HYDROLOGICAL AND HYDRODYNAMIC MODELING UNDER CLIMATE CHANGE SCENARIOS IN SNOW-GLACIER INDUCED HIMALAYAN CATCHMENT

Thesis submitted in partial fulfilment of the requirements

for the award of the degree of

DOCTOR OF PHILOSOPHY

in

Civil Engineering

by

VISHAL SINGH

(Roll No. 136104018)

Under guidance of

Dr. MANISH KUMAR GOYAL



DEPARTMENT OF CIVIL ENGINEERING

INDIAN INSTITUTE OF TECHNOLOGY GUWAHATI

GUWAHATI-781039, ASSAM, INDIA

MAY 2016

Department of Civil Engineering
Indian Institute of Technology Guwahati
Guwahati – 781039, Assam, India

Dr. Manish Kumar Goyal
Assistant Professor
0361-2583328
mkgoyal@iitg.ernet.in

Certificate

This is to certify that the thesis entitled "**Hydrological and Hydrodynamic Modeling under Climate Change Scenarios in Snow-Glacier Induced Himalayan Catchment**" being submitted by **Vishal Singh** to the Department of Civil Engineering, Indian Institute of Technology Guwahati, is a record of bona fide research work under my supervision and is worthy of consideration for the award of the degree of Doctor of Philosophy of the institute.

Date:

Place: Guwahati

Dr. Manish Kumar Goyal

TH-1643_136104018

Declaration of Authorship

I, Vishal Singh, declare that this thesis titled, '**Hydrological and Hydrodynamic Modeling under Climate Change Scenarios in Snow-Glacier Induced Himalayan Catchment**' and the work presented in it are my own. I confirm that:

- This work was done wholly or mainly wile in candidature for a research degree at this institute.
- Where any part of this thesis has previously been submitted for a degree or any other qualification at this institute or any other institutions, this has been clearly stated.
- Where I have consulted the published work of others, this is always clearly attributed.
- Where I have quoted from the work of others, the source is always given. With the exception of such quotations, this thesis is entirely my own work.
- I have acknowledged all main sources of help.
- Where the thesis is based on work done by myself jointly with others, I have made clear exactly what was done by other and what I have contributed myself.

Signed:

Date:

TH-1643_136104018

Dedicated to

My Parents

&

My Brother

TH-1643_136104018

"I am Shakti, as well as Shiva. I am everything male and female, light and dark, flesh and spirit. Perfectly balanced in one single moment lasting an eternity"

Lord Shiva

Lord Shiva, you my sunshine, my soul, Sivoham.

TH-1643_136104018

ACKNOWLEDGMENT

I am hearty obliging to my supervisor, **Dr. Manish Kumar Goyal** for his precious advises on academics, career and life's guidance. He has been extremely helpful throughout the completion of my PhD research work. He always pushed me hard and even harder because of which the study of this amount could be completed in relatively lesser period of time. I find myself very fortunate for being his student. He always has contemporary and diverse ideas which nurtured my thoughts and reasoning. He has been always very cooperative and caring during my tough times. He is very kind and always available despite of his busy academic schedule whenever I need help.

I am deeply thankful to the Chairman of my Doctoral Committee **Prof. Arup Kumar Sarma**, **Dr. Bimlesh Kumar** and **Dr. Pankaj Tiwari** for their valuable suggestions and kind support during completion of the research work. I have received help from numerous people in the course of the study and I would like to cordially thank them all. Without their help this study would not have been possible.

Particularly, I am indebted to my **Mummy-Daddy, Brother-Sister in Law and Mausaji-Mausiji** for their blessings and unconditional support for bringing me to such a level. Without their faith in me, I would not be able to carry out this study. A sweet thanks to my Nephew **Amritansh Singh** and my **Niece Sanskriti Singh** for their love. Special thanks to my dear **Shivam, Vivek Gupta, Uttam Puri Goswami, Juna Devi, Ashutosh Sharma, Suman Kumar Padhee and Manas Khan** for all their supports since the commencement of this research work. **Shivam** and **Uttam** provided me a great support during the thesis writing work. With their presence I always felt that I was accompanied by my family. I'm indebted to my good friends **Peeyush Gupta, Brij Kishore, Amanpreet Singh, Debhasish Bhakta, Ajeet Singh Chhabra, Ashutosh Srivastava, Sandeep Kumar Singh and Srinivas Reddy** for his great help throughout the course of this study.

I am thankful to the scientific Staffs of the Dept. of Civil Engineering for their support. I appreciate the staff members of various laboratories of the Dept. of Civil Engineering for the help they provided whenever it is required. I gratefully acknowledge the advises and supports provided by **Dr. Xuefeng Chu**, **Dr. Sanjay Kumar Jain** and **Dr. Apurba Kumar Bera** which were really very helpful in developing my morals and proceeding the research work. I would like to thank the

TH-1643_136104018

workers of Brahmaputra hostel mess, Brahmaputra hostel canteens for providing food and very kind to me. My special thanks to the owner of the utility store and his boys for being very kind to me. I am very thankful to the Indian Institute of Technology Guwahati for providing magnificent facilities and beautiful atmosphere to carry out my research work. I gratefully acknowledge the financial support that was received from the Department of Science and Technology, Govt. of India to carry out the research work presented in this thesis. Finally, above all he is **Supreme Lord** who has been present with me irrespective of my ups and downs. I thank him for his endless blessings.

TH-1643_136104018

ABSTRACT

In this study, a Teesta river Catchment (up to Chungthang gauge), which is a part of North Sikkim eastern Himalaya India, has been selected for the completion of the research work. In this study, the latest Coupled Model Intercomparison Phase 5 (CMIP5) Global Circulation Models (GCMs) with multiple Representative Concentration Pathway (RCP) experiments have been used for the downscaling of daily minimum, maximum temperature and precipitation datasets. For this research work, three GCM models such as CM3 model, CM2P1 model and ESM-2M model have been used. For downscaling of GCM variables such as maximum and minimum temperature, and precipitation, the Statistical Downscaling Model (SDSM) has been used. As per the observed precipitation and temperature datasets (1979-2005), the 21st century scenarios of daily precipitation and temperature have been projected utilizing the above three GCM models with their extreme (RCP8.5 & RCP4.5) to low emission (RCP2.6) scenarios of multiple RCP experiments. For downscaling, reanalysis data sets (e.g. AMIP controlled scenario) has been taken into account.

After downscaling of daily minimum-maximum temperature and precipitation data sets, significant increase and decrease in precipitation and temperature were evaluated using various statistical, non-parametric and parametric evaluation methods such as Mann-Kendall test, quantile regression method (QR) etc. Based on these test, a significant change in temperature and precipitation variables has been calculated. To find out the extremity in temperature and precipitation projection scenarios, temperature extreme indices (TEI) and precipitation extreme indices (PEI) have been computed. The TEI and PEI highlight the severity of climate change on the temperature and precipitation scenarios in the future time domain (2006-2100). Many TEI indices show that the temperature is increasing over eastern Himalayan catchment. The TEI also exhibited that the minimum temperature will be more acute in the 21st century decades. The PEI shows that the variability in precipitation pattern will be frequent and enhanced in future time decades.

Teesta river catchment shows large variation in topography and the elevation ranges, which vary from around 1400 meters to 7000 meters. By considering these elevation differences, the temperature lapse rate (TLR) and precipitation lapse rate (PLR) were measured and projected. The TLR showed a consistent decrease from the year 2006 to 2100, illustrating high warming over the eastern Himalayan catchment. The minimum TLR shows significant variations from the

TH-1643_136104018

year 2006 to 2100, which highlighted that the minimum temperature is increasing over the high hilly terrains of Teesta Himalayan catchment. The TLRs also exhibited significant variability from the year 2006 to 2100, as observed by the CMIP5 GCMs.

The remote sensing applications have used for the assessment of snow cover and glacier dynamics of Teesta river catchment. For the snow cover and glacier dynamics, MODIS, Landsat 7/8, LISS 3 and CARTOSAT digital elevation model (DEM) datasets have been used. For the snow cover dynamics, MODIS and LISS 3 temporal satellite imageries have been processed. Based on the computed snow covered area (SCA) using normalized difference snow index (NDSI) method, the monthly statistical analysis highlighted an enormous variations in the SCA during the year 2000 to 2014. The SCA has shown a slight decrease their area from the year 2000 to 2014. To characterize the debris cover of Zemu glacier, a novel approach based on the integration of optical and thermal bands from Landsat and LISS 3 satellite data sets has been developed. For the classification of debris cover of Zemu glacier, Maximum Likelihood Classification (MLC) and three dimensional hybrid classification (3DHC) method have applied. The accuracy assessment has done for the classified maps. Based on the classified maps, the Zemu glacier boundary has been derived. The Zemu glacier boundary derived from LISS 3 classified maps (2014) compared with surveyed toposheet of Zemu glacier region (1935), illustrated a significant variations and reduction in snout portion of the Zemu glacier.

Hydrological and hydrodynamic modeling of Teesta and Lachung river (a tributary of Teesta river) have been carried out to assess the various watershed components. For the hydrological and hydrodynamic modeling, Soil and Water Assessment Tool (SWAT) and Mike 11 by DHI (Dennis Hydraulic Institute) have been utilized. The main water balance components such as snowfall, snowmelt, precipitation, evapotranspiration, water yield and point source streamflow have been simulated and projected. The integrated modeling framework has been developed to rout the streamflow of Teesta and Lachung river up to Chungthang gauge. Based on the historical and projected hydro-meteorological variables, water level and discharge at various cross sections have been computed. Several cross sections are measured on the field using Total Station instrument and others are calculated using high resolution CARTOSAT DEM. Based on the integrated framework (e.g. SWAT and Mike 11), the rating curve equations have been developed at Lachung and Chungthang gauge stations. For the streamflow calibration/validation, and parameterization sensitivity and uncertainty analysis, SWAT Calibration and Uncertainty Program (SWAT CUP) based Sequential Uncertainty Parameter Fitting Approach (SUFI2), Generalized Likelihood Uncertainty Equation (GLUE) and Parametric Solution (ParaSol) optimization methods have

TH-1643_136104018

been applied. For the quantification and separation of snowmelt/icemelt from the glaciated region and snowmelt from non-glaciated region, a conceptual Glacier Hydrological Model (GSM-SOCONT) has been applied. However, several modifications have been done in the GSM-SOCONT model and three radiation parameters have been added, which were necessary for the Himalayan catchment.

A coupled hydrological and hydrodynamic modeling approach, utilizing SWAT and Mike 11, has been presented for the downstream river flow analysis of Lachung and Teesta river. Various river cross sections have been measured on the field. Based on the coupled approach, rating curve equations, utilizing projected water level and discharge datasets, have been developed. The water velocity, flood area, water level and discharge at various downstream river points have been computed. The daily minimum and maximum temperature show significant increase in the projected scenarios over the selected study region. The minimum temperature has found most increase than maximum temperature. The precipitation scenarios show significant variability in their intensity and frequency over the catchment. The projected streamflow show significant increase during 21st century. The snowmelt runoff is increasing and getting faster. The earlier melting is also detected due to warming. The snow cover and glacial changes are highly fluctuated.

TH-1643_136104018

Contents

Declaration of Authorship iii

Acknowledgements v

Abstract vii

List of Figures xxiii

List of Tables xxx

Symbols xxxiv

Abbreviations xxxviii

1 Introduction 1

1.1 Purpose of study 1

1.2 Problem statement 4

1.3 Research objectives 4

1.4 Thesis chapters 5

2 Literature Review 9

2.1 General.....9

2.2 Climate change 10

2.3 IPCC Assessment Report 5 (2013) and CMIP5 emission scenario 11

2.4 Climate change impacts on water resources 13

2.4.1 Effect of climate change on water resources around the world 16

TH-1643_136104018

2.4.2 Effect of climate change on water resources over Himalayan continents…….....18

2.5 Climate downscaling and future forecasting....…….……...21

2.5.1 Projection of temperature extremes …….....22

2.5.2 Projection of precipitation extremes …….. …….24

2.6 Remote sensing application in snow-cover and glacier studies …….....26

2.7 Hydrological and Hydrodynamic Modeling …….....29

2.7.1 Deterministic and Stochastic Hydrological Modeling……31

2.7.2 Hydrodynamic Models and River Flow Routing…….…..40

2.8 Conclusion of Literature Review ……..……41

3 Study Area and Data Used …… …….……43

3.1 Teesta River and its Major Tributaries ……43

3.2 Hydrological Characteristics of Teesta Catchment ……44

3.3 Snow Cover and Glacier Morphology of Teesta Catchment……46

3.4 Meteorological Characteristics of Teesta Catchment……...47

3.5 Geographical and Topographical Characterization of Teesta Catchment ……...48

3.6 Stream Channel Characteristics ……..50

3.7 Data Used ……50

TH-1643_136104018

3.7.1 Observed hydro-meteorological datasets ……50

3.7.2 CMIP5 GCMs and RCPs ……52

3.7.3 Remote sensing satellite datasets ……53

4 CMIP5 GCMs Downscaling …… …55

4.1 Downscaling of Precipitation and Temperature …… ……..55

4.1.1 Spatial interpolation of observed data sets …… …...55

4.1.2 Statistical-stochastic downscaling model (SDSM) ….....57

4.1.3 Selection of predictor variables ……57

4.1.4 Scenario generation ……..59

4.1.5 Bias correction ……64

4.1.6 Screening of predictor variables ……...…...64

4.1.7 Calibration and validation of SDSM ……...…65

4.2 Temperature and Precipitation Lapse Rates ……..……71

4.2.1 Average annual TLRs……...…71

4.2.2 Mann-Kendall trends of TLRs (Max and Min) as per CMIP5 ESM2M, CM3 and SM2P1 GCMs…….....74

4.2.3 PLR Scenarios ……..……..78

4.2.4 Trends evaluation in 21st century predicted Temperature scenarios ……....85

4.2.5 Temperature extremity evaluation using extreme indices ……..……90

TH-1643_136104018

4.2.6 Precipitation trends and change evaluation

in the 21^{s} century scenarios ……..……104

4.2.7 Precipitation extreme indices and changes ……..……111

4.2.8 Spatio-temporal variations in the PEIs ……..…..123

5 Remote Sensing Applications in Snow Cover and Glacial Change Analysis ……..131

5.1 Brief Overview about this Chapter ……131

5.2 Snow Cover and Glacier Extent Extraction Method ……132

5.2.1 MODIS (MOD09A1 and MOD10A2) data processing .132

5.2.2 LISS and Landsat sensors data processing ……134

5.2.3 Satellite data pre-processing and ortho-rectification …..135

5.2.4 Cloud removal and snow cover extraction from MODIS (MOD09A1 Terra 8 daily), LISS 3 and Landsat data Products……136

5.2.5 Characterization of debris cover of glaciers ……...142

5.3 Snow Cover Change Analysis ……...149

5.3.1 MODIS snow cover area (SCA), snow depletion curves (SDC) and change assessment ……149

5.3.2 SCA analysis and change assessment using LISS-3 satellite datasets ……161

5.3.3 Glacial lakes and water bodies extraction and change detection ……..167

5.4 Characterization of Debris Covers of Zemu Glacier ……172

TH-1643_136104018

5.4.1 MLC and 3HD classification approach for preparing glacier maps …….. .172

5.4.2 Characterization of SGD, PGD and other

glacier classes ……..178

5.4.3 Delineation, comparison and change assessment of Zemu glacier ……..185

6 Integrated Hydrological-Hydrodynamic Modeling and Projected Scenario………..189

6.1 Brief Framework ……...189

6.2 Methodology of SWAT, Glacier Hydrological Model and MIKE-11 ……..190

6.2.1 SWAT Model description and model setup.....190

6.2.2 Rationale behind the sub-watershed and model simulation setup ……195

6.2.3 SWATs Elevation band approach for snowfall and snowmelt calculation ……...196

6.2.4 SWAT calibration, validation, parameterization sensitivity and uncertainty analysis methods …….…….....198

6.2.5 Objective functions ……202

6.3 Snow Water Equivalent Reconstruction Approach …….....203

6.4 Improvements in Glacier Hydrological Model for Snowmelt Runoff Estimation ……205

6.5 Hydrodynamic Model MIKE 11 and Coupling with SWAT ……208

6.6 SWAT and SWAT CUP based Analysis Results ……..210

TH-1643_136104018

6.6.1 CN adjustment and improvement in SWAT simulated outcomes ……..…….210

6.6.2 SWAT model calibration/validation, parameterization sensitivity and uncertainty analysis ……..212

6.6.3 Simulations, projections scenarios and changes in main watershed components under CMIP5 GCMs ……..220

6.7 improved GSM-SOCONT Model: Coupling and Comparison with SWAT ……..……..236

6.8 Elevation Band Approach for Projecting Snowfall-Snowmelt and their Change Assessment under CMIP5 GCMs ……..……..244

6.9 Evaluation of Swat Modeled Snowmelt using Satellite Snow Cover Based SWE Reconstruction Approach ……..…….254

6.10 Coupled Approach: MIKE 11 and SWAT ……..…..259

6.10.1 MIKE 11 model setup and cross section profile ……..261

6.10.2 Mike 11 Historical Simulations ……..…...265

6.10.3 Mike 11 21st Century Projections under CMIP5 CM3 GCM ……268

6.10.4 Development of Rating-Curve Equations ……....272

7 Conclusions and Recommendations for Future Work……281

7.1 Downscale Scenarios and their Conclusion……...282

7.2 Remote Sensing Applicability in the Snow-Cover and Glacial Change Analysis……283

7.3 Hydrological and Hydrodynamic Modeling Applications

TH-1643_136104018

in the Assessment Watershed Components……284

7.4 Recommendations for Future Scope……..285

Appendix ……..287

References……297

TH-1643_136104018

LIST OF FIGURES

Fig. 2.1: IPCC assessment reports their scenarios……..... 11

Fig. 2.2: CMIP5 GCMs and their RCP details (Adopted: http://www.gfdl.noaa.gov/coupled-physical-model-CM3) …… 14

Fig. 3.1: Study area map showing Teesta catchment profile and meteorological observation details. …… 45

Fig. 3.2: Maximum and Minimum snow cover over the study area. 47

Fig. 3.3: Average monthly precipitation and temperature over the selected study area…….. 48

Fig. 3.4: Digital elevation model showing elevation variations over selected study area……... 49

Fig. 3.5: Soil map of the study area (FAO, 2005)……..... 49

Fig 4.1: Flow diagram of CMIP5 GCMs downscaling steps……..... 58

Fig. 4.2: Calibration/Validation results showing comparison between observed (Obs.) and bias corrected (BC) simulated (Sim.) datasets (1979-2005): (a) Precipitation (Pcp), (b) Maximum (max) Temperature (Temp) and (c) Minimum (Min) Temperature……..... 68

Fig. 4.3: Frequency Curves (FC) showing the comparison of Modeled Normal Frequency (NF) distribution of Observed data sets with Actual Frequency (AF) distribution of Observed data, AF of bias corrected (BC) simulated data and AF of without bias corrected (WBC) simulated data (1979-2005): (a) FC for Precipitation, (b) FC for Maximum Temperature and (c) FC plots for Minimum Temperature……..... 70

Fig. 4.4: Average annual TLRs (Max and Min) during the historical time periods (1979-2005). …….. 72

Fig. 4.5: Average annual TLRs scenarios in the 21st century domain as per CMIP5-ESM2M and their RCP experiment. ....…..... 73

Fig. 4.6: Monthly comparison of sensitivity of Minimum and Maximum temperature using Mann-Kendall test…..... 75

Fig. 4.7: Monthly inter-comparison of sensitivity results of Minimum and Maximum temperature using Mann-Kendall test. ……..... 77

Fig. 4.8: (a) Three months moving average of PLR (mm/km) for the observed time series (1979-2005) and (b) An average annual PLR (mm/km) for the future time series (2006-2100) data sets. …… 78

TH-1643_136104018

Fig. 4.9: Mann-Kendall test statistics (Z) results for the monthly averaged PLR as per the CMIP5 ESM-2M GCM and RCPs experiments (2.6, 4.5 and 8.5); (a) Observed time series plots (1979-2005), (b) Z statistics for the time series (2006-2100) (c) Z statistics for the time series (2011-2041) (d) Z statistics for the time series (2041-2070) and (e) Z statistics for the time series (2071-2100). 81

Fig. 4.10: Sen's slopes results for the monthly average PLR in an intra-decadal time series durations. 86

Fig. 4.11: Multimodel CMIP5 GCMs scenarios of average annual temperature warming at the whole catchment scale during 21st century with their emission scenarios (RCPs: 2.6, 4.5 and 8.5); (a) maximum temperature scenarios and (b) minimum temperature scenarios..... 87

Fig. 4.12: Mann-Kendall results for multimodel scenarios of annual averaged temperature growth rate across the study area during 2006 to 2100. 88

Fig. 4.13: Mann-Kendall trend results showing monthly variations in minimum temperature and maximum temperature during 2006-2100 under CMIP5-ESM2M GCM with RCP experiments (2.6, 4.5 and 8.5) across all the climate stations; (a) minimum temperature trends and (b) maximum temperature trends. 91

Fig. 4.14: Box plots showing projected scenarios of temperature extreme indices in a multi-temporal time series domain (TS1: 1981-2005, TS2: 2006-2030, TS3: 2041-2065 and TS4: 2076-2100) as per minimum and maximum temperature across all the climate stations..... 99

Fig. 4.15: Results show cluster based warming signatures of 12 most significant TEIs in intra-decadal time series durations as per multimodel 21st century (2006-2100) projected climate ensembles. 105

Fig. 4.16: Mann-Kendall trend results showing monthly variations in the precipitation during 2006-2100 under all RCP experiments (2.6, 4.5 and 8.5) across all the climate stations..... 112

Fig. 4.17: Quantile regression based plots for precipitation extreme indices in an intra-decadal time series durations: (a) observed quantile plots (1979-2005), (b) Plots for the intensity based extreme precipitation indices under RCPs 2.6, 4.5 and 8.5 experiments, (c) Plots for the frequency based extreme precipitation indices under RCPs 2.6, 4.5 and 8.5 experiments..... 123

Fig. 4.18: An intra-decadal spatial variation in the precipitation intensity 128

TH-1643_136104018

and frequency calculated from PEIs: (a) RCP2.6, (b) RCP4.5 and (c) RCP8.5……..…..

Fig. 5.1: DN to radiance and radiance to temperature brightness conversion flow chart in model maker tool, ERDAS Imagine. …… 138

Fig 5.2: Distinction between cloudy and non-cloudy patches in TIR band of Landsat sensor. …… 139

Fig. 5.3: Cloud removal steps for Landsat TIR bands. ……. 140

Fig. 5.4: Flow chart of snow cover extraction approach using NDSI and NDWI……..... 142

Fig. 5.5: Methodology chart of the classification of debris covers of Zemu glacier……..... 143

Fig. 5.6: Slope and elevation information over the Zemu glacier……... 147

Fig. 5.7: Temporal snow cover variation during minimum and maximum snow cover duration over the study area as per MOD09A. …… 151

Fig. 5.8: Minimum, maximum, temporal and average SCA (km^2) statistics at catchment scale using MODIS datasets during 2000 to 2014. …….. 156

Fig. 5.9: Monthly Snow Depletion Curves (SDC) during 2000 to 2014 as per MODIS (MOD09A1) multispectral satellite datasets. …….. 187

Fig. 5.10: Elevation band wise distribution of maximum and minimum SCA at each sub-catchment utilizing MODIS (TERRA and Aqua) 8 daily snow cover products during 2000 to 2014. …… 159

Fig. 5.11: NDSI showing maximum and minimum SCA from IRS LISS 3 multispectral satellite imageries during 2009-2014. …….. 162

Fig. 5.12: Flow chart of the extraction methodology of glacier lakes and waterbodies……. 167

Fig. 5.13: Highlighting changes in Glacial Lakes and Waterbodies during 1990 to 2014…… 171

Fig. 5.14: Spectral reflectance curves of optical bands from LISS 3 sensor and thermal bands from Landsat 7 and Landsat 8 sensors: (a) spatial location of the spectral profile (as per LISS 3 2009), (b) spatial spectral reflectance curves of LISS 3 and Landsat sensors during 2009 to 2014 and (c) reflectance curve for the transformed bands. …… 173

Fig. 5.15: Maps show the quality check based identification of the various glacial classes comparing GeoEye-1 GES image and satellite images from Landsat and LISS 3 sensors……. 175

Fig. 5.16: Maps (2009-2014) showing classified maps as per the integrated

TH-1643_136104018

combinations of optical, thermal infrared, transformed bands and new band ratio images from Landsat and LISS 3 sensors applying MLC and three dimensional hybrid classification approaches: (a) 2009, (b) 2010, (c) 2011, (d) 2012, (e) 2013 and (f) 2014. 176

Fig. 5.17: (a) Maps showing the area statistics of glacial classes calculated as per the different classified maps during 2009 to 2014, (b) glacial classes based hypsometric curve showing the glacial classes distribution as per the elevation variation and (c) maps showing the comparative statistics of the area of glacial classes (e.g. clean ice snow, ice snow mix debris and SGD) versus elevation..... 181

Fig. 5.18: SGD and PGD boundary and area characterization using semi-automated approach as per the hybrid classified map of the year 2014. 185

Fig. 5.19: Maps showing the semi-automated delineated boundary of the Zemu glaciers and its comparison with the surveyed toposheet and ICIMOD WGI database based glacier boundaries. 186

Fig. 6.1: Methodology chart of SUFI2, GLUE and ParaSol methods..... 200

Fig. 6.2: Flow chart of improved GSMSOCONT Glacier Hydrological Model coupled with SWAT. 205

Fig. 6.3: Implicit scheme computation grid..... 209

Fig. 6.4: Coupled approach between Mike 11 and SWAT parameters and modules for the projection of hydrodynamic variables. 210

Fig. 6.5: Comparisons of SWAT simulated adjusted CN based streamflow, without adjusted CN based streamflow and calibrated flow with reference to observed streamflow: (a) time series plots of Lachung and Chungthang and (b) regression plots of Lachung and Chungthang. 211

Fig. 6.6: Time series plot for the (a) calibration and (b) validation at main outlet of the catchment (Chungthang) 214

Fig. 6.7: SWAT simulated main water balance components (average annual) at each catchment (1991-2005) 221

Fig. 6.8: Projected precipitation (Pcp mm) scenarios during 2008-2100 at each catchment scale as per: (a) ESM-2M, (b) CM3 and (c) CM2P1 GCMs with their RCPs..... 222

Fig. 6.9: Projected evapotranspiration (ET) scenarios during 2008-2100 at each catchment scale as per: (a) ESM-2M, (b) CM3 and (c) CM2P1 GCMs with their RCPs..... 225

TH-1643_136104018

Fig. 6.10: Projected water yield scenarios during 2008-2100 at each catchment scale as per: (a) ESM-2M, (b) CM3 and (c) CM2P1 GCMs with their RCPs…… ……..…… 228

Fig. 6.11: Monthly projected trends of streamflow at Lachung outlet as per multimodel CMIP5 GCMs for the year 2008-2100……. 234

Fig. 6.12: Monthly projected trends of streamflow at Chungthang outlet as per multimodel CMIP5 GCMs for the year 2008-2100. …… 235

Fig. 6.13: Comparison of time series values simulated from GSMSOCONT implementing radiation components: (a) Obs vs Qsim_rad vs Qsim_wrad, (b) scatter plot between Qsim_rad vs Observed discharge and (c) Separation of GSM-SOCONT simulated discharge (Qgsmscon). ……. 238

Fig. 6.14: Times series plots and comparison between the SWAT projected streamflows and improved GSMSOCONT projected streamflows at the catchment outlet (Chungthang) (2008-2100). ……..... 240

Fig. 6.15: Total snowmelt contribution at Chungthang outlet simulated from improved GSMSOCONT model under CMIP5 GCMs and RCPs……. 241

Fig. 6.16: Projected scenarios of icemelt/glacier melt runoff and snowmelt runoff (non-glacier) from improved GSMSOCONT model for the year 2008-2100..... 242

Fig. 6.17: Annual snowfall and snowmelt at each sub-catchment for the historical time (1991-2005) simulated from SWAT. …….. 245

Fig. 6.18: SWAT simulated monthly variations in snowfall during January to April under CMIP5 ESM-2M GCMs and RCPs during 2008-2100. ……. 246

Fig. 6.19: SWAT simulated monthly variations in snowfall during October to December under CMIP5 ESM-2M GCMs and RCPs during 2008-2100... 247

Fig. 6.20: SWAT simulated monthly variations in snowfall during January to April under CMIP5 CM3 GCMs and RCPs during 2008-2100……..... 248

Fig. 6.21: SWAT simulated monthly variations in snowfall during October to December under CMIP5 CM3 GCMs and RCPs during 2008-2100. …… 249

Fig. 6.22: SWAT simulated monthly variations in snowmelt during March to November under CMIP5 ESM-2M GCMs and RCPs during 2008-2100. . 250

Fig. 6.23: SWAT simulated monthly variations in snowmelt during March to November under CMIP5 CM3 GCMs and RCPs during 2008-2100…….. 251

Fig. 6.24: SWAT simulated monthly variations in snowmelt during March to November under CMIP5 CM2P1 GCMs and RCPs during 2008-2100. … 252

Fig. 6.25: Teesta river cross section and stream network 262

TH-1643_136104018

details……..

Fig. 6.26: Longitudinal Cross profile of Teesta River catchment showing maximum discharge at each cross sections: (a) Teesta river cross sections and (b) Lachung river cross sections…….……. 263

Fig. 6.27: Water Level at different Chainages/cross sections over Teesta River…… 265

Fig. 6.28: Water Level at different Chainages/cross sections over Lachung Rive……. 265

Fig. 6.29: Cross section details at Chungthang and Lachung Chainages (gauge)……..... 266

Fig. 6.30: Rating curves (stage-discharge) at different downstream Chainages of Teesta River computed from Mike 11……... 267

Fig. 6.31: Rating curves (stage-discharge) at different downstream Chainages of Lachung River computed from Mike 11. ……. 268

Fig. 6.32: Comparison of Mike 11 simulated discharge and observed discharge at Chungthang and Lachung..... 269

Fig.6.33: Mike 11 simulated discharge at upstream Chainages at Teesta River…….. 269

Fig. 6.34: Mike 11 simulated discharge at downstream Chainages at Teesta River…… 269

Fig. 6.35: Mike 11 simulated discharge at upstream and downstream Chainages at Lachung river. ……..……..... 270

Fig. 6.36: Mike 11 simulated water velocities at downstream Chainages at Teesta and Lachung rivers. ……...…….. 271

Fig. 6.37: Mike 11 simulated Flood Area (sq. meter) at downstream Chainages at Teesta and Lachung rivers……. 272

Fig. 6.38: Future water level (August to October) at Lachung and Chungthang as per CMIP5 CM3 GCMs (2008-2100). …….. 273

Fig. 6.39: Future Discharge (May to July) at Lachung and Chungthang as per CMIP5 CM3 GCMs (2008-2100). ……... 274

Fig. 6.40: Future Discharge (May to July) at Lachung and Chungthang as per CMIP5 CM3 GCMs (2008-2100). ……... 275

Fig. 6.41: Future Water Velocity (August to October) at Lachung and Chungthang as per CMIP5 CM3 GCMs (2008-2100). …….. 276

Fig. 6.42: Future Water Velocity (May to July) at Lachung and 277

TH-1643_136104018

Chungthang as per CMIP5 CM3 GCMs (2008-2100).. ……..
Fig. 6.43: Future Water Velocity (August to October) at Lachung and Chungthang as per CMIP5 CM3 GCMs (2008-2100). …….. 278
Fig 7.1: Overall study based major components assessed in historic and future time domain……..……. 281
Fig A.1: Precipitation extreme indices PEI in observed period (1979-2006) 287
Fig. A.2: Water yield (2008-2100) ……. 288
Fig. A.3: ET for CM3 GCM…….……... 289
Fig. A.4: Water yield for ESM2M GCM…… 290
Fig. A.5: ET for ESM2M GCM……..... 291
Fig. A.6 Water yield for CM2P1 GCM……..…….. 292
Fig. A.7: ET for ESM2M GCM……..... 293
Fig. A.8: Measurement of snow density using snow density gauge: scientific 200..... 294
Fig. A.9: Measurement of river cross section using total station…… 295

TH-1643_136104018

LIST OF TABLES

Table 2.1: Development scenarios of hydrological and hydrodynamic models around the world. 32

Table 2.2: SWAT model applications in different fields of water resources..... 35

Table 3.1: Teesta river tributaries. 44

Table 3.2: Teesta glaciers and their details. 46

Table 3.3: Climate Zones and their elevation across the study area i.e. eastern north Sikkim Himalayas..... 51

Table 3.4: Band details of Landsat and LISS 3 sensors. 53

Table 3.5: LISS 3 and Landsat Sensors image row/path and date acquisition details..... 54

Table 4.1: Predictor details with statistics. 60

Table 4.2: Result of downscaled precipitation and temperature during observed/historical time periods (1979-2005). 66

Table 4.3: Results of monthly trend analysis of maximum and minimum temperatures across all the climate stations under CMIP5 ESM-2M GCM with multiple RCPs (2.6, 4.5 and 8.5)..... 93

Table 4.4: Temperature extreme indices details and their descriptions..... 96

Table 4.5: Average statistics of TEI as per the multimodel temperature scenarios (2006-2100) over the study area. 101

Table 4.6: Cluster based F-ratio test results for TELs showing estimated difference between the clusters in intra-decadal time series domain. 108

Table 4.7: Mann-Kendall results for historical/Observed precipitation (1979-2005)..... 110

TH-1643_136104018

Table 4.8: Mann-Kendall test based results of precipitation increase and decrease as per CMIP5 ESM-2M GCM. 113

Table 4.9: Description of the PEI. 115

Table 4.10: Mean and standard deviation statistics of the PEI in the historical (1979-2005) and future time series (2006-2100) calculated from CMIP5 ESM-2M GCM based downscaled daily precipitation datasets across the whole catchment..... 118

Table 4.11: Average statistics of Precipitation Indices as per ESM-2M RCP scenarios (2006-2100). 121

Table 4.12: Estimated coefficient values based on the quantile regression analysis along with t stat and P value tests for the precipitation indices as per upper and lower quantiles under different RCP experiments. 126

Table 5.1: MOD09A1 sensor characteristics and their reflectance (λ) conversion factor..... 133

Table 5.2: MOD10A2snow cover details. 133

Table 5.3: Combination (CMB) of the band images details of Landsat and LISS 3 sensors..... 146

Table 5.4: SCA (km^2) statistics of MODIS (MOD09A1) during 2000 to 2014 for the whole study area. 155

Table 5.5: Percent (%) of change in SCA (km^2) as per MOD09A1 satellite datasets during 2000-2014 at catchment scale. 160

Table 5.6: Maximum and minimum SCA (km^2) statistics at each-sub catchment scale estimated from LISS 3 satellite imageries during the year 2009-2014..... 165

Table 5.7: Change in SCA (km^2) as per IRS LISS3 satellite data during 2000-2014 at catchment scale. 166

Table 5.8: Details of glacial lakes and waterbodies identified in different temporal time durations over the selected study region..... 168

Table 5.9: Overall accuracy of the classified maps. 178

TH-1643_136104018

Table 5.10: The area (hectare) statistics of different band combinations based classified maps during 2009 to 2014. ……..…… 179

Table 6.1: Adjusted CN as per the slopes at each HRU……..…… 191

Table 6.2: Calibration (1991-2000)/validation (2001-2005) results as per SUFI2, GLUE and ParaSol on a daily and monthly basis. ……. 215

Table 6.3: Description of model calibration parameters……..……. 216

Table 6.4: Model parameterization and sensitivity analysis results on a daily basis process using SUFI2 approach……..... 218

Table 6.5: Model parameterization and sensitivity analysis results on a daily basis process using GLUE approach……..... 218

Table 6.6: Model parameterization and sensitivity analysis results on a daily basis process using ParaSol approach……..... 219

Table 6.7: Change in Streamflows amount at Lachung and Chungthang between two intra-decades (2008-2050) and (2058-2100) as per CMIP5 GCMs and RCP experiments……. 232

Table 6.8: Glacier Hydrological Model calibration parameter details and their coefficient values. ……..... 236

Table 6.9: Percent (%) of change statistics of average annual snowmelt and snowfall in intra-decadal time series (TS) domains (TS1-2011-2035, TS2-2041-2065, and 2076-2100) observed as per multi model GCMs and RCPs.. 253

Table 6.10: Field based measurement of snow density and snow depth samples over Teesta catchment. ……..... 255

Table 6.11: Sub-catchment (SB) wise snow cover fraction for the year 2005 extracted from MODIS (MOD09A1) cloud free snow cover datasets……..... 256

Table 6.12: Sub-catchment (SB) wise 8 daily average of net solar radiation for the year 2005…… 257

Table 6.13: Sub-catchment (SB) wise Mp_j for the year 2005……..... 258

TH-1643_136104018

Table 6.14: Sub-catchment (SB) wise M_j (SWE) for the year 2005……..... 258

Table 6.15: Details of Mike 11 HD model parameters used as inputs to the model……..... 260

Table 6.16: Development of rating curve equation utilizing projected future water level and discharge (2008-2100). ……..... 279

TH-1643_136104018

Symbols

Z_j	The unknown point
Z_i	A value of known point
d_{ij}	Distance to known point
n	The user selected exponent
P_B	The adjusted precipitation
Z_B	Centroid elevation of the respective catchment.
P	The sub-catchment precipitation
Z	Recording gauge elevation
$d_{daypcpyr}$	Represents the mean annual number of days with precipitation.
P_{laps}	Precipitation local lapse rate
T_B	The interpolated adjusted temperature
T	The sub-catchment temperature
Z	Recording gauge elevation (grid point)
$-\alpha$	Temperature local lapse rate (T_{laps})
T_{deb}	The de-biased (corrected) daily time series of temperature
P_{deb}	Precipitation respectively for future periods
T_{SCEN}	The daily time series of temperature
$\overline{T_{CONT}}$	The long term monthly values for temperature
P_{SCEN}	Precipitation generated by SDSM for future periods
P_{CONT}	Precipitation for the control period simulated by SDSM
T_{obs}	The long-term monthly observed values for temperature
P_{obs}	The long-term monthly observed values for and precipitation
$\overline{P}$	The long-term average of precipitation
$\overline{T}$	The long-term average of temperature
S	Statistics
t_k	The number of data points in the k^{th} tied group
n	The number of tied (zero difference between compared values) groups
T_i	Sen's estimator of slope
x_j	Data values at time j
x_k	Data values at time k
S_j	Data points
x_n	A vector representing the nth data point
μ_j	Geometric centroid of the data points in Sj
x_i	A random variable chosen uniformly in the range 0 to 1
y_i	A random variable chosen uniformly in the range 0 to 1.
β_0	The intercept coefficient of the linear regression line
β_1	The slope coefficient of the linear regression line
$Q_y(\tau\|x)$	The expected y for the τ^{th} quantile of x
$\beta_0(\tau)$	The intercept coefficient of the τ^{th} quantile regression line
$\beta_1(\tau)$	The slope coefficient of the τ^{th} quantile regression line
ρ_λ	Unit-less planetary reflectance
L_λ	Spectral radiance
D	Earth-Sun distance in astronomical units
$ESUN_\lambda$	Mean solar exo-atmospheric irradiances

TH-1643_136104018

θ_s	Solar zenith angle
T	At-satellite brightness (K)
K_1	Band specific thermal conversion constant from the metadata file of Landsat sensor
K_2	Band specific thermal conversion constant from the metadata file of Landsat sensor
SW_t	The final soil water content (mmH_2O)
SW_o	The initial soil water content (mmH_2O)
T	Time in days
R_{day}	Amount of precipitation on day i (mmH_2O)
Q_{surf}	The amount of surface runoff on day i (mmH_2O)
E_a	The amount of evapotranspiration on day i (mmH_2O)
W_{seep}	The amount of percolation and bypass exiting the soil profile bottom on day i (mmH_2O)
Q_{gw}	The amount of return flow on day i (mmH_2O)
Q_s	Total surface runoff (mm)
R	daily rainfall (mm)
I_a	The initial abstraction such as infiltration and interception prior to runoff (mm)
S	A retention parameter based on the combination of soil, LULC
$CN2_\alpha$	The moisture condition II CN adjusted for slope α is the fractional slope for each HRU
P_B	The adjusted precipitation for each elevation band
T_B	Temperature for each elevation band
Z_B	Mean elevation for each elevation band
P (mmH_2O)	The sub-watershed precipitation
T^o C	Temperature degree Celsius
Z	Recording gauge elevation (m)
$days_{pcp,\,yr}$	The mean annual number of days with precipitation
T_B	Updated elevation band mean temperature
SWE_{day}	The mass of liquid water in the snowpack
S_F	Snowfall
S_M	Snowmelt
E_S	Sublimation
$T_{snowpack\ (day)}$	The snowpack temperature (^oC) on a given day
$T_{snowpack\ (day-1)}$	The snowpack temperature (^oC) on the day preceding it
T_{av} (^oC)	The mean air temperature for the same given day
SNO	The water content of the snow pack on a given day (mmH_2O)
SNO_{cov}	The fraction of area covered by snow
SNO_{100}	the threshold depth of snow at 100% coverage (mmH_2O)
cov_1, cov_2	Coefficients that define the shape of the curve
T_{max}	The maximum air temperature on a given day
b_{mlt}	The melt factor for that day (mmH_2O/day^{-^oC})
$SMFMN$	The melt factor for 21stJune
$SMFMX$	The melt factor for 21st December
D_n	The day of the year
S_{2gi}	the variance of the objective function values resulting from the number of model runs
θ_j	The parameter θ_j for the best estimates (i.e. parameters which produce the optimal objective function)

TH-1643_136104018

V	The degrees of freedom (mn)
$y_{t\ M\ 1,97.5\%}$	The upper boundary of the 95PPU
$y_{j\ M\ ,2.5\%}$	The lower boundary of the 95PPU
σ_{obs}	The standard deviation of the measured data
$[\theta min, \theta\ max]$	The posterior parameter distribution
$L(\theta)$	Generalized likelihood measure
w_l	likelihood weight
N	The number of behavioral parameters sets
R^2	Coefficient of determination
Q	Variable (e.g. discharge)
m	Measured data
S	Simulated data
I	The i^{th} measured or simulated data.
SWE_n	Pixel-specific SWE at time n
SWE_0	The initial SWE
M_j	Snowmelt for time step j
Mp_j	The potential snowmelt
T_d	Degree-days (the average 8 daily air temperature above 0°C)
a_r	Degree-day coefficient for melt factor ($cm°C^{-1}day^{-1}$)
R_n	Average 8 daily net radiation above 0 Wm^{-2}
M_q	Energy to water depth conversation
SCA_j	SCA at time step j
SCA_i and SCA_k	Observed SCA values prior to and after j
$\sum n_{\ i=1}\ Mp_i$	The cumulative potential snowmelt values corresponding to the satellite acquisition time steps i
$\sum n_{\ k=1}\ Mp_k$	The cumulative potential snowmelt values corresponding to the satellite acquisition time steps k
Q	The mean specific runoff at the catchment outlet
I	An index for each of the two parts of the catchment
J	An index for each of the ni elevation bands in part i
$ai_{,j}$	The area of an elevation band j belongs to the catchment part I (km^2)
$Q_{i,j}$	The mean daily specific runoff the special unit (mm/d)
a_c	The area of entire catchment (km^2)
P_{snow}	The snowfall
P_{tot}	The total precipitation on a given day (mm/d)
P_{iq}	Rainfall
T (°C)	The mean daily air temperature
T_0	The temperature threshold
M_F	A melt factor for the radiation
$a_{snow\ /aice}$	Radiation coefficient for snow and ice surface
I	Potential clear-sky direct solar radiation at the ice or snow surface (Wm^{-2})
$Q_{snow(ti)}$	Discharge from the snow contribution at time step t_i (mm/d)
$Q_{snow(ti+1)}$	The discharge at the successive time step
k_{snow}	The time constant of the reservoir
$P_{liq,snow}$	The rainfall (liquid precipitation) falling on the snowpack (mm/d)
$P_{\ eq}$	Equivalent rainfall (mm/d)
P_{liq}	Liquid precipitation
M_{snow}	snowmelt

TH-1643_136104018

A	The cross section area (m^2)
Q	The lateral inflow (m^2/s)
H	The water level above a reference datum (m) (dependent)
X	Downstream direction (m) (independent)
t	Time (s) (independent)
n	The Manning resistance coefficient ($s/m^{1/3}$)
R	The hydraulic or resistance radius (m)
g	The acceleration due to gravity (m^2/s)
a	The momentum distribution coefficient (e)
C and n	Constants
H	Water level or height
Z_0	Height at which discharge is zero

TH-1643_136104018

Abbreviations

10^{th} P	10^{th} percentile
1D	One dimensional
2D	Two dimensional
3DHC	3 dimensional hybrid classification
95PPU	95% prediction uncertainty
AF	Actual frequency
ALPHA_BF	Alpha base flow
AMC	Antecedent moisture condition
AMIP	Atmospheric model inter-comparison project
AnnAGNPS	Artificial neural network agricultural non-point source
Aqua	Aquatic
ARM	Agricultural runoff model
Avg	Average
AWiFS	Advance wide field sensors
BC	Bias corrected
BIT	Binary index tree
Cal	Calibration
CASC2D	Cascade two dimensional
CH	Chainage
CM	Catchment model
CM3	Coupled physical model
CMB	Combination
CMG	Climate-modeling grid
CMIP5	Coupled model intercomparison phase 5
CN	Curve number
CREAMS	Chemicals, runoff, and erosion from agricultural management systems
CSM	Climate system model
C-type	Clean-ice type
CUP	Calibration and uncertainty program
CWC	Central water commission
DEM	Digital elevation model
DN	Digital number
Elev.	Elevation
ENSO	El nino–southern oscillation
ESMs	Earth system models
ET	Evapotranspiration
ETCCDI	Expert team on climate change detection and indices
FAO	Food and agricultural organization
FCs	Frequency curves
Fig	Figure
FRST	Forest
FSSP	First suitable super predictor
GCM	Global climate models /general circulation model
GCPs	Ground control point
GFDL	Geophysical fluid dynamics laboratory

TH-1643_136104018

GLEAMS	Groundwater loading effects of agricultural management system
GLERL	Great lakes environmental research laboratory
GLOF	Glacial lake outburst flood
GLUE	Generalized likelihood parameter uncertainty equation
GPS	Global positioning system
GSM-SOCONT	Glacier snowmelt – soil contribution
GW_DELAY	Groundwater delay
HD	Hydrodynamic
HDF-EOS	Hierarchical data format-earth observing system
HEC-HMS	Hydrologic engineering centre - hydrological modeling system
HRUs	Hydrological response units
HVC	High value cases
ICIMOD	International centre for integrated mountain development
IDWA	Inverse distance weightage approach
IITM	Indian institute of tropical meteorology
IMD	Indian meteorological department
IMG	Image
IPCC	Intergovernmental panel on climate change
IRS	Indian remote sensing satellite
ISRO	Indian space research organization
Km	Kilometer
Lat	Latitude
LCC	Lambert conformal conic
LHS	Latin hypercube sampling
LISS	Linear imaging spectral scanner
Long	Longitude
LRs	Lapse rates
LULC	Landuse / landcover
LVC	Low value cases
m	Meter
MALR	Mean moist adiabatic lapse rate
MATLAB	Matrix laboratory
Max	Maximum
Min	Minimum
MIR	Middle infrared
MK	Mann-Kendall
MLC	Maximum likelihood classification
MLP	Multilayer perceptron
MNDWI	Modified normalized difference water index
MOD	MODIS
MODIS	Moderate imaging spectro-radiometer
MVC	Moderate value cases
MW	Mega watt
NA	Not applicable
NASA	National aeronautics space administration
NDSI	Normalized difference snow index
NDV	No data values
NDVI	Normalized difference vegetation index
NDWI	Normalized difference water Index

TH-1643_136104018

NF	Normal frequency
NIR	Near infrared
NSE	Nash-Sutcliffe equation
NWH	Northwest Himalaya
Obs.	Observed
Parasol	Parametric solution
PAST	Pasture
PBIAS	Percent bias
Pcp	Precipitation
PEI	Precipitation extreme indices
PERCmm	Percolation millimeter
PET	Potential evapotranspiration
PGD	Periglacial debris
PGs	Precipitation gradients
PLR	Precipitation lapse rate
PRECIPmm	Precipitation millimeter
PRMS	Precipitation-runoff modeling system
PRP	Percent reduction partial correlation
RCP	Representative concentration pathway
RF	Radiative forcing
RMSE	Root mean square error
RS	Remote sensing
SB	Sub-catchment
SCA	Snow covered area
SCD	Snow-cover duration
SCE	Shuffle complex equation
SCM	Snow-cover melt
SCS	Soil conservation services
SD	Statistical downscaling
SDC	Snow depletion curves
SDSM	Statistical downscaling model
SF	Snowfall
SFTMP	Snowfall temperature
SGD	Supraglacial debris
SHP	Small hydropower projects
SHRB	Shrubs
SM	Snowmelt
SMFMX	Snowmelt factor maximum
SMFMN	Snowmelt factor minimum
SNO	Snow
SOL	Soil
SREX	Special report on managing the risks of extreme events and disasters to advance climate change adaptation
SRM	Snow melt runoff model
SRTM	Shuttle radar topographic mission
Stn	Station
SUFI2	Sequential uncertainty parameter fitting approach
SURQ	Surface runoff
SVAT	Soil-vegetation-atmosphere transfer
SWAT	Soil water assessment tool
SWE	Snow water equivalent

TH-1643_136104018

SWIR	Shortwave infrared
SWmm	Seepage water millimeter
SWRRB	Simulator for water resources in rural basins
TB1	Transformed band 1
TEI	Temperature extreme indices
TERRA	Terrestrial
TIFF	Tagged image file format
TIR	Thermal infrared
TLR	Temperature lapse rate
TM	Thematic mapper
TOA	Top of the atmosphere
TS	Time series
UBCM	University of British Columbia model
UNFCCC	United Nations Framework Convention on Climate Change
Val	Validation
VIC	Variable infiltration capacity
WBC	Without bias corrected
WETSPA	Water and energy transfer between soil, plants and atmospheric model
WGI	World glacier inventory
WYLD	Water yield

TH-1643_136104018

CHAPTER 1

INTRODUCTION

1.1 PURPOSE OF STUDY

The major river basins of India such as Ganga, Indus and Brahmaputra, originate from the Himalayan glaciers (Watershed Atlas of India, 2012; India-WRIS, 2012). In India, the glaciers are controlled to extra-peninsular region specifically Himalaya within the longitudes 72°E to 96°E and latitudes 27°N to 36°N. The Indian Himalayan region comprises about 9,575 glaciers and other permanent ice bodies covering an area of about 40,000 km^2, with an approximate ice volume of 2,000 km^3 (Raina and Srivastava, 2008). The glacier ranges over the entire Himalayas are among the largest and most spectacular in the world (Bajracharya and Shrestha, 2011). Himalayan glaciers are important for generating hydroelectricity, irrigation, drinking water supply and daily needs of over 0.5 billion people.

Climate change as per the UNFCCC (United Nations Framework Convention on Climate Change), is defined as "*a change of climate which is attributed directly or indirectly to human activity that alters the composition of the global atmosphere and which is in addition to natural climate variability observed over comparable time periods*" (Kagawa et al., 2015). Intergovernmental Panel on Climate Change (IPCC) 2013 concluded that the processes affecting climate can exhibit considerable natural variability over the Himalayan regions (Change, I.C., 2013). The impact of global changing climate is very often over the entire Himalayan regions and thus, periodic and chaotic variations on a vast range of spatial and temporal scales are also observed (Huang et al., 2015; Change, I.C., 2013). The Himalayan water resources will come under increasing pressure due to changing climate (Change, I.C., 2013; Kattelmann, 1987). Many glaciers and snowpacks are receding due to the warming trends of the lower atmosphere, which could be a significant cause of decreasing snow depth and snowpack duration over the snow-glacier induced Himalayan watersheds (Srivastava et al., 2014; Bolch et al., 2012; Rangwala and Miller, 2012). At present, more than 45% of the average annual precipitation, including rainfall and snowfall, in the Himalayan rivers, is wasted by natural runoff to the sea (Mall et al., 2006). There are many indicators of climate change such as surface and air temperature, atmospheric water vapour, precipitation, extreme events, glacier retreating, and melting of land ice have been noticed in the Himalayan regions (Bolch et al., 2012; Gardelle et al., 2012). Glacier

TH-1643_136104018

retreating is the most noteworthy phenomenon which has been noticed in last several decades by various researchers of the world (Goel, 2014; Kargel et al., 2011). Due to increasing trends of air temperature across the globe (Change, I.C., 2013), Himalayan glaciers are retreating with faster rate than it's normal (Kulkarni et al., 2010). In recent years, glacial retreat is a major concern has been noticed over the entire Himalayan regions (Palazzi et al., 2014; Kulkarni et al., 2007). A few studies focused on the Himalayas show Himalayan glaciers are under serious threat due to changing climate (Bolch et al., 2012; Bajracharya and Shrestha, 2011; Bhambri et al., 2011). On a regional scale, snow cover and valley glaciers are the important sources for the local water availability, streamflows and groundwater recharge over the entire Himalayan continents. The precipitation variability has also increased over the Himalayas (Palazzi et al., 2014). Several climate change issues have been noticed over the eastern and western Himalaya in India (Kulkarni et al., 2010; Krishna, 2005). Few recent studies showed a significant threat over the Himalayan watershed conditions (Palazzi et al., 2014; Rao et al., 2014; Kulkarni et al., 2010). Kedarnath disaster experienced in 2013 in the Uttarakhand state of India, which is a part of western Himalaya, itself explained about the lack of current research findings and its understanding (Rao et al., 2014).

Many important modes of climate variability and intra-seasonal to seasonal phenomena are reproduced by IPCC (2013), with some improvements evident since the IPCC Assessment Report 5 (AR5) (Change, I.C., 2013). IPCC has produced various global climate models (GCMs) based historical and futuristic scenarios for the various physical and meteorological predictors related to earth, ocean and atmospheric dynamics (Taylor et al., 2012). The only approach to comprehend the impact of global as well as regional climate issues in the 21st century on the Himalayan watershed conditions is to evaluate the changes by utilizing global climate models (GCMs) (Change, I.C., 2013). The climate downscaling approaches latest Coupled Model Intercomparison Phase 5 (CMIP5) GCMs with multiple Representative Concentration Pathways (RCP) experiments as per the (Palazzi et al., 2014; Taylor et al., 2012) may be utilized to evaluate the historical and future climate variations and their impacts on water resources.

In the present time, when significant evidences of global climate change are discussed by IPCC (Palazzi et al., 2014; Change, I.C. 2013), the severity of precipitation extreme events will increase in the 21st century. Cloud burst and flash floods are treated as the most damage causing disasters in the world (Rao et al., 2014), and these can be frequent in the 21st century, especially over the western and eastern Himalayas (Pramanik et al., 2010). However, a major challenge associated with flash floods is the quantitative character of the forecast. The proper forecasting and accurate prediction of extreme events require

TH-1643_136104018

advancement of the basic simulation methods (Rao et al., 2014). An integrated hydrological and hydrodynamic modeling approach along with latest CMIP5 GCMs would add advantage in hydrological assessment during the historical time and 21st century domains.

Integrated watershed management is the process of organizing and guiding land, water and other natural resource use on a watershed to provide desired goods and services to people without affecting adversely soil and water resources (Singh et al., 2014; Wardlaw and Sharif, 1999). In the present context, various hydrological modeling tools have been developed to assess the climate variability over the watershed parameters in an integrated manner in the presence of physical and meteorological parameters (Singh et al., 2014; Singh and Woolhiser, 2002). Hydrological simulation and prediction of watershed components using advance hydrological models in the highly variable topography brings several uncertainties in their outcomes apart from data input errors and model structure related uncertainties (Singh et al., 2013; Abbaspour, 2011; Abbaspour et al., 2007). This uncertainty is aggravated in snow-dominated catchments because of a larger interaction among snowmelt and hydrologic processes (Manandhar et al., 2013). A comprehensive parameter based sensitivity and uncertainty analysis under different climatic settings in the temporal scales are thus necessary (Zhang et al., 2014; Abbaspour et al., 2011).

To explore various global as well as regional climate change issues related to water resources over the Himalayan regions, a Teesta river catchment part of north Sikkim eastern Himalaya India, has been selected in the present research work. The study region of Teesta river catchment is almost covered by snow covers and glaciers. The Teesta river is a major tributary of Brahmaputra basin (Watershed Atlas of India, 2012). The meteorology of Teesta river part of north Sikkim eastern Himalayas is mostly influenced by Indian monsoon (Racoviteanu and Williams, 2012; Raina and Srivastava, 2008). The future hydrological cycle will vary significantly due to changes in meteorological variables (e.g. temperature and precipitation) (Change, I.C., 2013). Thus, evaluating near term and 21st century differences in the main water balance components of the hydrological cycle is urgent and necessary for the exploration and conservation of the water resources over the selected study region.

The accurate estimation of snow cover and glacier changes in the historical and 21st century time domain will help to understand the impact of changing climate on the watershed hydrology of this region. The availability of remote sensing (RS) based multispectral spatio-temporal high resolution satellite imageries could be utilized effectively to estimate the snow cover and glacial changes in the historical and current scenarios (Tiwari et al., 2014; Kulkarni et al., 2007). The accurate planning and management of the water resources

TH-1643_136104018

require good long-term hydrological and hydraulic investigation, which are too limited in the eastern Himalayas especially north Sikkim eastern Himalaya.

1.2 PROBLEM STATEMENT

The present research work shall explore four main disciplines namely climate change impact evaluation on temperature and precipitation extremes, remote sensing based analysis of snow cover and glacial changes, hydrological modeling and 21st century scenario generation of main water balance components and hydrodynamic modeling of Teesta river with special integration of hydrological components and projected scenarios. The climate extremity and characteristics of impact may vary from historical to 21st century time domain and from region to region, yet several regions are likely to experience climate extremity. Therefore, climate extremity using downscaled (global to point scale) meteorological variables such as temperature and precipitation datasets has been evaluated in the both historical and futuristic time domains under CMIP5 GCMs.

The snowmelt induced a Teesta river catchment, part of north Sikkim eastern Himalaya, requires similar attention towards current and future impacts of the climate change on the main watershed components. The aim of this research is primarily to downscale hydro-climatological variables, understanding temperature and precipitation extremity, impact of climate change on snow cover and glacier extent, hydrological simulation of main water balance components and hydrodynamic modeling of Teesta river. This research work also explores various hydrological uncertainty and sensitivity analysis methods to reduce the model simulation errors.

This study also integrates hydrological model to hydrodynamic model for assessment of streamflow, water velocity and water level in 21st century. This study also determines the rating curves at different points in the downstream portion of the river. A comparison of model simulations in the current and possible future hydrological characteristics etc. are performed. In this study, a snow water equivalent reconstruction approach has been presented to evaluate the model generated snowmelt.

1.3 Research Objectives

The purpose of this research work is to provide the advance research guidelines as per the adopted approaches and methodologies for the hydrological and hydrodynamic assessment of the snowmelt induced Teesta river catchment in the changing climate condition. Based on current research needs, following are the research objectives defined as below:

TH-1643_136104018

- Downscaling of temperature and precipitation using latest CMIP5 ESM GCMs under different RCP experiments implicating temperature lapse rate and precipitation lapse rate.
- Precipitation and Temperature trends and extremes analysis in historical (1979-2005) and futuristic time series (2006-2100) domains incorporating seasonally and intra-decadal variations.
- Geospatial study of snow cover, glacier extent and glacial lakes changes over Teesta river catchment by utilizing multi-spectral and multi-temporal, Moderate Imaging Spectro Radiometer (MODIS: MOD09A1 & MOD10A2), Landsat 7, Landsat 8 and Indian Remote Sensing satellite (IRS) Linear Imaging Spectral Scanner (LISS) 3 datasets. Characterization of Zemu glacier and its changes using novel proposed hybrid classification approach.
- Rainfall runoff, snowmelt runoff, surface flow and water yield simulation at sub-catchment scale in long term historical and 21st century times incorporating single slope, multiple slopes and modified CN formula using SWAT model.
- Streamflow calibration, parameterization and sensitivity analysis using a new SUFI2 (sequential uncertainty parameter fitting approach), GLUE (generalized likelihood parameter uncertainty equation) and ParaSol (parametric solution) methods using SWAT CUP (calibration and uncertainty program) at Teesta and Lachung outlets of the catchments.
- Snowfall and snowmelt runoff computations incorporating a novel "elevation band approach" and "degree day temperature index model" using SWAT model. Glacier melts contribution extracted by GSMSNOCONT model implementing Himalayan glacial conditions (improved version of GSMSOCONT model). Comparison of SWAT and GSMSNOCONT based snowmelt runoff modeling.
- Scenario generation of precipitation, water yield, streamflow, surface runoff, evapotranspiration (ET), snowmelt and snowfalls at over long term durations (2006-2100) utilizing downscaled temperature and precipitation datasets at sub-catchment scale.
- A newly linked methodology framework of SWAT and Mike 11 model for the hydrodynamic modeling of Teesta and Lachung rivers. Analyzing historical and futuristic changes in downstream flows, water levels, water velocities and flooded areas at multiple river cross sections of both Teesta and Lachung River.

1.4 Thesis chapters

Chapter 2 presents the research work pertaining to the literature reviewed during the course of the study. The literature review of this study is to emphasize on the theme of the research

TH-1643_136104018

work including past and 21st century climate change issues, climate change impacts on Himalayan water resources, climate downscaling and forecasting, the extremity of temperature and precipitation over the Himalayas, the applications of remote sensing in snow cover and glacier studies, integrated hydrological and hydrodynamic modeling for the management of water resources of Teesta river catchment part of north Sikkim eastern Himalaya.

Chapter 3 of the thesis presents a detailed description of the selected study area of Teesta river catchment, which is a part of north Sikkim eastern Himalayas. The topographical, geographical, geo-morphological, hydrological and meteorological descriptions of the study area have been discussed.

Chapter 4 presents about the climate change analysis using latest CMIP5 GCMs (ESM-2M, CM2P1 and CM3) predictors with multiple RCPs (RCP2.6, RCP4.5 and RCP8.5) experiments. The statistical and stochastic, and bias correction approaches have been discussed for the downscaling of daily minimum, maximum temperature and daily precipitation datasets in the 21st century scenarios. A daily temperature (minimum and maximum) and precipitation observed datasets for the year 1979 to 2005 have been utilized for the downscaling. The temperature trends, precipitation trends, temperature lapse rate (TLR) and precipitation lapse rate (PLR) changes have been explored and discussed in the historical and 21st century time series domain.

Chapter 5 explores the scope of remote sensing methods and satellite datasets for the analysis of snow cover and glacial changes in the temporal and spatial domains. MODIS (MOD09A1 and MOD10A2) daily), IRS LISS 3, Landsat 7 and Landsat 8 images derive snow cover and glacier properties of Teesta river catchment. The longest valley glacier of the eastern Himalayas namely Zemu glacier has been taken to explore the current scenario of glacier retreating over the north Sikkim eastern Himalayas.

Chapter 6 presents the hydrological modeling approaches to simulate and forecast the various major water balance components at point and sub-catchment scales using Soil Water Assessment Tool (SWAT). To comprehend the snowmelt runoff, an improved version of Glacier Hydrological Model (GSM-SOCONT) based on linear reservoir approach, modified specially for the Himalayan conditions, has been developed. An integrated approach of hydrological-hydrodynamic modeling utilizes SWAT and Mike 11 for the assessment of downstream river flows at Teesta river and Lachung river (a tributary of Teesta river). The rating curve equations have been developed using projected discharge and water level at two gauges of the Teesta river catchment (Chungthang and Lachung). The historical and 21st

TH-1643_136104018

century projected scenarios of water level, discharge and water velocities have been computed and discussed.

Chapter 7 summarizes the final conclusions and contributions of the present research work. The scope for further studies and research work and some implied limitations of this research are concisely discussed.

भारतीय प्रौद्योगिकी संस्थान गुवाहाटी • Indian Institute of Technology Guwahati •

TH-1643_136104018

CHAPTER 2

LITERATURE REVIW

2.1 GENERAL

Indian water resources establish one of its dynamic assets. The Indian water resources are grouped into 6 major water resource regions namely Indus drainage, drainage flowing into Arabian Sea, drainage flowing into Bay of Bengal, Brahmaputra drainage, minor rivers draining into other basins/countries such as Myanmar, Bangladesh and China, and island drainage (River Basin Atlas of India, 2010). The rainfall in India shows very high spatial and temporal variability and absurdity of the situation is that from north eastern parts of India (highest rainfall) to Rajasthan state of India (lowest rainfall) (Kumar et al., 2005). As per the IPCC, climate change is expected to affect precipitation and water availability around the globe and eastern Himalayan continent is no exception of it. In previous decades, several high intensity rainfall events have been recorded over the Himalayan continents such as the Kedarnath, Uttarakhand flash floods (2013) and Jammu and Kashmir floods (2014) (Mishra et al., 2015, Rao et al., 2014). Due to increasing population, changes in landuse/landcover pattern and incremental trend of urbanization are could be another cause of the disruption in the watershed hydrology over Himalaya regions (Bolch et al., 2012; Kulkarni et al., 2010).

An assessment of the availability of water resources in the context of 21st century requirements and expected impacts of changing climate is critical for relevant national and regional long-term development strategies and sustainable development. The present research work attempts to analyze the challenges of water resources due to abrupt consequences of climate change such as warming trend of lower atmosphere and high spatial and temporal variability in precipitation over the snow glacier induced Teesta river catchment part of north Sikkim eastern Himalaya. Therefore, the current research work shall be emphasized on the three broad categories as given below:

- ✓ Impact of climate change on water resources of Teesta river catchment
- ✓ Assessment and impact evaluation of major climate issues related to watershed components
- ✓ Analysis, development and representation of various advance methodologies to minimize the impact of climate change on snow glacier induced Himalayan watershed

TH-1643_136104018

2.2 CLIMATE CHANGE

Changes in the atmospheric abundance of greenhouse gases and aerosols, in solar radiation and in land surface properties alter the energy balance of the climate system (Kumar et al., 2005). The exact definition of the climate change given by the IPCC (2007), "*Climate change refers to a change in the state of the climate that can be identified (e.g., by using statistical tests) by changes in the mean and/or the variability of its properties, and that persists for an extended period, typically decades or longer*" (Stocker et al., 2013). Due to the adverse impacts and negative consequences of the climate change, the presence of people livelihoods, species diversity, ecosystems, environmental functions, services, and resources, infrastructure, or economic, social, or cultural assets in places and settings that could be affected adversely (Stocker et al., 2013). Many studies revealed that in the last few decades, changes in climate have caused impacts on natural and human systems on all continents and across the oceans. Although, their severity and extremity may vary from region to region (Pachauri et al, 2014). In the recent time, climate extremes, warming air temperature, droughts, floods, cyclones, and GLOF (Glacial Lake Outburst Flood) revealed significant vulnerability and exposures of some ecosystems and many human systems to current climate variability (Shrestha et al., 2012). Evidence of climate change impacts is strongest and most comprehensive for water resource systems (Mishra et al., 2015; Shrestha et al., 2012).

The globally averaged collectively land and ocean surface temperature data as computed by a linear trend, show a warming rise of 0.85 [0.65 to 1.06] °C, over the period 1880 to 2012 (Mishra et al., 2015), when multiple independently produced datasets exist. The total increase between the average of the 1850-1900 period and the average of the 2003-2012 period is 0.78 [0.72 to 0.85] °C, based on the single longest dataset available (Stocker et al., 2013). Since last two decades, the Greenland and Antarctic ice sheets have been losing mass, glaciers have continued to shrink almost worldwide, and Arctic sea ice and Northern Hemisphere spring snow cover have continued to decrease in extent (Vieli, 2015).

TH-1643_136104018

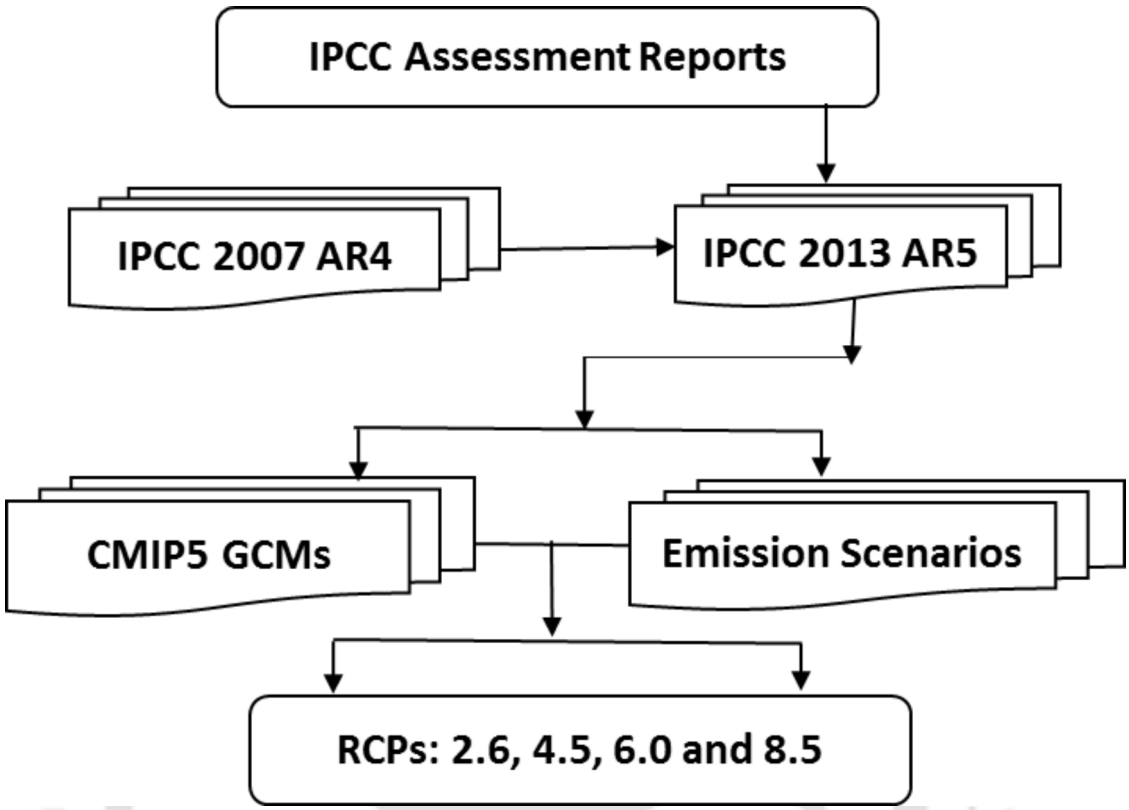


Fig. 2.1: IPCC assessment report their scenarios.

The atmospheric Radiative Forcing (RF) is recorded around 43% higher than the records from 2005 reported in the IPCC Assessment Report 4 (AR4). This is causing due to the continuous growth in greenhouse gas concentrations and indicating a frailer net cooling effect (Vieli, 2015; Stocker et al., 2013). On regional scales, the confidence in model ability to simulate surface temperature is less than for the larger scales (Stocker et al., 2013). The combined effect of alterations between atmospheric and surface warming, and fluctuations in water vapour, is exceptionally likely positive and thus intensifies changes in climate (Change I.C., 2013; Stocker et al., 2013; Vaughan et al., 2013).

2.3 IPCC ASSESSMENT REPORT 5 (2013) AND CMIP5 EMISSION SCENARIOS

The IPCC AR provides comprehensive assessment of climate change issues, their impacts and response strategies through the evaluation of scientific approaches. The first AR, IPCC report has produced in the year 1990 to analyze the scientific understandings and related uncertainties underlying assessment findings (Change, I.C., 2013; Mastrandrea et al., 2011). The IPCC AR5

TH-1643_136104018

explores the literature on the scientific and, technological, economic and social aspects of mitigation of climate change (Change, I.C., 2013). As per the IPCC AR5 (2014), fresh-water related risks of climate change increase significantly with increasing greenhouse gas concentration in the atmosphere (Field, 2014). During the last decades of 21st century, the extreme events such as river flood is projected to be three times greater for extreme emission scenarios (RCP8.5) than low emission scenarios (RCP2.6) (Field, 2014; Change, I.C., 2013; Taylor et al., 2012). In this report, it is also mentioned that the frequency and intensity of meteorological factors will be enhanced in 21st century. The drought will be more severe in the low rainfall regions and the intensity and amount of precipitation extreme event will be enhanced in the high rainfall regions around the world (Wong et al., 2014). Thus, climate change negatively alters the freshwater ecosystems through changing streamflows.

As per AR5, the regions with snow cover and glaciers, climate change has altered observed streamflow seasonality and melt runoff rate and earlier melting is projected. These alteration will be more severe in the last decades of 21st century (Pachauri et al., 2014). In the last few decades, the abrupt warming signatures have been recorded. These warming trends have reduced the maximum snow depth over few regions as analyzed and provoked the spring maximum of snowmelt runoff, smaller snowmelt floods, increased winter flows due to earlier snow melting and reduced summer low flows (Doll and Bunn, 2014; Pachauri et al., 2014, Change, I.C., 2013). In this report, it is concluded that the abrupt changes in the climatic factors due to continued warming, glacier retreating is likely to be enhanced and total melt water yields from glacier ice will increase in many regions during the 21st century (Barros et al., 2015; Doll and Bunn, 2014, Change, I.C., 2013). The permafrost warming is caused due to global warming and thawing in high-latitude regions and in high-elevation regions. This report also discussed about the uncertainty due to climate change, which will provide and adaptive approach for the management of the water resources.

The long-term scenarios measured in the IPCC AR5 were produced principally by large-scale coupled models or integrated models (Change, I.C., 2013). Integrated models deliver measureable, long-term projections of many of the most important characteristics of mitigation pathways. They accounting for many of the most important interactions between the natural systems and numerous relevant human systems (Change, I.C., 2014). The Fifth Generation Coupled Model Intercomparison Project (CMIP5) builds after the accomplishments of earlier phases of CMIP3 (Meehl et al., 2005). The CMIP5 models include two types experiment, (1) long term (century time scale) and (2) near – term scenarios (10-30 years). Both these

TH-1643_136104018

experiments are coupled with ocean-atmosphere GCMs (Taylor et al., 2012; Meehl et al., 2009). The CMIP5 scenarios of climate change are determined by emission scenarios reliable with the RCP experiments, which explores an estimate of the RF in the 21st century. (Taylor et al., 2012; Moss et al., 2010). The RCP8.5 categorized as the high emission scenarios experiment and as per RCP8.5, RF will be increased in the 21st century. Likewise, the RCP2.6 and RCP4.5 are the intermediate scenarios, in which the RF will be reached a maximum near the middle of the 21st century before decreasing.

A number of additions of CM3 (Coupled Physical Model) were achieved following the CMIP5 protocol, including all proposed "Core" simulations and most of the "Tier 1" and "Tier 2" simulations(Taylor et al. 2012). These simulations include an 1860 control, a 5-member historical ensemble, and 4 future scenarios (RCP2.6, RCP4.5, RCP6.0 and RCP8.5). The model responses are examined by the detection and attribution simulations of these model experiments to subsets of historical forcing which include well-mixed greenhouse gases and ozone only, natural forcing only, aerosol forcing only, and anthropogenic forcing only (Forster et al., 2013; Taylor et al., 2012).

The atmospheric component of the Earth System Models (ESMs) comprises physical parameters such as aerosols, cloud physics, and precipitation. The terrestrial and topographical factors includes precipitation, evaporation, streams, lakes, and streamflows to simulate dynamic reservoirs of carbon and other tracers (Arora et al., 2013; Dunn and Son et al., 2013).The ESMs based experiments include around 1860 control/historical and 4 future scenarios (RCP2.6, RCP4.5, RCP6.0 and RCP8.5) (Arora et al., 2013).

2.4 CLIMATE CHANGE IMPACTS ON WATER RESOURCES

As per the IPCC AR5, the negative effects of changing climate will be more severe on the terrestrial and fresh water ecosystems in the mid and last decades of 21st century under moderate to extreme RCP experiments (RCP4.5, RCP6.0 and RCP8.5) (Change, I.C., 2014; Change, I.C., 2013; Arnell and Hughes, 2014). Apart from the high emission scenarios and RCPs, the low emission scenario i.e. RCP2.6 will lead to major changes in environmental ecosystems especially over high altitude regions (Change, I.C., 2014).

TH-1643_136104018

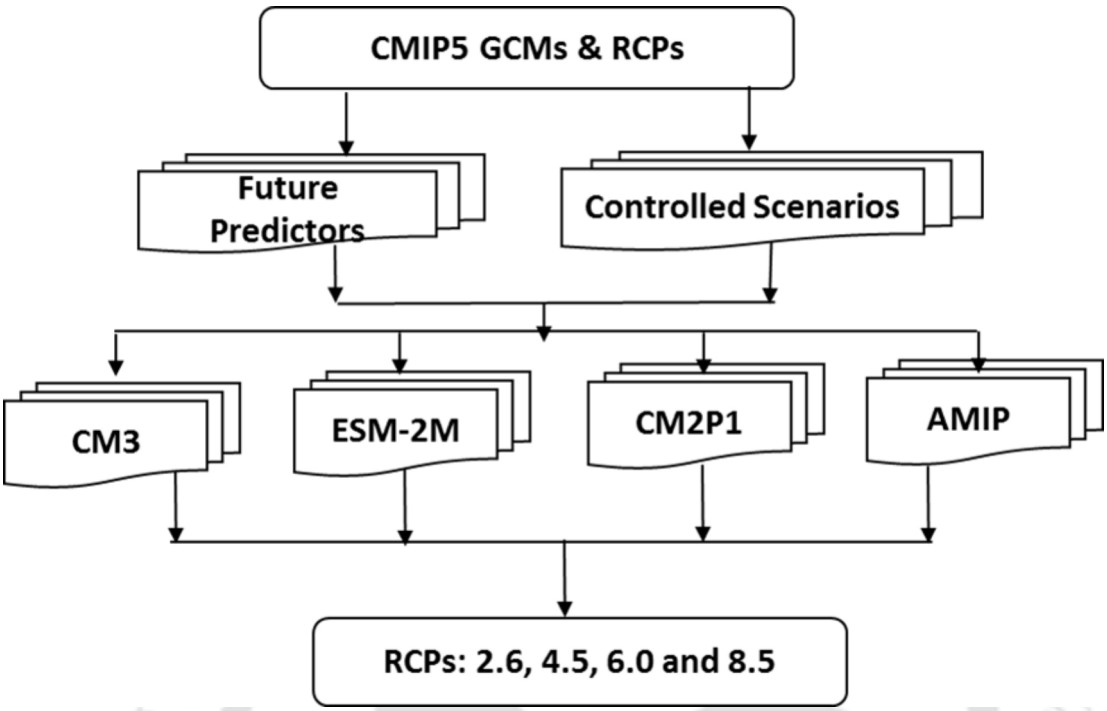


Fig. 2.2: CMIP5 GCMs and their RCP details (Adopted: *http://www.gfdl.noaa.gov/coupled-physical-model-cm3*).

Climate change induced changes in precipitation will substantially alter ecologically flow regimes of many rivers and wetland ecosystems (Whitehead et al., 2015; Change, I.C., 2014). The deterioration of landuse and landcover management practices affect the local as well as global climate and it can cause warming and cooling and bring significant changes in precipitation (Arnell, 1999). The vegetation density and species diversity influence the water use and rate of evapotranspiration (ET). Thus effective landuse strategies and management practices are needed to mitigate the effects of changing climate on water resources (Arnell and Hughes, 2013; Arnell, 1999).

Changes in the hydrological cycle which are associated with the negative impacts of climate will lead to diverse impacts and risks. The historical and 21st century predicted negative effects of climate change on water resource system will be severe due to increase in temperature and variability in the precipitation pattern (Whitehead et al., 2015; Change, I.C., 2014; Change, I.C., 2013). The negative consequences of climate change such as warmer water, more intense precipitation and longer periods of low flow in the rainfall dependent catchment could be greater during 21st century as per the predicted emission scenarios (Change, I.C., 2014). Climate change can certainly alter the probability of a specific extreme event such as flood. The

TH-1643_136104018

probability of such event can be estimated by analyzing the magnitude and fraction of events (Whitehead et al., 2015; Field, 2012; Jones et al., 2007). Potential ET and precipitation events are considered the main climate drivers which control the watershed hydrology on any region (Change, I.C., 2013). Precipitation is highly dependent on the atmospheric water vapor content and moist vapor content in the atmosphere depends on temperature. Thus, increasing temperature altering this physical process (Change, I.C., 2014; Change, I.C., 2013). Here, the some observations have been analyzed in the 21st century scenarios using CMIP5 simulations reported in the IPCC AR5 as below (Whitehead et al., 2015; Change, I.C., 2014; Change, I.C., 2013):

- Due to increasing surface temperature, the vapor carrying capacity is affecting and thus the variability and the ratio of precipitation to snowfall and rainfall are increasing non-uniformly.
- Warming rate affecting the snowmelt and glacier mass budgets.
- The precipitation as snowfall is decreasing and the extent of snow cover is reducing by earlier melting.
- Wet regions and seasons are becoming wetter and dry regions are becoming drier.
- Global average precipitation has increased in the warmer world and the variability from region to region is also increasing.
- Changes in evaporation are recorded similar patterns to precipitation with increase.

As per IPCC (2013), very high intensity extreme events are expected. The maxima of daily precipitation observed from 20 years return periods (1986-2005) are projected to shorter return period during 2081-2100. As per RCP2.6 it is 14 years, 11 years for RCP4.5 and 6 years for RCP8.5 (Kharin et al., 2013). As per the CMIP5 emission scenarios, it is observed that the frequency and magnitude of both floods and droughts will be altered. As per the SREX (Special Report on Managing the Risks of Extreme Events and Disasters to Advance Climate Change Adaptation), the flood frequency and intensity are projected to increase, and the regional changes by the implications of temperature and precipitation will also be increased (Kharin et al., 2013; Seneviratne et al., 2012). As per the CMIP5 and their RCP experiments, it is projected that the water resources is decreased in the mid-latitude and dry sub-tropical regions and will be increased at high latitudes and in many humid mid-latitude regions (Kharin et al., 2013). In the 21stcentury, the quality of fresh water lakes and availability of clean water can be reduced by the negative effects of the changing climate (Mehdi et al., 2015; Change, I.C., 2014; Kharin et al., 2013).

TH-1643_136104018

The hydrologist and civil engineers of water utilities and water resources have significant experience in familiarizing their policies and observations to the weather. However, with respect to the adverse effects of climate change, a long-term planning and conservation-management practices are needed to save our future which is extremely uncertain (Mehdi et al., 2015; Kharin et al., 2013). A flexible group of solutions that produces benefits regardless of the impacts of climate change and that can be implemented adaptively, step by step, is valuable because it allows policy to evolve increasingly, thus building on rather than losing the value of previous investments (Change, I.C., 2014; Change, I.C., 2013). Several adaptive procedures that may demonstrate predominantly operative include rainwater harvesting, conservation tillage, maintaining vegetation cover, planting trees in steeply sloping fields, mini-terracing for soil and moisture conservation, improved pasture management, water reuse, desalination, and more efficient soil and irrigation water management (Seneviratne et al., 2012).

2.4.1 Effect of climate change on water resources around the world

Floods, droughts, water scarcity, glacier retreating, earlier snowmelt, faster snowmelt, less precipitation as snowfall, increase global mean precipitation, decrease runoff in rainfall dependent inland based catchments and increase winter runoff in snow glaciated regions are the key impacts of climate change identified in the IPCC AR5 around the globe (Change, I.C., 2014; Change, I.C., 2013). A significant increment in rainfall intensities have been observed in most of the climate change-water studies, though their severity may higher and lower at some place and it varied from region to region (Harding et al., 2014). Many CMIP4 and CMIP5 based climate models recommended increases of rainfall in the northern hemisphere high latitudes and decreases of rainfall in the sub-tropical regions of the world (Hagemann et al., 2013; Seneviratne et al., 2012). As per the study conducted by Kalra et al. (2008), a significant increment in streamflows is observed in the Mississippi river basin, North America. Zhang et al. (2007) reported that the anthropogenic forcing (in 20th century) significantly affected to the observed changes in region and global precipitation. The authors concluded that the human influence on climate has been enhance and it influenced the surface air temperature, sea level pressure, free atmospheric temperature, and tropopause height and ocean heat content. This study showed that anthropogenic forcing had a detectable effect on observed changes in average precipitation within latitudinal bands. This study also revealed that these changes cannot be explained by internal climate variability or natural forcing.

Dai et al. (2009) conducted a study on the projection of streamflows and reported that the top rivers of the world such as Congo, Mississippi, Yenisei, Parana, Ganges, Columbia and Niger

TH-1643_136104018

showed significant increments in the simulated streamflows. This study concluded that the inter-annual variations are correlated with the El Nino–Southern Oscillation (ENSO) events for discharge into the Atlantic, Pacific, Indian, and global ocean as a whole. The authors also concluded that precipitation is a major driver for the discharge trends and large intra-decadal variations. Zhang et al. (2009) observed that the flood discharges in the lower Yangtze basin have increased in the last 40 years. At regional scale, significant increase in the annual maximum streamflow has been obtained in northwestern Europe by several researchers (Hattermann et al., 2013; Ellison et al., 2012). Significant decrease trends in snowmelt-flood magnitudes at almost one-fifth of 160 stations in Canada were reported by Cunderlik and Ouarda, (2009). Same decrease trends for spring and annual maximum flows were also recorded by Burn et al. (2010). Hattermann et al. (2013) identified consistent trends in precipitation extremes and flooding in Germany. However, few studies have considered variations in the hydrological drought (Mann and Gleick, 2015; Murphy and Timbal, 2008; Dale et al., 2001; Le, 1996).

Many studies have explored the severity of climate change on water resources used large ensembles of regional or global models (Pushpadas et al., 2015; Vicente-Serrano et al., 2015; Whitehead et al., 2015; Harding et al., 2014; Kharin et al., 2013; Arnell and Hughes, 2014). Several studies used probability distributions for the futuristic assessment by combining outcomes from multiple climate projection and emission scenarios (Liu et al., 2013; Christierson et al., 2012). A few studies evaluated the effects of climate change on groundwater and aquifer recharge especially before 2010 (Hua et al., 2015; Jena et al., 2015; Portmann et al., 2013; Crosbie et al., 2013; Jackson et al., 2011). Hua et al. (2015) provided insights about the optimal weights of allocating capital to each managed stages that maximize expected future return for the portfolio while minimizing overall portfolio risk in the future. Jackson et al. (2011) studied on the UK Chalk groundwater resources. In this study, a range of predictions is obtained by applying precipitation and temperature utilizing thirteen GCMs, to a distributed recharge model and a groundwater flow model. The authors resulted that the simulated changes in annual potential groundwater recharge ranged from a 26% decrease to a 31% increase by the 2080s, with ten models are predicting a decrease and three models are showing an increase.

Tennant et al. (2015) studied elevation-dependent response of streamflow to climate warming and resulted that the precipitation and streamflow are much shorter in low elevation regions than in mid- and high-elevation areas of the watershed. The authors concluded that low elevation annual percentiles of streamflow occur 30–50 days earlier than in higher elevation

TH-1643_136104018

watersheds. Jung et al. (2013) studied on the Korean streamflow seasonality based on multimodel climate projections and results showed that streamflow seasonality is likely to be provoked due to increases in wet season flow (July through September) and decreases in dry season flow (October through March). Most studies employed streamflow changes through climate-driven parameters from large, mainstream channels in order to detect trends or to calibrate hydrologic models (Tang and Lettenmaier, 2012). Bae et al. (2011) conducted a study over South Korea and used three semi-distributed hydrological models such as PRMS, SLURP and SWAT and seven different PET computation methods such as Hamon and Jensen–Haise methods for PRMS, Penman–Monteith, Granger and Spittlehous-Black for SLURP, Penman–Monteith, Priestley-Taylor and Hargreaves for SWAT have used for comparing differences of response to climate change in the Chungju Dam basin, Korea. The authors found a negative trend in spring streamflow and a positive trend in summer streamflow during the year 1968-2001. Kim et al. (2009) and Chang and Kwon (2007) demonstrated significant increasing trends in summer precipitation for 1973–2005 in South Korea.

As per the studies conducted by Dankers et al. (2014) and Hirabayashi et al. (2013), it is observed that the flood hazards increased over about half of the globe based on multiple CMIP5 GCMs, however, it also shows significant variability at the catchment scale. The regions such as South and Southeast Asia, tropical Africa, northeast Eurasia and South America have consistently increasing flood hazards and the regions such as Northern and Eastern Europe, Anatolia, central Asia, central North America and southern South America have shown decrease in projected flood hazard (Seneviratne et al., 2012). Several studies focused on the climate change impacts on small coastal basins, because of the coarser resolution of the GCMs (Elguindi et al., 2011). Elguindi et al. (2011) evaluated the ability of the CNRM-ARPEGE CLIMATE V4 general circulation model (GCM) over the Mediterranean-Caspian Sea to estimate the present-day hydrological budget components and characterized contrasted runoff pattern due to the climate change.

2.4.2 Effect of climate change on water resources over Himalayan continents

The total fresh water resources over the Himalayan terrains of China, India, Nepal, Bhutan and Pakistan estimated around 2100Gt to 5000Gt (Bolch et al., 2012). An inclusive understanding about the extent and severity of changes in glaciers due to climate change will support downstream hydrological planning and water resource management (Shrestha et al., 2012). Radic et al. (2014) studied on the projections and simulation of the glaciers mass changes utilizing CMIP5 projection from 14 GCMs. The authors resulted that the Himalayan glaciers

TH-1643_136104018

will be lost their mass around 29% from 2035 to 2100, though the range of losses is recorded around 15% to 78% as per RCP4.5. The mean loss to 2100 is recorded around 45% under RCP4.5 and up to 68% under RCP8.5. Huss (2011) noticed that the when glaciers shrinked, their relative contribution decreased and the annual runoff peak shifted toward spring. However, runoff shifts is expected higher in the western Himalaya than eastern Himalayas, where the monsoon and melt season overlapped (Huss (2011). Over the Himalayas, many climate variables lead to changes in snow melting and extent of ice (Sorg et al., 2012; Huss, 2011).

Shrestha et al. (2012) studied on the Hindu-Kush Himalayan (HKH) mountain system and resulted widespread climate change issues in the Himalayas and associated changes in local ecosystems. The authors observed significant spatial and seasonal changes in climate and phonological parameters over Himalayas. The authors observed that the rate of warming in the Himalayas is greater than the global average, which confirms that the Himalayas are among the regions most vulnerable to climate change. Many studies reported that the Himalayan glaciers are retreating and thinning due to the warming (Lutz et al., 2013; Scherler et al., 2011; Bajracharya and Shrestha, 20011; Kulkarni et al., 2007). Lutz et al. (2013) performed a comparison of climate change signals in CMIP3 and CMIP5 multi-model ensembles and implications for Central Asian glaciers. The authors evaluated that the CMIP5 ensemble has shown greater regional warming than the CMIP3 ensemble. Though, the authors observed the spread in projections of future glacier extent in Central Asia is similar for both ensembles.

Bajracharya et al. (2015) worked on the glaciers of the HKM regions and assessed the observed changes from the 1980s to 2010. The authors reported that due to the climate change and warming the Himalayan glacial lakes will be expanded, which could be the cause of glacial lake outburst floods. Snow water equivalent (SWE) reduces with an increase in air temperature. Collins et al. (2013) worked on the climatic variations over Himalayas and found that the streamflow in tributaries of the Ganges in Nepal fluctuated from year to year but the general background level of flow was usually maintained from the 1960s to 2000s. The central Himalayan Glaciers have clearly reduced in length and thickness from Little Ice Age maximum extension (Bolch et al., 2012). Srivastava (2012) studied on the Gangotri glacier and monitored the Gangotri glacier snout, from which the Bhagirathi tributary of the Ganges flows. The authors suggested that the ice-covered area of the Gangotri glacier is declined by 0.58 km^2 between 1935 and 1996. The runoff contribution from melting of snow and glaciers suggest that climatic warming may be having a significant impact on flows in Himalayan tributary flow (Bhambri et al., 2011).

TH-1643_136104018

Bhutiyani et al. (2008) determined that, due to the temperature warming, the discharge of the Satluj river has increased from1991 to 2004. In the entire Himalayan region, especially Indian sub-continents, most of studies have been conducted over western Himalayas, because the streamflow and observed precipitation datasets are not available in public domain for Ganga basin and Brahmaputra basin due to classified data sets (Ministry of Water Resources, 2013). As per the warming trends, from year-to-year, melt and runoff will be greater in warmer years over the Himalayan rivers (Bhambri et al., 2011). Due to the larger climatic variability, the accurate simulation and projection of hydrological scenarios, over the Himalayas, using multimodel GCMs will be affected and the chances of uncertainties will be more (Immerzeel et al., 2009). Immerzeel et al. (2012) studied on the hydrological response to climate change in a high altitude glaciered catchment in the Himalayas and resulted that both temperature and precipitation are projected to increase, which displays in a steady decline of the glacier area. The authors observed that the river flow is projected to increase significantly due to the increased precipitation and ice melt over the high altitude regions. The authors also revealed that the contribution of rain runoff and base flow will increase due to summation of glacier runoff.

Shah et al. (2015) studied on the central Himalayan glacier induced rivers to monitor the sensitivity of climate change as per the altitudinal gradient. The authors found an altitudinal sensitivity of climate change over several regions utilizing a generalized linear model. Ichiyanagi et al. (2007) initially and later Shah et al. (2015) proved the seasonal shifts in the monsoon over the Himalaya. Immerzeel et al. (2012) concluded that Asia's water towers have been threatened by climate change. However, the effects of climate change on water availability and food security in Asia differ substantially among basins and cannot be generalized. Immerzeel et al. (2012) and Bolch et al. (2012) revealed that the climate change effects in the Indus and Brahmaputra basins are likely to be severe due to the large population and the high dependence on irrigated agriculture and melt- water over the glaciated region. A less numbers study have been conducted on the eastern Himalayan regions, which could address the severity of 21st century climate change impacts (Apurv et al., 2015; Schickhoff et al., 2014; Krishna, 2005). As per the Bolch et al. (2012), more than 100 glaciers in the HKH region changed their length due to retreating since mid - 19th century. Though, some large glaciers have gained mass in the north western Himalaya and in the Karakoram. Though, the elevation dependent climate change issues utilizing CMIP5 emission scenarios are not discussed so far. In the Himalaya, few studies showed an elevation dependent consequences of climate changes in the water resources (Rangwala and Miller, 2012; Rangwala et al., 2010).

TH-1643_136104018

2.5 CLIMATE DOWNSCALING AND FUTURE FORECASTING

Statistical downscaling demonstrates a commonly used approach to downscale high resolution or in situ climate projections (Wojcik, 2015; Gutmann et al., 2014). A number of statistical downscaling methods are utilized by various researchers around the world, all these methods use the basic concept of founding quantitative relations between large-scale GCM predictors and point source observational predictands or observed datasets (Rashid et al., 2015; Taylor et al., 2012). Wojcik (2015) checked the reliability of CMIP5 GCM simulation and reproduced atmospheric circulation over Europe and North Atlantic using statistical downscaling of CMIP5 climate models. The author highlighted that reliability of GCMs varies seasonally as well as inter-model basis. Wang et al. (2015) compared the empirical statistical methods on a daily basis climate projections utilizing CMIP5 GCMs. The authors evaluated his findings over the Huai river basin, China and resulted that the "bias correction (BC)" based methods produce larger uncertainty bands of intra-annual variability the "change factor" based methods. The GCMs contain bias in the observations, thus GCMs need to be corrected prior to be used (Wilby et al., 2014; Jarosch et al., 2012; Mahmood and Babel, 2012). Hagemann et al. (2011) used Delta-change approach for GCM models. The delta change approach is a method that makes the output of GCMs useful for catchment scale analysis and hydrological modeling (Portmann et al., 2013).

Zhao et al. (2015) compared two different downscaling (e.g. $Pre_{sim1}$and Pre_{sim2}) methods using CMIP5 GCMs for precipitation in China. The authors resulted that without correction of the GCMs, it cannot be used. The authors found that Pre_{sim1}has better accuracy than Pre_{sim2}. In this study, the second method Pre_{sim2}, which establishes regression model based on the station data, has a tendency to overestimate or underestimate the real values. The accuracy of Pre_{sim1} method is recorded much better than $Pres_{im2}$ compared based on mean absolute error, mean relative error and root mean square error. The most straightforward approach of interpolation is linear or more sophisticated methods between large-scale grid points closest to the region to infer the regional scale (Wilby et al., 2014; Mahmood and Babel, 2012). To examine the impact of global climate change on the local climate, a new dynamical downscaling methodology has been utilized worldwide (Lauwaet et al., 2015; Dosio et al., 2015). Dosio et al. (2015) applied dynamical downscaling of CMIP5 GCMs over CORDEX-Africa with COSMO-CLM. The authors evaluated over the present climate and analysis of the added value. CORDEX generates high resolution (0.5°×0.5°) gridded historical and future climate projections using CMIP5 GCMs. Though, it is very challenging for climate models to replicate the various physical

TH-1643_136104018

processes and difficulty of their responses (Taylor et al., 2012). RCMs (Regional Climate Models) by adopting dynamic downscaling provide high resolution climate outputs but due to associated complexities, very less number of studies reported (Lee et al. 2014; Lee and Hong 2013; Paeth and Mannig 2012; Diallo et al. 2012). Dynamic downscaling suffers from several weaknesses, the mismatching of regional model physics with those of the global model (Emanuel, 2013).

Goyal et al. (2012) presented a nonparametric method K-Nearest Neighbor for statistical downscaling of the temperature, evaporation and precipitation datasets over a semi-arid region of India. The authors evaluated the performance of the K-NN approach through several statistical performance indicators. A comparison of K-NN has been made with a linear multiple regression (LMR)-based downscaling model and a simple multiplicative shifts was tested to correct the predictands values. Bloschl and Montanari (2010) found that using statistical downscaling methods, GCMs are able to simulate the mean features of the global climate at spatial and point scale. The statistical downscaling methods have progressively used by various researchers around the world (Ghosh and Mujumdar, 2008; Goyal and Ojha, 2010; Mahmood and Babel, 2012; Emanuel, 2013, Wilby et al., 2014). Statistical downscaling model (SDSM) developed by Wilby et al. (2006) is a hybrid of stochastic weather generator and multiple linear regression. The SDSM model has been evaluated by various researchers around the world for the downscaling of temperature, precipitation, evapotranspiration etc. (Singh et al., 2015; Wilby et al., 2014; Emanuel, 2013; Mahmood and Babel, 2012; Huang et al., 2011; Wilby, 2006). Statistical downscaling based bias correction methods are also produced by Mahmood and Babel (2012). SDSM has three sub-models such as monthly, seasonal, and annual to develop, though many authors concluded that the monthly sub-model can be utilized perfectly and more accurately (Mahmood and Babel, 2012; Huang et al. 2011), to develop SDSM for downscaling local climate variables.

2.5.1 Projection of temperature extremes

The studies conducted around 1990s concluded large scale and regional scale warming over the Earth's surface (Easterling et al. 1997; Horton, 1995). Horton (1995) studied and found the worldwide increase in the minimum daily air temperature. IPCC (2007) revealed that the increasing concentration of greenhouse gases and sulfate aerosols are the main cause of warming (Taylor et al., 2012; Rangwala and Miller, 2012). Easterling et al. (1997) found significant variations in minimum and maximum temperature and observed that the diurnal temperature variations. Zhou et al. (2007) observed that increase in cloudiness and precipitation,

TH-1643_136104018

which reduced the diurnal temperature ranges. Chu et al. (2010) worked on the GCMs and found that GCMs have significant capability to simulate and global and regional scale temperature variation. Tatsumi et al. (2015) utilized CMIP3 GCMs for the downscaling and projections of the minimum-maximum temperatures and cloudiness in the Shikoku region, Japan. The authors observed significant variations in the temperature and cloudiness, and explained that the dependency of future changes in temperatures on future changes in CLD were more evident in winter than in other seasons.

Horton et al. (2013) studied on the warming due to climate change and explained that the main cause of the high relative humidity is rise global average temperature, which could be dangerous for the high density urban cities and extreme heat has the potential to damage critical infrastructure. Kunkel et al. (2013) and Horton et al. (2013) determined that due to abrupt increase of warming can provoke to flash flooding in small streams from convective precipitation. Thibeault and Seth (2014) worked on the projection of future temperature extremes over Northeast United States utilizing CMIP5 GCMs. The authors found a significant shift is found in the distribution of observed total annual precipitation over 1981–2010.The authors also found largest decreases in cold extremes over northern and interior portions of the Northeast. This study provides a regional analysis as per the latest generation of CMIP global models specifically for the Northeast. This will be useful to stakeholders focused on understanding and adapting to climate change and its impacts in the region. Meehl et al. (2014) and Wuebbles et al. (2014) utilized CMIP5 climate models for the analysis of temperature extremes over United States. The authors also compared their results with CMIP3 scenarios and concluded that the spatial pattern and direction of change in temperature projection during 21st century do not vary extensively. Knutti and Sedlacek (2013) also observed the similar trend and revealed that the range in future projections due to uncertainty in climate sensitivity is also unchanged.

The variable frequency temperatures, as high or low monthly, is another measure of extreme temperature change (Meehl et al., 2014) in the CMIP5 RCPs. Under the low emission scenario RCP2.6, current annual maximum temperature extreme values are more frequent around 4 to 10 times at the beginning of the 21st century (Wuebbles et al., 2014). The moderate emission scenario RCP4.5 showed that the high monthly record temperature will be more frequent in the 21st century (Wuebbles et al., 2014; Sedlacek et al., 2012). Miao et al. (2014) worked on the CMIP5 models and projected the 21st century temperature scenarios over Northern Eurasia. The authors observed that the surface air temperature in the 21st century will be increased by

TH-1643_136104018

1.03°C/100 year as per RCP2.6, 3.11°C/100 year as per RCP4.5 and 7.14°C/100 year as per RCP8.5 scenarios. Miao et al. (2014) also revealed that the uncertainty of the surface air temperature can be increased with time over the Northern Eurasia. The authors evaluated the multi-model ensemble techniques to project the future surface air temperature changes under different emission scenarios. The results showed that most of GCMs overestimate the annual mean surface air temperature in Northern Eurasia and the difference between the observation and the simulations primarily comes from the winter season. Though, many GCMs can approximately capture the decadal surface air temperature trend but with less accuracy. Kharin et al. (2013) also evaluated CMIP5 multimodel emission scenarios for the projection of temperature and found significant increment in the global annual average temperature, which can be a significant cause of glacier retreating and increasing sea level rise.

Gardner et al. (2009) first time evaluated the near temperature changes as per the Temperature Lapse Rate (TLR) over Arctic glaciers. The authors observed the temperature warming as per the elevation differences. The authors concluded that the TLR near glacier surfaces vary on both daily and seasonal timescales, are consistently lower than the mean moist adiabatic lapse rate (MALR). The authors also found a significant fraction of the daily variability in lapse rates is associated with changes in free-atmospheric temperatures. Gardner et al. (2009) and Rangwala and Miller (2012) observed elevation dependent warming, which could a serious threat to the permanent snow cover and glaciers. The main climate factor such as air temperature is responsible for the snow accumulation over the glaciated regions and it is invariably linked to the altitude and topography, as local temperature lapse rate (TLR) existed (Hantel and Maurer, 2011; Etienne and Paris, 2010). TLR, which is dependent on the elevation, is recognized as one of the most important environmental factor that influences the precipitation and moisture conditions at local spatial scales (Chow et al., 2010). Kharin et al. (2013) detected the temperature extreme changes by the preparation of temperature extreme indices. The authors studied the extreme temperature changes over South Korea using quantile regression and found increasing trend of minimum temperature in both upper and lower quantiles.

2.5.2 Projection of precipitation extremes

Harding et al. (2014) worked on the future for global water assessment and mentioned that the global scenario of water resources under considerable pressure. The authors mainly revealed that dry areas will be more drier in the future and an increasing proportion of precipitation falling in extreme events, also leading to longer dry spells. The authors concluded that the evapotranspiration (ET) varies with the landcover and soils, as well as local significance of the

TH-1643_136104018

climate, so it is difficult to conclude. Hagemann et al. (2013) analyzed that water scarcity will be increased in China and India due to increasing population and over exploitation of natural water reserves. Pall et al. (2011) has studied on the UK flood in 2000 and presented a multi-step, physically based probabilistic event attribution framework which highlights that global anthropogenic greenhouse gas emissions substantially increased the risk of flood occurrence in England and Wales in autumn 2000. This study results revealed that the precise magnitude of the anthropogenic contribution remains uncertain. Though, in nine out of ten cases the model results indicate that twentieth-century anthropogenic greenhouse gas emissions increased the risk of floods occurring in England and Wales in autumn 2000 by more than 20%, and in two out of three cases by more than 90%. Wu et al. (2013) utilized the CMIP5 GCMs and RCPs, and resulted that due to increments in the greenhouse gases and aerosols, global hydrological cycle has been shifted.

Sayemuzzaman and Jha (2014) worked on the observed (1950-2009) precipitation datasets over North Carolina, United States and significant variability in the annual and seasonal time series. The authors resulted an increase in precipitation in mountain and coastal regions in general except during the winter applying regional trend analysis. Sonali and Nagesh (2013) performed the spatial and temporal trend analysis monthly and seasonal maximum and minimum temperatures used parametric and non-parametric tests to evaluate the precipitation. The authors found significant variability in the precipitation amount in Indian sub-continents. This study results agreed with the earlier observation that the trend in minimum temperature is significant in the last three decades over India. Palazzi et al. (2014) evaluated CMIP5 GCMs over Karakoram-Himalaya and gradual increments in the summer precipitation throughout the 21st century scenarios. Though, properly simulation of seasonal precipitation and its spatial and temporal distribution using GCMs has demonstrated many difficulties. Deng et al. (2015) analyzed the frequency of extreme precipitation over Ontario using GCMs and observed annual heavy precipitation days, very heavy precipitation days, very wet day and extreme wet days in the progressive manner over major parts of the Ontario.

Song et al. (2015) also used observed precipitation datasets to detect the recent changes in extreme precipitation and droughts during 1960 to 2013 over Songhua river basin, China. Song et al. (2015) generated precipitation indices and observed that wet days are increased and the regionally averaged consecutive dry days significantly increased. Qian et al. (2007) found that the frequencies of extreme precipitation events increased in eastern China. Zhang et al. (2011) recognized the large number of consecutive rainy days in China during 1960–2005 and

TH-1643_136104018

determined that the increasing fractional involvement of shorter consecutive rain days may suggest increasing precipitation. Kharin et al. (2013) prepared extreme precipitation indices to detect the annual, seasonal and intra-annual variability in 21st century precipitation scenario utilizing CMIP5 RCPs. The authors observed relative changes in the intensity of precipitation extremes and the annual mean precipitation is increased.

2.6 REMOTE SENSING APPLICATION IN SNOW COVER AND GLACIER STUDIES

Snow cover and glaciers changes and faster snowmelt are the indicators of global warming and climate change (Paul et al., 2004). Snow parameters are observed highly sensitive to the climate factors (Snehmani et al., 2015). Remote sensing has the benefits and ability to analyze spatial, spectral and temporal changes in snow cover and glacier generally in remote and inaccessible areas, where field measurements cannot be evaluated (Immerzeel et al., 2009; Kularni et al., 2007). It is observed that mountain regions, especially Himalayas, shows large variations in the topography and climate (Rangwala and Miller, 2012), thus snow cover also varied from high elevation areas to low elevation areas (Bradley et al., 2009). It is estimated that around 1/6 of the global population depends on snow and glacier for fresh water resources (Viviroli et al., 2009). Blanford (1984), initially suggested that the winter snow cover in Himalayas could be sensitive for the summer month's rainfall. Across the world, snow cover and glaciers are reducing their spatial and temporal distribution observed by many researchers (Viviroli et al., 2009; Immerzeel et al., 2009; Kularni et al., 2007). Thus, time to time accurate measurement of the snow cover and glaciers changes are necessary to conserve the water resources over snow glacier induced catchments (Immerzeel et al., 2009; Kulkarni et al., 2007).

Paudel and Andersen (2011) monitored snow cover variability in the Trans Himalayas utilizing MODIS snow cover datasets. The authors presented a very organized approach for the cloud removal. The authors revealed that the temporal and spatial variability of the snow cover is significantly affected over the Trans Himalayas. MODIS snow cover products are freely available on the NASA portal and can be downloaded (Hall et al., 2002). The MODIS snow product suite begins with a 500-m resolution, 2330-km swath snow-cover map, which is then gridded to sinusoidal grid to produce daily and 8-day composite tile products. The sequence proceeds to a climate-modeling grid (CMG) product at 250meter resolution, with both daily and 8-day composite products. Each pixel of the daily CMG contains fraction of snow cover from 40% to 100% (Paudel and Andersen, 2011; Hall et al., 2002).Himalayan glaciers have been grouped as clean-ice type (C-type) and debris-covered ice type (Pratap et al., 2015). Debris covered glaciers or moraine glaciers characterized by significant sediment transport agent in

TH-1643_136104018

cold mountainous environments (Pratap et al., 2015). Many research studies revealed that around 70–80% of Himalayan glaciers are debris-covered and have been retreating almost since the end of the Little Ice Age (Pratap et al., 2015; Immerzeel et al., 2012; Basnett et al., 2013; Boltch et al., 2012; Kulkarni et al., 2007), yet few studies do not agree in this and have different views (Gardelle et al., 2012; Himalayan, 2009). The details about the glacial retreating and shrinking around the world, including Himalayan continent, have been analyzed by few research centers (Pratap et al., 2015; Frey et al., 2012).

The glacial snowfields over Himalayan glaciers store about 12000 $km^3$of freshwater (Tiwari et al., 2014). However, less attention has been paid to enumerating the Himalayan glaciers especially over the eastern Himalayan region (Kulkarni et al., 2007). The influence of debris cover on the ablation process in different seasons (winter, summer and spring) is largely unknown over the eastern Himalayas (Kulkarni et al., 2007). Many glaciological studies based on the mass balance of glaciers show an increase of rate of glacial loss in the last decades (Basnett et al., 2013; Racoviteanu et al., 2008) and due to the recent retreat, the terminuses of the glaciers have shown continuous increase in the debris cover (Tiwari et al., 2014). These recent trends of glacial retreat may be endorsed due to the 20^{th} century climate fluctuations (Basnett et al., 2013). Though, several studies reported that the response of glaciers to such climate fluctuations may also depend on non-climatic factors such as ice dynamics, glacier hypsometry and topography (Tiwari et al., 2014; Racoviteanu et al., 2008).

Remote sensing based characterization of glaciers could be useful for their regular mapping in a comprehensive and effective manner (Shukla et al., 2010; Racoviteanu et al., 2008; Gupta, 2003). Many glaciological studies are monitoring and mapping glacier changes using remote sensing in mountain regions observing rapid changes in the glacier extents (Tiwari et al., 2014; Alifu et al., 2015; Shukla et al., 2010; Kulkarni et al., 2007). The increased availability of satellite remote sensing imageries with adequate spatial and temporal resolution with near global coverage allows extending the measurements of glaciers over larger areas (Khan et al., 2015). A few studies utilized remote sensing satellite datasets for mapping and characterizing debris properties of the glaciers with good accuracy (Khan et al., 2015; Tiwari et al., 2014). The mapping of debris covered glaciers in the optical region show similar spectral reflectance because SGD (debris cover within the glacier boundary) and PGD (debris cover outside the glacier boundary) have almost similar spectral response (Tiwari et al., 2014; Racoviteanu et al., 2008). The accurate mapping and characterization of debris covered glaciers even by remote sensing has always been a challenge (Gupta, 2003). The manual and field methods are time

TH-1643_136104018

consuming and much costly so cannot effectively utilize in extreme elevation ranges, yet could be manageable for the alpine and other glaciers.

The cloud cover extent and shadow regions in high hilly terrain are the major problems in remote sensing satellite datasets especially with the optical and thermal infrared bands. Cloud patches shows large anomalies in the reflectance and temperature brightness of the optical and thermal sensors, respectively. Thus, an accurate measurement of the SGD and PGD cannot possible without removal of it. Tiwari et al. (2014) has classified cloud and shadow as a separate class but the given methodology is not effective in case of temperature brightness. The area under these classes could not be significantly quantified and cannot be added into the glacial extent, which reduces the accuracy level. Many studies reported that this simplification may not always be true (Alifu et al., 2015; Paul et al., 2004). Shukla et al. (2010) and Tiwari et al. (2014) have used single satellite sensor (e.g. Landsat ETM^{+} and ASTER) for merging optical and thermal bands for characterizing debris of glaciers. However, the cloud cover can be removed by the adjacent scene of the same year same satellite datasets (Alifu et al., 2015).

Previous studies reported that the optical and thermal bands from the different satellite sensors are capable to explore glacier properties (Khan et al., 2015, Tiwari et al., 2014; Shula et al., 2010). Though, the visible and NIR sensors have several limitations to daylight, cloud free conditions, which are challenging to achieve over extensive glaciered areas like Himalaya. Kulkarni et al. (2007) studied the glacial retreat in the Himalaya in the optical region using IRS P6 LISS 3 and LISS 4 datasets. They indicated that a combination of glacial fragmentation, higher retreat of small glaciers and climate change influencing the sustainability of Himalayan glaciers. They identified the fluctuations in the glacier boundary and terminus of the glaciers by preparing the spectral reflectance curves (Narsimlu et al., 2013; Shrestha et al., 2012).

Khan et al. (2015) separated snow, clean and debris covered ice in the Hindukush-Karakoram-Himalayas using Landsat images between 1998 and 2002 at the end of the melting season. The author used a semi-automated method to separate perennial snow and glacier inventory based on by combining the surface slope information with optical bands of Landsat images and then applied the supervised MLC to map glaciers. Slopes can help to identify the ridge line between the PGD, SGD and other glacier classes (Alifu et al., 2015). The higher degree slope represents the clean ice glacier which covered by fresh snow. The slope also helps to identify the glacier boundary to separate the SGD and PGD. Initially, Lougeay (1974) presented a method to distinguish debris cover of glaciers using the temperature differences by analyzing field collected temperature datasets. The author found out that the PGD area is hotter than the SGD.

TH-1643_136104018

Tiwari et al. (2014), Shukla et al. (2010) has worked on this idea and analyzed the effectiveness of thermal data in differentiating SGD and PGD along with optical data from ASTER and Landsat sensors. Alifu et al. (2015) used the Landsat band ratios (e.g. Band 3/Band 5 and Band 4/Band 5) to distinguish debris free glacier ice from non-glaciered portions. Previous studies (Alifu et al., 2015; Kaabet al., 2012) have shown the effectiveness of the band ratio algorithm in the mapping of glaciers.

Chelamallu et al. (2014) demonstrated that snow cover mapping is important for snow and glacier-related research. The spatial and temporal distribution of snow cover area is a fundamental input to the atmospheric models, snowmelt runoff models and climate models, as well as other applications (Chelamallu et al., 2014; Dietza et al., 2013). Negi et al. (2013) developed a methodology for the mapping of snow cover in Beas basin, Indian Himalaya using Advance Wide Field Sensors (AWiFS) IRS-P6 satellite data. The complexities in the mapping of snow cover in the study area have shown under vegetation, contaminated snow and patchy snow. Tang et al. (2013) addressed a snow-mapping algorithm for the Tibetan Plateau region using MODIS data and studied that the effects of the atmosphere and terrain on the satellite observations at the top of the atmosphere (TOA), particularly in the rugged Tibetan Plateau region, the surface reflectance is retrieved from the TOA reflectance after atmospheric and topographic corrections. Negi et al. (2013) demonstrated the potential of hyperspectral imaging Hyperion data for the mapping of snow grain size and snow mixed objects in the Himalayan region. The spectral signatures collected using a field spectroradiometer for different types of snow grain size and vegetation-/soil-mixed snow were used for the identification/comparison of collected image spectra. Dietza et al. (2013) studied on the daily snow-cover time series for the whole of central Asia after cloud coverage was removed. Snow-cover duration (SCD), snow-cover start (SCS), and snow-cover melt (SCM) have been derived for each hydrological year from 2000/2001 to 2010/2011 and mean conditions were extracted that identify a distinct north–south gradient of these parameters. Sharma et al. (2014) presented a study which deals with spatio-temporal snow cover distribution in Northwest Himalaya (NWH) in a discourse on regional topography and prevalent climatology. Singh et al. (2014) provided an overview of various methods for estimating snow cover and properties in high mountains using remote sensing techniques involving microwaves.

2.7 HYDROLOGICAL AND HYDRODYNAMIC MODELING

A watershed is a natural unit of land from which the surface, sub-surface and groundwater runoff drain to a common/single outlet (Singh and Frevert, 2002; Black, 1995). The watershed

TH-1643_136104018

hydrology can be defined as that branch of hydrology that deals with the integration of hydrological processes (such as precipitation, evaporation, condensation, transpiration, the water budget, infiltration, antecedent moisture condition, time of concentration, interception, return period, environmental flow, overland flow etc.) at the watershed scale to determine the watershed response (Singh and Woolhiser, 2002). The optimum demands of water supplies to avoid flood damages require sufficient knowledge of hydrological processes (Singh and Frevert, 2002).It helps us in balancing and quality wise streams, lakes and other water bodies (Brooks et al., 2012). Embedded in the concept of integrated watershed management is the recognition of the inter-relationships among landuse, soil and water and the linkage between upland and downstream areas (Brooks et al., 2012; Gupta, 2003). Due to the intimate linkage between the hydrologic cycle and climate, climate change can influence hydrological components as well as streamflow/runoff. Thus, a long term deterministic and stochastic hydrological modeling is required to overcome the issues. Projected changes in climate are expected to change precipitation pattern and freshwater flow regimes in the form of high intensity and high volume runoff (Escurra et al., 2014; Gosh and Dutta, 2012), thus, accurate prediction of watershed parameters are necessary to assess future changes (Singh and Woolhiser, 2002).

A wide range of applications relevant for the planning and management of water resources have been demonstrated using the framework built at the macro level as well some patches developed at the larger scales by the actions of hydrological and hydrodynamic modeling (Singh et al., 2013; Singh and Woolhiser, 2002; Arnold et al., 1998). Apart from the above considerations, it is assumed that the model parameterization and sensitivity analysis are also the necessary tasks in the accurate prediction of hydrological scenarios (Jones and Carvalho, 2014; Abbaspour et al., 2011). Many researchers found that the accurate prediction of the modelled scenarios is difficult; when a watershed/catchment involves snow and glacier induced hydrological processes additionally (Mall et al., 2006). Taye and Willems (2013) analyzed that changes in catchment runoff variability are a function of changes in climate as well as catchment behavior. Taye and Willems (2013)used two conceptual hydrological models were calibrated and evaluated for their performance to simulate extreme high flows and changes in these flows for corresponding changes in rainfall conditions. Patil et al., (2014) studied on the spatial variability of climate and told that it can negatively affect catchment streamflow predictions using EXP-HYDRO model and it implemented at 41 mesoscale (500–5000 km^2) catchments in the Pacific Northwest region of USA. The large scale hydrological models are conceptual models having at least a small physical basis such as VIC ((Liang et al., 1994), LASCAM (Viney et al., 2000), TOPKAPI model (Liu and Todini, 2002), and IBIS–THMB (Coe et al., 2007).

TH-1643_136104018

Mishra et al. (2014) studied experimentally the effect of watershed (i.e. field plot of 22 m×5 m) slope on rainfall-generated runoff and, in turn, the runoff curve numbers (CN) resulting from field plots (with land use of maize and sugarcane on the soil falling in Hydrologic Soil Group C) located in Roorkee, India. The results indicated that the plot of 5 % slope yielded the largest runoff and, in turn, CN compared to those due to the plots of 3 and 1 % grades, for the same rainfall, soil, and land use. Immerzeel et al. (2014) worked on the glacier-hydrological models which simulate catchment response to climate variability depends to a large degree on the data used to force the models. The authors analyzed the results of a 1 year field campaign focusing on air temperature and precipitation observations in the Langtang valley in the Nepalese Himalayas. They used the observed time series to characterize both temperature lapse rates (LRs) and precipitation gradients (PGs).

Vansteenkiste et al. (2014) used five hydrological and hydrodynamic models and compared their utilities and calibration techniques. The authors demonstrated the response behavior of the catchment extracted from the river flow and input time series and focused on reproducing the quick and slow runoff sub-flows. Willems, (2015) concluded that the model calibration, based on multiple objectives functions, is qualitatively more balanced but does not necessarily statistically perform the best. A realistic and accurate river flow forecasting for the real-time river management, including flood control, flood warning, reservoir and integrated watershed management are needed , where the uncertainty is dominant (Vansteenkiste et al., 2014; Madson and Skotner, 2005). Hydrodynamic river flow routing in large scale resulted of other flow related variables, such as river stage, velocity and slope (Madson and Skotner, 2005). One dimensional (1D) hydrodynamic river models have well developed and used since the late 1970s (Paiva et al., 2013; Paiva et al., 2009; Paz et al., 2010; Cunge et al., 1980). Several other studies also noticed for flood inundation simulation ranging from simplified models utilizing composite cross section to 2D models (Bates and De Roo, 2000).

2.7.1 Deterministic and stochastic hydrological modeling

Himalayan streams contribute significant amount of discharge due to snowmelt and glacier melt water and also dignified by temporal flow variability due to large differences in the PLR (Gardener et al., 2009, Kumar and Singh, 2012). Accurate hydrological modeling over Himalayan river catchments remains a huge challenge due to associated complexities (Kumar and Singh, 2012). Thus, over these complexities stochastic and deterministic hydrological modeling can giver better understanding of the parameters and uncertainties too (Neistch et al., 2012; Abbaspour et al., 2007; Singh and Woolhiser, 2002). Deterministic hydrological models

TH-1643_136104018

which have been evaluated over mountainous catchments such as PRMS (Precipitation-Runoff Modeling System), TOPNET generated as per the Top Model (Beven et al., 1995) and SWAT (Soil Water Assessment Tool) (Neistch et al., 2011; Arnold et al., 1998) are shown their utilities over complex high hilly terrains. Combining deterministic and probabilistic methods for steep slopes and flood plain based catchments has been evaluated by Jain et al. (2010).

SRM (Snow Melt Runoff Model) used by various researchers to predict the melt runoff (Panday et al., 2014; Schaper and Seidel, 2000; Ferguson, 1999) but this model has several limitations. Schaper and Seidel (2000) studied snowmelt and glacier melt changes using SRM and found enforced summer icemelt and earlier snowmelt. Singh and Woolhiser (2002) provided a review over the applicability and behaviour of the various mathematical deterministic and stochastic hydrological models. The listing of various popular hydrological models and their details are given in the Table 1. Papers related to the present work show the recent hydrological significance have been emphasized here.

Table 2.1: Development scenarios of hydrological and hydrodynamic models around the world.

Model Name	Authors	Year	Model Features
Catchment Model (CM)	Dawdy and O' Domell	1965	Lumped, event based runoff model
Stanford Watershed Model	Crawford and Linsley	1966	Continuous, dynamic, steady state
U.S. Department of Agriculture Hydrograph Laboratory Model (USDAHL)	Holtan et al.	1974	Event based, process oriented, lumped hydrological model
Agricultural Runoff Model (ARM)	Donigian et al.	1977	Process-oriented, semi distributed, continuous stormflow model
University of British Columbia Model (UBCM)	Quick and Pipes	1977	Process oriented, lumped parameter, continuous simulation model
Chemicals, Runoff, and Erosion from Agricultural Management Systems (CREAMS)	USDA	1980	Process-oriented, lumped parameter, agricultural runoff and water quality model

TH-1643_136104018

Hydrologic Engineering Centre -Hydrological Modeling System (HEC-HMS)	Feldman	1981	Physically based, semi-distributed, event based runoff model
Great Lakes Environmental Research Laboratory (GLERL) Model	Croley	1983	Physically based, semi distributed continuous simulation model
Simulator for Water Resources in Rural Basins (SWRRB)	Williams et al.	1985	Process-oriented, semi distributed, runoff and sediment yield simulation model
Soil-Vegetation-Atmosphere Transfer (SVAT) Model	Ma et al.	1990	Macroscale, lumped parameter, streamflow simulation system
Cascade two dimensional Model (CASC2D)	Julien and Saghafian	1991	Physically based, distributed, event-based runoff simulation model
Variable Infiltration Capacity (VIC) Macroscale Model	Liang et al.	1994	large-scale, semi-distributed hydrologic mode
Generalized River Modeling Package—SystemeHydroloqueEuropeen (MIKE-SHE)	Refsgaard and Storm	1995	Physically based, distributed, continuous hydrologic and hydraulic simulation model
Groundwater Loading Effects of Agricultural Management Systems (GLEAMS)	Knisel and Williams	1995	Process-oriented, lumped parameter, event-based water quantity and quality simulation
Snowmelt Runoff Model (SRM)	Rango	1995	Lumped, continuous snowmelt-runoff simulation model
Water and Energy Transfer between Soil, Plants and Atmosphere (WETSPA) model	Wang et al.	1997	gridded based distributed hydrological model
Soil Water Assessment Tool (SWAT)	Arnold et al.	1998	Distributed, conceptual, continuous simulation model
Semi-distributed Land Use-based Runoff Processes (SLURP)	Geoff Kite	1997	Basin model, sub-basin, runoff, DEM

TH-1643_136104018

Distributed Hydrological Model (HYDROTEL)	Fortin et al	2001	Physically based, distributed, continuous hydrologic simulation model
Hydrological Predictions of the Environment (HYPE) Model	Lindstorm et al.	2010	daily/Hourly, small scale and large scale hydrological model
AnnAGNPS (Artificial Neural Network Agricultural Non-Point Source Model)	Bingner et al.	2011	watershed scale, continuous simulation model
Physically Based Runoff Production Model (TOPMODEL)	Beven and Kirkby	1979, 1995	Physically based, distributed, continuous hydrologic simulation model

Wurbs et al. (2005) used SWAT model for assessing the impact of changing climate in a watershed of Texas. They used Hadley center GCMs for the projection of future water balance components. Jain et al. (2010) utilized SWAT model for assessing the rainfall-runoff and sediment yield over the Satluj river catchment, India. Singh et al. (2013) used SWAT and SWAT CUP (Calibration Uncertainty Program) for assessing streamflow at Tungabhadra catchment, India. The authors also discussed about the various model calibration and sensitivity analysis parameters. Goyal et al. (2015) combined the SWAT and Geospatial data layers for assessing the site suitability of small hydropower projects over upper part of Mahanadi river basin, India. The authors presented a new multi-criteria approach for harnessing hydropower through establishing small hydropower projects (SHPs) (≤25 MW) instead of large hydropower projects. The multi-criteria approach is based on an integration of the advance raster data based preparation of geospatial data layers, hydrological modeling and weighted sum overlay analysis. Singh et al. (2015) used the SWAT model to determine the extreme peak and low flow conditions over snow glaciated and inland catchments and discussed about various model uncertainties in comparable manner. The authors examined model uncertainties associated with streamflow by characterizing it into extreme high (peak) flows and low flows. The streamflow was initially simulated and calibrated using the soil and water assessment tool (SWAT) model and SWAT CUP (calibration and uncertainty program) based sequential uncertainty fitting approach (SUFI2) by analyzing 14 different hydrological parameters.

Hydrological modeling using deterministic hydrological model SWAT has been reviewed significantly in this section of the chapter. Many authors have been utilized SWAT model in the historical and futuristic time series across the world and the results from the SWAT is well

TH-1643_136104018

globally accepted (Neistch et al., 2011). A few popular studies around the world utilizing various observed and downscaled GCMs for the assessment of streamflows, snowfall, snowmelt and other water balance components have been notified in the Table 2 given below:

Table 2.2: SWAT model applications in different fields of water resources.

Authors	Year	Title
Bhatt et al.	2015	Climate Change and Hill Agriculture in Northwest Himalaya.
Dahal et al.	2015	Estimating the impact of climate change on streamflow in Bagmati Watershed, Nepal.
Dakhlalla and Parajuli	2015	Evaluation of the Best Management Practices at the Watershed Scale to Attenuate Peak Streamflow Under Climate Change Scenarios.
Devkota and Gyawali	2015	Impacts of climate change on hydrological regime and water resources management of the Koshi River Basin, Nepal.
Ficklin et al.	2015	Assessing differences in snowmelt-dependent hydrologic projections using CMIP3 and CMIP5 climate forcing data for the western United States
Goyal et al.	2015	Geospatial and hydrological modeling to assess hydropower potential zones and site location over rainfall dependent Inland catchment.
Gummadi and Rao	2015	Addressing the Potential Impacts of Climate Change and Variability on Agricultural Crops and Water Resources in Pennar River Basin of Andhra Pradesh.
Gurung et al.	2015	Impact of climate change and watershed interventions on water balance and crop yield in West Seti river sub-basin of Nepal.
Guse et al.	2015	Eco-hydrologic model cascades: Simulating land use and climate change impacts on hydrology, hydraulics and habitats for fish and macroinvertebrates.
Herman et al.	2015	Impacts of Climate Change on Fish Biological Integrity within the Saginaw Bay Watershed.
Kang and Sridhar	2015	Evaluation of climate change impact on drought in Virginia.
Lee et al.	2015	Prediction of climate change impacts on agricultural watersheds and the performance of winter cover crops: Case study of the upper region of the Choptank River Watershed.
Lin et al.	2015	Evaluating Impacts of climate and land use changes on streamflow using SWAT and land use models based CESM1-CAM5 Climate scenarios
Maurer et al.	2015	Technical Note: The impact of spatial scale in bias correction of climate model output for hydrologic impact studies.
Mehdi et al.	2015	Simulated impacts of climate change and agricultural land use change on surface water quality with and without adaptation management strategies.

TH-1643_136104018

Mittal et al.	2015	Impact of Human Intervention and Climate Change on Natural Flow Regime.
Neupani et al.	2015	Projected hydrologic changes in monsoon-dominated Himalaya Mountain basins with changing climate and deforestation.
Omani et al.	2015	Impacts of climate change on the glacier melt runoff from five river basins.
Pervez and Henebry	2015	Assessing the impacts of climate and land use and land cover change on the freshwater availability in the Brahmaputra River basin.
Senzeba et al.	2015	Snowmelt runoff modelling in data scarce Nuranang catchment of eastern Himalayan region.
Singh et al.	2015	Multicriteria Evaluation Approach for Assessing Parametric Uncertainty during Extreme Peak and Low Flow Conditions over Snow Glaciated and Inland Catchments.
Uniyal et al.	2015	Assessing Climate Change Impact on Water Balance Components of a River Basin Using SWAT Model.
Verma et al.	2015	Climate Change Impacts on Flow, Sediment and Nutrient Export in a Great Lakes Watershed Using SWAT
Zhou et al.	2015	Integrated SWAT model and statistical downscaling for estimating streamflow response to climate change in the Lake Dianchi watershed, China.
Ashraf et al.	2014	Analyses of the impact of climate change on water resources components, drought and wheat yield in semiarid regions: Karkheh River Basin in Iran.
Dong et al.	2014	Relative effects of human activities and climate change on the river runoff in an arid basin in northwest China.
Ferrant et al.	2014	Projected impacts of climate change on farmers' extraction of groundwater from crystalline aquifers in South India.
Gassman et al.	2014	Applications of the SWAT model special section: overview and insights.
Hassan et al.	2014	Climate change and water availability in the Ganges-Brahmaputra-Meghna basin: impact on local crop production and policy directives.
Jha and Gassman	2014	Changes in hydrology and streamflow as predicted by a modelling experiment forced with climate models
Johnston and Smakhtin	2014	Hydrological modeling of large river basins: how much is enough?
Kulkarni et al.	2014	Assessing Hydrological Response to Changing Climate in the Krishna Basin of India

TH-1643_136104018

Mittal et al.	2014	Flow regime alteration due to anthropogenic and climatic changes in the Kangsabati River, India.
Molina-Navarro et al.	2014	Hydrological and water quality impact assessment of a Mediterranean limno-reservoir under climate change and land use management scenarios
Piniewski et al.	2014	Effect of climate change on environmental flow indicators in the Narew basin, Poland
Singh et al.	2014	Impact of water management interventions on hydrology and ecosystem services in Garhkundar-Dabar watershed of Bundelkhand region, Central India.
Wang et al.	2014	SWAT modeling with uncertainty and cluster analyses of tillage impacts on hydrological processes
Yasir et al.	2014	Sediment balances in the Blue Nile River Basin
Zhang et al.	2014	Uncertainties in SWAT extreme flow simulation under climate change.
Ficklin et al.	2013	Effects of projected climate change on the hydrology in the Mono Lake Basin
Garg et al.	2013	Hypothetical scenario–based impact assessment of climate change on runoff potential of a basin.
Jeuland et al.	2013	Implications of climate change for water resources development in the Ganges basin.
Jha et al.	2013	Regional changes in nitrate loadings in the Upper Mississippi River Basin under predicted mid-century climate
Jung et al.	2013	Possible change in Korean streamflow seasonality based on multi-model climate projections
Kalra et al.	2013	Increasing streamflow forecast lead time for snowmelt-driven catchment based on large-scale climate patterns.
Kim et al.	2013	Impacts of changes in climate and land use/land cover under IPCC RCP scenarios on streamflow in the Hoeya River Basin, Korea
Kumar et al.	2013	Climate change implications on water resources in India-review
Kushwaha and Jain	2013	Hydrological simulation in a forest dominated watershed in Himalayan Region using SWAT model.
Manandhar et al.	2013	Perturbation study of climate change impacts in a snow-fed river basin

TH-1643_136104018

Narula and Gosain	2013	Modeling hydrology, groundwater recharge and non-point nitrate loadings in the Himalayan Upper Yamuna basin.
Rahman et al.	2013	Streamflow modeling in a highly managed mountainous glacier watershed using SWAT: the Upper Rhone River watershed case in Switzerland
Shreshtha et al.	2013	Impact of climate change on sediment yield in the Mekong River basin: a case study of the Nam Ou basin, Lao PDR.
Sun et al.	2013	Effects of climate change on annual streamflow using climate elasticity in Poyang Lake Basin, China
Ahmed et al.	2012	Hydrology of mountainous areas in the upper Indus Basin, Northern Pakistan with the perspective of climate change.
Arnold et al.	2012	SWAT: Model use, calibration, and validation
Dixon and Earls	2012	Effects of urbanization on streamflow using SWAT with real and simulated meteorological data
Immerzeel et al.	2012	Hydrological response to climate change in a glacierized catchment in the Himalayas
Islam et al.	2012	Streamflow response to climate change in the Brahmani River Basin, India
Jin and Sridhar	2012	Impacts of Climate Change on Hydrology and Water Resources in the Boise and Spokane River Basins1
Kilonzo et al.	2012	Critical review of SWAT applications in the upper Nile basin countries
Luo et al.	2012	Baseflow simulation using SWAT model in an inland river basin in Tianshan Mountains, Northwest China
Mengistu et al.	2012	Sensitivity of SWAT simulated streamflow to climatic changes within the Eastern Nile River basin.
Opitz-Stapleton et al.	2012	Scientific and social uncertainties in climate change: the Hindu Kush-Himalaya in regional perspective
Pavelic et al.	2012	Role of groundwater in buffering irrigation production against climate variability at the basin scale in South-West India
Shen et al.	2012	Analysis of parameter uncertainty in hydrological and sediment modeling using GLUE method: a case study of SWAT model applied to Three Gorges Reservoir Region, China
Shreshtha et al.	2012	Modeling climate change impacts on hydrology and nutrient loading in the upper assiniboine catchment1

TH-1643_136104018

Singh et al.	2012	Comparison of soil and water assessment tool (SWAT) and multilayer perceptron (MLP) artificial neural network for predicting sediment yield in the Nagwa agricultural watershed in Jharkhand, India
Wang et al.	2012	Wang, Z., Ficklin, D. L., Zhang, Y., & Zhang, M. (2012). Impact of climate change on streamflow in the arid Shiyang River Basin of northwest China
Wu and Liu	2012	Automating calibration, sensitivity and uncertainty analysis of complex models using the R package Flexible Modeling Environment (FME): SWAT as an example.
Wu et al.	2012	Predicting impacts of increased CO 2 and climate change on the water cycle and water quality in the semiarid James River Basin of the Midwestern USA

Apart from the above considerations, it is assumed that the model parameterization and sensitivity analysis are also the necessary tasks in the accurate prediction of hydrological scenarios (Jones and Carvalho, 2014; Abbaspour et al., 2011). The detailed parameterization actually helps in the model optimization when random variables (e.g. precipitation) are associated in the model based simulation studies. The model randomness makes the hydrological process uncertain and less predictive (Abbaspour et al., 2011).In hydrological modeling, uncertainties can be introduced from various sources. Watershed model consists of deterministic description of precipitation, discharge, ET, storage and transport processes. Due to the representation of internal structure of the model, measurement errors and errors due to model structure itself lead to sequentially dependent errors in model results (Zhang et al., 2014; Abbaspour et al., 2007).Water balance models have been formulated at various time scales (e.g. hourly, daily, monthly and yearly), which vary with degrees of complexity and uncertainties (Xu and Singh, 1998).

Zhang et al. (2014) used SWAT model to calculate water balance parameters over mountainous watershed of northwest China. The outcomes of this study designated that the method was effective and feasible and the Coefficient of Determination (R^2) were greater than 0.81 and as high as 0.94 and the absolute values of the Percent Bias (PBIAS) were less than 2. The water balance in the Yingluoxia watershed showed that the mean annual precipitation, ET, and discharge of the watershed from 1990 to 2000 were optimized well. Narsimlu et al. (2013) used SWAT model for the futuristic assessment of the climate change impacts on water resources of Upper Sind River Basin, India. The model results indicated that the average annual streamflow increased by 16.4 % for the midcentury and 93.5 % for the end century. A very less numbers of studies have noticed that utilize SWAT model for the snowmelt runoff assessment (Singh et al., 2015; Ficklin and Barnhart, 2014; Narsimlu et al., 2013; Jain et al., 2010). Deb et al. (2015) worked on the sub-arctic watershed and utilized SWAT for assessing 21st century projection

TH-1643_136104018

scenarios of hydrological components. He observed the overall hydrology of the watershed is projected to remain snowmelt dominated through the mid-21st century without a major shift in regime. Ficklinand Barnhart (2014) worked on the hydrological uncertainty assessment in a snowmelt-dependent watershed utilizing SWAT and CMIP5 GCMs. He showed that hydrologic model parameterizations give comparable plenty calibration metrics, which could lead to statistically significant variations in hydrologic projections under climate change.

Calibration of a distributed hydrological model using streamflow data from a large catchment always leads to non-identifiable parameter due to strong over parameterization (Abbaspour et al., 2007). Bayesian inference operates parametric uncertainty within uncertainty domains (prior and posterior) associated with each parameter (Abbaspour et al. 2011). Parameter uncertainty is usually caused as a result of inherent non-uniqueness of parameters in inverse modeling and can be identified by the multiple objective functions (Abbaspour et al. 2011). The adaptation of inverse modeling approach is a very popular method for model calibration and uncertainty assessment using stochastic approach (Abbaspour et al., 2007; Gupta, 2003). Abbaspour (2007) demonstrated that the distributed hydrological models like SWAT (Soil and Water Assessment Tool) are often highly over- parameterized, making parameter specification and parameter estimation inevitable steps in model calibration. He used SWAT CUP based a multi-site semi-automated inverse modelling routine (SUFI-2) for calibration and uncertainty analysis. Zhang et al., (2014) studied on the understanding of the sensitivity of the SWAT model to the resolutions of Digital Elevation Models (DEMs) based on the analysis of multiple evaluation indicators. In the recent years, the hydrological modelling community has shown a strong interest in minimizing uncertainty issues through model identification and parameter estimation (Arnold et al., 2012). Several authors utilized SWAT CUP based SUFI2 and GLUE (Generalized Likelihood Uncertainty Equation) in the stochastic manner to calibrate watershed parameters and uncertainty assessment (Singh et al.,2015; Singh et al., 2013; Arnold et al., 2012; Rouholahnejad et al., 2012; Abbaspour et al., 2007)

2.7.2 Hydrodynamic models and river flow routing

Paiva et al. (2011) described the utilization of hydrological and hydrodynamic modeling in river flow and the validation using discharge and water level data shows that the model is capable of reproducing the main hydrological features of the Purus River basin. Yamazaki et al. (2012) adjusted DEM approach for floodplain hydrodynamic modeling. The DEM's accuracy was validated using hydrodynamic simulations with the LISFLOOD-FP model over the Amazon River. The simulated water surface elevations and flooded areas with the adjusted DEM shows

TH-1643_136104018

better agreement to observation data when compared to the results from the original SRTM3 DEM. Pramanik et al. (2009) worked on one dimensional hydrodynamic modeling of river flow using DEM extracted river cross-sections.

The principle of hydraulic routing of river flow has been applied to many river basins worldwide (Yamazaki et al., 2012; Pramanik et al., 2010). The space–time variation of flow and water level in the rivers are computed using St. Venant equations (Wang et al, 2006). Models such as MIKE 11HD, HEC-RAS and LISSFLOD-FP have been categorized as hydraulic models, which use the above numerical methods to compute flow and water level at different grid points along the rivers (Pramanik et al., 2010; Hunter et al. 2007; Wang et al. 2006). Loinaz et al. (2013) used hydrodynamic model and integrated flow and temperature modeling. The authors showed that a reduction of 10% in the groundwater flow in the Silver Creek Basin, has increased average and maximum temperature increases in Silver Creek over 0.3˚C and 1.5˚C. Mike 11 1D fully hydrodynamic model is capable to forecast long term water level, discharge, and flood area with their water velocities in large scale as well as small scale river watersheds (Awol et al., 2015; Zhao et al., 2012; Liu et al., 2007; Thompson et al., 2004; Havno et al., 1995).Zhao et al. (2012) studied on the MIKE SHE/MIKE 11 coupled model to simulate the dynamic exchanges between the overland flow plain in Florida. Yazdi and Neyshabouri (2012) used Mike 11 for the flood management at catchment scale and coupled Mike 11 with the NSGA-II multi-objective optimization model to provide the optimal Pareto solutions between two conflict objectives of minimizing the investment costs of flood mitigation measures and the potential damages of the floodplain.

2.8 CONCLUSION OF LITERATURE REVIEW

As per the IPCC AR5, because of climate change, water scarcity will be enhanced in the future. Extreme events will be more frequent in near future and the intensity and volume of precipitation and stream flow will also be increased in the coming years, especially over the Himalayan regions. As per the detailed literature, many studies across the world revealed that global average annual temperature has been increased in the last 100 years and it could be more in the 21st century as per opted in the latest CMIP5 GCMs and their emission scenarios. The warming trend of the surface and air temperature will increase the precipitation variability and this could be more severe in the 21st century last decades. Many authors reported that due to the temperature increase, glaciers are retreating. The snowmelt rate is getting faster than actual and earlier melting is also reported. Several authors also reported less precipitation as snowfall and increase precipitation as rainfall.

TH-1643_136104018

As per detailed literature review, the current study area is critically studied. Therefore, for this study, a Teesta river catchment has considered for the hydrological and hydrodynamic assessments. For the computation of snowmelt and snowpack using hydrological model SWAT, an elevation band approach has been applied at sub-catchment scale. The contribution of snowmelt and snowpack have been assessed at both point scale and spatial scale in historical and future time, which provide a significant scope of the study. As per literature review, most of the researchers used constant TLR and PLR for snowmelt calculation, which is not so much effective. The monthly variation in the TLR and PLR can improve snowmelt runoff computation. Snowmelt runoff computation using SWAT has been evaluated by various researchers around the world. However, a very few found several difficulties in the separation of snowmelt contribution from glaciated region and non-glaciated region. A glacio-hydrological model (GSM-SOCONT) model has been applied by Schaefli et al. (2005) can be utilized for the separation of snowmelt contribution from glaciated region and non-glaciated region. However, this model is initially developed for the Alpine river catchments and thus, several modifications are needed before applying it for Himalayan catchment studies.

For runoff computation, most of the researchers used single slope method in SWAT model. As per literature review, it has been concluded that for the hilly terrain catchments, the modification in curve numbers (CNs) are required as per slopes to minimize the errors. Mishra et al. (2014) produced a modified CN formula and adjusted the CNs based on the slope coefficient. These modifications in CNs can improve the modeling results. The hydrological models have been used by various researchers for the simulation and projection of various water balance components. As per literature review, a Mike 11 hydrodynamic model also utilized by various researchers for flood routing and development of rating curves but Mike 11, alone, cannot be used for the projection of water quality and other hydrodynamic variables. Thus an integrated approach could be useful for the simulation and projection of various hydrodynamic variables such water level, discharge, rating curves and water velocity.

TH-1643_136104018

CHAPTER 3

STUDY AREA AND DATA USED

3. 1 TEESTA RIVER AND ITS MAJOR TRIBUTARIES

For this research work, a Teesta river catchment (up to Chungthang gauge station the area is about 2587.4 km^2), part of north Sikkim Himalaya, Sikkim state of India, has been selected. Lachung is one of the major tributaries of Teesta river, selected for the study. Chungthang and Lachung are the two gauge stations have taken as outlet of the Teesta and Lachung river, respectively (Fig. 3.1). The upstream portion of the Teesta river catchment is mostly covered by snow and glaciers and thus the upstream portion (up to Chungthang gauge) has been selected for the study. The origin point of the Teesta river is Chhombo Chhu from a glacial lake namely Khangchun Chho at an elevation of 5280 meter, north Sikkim eastern Himalayas. The Khangchung Chho glacial lake is situated at the terminus of the Teesta Khangse glacier downwards from the peak of Pauhunri glacier at 7056 meter in north western direction. Several studies reported that Teesta Khangse and Chho Lhamo glaciers are the main sources of Teesta river (Krishna, 2005). The Teesta river, from its origin to plain, contributes and fedded by many small and large tributaries. Many shorter course streams are meeting the Teesta river on eastern flank, while the larger tributaries meet western flank (Table 3.1). The right bank tributaries drains are covered by significant amount of snow cover and glacier areas. On the other hand, the left bank tributaries originate from semi-permanent and much smaller snow fields as compared to right bank tributaries. The main tributaries of river Teesta have shown in Table 3.1.

The stream network of Teesta river catchment can be categorized into different sub-river systems such as:(a) Teesta river upstream of Zemu-Chhu-Teesta confluence, (b) Zemu Chhu, (c) Teesta river between Chungthang and Lachen towns, (d) Lachung Chhu, (e) Chungthnag-Mangan and Chakung Chhu sub-system, (f) Rangyong Chhu, (g) Dik Chhu, (h) Teesta river between Mangan and Singtam, (i) Rani Khola, (j) Teesta river between Teesta-Rani Khola confluence and Teesta-Rangpo Chhu confluence, (k) Rangpo Chhu, (l) Rangit river and (m) Jaldhaka river. A Teesta river, after traveling about 40 km distance in Sikkim state of India, it enters into West Bengal state of India. After perambulating a length of around 414 km in Indian and Bangladesh, finally it joins the Brahmaputra river in Bangladesh. The average depth of river

TH-1643_136104018

varies from 1.8 meter to 4.5 meter in India (Bawa and Ingty, 2012). The average maximum velocity of the river flow recorded around 8.5 meter/second at several locations along the Teesta river from upstream to downstream (Rahman et al., 2010). The river banks are highly steep and sloping as observed according to the river flow velocity.

Table 3.1: Teesta river tributaries.

SI. No.	Right-Bank tributaries	Left-Bank Tributaries
1	Lachung Chu	Zemu Chhu
2	Chakung Chu	Rangyong Chhu
3	Dik Chhu	Rangit river
4	Rani Khola	
5	Rangpo Chhu	

3.2 HYDROLOGICAL CHARACTERISTICS OF TEESTA CATCHMENT

Hydrological assessment of a river basin is an important element for planning, management and development of water resources for many purposes. The state of Sikkim, especially north Sikkim district, is characterized with enormous water resources available through snow and glaciers. Teesta is classified as a perennial river channel with substantial streamflows even in the lean season. The river streamflows generally in North South direction bisecting the State of Sikkim. Teesta river is the single major river in the State which drains about 95 % of the total area of the State.

A massive fall of the order of 3,300 m over a river stretch of 175 km. makes this river an ideal and reliable source of hydropower (Krishna, 2005).

TH-1643_136104018

TH-1643_136104018

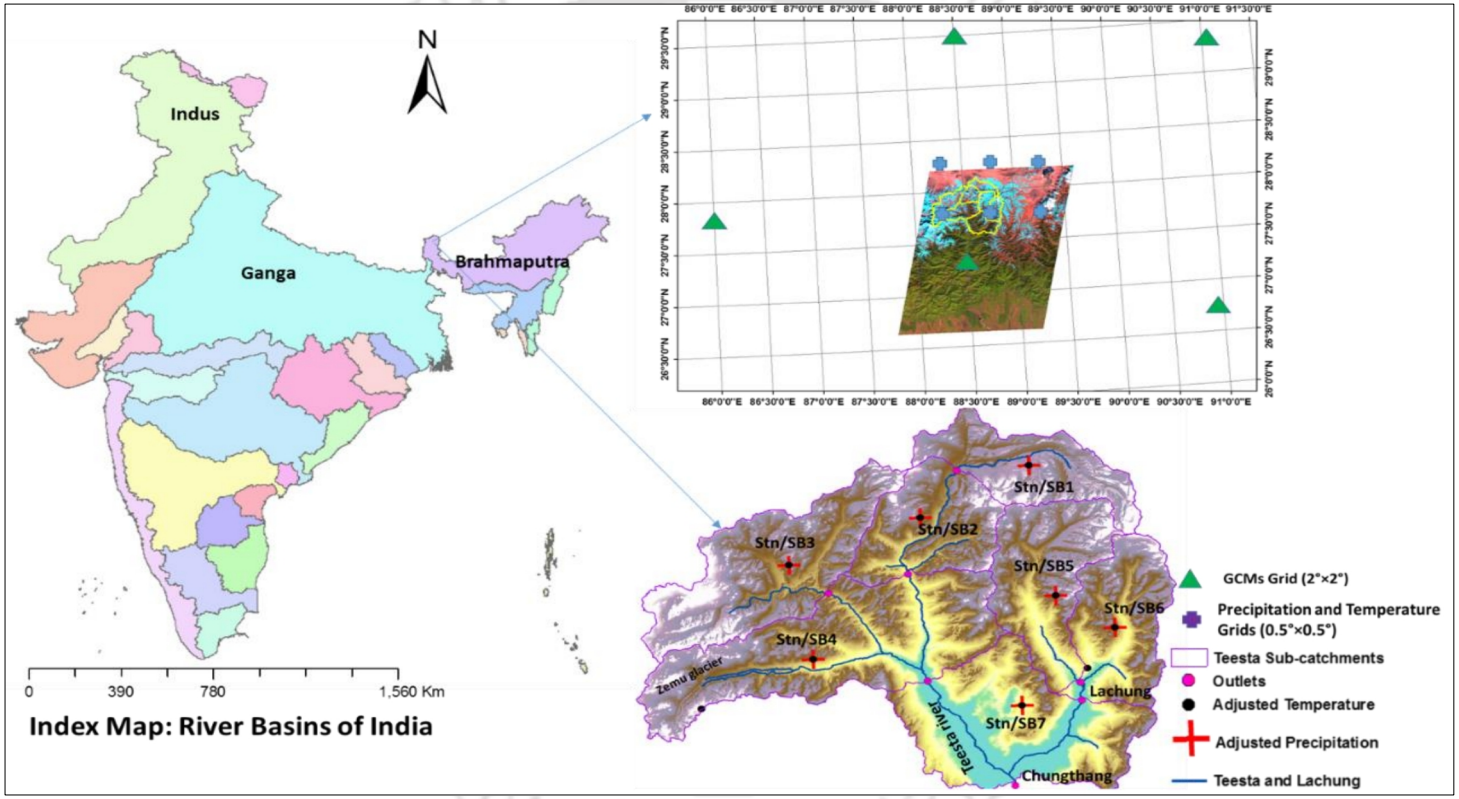


Fig. 3.1: Study area map showing Teesta catchment's profile and their meteorological observation details.

However, in the upper part of the Sikkim i.e. north Sikkim area, the establishment of additional hydro-meteorological networks for collecting the gauge, discharge and precipitation data to estimate the water availability in the Teesta valley for development of power could be beneficial for the future water requirements. Over the Teesta river catchment, the collection of discharge data during the lean as well as monsoon seasons is equally important to assess the negative and positive hydrological consequences.

3.3 SNOW COVER AND GLACIER MORPHOLOGY OF TEESTA CATCHMENT

As per the State of Environment (2007)-Sikkim, around 84 glaciers have been listed in the Teesta river catchment (Raina and Srivastava, 2006). The upstream portion of the Teesta river has perennial high permanent snow fields and glaciers. The total glacial area is recorded around 440.24 km^2. The total permanent snow cover was estimated around 251.224 km^2. The total glacial and snow cover (permanent) stored water in Teesta catchments is calculated as 145.05 cu Km (Raina and Srivastava, 2006) (Fig. 3.2). The average altitude of snow line is computed as 5039 meter. Zemu glacier has been identified as the longest and largest glacier over the Teesta river (Table 3.2), which followed by mainly Talung, Changsang and others (Krishna, 2005).

Table 3.2: Teesta glaciers and their details (Source: Krishna, 2005).

Glaciers	Snout Altitude (m.s.a.l.)	Max Ele. (m.s.a.l.)	Equilibrium Area Line (m.s.a.l.)	Length (m)	Width (m)	Slope trend
Zemu	3970	5300	4635	20550	3300	SE-EEN
Talung	3700	5050	4375	12750	1800	NW-NE
Changsang	5375	5800	5587.5	8850	1350	WWS-EEN
Tongshiong	4150	5050	4600	5700	1050	NW-SE
Onglakthang	4820	5150	4985	4650	600	NW-S
Jumthulphuk	3900	4550	4225	6750	900	NNW-EES
East Rathong	4475	5100	4787.5	4500	750	NW-SE
Simvo	4875	5650	5262.5	1800	525	SE-NW
Siniolchu	4475	5200	4837.5	4650	450	SSW-NNE
Twin	5200	5725	5462.5	4800	450	W-EES
Lhonak North	5225	5950	5587.5	4800	600	NW-SE
Lhonak North	5225	5950	5587.5	4650	750	WWS-EEN
Umramkhang	3750	4400	4075	6300	525	NNW-SSE
South Simvo	5150	5900	5525	4425	525	NW-SSE
TistaKangse	5350	6350	5850	4950	675	SSW-N

TH-1643_136104018

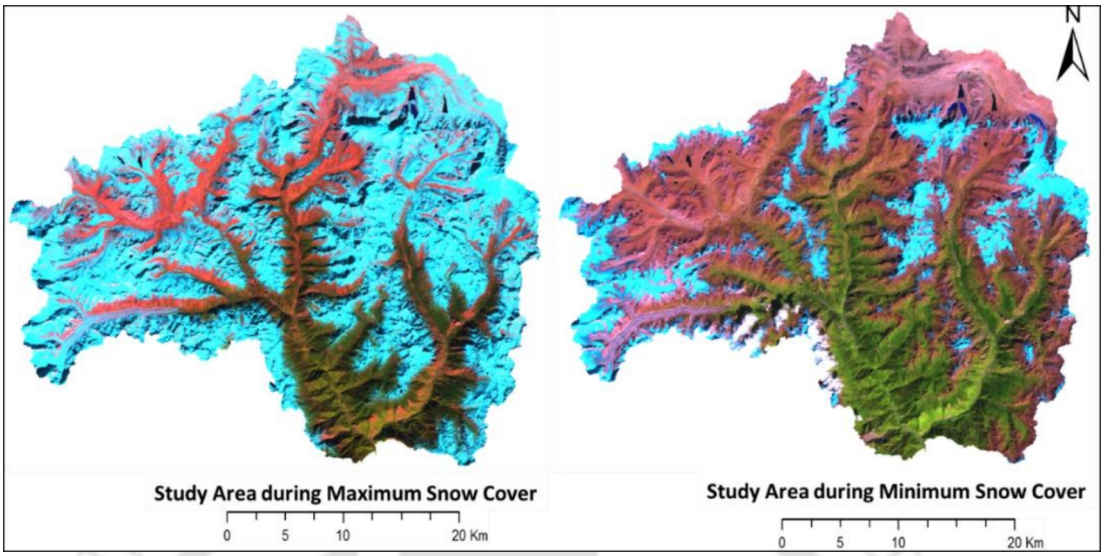


Fig. 3.2: Maximum and minimum snow cover in study area.

3.4 METEOROLOGICAL CHARACTERISTICS OF TEESTA CATCHMENT

The Teesta river catchment influences by mainly southwest monsoon, which normally sets around mid-June and withdraws by end of September. The average annual precipitation in Sikkim is about 2534 mm. The Teesta basin upstream portion is mainly fed by snowfall during winters and the downstream portion is fed by rainfall in summer and snowfall in winter. Due to the high altitudinal variations over the upstream catchment parts of Teesta river, the meteorological factors (e.g. temperature and precipitation) show high variability across the sub-catchments. In this research work, the whole Teesta catchment is not considered for the study and evaluation. The Teesta upstream portion, which corresponds up to Chungthang at the point where Teesta and Lachung meet, has been considered for the study.

The Teesta river catchments receives around 75% of the rainfall during monsoon season (June to October). The Teesta river catchment receives highest precipitation in the July and August, while the maximum snowfall receives during February and March months. The spatial and temporal variations in the precipitation also observed in the Teesta river catchment (Fig. 3.2). The average precipitation over the selected study region has been shown in Fig. 3.3.

TH-1643_136104018

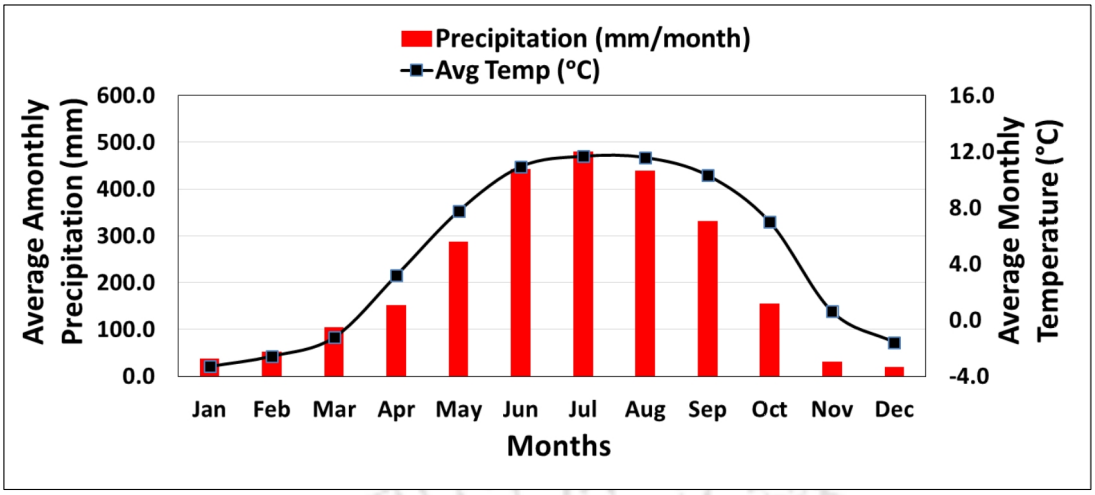


Fig. 3.3: Average monthly precipitation and temperature over the selected study area.

The temperature is highly variable over the Teesta river catchment due to its high variable topography. The upstream portion corresponds to extreme higher altitudinal zones than lower catchment portion. Thus, Temperature Lapse Rate (TLR) significantly varied over the catchment. The mean monthly temperature variations over the selected study region has been shown in Fig. 3.3. The mean daily Relative Humidity also significantly varied over the Teesta river catchment. It varies from 63.9% to 88.7% over the catchment.

3.5 GEOGRAPHICAL AND TOPOGRAPHICAL CHARACTERISTICS OF TEESTA CATCHMENT

For the current study, Teesta river catchment (up to Chungthang) has been considered for the study. This portion of the study area mainly comprises with snow covers and glaciers. At the Chungthang town, the river Lachung meets the river Teesta. The geographical extents of the selected study area fall between Latitudes 27° 30′ to 28° 30′ N and Longitudes 87° 30′ to 89° 30′ E. The upstream portion of the Teesta river catchment part of north Sikkim Himalaya is fully sheltered by rugged terrain including mountain and hills. The glacier of this region comprised an enormous amount of uninterrupted snow and ice and are found to create many glacial lakes, which are also quite susceptible to disastrous hazard due to glacial Lake Outburst Flood (GLOFs).

The glaciers and water bodies including glacial lakes especially in the upstream portion of the catchment, part of north Sikkim, are the reserves of fresh water which benefits millions of people in the downstream. The landuse/landcover (LULC) and soil maps have been prepared only for the selected study basin. The topographical, LULC and soil characteristics of the selected study area have been shown in Figs. (3.4 and 3.5).

TH-1643_136104018

The upstream portion of the Teesta river of north Sikkim eastern Himalayas shows a wide range of soil and vegetation diversity. These soils have been categorized as per the slope steepness (NBSSLUP, State of Environment 2007-Sikkim). Formation of soils on side slopes is influenced by the steepness of the slope. In the extreme high elevation, throughout the year, whole area is generally covered by snow and glaciers. In these regions the soil temperature is low.

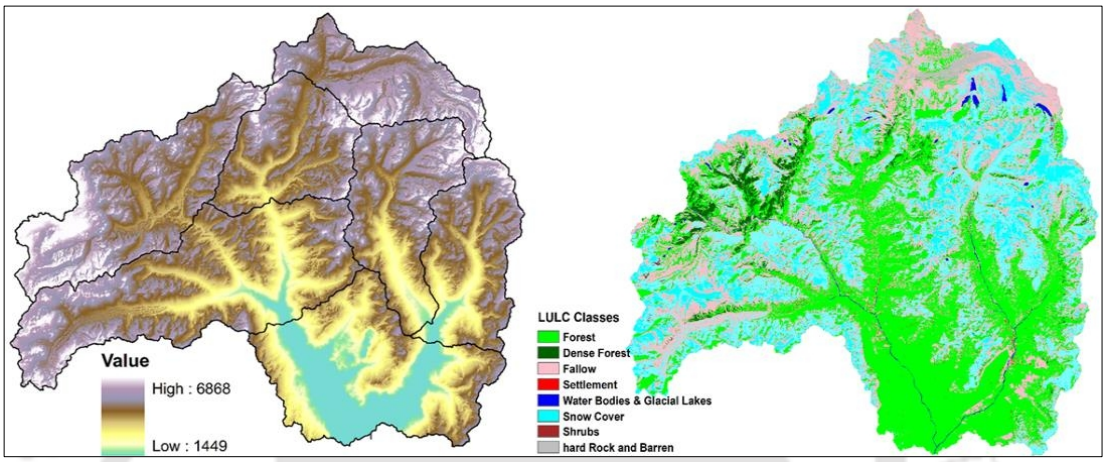


Fig.3.4: Digital elevation model showing elevation variations in study area.

Valley of the Teesta river are very narrow with moderate to high steep slopes (15-30%). The LULC map is prepared from the IRS (Indian Remote Sensing Satellite) LISS 3 sensor data sets for the period of 2014 (Fig. 3.4). The soil maps is taken from the FAO (Food and Agricultural Organization, USA) (at 1.250000 scale) (Fig. 3.5) and then re-corrected as per the State of Environment 2007-Sikkim.

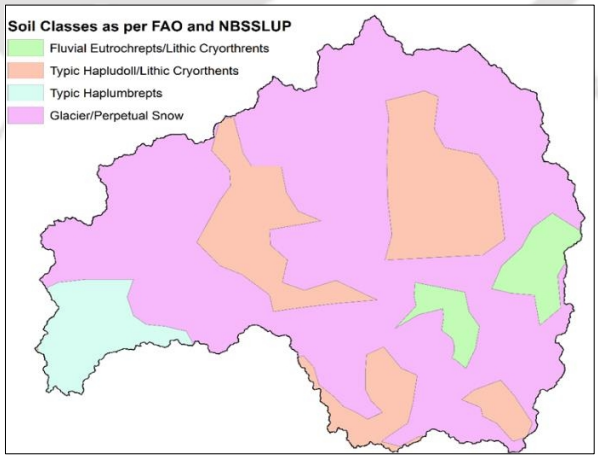


Fig.3.5: Soil map of the study area (FAO, 2005).

TH-1643_136104018

3.6 STREAM CHANNEL CHARACTERISTICS

Teesta river catchment represents a unique and diverse drainage characteristics. Teesta drainage channels corresponded with river deposits and fluvioglacial processes in the north Sikkim eastern Himalayan terrains have been processed for more than decades. The Teesta river catchment and their landforms include canyons at different altitudes, asymmetric valleys, U-shaped valleys and steps, lakes, alluvial cones, truncated ridge-spurs, terracettes, rectangular barbed trellised radial subdendric drainage channels. The Teesta river corresponded to rain in the summer and spring months, while it receives snow during the winter months (October - April). The upstream extreme high hilly (elevation >5039 meter) terrains of the catchment is covered with snow (Raina and Srivastava, 2006).

The Teesta river catchment represents a complex hydrographic networks of branching streams in the hierarchical order form such as Andherijihora tributary, while the main stream i.e. Teesta river shows trunk stream network. The Teesta river catchment corresponded with water bodies and glacial lakes. The three kind of stream channels have been categorized in the Teesta river catchment as per their surface drainage system: (i) precipitation of moisture or rainfall and flowing in accordance with the varied topography, (ii) drainage noticeably restricted along these streams, especially during dry or non-dry periods and (iii) the static water bodies and glacial lakes. The water surface runoff is mainly corresponded with rainfall. However their flow velocities vary at different sections of the stream channel (Raina and Srivastava, 2006).

The Teesta drainage represented both physical and cultural environments in the course of geo-ecological alteration of those Himalayan geo-complex like climate, structure, vegetation, soil, topography or other terrain factors determining the rapidity of runoff. The Teesta basin has per-humid climate in Sikkim, which can be characterized by enormous water surpluses. The prevalent monsoon climates of the Teesta river catchment supports evergreen rainforests including grasses and in some parts of middle Teesta basin, it is characterized by dense and luxuriant vegetation. In the last several years, due to adverse influence of the climate and variable monsoon activity, the precipitation recorded much greater than normal (Bawa and Ingty, 2012).

3.7 DATA USED

3.7.1 Observed hydro-meteorological datasets

TH-1643_136104018

A high-resolution daily gridded precipitation (0.5°×0.5°) and daily gridded temperature (1°×1° and 0.5°×0.5°) datasets for the period of 1980 to 2005 (around 26 years) are available at Indian Meteorological Department (IMD) and Indian Institute of Tropical Meteorology (IITM) India. These 26 years datasets are utilized for the downscaling as per availability. This dataset is prepared from quality-controlled observed precipitation/rainfall data from more than 1800 gauges and is increasingly being used in studies on the Indian and Himalayan continents (Subas and Sikka 2014). Apart from this, two gauge stations such as Lachung and Chungthang point source measured daily precipitation dataset (1980-2005) are also available and thus, utilized for the study.

Initially, the whole study area catchment was divided into seven sub-catchments. Each sub-catchment has varied topography and climatology (Fig. 3.4). Thus, there are seven climate stations such as Chopta valley (Stn1/SB1), Thangu (Stn2/SB2), Muguthang (Stn3/SB3) Lachen (Stn4/SB4), Yumthang (Stn5/SB5), Lachung (Stn6/SB6) and Chungthang (Stn7/SB7) were derived as per the delineated sub-catchments. These climate stations were chosen to highlight the local climate variations over the selected study region, part of north Sikkim eastern Himalaya (Table3.3). At Lachung and Chungthang gauge stations, daily point source observed discharge data sets were available for the year1991 to 2005 at Central Water Commission (CWC), India and hence, utilized for the study.

Table 3.3: Climate Zones and their elevation across the study area i.e. eastern north Sikkim Himalayas.

Climate Zones	Area (Sq.km)	Elev. Min (m)	Elev. Max (m)	Elev. Mean (m)	Centroid Elev. (m)	LAT	LONG
Chopta Valley (Stn1)	238.46	4714	6652	5633	5283	28.035	88.704
Thangu (Stn2)	265.02	3777	6705	5219	4920	27.969	88.556
Mugithang (Stn3)	311.76	4382	6878	5588	5275	27.911	88.378
Lachen (Stn4)	306.27	3006	6679	4790	4897	27.850	88.727
Yumthang (Stn5)	721.8	2612	7392	4970	4909	27.777	88.401
Lachung	269.03	2675	6338	4494	4683	27.801	88.802

TH-1643_136104018

(Stn6)							
Chungthang (Stn7)	475.06	1495	5442	3441	3566	27.698	88.672

3.7.2 CMIP5 GCMs and RCPs

CMIP5 (as per IPCC 2013/14) model runs incorporate substantial changes that are associated with the use of Representative Concentration Pathways (RCPs) to characterize alternative future greenhouse gas emissions scenarios (Zhang et al. 2014) in contrast to the previous SRES (Special Reports on Emission Scenarios) (Kharin et al. 2013; Zhang et al. 2014; Taylor et al. 2012). The estimated radiative forcing values by the year 2100 are 2.6 Wm^{-2} in the RCP2.6 experiment, peaking at about 3 Wm^{-2} before 2100 and declining afterwards, and 4.5Wm^{-2} and 8.5Wm^{-2} in the other two experiments considered here, RCP4.5 and RCP8.5 (Taylor et al. 2012). Moreover, the CMIP5 models include the standard Climate System Models (CSMs) as used in CMIP3 (albeit mostly with updates, including higher spatial resolution) which incorporate additional biogeochemical components (e.g. aerosols, chemistry, and dynamic vegetation) (Zhang et al. 2014; Taylor et al. 2012).

The five GCM grid (2.5°×2.5°) points surrounding the study region were selected as the spatial domain of the 16 most relevant predictors (Zhang et al. 2014; Taylor et al. 2012) to adequately cover the various circulation domains of the predictors considered in this study (Fig. 3.1). For the point scale downscaling of GCMs predictor at each climate station, an Inverse Distance Weightage Approach (IDWA) (Lu and Wong 2008; Snell 1998; Snell et al. 2000) was performed (Kharin et al. 2013; Goyal and Ojha 2011). The IDWA method interpolates the GCM grid points (predictors), as per the weighted average of each grid point, at the known observed gridded points (predictands). The utility of this interpolation algorithm was examined in previous downscaling studies (Goyal and Ojha 2010; Ghosh and Mujumdar 2008).

After the spatial interpolation of observed meteorological variables (1980-2005), we performed the downscaling of CMIP5 ESM-2M, CM2P1 and CM3 with their RCP experiments (2006-2100) based GCM datasets at each climate station. The observed datasets used as the predictands and AMIP used as controlled scenarios (1980-2005) as per the CMIP5 GCMs. The downscaling performed to generate the point source daily precipitation, daily minimum and maximum temperature scenarios in the 21st century (2006-2100), at each sub-catchment (SB) and climate stations (Stn). CMIP5 model runs incorporate substantial changes that are

TH-1643_136104018

associated with the use of RCPs to characterize alternative future greenhouse gas emissions scenarios (Zhang et al. 2014) in contrast to the previous SRES (Special Reports on Emission Scenarios) (Kharin et al. 2013; Zhang et al. 2014; Taylor et al. 2012).

3.7.3 Remote sensing satellite datasets

The remote sensing satellite datasets such as MODIS (MOD09A1 Terra/Aqua cloud free & MOD10A2 classified 8 daily snow cover products), LANDSAT 7 (with all available bands), LANDSAT 8 (with all available bands) and IRS LISS 3 (with all available bands) have been used for the study. The MODIS and Landsat datasets collected from the Earth Explorer Web portal NASA (www.earthexplorer.usgs.gov). The IRS P6 (Resourcesat-1 Satellite Mission Payload 6) LISS 3 during 2009 to 2014, for various months, have been purchased from National Remote Sensing Centre (ISRO), India.

The other Landuse, Soil data sets and meteorological datasets (e.g. daily humidity, daily net radiation and daily wind speed) have been downloaded (www.*rda.ucar.edu/datasets/ds093.1/)* from the SWAT (Soil and Water Assessment Tool) Web Portal (*www.swat.tamu.edu*). The high resolution Digital elevation Model (DEM) with 30 meter and 10 meter spatial resolution have been opted from the BHUWAN portal, ISRO (Indian Space Research organization), India. Various hydraulic river cross sections, snow density, snow water equivalent and LULC ground truth data have been collected from the field measurement. The remote sensing satellite datasets details have shown in the Table 3.4 and Table 3.5.

Table 3.4: Band details of the Landsat and LISS 3 sensors.

Sensors	Band No.	Bands Name	Bands Abbreviation
Landsat 7	Band 1	Blue	B
	Band 2	Green	G
	Band 3	Red	R
	Band 4	Near Infra Red	NIR
	Band 5	Middle Infra Red	MIR
	Band 6	Thermal Infra Red	TIR
	Band 7	Short Wave Infra Red	SWIR
	Band 8	Panchromatic Band	PB
Landsat 8	Band 1	Coastal Aerosol	CA
	Band 2	Blue	B
	Band 3	Green	G

TH-1643_136104018

	Band 4	Red	R
	Band 5	Near Infra Red	NIR
	Band 6	Short Wave Infra Red 1	SWIR 1
	Band 7	Short Wave Infra Red 2	SWIR 2
	Band 8	Panchromatic Band	PB
	Band 9	Cirrus	Cirrus
	Band 10	Thermal Infra Red 1	TIR 1
	Band 11	Thermal Infra Red 2	TIR 2
LISS 3	Band 1	Green	G
	Band 2	Red	R
	Band 3	Near Infra Red	NIR
	Band 4	Short Wave Infra Red	SWIR

Table 3.5: The row/path and date acquisition details of LISS 3 and Landsat sensors images.

Years	Row/Path	2009	2010	2011	2012	2013	2014
LISS 3	107-51, 107-52	1-10-2009, 10-03-2009	20-10-2010, 11-04-2010	08-11-2011, 06-04-2011	26-11-2012, 07-03-2012	29-10-2013, 26-03-2013	23-10-2014, 21-03-2014
Landsat 7	139-041	05-11-2009	07-11-2010	NA	NA	NA	NA
Landsat 8	NA	NA	NA	08-11-2011	08-10-2012	11-10-2013	07-11-2014

TH-1643_136104018

CHAPTER 4

CMIP5 GCMs DOWNSCALING

4.1 DOWNSCALING OF PRECIPITATION AND TEMPERATURE

The whole selected catchment area is classified into seven climate stations (Stn)/sub-catchments (SB) such as Chopta valley (Stn1/SB1), Thangu (Stn2/SB2), Muguthang (Stn3/SB3) Lachen (Stn4/SB4), Yumthang (Stn5/SB5), Lachung (Stn6/SB6) and Chungthang (Stn7/SB) as per their topographical variations. This division of catchment into seven climate stations actually highlights the local climate variations of the Teesta upstream portion part of north Sikkim eastern Himalayas, based on their topographical significant (Chapter 3, Table 3.3). The division of the whole catchment area into seven sub-catchment/climate stations have been performed into SWAT model. Then the GCMs were interpolated for each climate station with reference to precipitation and temperature datasets. Initially, the observed daily gauge and gridded precipitation and minimum (Min)-maximum (Max) temperature datasets (1979-2005) have been interpolated at each catchment scale. The two gauge stations such as Lachung and Chungthang based measured (observed) /historical (1979-2005) precipitation datasets used directly without any interpolation.

4.1.1 Spatial interpolation of observed data sets

A high-resolution daily gridded precipitation (0.5°×0.5°) and daily gridded temperature (0.5°×0.5° and 1.0°×1.0°) datasets for the period of 1979 to 2005 are prepared from quality-controlled observed precipitation/rainfall data sets from more than 1800 gauges. Two gauge stations such as Lachung and Chungthang point source measured daily precipitation datasets (1979-2005) are utilized as per the availability. All seven climate stations such as Chopta valley (Stn1), Thangu (Stn2), Muguthang (Stn3) Lachen (Stn4), Yumthang (Stn5), Lachung (Stn6) and Chungthang (Stn7) were chosen to highlight the local climate variations over eastern Himalayan regions together with global scale climate variables. The spatial interpolation has been carried out using Inverse Distance Weighted Approach (IDWA) (Lu and Wong, 2008; Snell, 1998) to maintain the spatial significance of the variables. The whole methodology is shown in Fig. 4.1.

The equation is given below (Eq. 4.1)

TH-1643_136104018

$$Z_j = \frac{\sum_i \frac{Z_i}{d_{ij}^n}}{\sum_i \frac{1}{d_{ij}^n}} \ldots\ldots\ldots\

the sub basin meteorological station (Z) and each elevation band (Z_B) multiplied by the lapse rate of (˚C/km) per event (T) (Neistch et al., 2011) (Eqs. 4.5 and 4.6).

$$T_B = T + (Z_B - Z)\frac{dT}{dZ} \quad \text{..... (4.5)}$$

$$\frac{dT}{dZ} = -\alpha \quad \text{..... (4.6)}$$

where, $\frac{dT}{dZ} = -\alpha$ is the mean local lapse rate (T_{laps}) and can be calculated for all the stations.

4.1.2 Statistical-stochastic downscaling model (SDSM)

Statistical downscaling (SD) methods produce empirical/statistical links among the large-scale and local-scale variables. SD is not only useful in numerical weather prediction and synoptic climatology, but is also applied for a wide range of climate applications (Mahmood and Babel, 2012). The main advantage of SD is that it provides local-scale information, which is very useful in climate change impact assessment studies. On the downside, the main disadvantage of this approach is that it requires long historical meteorological weather station data to construct an appropriate link with large-scale variables.

The SDSM downscaling tool implies on empirical relationships between the local-scale predictands and large-scale predictor(s) (Willby et al., 2014; Wilby et al., 2006). It is developed by Robert L. Wilby based on the visual basic 6.0 coding platform (for the detailed methodology see Wilby et al., 2014). SDSM can be classified as a conditional weather generator in which regression equations are used to estimate the parameters of daily minimum-maximum temperature and precipitation rate and amount, separately, so it is slightly more sophisticated than a straightforward regression model.

The main feature of the SDSM tool is to provide the station-scale climate information from GCM-scale output. The large-scale variable fields from GCMs or reanalysis data (the predictors) are chosen such that they are strongly related to the local scale conditions of interest (the predictands or response variable) (Goyal and Ojha 2010).

4.1.3 Selection of predictor variables

Because of the linear concepts of SDSM, the selection of predictors was performed based on the correlation and partial correlation analysis between the interested predictands and the predictors, and weights of the predictors which are estimated via ordinary least-square method (Willby et al., 2014; Mahmood and Babel, 2012). Among the 16 predictors, the negatively correlated predictors were dropped. Thus out of 16 GCM predictors, finally 12 best correlated predictors were selected for the study.

TH-1643_136104018

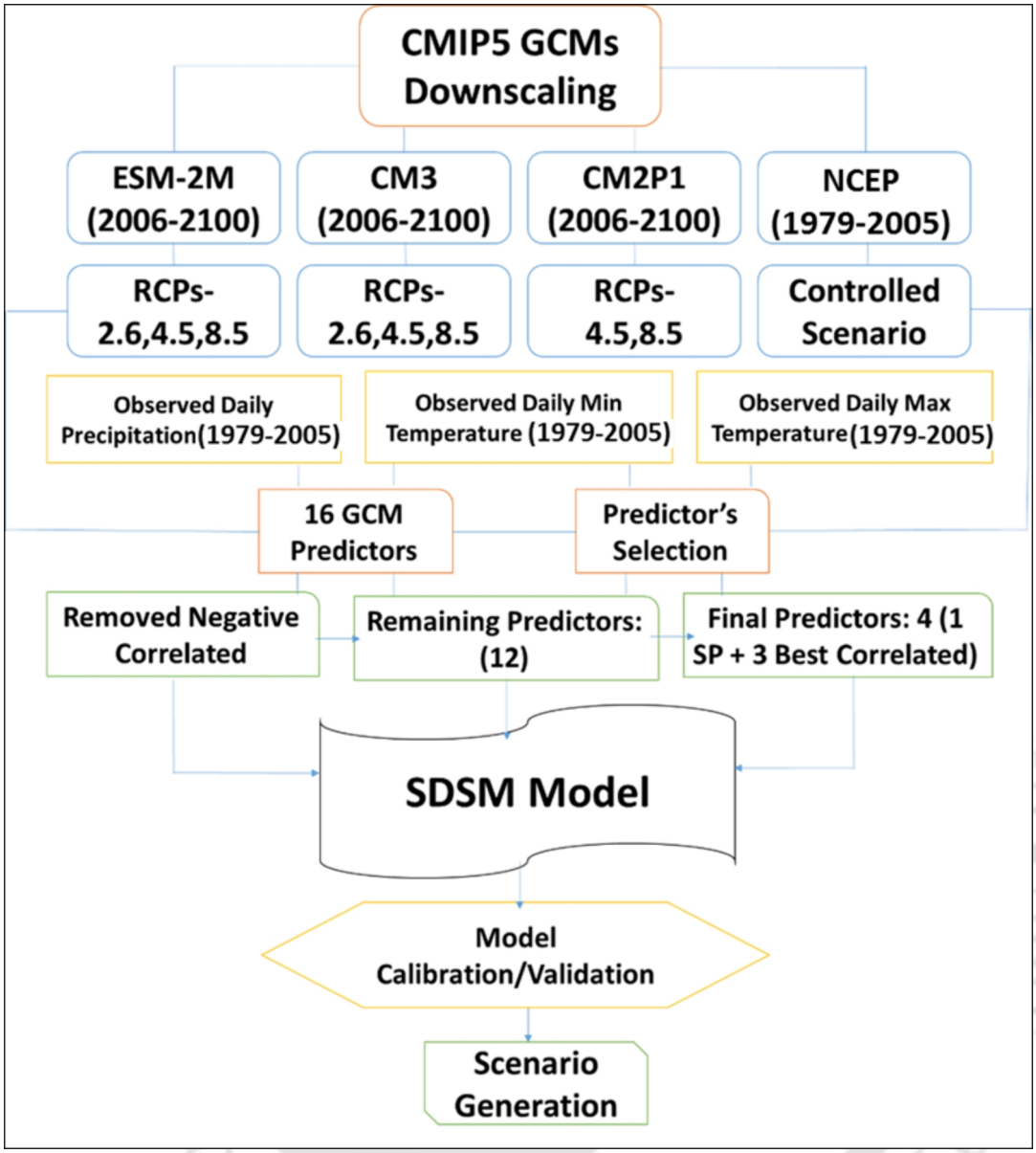


Fig4.1: Flow diagram of CMIP5 GCMs downscaling steps.

To select the first and most suitable large scale variable is relatively easy, though the judgment of the second, third and fourth and so on is much more subjective. Thus, a more quantitative method is performed for screening large scale variables for each local scale variable at each of the climate stations.

First a correlation matrix between 16 AMIP/NCEP predictors and the predictand is prepared. Then the predictors of high correlation coefficient (12 in this case) were taken and arranged in descending order. Out of 16 predictors, the negative correlated predictors have dropped for the analysis and thus 12 positive correlated predictors are selected for the study. The first ranked predictor, having the highest correlation coefficient among others, is

TH-1643_136104018

selected and defined as the first suitable super predictor (FSSP). After this the absolute correlation (R) between predictor and predictand, and the correlation coefficient between individual predictors are also calculated. Then the other highly correlated predictors (for precipitation it is 0.5 and above, and for temperature it is 0.7 and above in this case) are taken out in order to remove any multi-co-linearity (Table 4.1). The correlation coefficient up to 0.7 between two predictors is acceptable (Mahmood and Babel, 2012).

The selection of the second, third and so on AMIP predictors was performed using percentage reduction in an partial correlation (PRP) with respect to absolute correlation is calculated for each predictor (Mahmood and Babel, 2013). The PRP is the percentage reduction in partial correlation with respect to correlation coefficient. The predictor which has a minimum PRP in partial correlation (Table 4.2) is selected as the second most suitable predictor. As a result, this predictor has almost no or a very insignificant multi-co-linearity with the FSSP. The third, fourth and following predictors could be obtained by repeating the same procedure.

4.1.4 Scenario generation

For the 21st century (2006-2100) scenario generation, the combined calibration/validation of SDSM model is performed using daily observed minimum and maximum temperature, and precipitation datasets (predictands) with AMIP/NCEP controlled predictors (1979-2005). For the model calibration and parameterization, SDSM is developed on the monthly sub-models. The model performance is evaluated using multiple well know and best utilized statistical evaluation methods such as R, coefficient of determination R^2, Root Mean Square Error ($RMSE$), Mean and Standard Deviation (σ) (Hamilton, 1994). The conditional sub-model is used for maximum and minimum temperature without any transformation and unconditional sub-model for precipitation with fourth root transformations. R is used for the predictor selection. Based on R, the partial R is calculated.

With the developed models, maximum temperature, minimum temperature and precipitation are simulated for 1979-2005 using AMIP predictors. Total 25 ensembles are generated using the monthly SDSMs and the mean of these ensembles is used in the study. The R^2, mean SD and RMSE are used for the accuracy estimation. The above performance indicators are calculated for each climate stations. In this study, the monthly mean simulated data for precipitation variable, and daily simulated data for minimum and maximum temperature variables computed by both models utilizing AMIP/NCEP predictors, are plotted against the observed datasets. After successful calibration of the models, 21st century scenarios (2006-2100), as per their RCP experiments, are generated.

TH-1643_136104018

TH-1643_136104018

Table 4.1: Predictor details with statistics.

Variables	Stns	Statistics	hfls	pr	prc	rhs	rhsmax	rhsmin	rlds	sfcwind	tas	tasmax	tasmin	vas
Precipitation	Stn1	R	0.38	0.52	0.32	0.29	0.21	0.31	0.41	0.11	**0.62**	0.41	0.42	0.24
		Partial r	0.03	0.01	0.01	-0.03	0.01	0.04	0.01	0.01	-0.02	0.04	0.04	0.00
		PRP	-0.91	-0.97	-0.97	-1.10	-0.95	-0.88	-0.98	-0.95	-1.04	-0.91	-0.90	-1.00
	Stn2	R	0.37	0.31	0.32	0.28	0.20	0.30	0.40	0.10	0.42	0.40	**0.42**	0.24
		Partial r	0.03	0.01	0.01	-0.02	0.01	0.03	0.01	0.01	-0.02	0.03	0.05	0.00
		PRP	-0.93	-0.97	-0.97	-1.09	-0.96	-0.89	-0.99	-0.95	-1.04	-0.93	-0.88	-0.99
	Stn3	R	0.37	0.31	0.31	0.27	0.19	0.30	0.40	0.10	**0.53**	0.40	0.42	0.24
		Partial r	0.03	0.02	0.01	-0.02	0.00	0.03	0.01	0.00	-0.02	0.03	0.05	0.00
		PRP	-0.91	-0.95	-0.97	-1.09	-0.98	-0.89	-0.98	-0.98	-1.03	-0.94	-0.88	-1.00
	Stn4	R	0.38	0.32	0.32	0.28	0.20	0.31	0.41	0.10	0.43	0.41	0.43	**0.63**
		Partial r	0.03	0.01	0.01	-0.02	0.01	0.03	0.01	0.01	-0.02	0.03	0.05	0.00
		PRP	-0.92	-0.96	-0.97	-1.08	-0.96	-0.89	-0.99	-0.95	-1.04	-0.94	-0.89	-1.00
	Stn5	R	0.40	0.34	0.34	0.31	0.21	0.33	0.44	0.11	0.44	0.42	**0.45**	0.27
		Partial r	0.04	0.02	0.01	-0.02	0.00	0.04	0.00	0.00	-0.01	0.02	0.05	0.01

TH-1643_136104018

		PRP	-0.89	-0.95	-0.96	-1.08	-0.99	-0.88	-0.99	-1.03	-1.01	-0.96	-0.89	-0.95
	Stn6	R	0.38	0.32	**0.65**	0.28	0.20	0.31	0.41	0.10	0.43	0.41	0.43	0.24
		Partial r	0.03	0.01	0.01	-0.03	0.01	0.03	0.01	0.01	-0.02	0.03	0.05	0.01
		PRP	-0.92	-0.96	-0.98	-1.09	-0.95	-0.89	-0.97	-0.95	-1.04	-0.93	-0.89	-0.95
	Stn7	R	0.38	**0.56**	0.32	0.28	0.19	0.30	0.41	0.10	0.43	0.41	0.43	0.24
		Partial r	0.02	0.01	0.01	-0.02	0.01	0.03	0.00	0.00	-0.01	0.02	0.05	0.01
		PRP	-0.94	-0.98	-0.96	-1.07	-0.96	-0.91	-1.00	-0.97	-1.01	-0.96	-0.88	-0.95
Max Temperature	Stn1	R	0.73	0.51	0.52	0.50	0.39	0.54	0.77	0.10	**0.85**	0.82	0.83	0.39
		Partial r	-0.04	-0.06	0.05	-0.07	0.15	0.07	-0.07	0.02	0.13	-0.03	0.06	-0.05
		PRP	-1.05	-1.12	-0.90	-1.15	-0.63	-0.88	-1.10	-0.80	-0.85	-1.04	-0.93	-1.12
	Stn2	R	0.73	0.51	0.52	0.50	0.38	0.53	0.77	0.07	**0.86**	0.83	0.84	0.39
		Partial r	-0.03	-0.05	0.05	-0.08	0.14	0.06	-0.07	0.00	0.15	-0.06	0.08	-0.03
		PRP	-1.03	-1.10	-0.91	-1.16	-0.64	-0.89	-1.09	-0.95	-0.83	-1.07	-0.91	-1.07
	Stn3	R	0.73	0.50	0.51	0.49	0.36	0.52	0.77	0.08	**0.86**	0.83	0.83	0.39
		Partial r	-0.02	-0.05	0.04	-0.08	0.13	0.06	-0.07	-0.01	0.16	-0.07	0.08	-0.02
		PRP	-1.02	-1.09	-0.91	-1.17	-0.65	-0.89	-1.09	-1.10	-0.82	-1.09	-0.90	-1.05
	Stn4	R	0.74	0.51	0.52	0.50	0.38	0.53	0.77	0.08	**0.86**	0.83	0.83	0.38
		Partial r	-0.03	-0.06	0.05	-0.08	0.14	0.06	-0.08	0.01	0.15	-0.06	0.07	-0.03
		PRP	-1.04	-1.11	-0.91	-1.15	-0.64	-0.88	-1.10	-0.91	-0.83	-1.07	-0.91	-1.09
	Stn5	R	0.72	0.50	0.51	0.49	0.35	0.52	0.77	0.08	**0.86**	0.82	0.83	0.39
		Partial r	-0.02	-0.05	0.05	-0.08	0.12	0.06	-0.07	-0.01	0.16	-0.08	0.09	-0.02
		PRP	-1.02	-1.09	-0.91	-1.16	-0.65	-0.89	-1.10	-1.14	-0.81	-1.09	-0.90	-1.04

TH-1643_136104018

		R	0.73	0.51	0.52	0.50	0.38	0.53	0.77	0.08	**0.85**	0.83	0.83	0.38
		Partial r	-0.03	-0.05	0.05	-0.07	0.14	0.06	-0.07	0.01	0.14	-0.05	0.07	-0.03
	Stn6	PRP	-1.04	-1.10	-0.91	-1.15	-0.64	-0.89	-1.10	-0.88	-0.83	-1.06	-0.91	-1.09
		R	0.66	0.45	0.46	0.44	0.33	0.47	0.69	0.05	**0.78**	0.75	0.75	0.33
		Partial r	-0.02	-0.05	0.05	-0.08	0.13	0.06	-0.07	-0.01	0.16	-0.07	0.08	-0.02
	Stn7	PRP	-1.03	-1.10	-0.90	-1.17	-0.62	-0.88	-1.10	-1.13	-0.80	-1.09	-0.89	-1.05
Min Temperature		R	0.81	0.58	0.58	0.59	0.45	0.62	0.85	0.11	**0.91**	0.87	0.90	0.44
		Partial r	0.10	0.02	0.00	-0.09	0.13	0.12	-0.02	-0.05	0.04	0.07	0.13	-0.05
	Stn1	PRP	-0.88	-0.96	-1.01	-1.16	-0.72	-0.81	-1.02	-1.42	-0.95	-0.92	-0.86	-1.11
		R	0.80	0.58	0.58	0.58	0.44	0.62	0.85	0.08	**0.91**	0.87	0.90	0.44
		Partial r	0.10	0.03	0.00	-0.10	0.12	0.12	-0.02	-0.06	0.08	0.03	0.15	-0.03
	Stn2	PRP	-0.87	-0.95	-1.01	-1.17	-0.73	-0.81	-1.02	-1.68	-0.92	-0.97	-0.84	-1.07
		R	0.79	0.57	0.57	0.58	0.42	0.61	0.85	0.08	**0.91**	0.87	0.90	0.44
		Partial r	0.11	0.03	0.00	-0.10	0.11	0.12	-0.02	-0.06	0.10	0.01	0.16	-0.02
	Stn3	PRP	-0.87	-0.95	-1.01	-1.17	-0.73	-0.81	-1.03	-1.76	-0.89	-0.99	-0.82	-1.04
		R	0.80	0.58	0.58	0.59	0.45	0.62	0.85	0.08	**0.91**	0.87	0.90	0.44
	Stn4	Partial r	-0.13	0.11	0.04	-0.01	-0.10	0.12	0.11	-0.02	-0.05	0.07	0.03	0.14
		PRP	-1.16	-0.82	-0.93	-1.02	-1.22	-0.80	-0.87	-1.24	-1.06	-0.92	-0.96	-0.67
		R	0.79	0.57	0.57	0.57	0.42	0.61	0.85	0.08	0.91	**0.86**	0.90	0.44
	Stn5	Partial r	0.13	0.04	-0.01	-0.11	0.13	0.13	-0.03	-0.07	0.12	0.00	0.18	-0.02
		PRP	-0.84	-0.94	-1.01	-1.20	-0.68	-0.78	-1.04	-1.84	-0.87	-1.00	-0.80	-1.05
	Stn6	R	0.80	0.58	0.58	0.59	0.45	0.62	0.85	0.08	**0.91**	0.87	0.90	0.44

TH-1643_136104018

		Partial r	0.12	0.03	-0.01	-0.11	0.15	0.13	-0.02	-0.06	0.08	0.05	0.16	-0.04
		PRP	-0.85	-0.95	-1.01	-1.19	-0.68	-0.79	-1.03	-1.68	-0.91	-0.95	-0.83	-1.10
	Stn7	R	0.76	0.54	0.55	0.56	0.42	0.59	0.81	0.06	**0.86**	0.82	0.85	0.41
		Partial r	0.12	0.04	-0.01	-0.11	0.14	0.13	-0.03	-0.07	0.11	0.01	0.17	-0.03
		PRP	-0.84	-0.94	-1.01	-1.20	-0.67	-0.77	-1.03	-2.11	-0.87	-0.98	-0.80	-1.06

*Highlighted values are selected as the first suitable super predictors (FSSP)

4.1.5 Bias correction

The CMIP5 GCMs data have some bias in their time series values (Torres and Marengo, 2014). Moreover, all model outputs involve a great deal of biases that, if not corrected, can lead to significant errors in impact assessments. Therefore, a bias correction of GCM outputs is necessary before analyzing regional/local impacts (Goyal and Ojha, 2010). For this reason, bias corrections of the downscaled temperature (Eqs. 4.7) and precipitation (Eq. 4.8) datasets have done (Mahmood and Babel, 2012):

$$T_{deb} = T_{SCEN} - (\overline{T_{CONT}} - \overline{T_{obs}}) \quad \text{(4.7)}$$

$$P_{deb} = P_{SCEN} \times \left(\frac{\overline{P_{obs}}}{\overline{P_{CONT}}}\right) \quad \text{(4.8)}$$

where T_{deb} and P_{deb} are the de-biased (corrected) daily time series of temperature and precipitation respectively for future periods. SCEN represents the scenario data downscaled by SDSM for future periods (2006-2100), and CONT represents downscaled data by SDSM for the present period (1979-2005). T_{SCEN} and P_{SCEN} are the daily time series of temperature and precipitation generated by SDSM for future periods respectively. T_{CONT} and P_{CONT} are the long term monthly values for temperature and precipitation for the control period simulated by SDSM. T_{obs} and P_{obs} represent the long-term monthly observed values for temperature and precipitation respectively. The bar over P and T shows the long-term average. The frequency and intensity of precipitation are the two main factors affecting precipitation variability (Mahmood and Babel, 2012). The characteristic of this method of study is to correct the precipitation amount and not the frequency, and also to remove any systematic errors belonging to SDSM during downscaling. It is assumed that the frequency is accurately simulated by SDSM. The normal frequency curves (FCs) have been plotted and comparison has been done among the simulated and observed datasets. Frequency distributions can demonstrate either the actual observational datasets falling in each range or the percentage of observations, which summarizes the distribution of values. In this research work, FCs have prepared to evaluate the feasibility of calibration/validation outcomes against the bias corrected (BC) and without bias corrected (WBC) simulated precipitation and temperature variables.

4.1.6 Screening of predictor variables

The selected predictors and their screening results for minimum temperature, maximum temperature and precipitation are shown in Table 4.2. It is observed that the AMIP precipitation predictors such as *tas*, *tasmin*, *tas*, *vas*, *tasmi*n, *prc* and *pr* are observed as FSSP for Stn1, Stn2, Stn3, Stn4, Stn5, Stn6 and Stn7 respectively. Likewise, the predictor

TH-1643_136104018

such as *tas* is observed as the FSSP for the maximum temperature for all of the climate stations and the predictor such as *tas* recorded as FSSP for the minimum temperature for all of the climate stations except Stn5. For the Stn5, *tasmin* is recorded as the FSSP. These predictors also covey a physical relationship regarding the local scale minimum temperature, maximum temperature and precipitation. As per the latest CMIP5 GCMs, several new predictors have been added (Taylor et al., 2012). In this study, the basic concept of predictor's selection is adopted as per the methodology proposed by Mahmood and Babel (2013).

4.1.7 Calibration and validation of SDSM

For the calibration/validation between the controlled AMIP/NCEP reanalysis simulated and observed datasets (1979-2005), a monthly SDSM model is setup and run. For the calibration/validation minimum 4 best predictors were selected for all the variables at each climate station (Table 4.1). Here, the calibration and validation outputs for the precipitation and temperature downscaling variables have shown together in Table 4.2. Table 4.2 shows the calibration/validation results for the SDSM model. The calibration and validation outcomes did not assume significant variations (e.g. R, R^2, Mean, standard deviation and RMSE). The calibration and validation outcomes did not assume significant variations (e.g. R, R^2, Mean, standard deviation and RMSE).

In Table 4.2, the objective functions such as standard deviation (SD), R, R^2 and RMSE showed the monthly basis prediction outcomes of the precipitation variable. Whereas, the minimum and maximum temperature outcomes showed a daily basis result. The mean values of these variables showed the average annual mean for the precipitation and temperature.

In Table 4.2, one can clearly see that the average monthly/annual mean for precipitation and temperature are significantly varied across all the climate stations. The regression plots showed a very good agreement between the observed and bias corrected simulated precipitation and temperature data sets. In case of the precipitation, the RMSE computed between the bias corrected (BC) simulated and observed datasets across all the climate stations, ranged from 15.54 (recorded minimum at Stn3) to 45.92 (recorded maximum at Stn2), is fairly acceptable and comparable to several previous studies (Mahmood and Babel, 2012, Wetterhall et al. 2006).

TH-1643_136104018

TH-1643_136104018

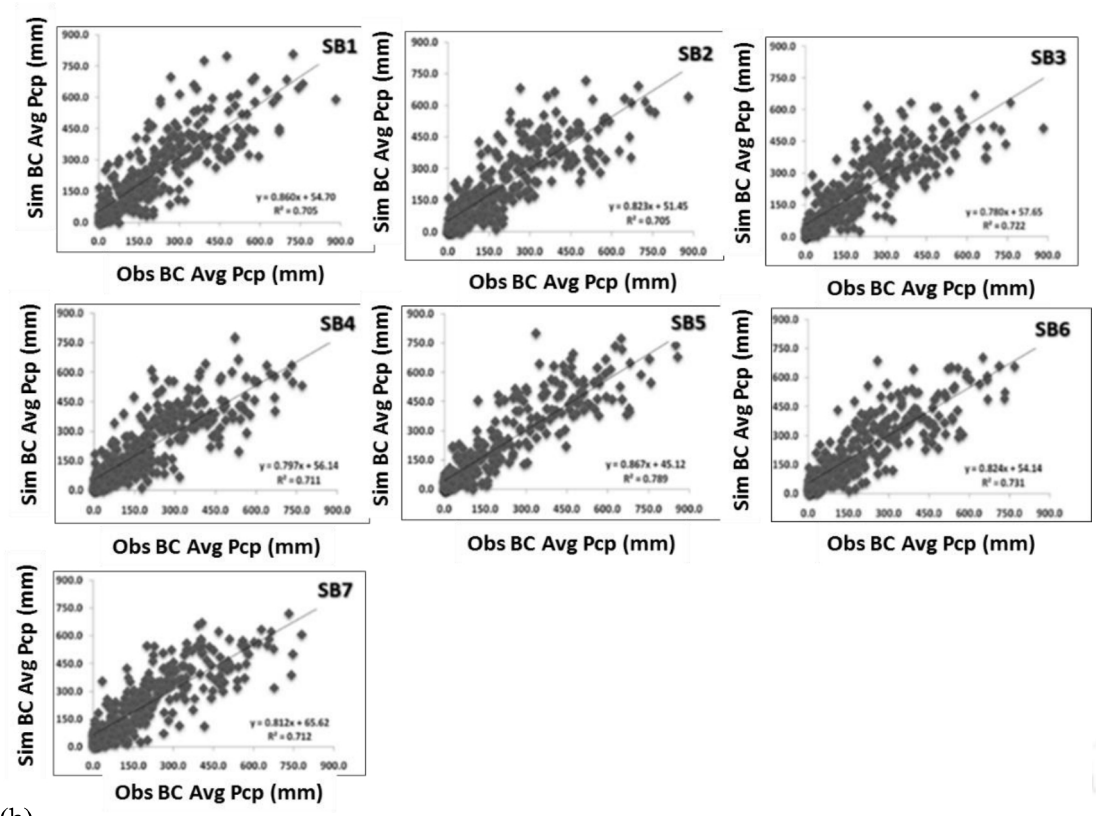
Table 4.2: Result of downscaled precipitation and temperature during observed/historical time periods (1979-2005).

Variables	Scenarios	Statistics	SB1	SB2	SB3	SB4	SB5	SB6	SB7
Precipitation	Observed	Annual Mean (mm)	2405.76	2384.04	2397.00	2391.96	2375.52	2382.00	2427.84
		Standard Deviation	183.78	183.73	184.4	185.16	212.99	184.92	188.51
	Calibration/Validation (BC)	R	0.84	0.84	0.85	0.83	0.89	0.86	0.84
		R^2	0.71	0.70	0.72	0.71	0.79	0.73	0.72
		RMSE (mm)	32.36	45.92	15.54	16.46	40.58	21.21	28.76
		Annual Mean (mm)	2725.68	2579.76	2563.56	2580.24	2602.44	2614.08	2759.04
		Standard Deviation	188.23	180.02	170.61	177.53	207.93	178.275	181.35
Max Temperature	Observed	Annual Mean (°C)	7.81	9.79	9.83	9.83	9.24	9.47	12.58
		Standard Deviation	4.87	4.88	4.87	4.87	4.83	4.81	4.64
	Calibration/Validation (BC)	R	0.92	0.91	0.96	0.90	0.91	0.92	0.84
		R^2	0.82	0.84	0.92	0.82	0.84	0.84	0.72

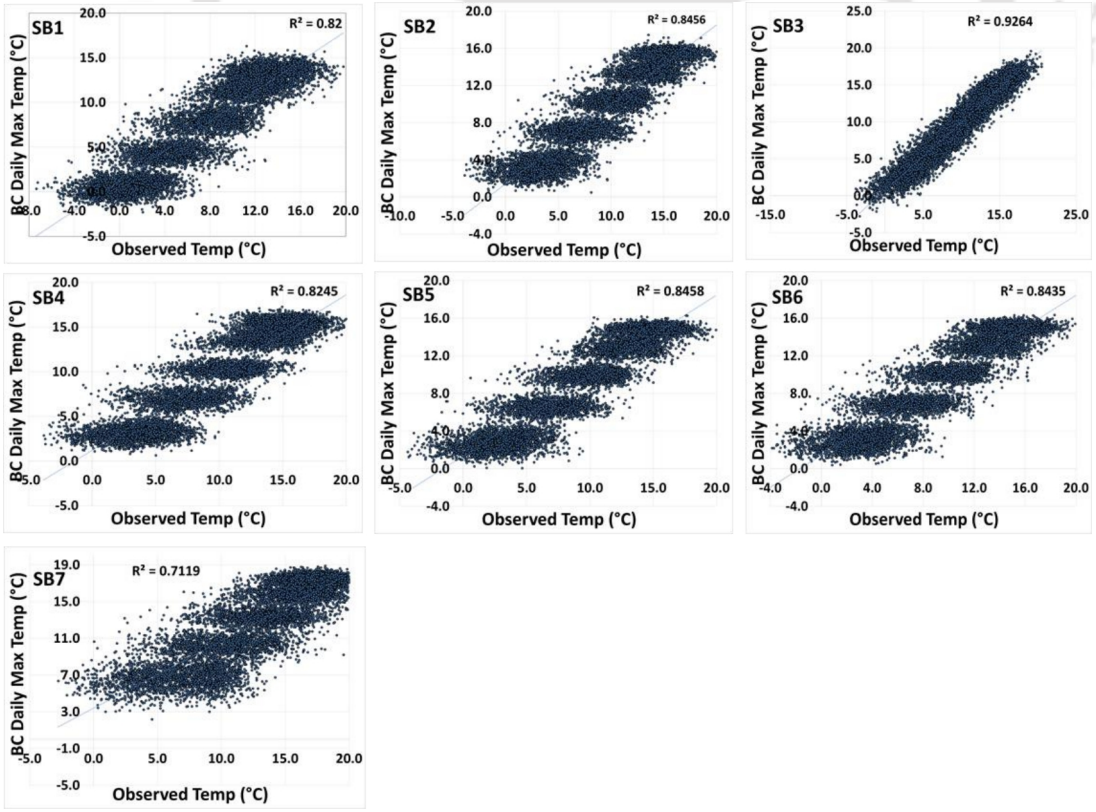
TH-1643_136104018

		RMSE (°C)	0.85	1.13	0.59	1.29	1.13	1.14	0.81
		Annual Mean (°C)	7.8	9.78	9.75	9.75	9.24	9.47	12.57
		Standard Deviation	4.75	4.74	4.83	4.83	4.7	4.66	4.25
Min Temperature	Observed	Annual Mean (°C)	-4.08	-1.67	-2.02	-1.65	-1.09	-0.87	2.24
		Standard Deviation	7.4	6.95	7	6.95	6.99	6.96	6.73
	Calibration/Validation (BC)	R	0.93	0.97	0.97	0.97	0.94	0.94	0.92
		R^2	0.93	0.93	0.94	0.93	0.93	0.93	0.84
		RMSE (°C)	1.48	1.27	1.24	1.27	1.28	1.3	1.23
		Annual Mean (°C)	-4.09	-1.66	-2.02	-1.66	-1.09	-0.87	2.26
		Standard Deviation	7.24	6.83	6.89	6.83	6.87	6.84	6.31

(a)



(b)



TH-1643_136104018

(c)

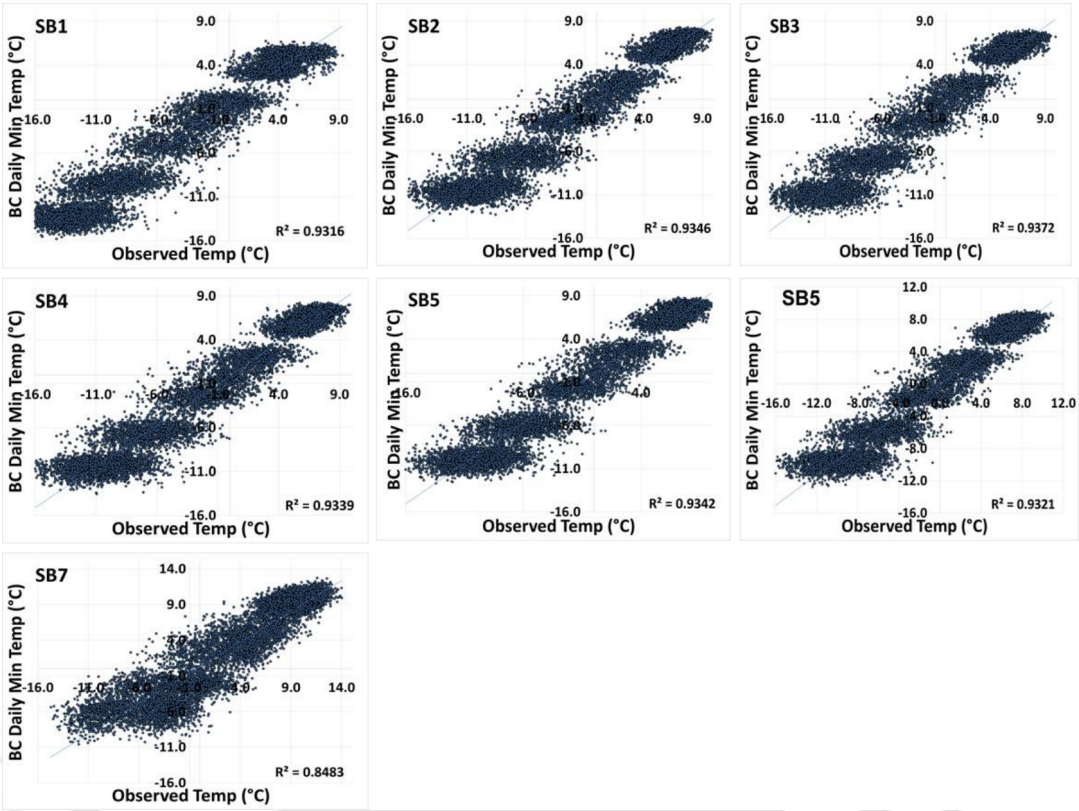


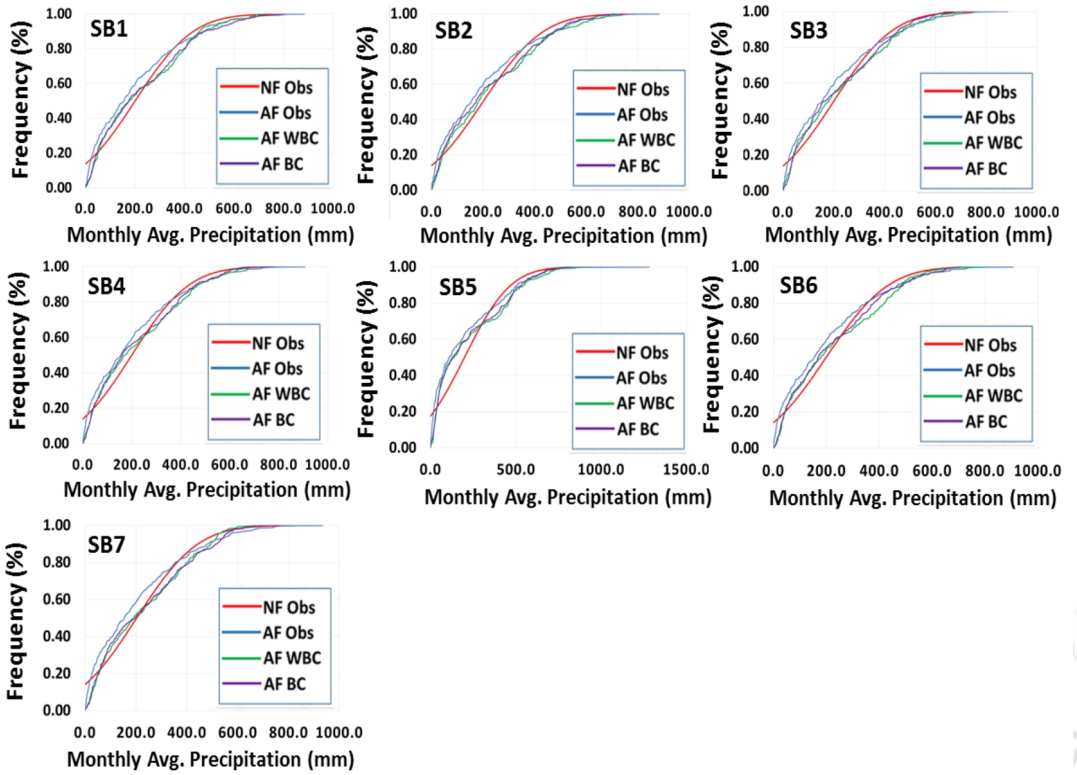
Fig. 4.2: Calibration/validation results showing comparison between observed (Obs.) and bias corrected (BC) simulated (Sim.) datasets (1979-2005): (a) avg. precipitation (Pcp), (b) maximum (max) temperature (temp) and (c) minimum (min) temperature.

For the precipitation, the calculated *R* values are also acceptable, which range from 0.89 (recorded maximum at Stn5) to 0.84 (recorded minimum for most of the Stns). In case of the minimum and maximum temperature, the *R* and R^2 results showed by minimum temperature are better than maximum temperature. Though, the maximum temperature computed RMSE from 0.59°C (at Stn3) to 1.29°C (at Stn4) and the minimum temperature calculated RMSE from 1.24°C (at Stn3) to 1.48°C (at Stn4) which is little bit high than maximum temperature. Though, these objective functions showed a good combination of the predictands and predictors. The regression plots (Figs 4.2a, 4.2b and 4.2c) highlight the difference between the without bias corrected (WBC) simulated datasets and BC simulated datasets during 1979-2005. The NF distribution for the observed meteorological variables was computed to compare the AFs for simulated variables. The FCs based comparison of the calibration/validation outcomes for the BC and WBC simulated datasets with observed datasets have been evaluated, for all of the meteorological variables, which showed a better justification of the accuracy level of the SDSM. In case of the precipitation, the BC simulated AF showed less variation through the NF than WBC simulated AFs. Though, we

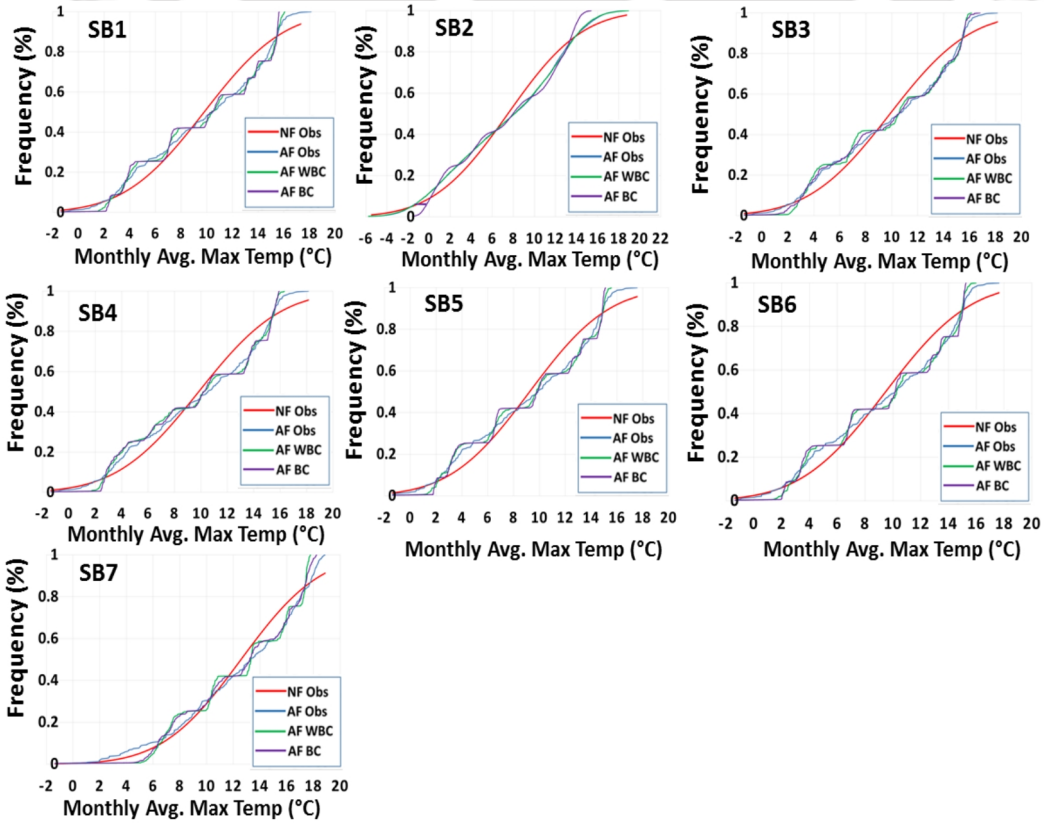
TH-1643_136104018

did not account much difference between the BC and WBC simulated precipitation (Figs. 4.2a, 4.2b and 4.2c).

(a)



(b)



TH-1643_136104018

(c)

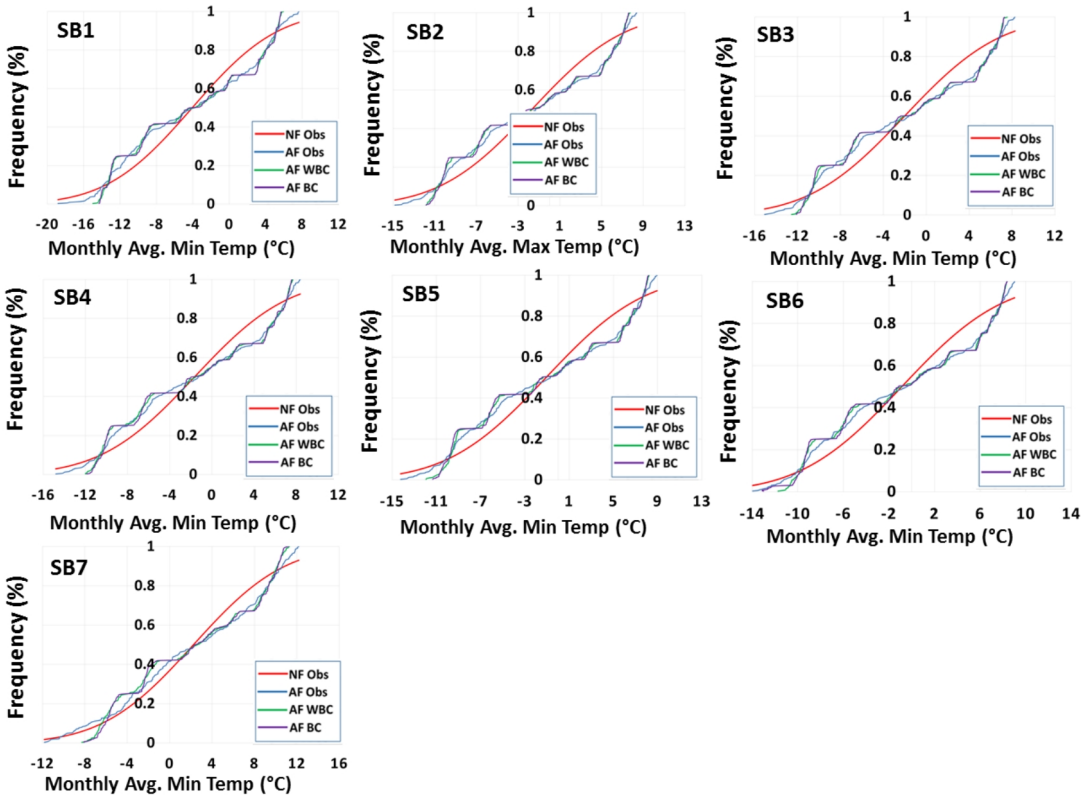


Fig.4.3: Frequency Curves (FC) showing the comparison of Modeled Normal Frequency (NF) distribution of Observed data sets with Actual Frequency (AF) distribution of Observed data, AF of bias corrected (BC) simulated data and AF of without bias corrected (WBC) simulated data (1979-2005): (a) FC for Precipitation, (b) FC for maximum temperature and (c) FC plots for minimum temperature.

In case of the minimum and maximum temperature, the BC and WBC simulated values showed enormous variations in the values from the NF of observed datasets. The minimum temperature based FCs showed better correlations with the NFs of observed datasets than maximum temperature. Here, it is observed that the BC FCs were found more consistent than the WBC simulated temperatures (Figs. 4.2b and 4.2c).

4.2 TEMPERATURE AND PRECIPITATION LAPSE RATES

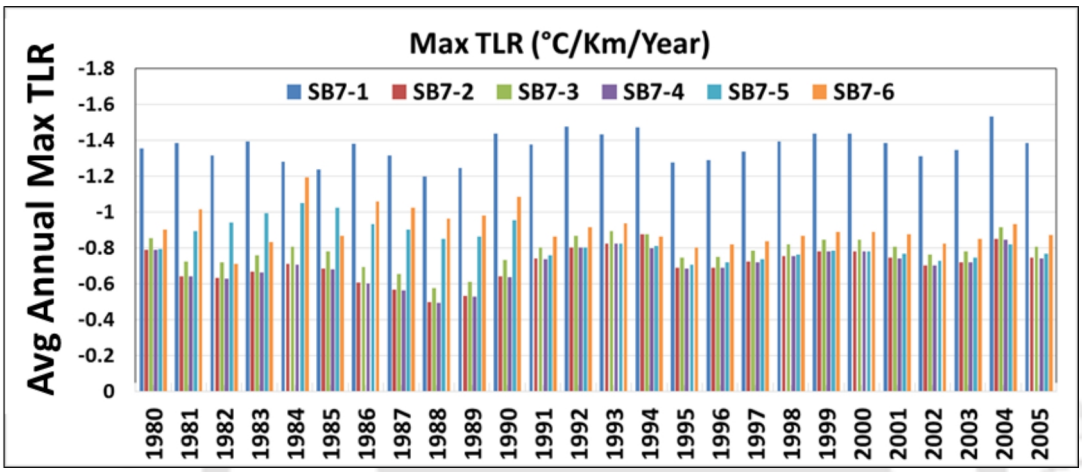
4.2.1 Average annual TLRs

The average annual TLRs have been calculated based on the monthly minimum and maximum temperature datasets by doing annual average. Figs (4.4a and 4.4b) show the average annual TLRs (max and min) during the historical time series (1979-2005). As per the TLR equation (explained above), the TLR has been calculated for SB1, SB2, SB3, SB4,

TH-1643_136104018

SB5 and SB6 with respect to SB7. The SB7 is the main outlet station of the selected study area and corresponds to minimum elevation over the catchment. Thus at each station, TLRs have been calculated with reference to SB7 (Stn7). In Figs. (4.4a and 4.4b), one can easily identified the existed spatial variability in the TLRs in the both minimum and maximum temperature. The maximum difference in the TLRs have been calculated between the SB7-SB1 for both Min and Max temperatures.

(a)



(b)

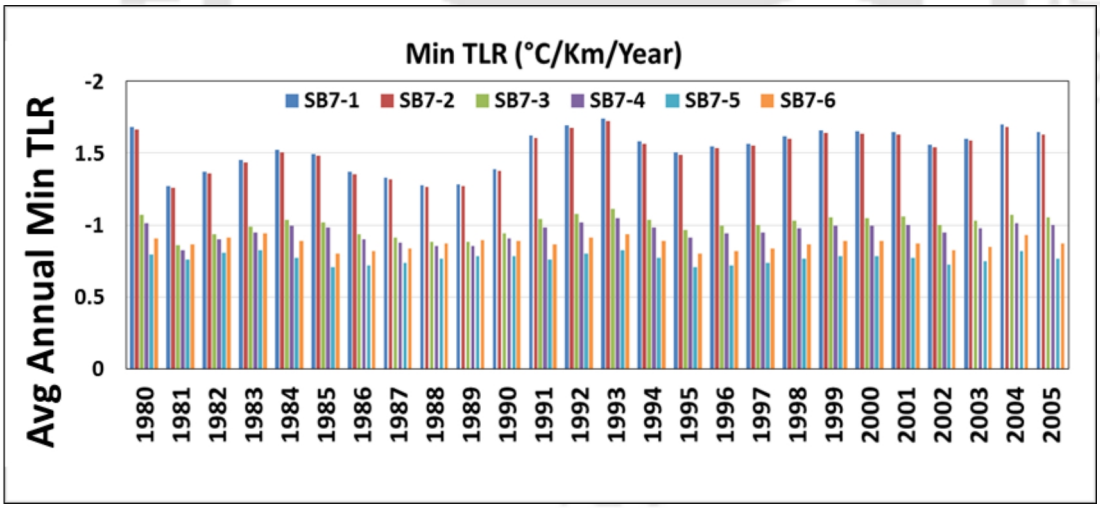


Fig.4.4: Average annual TLRs (Max and Min) during the historical time periods (1979-2005).

Fig. (4.5) shows average annual TLRs as per the CMIP5 ESM-2M GCM and RCPs (2006-2100). The 21st century scenarios of TLRs are calculated at the whole catchment scale by doing the average of all climate stations dataset. The Stn1 is corresponded to the highest elevation and Stn7 corresponded with the lowest elevation over the selected study area. Thus, each climate station reflects unique characteristics of meteorological variables and hence, the TLRs computed and compared with respect to the Stn7. In Fig. (4.5), the TLR,

TH-1643_136104018

calculated between the Stn7-Stn1, highlights maximum variations due to higher elevation differences among these two stations. The TLRs variability has been assessed during the 21st century time under the moderate and extreme RCP experiments. The RCP8.5 show largest variations in the TLRs than RCP2.6 and RCP4.5. This long time series (2006-2100) duration of TLRs exhibits a decrement in the TLRs across all of the climate stations. The 21st century changes in the TLRs as per the RCP experiments can be understood as per the plotted average trend line. The plotted trend line showed a consistent decrement in the TLRs among all the stations which have been compared. However the stations between Stn7-Stn1, Stn7-Stn3 and Stn7-Stn7 showed a consistent decreasing line, which highlights that the high altitude portion of the catchment are changing their TLRs. This could be interpreted as between these climate stations, the maximum and minimum temperature is extremely enhanced. In plots (Fig. 4.5), it is also observed that the fluctuations in the peaks of TLRs also enhanced after 2060s.

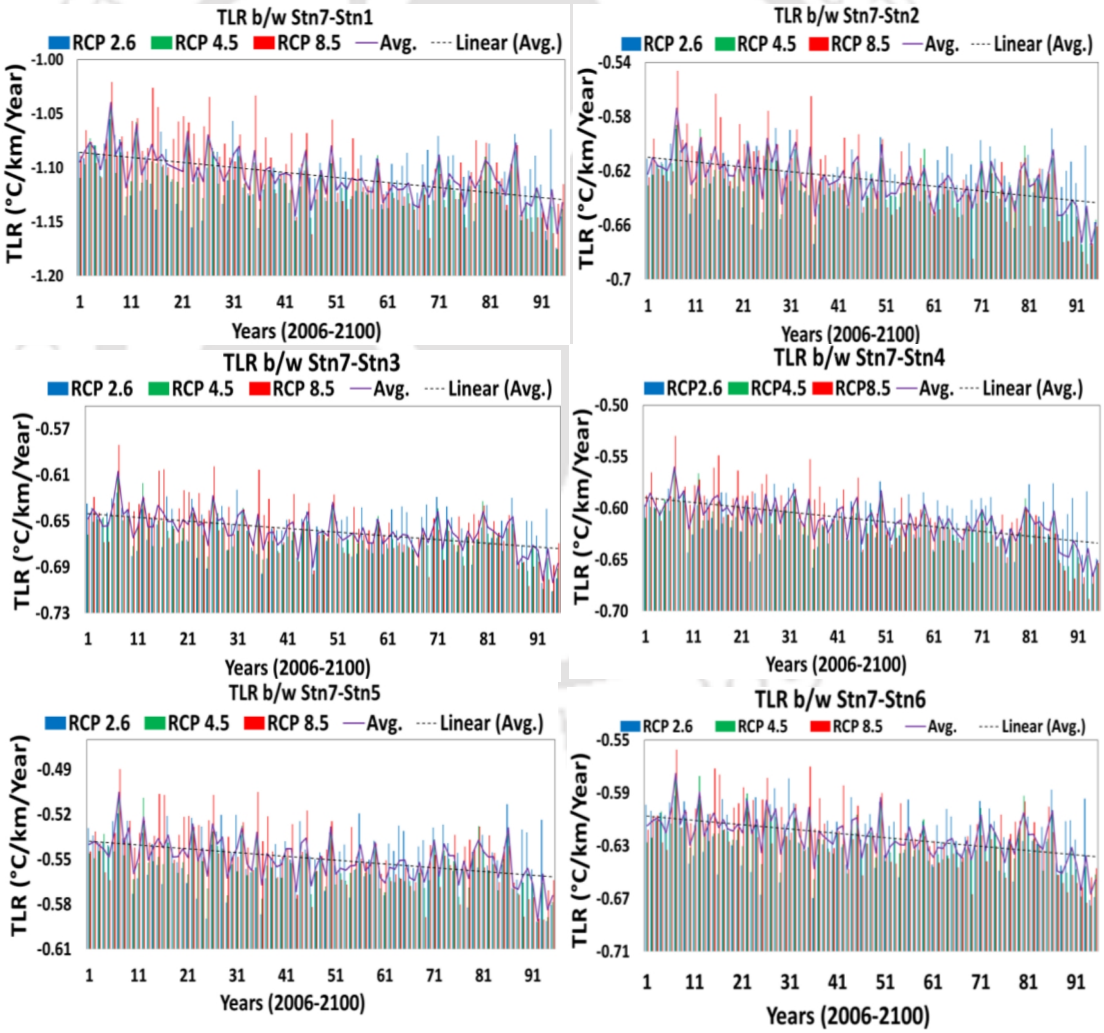


Fig. 4.5: Average annual TLRs scenarios in the 21st century domain as per CMIP5-ESM2M and their RCP experiment.

TH-1643_136104018

4.2.2 Mann-Kendall trends of TLRs (Max and Min) as per CMIP5 ESM-2M, CM3 and CM2P1 GCMs

The Mann-Kendall test (Burn and Elnur, 2002; Mann, 1975; Kendall, 1975) significantly utilized by various authors to detect the magnitude of change in the long term time series datasets (Choi et al., 2013; Goyal, 2014; Jain and Kumar, 2012). In this study, the Mann-Kendall test was applied to detect the long term trends in TLRs (Min and Max) during 2006 to 2100 as per multi-model CMIP5 GCMs and RCPs. The significance level of TLR is evaluated as α = 0.05. The alpha value of 0.05 was chosen as the local significance level for a two-sided test (Goyal, 2014). Based on this significance level (α), values larger than 1.96 or lower than 1.96, indicated a significantly ($p<0.05$) increasing or decreasing behaviour of the time series, respectively (Choi et al., 2013). The Mann-Kendall equations are described below as:

The statistics (S) is defined as (Eq. 4.9):

$$S = \sum_{i=1}^{N-1} \sum_{j=i+1}^{N} sgn(x_j - x_i) \quad \text{..... (4.9)}$$

Where, N is the number of data points. Assuming $(x_j - x_i) = \theta$, the value of $sgn\,(\theta)$ is computed as follows (Eq. 4.10):

$$sgn\,(\theta) = \begin{cases} +1 & if \;\; \theta > 0 \\ 0 & if \;\; \theta = 0 \\ -1 & if \;\; \theta < 0 \end{cases} \quad \text{.....(4.10)}$$

This statistics represents the number of positive differences minus the number of negative differences for all the differences considered. For large samples (N>10), the test is conducted using a normal distribution (Jain and Kumar, 2012) (Eq. 4.11)

$$E[S] = 0$$

$$var\,(S) = \frac{N(N-1)(2N+5) - \sum_{k=1}^{n}(t_k-1)(2t_k+5)}{18} \quad \text{..... (4.11)}$$

Where n is the number of tied (zero difference between compared values) groups and t_k the number of data points in the k^{th} tied group. The standard normal deviate (Z-statistics) is then computed as (Jain and Kumar, 2012) (Eq. 4.12):

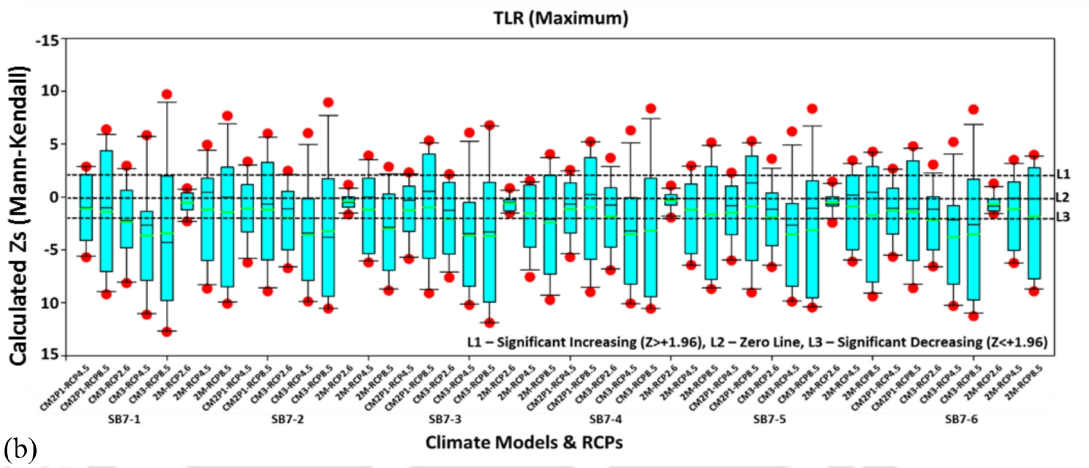
$$Z = \begin{cases} \frac{S-1}{\sqrt{var(S)}} & if \;\; S > 0 \\ 0 & if \; S = 0 \\ \frac{S+1}{\sqrt{var\,(S)}} & if \; S < 0 \end{cases} \quad \text{..... (4.12)}$$

TH-1643_136104018

If the computed value of $|Z| > Z\alpha/2$, the null hypothesis (H_0) is rejected at alpha (α) level of significance in a two-sided test (Choi et al., 2013).

The Mann-Kendall based trends of TLRs (2006 to 2100) are presented in Figs. 4.6(a) and 4.6(b). Fig. 4.6(a) shows the box plot representation of the Mann-Kendall test statistics (Z) at Y axis (vertical) for maximum TLR for each station. The Z value shows the TLR variation from January to December months during the year 2006 to 2100. Likewise, Fig. 4.6(b) shows the box plot representations of the Mann-Kendall test statistics (Z) at Y axis (vertical) for minimum TLR. Most of the months, for both the TLRs, showed significant variability in the TLR, which can be clearly seen in the box plots across all the experiments.

(a)



(b)

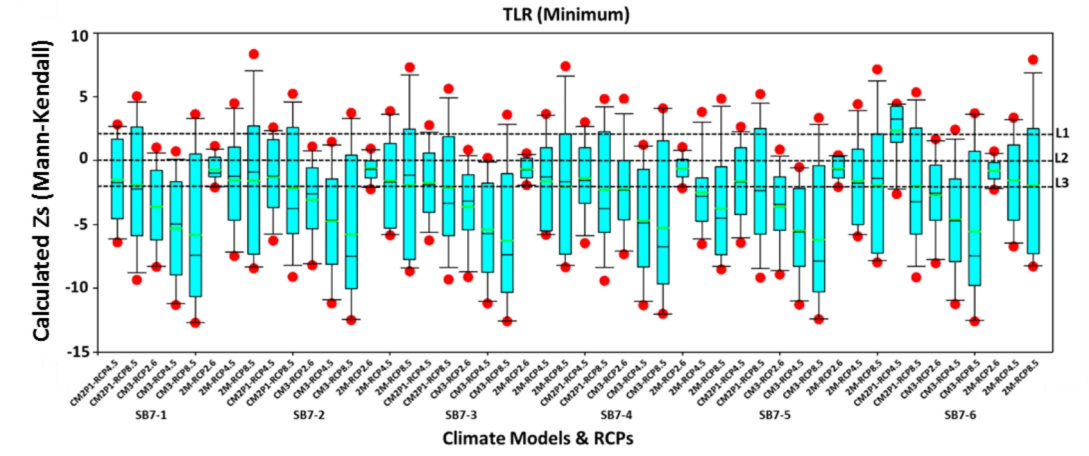


Fig. 4.6: Monthly comparison of sensitivity of Minimum and Maximum temperature using Mann-Kendall test.

The Mann-Kendall Z value, for both the TLRs (Min and Max), showed significant increasing or decreasing trends compared from January to December among all the CMIP5 and RCP experiments. These trends can be clearly interpreted through the plotted trend lines

TH-1643_136104018

(L1, L2 and L3) showed in Figs. 4.6(a) and 4.6(b). In these plots, very few observations, associated with maximum TLR, also showed increasing trends. These trends support strong temperature inversions from December to January during 2006 to 2100, which can be observed in all the CMIP5 GCMs and RCP experiments.

Here, it can be concluded that the obtained variability in the frequency/duration of temperature inversions (from January to December) could be a main driver of minimum and maximum TLRs changes between SB1 and SB7. Fig. 4.7 shows a month wise comparison of TLR trends between minimum TLR and maximum TLR. The Mann-Kendall (Z) values have been used to imply the TLR changes. In Fig. 4.7, one can observe significant variations in the Z values among all scenarios. A Red Color Circle has been drawn over the plots to highlight the variations between minimum and maximum TRL. In Fig. 4.7, most of the months (e.g. January, March, April, May, June, August, October and November) have shown significant increasing and decreasing trend.

The trend line which corresponds to maximum TLR has shown frequently increasing trends, while the trend line which corresponds to minimum TLR has shown nearly decreasing trends. This variation indicated that the minimum and maximum TLRs have been affected significantly in the projected time series durations (2006-2100). In Fig. 4.7, several months did not show any significant variation in the minimum and maximum TLRs, could be less sensitive for the changes.

The computed TLR values are computed lower in winter months than summer months and thus it represents high temperature inversions during summer months. The annual average plots of observed temperature scenarios (1979-2005) and 21st century scenarios (2006-2100) conclude that the SB7 and SB7 were corresponded to higher temperature values than other climate stations. These observations support temperature inversion and TLR viability over the upstream portion of Teesta river part north Sikkim eastern Himalayas.

The inversions of temperature appeared to be responsible for decreasing minimum and maximum TLR values during the year 2006 to 2100. This observation supports minimum and maximum temperature increments between SB7 to SB1. The resulted differences associated maximum and minimum TLRs are likely due mostly to inversions for the minimum temperature values than maximum temperature values. Overall Figs. (4.5 and 4.6) showed a significant changing pattern and fluctuations in the minimum and maximum TLRs.

TH-1643_136104018

TH-1643_136104018

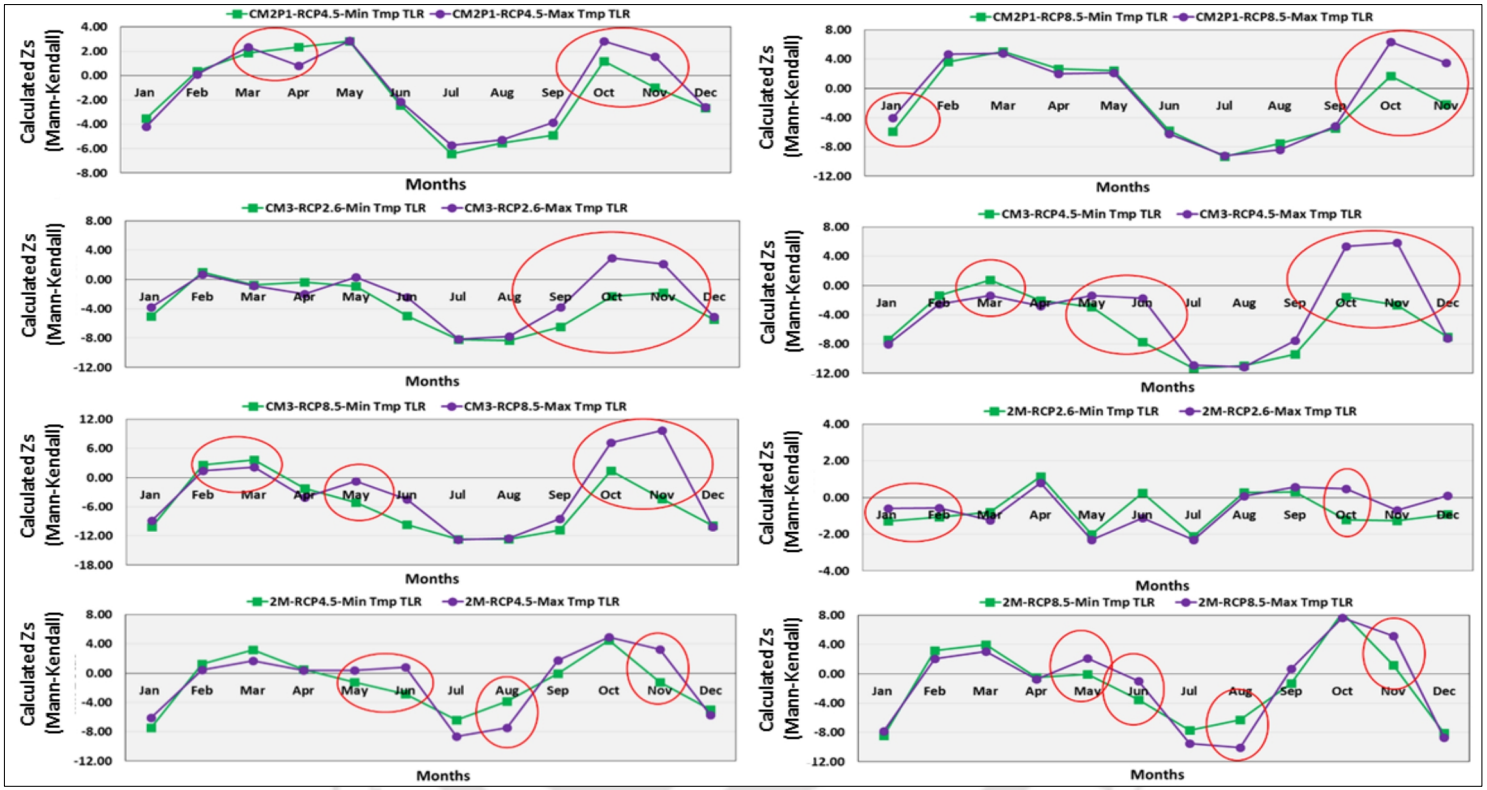


Fig. 4.7: Monthly inter-comparison of sensitivity results of minimum and maximum temperature using Mann-Kendall test.

4.2.3 PLR scenarios

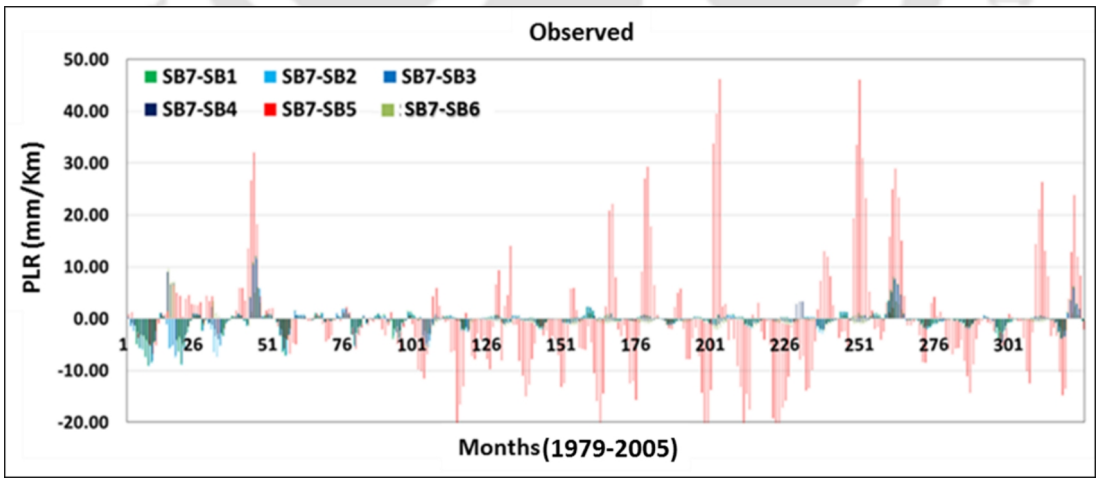
The computed PLR values have shown on a monthly and annual basis in the 21st century time series domain using CMIP5 ESM-2M and RCPs. Trends in PLR and PEI are estimated using Mann-Kendall test (Mann, 1975; Kendall, 1975). The magnitude of change in the time series was estimated using Sen's slopes. A Sen's estimation (Sen, 1968) is used to predict the rate of change of PLR and precipitation amounts per year (Choi et al., 2013). These methods are nonparametric and do not assume the distribution form for the data under investigation. In addition it is not sensitive to outliers (Choi et al., 2013). The possible autocorrelation in the time series that may render the test of statistical significance of a trend unreliable was taken into account by using an iterative procedure (Goyal, 2014; Choi et al., 2013).

In continuation of the Mann-Kendall test, the slopes (*Ti*) of all data pairs are first calculated by (Eq. 4.13)

$$T_i = \frac{x_j - x_k}{j-k} \quad \text{for } i = 1, 2, \ldots, N \ldots\ldots\ldots\ldots\ldots\ldots\ldots\ldots (4.13)$$

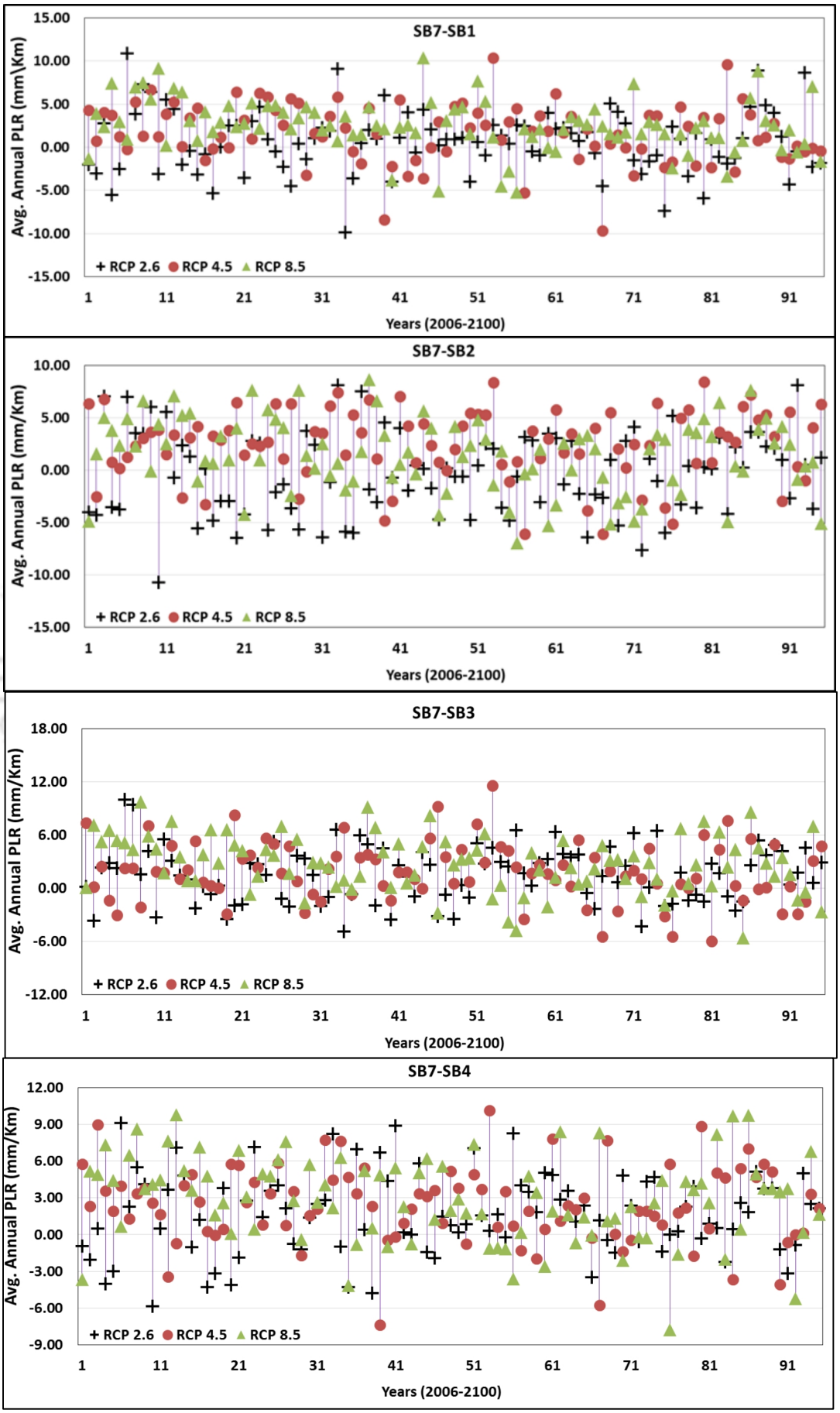
where x_j and x_k are data values at time j and k (j > k) respectively. The median of these N values of T_i is Sen's estimator of slope (Goyal, 2014; Choi et al., 2013; Sen, 1968). Fig. (4.8a) shows the trend of PLR calculated on a monthly basis in a historical times series **(1979-2005).**

(a)



TH-1643_136104018

(b)


SB7-SB1
Avg. Annual PLR (mm\Km)
15.00
10.00
5.00
0.00
-5.00
-10.00
-15.00
RCP 2.6 RCP 4.5 RCP 8.5
1 11 21 31 41 51 61 71 81 91
Years (2006-2100)
SB7-SB2
Avg. Annual PLR (mm/Km)
10.00
5.00
0.00
-5.00
-10.00
-15.00
RCP 2.6 RCP 4.5 RCP 8.5
1 11 21 31 41 51 61 71 81 91
Years (2006-2100)
SB7-SB3
Avg. Annual PLR (mm/Km)
18.00
12.00
6.00
0.00
-6.00
-12.00
RCP 2.6 RCP 4.5 RCP 8.5
1 11 21 31 41 51 61 71 81 91
Years (2006-2100)
SB7-SB4
Avg. Annual PLR (mm/Km)
12.00
9.00
6.00
3.00
0.00
-3.00
-6.00
-9.00
RCP 2.6 RCP 4.5 RCP 8.5
1 11 21 31 41 51 61 71 81 91
Years (2006-2100)

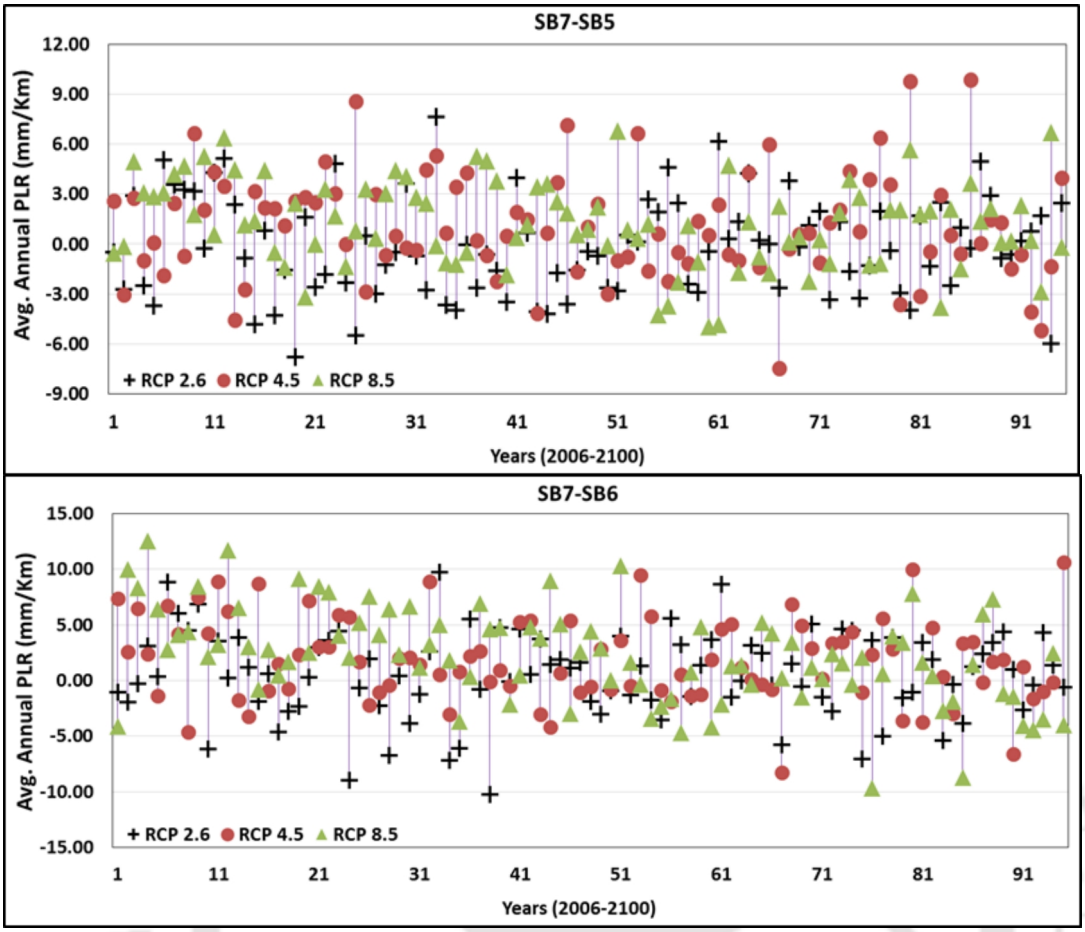


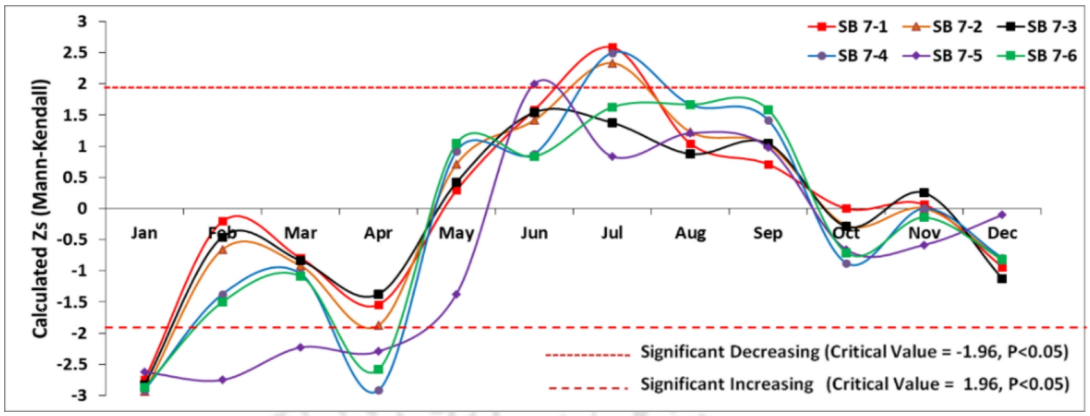
Fig. 4.8: (a) Three months moving average of PLR (mm/km) for the observed time series (1979-2005) and (b) An average annual PLR (mm/km) for the future time series (2006-2100) data sets.

Fig. (4.8a) showed that the earlier time series values (before 1990s) showed significant variations in the PLRs (several values recorded near 14mm/Km), whereas the time series values between 1990 to 2000 time periods showed less variations in their peaks. Fig. (4.8b) showed the comparative response of PLR on an annual average basis in a projected time series domain (2006-2100). Most of the plots, prepared based on the different RCPs, showed significant positive trends in the PLR except several trends.

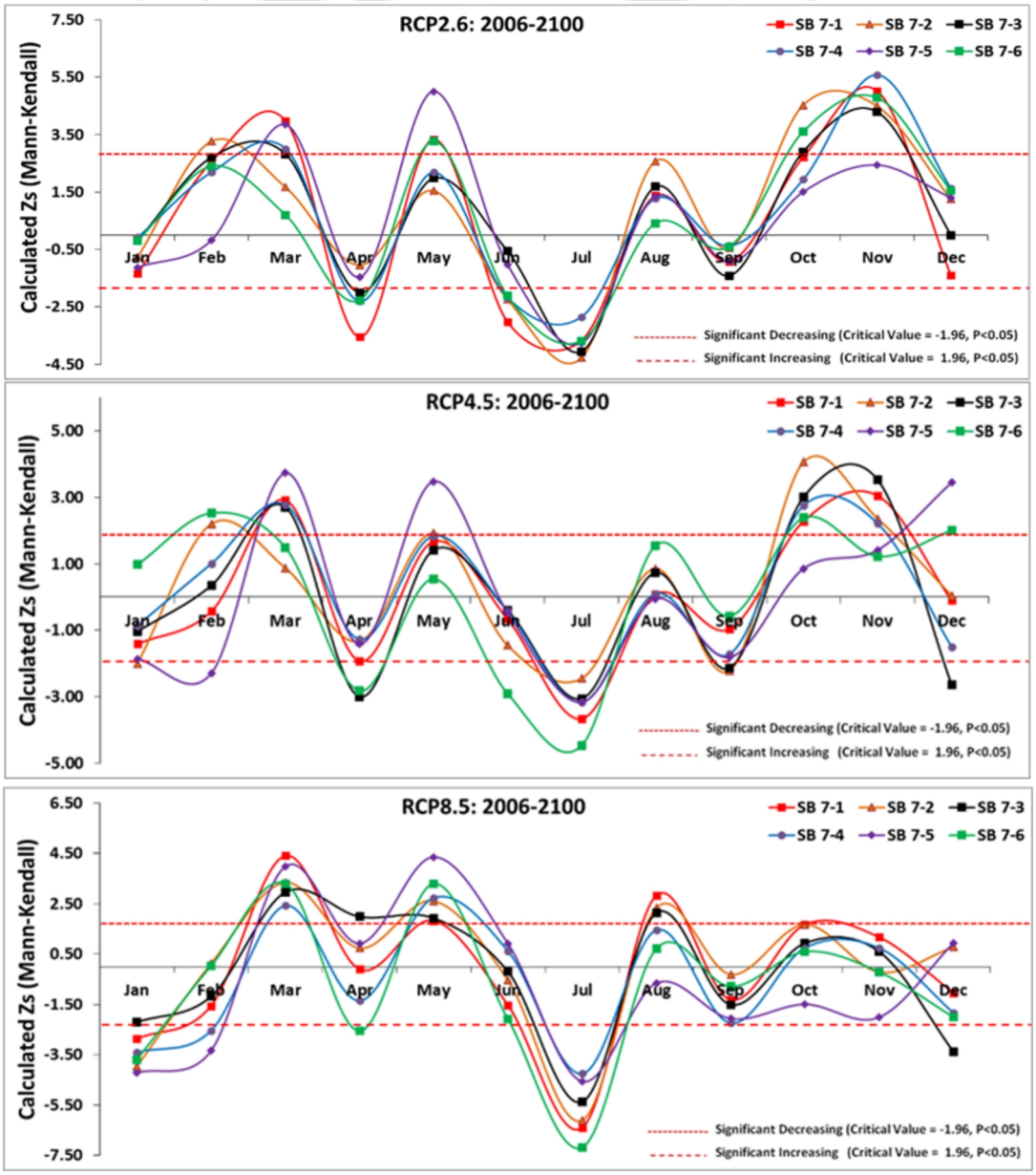
A number of plots as per Fig. (4.9) showed Mann-Kendall based trends in the PLR in an intra-decadal time series (1979-2005, 2006-2100, 2011-2040, 2041-2070 and 2071-2100) domain. Fig. (4.9a) showed a monthly Mann-Kendall statistics of the PLR in the observed/historical time series (1979-2005). Here, most of the positive trends (increasing trend) recorded in the monsoon months (May to September), whereas the negative trends are recorded in the spring months (October to April).

TH-1643_136104018

(a)

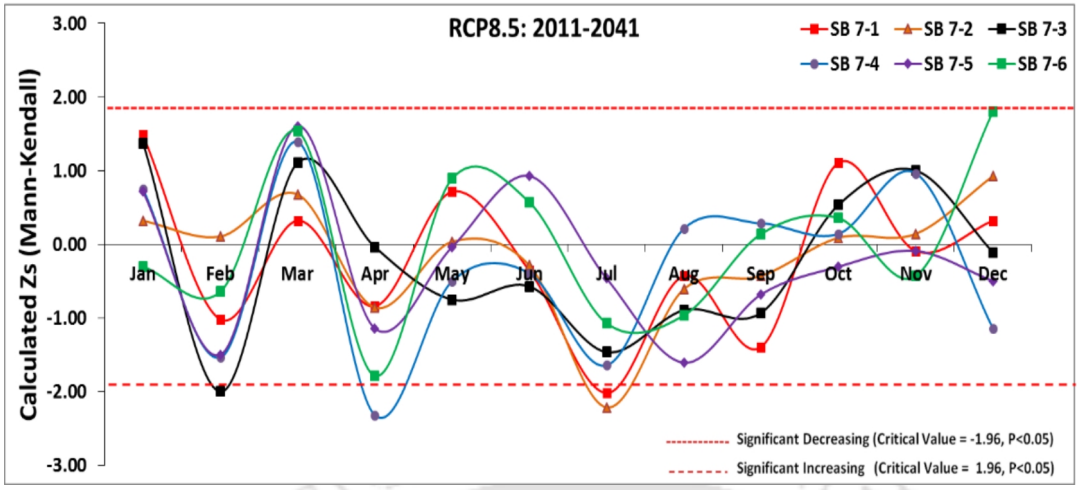


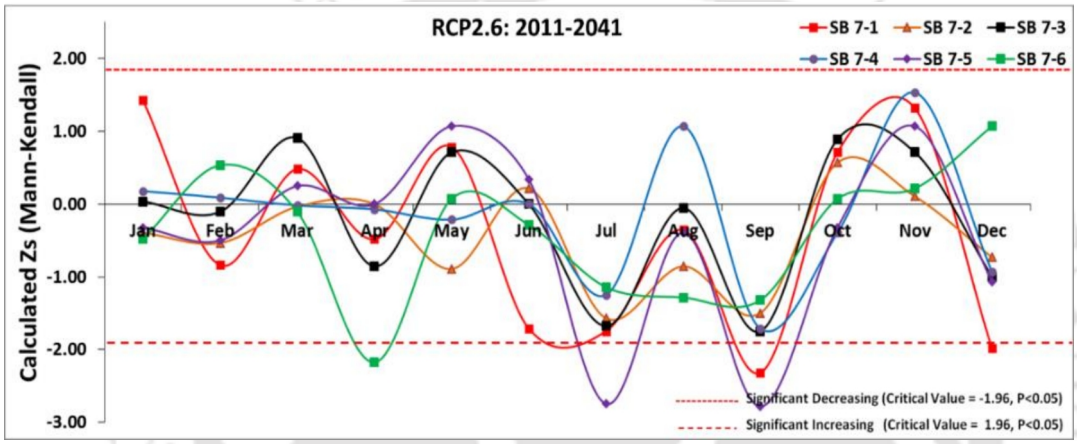
(b)

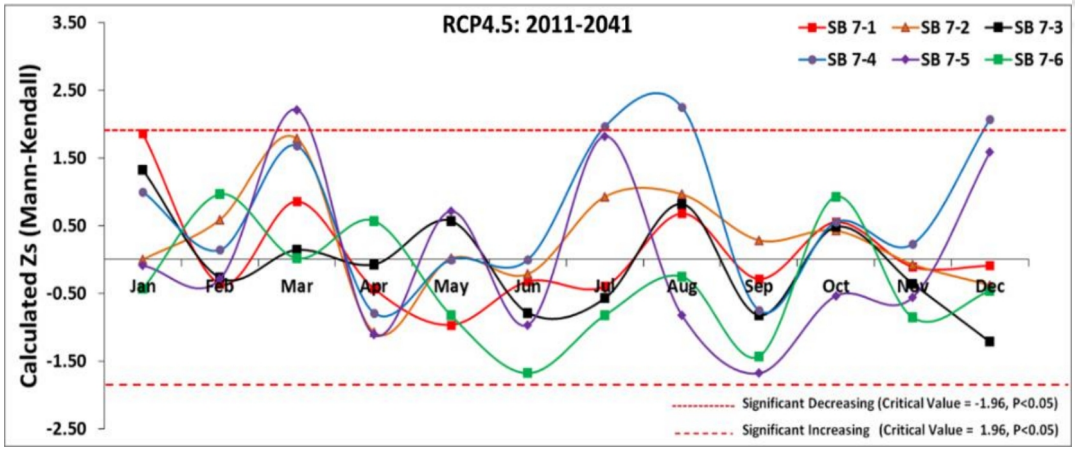


TH-1643_136104018

(c)

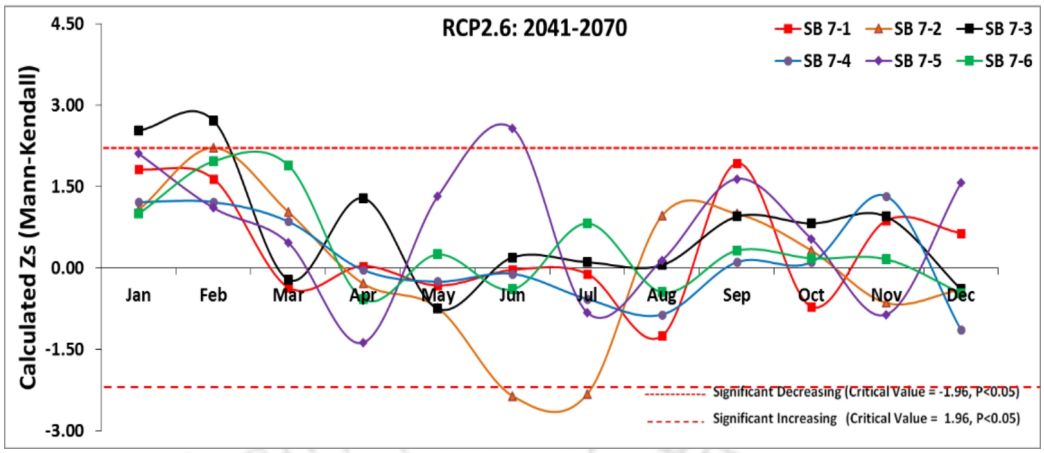


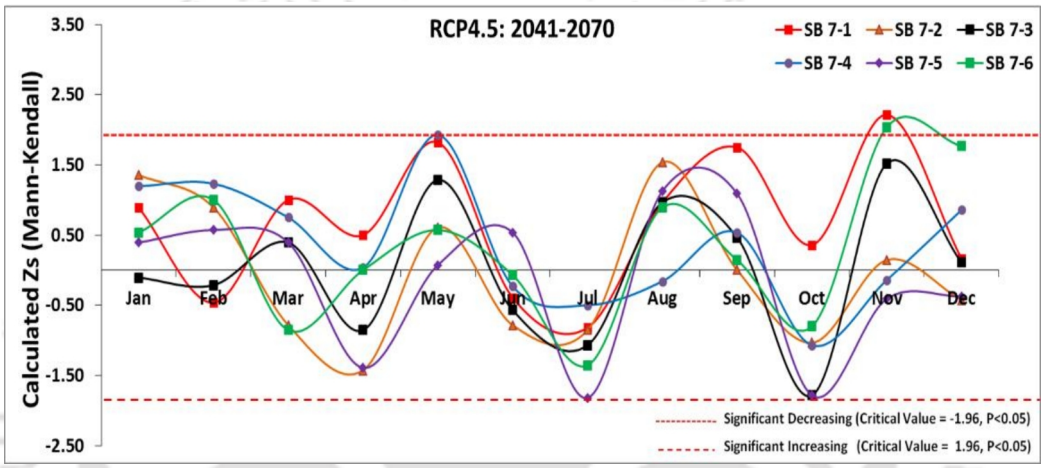


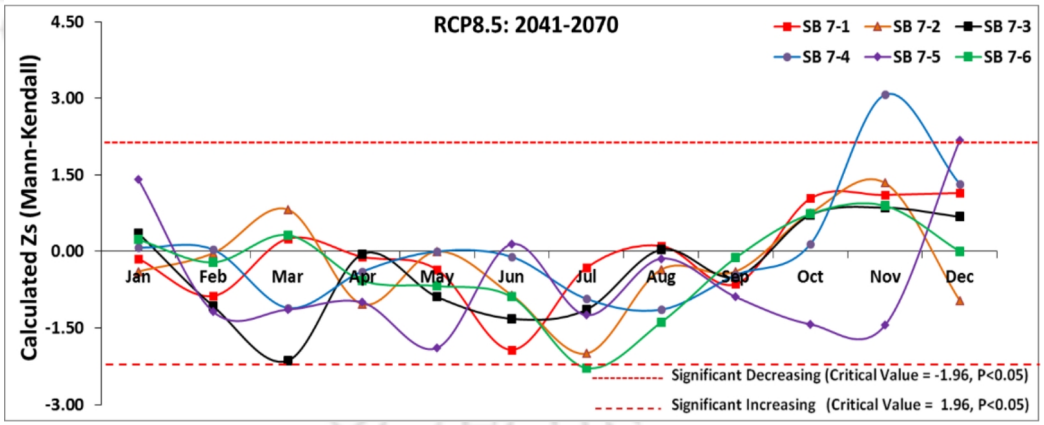


TH-1643_136104018

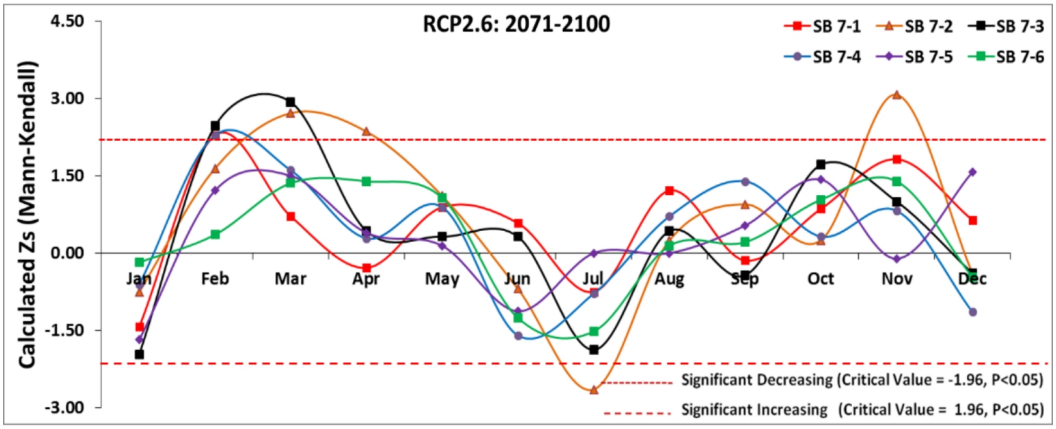
(d)







(e)



TH-1643_136104018

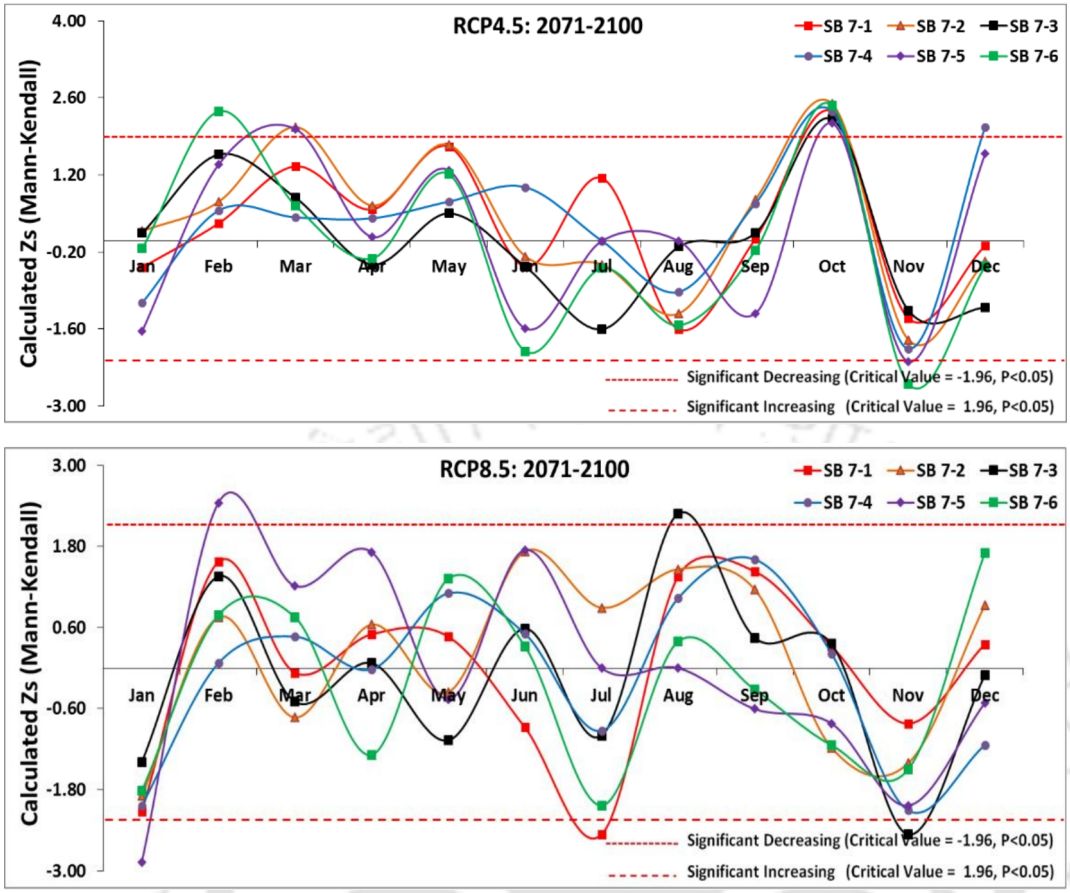


Fig. 4.9: Mann-Kendall test statistics (Z) results for the monthly averaged PLR as per the CMIP5 ESM-2M GCM and RCPs experiments (2.6, 4.5 and 8.5); (a) Observed time series plots (1979-2005), (b) Z statistics for the time series (2006-2100) (c) Z statistics for the time series (2011-2041) (d) Z statistics for the time series (2041-2070) and (e) Z statistics for the time series (2071-2100).

In Fig. (4.9a), one can notice that the PLR is significantly increased (positively) during June to August. Though, more or less decrement in the PLR was also observed during March to May, especially for the plots between SB7-6, SB7-4, SB7-5 and SB7-2.

From Fig. (4.9b), one can observe that most of the increasing trends are recorded during February, March, May, August, and October to December months. While, several negative trends were observed mostly in the January, April, July and December months. Likewise in Figs. (4.9c, 4.9d and 4.9e), most of the plots did not show any significant changes in the PLRs except RCP8.5 scenario which showed a significant decreasing trend for the SB7-1, SB7-2, SB7-3 and SB7-4.

TH-1643_136104018

To identify a magnitude of change in the PLRs during projected time scale (2006-2100), Sen's slopes are measured. Fig. (4.10) showed the results of Sen's slopes estimation on a monthly PLR in an intra-decadal time series domain (1979-2005, 2006-2100, 2011-2040, 2041-2070 and 2071-2100). As per Fig. (4.10), a RCP8.5 scenario based computations showed a maximum magnitude of change in the PLR (approx. -1 to 0.8 mm/km) than RCP2.6 and RCP4.5. Here, it is also observed that the Sen's slopes values, which are correspond to May to September months, have shown large fluctuations (increment or decrement) in the PLRs than the spring months. The months such as March, May, July, August, October and November showed mostly positive trends except few values.

4.2.4 Trends evaluation in 21st century predicted Temperature scenarios

For the evaluation of temperature warming in the 21st century, CMIP5 GCMs with their RCP experiments based temperature forecasting (max and min) have been done. For the assessment of significant increments, or decrements if so, non-parametric Mann-Kendall test, spatial standard deviation and mean monthly statistical evaluation at each climate station, have been applied. Figs. 4.11(a) and 4.11(b) show the average annual trend of maximum and minimum temperature at the whole catchment during the year 2006 to 2100, respectively.

In Fig. (4.11), one can observe the increasing trends in all of the multimodel GCMs and their RCPs. The maximum growth of warming can be assessed in the extreme emission scenario based RCP8.5. As per the numerical value, the temperature growth rate is observed between 0.5°C to 2.0°C in all the scenarios. In the projected scenarios, the severity of temperature rapidly enhanced after 2060s and showed sudden increments in the temperature mean values (Figs. 4.11a and 4.11b).

TH-1643_136104018

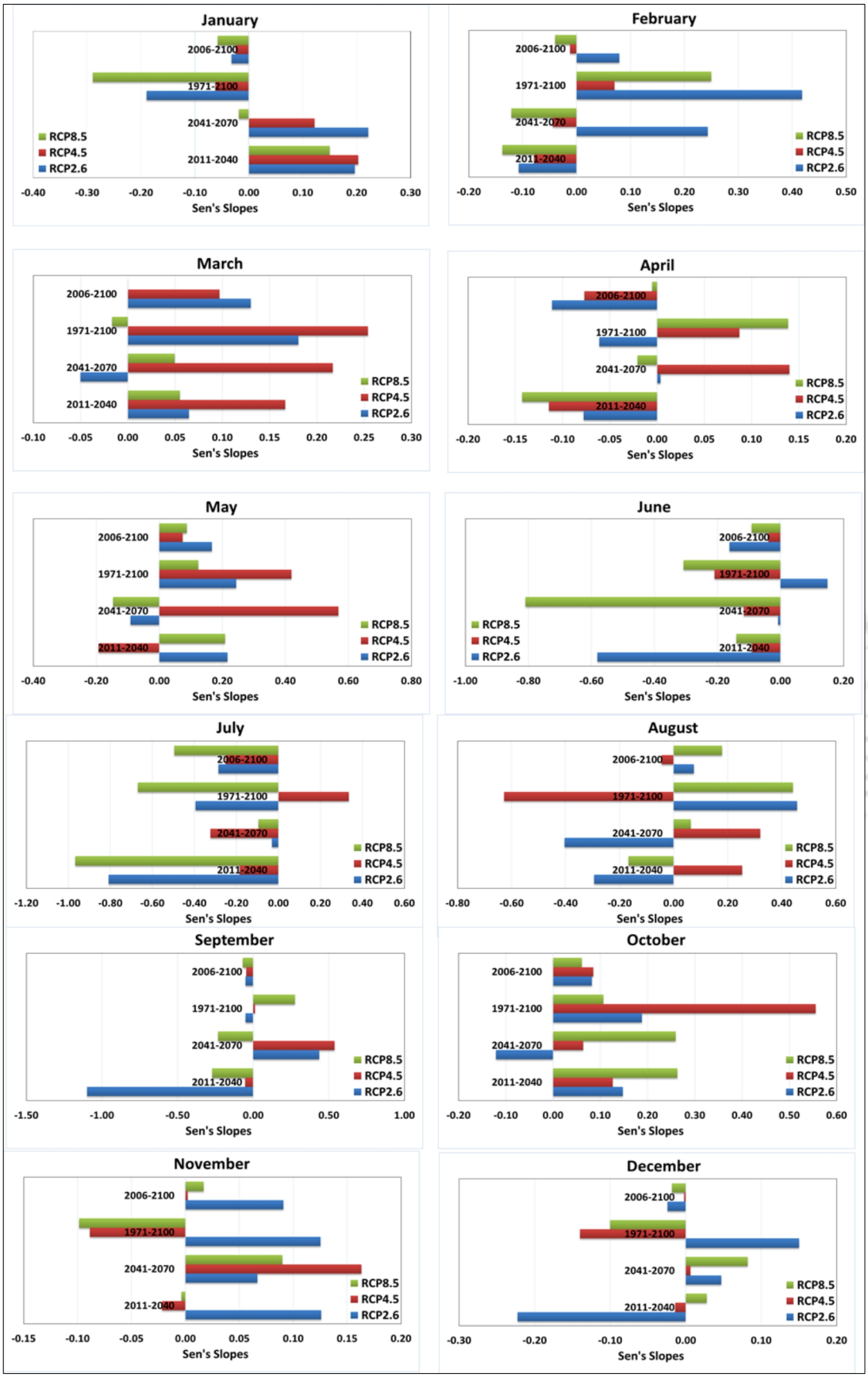
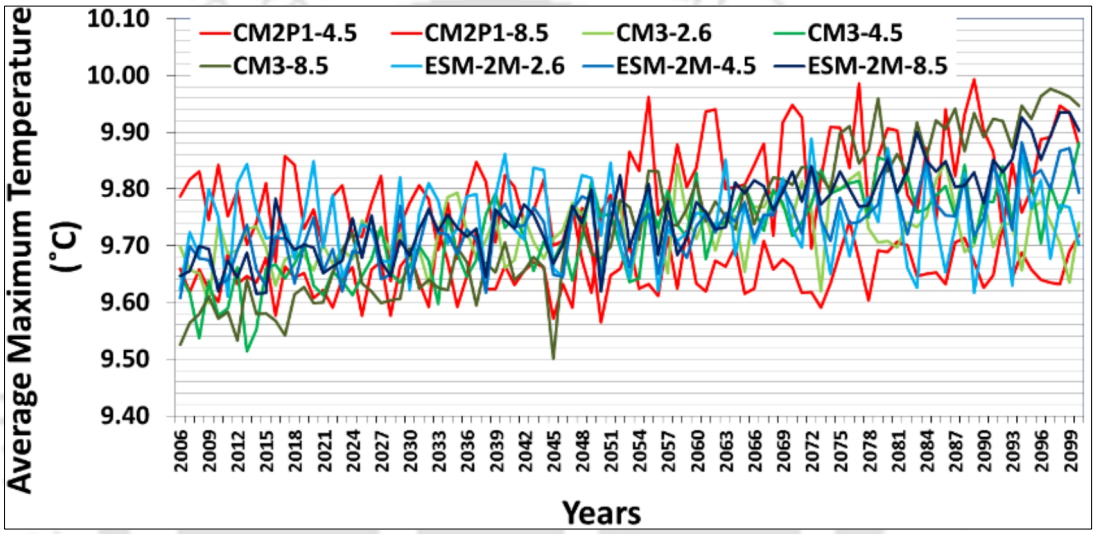


Fig. 4.10: Sen's slopes results (monthly average) of PLR in an intra-decadal times.

TH-1643_136104018

The average ensembles of temperature, as per CMIP5 GCMs, revealed warming signatures over the eastern Himalayas. In the next part, a spatial scale monthly basis prediction have been done to evaluate the temperature extremity over the selected catchment. Fig. (4.12) shows multimodel results employing Mann-Kendall test over averaged temperature at each station. Each model (e.g. CM2P1, CM3 and ESM-2M) datasets has been grouped into respective RCPs (e.g. 2.6, 4.5, 8.5), to compare the significant changes in temperature. The monthly basis predictions give a better understanding of the time series trends than annual predictions. The Mann-Kendall test results clearly showed significant warming trends in the projected scenarios.

(a)



(b)

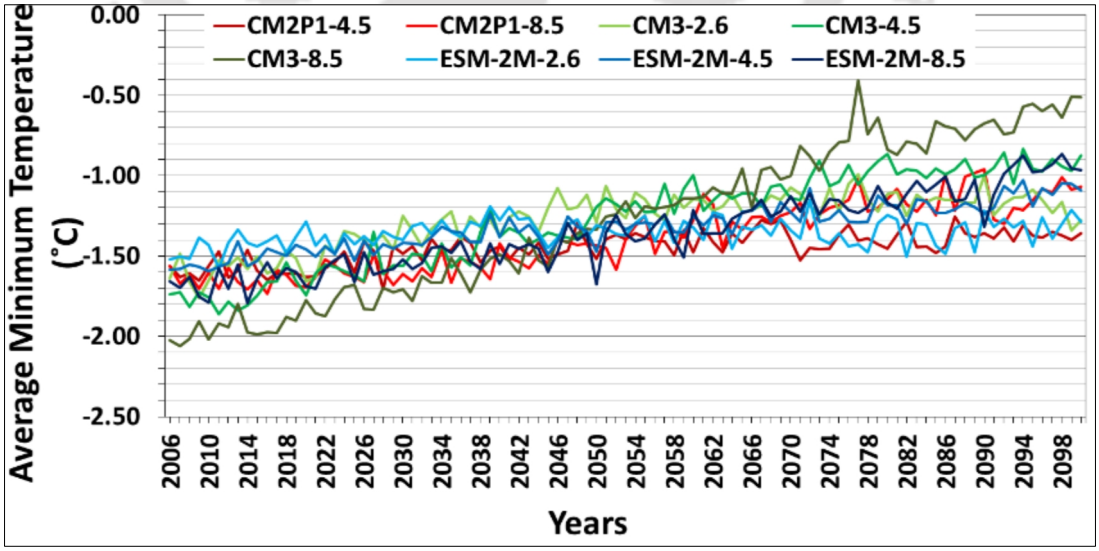


Fig. 4.11: Multimodel CMIP5 GCMs scenarios of average annual temperature warming at the whole catchment scale during 21st century with their emission scenarios (RCPs: 2.6, 4.5 and 8.5); (a) maximum temperature scenarios and (b) minimum temperature scenarios.

TH-1643_136104018

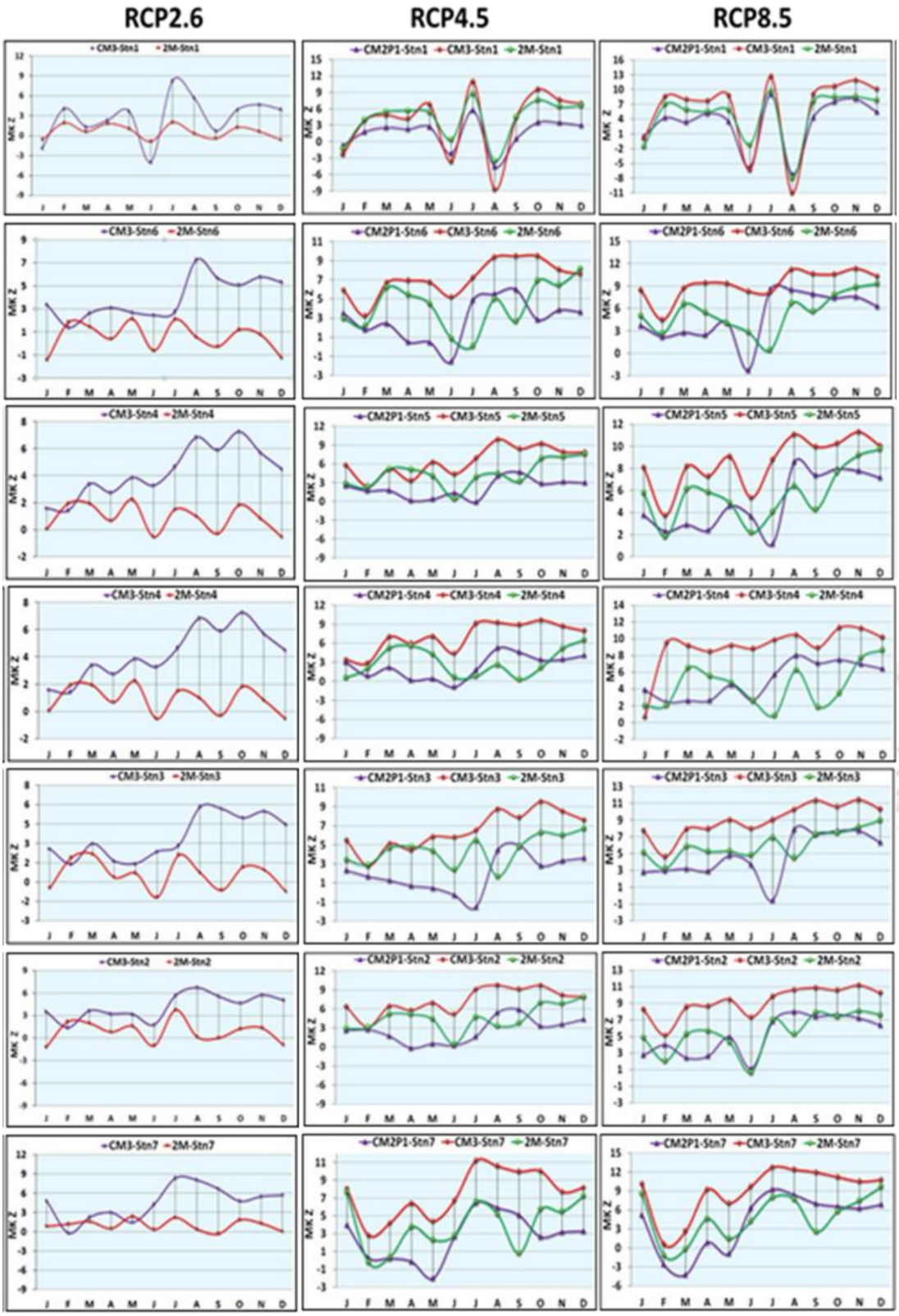


Fig. 4.12: Mann-Kendall results for multimodel scenarios of annual averaged temperature growth rate across the study area during 2006 to 2100.

TH-1643_136104018

In the present study, a significant elevation variation exists across the Chungthang (Stn7) to Chopta Valley (Stn1) (Fig. 4.12). Thus, the TLR and PLR also varied across the climate stations. The higher elevative parts of the study area, such as Chopta valley (Stn1), Thangu (Stn2) and Yumthang (Stn5) climate stations, showed larger variations in the Mann-Kendall statistics (Z) than moderate elevative climate stations (Fig. 4.12).

As per the monthly projection of Mann-Kendall Z stat value (based on the significance level α=0.01, where, if Z > +2.58 trend will be significant increase and if Z <-2.58 trend will be significant decrease), most of the months showed significant increasing trends among all of the multimodel projected scenarios except July (J), August (A) and March (M) months. They (July, August and March) have showed decreasing trends, especially over Chopta valley (St1) whose Z value recorded larger than +2.58. Though, the extremity of significant trends also varied as per the multimodel emission scenarios (RCPs).

The highest significant increasing trends are recorded for the RCP8.5 experiments. The other RCPs, lower (RCP2.6) to moderate (RCP4.5), also exhibit significant increasing trends. The asymmetry in the magnitude of the changes in warm extremes versus cold extremes reported in the previous studies is also evident in the CMIP5 ensemble. In Fig. (4.12), it is clearly observed that the high elevative parts of the eastern Himalayas (e.g. Chopta Valley Station) corresponded to maximum Z values than other stations. As per the increasing trends, high elevation zones such as Chopta Valley, Thangu and Yumthang were recorded as the warmest stations over the study region. Among all the climate stations, around 6 stations showed consistent significant warming.

There is a significant seasonal variability in warming rates on the entire Himalayas is also reviewed by Guan et al. (2015) and Rangwala and Miller (2012). The studies carried out by another authors using the same CMIP5 GCMs, Karin et al. (2013) and Taylor et al. (2012), reported that the median warming of cold extremes over the globe by the end of the 21stcentury is 1.5°C, 2.4°C, and 4.9°C in the RCP2.6, RCP4.5 and RCP8.5 experiments, respectively, as compared to the corresponding changes of 0.8°C, 1.7°C and 3.8°C for warm extremes. The overall trends revealed a significant warming signature over the eastern Himalayas. As per the above Mann-Kendall results, the emission scenarios based trends of average temperature gave broader perspective of the identification of the average temperature warming over the present study region.

To highlight the monthly variation in the min and maximum temperatures, a CMIP5-ESM2M GCM with multiple RCPs based downscaled scenarios have been utilized for the trends. The Mann-Kendall trends plotted in the spatial domain, which highlight the spatial and temporal variations across all the sub-catchments over the selected study region. Figs.

TH-1643_136104018

(4.12a and 4.12b) and Table (4.3) show the result of Mann-Kendall test. Fig. 4.13 (a) highlights the minimum temperature trends and Fig. 4.13 (b) shows maximum temperature trends on a monthly basis.

The results of the Mann-Kendall test clearly notified a significant warming trends the projected scenarios. As per the estimation of Mann-Kendall Z value, most of the months displayed significant increasing trends (Here, significance level α=0.05, $Z > +1.96$) in the minimum and maximum temperature both except January (Jan), February (Feb) and June (Jun). These months decreasing trends, especially over Stn4 and Stn5 (Fig. 4.13b). In the overall minimum and maximum temperature trends, it showed a consistent significant warming across all the climate stations, except few observations which are associated with maximum temperature (Table 4.3). In Fig. 4.13 (a), as per the minimum temperature trends, all months have shown almost increasing trends, while in maximum temperature based scenarios, except January all months have shown almost increasing trends across all the sub-catchments.

However, the severity of temperature increments, as per the spatial variations, varied from upstream to downstream portions of the catchment. In another way, the extreme scenarios (RCP8.5) showed maximum Z than other RCPs. These spatial variations in the Mann-Kendall Z are notice in the both min and max temperatures.

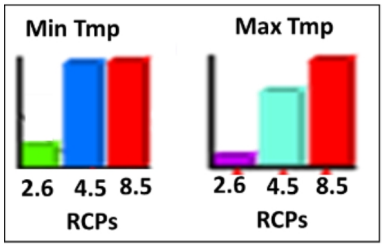
4.2.5 Temperature extremity evaluation using extreme indices

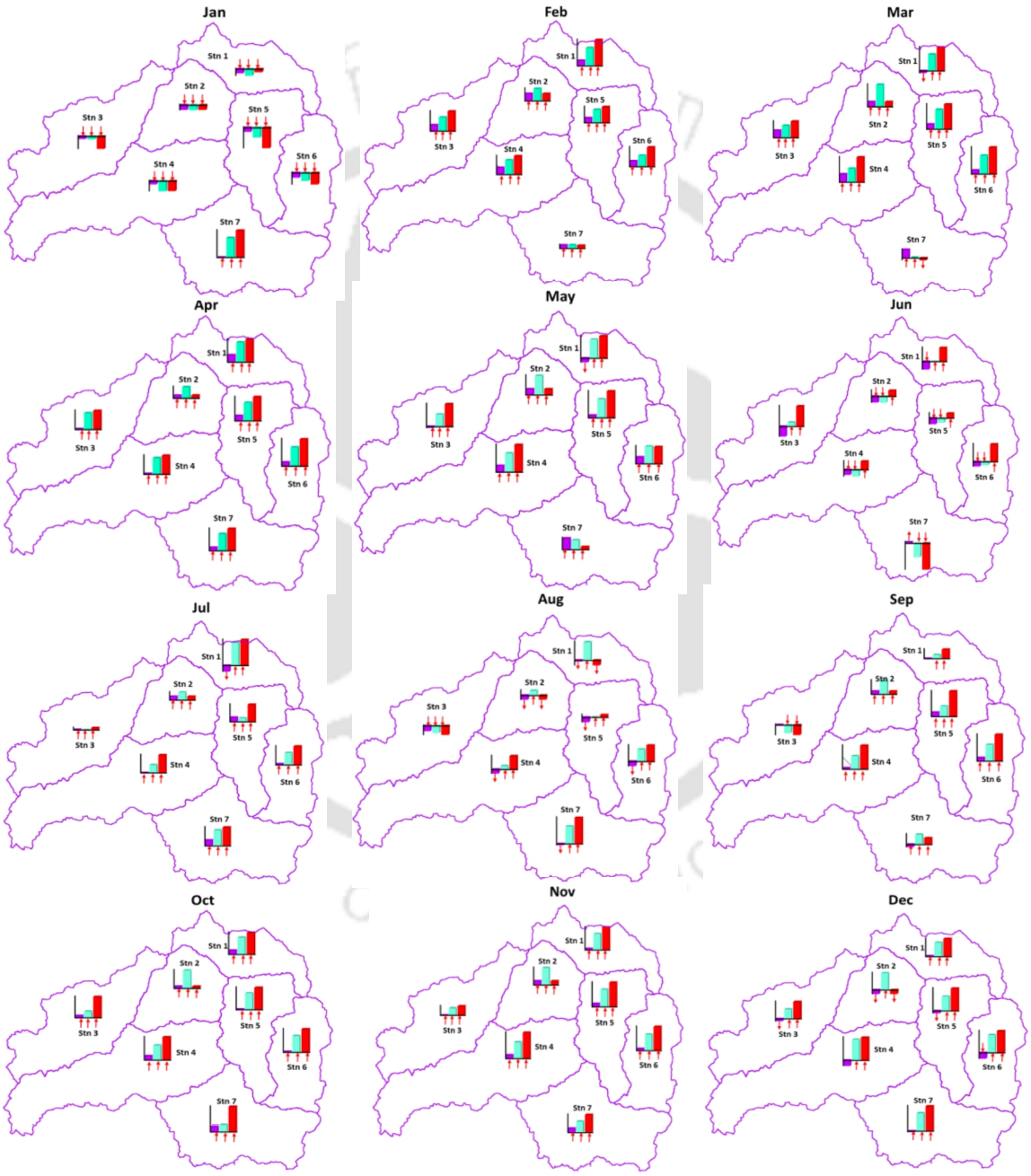
In this study, a set of 14 temperature extreme indices were selected and computed. The Expert Team on Climate Change Detection and Indices (ETCCDI) has given the justification and criteria of precipitation indices accepted by the Fourth Assessment Report of IPCC (IPCC, 2007). In this study, the temperature extreme indices (TEI) have been generated by the guidelines given by Guan et al. (2015), Wang et al. (2013), Li et al. (2012) and Rahimzadeh et al. (2009).

The details of the TEI are provided in Table 4.4. These TEIs were selected to evaluate the temperature extremity based on the frequency and intensity. The percentile based indices, Hottest day, Coldest day, Diurnal variation are grouped into intensity (°C) based indices, and Summer days, Warmest days, Coldest nights and tropical nights are grouped into frequency (days) based indices. All the indices calculated using daily minimum and maximum temperature datasets under CMIP5 GCMs.

TH-1643_136104018

(a)





TH-1643_136104018

(b)

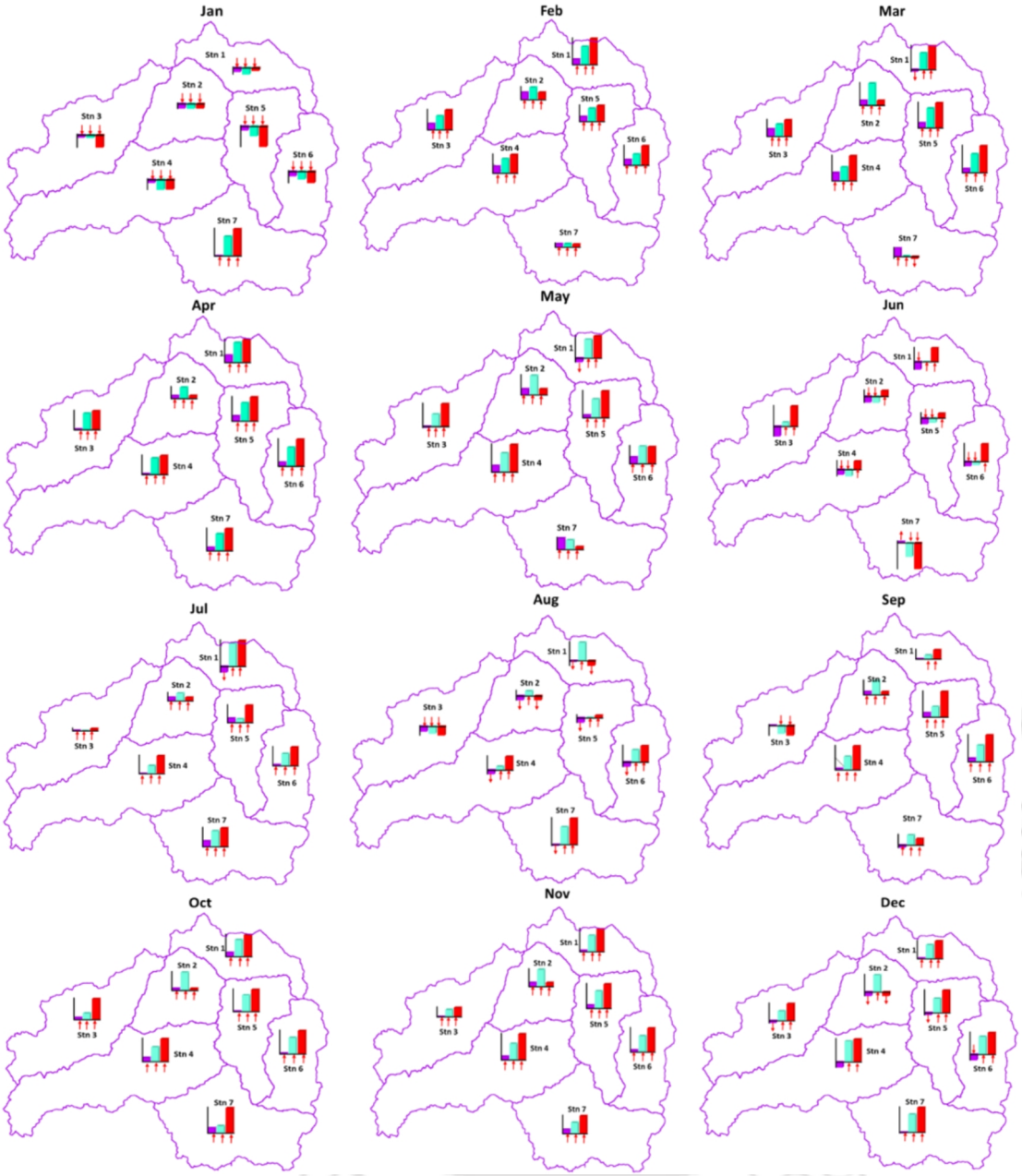


Fig. 4.13: Mann-Kendall trend results showing monthly variations in minimum temperature and maximum temperature during 2006-2100 under CMIP5-ESM2M GCM with RCP experiments (2.6, 4.5 and 8.5) across all the climate stations; (a) minimum temperature trends and (b) maximum temperature trends.

The TEIs were calculated in an intra-decadal time series (TS) domain by dividing the whole time series (1979-2100) including historical and 21st century scenarios) into multiple time series sets (each time = 25 years), where a series of 1981-2005 represents as TS1, a series of 2006-2030 represents as TS2, a series of 2041-2065 represents as TS3 and a series of 2076-2100 represents as TS4.

TH-1643_136104018

TH-1643_136104018

Table 4.3: Results of monthly trend analysis of maximum and minimum temperatures across all the climate stations under CMIP5 ESM-2M GCM with multiple RCPs (2.6, 4.5 and 8.5).

Variables	RCPs	Stations	Jan	Feb	Mar	Apr	May	Jun	Jul	Aug	Sep	Oct	Nov	Dec
Max Temperature	RCP 2.6	Stn1	-1.1	1.5	-0.3	1.2	-0.7	-1.1	-2.2**	-0.2	0.0	1.5	0.4	0.2
		Stn2	-1.2	2.1*	1.0	0.4	1.1	-0.8	1.7	-1.3	0.8	0.7	1.3	-1.3
		Stn3	-0.6	1.8	1.5	0.1	-0.1	-1.4	0.4	-1.6	0.07	0.7	-0.0	-0.7
		Stn4	-0.8	2.0*	1.7	0.1	1.2	-0.7	-0.2	-1.2	0.3	1.5	1.2	-1.8
		Stn5	-1.1	1.4	1.0	0.9	0.4	-0.8	1.6	-1.4	1.2	0.1	1.1	-0.7
		Stn6	-1.3	1.6	0.7	0.6	1.2	-0.6	0.3	-1.4	0.9	0.2	0.6	-1.9
		Stn7	-0.0	1.0	1.7	0.5	2.2*	0.1	2.1*	-0.3	-0.7	1.9*	1.3	-0.2
	RCP 4.5	Stn1	-1.8	5.4*	3.5*	3.5*	3.7*	-0.0	8.9*	6.0*	1.2	6.4*	5.7*	5.0*
		Stn2	-1.3	3.6*	4.7*	2.0*	3.7*	-0.8	3.0*	1.6	4.3*	6.9*	6.0*	6.1*
		Stn3	-0.7	4.1*	2.5*	2.9*	2.4*	0.6	0.0	-2.2**	-2.3**	2.5*	2.5	3.5*
		Stn4	-2.8**	4.3*	2.9*	2.9*	3.7*	-0.9	3.1*	1.2	4.0*	5.6*	5.8**	7.4*
		Stn5	-2.7**	3.9*	4.1*	3.2*	3.6*	-0.6	1.0	0.0	3.2*	6.3*	6.1*	5.1*
		Stn6	-2.2**	3.3*	3.9*	3.3*	3.4*	-0.5	4.7*	4.0*	5.0*	6.2*	5.7*	6.4*
		Stn7	5.6*	1.0	0.1	3.0*	1.8	-2.0**	6.1*	5.8*	3.1*	2.7*	3.9*	6.4*

TH-1643_136104018

	RCP 8.5	Stn1	-0.8	7.8*	4.9*	4.0*	4.3*	2.1*	10.0*	-1.5	2.8*	8.2*	8.0*	6.3*
		Stn2	-1.2	2.1*	1.0	0.5	1.1	0.8	1.3	-1.3	0.8	0.4	1.7	-1.3
		Stn3	-3.5**	5.9*	3.4*	3.3*	4.4*	3.0*	0.8	-2.9**	-2.9**	8.0*	3.2*	6.1*
		Stn4	-2.7**	5.5*	5.2*	3.3*	5.3*	1.2	6.9*	4.4*	7.3*	8.7*	9.2*	8.2*
		Stn5	-5.8**	4.7*	5.2*	4.2*	5.2*	0.7	6.6*	0.8	7.8*	8.4*	8.6*	8.0*
		Stn6	-3.2**	5.7*	5.6*	4.8*	3.2*	2.6*	7.2*	5.3*	8.1*	8.8*	8.4*	7.7*
		Stn7	7.8*	0.9	-0.3	3.9*	0.5	-3.9**	7.2*	8.7*	1.9	9.3	6.2*	8.8*
Min Temperature	RCP 2.6	Stn1	0.9	1.5	1.6	1.5	2.1*	1.0	-0.8	-0.3	-0.5	0.9	0.9	-1.2
		Stn2	-0.6	2.2*	2.1*	1.1	1.9	0.0	3.1*	0.3	-0.7	1.4	1.4	-0.5
		Stn3	-0.2	1.7	2.1*	1.0	2.0*	0.7	2.8*	-0.0	-0.4	1.2	1.3	-0.3
		Stn4	0.5	1.5	1.3	1.0	2.6*	0.8	2.3*	-0.8	-0.3	1.3	0.3	-0.1
		Stn5	-0.6	1.6	1.4	0.6	2.4*	0.5	2.8*	-0.1	-0.2	1.4	0.9	0.4
		Stn6	-0.4	1.8	1.9	0.4	2.1*	0.0	2.8*	0.13	-1.0	1.4	0.9	-0.4
		Stn7	1.3	1.3	1.6	0.5	2.5*	0.1	2.2*	-0.2	-0.1	1.4	1.2	0.1
	RCP 4.5	Stn1	1.0	1.6	6.5*	5.9*	5.2*	0.8	3.4*	5.6*	5.9*	7.7*	6.5*	6.8*
		Stn2	5.6*	1.5	4.4*	5.1*	3.6*	2.7*	6.9*	3.8*	6.3*	6.3*	6.7*	7.1*
		Stn3	5.0*	0.8	4.9*	4.5*	5.0**	2.9*	7.3*	3.7*	6.7*	6.5*	6.8*	8.3*
		Stn4	2.1*	-0.3	6.4*	5.0*	3.8*	2.9*	4.5*	3.0*	2.0*	-0.1	3.6*	4.1*
		Stn5	5.2*	0.2	5.4*	4.9*	3.6*	2.6*	7.3*	4.8*	5.3*	6.7*	7.1*	7.7*
		Stn6	6.1*	1.0	6.0*	5.0*	4.1*	3.6*	5.1*	4.8*	5.4*	6.4*	6.5*	7.4*
		Stn7	7.3*	-0.8	0.7	3.7*	2.5*	4.3*	6.7*	4.7*	2.3*	5.7*	5.5*	7.4*
	RCP 8.5	Stn1	-0.6	3.3*	5.9*	5.6*	5.7*	1.9	5.7*	8.0*	0.5	5.7*	8.6*	9.6*

TH-1643_136104018

		Stn2	6.6*	0.7	6.2*	5.4*	4.3*	4.4*	7.9*	5.9*	4.3*	1.1	3.6*	4.0*
		Stn3	7.0*	-0.4	6.5*	4.9*	4.8*	3.2*	8.0*	6.5*	4.3*	0.5	4.1*	3.2*
		Stn4	2.8*	-0.8	6.5*	5.0*	3.8*	3.8*	6.1*	6.3*	4.2*	-1.2	3.3*	2.4*
		Stn5	7.1*	-0.6	6.0*	5.6*	4.1*	4.9*	8.3*	7.1*	4.8*	-0.4	3.7*	2.6*
		Stn6	6.4*	0.0	6.4*	4.8*	3.8*	5.4*	6.1*	7.0*	3.9*	0.3	3.5*	2.5*
		Stn7	8.6*	-2.3**	-0.1	4.6*	2.1*	5.5*	8.0*	7.2*	5.9*	-2.1**	-3.4**	1.7

*significant increase (Z>+1.96) and **significant decrease (Z<-1.96)

Table 4.4: Temperature extreme indices details and their descriptions.

Variable	Indices	Description	Unit
Temperature Indices	10^{th} P - Min. Temp	10^{th} Percentile of daily min. temperature	°C
	80^{th} P - Min Temp	80^{th} Percentile of daily min. temperature	°C
	99^{th} P - Min Temp	99^{th} Percentile of daily min. temperature	°C
	10^{th} P - Max. Temp	10^{th} Percentile of daily max. temperature	°C
	80^{th} P - Max. Temp	80^{th} Percentile of daily max. temperature	°C
	99^{th} P - Max. Temp	99^{th} Percentile of daily max. temperature	°C
	Hottest Day	Max value of daily max. temperature	°C
	Coldest Day	Min value of daily max. temperature	°C
	Summer Days	Annual count when daily max temperature >25°C	Days
	Warmest Night	Max value of daily min. temperature	Days
	Coldest Night	Min value of daily min. temperature	Days
	Frost Days	Annual count when daily min temperature <0°C	Days
	Tropical Nights	Annual count when daily min temperature >10°C	Days
	Diurnal Variation	Difference of the average daily min and max temperature	°C

A K-means clustering approach (Hartigan and Wong, 1979) is generally utilized for the regionalization and classification of hydro-meteorological variables (Goyal and Gupta, 2014; Whitfield et al., 2002; Gong and Richman, 1995). K-means clustering method is employed to detect the intra-decadal temperature extremity in each TEI and it gave significant signatures of temperature warming over the study region.

A non-hierarchical K-means clustering method is mainly applied to detect the intra-decadal warming signature in the long term time series of each TEI. A K-means clustering is an algorithm to classify or to group the objects based on attributes/features into K number of group. K is positive integer number. The grouping is done by minimizing the sum of squares of distances between data and the corresponding cluster centroid (Hartigan and Wong, 1979). In this study, the purpose of K-mean clustering was to classify the long term time series (2006-2100) of TEI into intra-decadal time series durations (2006-2030, 2041-2065 and 2076-2100) which identified the magnitude of temperature extremity in the respective intra-decadal time series duration. Thus, the whole time series was divided into intra-decadal time series durations and then we classified each time series into 3 clusters. Each

TH-1643_136104018

cluster contains several cases of each time series datasets and this grouping of the cases is done by Euclidian Distance method (Goyal and Gupta, 2014). Each cluster group was re-categorized into High Value Cases (HVC), Moderate Value Cases (MVC) and Low Value Cases (LVC) by calculating arithmetic means of each time series of TEI.

The K-means algorithm is an algorithm to cluster n objects based on attributes into k partitions where $k<n$. An algorithm for partitioning (or clustering) N data points into K disjoint subsets S_j containing data points so as to minimize the sum-of-squares criterion. The mathematical function can be written as (Goyal and Gupta, 2014) Eq. 4.14:

$$J = \sum_{j=1}^{K} \sum_{n \in S_j} \left| x_n - \mu_j \right|^2 \ldots\ldots\ldots\ldots\ldots\ldots\ldots\ldots (4.14)$$

where x_n is a vector representing the n^{th} data point and μ_j is the geometric centroid of the data points in S_j. The Euclidean distances given by Eq. 4.15 as:

$$d(x, y) = \sqrt{\sum_{i=1}^{p} (x_i - y_i)^2} \ldots\ldots\ldots\ldots\ldots\ldots\ldots\ldots (4.15)$$

Here each x_i and y_i is a random variable chosen uniformly in the range 0 to 1. The significant F-ratio test (Winkler, 2014) is also applied to evaluate the significance level of each TEI in warming identification. It is the ratio of sum of squares (variances), which is used to analyze if the expected values of a variable within predefined groups differ from one another. The F-Ratio is applied to calculate the difference between the two clusters. From these values, the role of different mean variables in the formation of clusters is determined. F-Ratio is a statistical ratio that can be employed to analyze if the expected values of a variable within predefined groups differ from one another. Higher the value of significance (F-Ratio), lesser is the contribution of the variable to the separation of clusters.

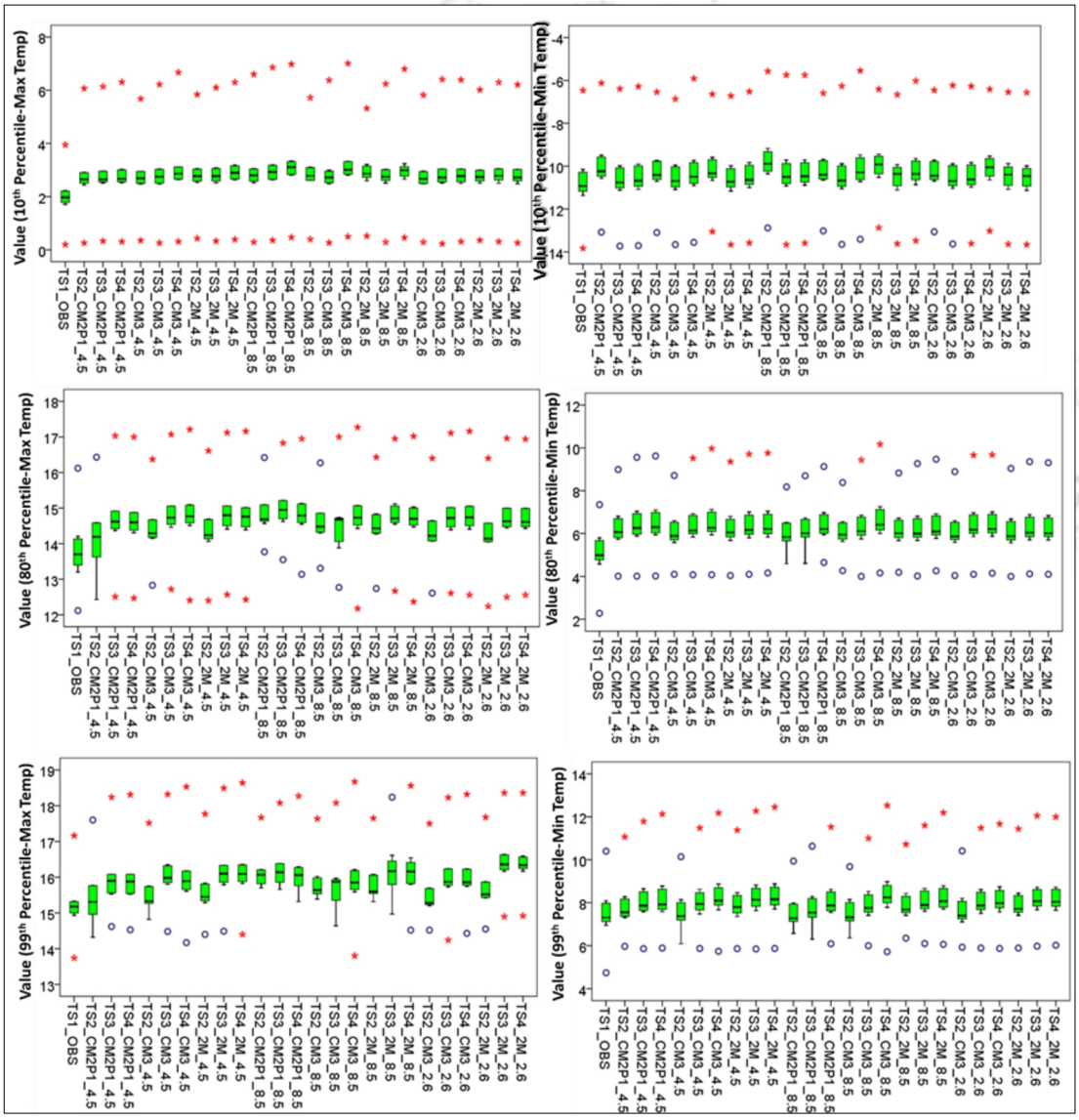
F= Between Group Variability/Within Group Variability

Fig. (4.14) displays the characteristics of temperature extreme indices as per the projected multimodel minimum and maximum temperature datasets across the study area. To highlight the spatial variations between the temperature indices in a long term decade (2006-2100), a number of statistical parameters such as minimum, maximum, standard deviation and mean have been calculated (Table 4.5).

Table 4.5 clearly shows a widespread significant changes in all temperature indices computed in the form of statistical parameters. As per Table 4.5, a percentile based indices (e.g. 10^{th} P, 80^{th} P and 99^{th} P) showed significant variations in their minimum and maximum value ranges (around 1°C to 2.0°C).

TH-1643_136104018

This shows a significant increment in the projected temperature scenarios. Another indices such as Hottest Day, Coldest Day, and Coldest Night and Warmest night also showed around 1°C to 2.5°C variations among their minimum and maximum value range. The frequency based indices such as Summer Days, Frost Days and Warmest Nights are also recorded to be having significant variations in their minimum and maximum values. The Diurnal Variation is computed as the most significant indices over the eastern Himalaya. The 10th P based on the minimum temperature showed extreme low values of the particular time series records during 2006 to 2100.



TH-1643_136104018

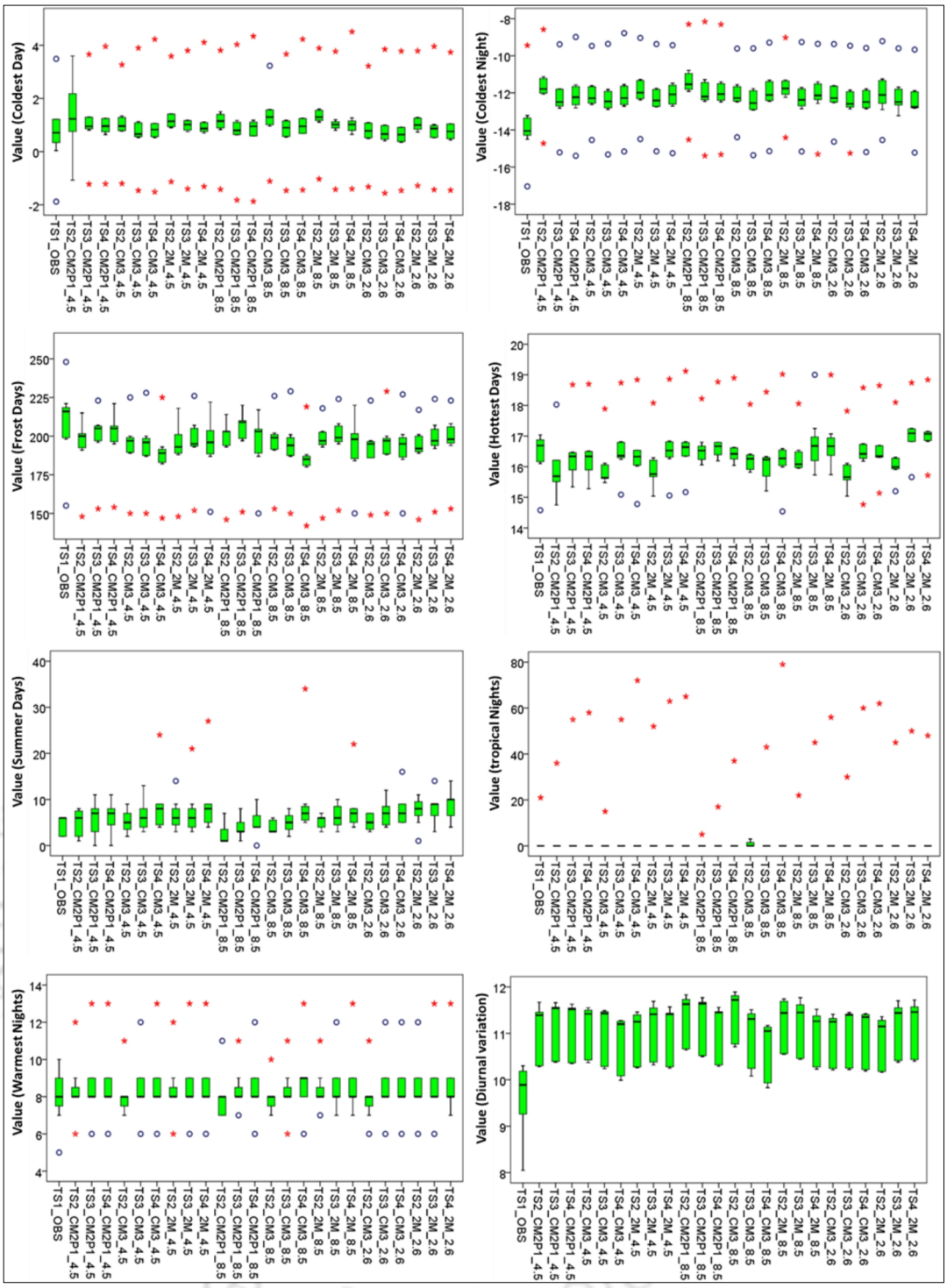


Fig. 4.14: Box plots showing projected scenarios of temperature extreme indices in a multi-temporal time series domain (TS1: 1981-2005, TS2: 2006-2030, TS3: 2041-2065 and TS4: 2076-2100) as per minimum and maximum temperature across all the climate stations.

Table 4.5 shows the average statistics of TEIs, which characterizes the temperature extremity over the selected study area under multimodel projected scenarios of temperature during the year 2006 to 2100. As per the results showed in the Table (4.5), if one compares the average response of Diurnal Variation with 10th P (minimum temperature) indices, then large variations can be noticed. This shows the severity of temperature changes in a long time duration. Rangwala and Miller (2012) reviewed the climate change impacts on the

TH-1643_136104018

Tibetan Plateau and Himalayas and found this region comes under significant sensitive regions to the ongoing global climate change and also analysed the same by various researchers (Kulkarni et al., 2010; Kulkarni et al., 2007; Wang et al., 2006). The mean and standard deviation also showed a significant variability in the multimodel projected temperature scenarios. The statistical parameters, which are computed based on the ESM-CM2P1 and ESM-CM3 model, showed higher values than the ESM-2M based experiments (Table 4.5). The box plots (Fig. 4.14) showed the temperature indices on an average basis, to highlight their statistical ranges and differences. In Fig. (4.14), one can observe the extremity of temperature indices and can compare the minimum temperature extremity and maximum temperature extremity across the climate stations. In box plots (Fig. 4.14), every climate scenario, which is showed on the horizontal axis, represents the distribution of value ranges of a particular index across all the climate stations. Here, it is found that the minimum temperature based indices have shown a significant distribution in their ranges than the maximum temperature based indices.

Fig. 4.15 shows the result of intra-decadal warming trends for each TEI. These intra-decadal warming trends or signatures have identified by applying K-means clustering approach. Here each intra-decadal TEI series for each climate model was divided into three clusters. These three clusters were re-grouped into HVC, MVC and LVC, which is based on their mean values. Table 4.6 shows the results of F-ratio test for each TEI for each climate ensemble. In Table 4.6, F-ratios estimated the difference between all the clusters in intra-decadal time series duration. Higher the value of significance, lesser is the contribution of the variable to the separation of the clusters. Table 4.6 indicates that significant differences are existed among all the TEIs in intra-decadal time series durations. It displays a significant temperature warming in each TEI. Several observations recorded high values, which correspond to less variations in the TEIs in intra-decadal time series duration.

As per the observations plotted in Fig. (4.15), a significant increment was observed in each intra-decadal time series for each TEIs except few ones. Though, in each cluster, their cases values are fluctuated and do not correspond any significant trend. The TEIs, which are calculated based upon HVC, show larger variations in their mean values than MVC and LVC. The comparative increment in temperature rate was recorded from 0.5°C to 2.5°C for all the clusters. The maximum temperature increments were recorded for the 10^{th} P (for minimum temperature) and Coldest Day (1°C to 2.5°C), while in others it varies from 0.5°C to 1°C. The frequency based indices show significant differences in the HVC, MVC and LVCs.

TH-1643_136104018

TH-1643_136104018

Table 4.5: Average statistics of TEI as per the multimodel temperature scenarios (2006-2100) over the study area.

Indices	Statistics	ESM-CM2P1		ESM-CM3			ESM-2M		
		CM2P1-RCP4.5	CM2P1-RCP8.5	CM3-RCP2.6	CM3-RCP4.5	CM3-RCP8.5	2M-RCP2.6	2M-RCP4.5	2M-RCP8.5
10^{th} P - Max Temp	Min	2.59	2.69	2.54	2.36	2.28	2.64	2.72	2.64
	Max	3.16	3.60	3.26	3.28	3.73	3.26	3.36	3.41
	Mean	2.87	3.12	2.91	2.90	2.96	2.94	2.92	2.96
	Stdev	0.11	0.19	0.15	0.18	0.27	0.12	0.13	0.17
80^{th} P - Max Temp	Min	14.18	14.56	14.37	14.30	13.38	14.24	14.22	14.17
	Max	14.91	15.37	15.01	15.07	15.14	14.95	15.06	15.07
	Mean	14.65	15.03	14.82	14.83	14.76	14.74	14.79	14.79
	Stdev	0.15	0.15	0.10	0.10	0.32	0.12	0.11	0.10
99^{th} P - Max Temp	Min	15.48	15.87	15.65	15.48	15.19	15.47	15.42	15.59
	Max	16.34	16.77	16.58	16.94	16.75	17.59	16.81	16.59
	Mean	16.00	16.36	16.10	16.09	16.05	16.44	16.22	16.28
	Stdev	0.16	0.15	0.14	0.17	0.24	0.34	0.18	0.13
Coldest Day	Min	-0.14	-0.25	-3.37	-1.06	-0.65	0.33	0.46	0.70
	Max	2.50	1.35	1.37	1.37	1.45	1.31	1.37	1.43
	Mean	1.13	0.93	0.76	0.92	1.01	0.94	1.05	1.10

TH-1643_136104018

	Stdev	0.45	0.29	0.73	0.34	0.27	0.24	0.16	0.14
Hottest Days	Min	15.84	16.44	16.02	15.80	15.53	16.00	15.70	16.03
	Max	16.91	17.41	17.31	17.75	17.58	18.21	17.64	17.55
	Mean	16.45	16.85	16.56	16.50	16.46	17.03	16.69	16.81
	Stdev	0.18	0.21	0.25	0.27	0.30	0.44	0.28	0.22
Summer Days	Min	0	0	0	0	0	1	0	0
	Max	3	2	4	5	7	5	6	5
	Mean	1	1	2	2	2	2	3	2
	Stdev	0.52	0.48	0.74	1.30	1.93	0.80	1.10	1.21
10^{th} P - Min Temp	Min	-10.74	-10.55	-10.99	-11.08	-11.25	-10.70	-10.77	-10.93
	Max	-9.91	-9.83	-10.03	-9.78	-9.61	-10.09	-10.06	-9.80
	Mean	-10.43	-10.24	-10.40	-10.42	-10.37	-10.41	-10.48	-10.35
	Stdev	0.14	0.17	0.20	0.26	0.39	0.14	0.15	0.23
80^{th} P - Min Temp	Min	6.20	5.87	5.90	5.86	5.80	6.09	6.26	5.89
	Max	6.83	6.72	6.72	6.81	6.90	6.69	6.79	6.76
	Mean	6.49	6.30	6.47	6.46	6.42	6.38	6.51	6.33
	Stdev	0.14	0.22	0.15	0.20	0.28	0.14	0.11	0.18
99^{th} P - Min Temp	Min	7.79	1.02	7.80	7.62	7.45	8.05	8.09	7.78
	Max	8.78	1.87	8.46	8.73	8.78	8.69	8.71	8.70
	Mean	8.26	1.39	8.17	8.17	8.10	8.41	8.43	8.27
	Stdev	0.18	0.22	0.16	0.26	0.38	0.12	0.15	0.20

TH-1643_136104018

Coldest Nights	Min	-12.76	-12.74	-13.34	-13.39	-13.56	-13.41	-12.79	-13.00
	Max	-11.66	-11.39	-11.79	-11.66	-11.64	-11.94	-11.74	-11.59
	Mean	-12.25	-12.03	-12.46	-12.41	-12.42	-12.39	-12.31	-12.28
	Stdev	0.22	0.26	0.30	0.35	0.45	0.26	0.22	0.29
Frost Days	Min	190	189	186	182	177	190	190	187
	Max	205	205	202	206	207	203	203	205
	Mean	199	198	194	193	193	197	196	197
	Stdev	3	4	4	6	8	3	3	5
Tropical Nights	Min	3	0	2	0	0	4	5	1
	Max	11	7	10	12	13	10	12	10
	Mean	7	3	7	7	6	7	9	6
	Stdev	2	2	2	3	5	1	1	2
Warmest Nights	Min	8.11	7.79	8.05	7.91	7.75	8.46	8.33	8.09
	Max	10.06	9.04	8.79	9.13	9.13	9.23	9.08	9.26
	Mean	8.78	8.31	8.47	8.47	8.39	8.81	8.78	8.67
	Stdev	0.37	0.27	0.17	0.25	0.38	0.16	0.17	0.24
Diurnal Variations	Min	10.95	10.86	10.78	10.67	10.38	10.92	10.83	10.77
	Max	11.41	11.45	11.39	11.45	11.59	11.26	11.26	11.41
	Mean	11.11	11.19	10.99	10.99	10.99	11.09	11.05	11.10
	Stdev	0.11	0.17	0.14	0.23	0.36	0.08	0.10	0.17

In Fig. (4.15), one can detect that the maximum increments in the temperature values are corresponded to the middle (2041-2065) and long decade (2076-2100) time series based experiments than near term decade (2006-2030) experiments. The extremity of the temperature was observed in the long term decade (2076-2100) based experiments, especially which are corresponded to the RCP8.5 experiments. Indices such as Diurnal Variation also exhibits a significant decrement in the temperature bands (difference in the minimum and maximum temperature) among all the clusters' cases. Indices such as Tropical Night is significantly enhanced its frequency (days) during 2006 to 2100.

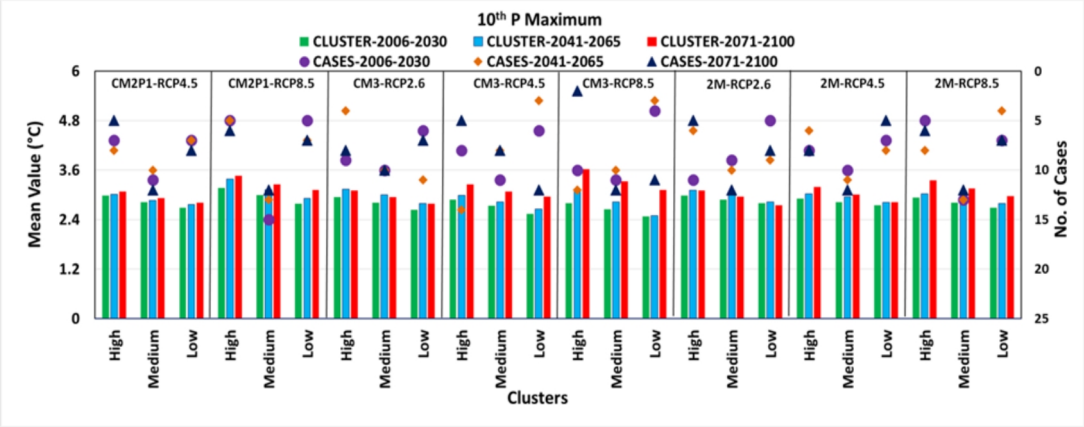
These TEIs based observations represent significant warming signatures over the north Sikkim Himalayas. The above TEIs based findings have clearly shown that each group of cluster corresponded to a significant increment in the temperature values. Clusters based identification of warming signatures clearly show consistent increments in the mean Temperature in intra-decadal time series durations. The K-means clustering approach is significantly utilized over this study region and provided better observational outputs to identify a warming signature.

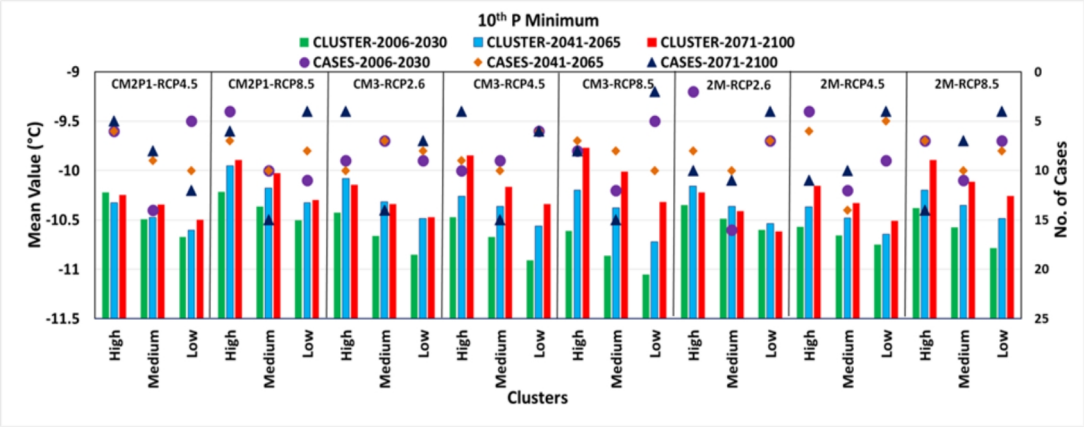
4.2.6 Precipitation trends and change evaluation in the 21st century scenarios

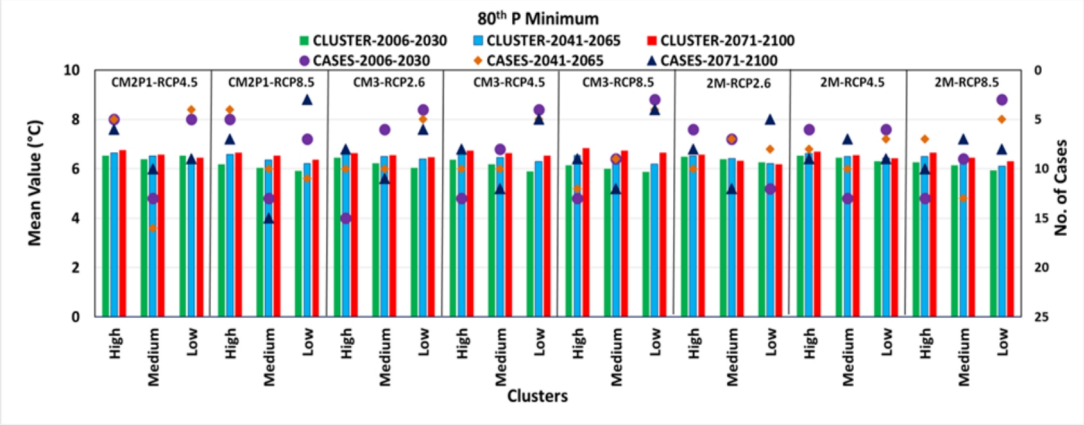
Precipitation trend analysis and precipitation variability have been evaluated in the historical (1979-2005) and 21st century time series domains (2006-2100) on a monthly basis using CMIP5 ESM-2M GCM. A Mann-Kendall (MK) test has been applied to detect the significant increase and decrease. To highlight the spatial variation in the precipitation changes, spatial plots of precipitation trends have been prepared as per the multiple RCPs.

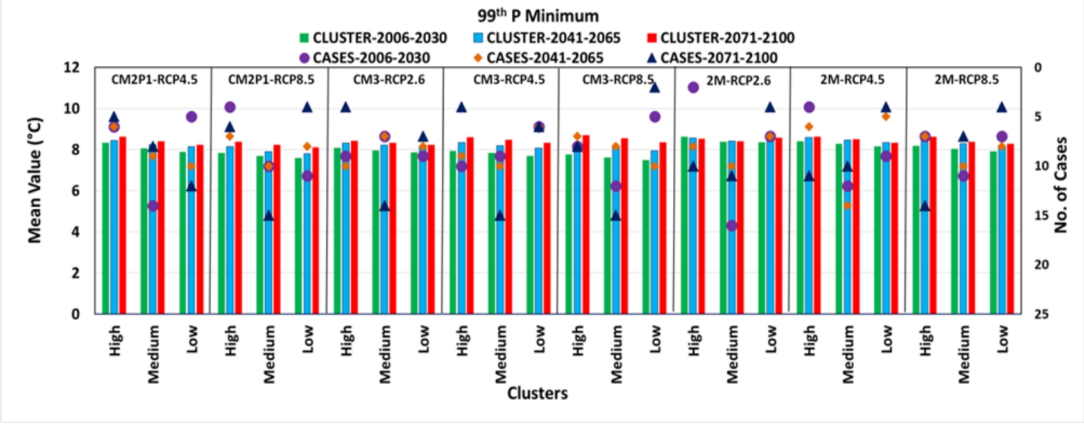
Table 4.7 shows the monthly precipitation trend analysis for historical time series (1979-2005) and here it was observed that the overall precipitation amount is increased during the historical time series also. As per significance level test Z (values larger than +1.96 as significant increase or lower than -1.96 as significant decrease) shown in Table 4.7, the precipitation trends for the February, March and April months are found significant (increasing) for almost all the sub-basins, whereas, the month of September has shown significant decreasing trend for all the sub-basins. As per Table 4.7, the decreasing trends were observed mostly in the monsoon (July to September) time periods across all the sub-basins. Table 4.7 clearly shows that most of the decreasing trends in the historical time series were observed in lower part of the catchment (SB5, SB6 and SB7). Table 4.1 shows the high intensity changes in the precipitation amounts were mostly calculated at the upstream sub-basins (SB1 and SB2) and downstream portions (SB6 and SB7).

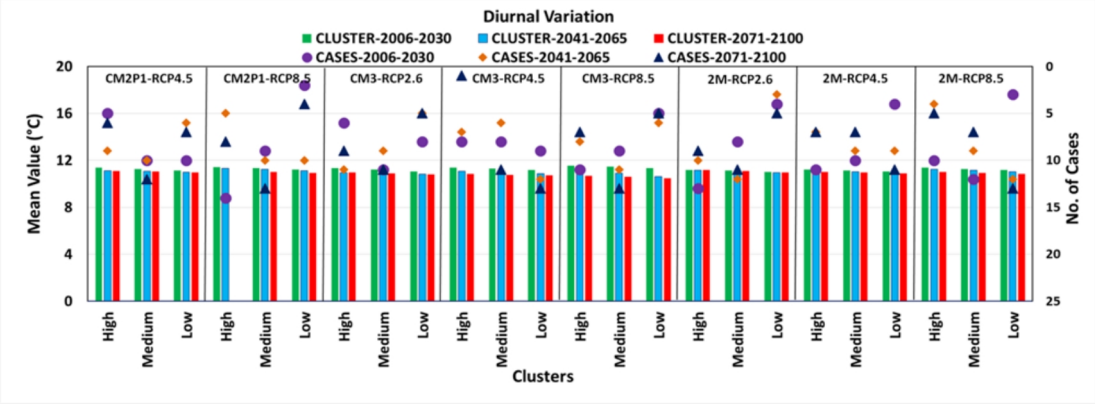
TH-1643_136104018

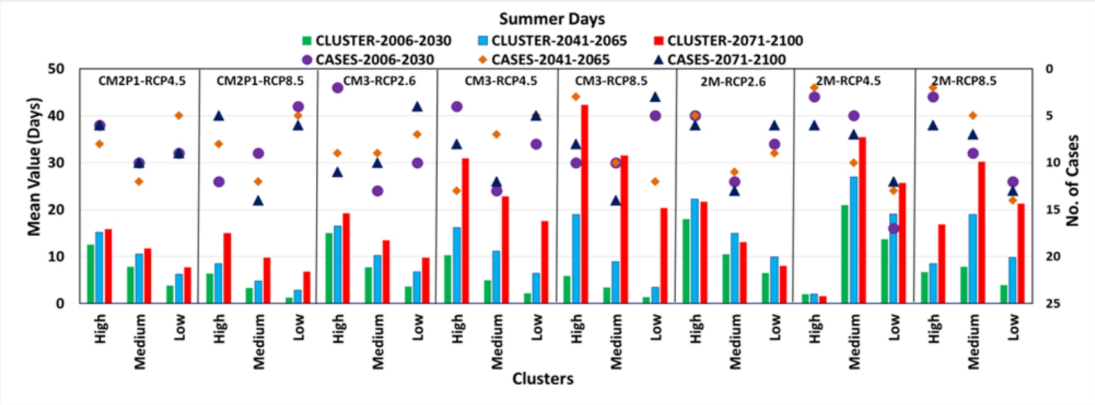

10th P Maximum
CLUSTER-2006-2030
CLUSTER-2041-2065
CLUSTER-2071-2100
CASES-2006-2030
CASES-2041-2065
CASES-2071-2100
CM2P1-RCP4.5
CM2P1-RCP8.5
CM3-RCP2.6
CM3-RCP4.5
CM3-RCP8.5
2M-RCP2.6
2M-RCP4.5
2M-RCP8.5
Mean Value (°C)
No. of Cases
High
Medium
Low
Clusters

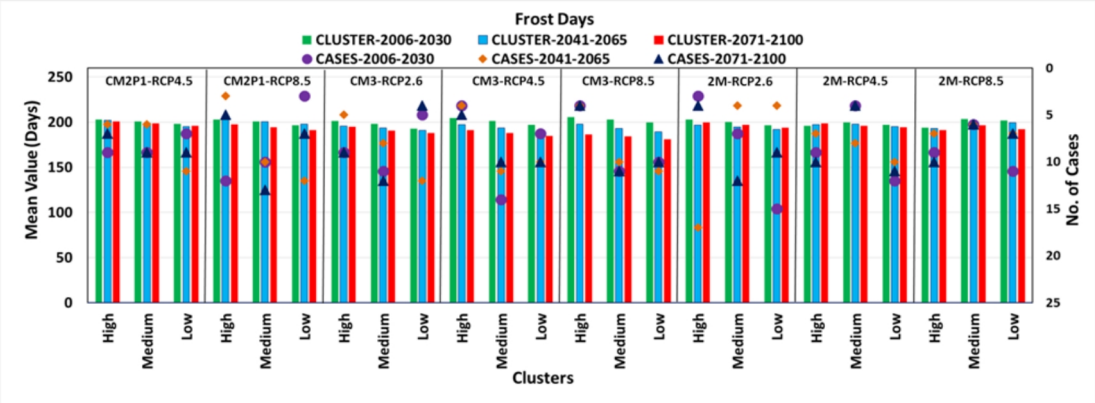

10th P Minimum
CLUSTER-2006-2030
CLUSTER-2041-2065
CLUSTER-2071-2100
CASES-2006-2030
CASES-2041-2065
CASES-2071-2100
CM2P1-RCP4.5
CM2P1-RCP8.5
CM3-RCP2.6
CM3-RCP4.5
CM3-RCP8.5
2M-RCP2.6
2M-RCP4.5
2M-RCP8.5
Mean Value (°C)
No. of Cases
High
Medium
Low
Clusters

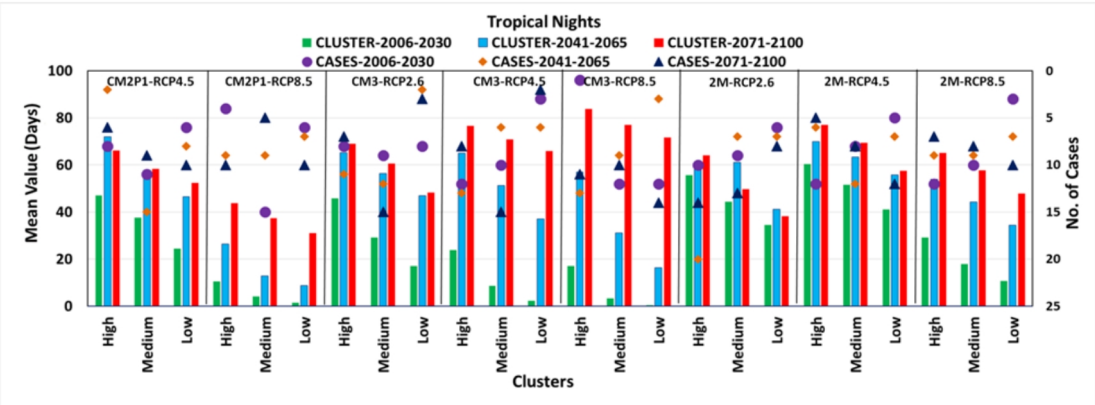

80th P Minimum
CLUSTER-2006-2030
CLUSTER-2041-2065
CLUSTER-2071-2100
CASES-2006-2030
CASES-2041-2065
CASES-2071-2100
CM2P1-RCP4.5
CM2P1-RCP8.5
CM3-RCP2.6
CM3-RCP4.5
CM3-RCP8.5
2M-RCP2.6
2M-RCP4.5
2M-RCP8.5
Mean Value (°C)
No. of Cases
High
Medium
Low
Clusters


99th P Minimum
CLUSTER-2006-2030
CLUSTER-2041-2065
CLUSTER-2071-2100
CASES-2006-2030
CASES-2041-2065
CASES-2071-2100
CM2P1-RCP4.5
CM2P1-RCP8.5
CM3-RCP2.6
CM3-RCP4.5
CM3-RCP8.5
2M-RCP2.6
2M-RCP4.5
2M-RCP8.5
Mean Value (°C)
No. of Cases
High
Medium
Low
Clusters


Diurnal Variation
CLUSTER-2006-2030
CLUSTER-2041-2065
CLUSTER-2071-2100
CASES-2006-2030
CASES-2041-2065
CASES-2071-2100
CM2P1-RCP4.5
CM2P1-RCP8.5
CM3-RCP2.6
CM3-RCP4.5
CM3-RCP8.5
2M-RCP2.6
2M-RCP4.5
2M-RCP8.5
Mean Value (°C)
No. of Cases
High
Medium
Low
Clusters


Summer Days
CLUSTER-2006-2030
CLUSTER-2041-2065
CLUSTER-2071-2100
CASES-2006-2030
CASES-2041-2065
CASES-2071-2100
CM2P1-RCP4.5
CM2P1-RCP8.5
CM3-RCP2.6
CM3-RCP4.5
CM3-RCP8.5
2M-RCP2.6
2M-RCP4.5
2M-RCP8.5
Mean Value (Days)
No. of Cases
High
Medium
Low
Clusters


Frost Days
CLUSTER-2006-2030
CLUSTER-2041-2065
CLUSTER-2071-2100
CASES-2006-2030
CASES-2041-2065
CASES-2071-2100
CM2P1-RCP4.5
CM2P1-RCP8.5
CM3-RCP2.6
CM3-RCP4.5
CM3-RCP8.5
2M-RCP2.6
2M-RCP4.5
2M-RCP8.5
Mean Value (Days)
No. of Cases
High
Medium
Low
Clusters


Tropical Nights
CLUSTER-2006-2030
CLUSTER-2041-2065
CLUSTER-2071-2100
CASES-2006-2030
CASES-2041-2065
CASES-2071-2100
CM2P1-RCP4.5
CM2P1-RCP8.5
CM3-RCP2.6
CM3-RCP4.5
CM3-RCP8.5
2M-RCP2.6
2M-RCP4.5
2M-RCP8.5
Mean Value (Days)
No. of Cases
High
Medium
Low
Clusters

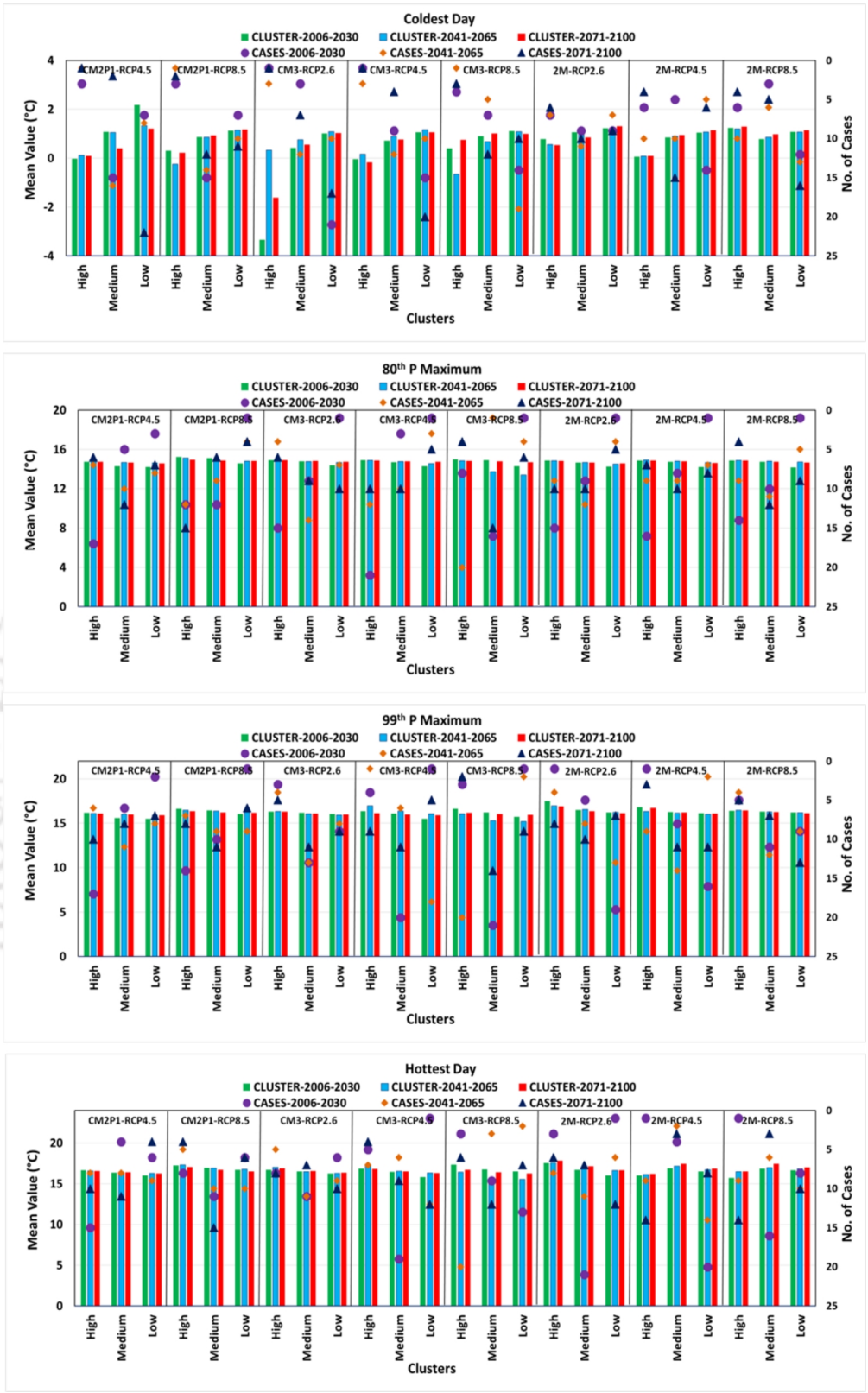


Fig. 4.15: Results show cluster based warming signatures of 12 most significant TEIs in intra-decadal time series durations as per multimodel 21st century (2006-2100) projected climate ensembles.

TH-1643_136104018

TH-1643_136104018

Table 4.6: Cluster based F-ratio test results for TEIs showing estimated difference between the clusters in intra-decadal time series domain.

Models	Time Series	10^{th} P - Min	80^{th} P - Min	99^{th} P - Min	Hottest Day	Coldest Day	Summer Days	Frost Days	Tropical Nights	Diurnal Variations	10^{th} P - Max	80^{th} P - Max	99^{th} P - Max
CM2P1-RCP4.5	2006-2030	7.96	9.38	5.64	7.03	20.44	8.94	4.46	6.43	11.35	4.09	16.14	11.83
	2041-2065	8.74	3.30	6.87	10.00	7.19	3.59	6.08	6.10	5.30	5.34	5.79	5.92
	2076-2100	7.21	13.04	7.79	3.94	6.18	8.42	5.23	5.70	8.33	5.42	5.79	9.47
CM2P1-RCP8.5	2006-2030	8.26	5.23	6.60	7.07	13.97	10.06	4.94	4.44	10.64	4.45	9.04	6.15
	2041-2065	6.34	7.88	9.74	6.95	8.37	4.60	5.98	4.23	8.11	4.57	11.31	3.70
	2076-2100	7.47	4.81	3.16	3.37	4.45	8.99	5.65	10.71	3.40	4.09	4.69	4.18
CM3-RCP2.6	2006-2030	5.30	7.57	6.27	4.11	56.06	6.30	7.11	22.65	5.08	5.63	6.58	7.08
	2041-2065	4.01	5.08	5.04	12.74	4.54	2.97	9.48	4.47	6.00	5.91	4.26	7.66
	2076-2100	6.48	5.06	5.78	5.09	10.03	5.45	4.12	5.02	6.00	8.51	9.83	8.22
CM3-RCP4.5	2006-2030	5.38	7.40	7.06	4.71	6.81	6.17	2.47	3.50	4.54	4.47	5.29	5.74
	2041-2065	6.91	7.83	3.43	6.19	3.25	2.61	4.61	11.57	8.67	3.24	6.88	10.14
	2076-2100	8.71	4.71	3.88	5.20	6.75	6.79	4.92	3.82	6.17	9.70	9.89	3.50
CM3-RCP8.5	2006-2030	5.09	4.83	9.90	6.70	11.11	5.88	4.72	8.56	7.62	3.60	9.04	5.63
	2041-2065	6.16	6.87	6.79	16.04	11.88	8.83	5.79	9.77	5.99	4.51	117.83	31.35
	2076-2100	5.73	3.89	5.95	6.37	4.67	4.48	3.55	5.36	5.34	25.05	4.21	4.67
2M-RCP2.6	2006-2030	7.89	5.44	7.08	4.05	9.00	2.33	3.62	7.18	7.73	5.04	5.76	15.98
	2041-2065	6.77	6.41	8.84	6.10	5.98	6.25	4.18	8.09	4.21	7.97	9.53	6.66

TH-1643_136104018

	2076-2100	6.74	6.28	6.32	7.61	12.44	7.15	3.83	5.20	6.28	6.15	10.52	3.69
2M-RCP4.5	2006-2030	4.46	5.66	4.73	2.78	7.39	4.81	3.83	7.27	7.91	3.56	13.18	17.14
	2041-2065	4.26	9.38	2.95	7.77	11.28	3.78	3.96	8.21	8.14	5.89	9.21	3.03
	2076-2100	8.52	5.56	8.52	8.81	5.70	6.82	7.73	4.44	7.45	5.00	6.75	10.71
2M-RCP8.5	2006-2030	8.19	6.64	2.90	3.33	8.68	3.53	4.74	4.89	4.83	4.37	13.26	3.77
	2041-2065	7.13	5.64	6.30	8.51	5.80	3.56	5.17	5.04	5.38	4.03	3.37	5.58
	2076-2100	5.30	9.02	5.06	5.96	6.65	5.07	10.45	5.50	5.92	7.21	7.47	7.02

Indian Institute of Technology Guwahati

Table 4.7: Mann-Kendall results for historical/Observed precipitation (1979-2005).

Months	SB1	SB2	SB3	SB4	SB5	SB6	SB7
	MK Z	MK Z	MK Z	MK Z	MK Z	MK Z	MK Z
Jan	1.104	1.063	1.063	1.064	0.542	1.063	1.313
Feb	2.459	2.46	2.543	2.585	1.25	2.501	2.459
Mar	1.917	1.938	1.917	1.96	0.667	1.959	2.022
Apr	2.585	2.668	2.626	2.293	1.256	2.084	3.127
May	0.542	0.521	0.542	0.5	-0.271	0.5	0.25
Jun	0.541	0.5	0.501	0.291	1.252	0.291	0.375
Jul	-1.5	-1.46	-1.501	-1.542	-1.584	-1.626	-1.626
Aug	1.25	1.23	1.209	1.209	1.209	1.209	1.042
Sep	-2.293	-2.251	-2.293	-2.293	-2.16	-2.334	-2.501
Oct	1.626	1.605	1.626	1.5	0.479	1.5	1.584
Nov	0.416	0.375	0.416	0.333	0.145	0.291	0.291
Dec	-0.125	-0.145	-0.166	-0.042	-0.208	-0.041	-0.271

(MK Z Values >+1.96, significant increase and values <-1.96, significant decrease)

Figs. 4.15 displays the comparative statistics of Mann-Kendall on a monthly average precipitation under different RCP experiments for each of the climate station. These tests show significant variations in the precipitation in spatio-temporal domain. Most of the months showed significant variability in the precipitation across all the climate stations. Here it is observed that the overall precipitation amount has been increased during the 21st century time series, because most of the months have shown significant increase in the precipitation. The statistics of significant increasing or decreasing trends are shown in Table 4.8. In Fig. 4.16, the upward directions of the arrows show increasing trends and downward directions show decrement in the values. The significance of increasing or decreasing trends were tested using significance level α=0.05. In Fig. (4.16), one can clearly observe that the precipitation trends are computed high for the RCP4.5 and RCP8.5 experiments in comparison to the RCP2.6 experiment.

The Mann-Kendall test statistics (Z) based on the significance level show that the precipitation trends significantly increased during March to June and October to November months for all the RCP scenarios, while the precipitation trends found in the July to September months are significantly decreased for all the RCPs and across all the climate stations (Table 4.8).

TH-1643_136104018

4.2.7 Precipitation extreme indices and changes

Like TEI, 12 precipitation extreme indices also generated using CMIP5 ESM-2M GCM based downscaled precipitation datasets (Guan et al., 2015; Li Rahimzadeh et al., 2009) at each climate station. The description and details of precipitation extreme indices have been shown in Table 4.9. To explore the precipitation changes, different percentiles (99^{th}, 95^{th}, 90^{th}, 85^{th}, 80^{th}) of daily total precipitation (>1mm) in a year and the number of days per year with daily precipitation exceeding 10 mm (N10), 20 mm (N20), 40 mm(N40) were calculated in long term spatio-temporal domain. The other important indices viz.SD11 (daily intensity index), RX1-Day (max-1 day precipitation), wet days and dry days were also calculated.

The long term geographical heterogeneity was assessed using quantile regression by built 99^{th}, 95^{th}, 90^{th}, 85^{th} and 80^{th} quintiles. To estimate the linear trends in the precipitation extreme indices (PEI) at high tails and lower tails, we applied the quantile regression model (Choi et al., 2013; Koenker, 2005) with year as an explanatory variable and PEI is taken as the independent variable. The quantile regression models allow one to examine changes in specific parts (quantiles) of the distribution (Choi et al., 2013). Thus, this model is suitable for calculating extreme event values (Choi et al., 2013; Tareghian and Rasmussen, 2013).

As per the Choi et al. (2014), the τ^{th} quantile ($0<\tau<1$) represents the value of the variable below which the proportion of population is τ. The central location of a distribution is represented by the median that is 0.5^{th} quantile (Koenker, 2005). In the standard regression, the expectation of the dependent variable Y, given the observation of $X=x$, can be described as (Eq. 4.16):

$$E[(Y|x)] = \beta_0 + \beta_{1x} \ldots\ldots\ldots\ldots\ldots\ldots\ldots\ldots (4.16)$$

where β_0 and β_1 are the intercept and slope coefficient of the linear regression line, respectively. The standard regression focuses on determining a conditional mean. The quantile regression is mainly concerned with the determination of a conditional quantile (Choi et al., 2014; Koenker, 2005). The linear conditional quantile function can be written in the following form (Eq. 4.17):

$$Q_y(\tau|x) = \beta_0(\tau) + x\beta_1(\tau) \ldots\ldots\ldots\ldots\ldots\ldots\ldots\ldots (4.17)$$

where $Q_y(\tau|x)$ is the expected y for the τ^{th} quantile of x and $\beta_0(\tau)$ and $\beta_1(\tau)$ are the intercept and slope coefficient of the τ^{th} quantile regression line, respectively. Further details about quantile regression models are given here (Choi et al., 2013; Hao and Naiman, 2007; Koenker, 2005).

TH-1643_136104018

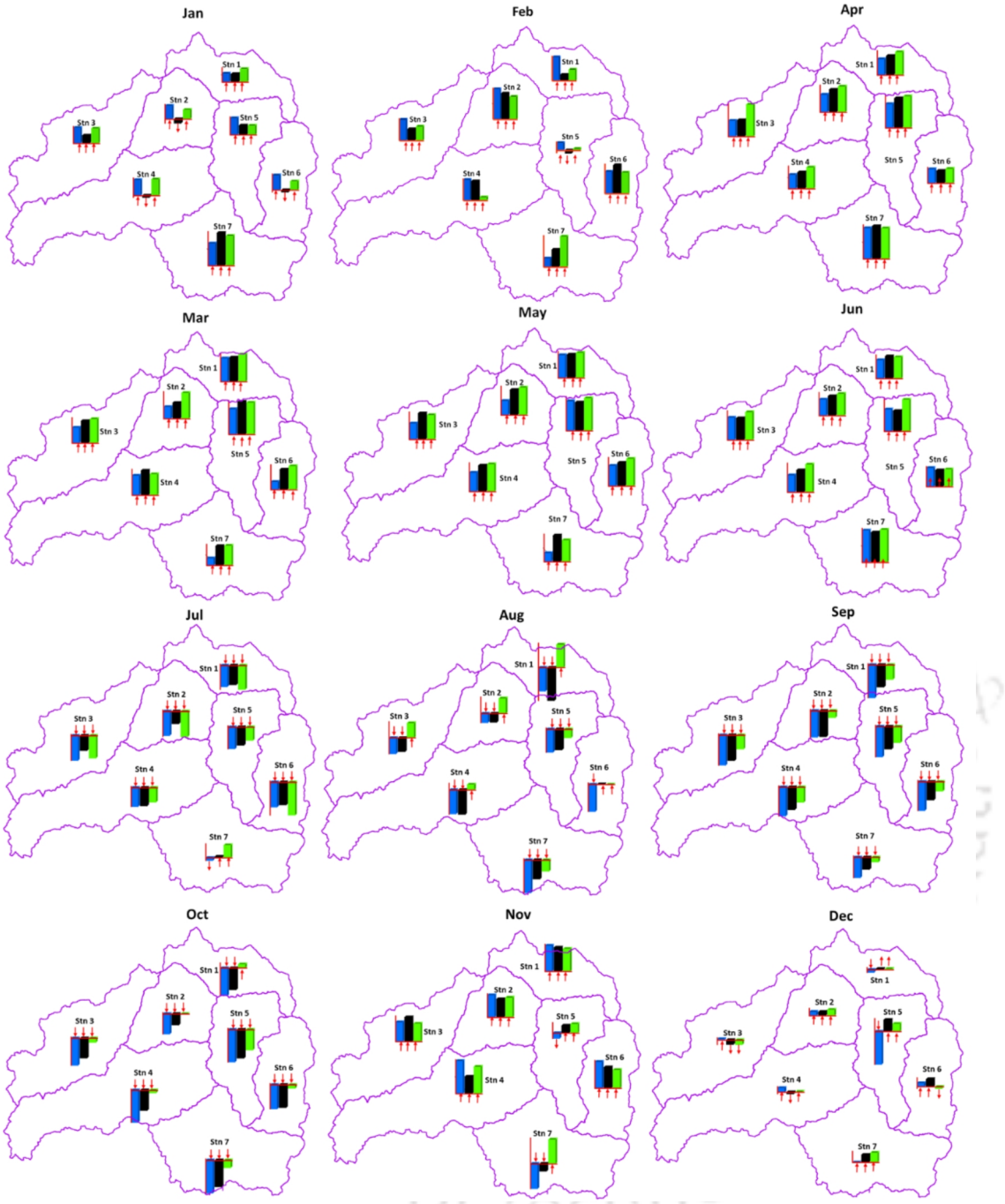


Fig. 4.16: Mann-Kendall trend results showing monthly variations in the precipitation during 2006-2100 under all RCP experiments (2.6, 4.5 and 8.5) across all the climate stations.

TH-1643_136104018

TH-1643_136104018

Table 4.8: Mann-Kendall test based results of precipitation increase and decrease as per CMIP5 ESM-2M GCM.

RCP	Stns	Jan	Feb	Mar	Apr	May	Jun	Jul	Aug	Sep	Oct	Nov	Dec
RCP 2.6	Stn1	1.6	3.7*	5.5*	3.5*	5.6*	4.2*	-5.0**	-2.9**	-7.2**	-5.6**	4.0*	-1.1
	Stn2	2.4*	4.8*	2.7*	3.8*	3.5*	3.7*	-5.7**	-1.1	-5.7**	-4.1**	3.4*	1.6
	Stn3	2.9*	3.3*	3.6*	3.4*	3.9*	5.1*	-5.9**	-1.9	-6.5**	-5.5**	3.0*	0.4
	Stn4	2.9*	3.3*	4.6*	3.0*	4.9*	3.9*	-4.5**	-2.9**	-6.3**	-6.5**	5.0*	1.8
	Stn5	3.1*	1.2	5.9*	5.2*	7.3*	5.0*	-5.2**	-2.8**	-6.6**	-6.6**	-0.8	-14.1*
	Stn6	2.7*	3.5*	1.8	3.1*	5.0*	4.3*	-5.9**	-3.3**	-6.3**	-4.9**	4.1*	1.5
	Stn7	4.1*	1.3	1.7	6.8*	2.1*	7.3*	-0.6	-4.0**	-4.4**	-6.7**	-3.8**	0.0
RCP 4.5	Stn1	2.4*	1.0	5.7*	4.2*	5.8*	5.1*	-4.6**	-4.0**	-4.8**	-4.4**	3.7*	0.4
	Stn2	1.7	4.1*	3.7*	4.9*	6.2*	4.5*	-2.5**	-1.5	-5.6**	-2.2**	2.8*	1.6
	Stn3	2.8*	1.8	5.2*	3.6*	6.4*	5.0*	-3.5**	-1.8	-5.5**	-4.0**	3.7*	-1.8
	Stn4	3.0*	3.1*	5.8*	3.6*	6.4*	5.0*	-4.3**	-3.0**	-4.9**	-4.1**	2.6*	-0.6
	Stn5	1.7	-0.4	7.7*	6.5*	7.0*	4.7*	-4.3**	-2.5**	-4.9**	-5.8**	1.1	5.0*
	Stn6	1.6	4.5*	4.7*	2.7*	5.7*	3.8*	-5.4**	0.4	-3.9**	-4.6**	3.2*	3.2*
	Stn7	5.5*	2.7*	4.5*	7.2*	6.5*	6.9*	0.2	-2.3**	-2.6**	-5.4**	-1.1	3.2*
RCP 8.5	Stn1	1.2	1.8	6.4*	5.1*	6.2*	4.9*	-5.7**	2.6*	-3.1**	0.9	3.5*	0.3
	Stn2	-0.5	3.6*	6.0*	5.6*	6.0*	5.0*	-6.0**	1.7	-1.9	0.0	3.0*	2.6*

TH-1643_136104018

	Stn3	1.5	2.2*	5.6*	7.0*	6.4*	6.4*	-5.3**	1.3	-3.0**	-0.2	2.8*	-1.9
	Stn4	-0.3	0.5	4.9*	4.7*	6.0*	6.4*	-3.4**	0.8	-3.3**	-0.1	4.1*	0.2
	Stn5	1.7	0.2	7.5*	6.9*	8.1*	7.3*	-3.1**	-1.4	-3.5**	-4.1**	1.4	3.3*
	Stn6	-0.3	3.4*	5.5*	3.2*	6.7*	4.0*	-7.8**	-0.3	-2.0**	-0.7	2.8*	-0.7
	Stn7	6.1*	4.9*	4.6*	6.7*	5.3*	7.5*	3.0*	-1.8	-1.0	-1.4	3.7*	4.2*

(*Significant increase and **significant decrease)

Table 4.9: Description of the PEIs.

Acronym	Description	Unit
99^{th} P	99^{th} Percentile of daily total precipitation amounts > 1 mm in a year in the given period	mm
95^{th} P	95^{th} Percentile of daily total precipitation amounts > 1 mm in a year in the given period	mm
90^{th} P	90^{th} Percentile of daily total precipitation amounts > 1 mm in a year in the given period	mm
85^{th} P	85^{th} Percentile of daily total precipitation amounts > 1 mm in a year in the given period	mm
80^{th} P	80^{th} Percentile of daily total precipitation amounts > 1 mm in a year in the given period	mm
N10	Number of days with precipitation of 10 mm or more in a year in the given period	days
N20	Number of days with precipitation of 20 mm or more in a year in the given period	days
N40	Number of days with precipitation of 40 mm or more in a year in the given period	days
SD11	Annual precipitation divided by the number of wet days	mm/day
RX1-day	Annual highest daily precipitation	mm
Wet days	Number of wet days in a year in the given period	days
Dry days	Number of dry days in a year in the given period	days

Table 4.10 shows the statistics of extreme and annual precipitation indices (>1mm). The description and details about the precipitation indices are shown in Table 4.9. These precipitation indices were calculated for historical time series daily precipitation data sets (1979-2005) and present and futuristic time series data sets (2006-2100) for all the RCPs at each sub-basin scale, respectively. The average values of all precipitation indices for the both time series domain for all the RCPs are shown in Table 4.10. The highest value of 99^{th} percentile at any sub-basin was almost five times the statewide mean. While the annual total precipitation is just about two times the mean. In Table 4.10, considering the standard deviation for all the RCPs, for all the sub-basins, the maximum of 99^{th} percentile was particularly large in comparison to other maxima. The mean of extreme precipitation indices for historical time series (1979-2005) such as 99^{th}, 95^{th}, 90^{th}, 85^{th}, 80^{th} percentiles vary from 55.28 to 62.08, 36.42 to 40.59, 28.22 to 30.77, 23.00 to 24.28, 19.77-20.90, respectively (Table 4.10) across all the sub-basins.

TH-1643_136104018

As per Table (4.10), for the historical time series precipitation indices (1979-2005), sub-catchment 5 has shown the extreme condition and recorded the maximum standard deviation for the all the indices calculated. In the comparison of historical time series precipitation indices (1979-2005) and futuristic precipitation indices (2006-2100) based on RCP 2.6, RCP 4.5 and RCP 8.5, as per the mean statistics from the Table 4.10, the number of wet days have been reduced in futuristic scenarios and the number of dry days have been increased. While comparing the frequency of the precipitation indices between historical and futuristic time series data sets, as per the calculated mean and standard deviation statistics taken from the Table 4.10, N10 shows increased number of frequencies for all the RCPs and across all the watersheds, however, the precipitation frequencies such as N20 and N40 have shown decreasing trend except SB7. The other indices such as RX-1 day and SD 11 has shown decreasing and increasing trends in futuristic scenarios (2006-2100), respectively, for all the sub-basins (Table 4.10).

Table (4.11) shows the mean statistics of the 8 most significant PEI in a multiple/intra-annual time series domain. These indices highlight the long term changes in the precipitation amount in terms of frequency and intensity (Table 9). As per the calculated mean and standard deviation of the extreme indices, showed in Table (4.11), one can clearly observe the existing variations in the extreme precipitation indices from Stn1 to Stn3. The mean values of these extreme indices showed significant variations between all the TS (e.g. TS 2006 to 2030, 2041 to 2065 and 2076 to 2100). The intra-decadal discrimination of these precipitation indices, based upon minimum and maximum statistics, also showed a significant heterogeneity in the multiple TS domain. The higher order TS (2041-2065 and 2076-2100) showed extreme effects of the precipitation indices which correspond to high degree magnitude of change in their frequencies and intensities.

The frequency based precipitation indices (e.g. N10, N20, Wet Days and Dry Days), which correspond to RCP4.5 and RCP8.5 experiments, showed significant increments (N10, N20 and Wet Days) and decrements (Dry Days) on an average basis prediction (Table 4.11). The intensity based indices such as 99^{th} P, 90^{th} P and 80^{th} P showed significant increments in the given TS domain. The RCP8.5 based scenarios showed extremity of the precipitation indices. Joshi et al. (2014) studied on the precipitation extremes over Central Himalayas and confirmed significant change in precipitation in the form of reduction in annual and monsoon precipitation and variations of precipitation patterns.

Here over eastern north Sikkim Himalayas, we also observed significant decrement in the average annual wet Days and increment in the Dry Days, while we also observed increased precipitation intensity as per the calculations by N10 and N20. Figs. (4.16a, 4.16b and

TH-1643_136104018

4.16c) and Table (4.11) show the results of PEI calculated using quantile regression model. The plots for observed indices (1979-2005), intensity based indices (2006-2100) and frequency based PEIs (2006-2100), are arranged separately to highlight the change in their indices values under different quantile ranges (Table 4.11). To demonstrate the increase or decrease trends in the different quantile ranges, a statistical t-test (Abbaspour et al., 2007) and P-value test (Abbaspour et al., 2011) were successfully applied (Table 4.11).As per the observed quantile regression plots (Fig. 4.17c), the frequency based PEIs such as N10, N20 and Wet Days showed increasing trends in all the quantiles (99^{th}, 95^{th}, 90^{th} defined as upper and 85^{th}, 80^{th} defined as lower quantiles). Though, a Dry Days showed a decreasing trend in their upper and lower quantiles both. It shows that the precipitation intensity and frequency both have changed.

In order to identify the changes in precipitation with respect to time (2006-2100), 95% confidence interval around the estimated coefficient (slope of the regression model), for the median quantile (which is also a 50^{th} quantile), is calculated showed in Figs. (4.17a, 4.17b and 4.17c). The t-test is evaluated based on the significance level alpha ($\alpha = 0.05$) and P values. The alpha value of 0.05 was chosen as the local significance level. Based on this significance level, values larger than 1.96 or lower than 1.96, respectively, indicate a significantly ($p<0.05$) positive (increasing) or negative (decreasing) trend. If the P values will be closer to zero, the corresponding values will be more significant for the trend.

In Table 4.11, as per the intensity based PEIs (e.g. 99P, 90P, 80P), it is observed that the estimated coefficient (slope of the regression for the respective quantile as an explanatory variable x with respect to time as an independent variable Y) and corresponding t statistics values showed almost increasing trends except 99P. In the overall comparison of all the quantiles, for both kind of PEIs, RCP8.5 showed an extreme responses and almost zero P values; that means, these trends are found most significant/vulnerable in terms of extreme precipitation in the given time series domain (2006-2100).

The increasing trends of the extreme precipitation events (PEIs) showed a significant variability in their magnitudes and amount in an intra-decadal time scales and scenarios being considered. The trends showed that the magnitude of change (intensity indices) of various PEIs is increased for the 21^{st} century projected experiments. However, their severity and variability varied as per the RCP experiments. A quantile regression approach significantly explored the spatio-temporal and geographical heterogeneity in the PEI at higher scales using t-test and P-value test. A different quantiles (99^{th}, 95^{th}, 90^{th}, 85^{th}, and 80^{th}) of PEIs showed significant increase or decrease in their frequencies and intensities.

TH-1643_136104018

TH-1643_136104018

Table 4.10: Mean and standard deviation statistics of the PEI in the historical (1979-2005) and future time series (2006-2100) calculated from CMIP5 ESM-2M GCM based downscaled daily precipitation datasets across the whole catchment.

Scenarios	Indices	Mean							Standard deviation						
		SB1	SB2	SB3	SB4	SB5	SB6	SB7	SB1	SB2	SB3	SB4	SB5	SB6	SB7
Historical 1979-2005	99th Percentile	55.61	55.66	55.61	55.34	62.08	55.28	55.91	14.31	14.41	14.31	13.98	14.84	13.99	14.21
	95th Percentile	37.11	37.17	37.11	36.48	40.59	36.42	36.64	10.54	10.63	10.54	9.92	9.01	9.97	9.83
	90th Percentile	28.71	28.80	28.71	28.29	30.77	28.22	28.21	9.07	9.05	9.07	8.78	8.20	8.79	8.20
	85th Percentile	23.38	23.42	23.39	23.03	24.28	23.00	23.09	7.49	7.51	7.49	6.89	6.43	6.91	6.44
	80th Percentile	20.16	20.22	20.17	19.81	20.90	19.77	19.95	6.15	6.18	6.15	5.56	5.48	5.57	5.36
	N10	84.96	84.85	85.04	83.81	78.30	83.70	86.67	17.65	17.70	17.70	17.85	13.52	17.74	19.68
	N20	35.96	35.81	36.00	35.63	37.67	35.44	36.81	12.76	12.92	12.77	13.03	12.10	12.83	13.03
	N40	8.74	8.78	8.78	8.56	11.04	8.48	8.48	6.29	6.30	6.30	6.02	6.22	6.05	5.32
	SD11	12.85	12.80	12.86	12.74	13.12	12.72	12.65	3.27	3.28	3.27	3.02	2.88	3.03	2.84
	RX1-Day	75.60	75.36	75.60	74.48	82.34	74.33	74.45	28.44	28.44	28.44	27.31	28.11	27.30	26.43
	Wet Days	198.22	198.15	198.19	198.41	188.52	198.11	201.85	36.21	36.18	36.18	32.92	28.04	32.89	31.67
	Dry Days	166.78	166.85	166.81	166.59	176.48	166.89	163.15	36.21	36.18	36.18	32.92	28.04	32.89	31.67
RCP2.6	99th Percentile	38.56	39.52	39.35	39.02	45.83	38.86	37.83	3.77	3.68	3.35	3.49	5.34	4.05	2.91

TH-1643_136104018

	95th Percentile	29.47	30.34	30.11	30.01	34.10	29.78	30.74	2.05	2.11	1.97	1.90	2.52	2.17	1.95
	90th Percentile	24.83	25.48	25.39	25.12	28.26	25.02	26.28	1.74	1.50	1.60	1.58	2.41	1.68	1.74
	85th Percentile	21.87	22.43	22.31	22.10	24.69	22.08	23.24	1.72	1.45	1.35	1.51	2.03	1.45	1.60
	80th Percentile	19.61	20.19	20.05	19.85	21.90	19.82	20.98	1.58	1.30	1.20	1.30	1.96	1.31	1.49
	N10	98.96	95.31	102.40	101.77	89.27	98.15	97.80	7.58	8.38	7.41	7.93	7.18	8.06	6.98
	N20	33.95	34.71	36.24	35.47	38.61	34.93	37.36	5.81	5.74	5.01	5.60	5.89	5.61	5.85
	N40	1.77	1.98	2.04	1.91	4.27	1.73	1.41	1.33	1.23	1.38	1.36	1.91	1.31	1.22
	SD11	12.92	13.31	13.22	13.15	13.93	12.98	13.75	0.76	0.72	0.66	0.71	0.86	0.66	0.73
	RX1-Day	46.54	47.41	47.19	46.25	53.25	46.04	43.64	6.48	6.58	6.21	6.13	8.55	5.73	5.22
	Wet Days	179.29	168.85	179.73	180.94	162.73	177.55	165.53	9.79	9.49	8.89	8.99	9.16	8.85	8.27
	Dry Days	185.71	196.15	185.27	184.06	202.27	187.45	199.47	9.79	9.49	8.89	8.99	9.16	8.85	8.27
RCP4.5	99th Percentile	38.47	38.63	38.82	39.69	44.80	38.21	37.83	3.56	3.67	3.69	4.45	4.74	3.94	3.19
	95th Percentile	29.65	30.44	29.58	30.32	34.18	29.82	30.32	2.05	2.22	2.24	2.09	2.47	2.35	1.91
	90th Percentile	25.14	25.91	25.16	25.21	28.44	25.26	26.00	1.56	1.54	1.69	1.60	1.91	1.76	1.56
	85th Percentile	22.02	22.91	22.08	22.16	25.04	22.17	23.16	1.40	1.36	1.43	1.31	1.73	1.47	1.44
	80th Percentile	19.68	20.69	19.68	20.02	22.12	19.76	20.86	1.17	1.24	1.21	1.16	1.58	1.32	1.28
	N10	99.76	101.05	100.37	100.92	90.11	99.81	95.41	6.85	8.08	6.79	7.98	7.17	8.31	8.14
	N20	34.34	38.59	34.35	36.08	39.91	35.16	36.58	5.00	5.49	5.36	5.53	5.33	5.87	5.58
	N40	1.78	1.78	1.86	2.28	4.00	1.74	1.28	1.28	1.23	1.29	1.60	1.86	1.51	1.15
	SD11	13.08	13.58	13.11	13.19	14.06	13.04	13.67	0.61	0.67	0.61	0.60	0.74	0.69	0.66
	RX1-Day	46.78	46.07	46.71	46.85	54.06	44.34	43.62	6.27	5.88	6.25	6.92	7.63	5.36	5.40
	Wet Days	177.62	174.57	178.16	179.43	163.01	178.25	162.33	9.15	9.48	9.36	9.88	8.44	8.63	9.33

TH-1643_136104018

	Dry Days	187.38	190.43	186.84	185.57	201.99	186.75	202.67	9.15	9.48	9.36	9.88	8.44	8.63	9.33
RCP8.5	99th Percentile	39.05	39.78	38.74	39.21	45.30	39.37	37.27	3.59	3.71	3.47	3.67	4.40	3.77	3.21
	95th Percentile	30.19	30.58	29.86	29.93	34.20	29.92	29.91	2.22	2.48	2.09	2.04	2.25	2.33	2.27
	90th Percentile	25.23	25.59	25.28	25.16	28.66	25.02	25.39	1.54	2.01	1.48	1.48	1.75	1.79	1.66
	85th Percentile	22.07	22.47	22.17	22.08	24.91	21.94	22.73	1.41	1.53	1.39	1.42	1.56	1.48	1.50
	80th Percentile	19.68	20.02	19.89	19.85	21.95	19.56	20.42	1.18	1.55	1.26	1.25	1.43	1.37	1.34
	N10	100.23	97.08	101.92	101.05	89.53	98.76	94.47	9.62	10.32	9.21	9.96	7.72	7.98	9.82
	N20	34.80	35.51	35.90	36.14	39.43	34.53	34.83	5.39	6.47	6.02	6.05	4.50	5.64	5.72
	N40	1.83	2.21	1.98	2.14	4.40	2.04	1.25	1.38	1.49	1.36	1.48	1.84	1.41	1.18
	SD11	13.07	13.25	13.16	13.06	13.94	12.96	13.36	0.68	0.81	0.62	0.68	0.66	0.67	0.71
	RX1-Day	46.73	47.09	47.27	46.97	55.16	47.11	43.29	7.27	6.74	7.08	6.17	9.37	6.19	5.14
	Wet Days	180.17	172.69	180.74	182.01	164.00	179.75	164.45	10.61	11.45	10.42	9.98	11.67	8.96	11.99
	Dry Days	184.83	192.31	184.26	182.99	201.00	185.25	200.55	10.61	11.45	10.42	9.98	11.67	8.96	11.99

TH-1643_136104018

Table 4.11: Average statistics of Precipitation Indices as per ESM-2M RCP scenarios (2006-2100).

Statistics	PEI	2006-2040			2041-2065			2071-2100		
		RCP 2.6	RCP 4.5	RCP 8.5	RCP 2.6	RCP 4.5	RCP 8.5	RCP 2.6	RCP 4.5	RCP 8.5
Mean	99th Percentile	39.85	39.49	39.82	39.88	39.61	40.02	39.52	39.4	39.59
	90th Percentile	25.77	25.87	25.76	25.84	25.76	25.7	25.75	25.83	25.78
	80th Percentile	20.34	20.4	20.2	20.37	20.34	20.06	20.36	20.32	20.21
	N10	98	98	98	98	96	93	98	98	97
	N20	36	36	36	36	35	34	36	36	36
	RX-1 Day	47	47	48	47	47	48	47	47	47
	Wet Days	174	173	175	173	170	168	174	173	174
	Dry Days	191	192	190	192	195	197	191	192	191
Standard deviation	99th Percentile	1.38	1.46	1.45	1	1.47	1.82	1.51	1.66	1.21
	90th Percentile	0.72	0.63	0.64	0.55	0.66	0.73	0.86	0.71	0.6
	80th Percentile	0.63	0.53	0.51	0.51	0.52	0.41	0.7	0.5	0.56
	N10	3.14	3.92	6	3.66	3.57	3.36	2.73	3.06	3.42
	N20	2.43	2.34	2.83	2.14	2.28	1.49	2.7	2.04	2.31
	RX-1 Day	2.22	2.36	2.75	2.11	2.27	2.53	1.99	2.55	2.34
	Wet Days	4.26	5.44	7.86	3.28	4.58	4.78	4.17	3.63	5.15
	Dry Days	4.26	5.44	7.86	3.28	4.58	4.78	4.17	3.63	5.15
Minimum	99th Percentile	36.52	35.29	36.48	37.7	36.74	36.69	36.52	35.29	36.48
	90th Percentile	24.07	24.18	24.29	24.42	24.42	24.29	24.2	24.18	24.75
	80th Percentile	18.94	18.96	18.79	19.36	19.13	19.15	18.94	18.96	19.25

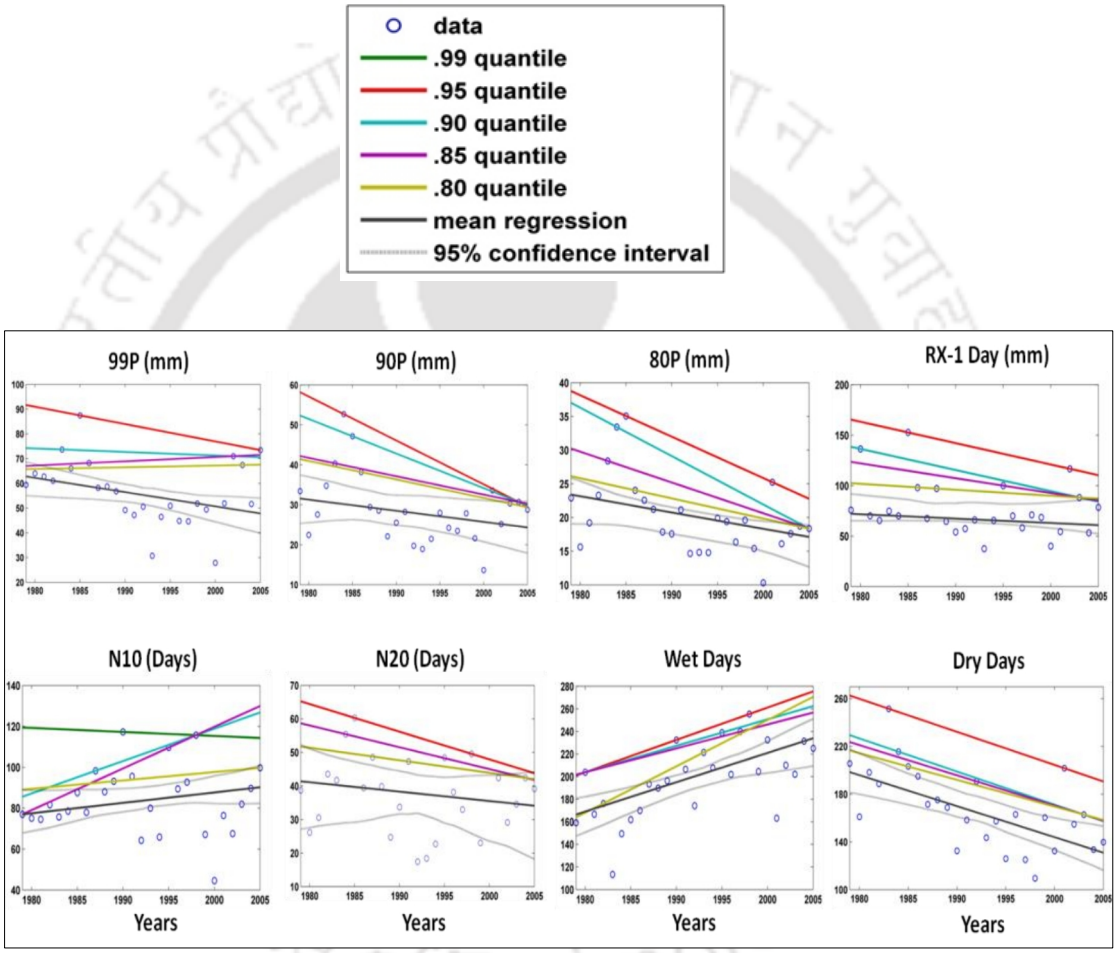
TH-1643_136104018

	N10	90	87	84	91	87	84	93	90	88
	N20	30	30	29	31	30	30	30	30	32
	RX-1 Day	42	41	41	44	43	43	42	42	43
	Wet Days	162	159	159	167	159	160	162	167	163
	Dry Days	182	177	173	185	188	188	184	185	181
Maximum	99th Percentile	44.04	43.53	43.29	42.88	42.38	43.29	42.59	43.53	41.33
	90^{th} Percentile	27.49	27.69	27.3	26.53	27.69	27.11	27.49	27.17	27.3
	80^{th} Percentile	22.15	21.86	21.86	21.34	21.86	20.8	22.15	21.12	21.86
	N10	106	107	111	106	104	98	105	103	103
	N20	42	42	43	40	40	36	42	38	42
	RX-1 Day	55	53	54	51	52	53	51	53	53
	Wet Days	183	188	192	180	177	177	181	180	184
	Dry Days	203	206	206	198	206	205	203	198	202

4.2.8 Spatio-temporal variations in the PEIs

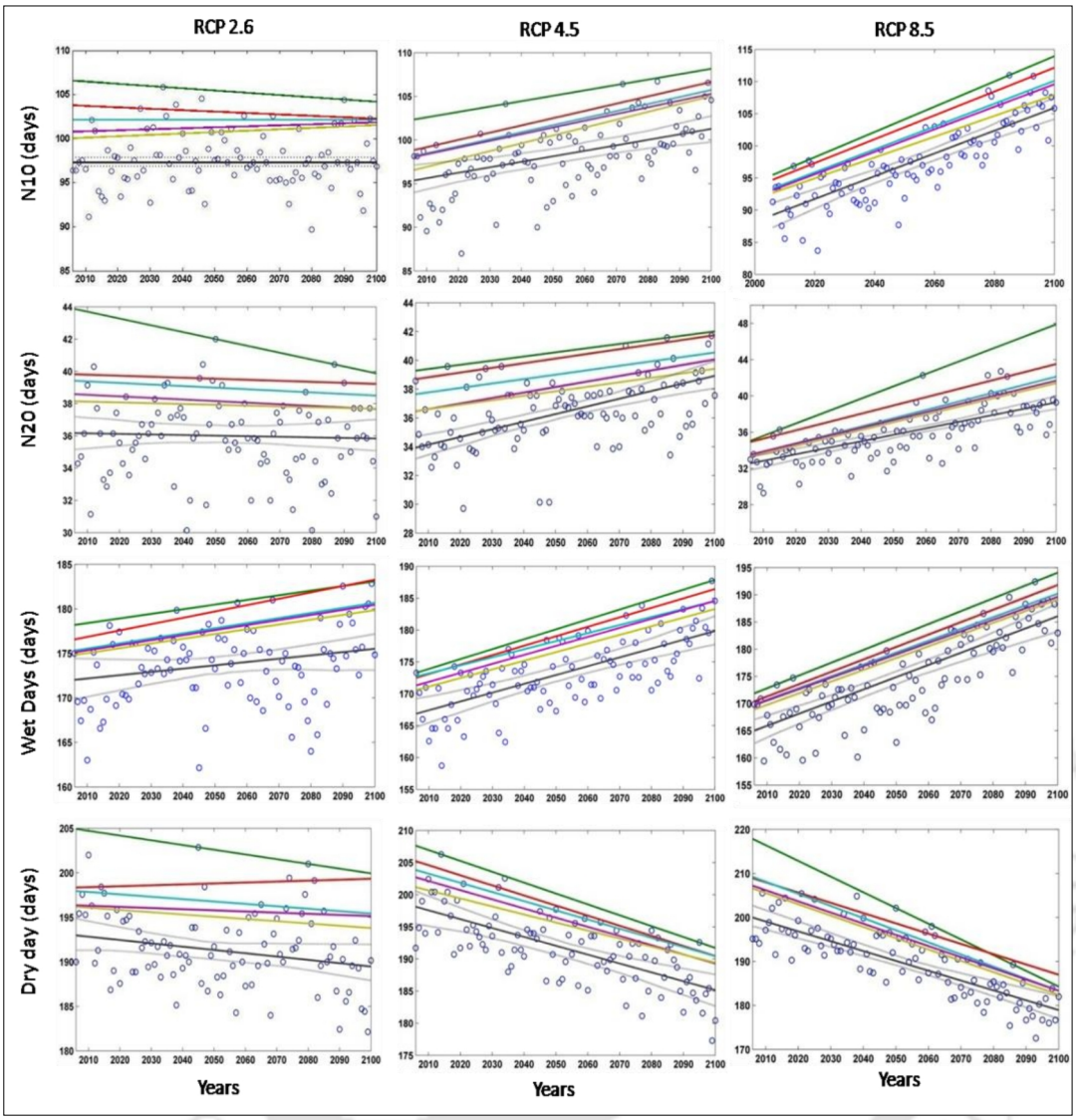
To highlight the spatial variations in the precipitation extremes, most significant PEIs were interpolated using IDWA method at the selected study region under CMIP5 ESM-2M GCM and RCPs (2006-2100). Each PEI highlights the spatial variation in the precipitation based on their frequencies and intensities in an intra-decadal time series domains. The PEIs results showed an enormous variation in their frequency and intensity over the study area.

(a)



TH-1643_136104018

(b)



TH-1643_136104018

(c)

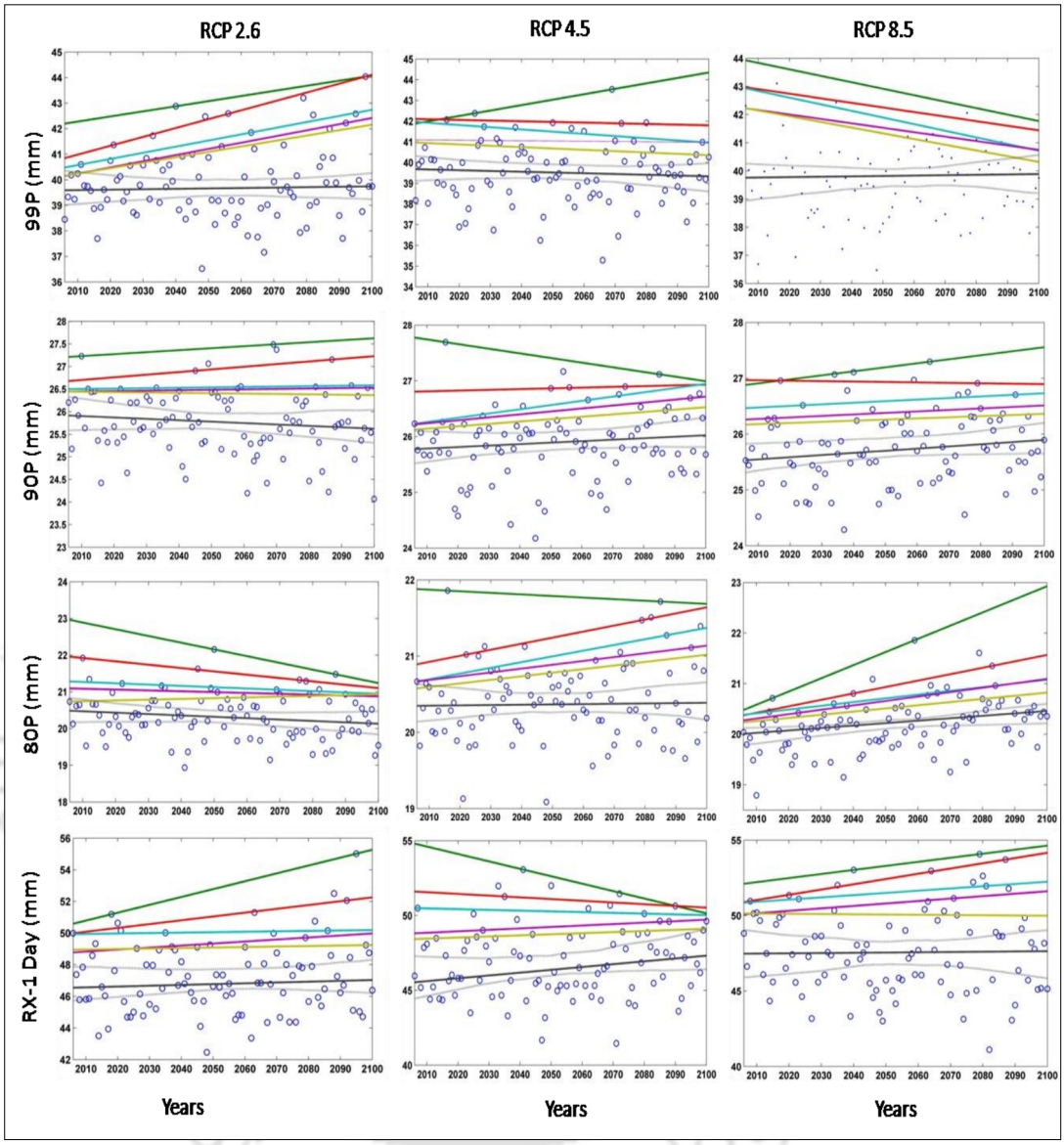


Fig. 4.17: Quantile regression based plots for precipitation extreme indices in an intra-decadal time series durations: (a) observed quantile plots (1979-2005), (b) Plots for the intensity based extreme precipitation indices under RCPs 2.6, 4.5 and 8.5 experiments, (c) Plots for the frequency based extreme precipitation indices under RCPs 2.6, 4.5 and 8.5 experiments.

TH-1643_136104018

Table 4.12: Estimated coefficient values based on the quantile regression analysis along with t stat and P value tests for the precipitation indices as per upper and lower quantiles under different RCP experiments.

Indices	Quantiles	t-stat	P-value	t-stat	P-value	t-stat	P-value
		RCP2.6		RCP4.5		RCP8.5	
99P	99th Quantile (Q1)	1.412	0.161	1.353	0.179	-3.281	0.001
	95th Quantile (Q2)	2.87	0.005	-0.245	0.806	-2.154	0.033
	90th Quantile (Q3)	2.83	0.005	-0.845	0.399	-2.908	0.004
	85th Quantile (Q4)	2.62	0.01	-0.141	0.887	-1.452	0.149
	80th Quantile (Q5)	2.21	0.029	-0.877	0.382	-1.668	0.098
90P	99th Quantile (Q1)	0.612	0.541	-0.694	0.488	1.081	0.282
	95th Quantile (Q2)	0.663	0.508	0.205	0.838	-0.151	0.879
	90th Quantile (Q3)	0.236	0.813	1.699	0.092	0.55	0.583
	85th Quantile (Q4)	0.353	0.724	2.146	0.034	0.672	0.502
	80th Quantile (Q5)	-0.28	0.78	1.884	0.062	0.707	0.481
80P	99th Quantile (Q1)	-1.41	0.161	-0.303	0.762	2.792	0.006
	95th Quantile (Q2)	-1.52	0.131	1.462	0.146	2.195	0.03
	90th Quantile (Q3)	-0.76	0.446	1.732	0.086	1.852	0.067
	85th Quantile (Q4)	-0.55	0.58	1.469	0.144	2.734	0.007
	80th Quantile (Q5)	0.507	0.612	1.645	0.103	2.177	0.032
N10	99th Quantile (Q1)	-1.39	0.166	2.336	0.021	16.06	0
	95th Quantile (Q2)	0	1	4.334	0	7.281	0
	90th Quantile (Q3)	0	1	5.194	0	6.314	0
	85thQuantile (Q4)	0.579	0.563	4.35	0	8.699	0
	80th Quantile (Q5)	0	1	5.028	0	8.831	0
N20	99th Quantile (Q1)	-1.33	0.188	4.455	0	5.576	0
	95th Quantile (Q2)	-0.89	0.378	1.85	0.067	4.806	0
	90th Quantile (Q3)	0	1	2.017	0.046	4.273	0

TH-1643_136104018

	85thQuantile (Q4)	0	1	1.388	0.168	6.404	0
	80th Quantile (Q5)	0	1	1.117	0.266	9.285	0
RX-1 Day	99th Quantile (Q1)	2.83	0.005	-2.583	0.011	2.218	0.028
	95th Quantile (Q2)	1.136	0.258	0	1	2.514	0.013
	90th Quantile (Q3)	0	1	0	1	1.157	0.25
	85thQuantile (Q4)	0.917	0.361	1.216	0.226	1.123	0.264
	80th Quantile (Q5)	0	1	1.702	0.092	0	1
Wet Days	99th Quantile (Q1)	2.7	0.008	11.8	0	16.92	0
	95th Quantile (Q2)	4.38	0	6.31	0	10.02	0
	90th Quantile (Q3)	3.14	0.002	5.952	0	10.93	0
	85thQuantile (Q4)	3.05	0.002	6.418	0	11.93	0
	80th Quantile (Q5)	2.65	0.009	6.85	0	9.615	0
Dry Days	99th Quantile (Q1)	-1.01	0.313	-7.098	0	-4.885	0
	95th Quantile (Q2)	0.371	0.711	-5.074	0	-4.081	0
	90th Quantile (Q3)	-0.88	0.378	-4.367	0	-9.299	0
	85thQuantile (Q4)	-0.57	0.568	-4.352	0	-9.852	0
	80th Quantile (Q5)	-1.12	0.266	-5.995	0	-8.473	0

Note: The Bold values are significant trends

They showed significant variations in each PEI in intra-decadal time durations. Based on the spatial plots, a significant increment was observed in the frequencies and intensities of the precipitation indices. Figs. (4.18a, 4.18b, 4.18c and 4.18d) showed that an intensity based indices such as 99P, 90P and 80P significantly suffered from the precipitation variability. The variability could be observed in an intra-decadal time series and it is found quite high for the RCP8.5 based scenario results. In Figs. (4.18a, 4.18b, 4.18c and 4.18d), one can observe that the frequency based indices such as Dry days and Wet days are increased over the upstream (e.g. SB1, SB2) and downstream portions (e.g. SB6, SB7) of the catchment, respectively.

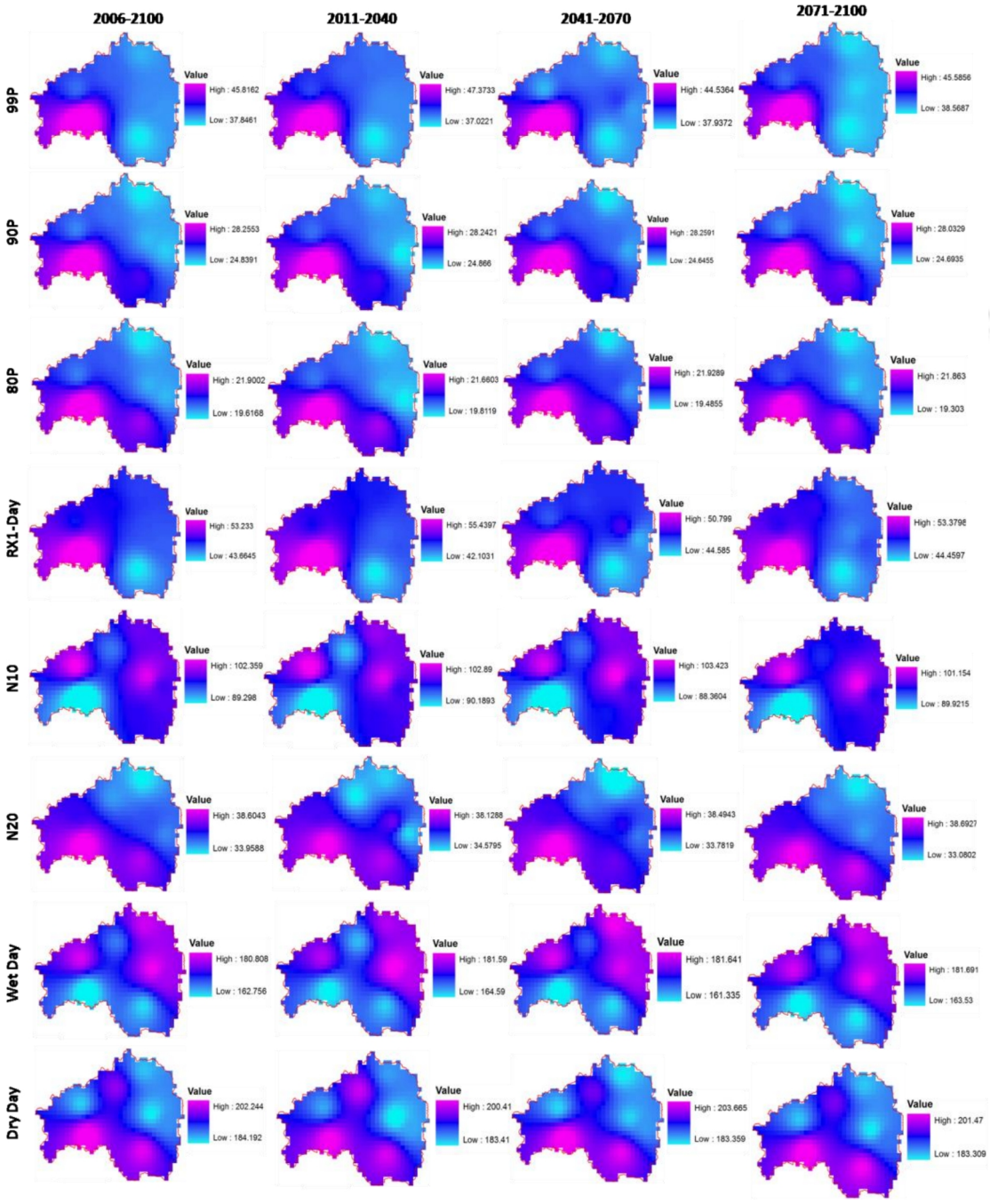
The increasing trends of the extreme precipitation events (PEIs) showed a significant variability in their magnitudes and amount in an intra-decadal time scales and scenarios

TH-1643_136104018

being considered. The CMIP5 ESM-2Mmodel based predictions of extreme precipitation heterogeneity tended to expect increases over the eastern Himalayan catchment, could be a cause of increasing temperature due to enhanced anthropogenic activities and increasing level of carbon dioxide concentrations (Taylor et al., 2012).

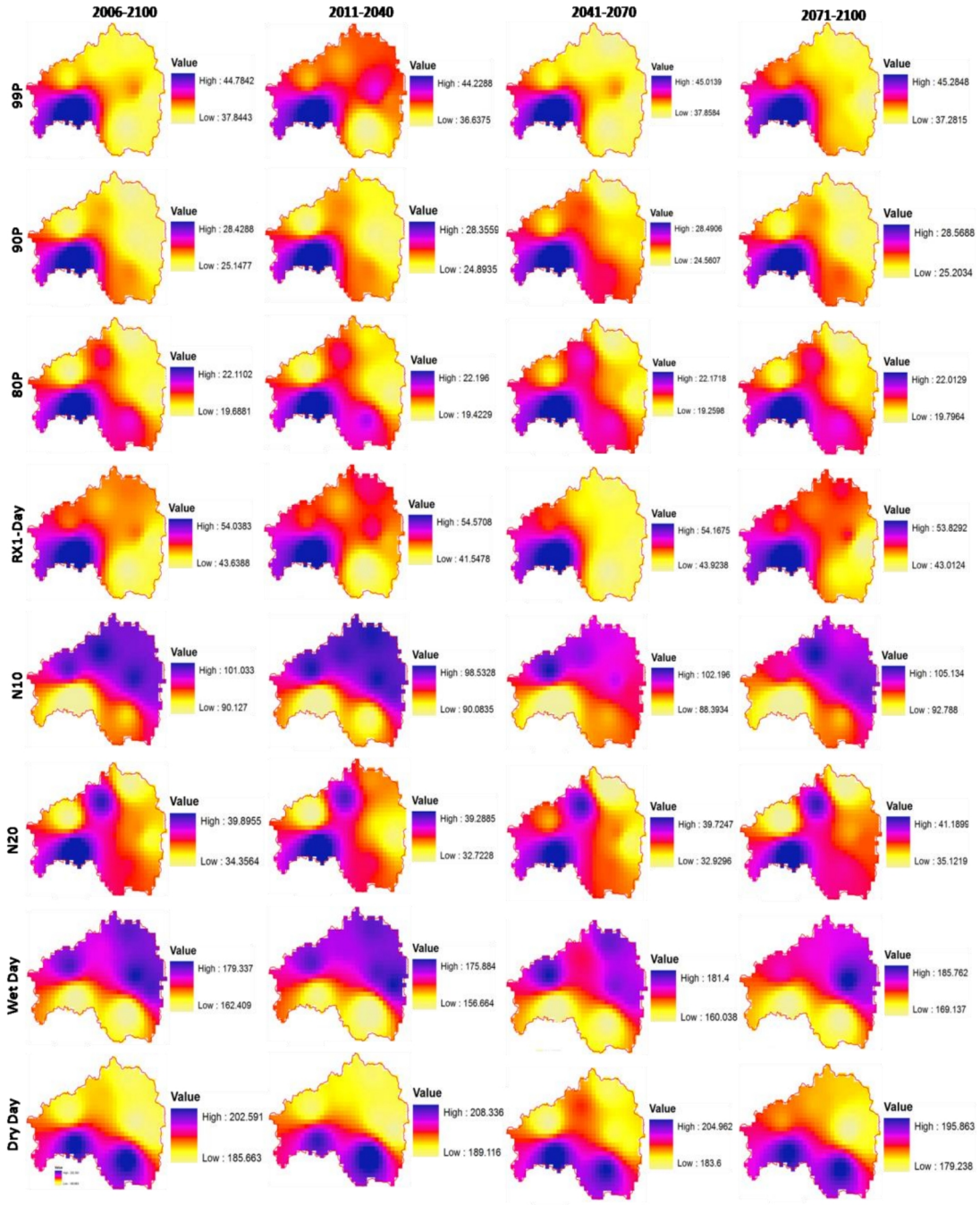
The SB wise estimation of the precipitation extreme events increased the understanding to interpret the heterogeneity and changes in the long term spatio-temporal domain (2006-2100).

(a)



TH-1643_136104018

(b)



TH-1643_136104018

(c)

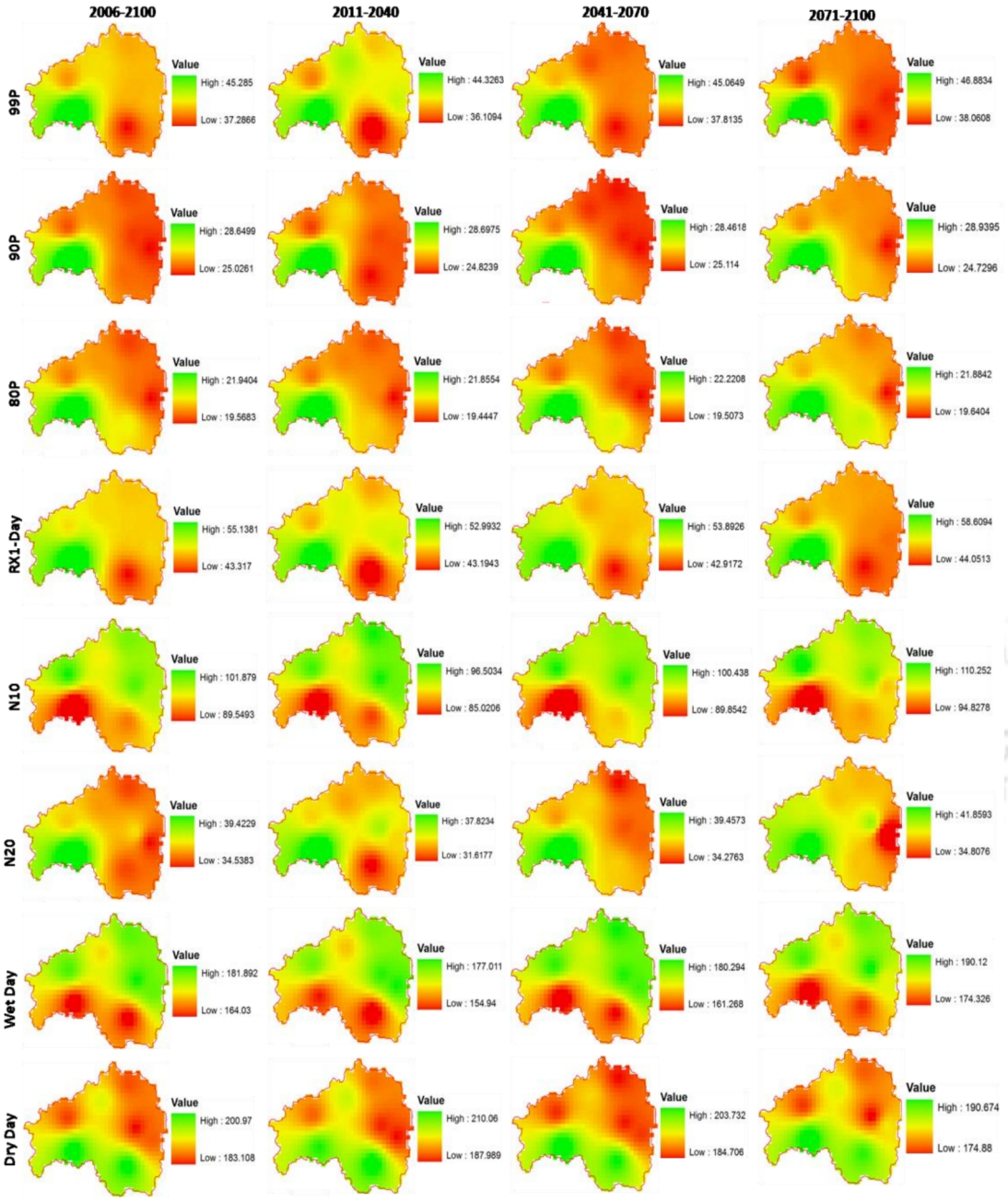


Fig. 4.18: An intra-decadal spatial variation in the precipitation intensity and frequency calculated from PEIs: (a) RCP2.6, (b) RCP4.5 and (c) RCP8.5.

TH-1643_136104018

CHAPTER 5

REMOTE SENSING APPLICATIONS IN SNOW COVER AND GLACIAL CHANGE ANALYSIS

5.1 GENERAL

In this chapter, snow cover, glacier extent and glacial lakes changes have been explored utilizing high resolution and multispectral and multi-temporal remote sensing (RS) satellite data sets. The respective analysis outcomes in the form of figures and tables are displayed and discussed in a geospatial domain. The temporal and spatial variations of snow covers and glaciers extent have been explored utilizing mathematical and image processing techniques and models. The effect of altitudinal variations in the snow cover and glaciers extent have been analysed. To do so, the whole catchment was divided into seven sub-catchments and each sub-catchment also divided into 10 elevation bands. Elevation band wise analysis of snow cover and glacial changes provided a significant scope for the assessment of snow cover changes. The multi spectral, multi-spatial and temporal characterization of the snow covers and glacier features have been assessed utilizing IRS P6 LISS 3, Landsat 7, Landsat 8 and MODIS (MOD09A1 and MOD10A2 8 daily) snow cover products. For the characterization of debris covers of glaciers by presenting a new innovative methodology, Zemu glacier located in the study area catchment has been chosen for the study.

There are certain limitations with regard to using RS for mapping of geophysical parameters such as slope steepness, glacial features under shadow region and relief displacement due to extreme hilly terrains. Thus field-based data is integrated to improve the RS products. Many studies highlighted that cloud cover and spectral overlap are major issues in mapping of snow cover using RS techniques (Tiwari et al., 2015; Shukla et al., 2010). The cloud infection limits the capability of satellite imageries to measure the accurate snow-covered glacial area. Thus, cloud removal and improving the object information for the cloudy parts in satellite images are essential in snow cover mapping and glacier analysis. Cloud cover is a particular challenge to optical RS in the Himalayan region, where skies remain overcast for much of the year. The presence of cloud pixels in MODIS snow cover products is significant during the monsoon season, and leads to an underestimation of snow covered area (SCA), which in turn influences application products such as hydrographs. Thus, for this study, a cloud free MODIS product (MOD09A1 Terra/Aqua 8 daily 500 meter spatial resolution with 7 bands) has been taken into an account (Vermote et al., 2015).

TH-1643_136104018

In this research work, for the snow cover and glacier mapping, MODIS (MOD09A1 and MOD10A2 8 daily) having 500 meter spatial resolution, Landsat 7 (30 m), Landsat 8 (30 m) and LISS 3 (23.5 m) satellite datasets have been accounted for the study. The satellite data sensor characteristics and imagery details are already provided in Chapter 3 (Study area and data used). In this chapter, various remote sensing based image processing and geospatial data utilization methods have been presented and discussed. The overall methodology for the snow cover and glacial change assessment include a number of equations and conceptual formulation steps such as geometric and radiometric corrections, ortho-georectification, image enhancement techniques, DN (Digital Number) to Radiance and Radiance to Reflectance conversion, image band transformation, band ratioing, image classification etc.

5.2 SNOW COVER AND GLACIERS EXTENT EXTRACTION METHODS

5.2.1 MODIS (MOD09A1 and MOD10A2) data processing

The MODIS surface reflectance products delivers an appraisal of the surface spectral reflectance as it will be measured at ground level in the absence of atmospheric scattering or absorption. The MODIS product such as MOD09A1 provides total 7 bands data sets at 500 meter spatial resolution in an 8-day gridded level-3 product in the Sinusoidal projection (Vermote, 2015). Every MOD09A1 pixel contains the finest likely L2G observation during an 8-day period. MOD09A1 can be categorized as low-view angle with high-observation coverage datasets. It contains very less clouds/almost zero cloud cover or cloud shadow, and aerosol loading, hence, this data sets could be useful for the monitoring of snow cover and glaciers, especially over the mostly cloud induced Himalayan terrains. The sensor properties of MOD09A1 data sets have been provided in Table 5.1. The MOD09A1 is a normalized product and thus, the initial reflectance conversion is must for this datasets before further processing.

TH-1643_136104018

TH-1643_136104018

Table 5.1: MOD09A1 sensor characteristics and their reflectance (λ) conversion factor.

Data Sets (HDF Layers)	Units	BIT Type	Fill	Valid Range	Scale factor
Band 1 (620–670 nm)	(λ)	16-bit signed integer	-28672.00	-100–16000	0.0001
Band 2 (841–876 nm)	(λ)	16-bit signed integer	-28672.00	-100–16000	0.0001
Band 3 (459–479 nm)	(λ)	16-bit signed integer	-28672.00	-100–16000	0.0001
Band 4 (545–565 nm)	(λ)	16-bit signed integer	-28672.00	-100–16000	0.0001
Band 5 (1230–1250 nm)	(λ)	16-bit signed integer	-28672.00	-100–16000	0.0001
Band 6 (1628–1652 nm)	(λ)	16-bit signed integer	-28672.00	-100–16000	0.0001
Band 7 (2105–2155 nm)	(λ)	16-bit signed integer	-28672.00	-100–16000	0.0001

Table 5.2: MOD10A2snow cover details.

Sample Value	0	1	11	25	37	39	50	100	200	254	255
Explanation	data missing	no decision	night	no snow	lake	ocean	cloud	lake ice	snow	detector saturated	fill

The MOD09A1 product is downloaded into the .HDF-EOS (Hierarchical Data Format-Earth Observing System) file format and later it converted into the .IMG (Image) file format to generate the raster data properties (Vermote, 2015).

MODIS/Terra Snow Cover 8-Day L3 Global 500m Grid (MOD10A2) data set is a classified snow cover product of MODIS sensor and hence used for the SCA validation. MOD10A2 contains maximum snow cover extent over an 8-day period in the HDF-EOS format with corresponding metadata. MOD10A2 has1200km by 1200km tiles with 500 m resolution data grids in a sinusoidal map projection. The snow cover has been generated using a Normalized Difference Snow Index (NDSI) and other criteria tests (Hall et al., 2006). In this research work, the classified snow cover product i.e. MOD10A2 has been utilized for the comparison of snow cover accuracy using MOD09A1. The details about the MOD10A2 product have been given in Table 5.2.

All the image processing tasks have been completed into the ERDAS Imagine software (Erdas Imagine, 2014). Before extracting the snow cover information from the MOD09A1, the Sinusoidal projection system is transformed into the Lambert Conformal Conic(LCC) projection system, which is defined as the most accurate projection system of India, imageries of MOD091 (Bera et al., 2014; Manjunath et al., 2006). For the snow cover extract from MODIS data sets, the 8-daily data sets from the year 2000 to 2014 have been downloaded. However, for the snow cover extraction and change analysis, the MODIS scenes were selected during snow accumulation (February, March and April) and snow ablation (August, September, October and November) time periods, as per the Himalayan snow properties (Gurung et al., 2011; Kulkarni et al., 2010; Kulkarni et al., 2007).

5.2.2 LISS and Landsat sensors data processing

Another high spatial resolution sensor such as IRS LISS 3 satellite datasets (2009-2014) were also utilized for the snow cover change detection. The LISS 3 satellite datasets for the months such as February and March during accumulation time and October and November during ablation time, less than 10% cloud cover, used for the snow cover mapping over the selected study area. The details about the LISS 3 sensors and scenes are already discussed in Chapter 3. In this study, glaciers classification, characterization of debris cover of Zemu glaciers, and glacial lakes changes have also been studied using Landsat TM (Thematic Mapper), Landsat 7 and Landsat 8 sensors along with LISS 3 sensors. The LISS 3 datasets have been obtained for the current change assessment (2009-2014) and quality evaluation of the MODIS snow cover products. For the glacial lakes and debris covers of glaciers classification, Landsat TM (1980, 2000), Landsat 7 (2010, 2009-2012) and Landsat 8 (2013-

TH-1643_136104018

2014) were utilized. The metadata information of LISS 3 and Landsat sensors are given in Chapter-3.

5.2.3 Satellite data pre-processing and orthorectification

The MODIS, Landsat and LISS 3 satellite scenes were re-projected into LCC projection system to maintain the uniqueness in the satellite datasets. The LCC projection parameters such as datum, ellipsoid etc. were opted from the work done by Bera et al. (2014) and NRSC (2010). The Landsat datasets were orthorectified. Thus, with reference to Landsat datasets, all the scenes of LISS 3 and MOD09A1 have been orthorectified before the image enhancement. Initially, LISS 3 and Landsat scenes were opted in the mono bands, thus, all the bands were stacked and formulated the multispectral scenes. After stacking the bands, radiometric and geometric corrections have been done for the LISS3 satellite imageries.

The radiometric and geometric properties were opted from the metadata file associated with LISS 3 imageries. The Landsat sensors provide orthorectified datasets thus, for Landsat imageries, geometric and radiometric corrections have not performed. After radiometric and geometric corrections of LISS 3 data sets, the DN values of Landsat and LISS sensors are converted into reflectance values. The conversion formula is given below as (YCEO 2013: www.yale.edu/ceo; Thome, 2001):

The conversion from DN to Radiance computed as Eq. 5.1:

$$L_\lambda=((LMAX_\lambda - LMIN_\lambda)/(QCALMAX - QCALMIN)) * (QCAL - QCALMIN) + LMIN_\lambda \ldots\ldots\ldots\ldots\ldots\ldots\ldots\ldots (5.1)$$

where,

L_λ is the cell value as radiance, QCAL = digital number, $LMIN_\lambda$ = spectral radiance scales to QCALMIN, $LMAX_\lambda$ = spectral radiance scale to QCALMAX, QCALMIN = the minimum quantized calibrated pixel (typically = 1), QCALMAX = the maximum quantized calibrated pixel (typically = 255). The above parameters such as QCAL, QCALMIN, QCALMAX, $LMIN_\lambda$ and $LMAX_\lambda$ were obtained from the metadata file associated with the Landsat bands.

The conversion from Radiance to Reflectance:

$$\rho_\lambda = \pi * L_\lambda * d^2/ESUN_\lambda * cos\theta s \ldots\ldots\ldots\ldots\ldots\ldots (5.2)$$

Where, ρ_λ = unitless plantary reflectance, L_λ = spectral radiance, d = Earth-Sun distance in astronomical units, $ESUN_\lambda$ = mean solar exoatmospheric irradiances and θs = solar zenith angle. These variables are also obtained from the metadata file associated with the Landsat

TH-1643_136104018

bands (YCEO 2013: www.yale.edu/ceo). Likewise, the LISS 3 sensors DN values are also converted into reflectance values (Nayak, 2006). The model formulation for the DN to reflectance conversion has been done using the 'model maker' tool of ERDAS Imagine. The formulation of the model maker tool is displayed in Fig. 5.1. Similarly, the thermal bands of Landsat sensors, whose DN values are converted into reflectance for the image analysis. The equation is given below as Eq. 5.3:

$$T = \frac{K_2}{\ln(\frac{K_1}{L_\lambda}+1)} \ldots\ldots\ldots\ldots\ldots\ldots (5.3)$$

Where, T = At-satellite brightness (K), K_1= band specific thermal conversion constant from the metadata file of Landsat sensor, K_2 = band specific thermal conversion constant from the metadata file of Landsat sensor. The thermal constants K_1 and K_2 values can be opted from the metadata file, which comes by default with the Landsat data sets (*http://landsat.usgs.gov/Landsat8_Using_Product.php*).

Bhambri and Chaujar (2011) reported that the relief displacement is a major problem in the high hilly terrains based satellite imageries and thus accurate area information of the glacier cannot measure without improving this distortion. Several authors also notified the similar problems in the glacier mapping (Alifu et al., 2015; Bhambri and Chaujar, 2011; Shukla et al., 2010). Thus, this study involved the orthorectification of LISS 3 satellite datasets using orthorectified CARTOSAT DEM (Bera et al., 2014) and Landsat imageries to improve the accuracy of the results. The orthorectification is done using Autosync geo-referencing tool by "Projective Transform" method. The Projective Transform models can be solved by the minimal number of GCPs (Ground Control Points). The GCPs are collected from the field survey. However, due to less number of GCPs, an automatic GCP tie points are also generated with reference to orthorectified Landsat imagery. The terrain relief displacement was solved using the CARTOSAT high resolution (30meter) digital elevation model. The orthorectification of satellite imageries are necessary to reduce the RMSE (Root Mean Square Error) and terrain relief displacements in the mountainous parts.

5.2.4 Cloud removal and snow cover extraction from MODIS (MOD09A1 Terra 8 daily), LISS 3 and Landsat data products

Because of the cloud contamination in the satellite imageries, without removing clouds from the datasets, it cannot be used for the snow cover monitoring. In the Himalayas like north Sikkim eastern Himalayas, terrains are extremely high. Thus, cloud removal is needed before snow cover extraction.

TH-1643_136104018

Thus, a cloud free snow cover product i.e. MOD09A1 has been utilized for the snow cover extraction (Vermote, 2015). Many authors revealed that MOD09A1 8 daily data sets with 500 meter spatial resolution is sufficient for the snow cover monitoring over the high hilly terrains (Vermote, 2015; Lie et al., 2012; Gafurov and Bardossy, 2009; Miller and Thomas, 2005) The LISS 3 satellite scenes were chosen such that as the cloud cover is found less than 10%.

In the Himalayan terrains, cloud cover density shows maximum during the monsoon months (May to August). Thus, we avoided to purchase the scenes within these months. In the Landsat datasets, several scenes contained cloud more than 20%, thus, a cloud removal method is formulated by adopting TIR bands of Landsat datasets. The TIR bands and other Landsat datasets were used in the characterization of debris covers of Zemu glacier.

Cloud has similar reflectance as that of snow, thus it can be a problem in high hilly terrains for classifying the glaciers (Tiwari et al., 2015). However, the cloud cover can be easily identified in the TIR bands by converting the TIR DN values to temperature brightness. The cloudy part in the TIR band shows lowest temperature (˚K) than normal temperature ranges when compared to non-cloudy images of TIR bands.

The idea of cloud removal using the thermal differences based on the TIR bands has been obtained by the work done by (Gafurov and Bardossy, 2009). Thus, a temperature threshold has been determined (here it is taken as less than 240˚K) and then cloudy pixels were removed from the given temperature threshold.

TH-1643_136104018

TH-1643_136104018

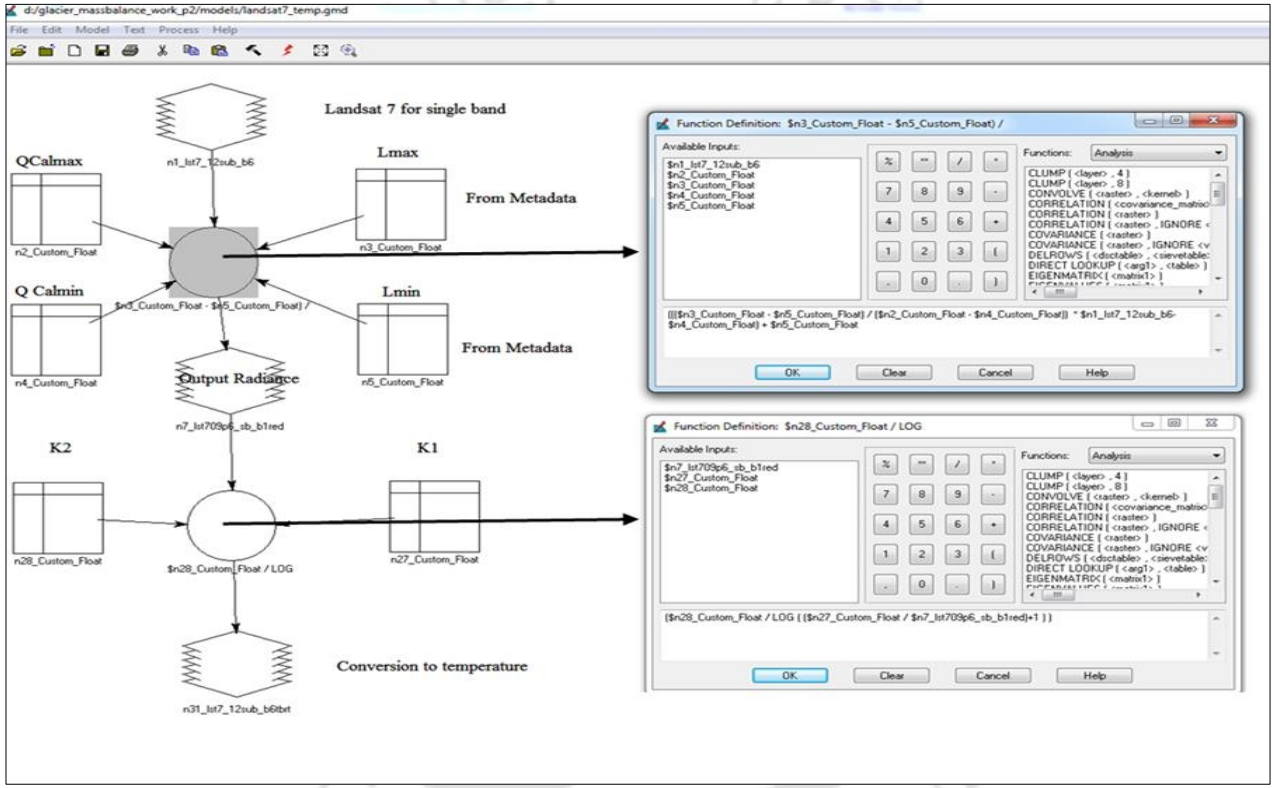


Fig. 5.1: DN to radiance and radiance to temperature brightness conversion flow chart in model maker tool, ERDAS Imagine.

The temperature differences can be notified in the cloudy versus non-cloudy TIR bands at the same area (Fig. 5.2). The replaced pixels were assigned the new values as per the mean TIR band image prepared by doing average of the TIR bands (2009 to 2014).The cloud removal process has been performed in the MATLAB and ERDAS imagine software, and this cloud removal technique could be useful for the other remote sensing applications (e.g. MATLAB code is provided in the APPENDIX Section) (Fig. 5.3).The whole process can be grouped into three broader sections as below:

(i) Cloudy pixel identification: The cloudy pixels are identified by creating spatial spectral profile. In the present study, the cloudy pixel threshold is defined as the 240°K, if temperature is above this range then pixels are non-cloudy and if pixel value is less than 240°K, then pixels are cloudy. These cloudy pixel are assigned as No Data Values (NDV).

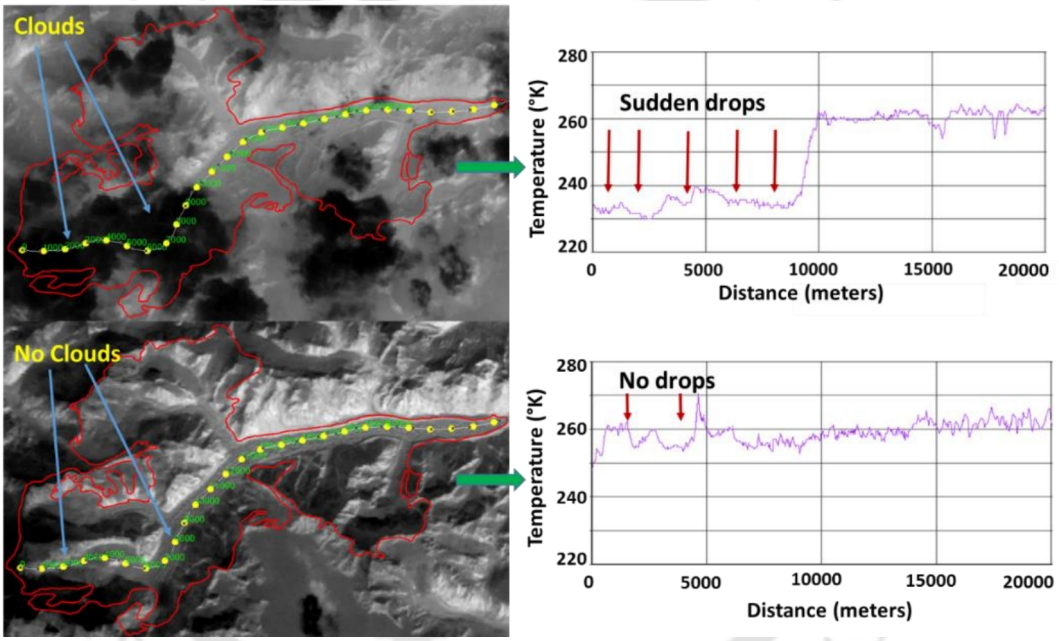


Fig 5.2: Distinction between cloudy and non-cloudy patches in TIR band of Landsat sensor.

(ii) Formulation of TIR hybrid image: The hybrid TIR image are made as per the combinations of all the TIR bands for the years 2009-2014. Based on the temperature threshold, cloudy patches has been identified in the images. Based on this, for each the respective year, a polygon of cloudy pixel extent has been drawn in the vector format.

If {Pixel value/image} is >240°K, Pixel Value = (Same) Non-Cloudy and

If {Pixel value/image} is ≤ 240°K, Pixel value = (NDV), Cloudy Pixels

TH-1643_136104018

The above operation has been applied to assign the cloudy pixel as NDV. As per the cloudy image polygon, cloudy patches are extracted from the entire bands.

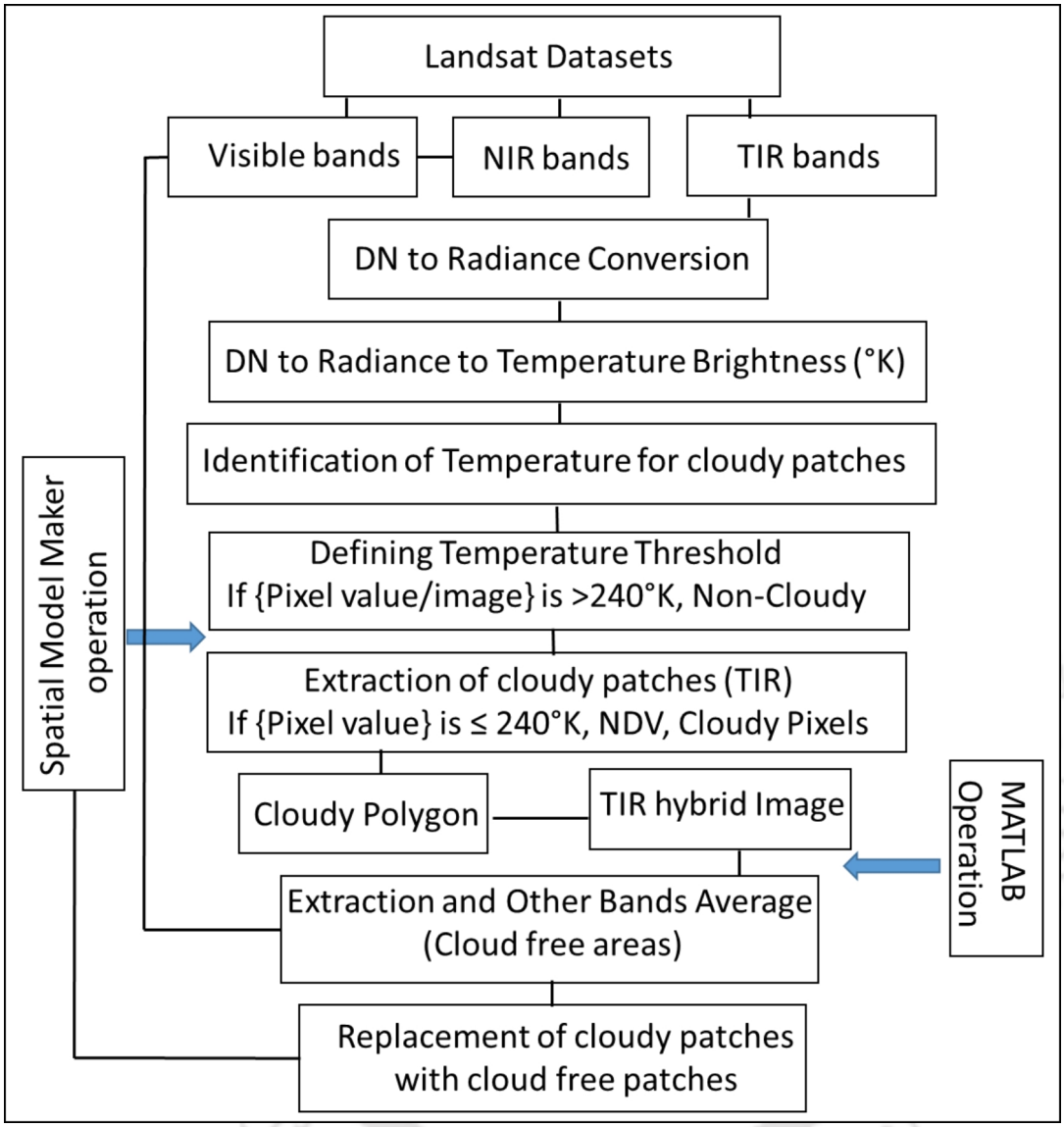


Fig. 5.3: Cloud removal steps for Landsat TIR bands.

(iii) Cloud removal from other bands: For each band including TIR, the hybrid image combinations for each bands (Visible and NIR) have been prepared. Then, the cloudy patches (e.g. contain around 20%-25% cloud cover) have been replaced by the hybrid bands of Visible and NIR regions. This method is useful for the cloud cover extraction, if the cloud percentage (%) is below 25%, otherwise the temporal utility of the datasets can be reduced.

For the snow cover extraction, a Normalized Difference Snow Index (NDSI) has been used (Chelamallu et al., 2014; Dietz et al., 2013; Paudel and Andersen, 2011; Kulkarni et al., 2010). NDSI adopts the snow reflectance in visible (Green) with high reflectance and

TH-1643_136104018

Shortwave Infrared (SWIR) with low reflectance. The clouds have high reflectance in the SWIR region, thus TIR band could be analyzed for the discrimination between the clouds and snow. The NDSI ranges from -1 to +1. In MODIS, the NDSI adopts the reflectance in the visible band such as MODIS band 4 (545nm-565nm) and SWIR band such as band 6 (1628nm-1652nm) divided by the addition of these two bands. The NDSI equation is given (Eq. 5.4).

$$NDSI = \frac{Green(MODIS\ Band\ 4) - SWIR\ (MODIS\ Band\ 6)}{Green(MODIS\ Band\ 4) + SWIR\ (MODIS\ Band\ 6)} \ldots\ldots\ldots (5.4)$$

As snow has low reflectance in SWIR portion and high reflectance in visible (Green) region, it can be differentiate very easily from the other objects. However, in NDSI, vegetation and water pixels can be mixed up with the snow pixels (Kulkarni et al., 2010). In Himalayas, the snow can be obscured by vegetation and water-bodies (Lie et al., 2012). However, in the present study area, the vegetation density was found less, especially in the snow induced regions, yet, it contains many small to big water bodies across all the catchment. Thus, Normalized Difference Water Index (NDWI), Modified NDWI and $MNDWI_{GAO}$ were formulated to extract the water bodies and glacial lakes within the catchment (Li et al., 2015; Feyisa et al., 2014; Gao, 1996). Every NDWI method give a scope to provide the better characterization of the water pixels and non-water pixels. Based on these methods, finally a unique water pixel range has been determined. The mixed water pixels have been removed from the snow covered areas. The NDWI formulas are given below as (Eqs. 5.5, 5.6 and 5.7):

$$NDWI = \frac{SWIR - Near\ Infrared\ (NIR)}{SWIR - Near\ Infrared\ (NIR)} \ldots\ldots\ldots\ldots\ldots\ldots\ldots\ldots (5.5)$$

$$MNDWI = \frac{GREEN - Middle\ Infrared\ (MIR)}{GREE + Middle\ Infrared\ (MIR)} \ldots\ldots\ldots\ldots\ldots\ldots (5.6)$$

$$MNDWI_{GAO} = \frac{NIR - MIR}{NIR + MIR} \ldots\ldots\ldots\ldots\ldots\ldots\ldots\ldots\ldots\ldots\ldots\ldots (5.7)$$

$0.2 \leq NDWI \leq 0.35$, Pixels are Water (Gao, 1996)

$NDWI \geq 0.36$, Pixels are Snow/Glacier (Gao, 1996)

After the calculation of NDSI and NDWI, the snow cover has been extracted according to these two values and the above criteria. The 0.4 NDSI is the standard and adopted in many studies (Li et al., 2015; Feyisa et al., 2014) but this threshold. The NDSI range for Hindu Kush Himalayas region can vary from 0.3 to 0.4 (Tang et al., 2013) due to vegetation and waterbodies/glacial lakes. Thus, in the present study, 0.35NDSI has been opted for the snow cover extraction. Similar approach has been adopted for the IRS LISS 3 satellite datasets for snow cover extraction. The separation of the water pixels from the snow cover pixels

TH-1643_136104018

improved the accuracy of the snow cover extraction. The whole methodology of snow cover extraction has been shown in the flow chart (Fig. 5.4).

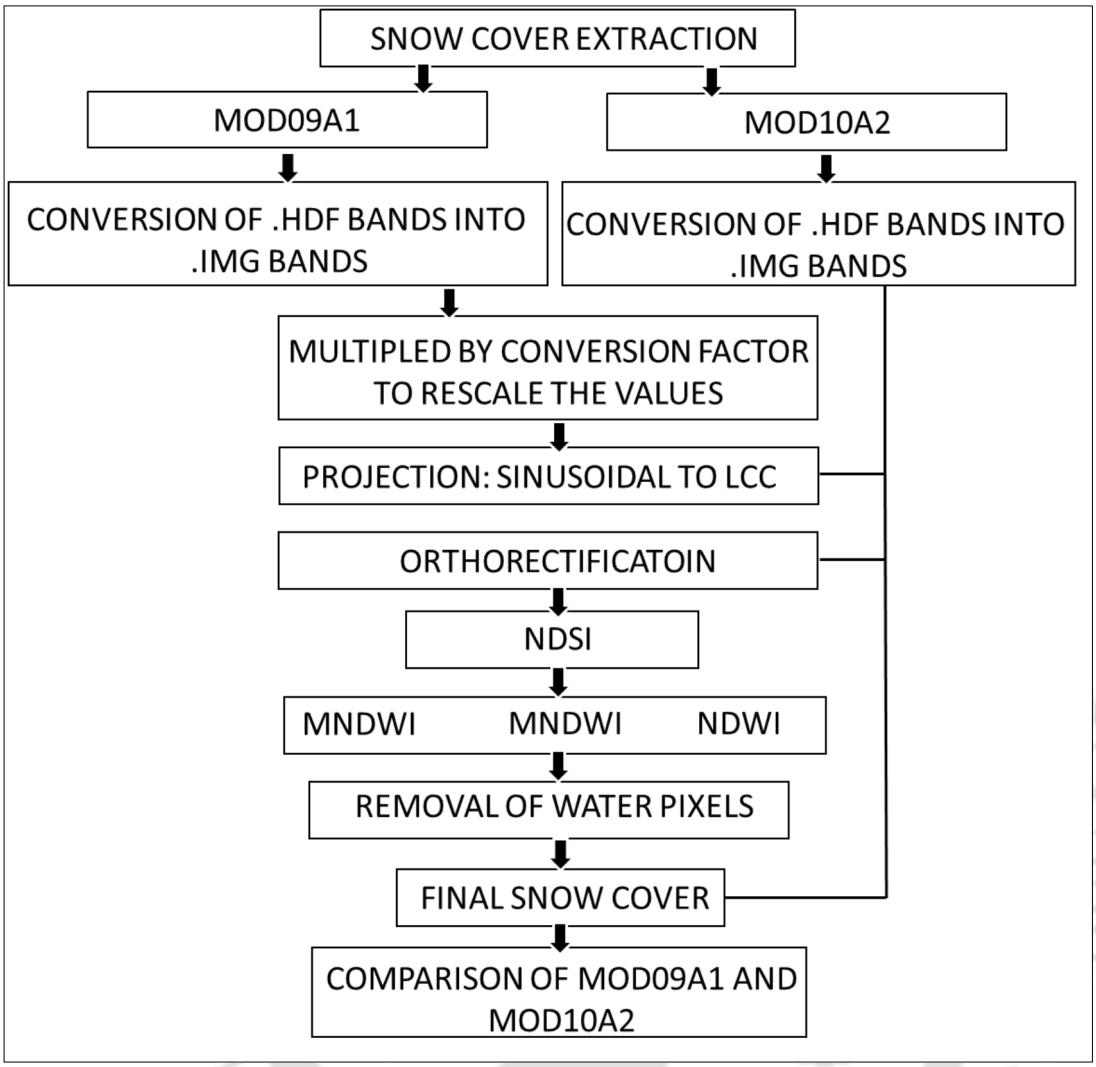


Fig. 5.4: Flow charts of snow cover extraction approach using NDSI and NDWI.

5.2.5 Characterization of debris cover of glaciers

In the eastern Himalaya, Zemu glacier is characterized as the longest valley glacier which contributes more than 70% water to the Teesta river. Zemu glacier is located at the base of Kanchenjunga in the north Sikkim Himalaya, India. It extends from Latitude 27° 42′ 00′′ N to 27° 47′ 00′′ N and Longitude 88°08′ 00′′E to 88°23′ 00′′E. The Zemu glacier boundary elevation varies from 4129 meter to 6289 meter. The snout of the Zemu glacier is located at about 4136 meter AMSL. The thickness of the debris cover of Zemu glaciers varies from few centimeters to meters (Racoviteanu and Williams, 2012). A thick layer of debris is available on the Zemu glacier which prevents ablation. However, numerous glacial lakes have been formed on the surface of these debris-covered sections of the Zemu glacier. Zemu Glacier remnants is a less studied and monitored glacier among the other Himalayan glaciers. Thus, for the characterization of the debris cover of glaciers, Zemu glacier has been

TH-1643_136104018

selected for the evaluation. Differentiating supraglacial debris (part of the glacier boundary), clean ice and ice covered glaciers from periglacial debris (outside the glacier boundary) cover is a challenging task due to similar responses of remote sensing spectral bands (Pratap et al., 2014; Marston et al., 1996) (Fig. 5.5).

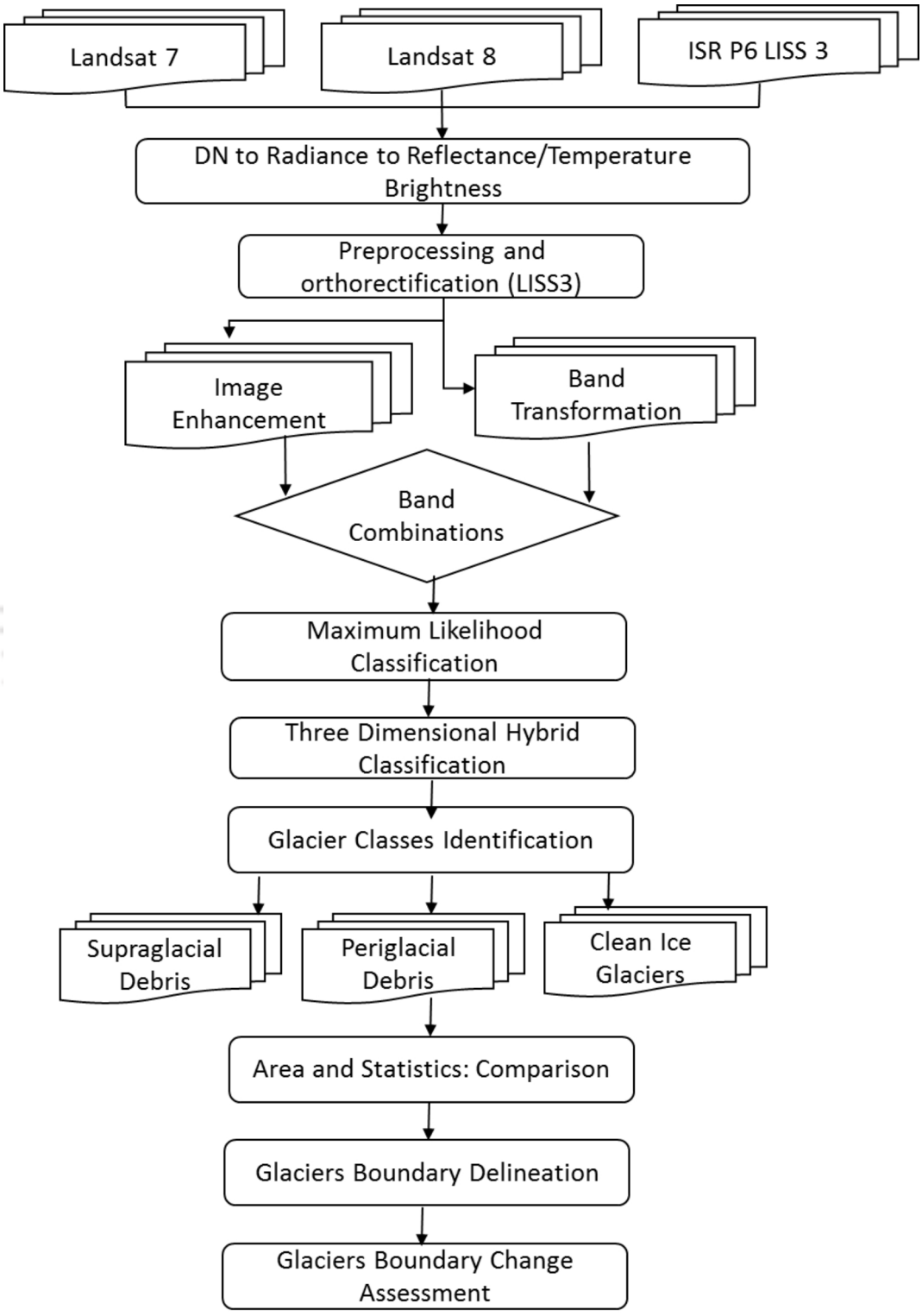


Fig. 5.5: Methodology chart of the classification of debris covers of Zemu glacier.

TH-1643_136104018

This study presents an innovative hybrid multicriteria decision making approach utilizing optical and thermal infrared bands, maximum likelihood classification (MLC) and the formulation of three dimensional hybrid classification (3DHC) approach in the temporal time domain (2009-2014). For the characterization of the debris cover of the Zemu glacier, Landsat 7 (2009-2012), Landsat 8 (2013-2014) and LISS 3 (2009-2014) remote sensing satellite sensors data sets have been used. The LISS 3 and Landsat scenes details have been provided in Chapter 3. LISS 3 sensor has two visible (GREEN, RED) and two Infrared Bands (NIR and SWIR), whereas Landsat sensors are the combination of multiple visible, NIR, MIR, SWIR and TIR bands. The spatial resolution of these two sensors are 23.5 meter and 30.0 meter for LISS 3 and Landsat, respectively. The overall methodology has been grouped into the following steps:

(i) Pre-processing of remote sensing datasets (dataset generation, preprocessing, and orthorectification of LISS 3 satellite imageries): The initial step for the image pre-processing involved the layer stacking of LISS 3 and Landsat datasets. After layer stacking, the radiometric and geometric corrections have been applied. To explore the spectral characteristics of the Zemu glacier classes such as Supraglacial Debris (SGD) and Periglacial Debris (PGD), the radiance values of the optical bands for all the satellite sensors have been converted into the reflectance values, and the thermal bands radiance values have been converted into temperature brightness values by applying the unit conversion coefficients and conversion algorithms.

(ii) Image enhancement to set up band combinations (density slicing, band ratioing and band transformations): Tiwari et al. (2015) and Shukla et al. (2010) observed that the reflectance of ice snow mix debris and SGD conflates in different bands at several places. This shows superfluous or similar spectral information in the optical bands. To overcome this issue and to enhance the difference between the reflectance of different classes, an image enhancement based on band transformations using simple addition and subtraction of bands obtained from Landsat (Blue band) and LISS 3 (Green, Red NIR and SWIR bands) satellite sensors has been proposed as:

B1 (Blue Band from Landsat) + B1 (Green Band from LISS 3) = TB1

B2 (Red Band from LISS 3) – B3 (NIR Band from LISS 3) = TB2

B3 (NIR Band from LISS 3) – B4 (SWIR Band from LISS 3) = TB3

Band transformation could lead to fluctuations (increase/decrease) in the dynamic range of the reflectance and thus it can produce enormous contrast between the image objects, resulting into or highlighting 'off-beat' objects (Tiwari et al., 2015; Gupta, 2003). The

TH-1643_136104018

spatial reflectance profile has been created to explore the Zemu glacier features under the different transformed (e.g. 2009) and original bands (2009-2014). The band transformation could also be more useful in the removal of cloud cover and hence, the accuracy of classified maps can be enhanced (Tiwari et al., 2015).

The clean snow ice covered glaciers have a high reflectivity in the visible to NIR portions and it has low reflectivity in the SWIR wavelength region. Thus, visible, NIR and SWIR bands have advantages to separate clean glacier ice from non-glacier surfaces by doing band ratios (e.g. Red/SWIR and NIR/SWIR) as per their spectral differences at different wavelengths. The TIR band could be used to distinguish the different glacier classes as per the temperature differences (Tiwari et al., 2015). Hence, a new band ratio images combination has been presented to classify the SGD, clean ice snow covered glacier and PGD more accurately. The new band ratio is given (Eq. 5.8).

New band ratio = (TIR/ (NIR or MIR/SWIR)…… (5.8)

(iii) Cloud removal in optical and thermal bands from Landsat and LISS 3 datasets: This has been done using cloud pixel identification and formulation of TIR hybrid images as discussed in Chapter 5 Section 5.2.4.

(iv) Formulation band combinations by integrating optical and thermal bands: The main intention of this novel approach is to characterize the SGD and PGD with maximum accuracy. Every spectral band has its own specialties in the exploration of glacier features. Thus, a set of band combinations in the optical (visible, NIR, MIR and SWIR) and TIR regions can help to identify the glacier features (Alifu et al., 2015). Thus, maximum possible band combinations, in this case it is six, integrating optical and thermal bands from the high resolution satellite sensors such as Landsat 7, Landsat 8 and LISS 3 have been formulated (Table 5.3). Every combination has a set of pair of optical and thermal bands which represent the unique spectral differences in the glacial features. For the formulation of the band combinations, the Blue and TIR bands intersected from the Landsat sensor and integrated with the LISS 3 sensor of the same year and near time duration.

The Landsat 8 imageries (2013-2014) are obtained in the 16 bit data system, while LISS 3 imageries are obtained in the 8 bit data system. Thus, Landsat 8 Blue and TIR bands rescaled into 8 bit data, which is the necessary requirement for the layer stacking and resolution merging of the remote sensing datasets (Bhardwaj et al., 2015). The higher bit to lower bit data conversion does not reduce the quality of the datasets (Yang et al., 2015). In the merging of Landsat bands to LISS 3 bands, the images geometric projection system, data type (bit system) and their extent (coordinate boundary) should be same.

TH-1643_136104018

Initially, LISS 3 optical bands were stacked as per the details given in Table 5.3. Then, Landsat 7 and Landsat 8 Blue and TIR bands were merged into the LISS 3 as per the methodology initially presented by Tiwari et al. (2015) (Table 5.3). In this approach, the optical bands, band ratio and thermal differences are determined as the key factors to classify the Zemu glaciers into clean ice glaciers, SGD and PGD. These six band combinations have been subjected to image classification and accuracy assessment of the classified maps.

Table 5.3: Combination (CMB) of the band images details of Landsat and LISS 3 sensors.

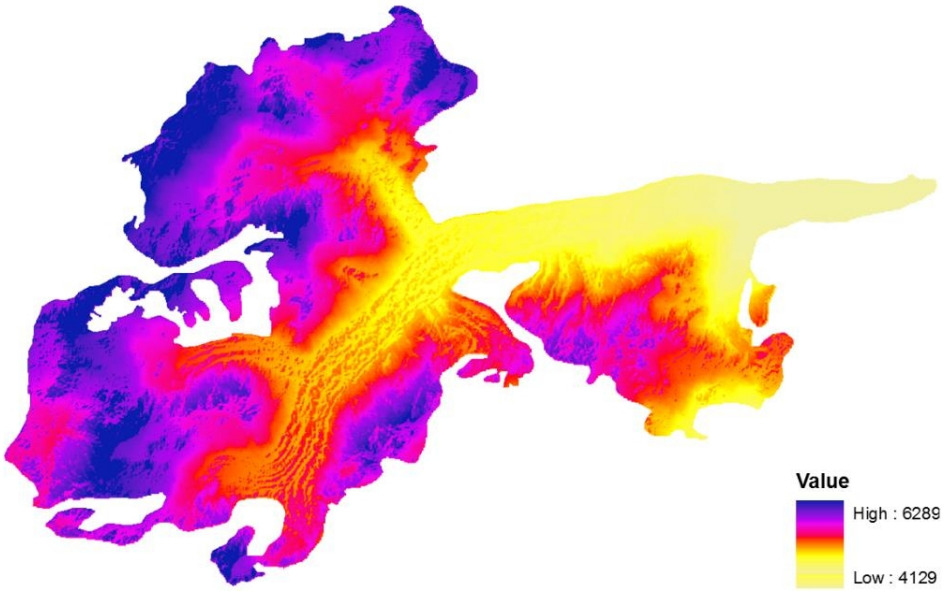
Band Combinations	2013-2014		2009-2012	
	LISS 3	Landsat 8	LISS 3	Landsat 7
CMB 1	B1, B2	B2	B1, B2	B1
	B3	-	B3	-
	-	B10, B11	-	B6
	Total Band CMBs = 5		Total Band CMBs = 5	
CMB 2	B3	-	B3	-
	B4	-	B4	-
	-	TIR1, TIR2	-	B6
	Total Band CMBs = 4		Total Band CMBs = 3	
CMB 3	B1, B2	B2	B1, B2	B1
	B10/(B3/B6)	B11/(B3/B6)	B3	B5, B6
	B4	-	B4	-
	Total Band CMBs = 6		Total Band CMBs = 7	
CMB 4	B2-B3=TB2	B1+B1 = TB1	B2-B3=TB2	B1+B1 = TB1
	B3-B4=TB3	-	B3-B4=TB3	-
	-	B10, B11	-	B6
	Total Band CMBs = 5		Total Band CMBs = 4	
CMB 5	B2-B3	-	B2-B3	-
	B3-B4	-	B3-B4	-
	-	B10, B11	-	B6
	Total Band CMBs = 4		Total Band CMBs = 3	
CMB 6	B1, B2	-	B1, B2	-
	B3	-	B3	-
	B4	-	B4	-
	Total Band CMBs = 4		Total Band CMBs = 4	

TH-1643_136104018

(v) Improvements in the Maximum Likelihood Classification (MLC) methodology: Since cloud cover limitations, the cloud cover can be easily identified in the TIR band by converting the TIR digital number (DN) values to temperature brightness (TB). The cloudy part in the TIR band shows lowest temperature (˚K) and sudden drops than normal temperature ranges, when compared to non-cloudy TIR bands. The cloud removal methodology is already explained in the above sections. In the valley glaciers several pixels of SGD, PGD and valley rocks exhibit similar temperature brightness in the TIR band (Tiwari et al., 2015). Due to this, it is the whole difficult to identify the spectral signatures of these surfaces to put up information for MLC. To overcome this problem, additional parameters such as slope and elevation information have been generated from the CARTOSAT DEM to enhance the accuracy level (Figs. 5.5 and 5.6). The spectral differences within the different surfaces help in identifying the unique spectral signature for the MLC. To verify the precision of the spectral signatures collected for the MLC, google earth based Quickbird image (at 1:10000 scale) used to extract the glacial signatures.

Based on the detailed quality checks using Quickbird image based extracted signatures, GPS survey points, spatial spectral plots and visual image interpretation, the Zemu glaciers has been categorized into clean ice snow, ice snow mix debris, SGD, rocks, vegetation, PGD and glacial lakes. These spectral signatures are then subjected to MLC as per the formulated six different band combinations (2009 to 2014). The MLC method has been performed in the ERDAS Imagine (Erdas Imagine, 2014). For identification of the spectral signatures to perform the MLC, maximum possible unique signatures have been extracted and then reclassified into the respective classes.

(a)



TH-1643_136104018

(b)

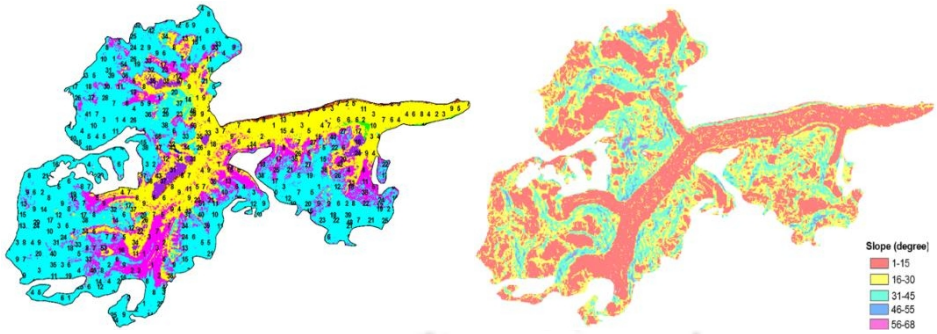


Fig. 5.6: Slope and elevation information over the Zemu glacier.

(vi) Three dimensional hybrid classification (3DHC) approach: Each MLC classified map formulated by optical and TIR bands combination shows mixing of the glacial classes pixels. Each MLC based classified maps for each band combination has given unique response of the glacial classes. Thus, a 3DHC classification approach has been presented to make the hybrid classified maps for all the six image bands combination of classified maps (2009-2014).

In this method, initially, all the classified maps grouped into a single layer and then all the classified maps converted into *.tiff*, which is necessary to maintain the projection parameters. All the classified maps should have same spatial extent, pixel resolution, pixel values, number of classes and their coding structure, and coordinate system. All the pixel values should be arranged into same number of rows and columns (in two dimensions i.e. row and column). This overall classification methodology has been incorporated into the MATLAB platform. To make the hybrid of all the classified maps, a mode of probability mass function has been applied (Krakauer et al., 2015). Finally, to display the image with defined projection system (third dimension used for projection system), a hybrid three dimension classified map has been created. The MLC based classified maps (six maps for each band combination for each year during 2009-2014) showed significant variability in their glacier classes.

(vi) Delineation of the Zemu glacier boundary:

The fully automatic digitization approach does not give authentic representation of the glacier boundary as discussed by many authors and its time consuming also (Tiwari et al., 2015; Shukla et al., 2015; Alifu et al., 2015). For the Zemu glacier boundary delineation, a semi-automated approach has been adopted to classify the Zemu glaciers features and the whole glacier boundary outline. The glacier features are generated as per the MLC and 3HDC approaches in the raster grid format. For finalizing the Zemu glacier boundary, the

TH-1643_136104018

3DHC maps produced (2009-2014) after post-processing, having the highest accuracy, are used. Then automatic digitization and manual corrections over the glacial features have been done to refine the glacier classes such as SGD and PGD. ICIMOD WGI glacier boundary (created in the year 2000) and surveyed toposheet (downloaded from the Himalayan journal, prepared in 1935 at 1:25000 scale) have been used as the reference datasets (Hooker, 2003) for the correction of the glacier boundaries. The semi-automated approach saves the time and effort, and delivers a better accuracy level in the discrimination of the SGD and PGD, and other glacier classes.

In this study, the outer shape of the Zemu glacier has been delineated and the boundary area is compared with the previous two datasets such as ICIMOD WGI glacier boundary and surveyed toposheet based Zemu glacier boundary. The semi-automatic digitization of the glacier boundary is performed by fixing the mapping scale at 1:25000, which is good enough to characterize the accurate boundary area. The significance about the glacier Zemu boundary and its changes are discussed in the next section.

5.3 SNOW COVER CHANGE ANALYSIS

5.3.1 MODIS snow cover area (SCA), snow depletion curves (SDC) and change assessment

The snow cover extracted from MODIS (MOD09A1) 8 daily Terra/Aqua cloud free satellite datasets for the year 2000 to 2014. The LISS 3 data sets were available for the year 2009 to 2014 during accumulation and melting time periods, hence, utilized for the snow cover extraction.

The snow cover extraction methodology has been shown in Fig. (5.4). The temporal snow cover variations (2000-2014) as per MODIS datasets, during accumulation (February, March and April) and melting (August, September and October) times, have been shown in Fig. (5.7). In the current study area, the snow melt starts from the April and the snow accumulation starts from the October.

In Fig. (5.7), a monthly snow cover variation has been displayed, which shows maximum and minimum snow cover area during 2000 to 20014. In Fig. (5.7), one can notice the snow cover fluctuations at different parts of the selected study area. Among all the months, the February and March months have shown maximum snow cover during all the years.

While the lowest or almost zero snow cover is opted in the month of August. Thus, in the April month, many years showed comparatively less snow cover than February and March months. Till August almost temporary snow cover melts but it again starts in the October. This snowfall could be noticed in the October months, in all the years (2000-2014). All the

TH-1643_136104018

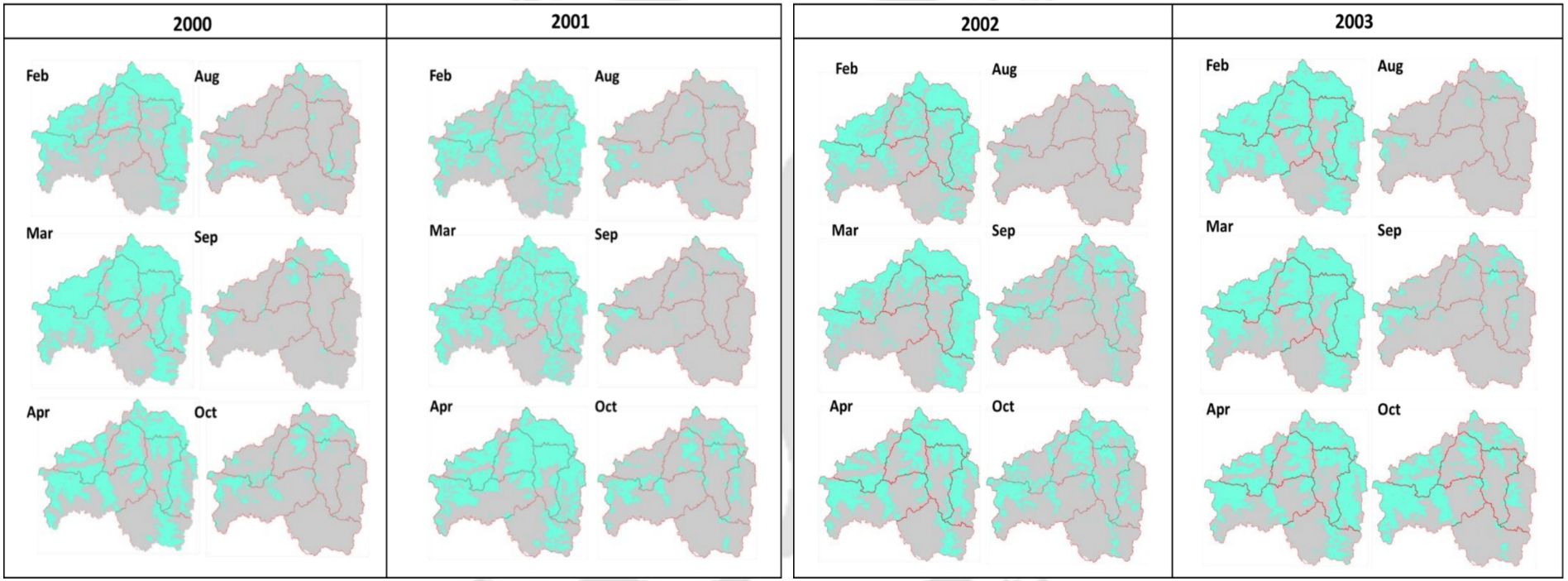
Figs. (5.7) show that the high elevative portions of the catchment correspond maximum snow cover than moderate terrains of the catchment. Table 5.4 gives clear information about the monthly SCA over the catchment 2000 to 2014 during accumulation and melt time periods. In Table 5.6 it can be seen that the SCA is highly fluctuated during all the temporal years. In the recent years, from 2007 to 2014, SCA is slightly decreased in few years during accumulation months such as 2007, 2009, 2011 and 2014. In Table 5.5 one can clearly observe that the October month has gained little amount of snow cover. The August month have shown minimum SCA than other maximum.

Fig. 5.8 displays the comparison between minimum, maximum and temporary SCA at each sub-catchment scale during 2000 to 2014. This highlights that the SCA is highly fluctuated in the given temporal years. In Fig. (5.8), it can be observed that the initial years (2000-2007) showed highest maximum SCA during (high peaks), while recent years (after 2007) showed slight decrement in the SCA. Because the recent year peaks are lesser than initial years. In Fig. (5.8), the SB1, SB3 and SB4 corresponded to highest maximum snow cover than other SBs. This showed the elevation dependent characteristics of SCA. Because SB1, SB2, SB3 and SB4 corresponded with extreme high elevations. In the high elevation portion of the catchment such as SB1, SB2, SB3 and SB4, the temporal SCA statistics shows consistency than other SBs. It reflects a fast melting over these SBs.

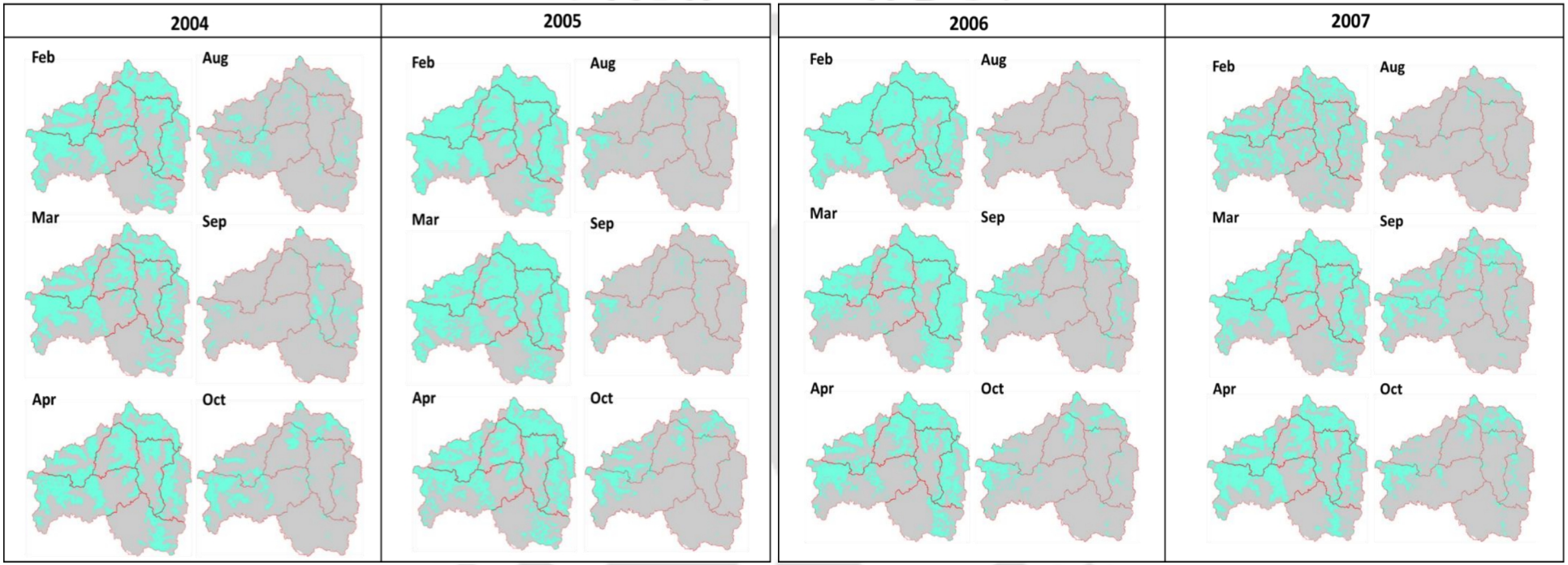
Snow duration/depletion curves (SDCs) are very important parameter in snow hydrological modeling and to assess the snow cover dynamics of the region. SDCs are very much required for snowmelt runoff modeling in a snowmelt induced river catchment. The SDCs provides the information about the pattern of snowfall and snowmelt in the given months and year. Remote sensing satellite imageries can be utilized significantly to plot the SCD of the area in the temporal and spatial domain. SDCs can be computed by interpolating percentages of SCA for the given days/months/years. SDC can be plotted accurately, if there is no cloud in the datasets. In high hilly terrain catchment such as current study area, SDC significantly fluctuates as per the elevation differences. Fig. 5.9 shows the monthly SDCs over the selected study region during the 2000 to 2014. The plotted SDCs show significant fluctuation in the SCA (%) across all the months and years. SCA (%) derived from the MODIS datasets using NDSI calculations as per the existed elevation. SCA is required for elevation zones/bands.

TH-1643_136104018

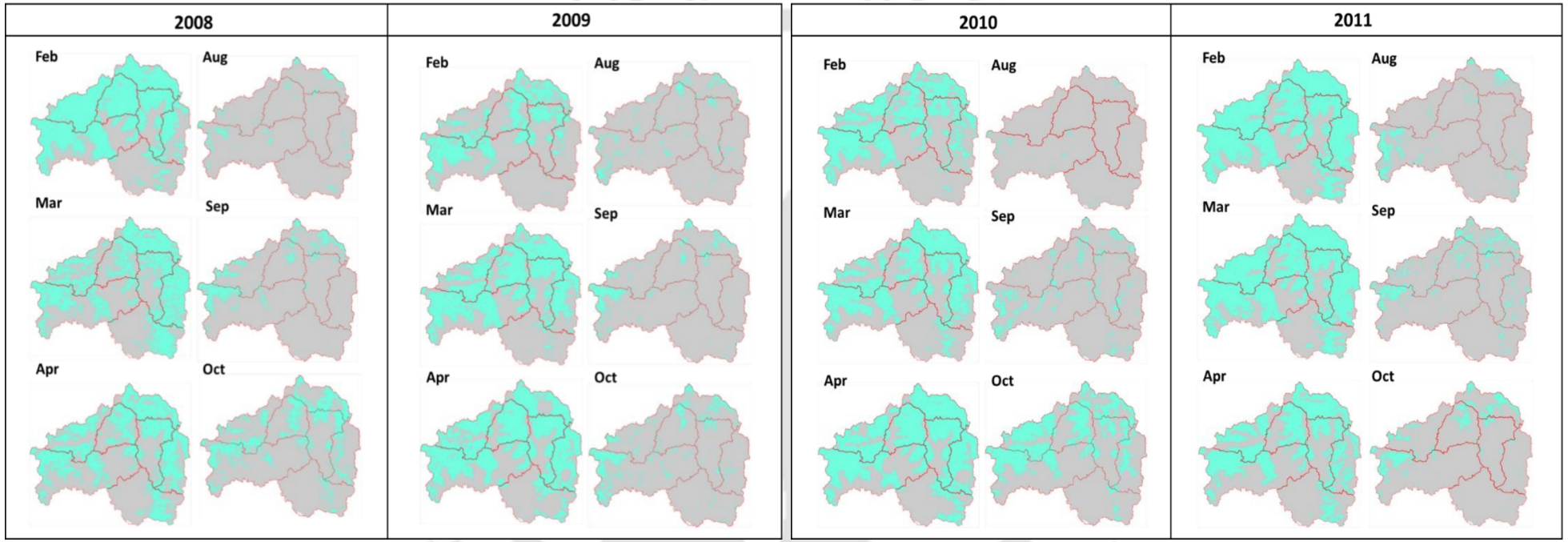
TH-1643_136104018



TH-1643_136104018



TH-1643_136104018



TH-1643_136104018

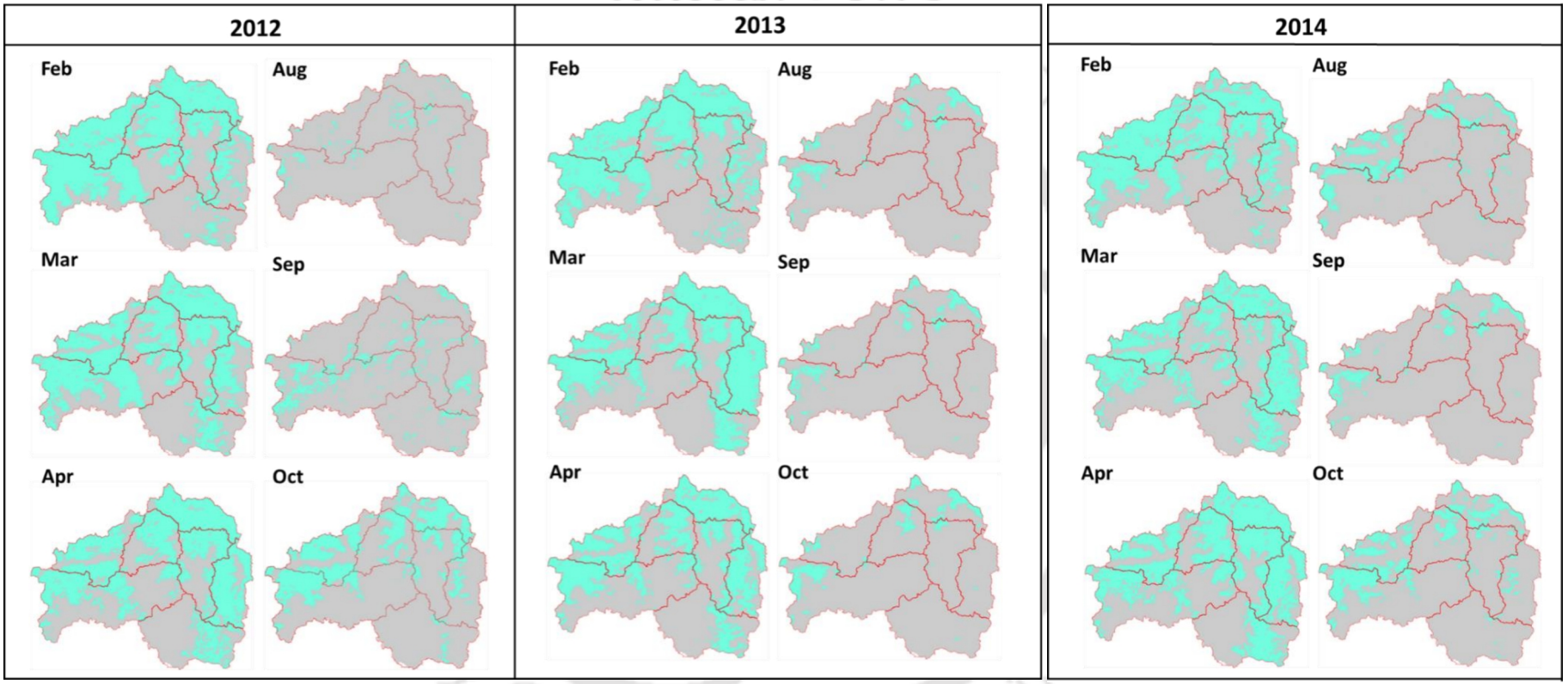


Fig. 5.7: Temporal snow cover variation during minimum and maximum snow cover duration over the study area as per MOD09A.

Table 5.4: SCA (km^2) statistics of MODIS (MOD09A1) during 2000 to 2014 for the whole study area.

Years	Feb	Mar	Apr	Aug	Sep	Oct
2000	1149.96	1678.36	1291.21	116.82	115.53	147.68
2001	1190.97	1412.92	1374.71	79.46	146.23	327.21
2002	1230.81	1154.47	1140.73	62.70	77.94	44.93
2003	1571.11	1565.33	1282.84	43.89	88.48	754.52
2004	1218.99	1055.08	1141.80	78.11	115.52	96.00
2005	1649.65	1623.59	1239.91	45.64	73.65	179.32
2006	1335.25	1363.83	1020.95	55.84	95.98	241.94
2007	938.31	1378.85	1149.96	14.40	106.92	79.13
2008	1578.12	1260.51	1175.51	77.32	94.92	275.05
2009	771.30	1313.10	1592.59	55.41	61.19	280.13
2010	1130.64	1199.55	615.45	23.10	76.25	213.42
2011	670.84	1627.79	1143.52	66.57	102.00	231.22
2012	1419.14	1376.64	1338.22	51.33	65.49	451.26
2013	1223.38	1272.96	1120.34	66.78	147.73	148.37
2014	1214.79	1141.38	1323.84	61.56	105.07	276.95

To calculate the fractional SCA, around 10 numbers of elevation bands have been created based on the topographical variations over the study region. For the elevation bands, high spatial resolution (30 meter) based CARTOSAT DEM was utilized. The centroid elevation for 1st and 10^{th} bands varies from 1400 meter to 6800 meter, respectively.

Fig. 5.9 shows a consistent increment in the SCA with elevation except a very few one. A typical shape, superficial on many years, is that the elevation band where for example around 40% to 50% of the area is snow covered is at a higher elevation. The faster decrease in the SCA at the moderate to lower elevation bands noticed in all the years. In Fig. 5.9, an enormous fluctuations have been noticed in the January (Jan), August (Aug) and October (Oct) months in all the years. As per the elevation wise distribution of SCA, moderate high elevation band ranges show maximum fluxions in the SCA during all the years and months.

TH-1643_136104018

TH-1643_136104018

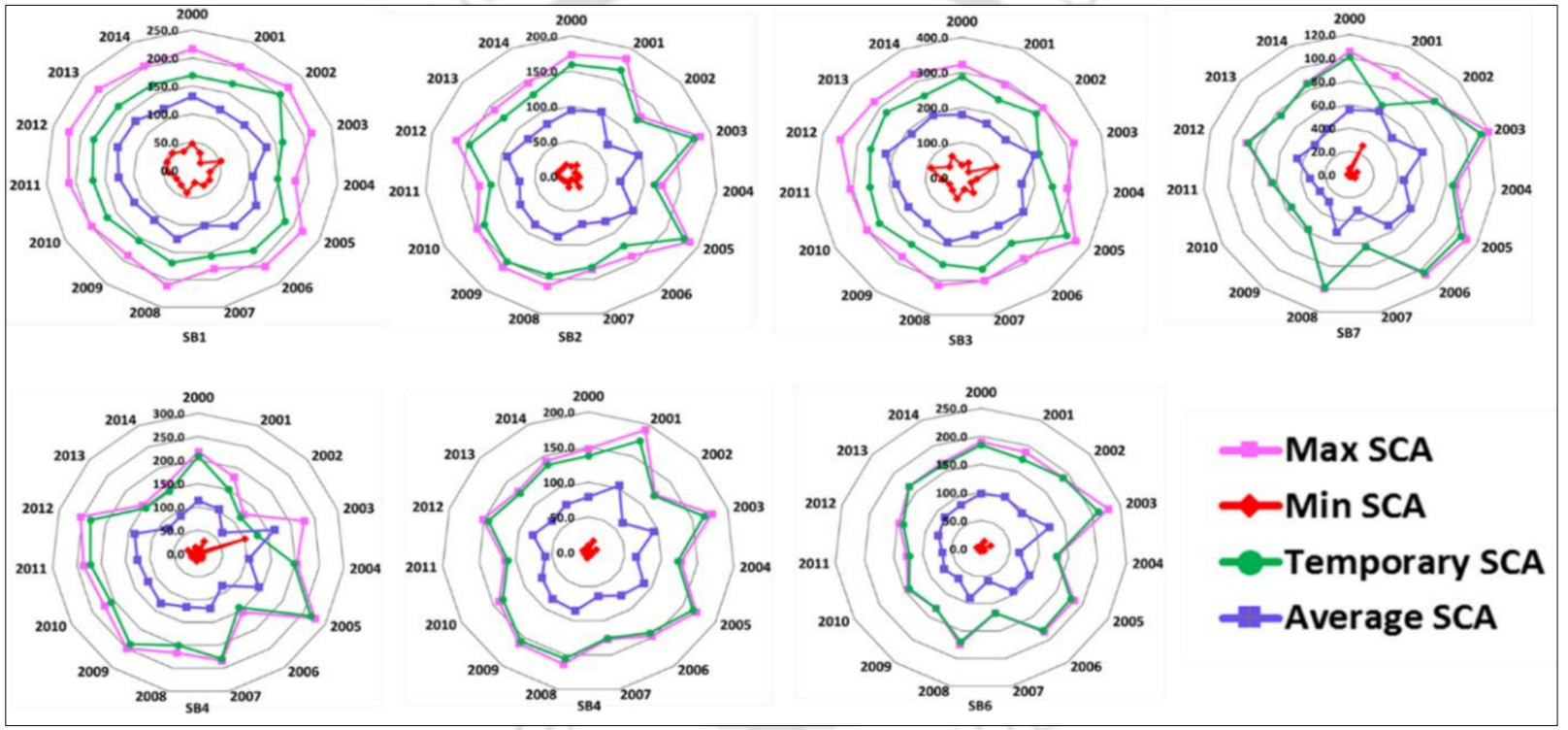


Fig. 5.8: Minimum, maximum, temporal and average SCA (km^2) statistics at catchment scale using MODIS datasets during 2000 to 2014.

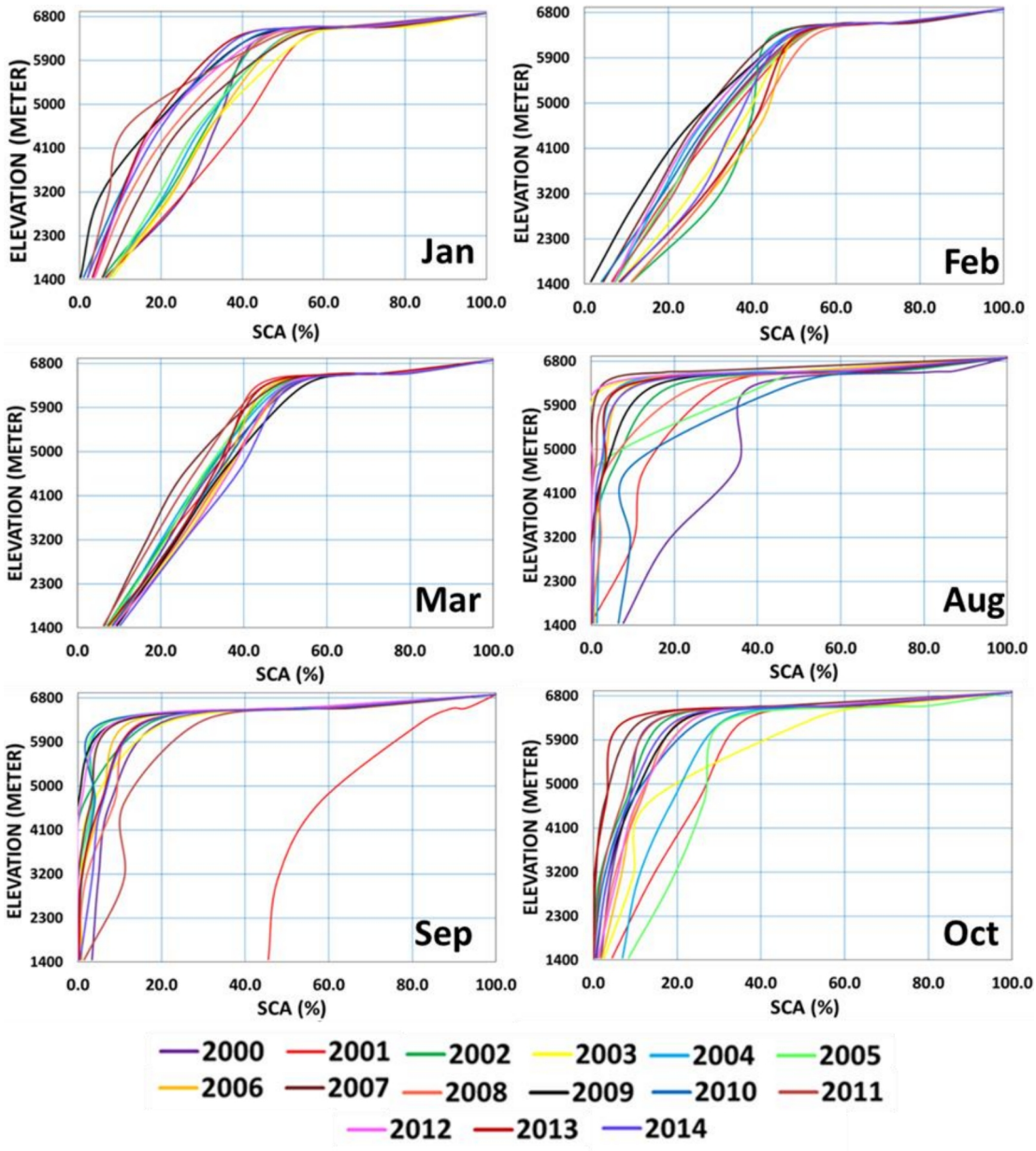


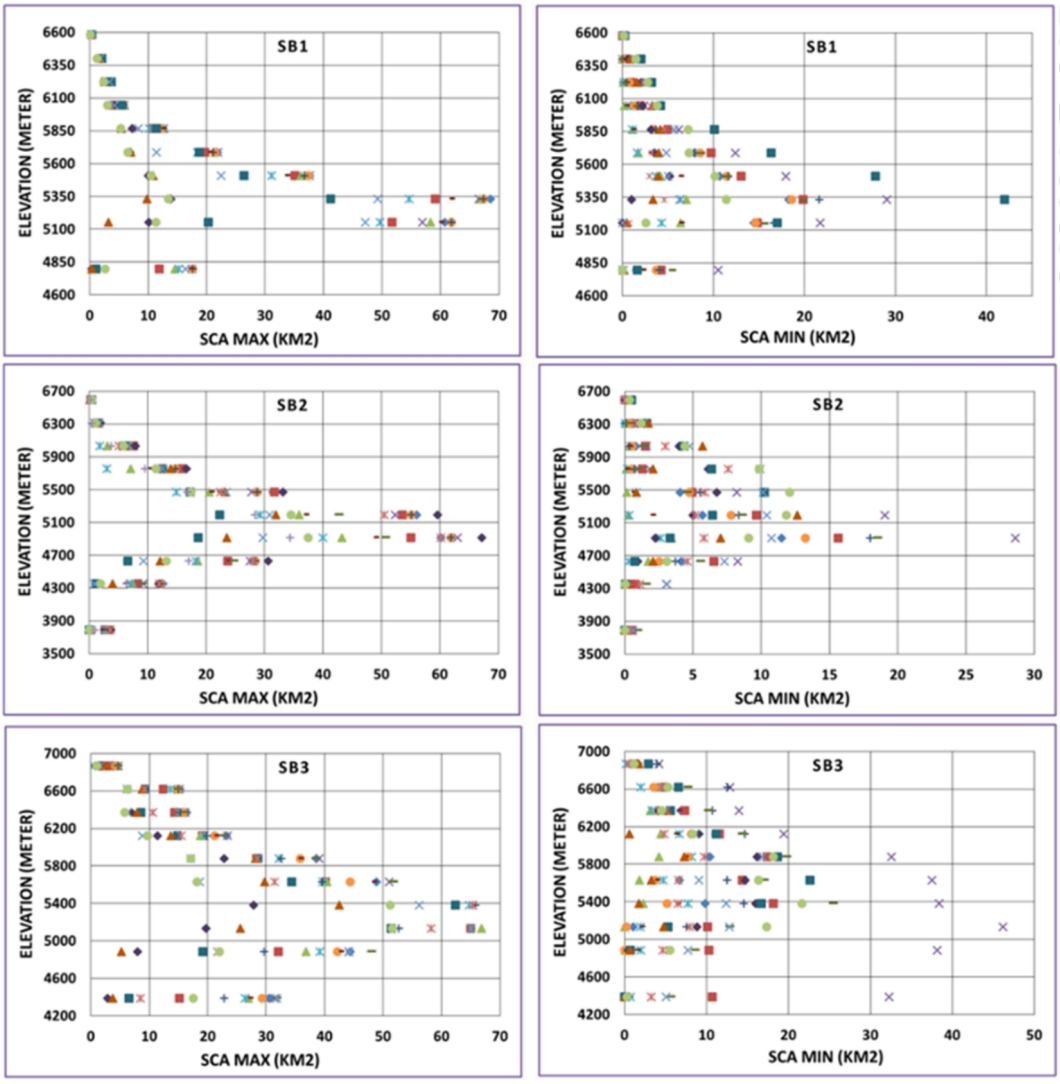
Fig. 5.9: Monthly Snow Depletion Curves (SDC) during 2000 to 2014 as per MODIS (MOD09A1) multispectral satellite datasets.

Fig. 5.10 showed the elevation band wise distribution of maximum and minimum SCA at each sub-catchment scale during temporal time duration (2000-2014) as per MOD09A1 MODIS snow cover datasets. This shows the elevation dependent spatial distribution of SCA within the sub-catchments. In Fig. 5.10, one can notice that the maximum SCA based plots show large spatial distribution of SCA across all the sub-catchments. In case of the minimum SCA, at high elevation based SBs such as SB1, SB2, SB3 and SB4 show significant spatial distribution, while lower to moderate elevation based SBs did not highlight significant spatial distribution of SCA. In Fig. 5.10, it is observed that the

TH-1643_136104018

maximum SCA based plots corresponded around 80% SCA in the high to extreme high hilly elevation bands, while moderate elevation bands corresponded only up to 20% SCA across all the sub-catchments during 2000 to 2014. In case of the minimum SCA, most of SCA percentages corresponded to high hilly portion of the catchment. In case of the minimum SCA, very less amount of SCA has been calculated, especially moderate elevation based SBs such as SB5, SB6 and SB7. The distribution of SCA in these SBs was also not significant. In case of the minimum SCA, 10% to 20% SCA corresponded only for high hilly terrain based SBs such as SB1, SB2 and SB3. This displays the snow cover distribution characteristics over the catchment, which can be useful for the snowmelt runoff computation. The MODIS cloud free snow cover data used for SCA estimation and based on that the SDCs are plotted over the Teesta river catchment.

Table 5.5 shows the change in SCA (%) as per the monthly calculation during 2000 to 2014. In Table 5.5, the February, April and October months show significant decrement (SCA %), while March have shown an increase in SCA.



TH-1643_136104018

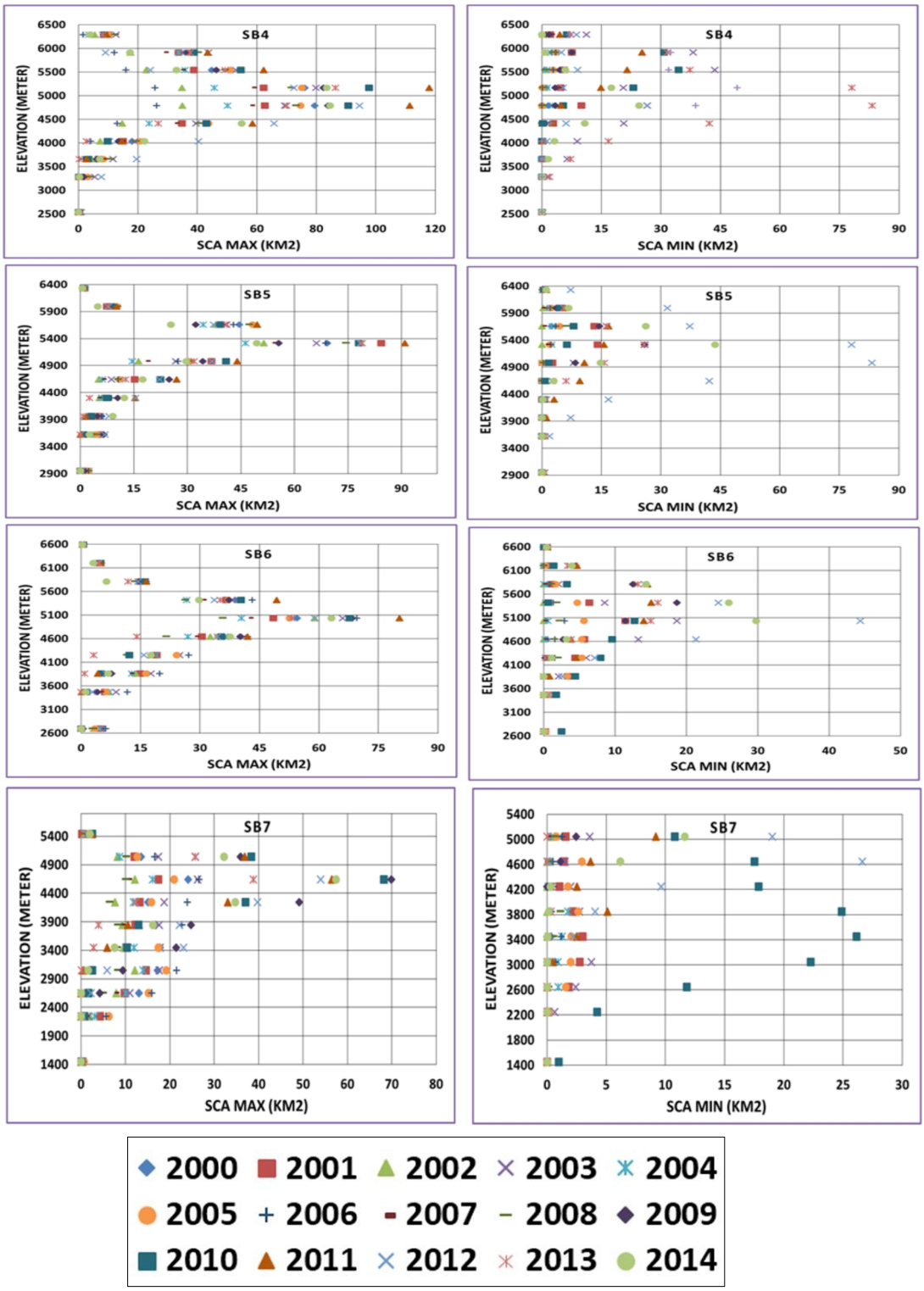


Fig. 5.10: Elevation band wise distribution of maximum and minimum SCA at each sub-catchment utilizing MODIS (TERRA and Aqua) 8 daily snow cover products during 2000 to 2014.

TH-1643_136104018

Table 5.5: Percent (%) of change in SCA (km^2) as per MOD09A1 satellite datasets during 2000-2014 at catchment scale.

Years	Feb	Mar	Apr	Aug	Sep	Oct
2000-2001	-1.603	10.379	-3.265	1.461	-1.200	-7.019
2000-2002	-3.161	20.484	5.884	2.116	1.470	4.017
2000-2003	-16.467	4.420	0.327	2.851	1.058	-23.727
2000-2004	-2.699	24.370	5.842	1.514	0.000	2.021
2000-2005	-19.538	2.142	2.006	2.783	1.638	-1.237
2000-2006	-7.245	12.298	10.567	2.384	0.764	-3.685
2000-2007	8.276	11.711	5.523	4.005	0.337	2.680
2000-2008	-16.741	16.338	4.524	1.544	0.806	-4.980
2000-2009	14.805	14.282	-11.784	2.401	2.125	-5.179
2000-2010	0.755	18.721	26.422	3.664	1.536	-2.570
2000-2011	18.733	1.977	5.774	1.965	0.529	-3.266
2000-2012	-10.525	11.797	-1.838	2.561	1.956	-11.870
2000-2013	-2.870	15.851	6.681	1.956	-1.259	-0.027
2000-2014	-2.535	20.996	-1.276	2.161	0.409	-5.054

These trends does not give any significant idea about consistent decrease or increase in SCA over the catchment. However, between several years SCA is decreased more than 15%. The October and February months are very critical months for snowfall over the Teesta river catchment, because most of the snowfall it receives during January and February months only. Thus, decrease in SCA during February could be serious threat to the Teesta river catchment. The overall analysis shows highly fluctuating response of SCA over this region.

The maximum decrease in SCA is estimated around 1 to 23 % during the February and October months, while increase in SCA is estimated around 1 to 26 % during March and April. The melting also starts in the April months and if it shows an increase in SCA in April as per Table 5.5, then this means there is shift in the precipitation and snowfall

TH-1643_136104018

pattern. The shifts in the snowfall will increase the higher and faster melting over the Teesta river catchment. However, a few years (e.g. 200-20011, 2007-2009 and 2013-2014) in the April month also exhibits decrease in SCA.

5.3.2 SCA analysis and change assessment using LISS 3 satellite datasets

Due to less temporal resolution (25 days) and high cloud cover contamination as Himalayan terrain topography, LISS 3 satellite imageries for the maximum (February/March) and Minimum (October/November) time durations, which has minimum cloud cover (less than 20%) scenes, from 2009 to 2014, have been obtained for the snow cover estimation and change assessment. LISS 3 sensor has very high spatial resolution (23.5 meter) and better radiometric resolution than MODIS, thus, provides a better accuracy outcomes. The LISS 3 imageries are initially orthorectified and then applied NDSI approaches for the extraction of SCA. The details about the LISS 3 sensors have been provided in the above sections. The NDSI based extraction of SCA during maximum and minimum time duration has been shown in Fig. 5.11.

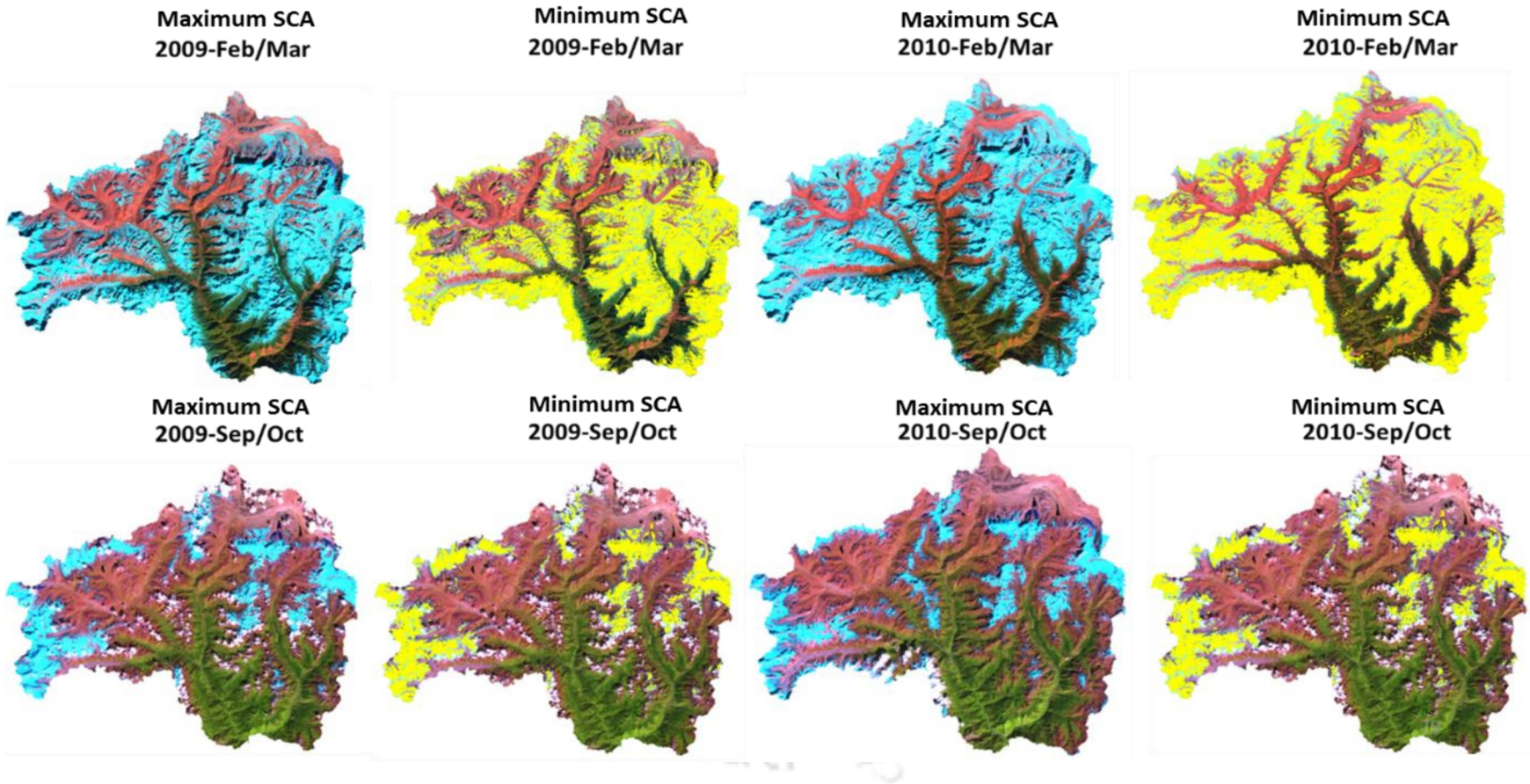
In Fig. 5.11, one can observe a significant variation the SCA during maximum and minimum time periods during the year 2009-2014. In the maximum SCA extraction, most of the scenes are collected for the February and March months. While in the minimum SCA extraction, the LISS 3 satellite imageries are considered from the October and November months with minimum cloud covers. However, except two or three scenes, all the scenes have less than 10% cloud cover. Thus, better accuracy can be estimated in the SCA calculation.

In Fig. 5.11, it can be clearly observe that the high elevative portion of the catchment corresponded maximum SCA even during the melt periods. In the maximum SCA duration, almost whole study area is covered by snow cover, but in minimum time periods, it melts from the moderate hilly portions of the catchment and it only remains at the high elevative portions of the catchment.

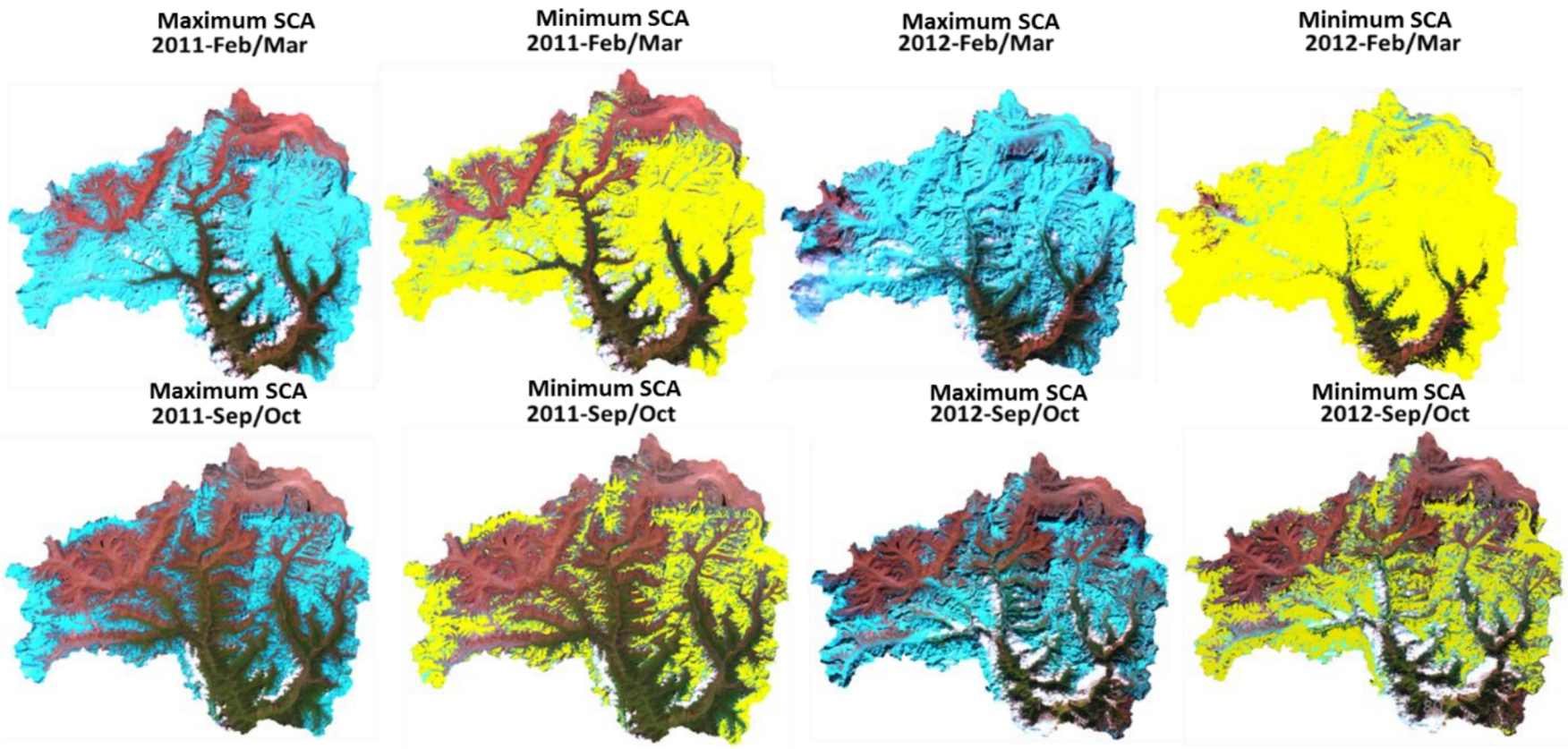
In Table 5.6 SCA statistics from LISS 3 satellite imageries have been shown at each sub-catchment scale. The sub-catchment wise estimation of SCA gives spatial distribution information of snow covers over the Teesta catchment. The whole time series (2009-2014) is grouped into two time scenarios (e.g. 2009-2011 as Avg. 1 and 2012-2014 as Avg. 2) to compare the average statics. The average statistics show significant variations in the SCA during maximum and minimum time scale even in the less temporal time durations. A slight decrease in SCA is observed in Avg. 2 (Table 5.6).

TH-1643_136104018

TH-1643_136104018



TH-1643_136104018



TH-1643_136104018

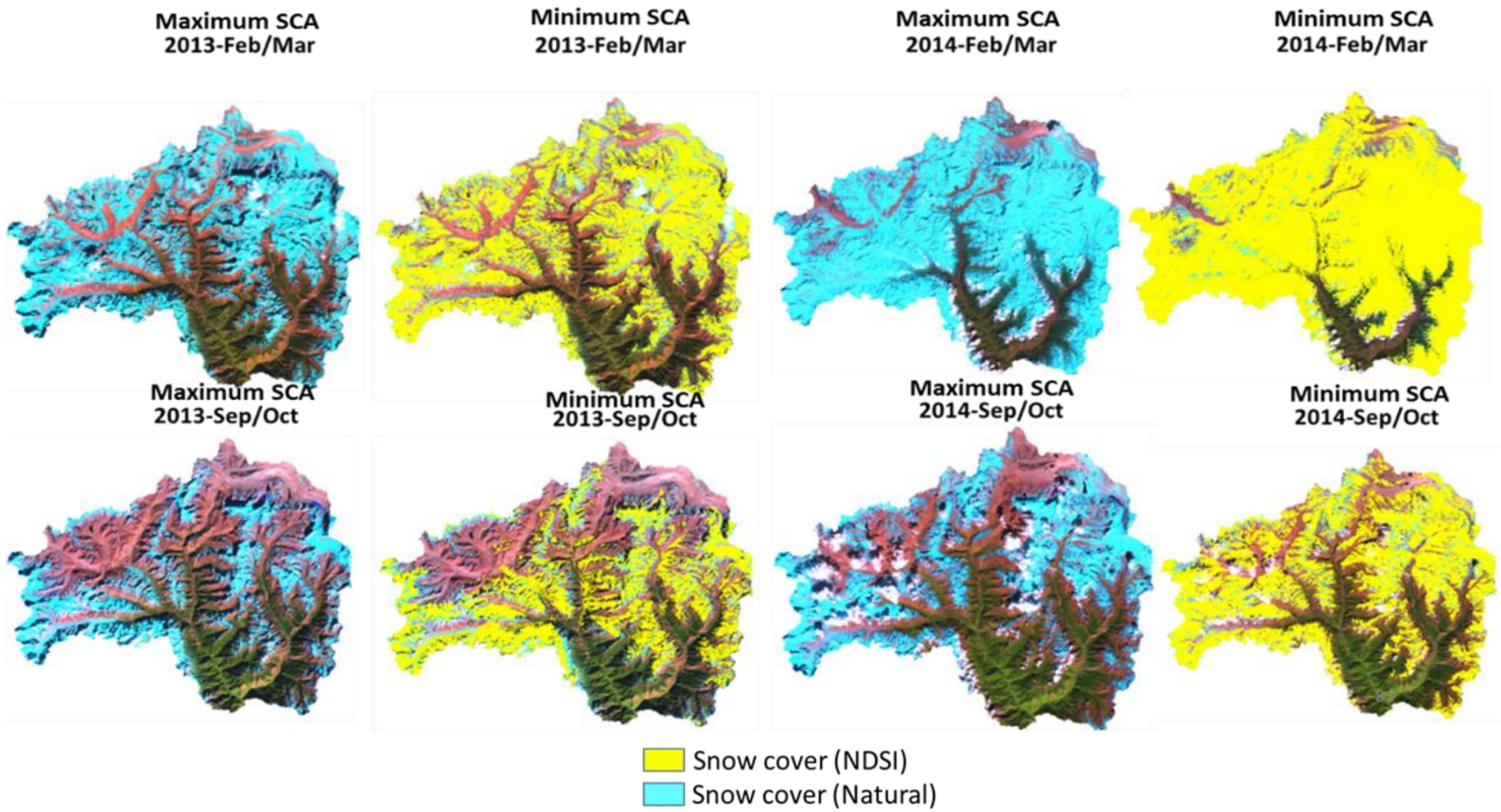


Fig. 5.11: NDSI showing maximum and minimum SCA from IRS LISS 3 multispectral satellite imageries during 2009-2014.

Table 5.6: Maximum and minimum SCA (km^2) statistics at each-sub catchment scale estimated from LISS 3 satellite imageries during the year 2009-2014.

SBs	SCA (km^2)	2009	2010	2011	Avg. 1	2012	2013	2014	Avg. 2
SB1	Min	13.69	125.40	12.39	50.49	28.76	23.18	43.96	31.97
	Max	52.57	131.05	45.13	76.25	164.72	131.51	56.60	117.61
	Change	38.88	5.66	32.74	25.76	135.96	108.33	12.64	85.64
SB2	Min	27.14	30.82	14.93	24.30	55.77	32.89	52.30	46.99
	Max	87.22	112.98	111.46	103.89	195.18	123.92	118.00	145.70
	Change	60.07	82.16	96.53	79.59	139.41	91.03	65.70	98.71
SB3	Min	76.58	91.24	21.09	62.97	83.59	53.47	99.52	78.86
	Max	126.28	237.67	169.31	177.75	265.07	251.12	201.52	239.24
	Change	49.70	146.43	148.21	114.78	181.48	197.65	102.00	160.38
SB4	Min	100.36	74.31	112.94	95.87	305.40	64.80	161.86	177.36
	Max	322.94	347.91	421.06	363.97	336.84	281.95	305.79	308.19
	Change	222.58	273.60	308.12	268.10	31.44	217.15	143.93	130.84
SB5	Min	56.95	23.15	110.61	63.57	119.22	71.99	96.17	95.80
	Max	180.66	202.57	240.66	207.96	214.93	177.65	151.47	181.35
	Change	123.71	179.42	130.05	144.39	95.71	105.65	55.30	85.56
SB6	Min	50.88	44.82	18.73	38.14	119.09	52.41	79.25	83.58
	Max	195.65	184.12	216.27	198.68	171.25	123.38	165.83	153.49
	Change	144.77	139.30	197.54	160.54	52.15	70.97	86.58	69.90
SB7	Min	3.87	137.22	4.21	48.43	63.28	0.00	19.99	27.76
	Max	219.71	175.62	146.39	180.57	175.27	86.08	152.00	137.78
	Change	215.84	38.40	142.18	132.14	111.98	86.08	132.00	110.02

The highest fluctuation in the maximum SCA has been determined for the SB7, while the highest fluctuation in the minimum SCA was obtained at the SB 1 and SB2.Table 5.7 shows the absolute change in SCA statistics during the year 2009-2014 at catchment scale from LISS 3 sensor datasets. In Table (5.6), most of the values are negative except few positive values, which shows significant decrease and increase in SCA during 2009-2010. This is a similar response to MODIS satellite datasets. The maximum decrease is recorded as -205 km^2between 2009 and 2012, while the maximum increase is recorded as 177 between 2009 and 2010.This shows a significant variability in the SCA over the Teesta catchment. However, most of the trends show decrease in SCA over the selected study region.

TH-1643_136104018

Table 5.7: Change in SCA (km^2) as per IRS LISS3 satellite data during 2000-2014 at catchment scale.

Avg1-Avg2	2009-2010	2009-2011	2009-2012	2009-2013	2009-2014
18.52	-111.71	1.30	-15.07	-9.49	-30.27
-41.36	-78.49	7.44	-112.15	-78.95	-4.03
-59.88	33.22	6.13	-97.08	-69.46	26.24
-22.69	-3.68	12.21	-28.63	-5.74	-25.16
-41.81	-25.77	-24.24	-107.96	-36.70	-30.78
-19.12	-22.09	-36.46	-79.34	-30.96	-5.62
-15.89	-14.66	55.49	-7.01	23.12	-22.93
-61.49	-111.38	-43.02	-138.79	-124.83	-75.24
-45.60	-96.73	-98.51	-131.78	-147.95	-52.31
-81.49	26.05	-12.58	-205.05	35.56	-61.50
55.77	-24.97	-98.12	-13.91	40.99	17.14
137.26	-51.02	-85.54	191.14	5.43	78.65
-32.23	33.80	-53.67	-62.27	-15.04	-39.22
26.61	-21.90	-60.00	-34.27	3.02	29.19
58.84	-55.70	-6.33	28.00	18.06	68.41
-45.44	6.06	32.15	-68.21	-1.53	-28.37
45.19	11.53	-20.62	24.41	72.27	29.82
90.63	5.47	-52.77	92.62	73.80	58.19
20.67	-133.34	-0.34	-59.41	3.87	-16.12
42.79	44.09	73.31	44.44	133.63	67.71
22.12	177.43	73.65	103.85	129.76	83.83

This portion of the study demonstrates an effort to comprehend the present state of a snow cover regime and its dynamics along with its temporal and spatial variability in the selected study region part of north Sikkim eastern Himalaya, utilizing multispectral multi-resolution satellite senor datasets. The data set time frame is not so long to allow for robust decisions in the assessment of snow cover. Though, around 15 years temporal variations study of the SCA is found sufficient to monitor the recent changes over Sikkim Himalaya. Overall, including LISS 3 and MODIS snow cover assessment, a high variability in the SCA has been obtained during the snow accumulation time periods than snow melt seasons. It also fluctuates from high elevation to low elevation portions of the catchment.

TH-1643_136104018

5.3.3 Glacial lakes and waterbodies extraction and change detection

A Teesta river catchment part of north Sikkim eastern Himalaya comprises with snow covers and glaciers especially at their upstream portions. The Sikkim glaciers are valley type glaciers, which consist many glacial lakes in the depression of glacier and valley portion due to glacier dynamics. Though several waterbodies are also present with in the region. Due to the changing climate, many glaciers are retreating around the world and increasing the volume of these glacial lakes and water bodies.

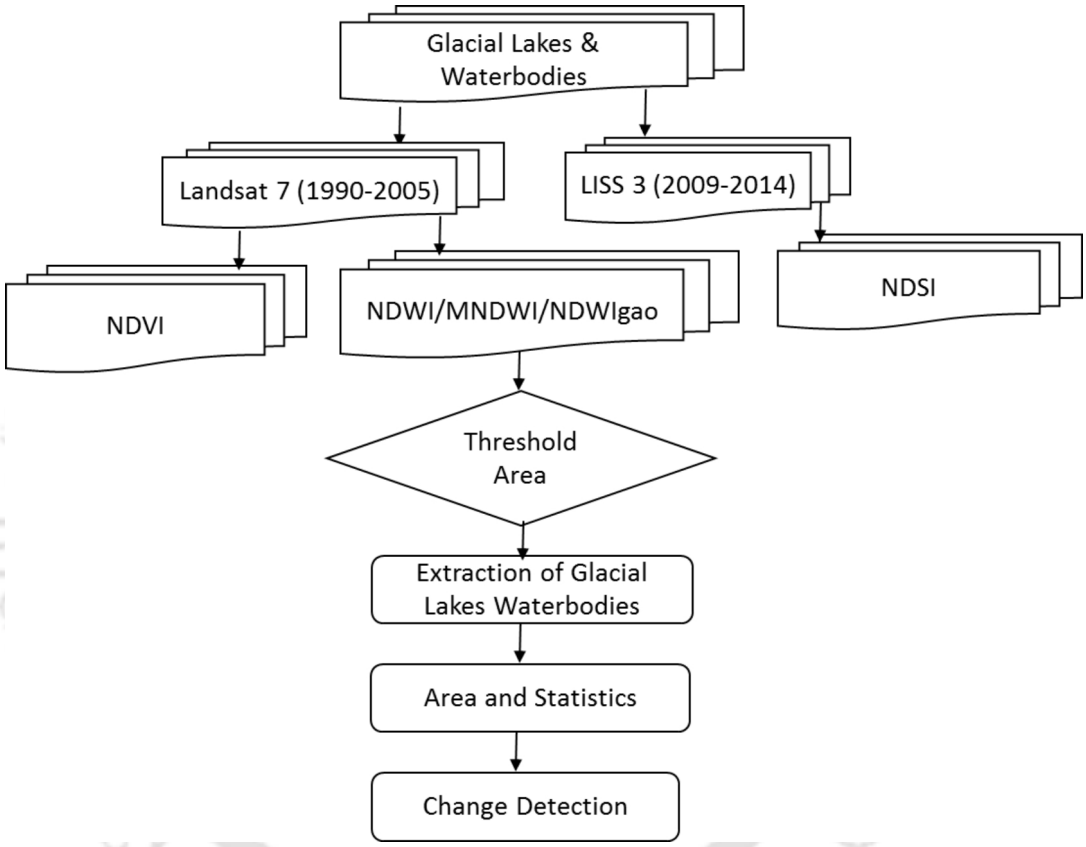


Fig. 5.12: Flow chart of the extraction methodology of glacier lakes and waterbodies.

The new formation of moraine-dammed glacial lakes and glacial lake outburst flood (GLOF) is major concern in the high hilly terrain based catchments (Kulkarni et al., 2008). Thus, there is an argent need to carry out a detail glacier lakes inventory, to monitor the current status of the glacial lakes and water bodies, for the sustainable water management and to prevent this region from severe flash flood hazards.

In the snow and glaciated Teesta river catchment part of north Sikkim eastern Himalaya, remote sensing based assessment of many of the glacial lakes are easier as these are located at very high altitude, cold weather and rocky extremely high hilly terrain conditions. The remote sensing based extraction of glacial lakes sometimes fail, if the glacial lakes are covered by ice, under mountain shadows and cloud contamination. Therefore, almost cloud

TH-1643_136104018

free satellite images are selected in the melt time periods (during October/November) with less than 10 % cloud cover. For this purpose, two high spatial remote sensing satellite sensors such as Landsat and Indian Remote Sensing Satellite (IRS) LISS 3 imageries were obtained in the temporal duration (1990, 2000, 2005, 2010, and 2014).

Table 5.8: Details of glacial lakes and waterbodies identified in different temporal time durations over the selected study region.

Lake-ID	Lat	Long	Area (km^2) 1990	Area (km^2) 2000	Area (km^2) 2005	Area (km^2) 2009/10	Area (km^2) 2014
GL-1	27.99	88.81	1.565149	1.461113	1.53874	1.512132	1.758543
GL-2	28.01	88.71	1.324957	1.132249	1.23125	1.139179	1.151697
GL-3	28.01	88.76	1.0628	0.999108	0.92431	0.930792	1.08377
GL-4	28.03	88.71	1.054443	1.080942	1.07225	1.091195	1.08436
GL-5	28.01	88.70	0.765436	0.799475	0.78174	0.897351	0.92661
GL-6	27.90	88.78	0.589842	0.285782	0.27943	0.325034	0.298906
GL-7	27.98	88.62	0.569183	0.561254	0.56102	0.563258	0.571565
GL-8	27.95	88.33	0.574318	0.567535	0.48435	0.567865	0.622453
GL-9	27.99	88.55	0.535879	0.533151	0.55717	0.573525	0.786895
GL-10	27.91	88.20	0.562275	0.664051	0.53728	NA	NA
GL-11	28.06	88.63	0.478717	0.125985	0.48425	0.121293	0.149456
GL-12	28.00	88.64	0.384494	0.342615	0.33265	0.315766	0.300169
GL-13	27.90	88.76	0.334788	0.342137	0.37404	0.419097	0.388735
GL-14	27.94	88.78	0.34118	0.118912	0.2881	0.132273	0.120971
GL-15	28.01	88.49	0.350909	0.390955	0.36986	0.448316	0.409336
GL-16	27.92	88.16	0.311256	NA	NA	NA	NA
GL-17	27.67	88.51	0.318836	0.23123	0.19228	0.203512	0.322012
GL-18	27.96	88.74	0.25383	0.226575	0.14633	0.214281	0.211956
GL-19	27.95	88.31	0.240439	0.3574	0.33656	0.374169	0.332029
GL-20	28.01	88.56	0.227473	0.254551	0.23425	0.255801	0.275903
GL-21	28.01	88.57	0.209363	0.25952	0.21003	0.24285	0.271025
GL-22	27.96	88.65	0.183929	0.190094	0.18523	0.209035	0.136445
GL-23	27.96	88.36	0.180664	0.166191	0.20005	0.18307	0.178595
GL-24	27.97	88.80	0.191578	0.196385	0.10308	0.188138	0.191471
GL-25	27.91	88.34	0.191963	NA	NA	NA	NA
GL-26	27.73	88.83	0.164956	0.185274	0.16192	0.073708	0.171306
GL-27	27.89	88.24	0.200935	0.162623	NA	NA	NA
GL-28	27.72	88.45	0.15444	0.153737	0.12885	NA	0.148551

TH-1643_136104018

GL-29	27.83	88.32	0.184994	0.092312	0.12149	0.112961	0.134875
GL-30	28.01	88.65	0.140764	0.138423	0.13472	0.115291	0.120598
GL-31	27.97	88.43	0.15414	0.135768	0.15271	0.140689	0.145141
GL-32	27.76	88.48	0.14314	0.087154	0.12675	0.127853	0.183861
GL-33	27.97	88.44	0.138726	0.058831	0.06827	0.087363	0.104037
GL-34	27.85	88.81	0.133142	0.081399	0.08426	0.84256	0.084373
GL-35	27.82	88.26	0.135359	0.059962	0.06582	0.104196	0.136402
GL-36	27.82	88.66	0.13857	0.137715	0.13433	0.14465	NA
GL-37	27.72	88.69	0.130741	0.116081	0.11525	0.126695	0.128333
GL-38	27.86	88.86	0.126894	0.127368	0.11059	0.138763	0.158338
GL-39	27.85	88.24	0.126966	0.0646	0.13529	0.288779	0.308192
GL-40	27.84	88.80	0.121915	NA	NA	NA	NA
GL-41	27.98	88.79	0.120827	0.091267	0.14454	0.097385	0.073666
GL-42	27.88	88.25	0.119967	0.133156	0.11493	0.149534	NA
GL-43	27.99	88.74	0.118076	0.08579	0.10419	0.11829	NA
GL-44	27.92	88.31	0.155026	0.105704	0.09361	0.108049	0.127636
GL-45	27.97	88.42	0.124275	0.11295	0.13427	0.130054	0.130009
GL-46	27.95	88.35	0.132015	0.195944	0.2809	0.126541	0.210515
GL-47	27.97	88.59	0.117867	0.119311	0.1019	0.111717	0.111741
GL-48	27.66	88.69	0.117618	0.13256	0.14358	0.145089	0.181619
GL-49	27.70	88.51	0.100036	0.0765285	0.07271	NA	NA
GL-50	27.75	88.69	0.124857	0.092271	0.06313	0.109839	NA
GL-51	27.92	88.67	0.122552	0.102069	0.21745	0.2106735	0.2104466
GL-52	27.96	88.80	0.113565	0.087916	0.12214	0.112352	0.121917
GL-53	27.67	88.69	0.107054	NA	0.12676	0.124809	0.109206
GL-54	27.99	88.60	0.105895	0.104732	0.10537	NA	0.103396
GL-55	27.84	88.23	0.102511	0.102541	NA	0.127013	0.11711
GL-56	27.87	88.79	0.098676	0.095763	0.11076	0.110543	0.11241
GL-57	27.82	88.45	0.088949	0.076402	0.11671	0.083298	0.079252
GL-58	27.89	88.27	0.096424	0.09075	NA	0.093051	0.108304
GL-59	27.89	88.26	0.120625	0.085011	0.0764	NA	0.075992
GL-60	27.75	88.68	0.090187	0.07378	0.08223	0.071979	0.063179
GL-61	27.95	88.22	0.092477	NA	0.0545	NA	NA
GL-62	27.87	88.64	0.078957	0.078553	0.09522	0.095	NA
GL-63	27.70	88.72	0.090098	NA	0.24938	0.077413	NA
GL-64	27.99	88.80	0.079751	0.070663	NA	0.073755	0.078101
GL-65	27.88	88.26	0.079902	0.090878	0.07021	0.08579	0.111732
GL-66	28.00	88.55	0.070937	0.101387	0.07445	0.093716	0.09513
GL-67	27.94	88.27	0.074558	0.071418	0.08858	0.062694	0.091647

TH-1643_136104018

GL-68	27.76	88.61	0.065472	NA	NA	NA	0.057839
GL-69	27.68	88.81	0.074075	0.0762568	0.09068	0.058802	0.056987
GL-70	27.77	88.85	0.078327	0.06212	NA	NA	0.067925
GL-71	27.85	88.50	0.080879	0.06272	NA	NA	0.085022
GL-72	27.83	88.42	0.065666	NA	NA	NA	NA
GL-73	27.94	88.27	0.063639	NA	NA	NA	NA

A semi-automated methodology including Normalized Difference Water Index (NDWI), Modified NDWI and manual digitization of glacier lakes and water bodies have been adopted. The methodology of the waterbodies and glacial lakes extraction using NDWI has been explained already in the above sections. Table 5.8 show the area statistics and Latitudes and Longitudes of glacial lakes and water bodies calculated using LISS 3 and Landsat multispectral satellite snow cover products in different time decades (1990, 2000, 2010 and 2014). Total 73 numbers of glacial lakes and waterbodies, having area greater than 0.05 km^2, are extracted. As per the temporal analysis from 1990 to 2014, few glacier lakes and water bodies have been disappeared.

Among all, specifically, the glacial lakes are increasing their sizes in the progressive manner. Though several water bodies have also reduced their extent in the temporal domain (1990-2014). A few glacial lakes and water bodies have significantly increased their extent in the temporal time and can be seen in Table 5.8. Most of the glacial lakes, which are having area greater than 0.7 km^2 are significantly increased their sizes from 1990 to 2014 and still consistently increasing. These glacial lakes are situated in the high hilly terrains of this region and thus, could be severe in the near future for flash flood hazards.

Fig. 5.13 shows the increase and decrease in the area of glacial lakes and water bodies. In Fig. (5.13), the largest glacial lakes have been highlighted, which showed significant increase and decrease. In Fig (5.13), one can observe that many new glacial lakes have been formed and some of them have been disappeared too. The larger size glacial lakes are significantly increased. The glacial lakes which are situated at the top of the catchment showed enormous change in their size when compared between 1990 and 2014.

TH-1643_136104018

TH-1643_136104018

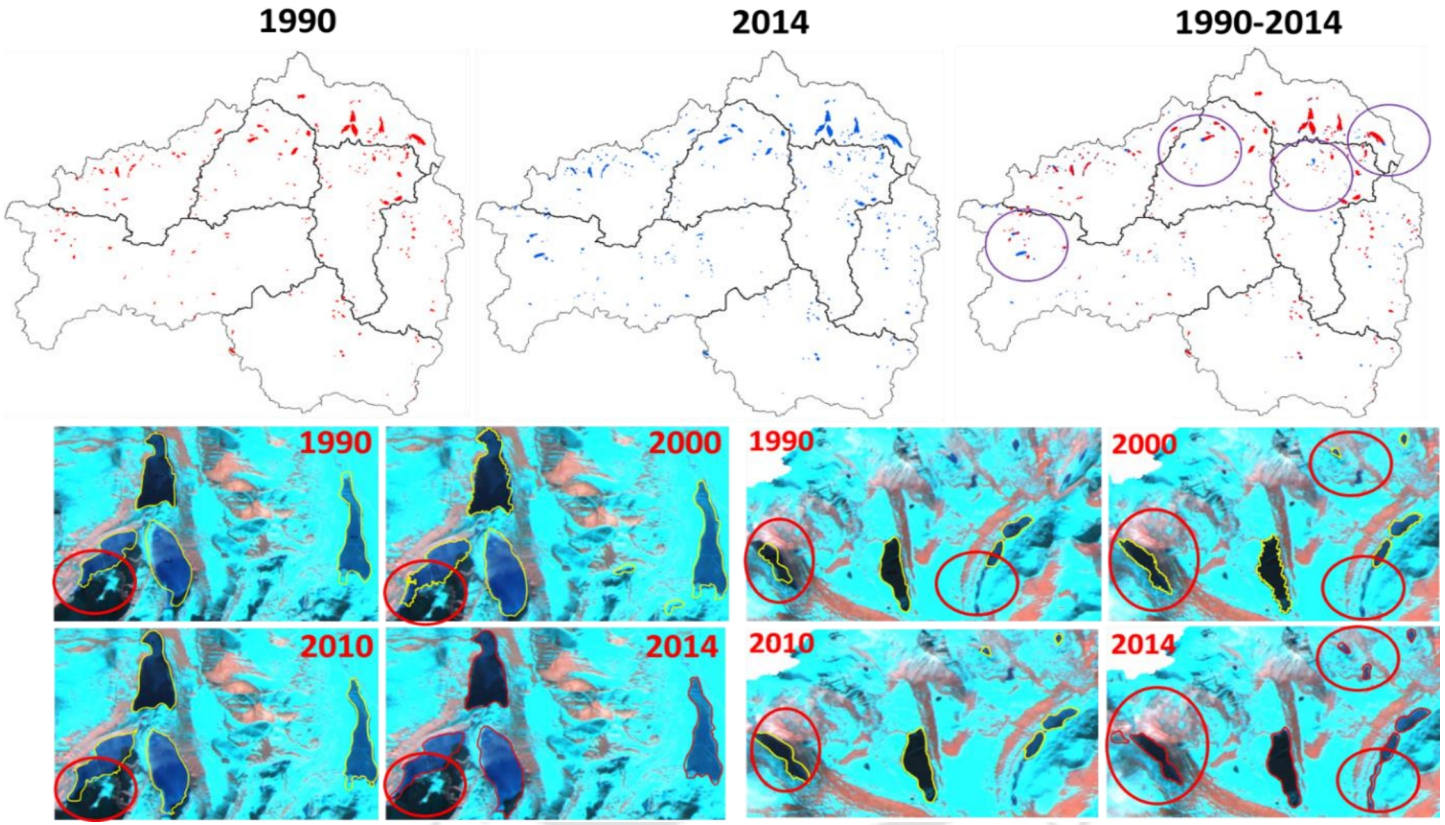


Fig. 5.13: Highlighting changes in Glacial Lakes and Waterbodies during 1990 to 2014.

In Fig. (5.13), it can also be interpreted that most of the glacial lakes are situated at the upstream portion or extreme hilly terrain portions of the catchment. The formation of new glacial lakes and the glacial lakes which have increased their sized could be disastrous in the near future.

5.4 CHARACTERIZATION OF DEBRIS COVER OF ZEMU GLACIER

Differentiating SGD, clean ice and ice covered glaciers from PGD cover is a challenging task due to similar responses of remote sensing spectral bands. As per the detailed literature review it is concluded that the differences between thermal and optical wavelength bands could be used to separate the SGD and PGD accurately. To characterize the debris cover of Zemu glacier, total six different combinations of bands including optical and thermal bands from two high spatial resolution multispectral sensors such as Landsat and LISS 3, have been formulated under various mathematical and image processing operations (as already explained).

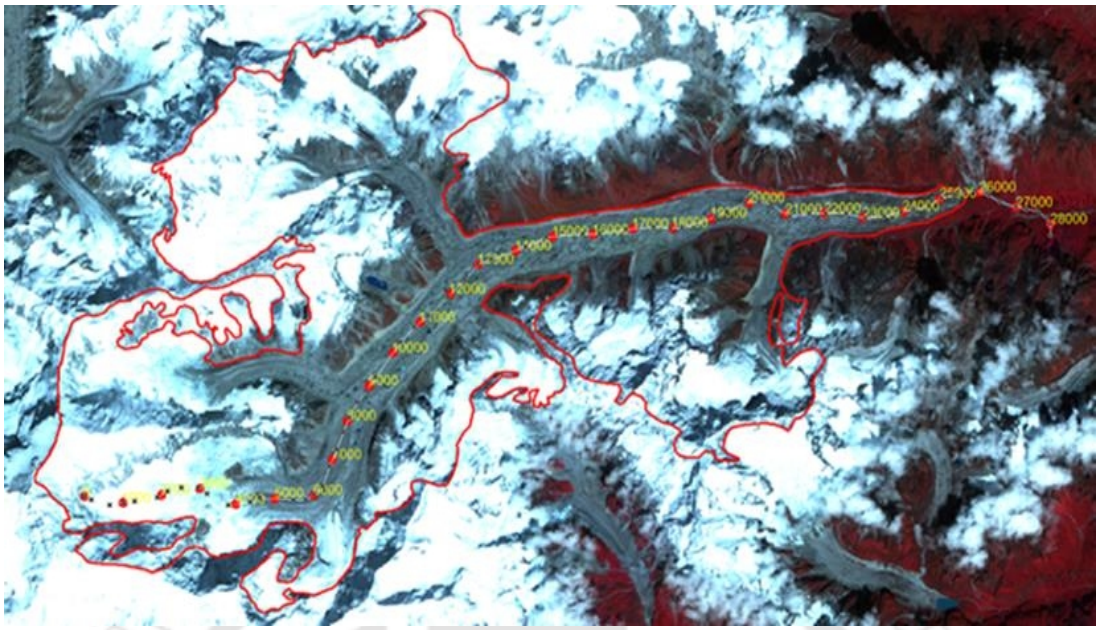
5.4.1 MLC and 3HDC classification of approaches for preparing glacier maps

To explore the glacier features over the Zemu glacier, spatial spectral reference curves have been plotted (Fig. 5.14). The spectral differences of the different glacial features will be helpful in identifying the unique spectral signatures, which are required for the MLC. To verify the accuracy of the spectral signatures, google earth based Quickbird image (at 1:10000 scale) has been used to extract the glacial signatures. These procedures have facilitated in identifying PGD, valley rocks and shadow regions in the complex topography of the Zemu glaciers (Fig. 5.15).

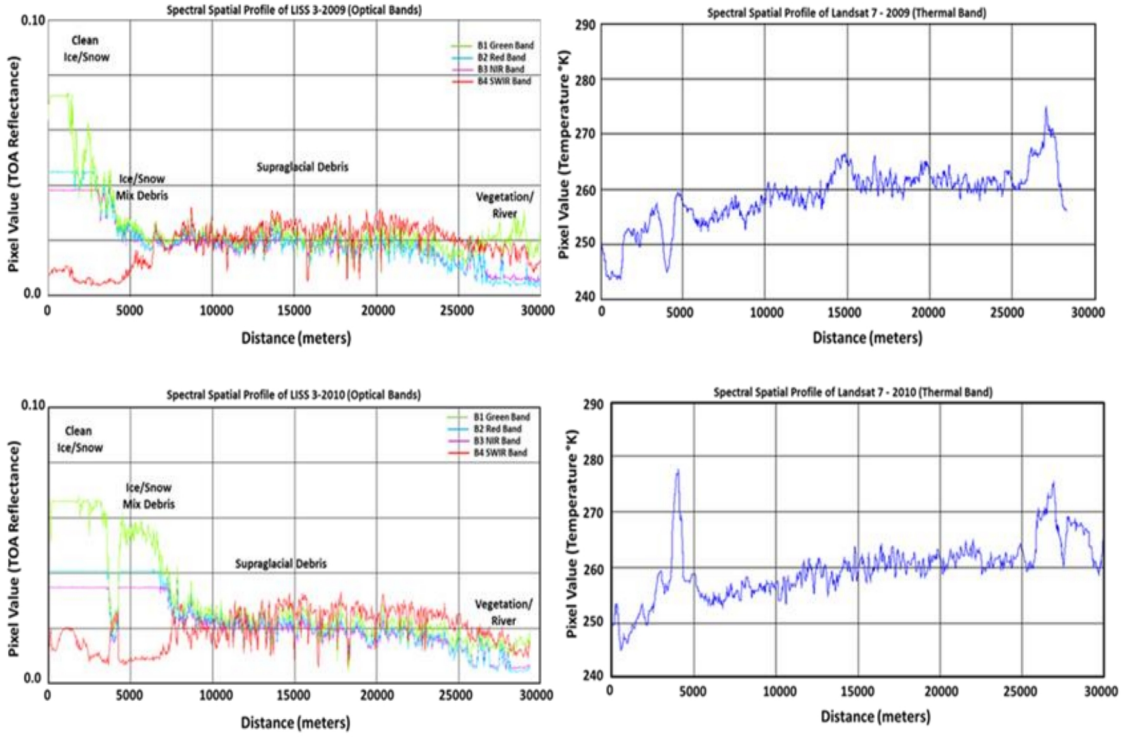
The temporal fluctuations in the SGD, clean ice snow glaciers and ice snow mixed debris covers have been evaluated based on the computed area and histograms with respect to each band combinations. The results of the MLC and 3HDC based classified maps have been showed in the Fig. (5.16) and in this, it shows all the classified maps as per the six band combinations and 3HDC based hybrid maps of these classified maps (2009-2010). The six classified maps based on MLC show significant variations in the glacial classes. Several mixing of the glacial classes have been identified in MLC based classified maps.

TH-1643_136104018

(a)



(b)



TH-1643_136104018

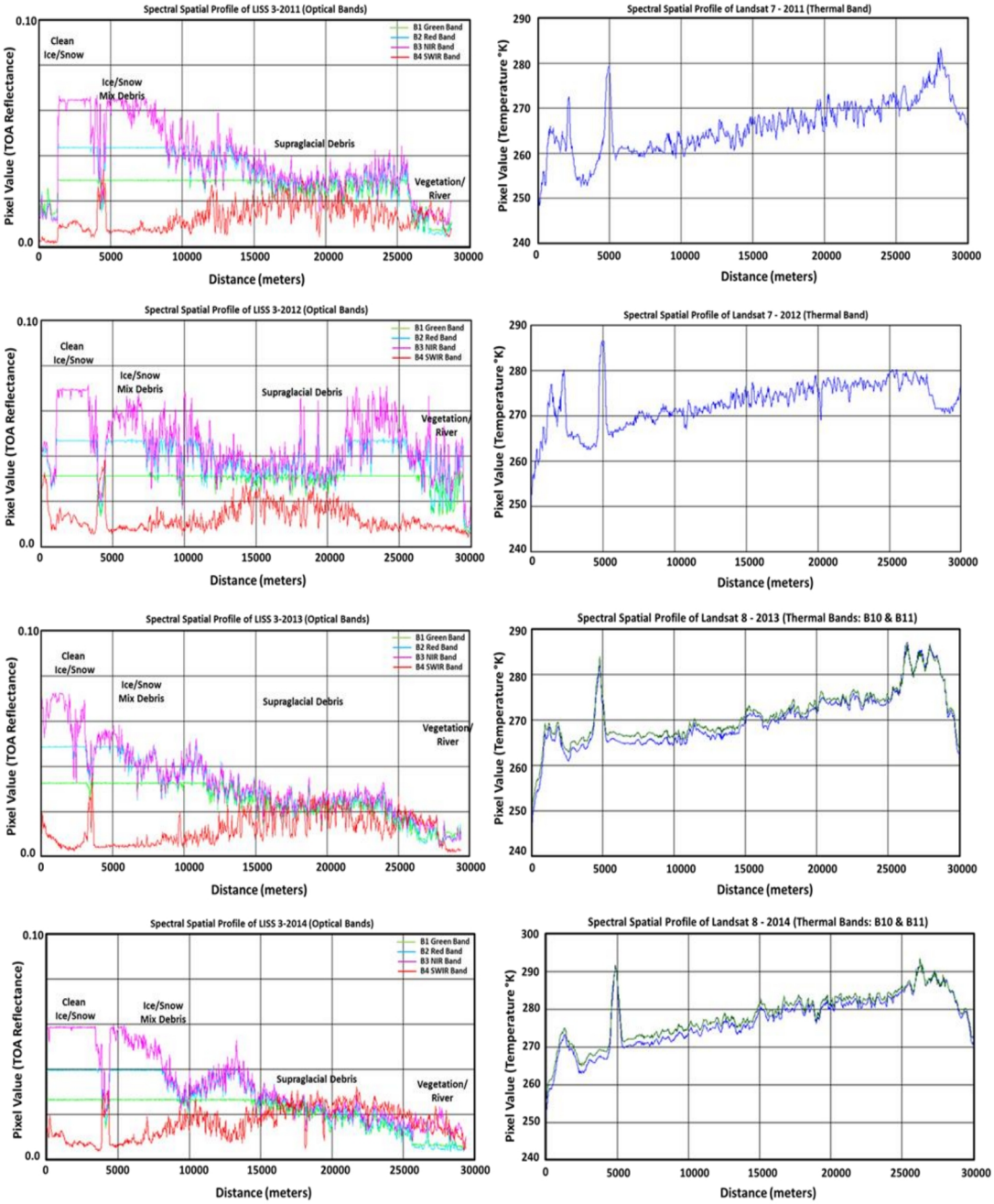


Fig. 5.14: Spectral reflectance curves of optical bands from LISS 3 sensor and thermal bands from Landsat 7 and Landsat 8 sensors: (a) spatial location of the spectral profile (as per LISS 3 2009) and (b) spatial spectral reflectance curves of LISS 3 and Landsat sensors during 2009 to 2014.

To minimize the effect of mixing of pixels, a very high resolution based Quickbird image (1:10000 scale) is adopted and processed it for the accurate identification of the glacial signatures for the MLC (Fig. 5.16). Still some fixing of pixels were remained. At many places, due to mixed pixels, it is found difficulty to identify the accurate glacial classes.

TH-1643_136104018

TH-1643_136104018

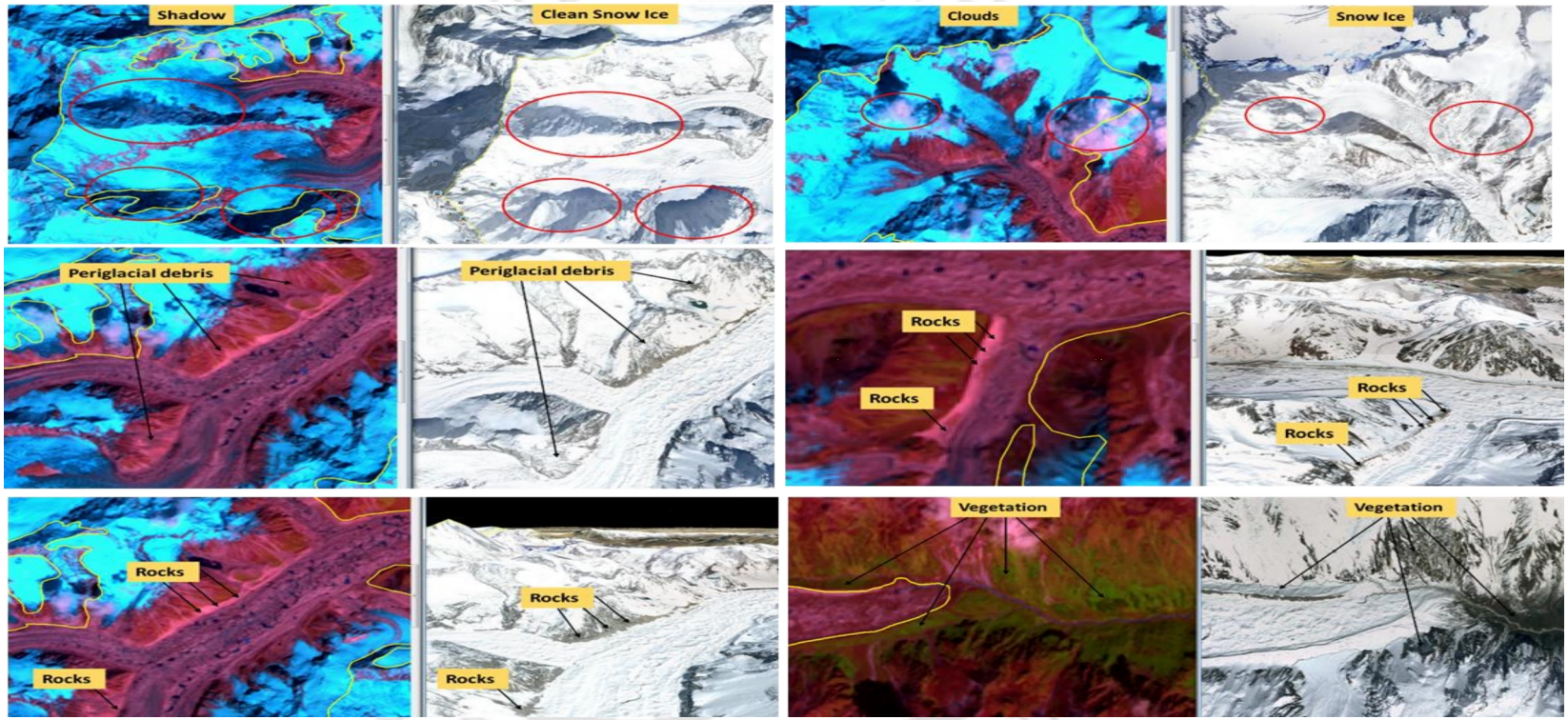
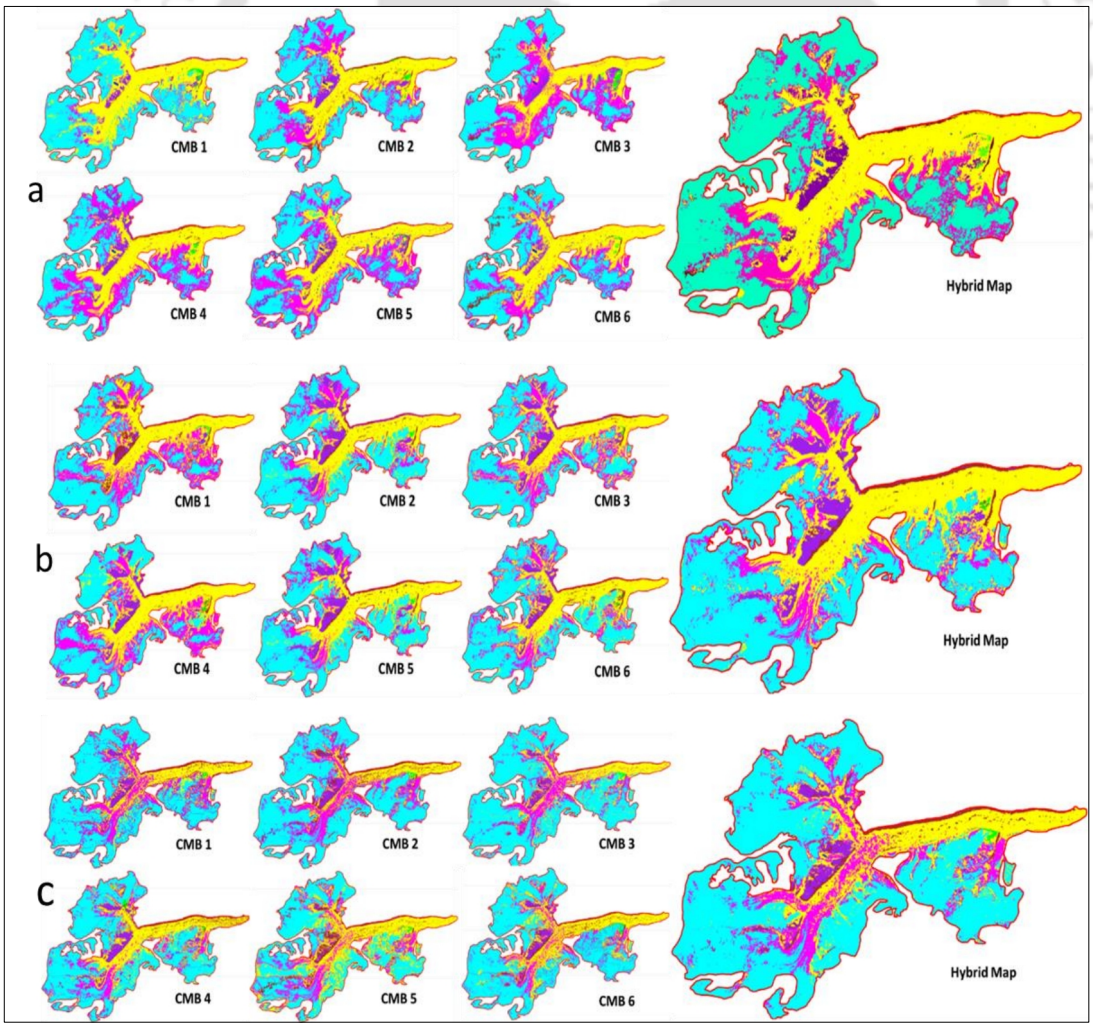


Fig. 5.15: Maps show the quality check based identification of the various glacial classes comparing GeoEye-1 GES image and satellite images from Landsat and LISS 3 sensors.

Thus, 3DHC method has been incorporated into the MATLAB image processing tool and the hybrid maps have been made for each year based on the six image band combinations using probabilistic mode function to separate the glacier features (Fig. 5.16). The accuracy assessment of all the thematic classified maps as per MLC and 2DHC methods have been performed.

Table 5.9 shows the overall accuracy of the classified maps generated by MLC and 3HDC methods. The accuracy assessment has been performed in the ERDAS Imagine software applying accuracy assessment tool with reference to the collected GPS samples and extracted spectral signature from the Quickbird (true color composite) images. Several quality check points highlighted the spectral signatures of the different glacier classes already shown in Fig. (5.15).

The accuracy assessment has been done for each individual image combination during each temporal year (2009-2014) and compared with the hybrid classified maps. It shows good agreement in the classified maps. The overall accuracy has been ranged from 74.25% to 92.65%.



TH-1643_136104018

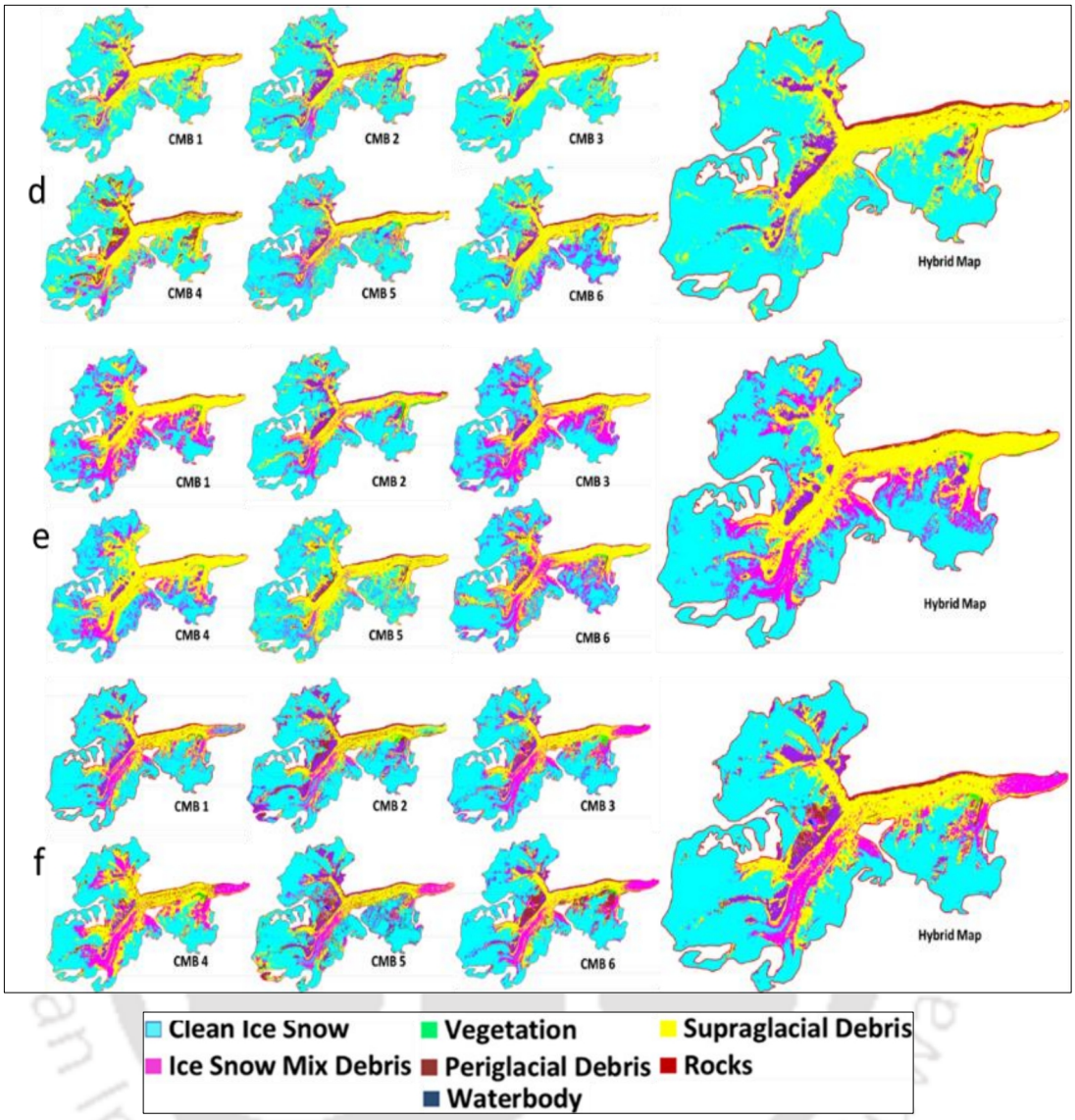


Fig. 5.16: Maps (2009-2014) showing classified maps as per the integrated combinations of optical, thermal infrared, transformed bands and new band ratio images from Landsat and LISS 3 sensors applying MLC and three dimensional hybrid classification approaches: (a) 2009, (b) 2010, (c) 2011, (d) 2012, (e) 2013 and (f) 2014.

The higher accuracy level has been recorded for the hybrid classified maps and the maximum accuracy has been obtained for the hybrid classified map for the year 2009 recorded as 92.65%, which is comparatively better than previous studies. To compare the classification accuracy for all the combinations for a respective year and year to year variation for a given combination, average accuracies have been calculated (Table 5.5).

TH-1643_136104018

Table 5.9: Overall accuracy of the classified maps.

Maps	Methods	Overall accuracy (%)						
		2009	2010	2011	2012	2013	2014	Average
CMB 1	MLC	84.56	84.12	85.62	85.64	79.85	80.15	83.32
CMB 2	MLC	85.63	86.63	86.54	83.39	80.21	74.25	82.78
CMB 3	MLC	80.95	79.56	84.33	84.75	75.35	85.65	81.77
CMB 4	MLC	88.21	86.58	81.26	82.56	76.23	86.65	83.58
CMB 5	MLC	89.23	87.63	88.21	78.54	80.29	80.12	84.00
CMB 6	MLC	79.21	83.33	79.85	84.23	89.33	82.62	83.10
Hybrid	MLC + Hybrid	92.65	90.14	89.21	90.23	87.21	88.98	89.74
Average		85.49	85.78	85.43	85.00	84.19	81.21	82.63

The majority of the combinations have obtained more than 85% accuracy and these values are above the acceptable value of 85% as suggested in the USGS classification scheme (Tiwari et al., 2015). It is also observed that the overall accuracy has been significantly varied from combination (CMB) 1 to CMB 6. As observed in Table 5.9, among all, three band combinations (CMB 1, CMB 4 and CMB 5 as referred to Table 5.9) have secured maximum accuracy level. The combination detail has been provided in Table 5.9, which shows that the transformed bands and thermal and optical band integration could be effectively used to distinguish the glacial properties.

5.4.2 Characterization of SGD, PGD and other glacier classes

Over the Zemu glacier boundary, the elevation varies from the 4129 meters to 6289 meters, while the slopes vary from 1° to 67° (Fig. 5.18). The elevation map of the Zemu glacier clearly shows that the extreme high elevation portion of the catchment is mostly covered by the clean ice snow, while the moderate and lowest elevation portion are mostly covered by the ice snow mix debris and SGD classes (Fig. 5.18). The high degree slopes have been recorded for the clean ice snow covered areas (highlighted in two digits), while low degree slopes recorded for the SGD (1° to 15°) except few portions as already seen in Fig. (5.18). These variations in the slopes were helpful to identify the accurate area and extent of the SGD during semi-automatic delineation of the SGD and other glacier classes.

TH-1643_136104018

Table 5.10: The area (hectare) statistics of different band combinations based classified maps during 2009 to 2014.

Classes	CMBs	2009	2010	2011	2012	2013	2014
Clean Ice/Snow	CMB 1	7435.22	5408.62	7593.19	8270.03	8203.84	5984.51
	CMB 2	6447.69	6667.22	8051.13	7666.42	8305.31	8197.60
	CMB 3	6163.02	6293.61	8642.83	7785.72	9496.57	6977.72
	CMB 4	5200.22	5177.45	7346.14	6420.76	6810.97	6372.79
	CMB 5	5250.15	6889.81	6396.80	7549.03	8614.01	7843.76
	CMB 6	6348.49	6716.11	7735.93	7826.78	7930.93	6801.26
	Hybrid	6584.42	6844.52	8388.65	8157.01	9027.02	7570.53
Ice/Snow Debris	CMB 1	610.45	3447.79	2404.55	1286.19	417.44	3476.36
	CMB 2	2395.15	1968.23	2652.93	1117.03	692.19	1363.48
	CMB 3	3816.49	2661.61	2173.99	2014.51	37.64	3417.01
	CMB 4	3716.57	3390.34	1656.09	2433.28	1061.50	2221.38
	CMB 5	3680.72	1745.64	2040.63	1295.51	1193.44	944.01
	CMB 6	2300.26	1990.33	1628.62	1617.62	1108.78	3094.54
	Hybrid	2458.17	1895.31	2015.48	1497.40	149.00	2338.31
SGD	CMB 1	5090.11	3992.22	2444.83	2906.93	4192.45	3954.01
	CMB 2	3936.60	3649.09	1743.39	2685.38	3384.49	3029.42
	CMB 3	3001.63	3654.61	2242.82	2677.28	3230.19	2734.74
	CMB 4	3797.10	4097.65	3196.44	3984.32	4571.77	4812.97
	CMB 5	3845.49	3644.89	4228.39	2502.49	3025.33	4484.22
	CMB 6	4094.82	3968.30	3064.82	2584.98	3550.68	3429.36
	Hybrid	4200.05	3928.61	2552.60	2964.62	3701.25	3485.54
Rocks	CMB 1	85.55	700.83	372.40	220.86	282.53	110.36
	CMB 2	400.30	226.04	838.82	817.18	343.40	229.70
	CMB 3	239.81	218.34	263.14	316.33	313.25	170.73
	CMB 4	181.60	270.61	639.34	584.10	1064.50	167.90
	CMB 5	108.46	364.37	1047.63	1026.25	262.92	412.41
	CMB 6	495.32	366.41	815.92	915.44	313.38	181.55
	Hybrid	129.17	261.32	443.43	371.21	268.36	125.10
Vege.	CMB 1	102.42	25.92	20.05	27.11	17.21	34.74
	CMB 2	116.53	34.90	42.08	71.69	12.08	110.25
	CMB 3	122.04	18.09	29.66	52.02	13.28	5.09
	CMB 4	54.59	20.75	35.53	36.18	29.59	23.36
	CMB 5	36.71	40.97	24.49	154.11	73.08	22.48
	CMB 6	42.19	19.13	33.68	22.75	21.92	55.13
	Hybrid	44.51	13.55	21.33	13.79	12.87	31.91

TH-1643_136104018

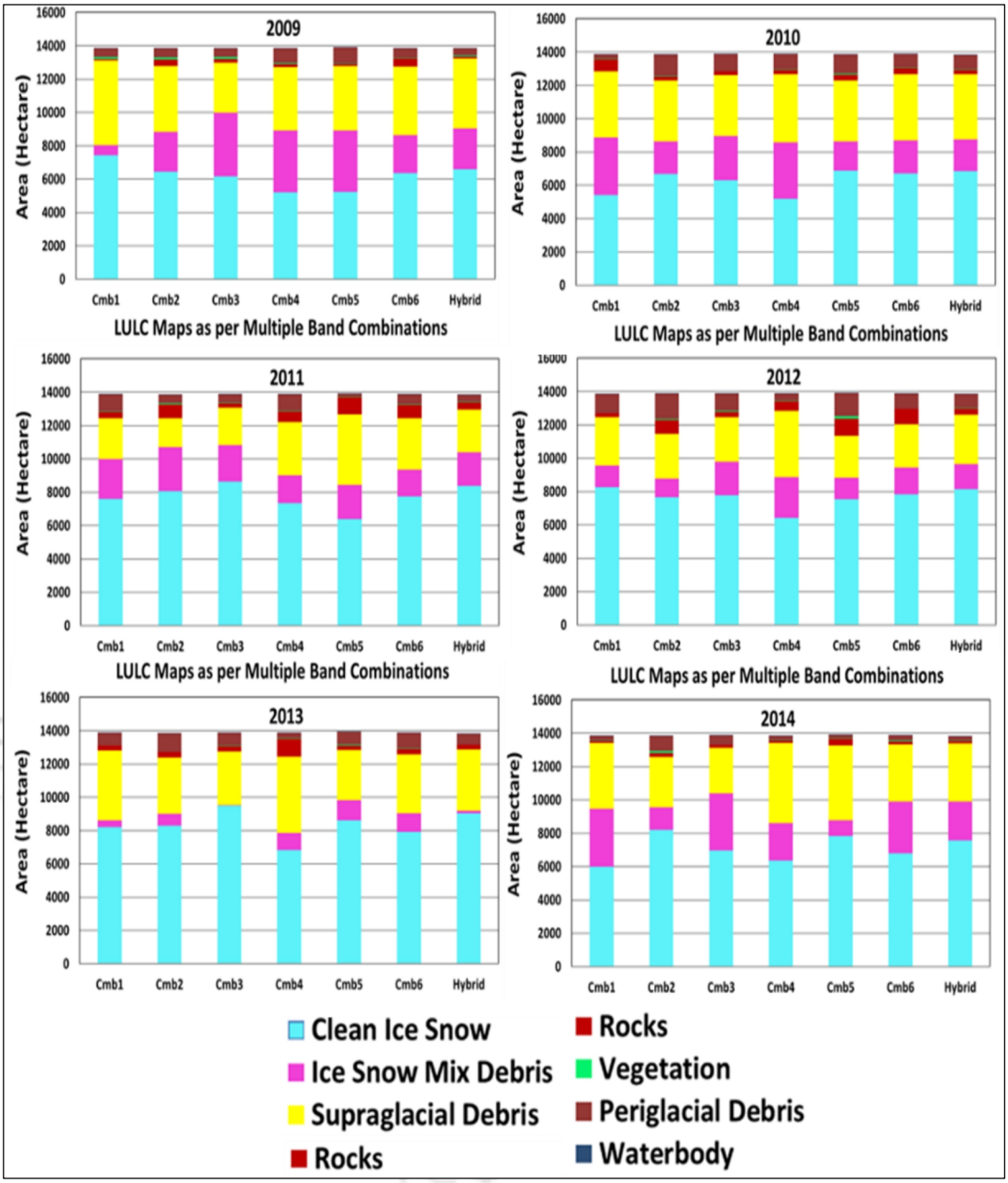
PGD	CMB 1	523.67	285.66	1030.86	1151.91	752.67	285.80
	CMB 2	554.56	1312.88	524.25	1513.55	1121.63	923.74
	CMB 3	518.47	1024.00	512.89	1019.72	778.39	558.14
	CMB 4	904.88	912.89	992.99	411.30	326.61	252.52
	CMB 5	972.31	1167.08	161.02	1388.01	760.17	198.72
	CMB 6	573.95	810.50	587.03	902.54	941.22	303.14
	Hybrid	439.09	882.92	432.36	838.53	668.70	282.94
Waterbody	CMB 1	21.13	10.85	5.38	10.58	4.07	22.07
	CMB 2	17.71	13.52	18.65	2.36	11.12	13.66
	CMB 3	7.07	1.62	5.92	8.03	0.90	4.43
	CMB 4	13.57	2.18	4.73	3.67	5.27	16.94
	CMB 5	31.93	19.13	33.54	8.13	0.81	22.19
	CMB 6	13.50	1.10	5.27	3.51	3.31	2.88
	Hybrid	12.96	1.46	3.47	4.23	1.94	5.29

Fig. (5.17a) and Table (5.10) show the area of the glacier classes (in hectares) computed from the raster based hybrid classified maps and MLC based classified maps (2009-2014). The area statistics of the glacier classes fluctuated from CMB 1 to CM6 (2009-2014). The Figs. (5.17a, 5.17b and 5.17c) and Table (5.10) show that the classes such as clean ice snow and ice snow mixed debris are maximally fluctuated, while the other classes such as SGD and PGD have shown lesser fluctuations in the area. This showed that a significant climatic variations existed over the Zemu glaciated region. Debris mixed glaciers are important for the snowmelt processes. The glacier area depletion curves also highlight the distribution of the glacier debris covers and other classes as per the elevation changes (Fig. 5.17b). Thus, to evaluate the temporal fluctuations (2009-2014) in the debris cover of the glaciers, the three main glacial classes such as clean ice snow, ice snow mix debris and SGD have taken into the consideration (Fig. 5.16c).

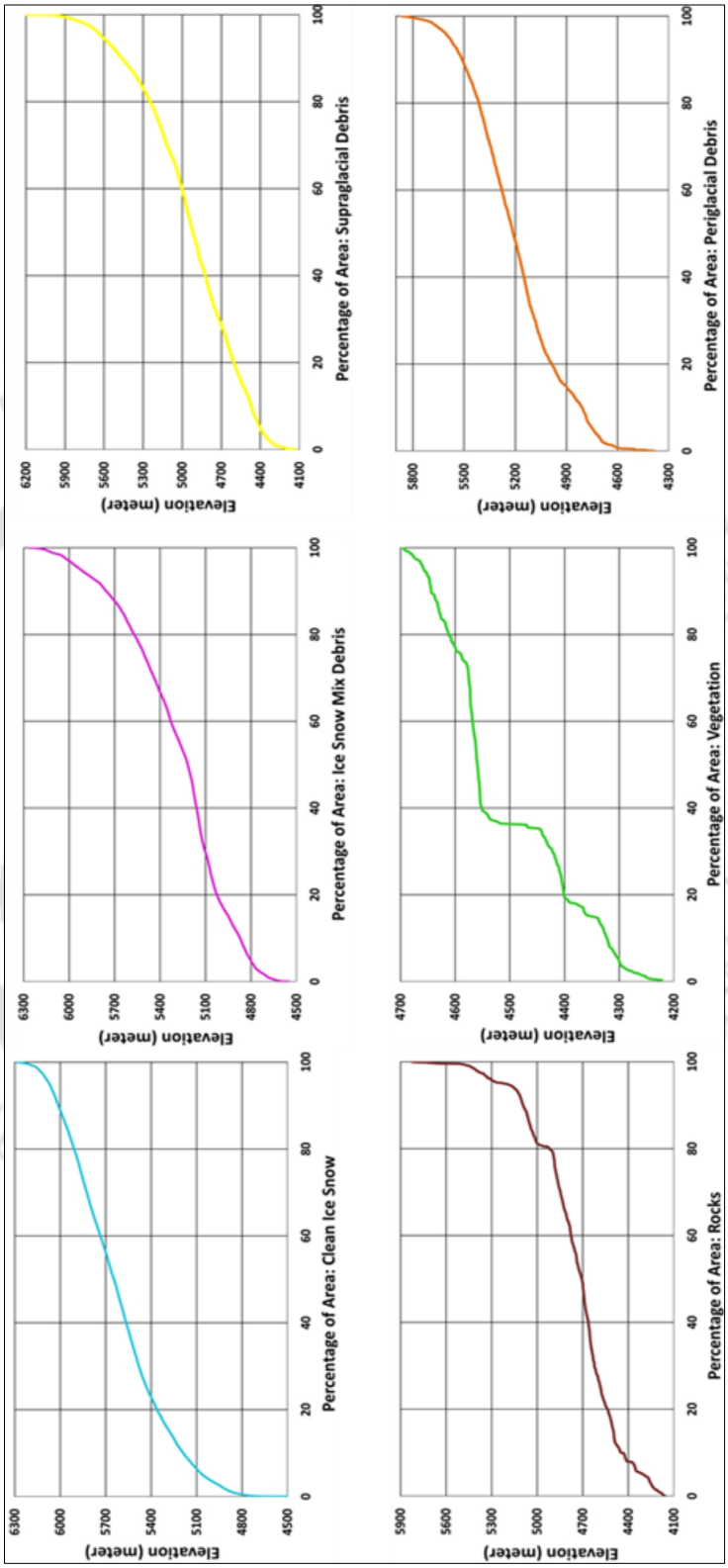
Fig. (5.17c) shows the temporal fluctuations in the clean ice snow, ice snow mix debris and SGD during 2009 to 2014. All these glacial classes area have been fluctuated enormously during the year 2009 to 2014, though, the ice snow mix debris class has fluctuated maximally. A constant trend, consistent rate of increasing and decreasing in their glacial area with elevation, was not obtained because of the short temporal duration (2009-2014). But Fig. (5.17c) shows significant fluctuations in the ice snow mixed debris covers and supra glacial debris. The PGD covers also fluctuated from 2009-2014. The temporal evaluation gave broader idea about the climate severity over the glaciated environment.

TH-1643_136104018

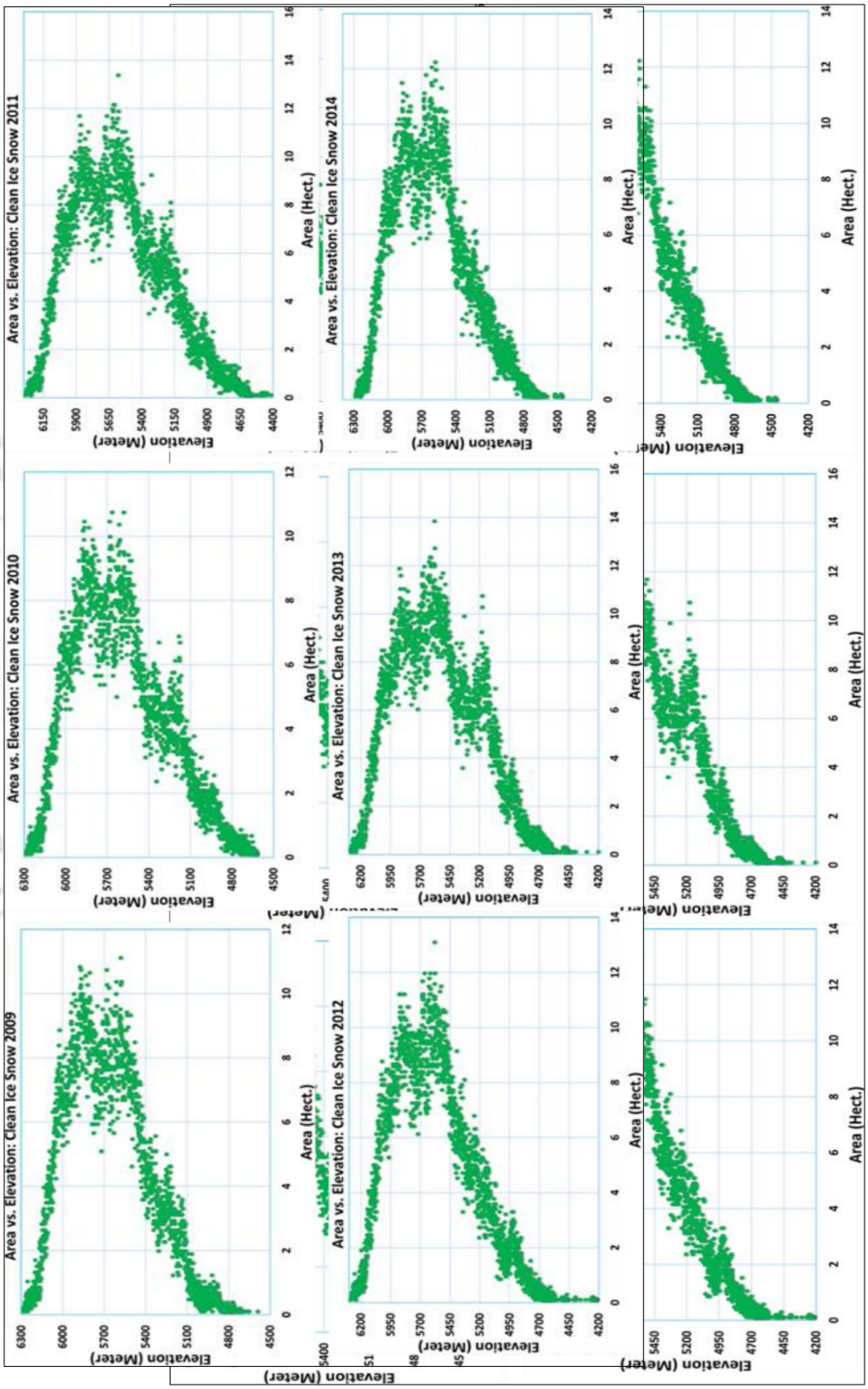
(a)



TH-1643_136104018


Elevation (meter)
Percentage of Area: Supraglacial Debris
Elevation (meter)
Percentage of Area: Periglacial Debris
Elevation (meter)
Percentage of Area: Ice Snow Mix Debris
Elevation (meter)
Percentage of Area: Vegetation
Elevation (meter)
Percentage of Area: Clean Ice Snow
Elevation (meter)
Percentage of Area: Rocks

(b)



(c)

TH-1643_136104018

TH-1643_136104018

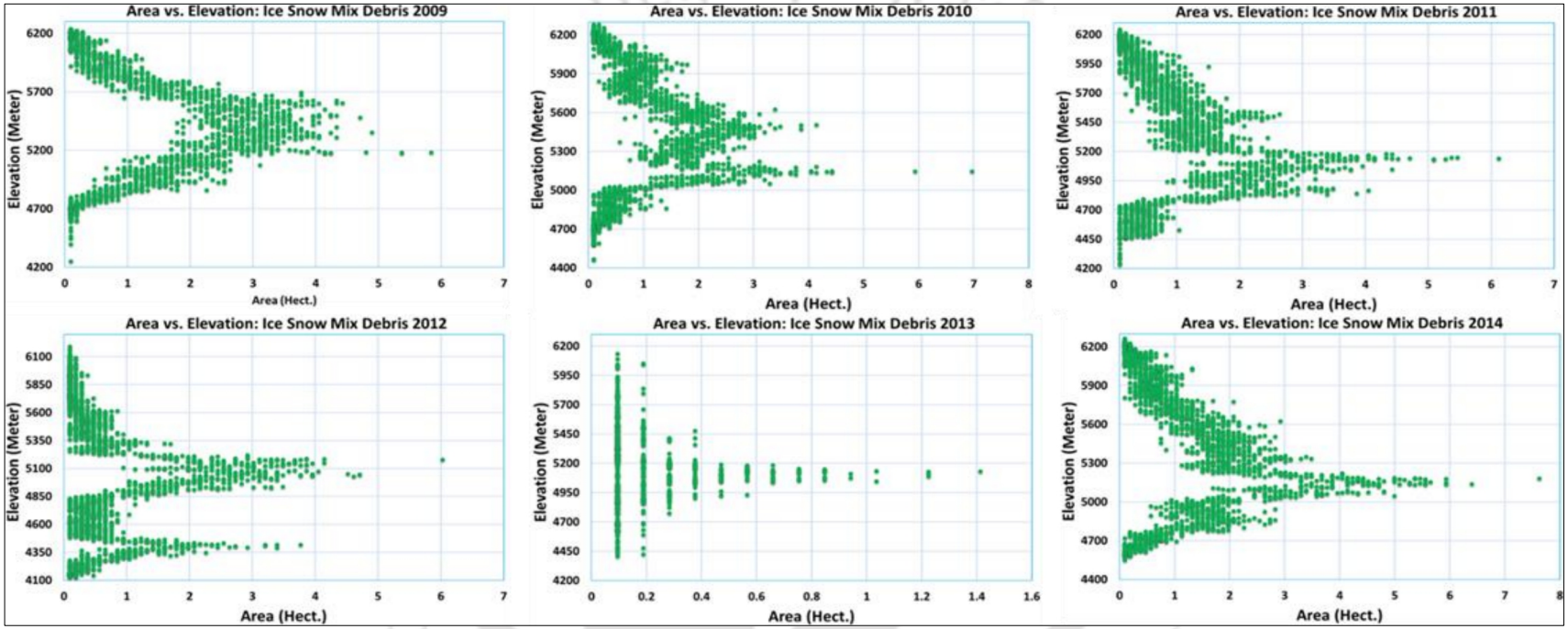


Fig. 5.17: (a) Maps showing the area statistics of glacial classes calculated as per the different classified maps during 2009 to 2014, (b) glacial classes based hypsometric curve showing the glacial classes distribution as per the elevation variation and (c) maps showing the comparative statistics of the area of glacial classes (e.g. clean ice snow, ice snow mix debris and SGD) versus elevation.

5.4.3: Delineation, comparison and change assessment of Zemu glacier

The automated delineated glacial boundary (SGD and PGD) highlights the Zemu glacial classes and displayed a nice agreement of the semi-automated delineation process (Fig. 5.18). In Fig. (5.18), we have shown the SGD and PGD boundary delineated as per the Hybrid classified map for the year 2014. The integrating approach of all the classification methods such as MLC, 3DHC etc. and step by step improvements in the glacier delineation provided a significant scope of this new innovated methodology.

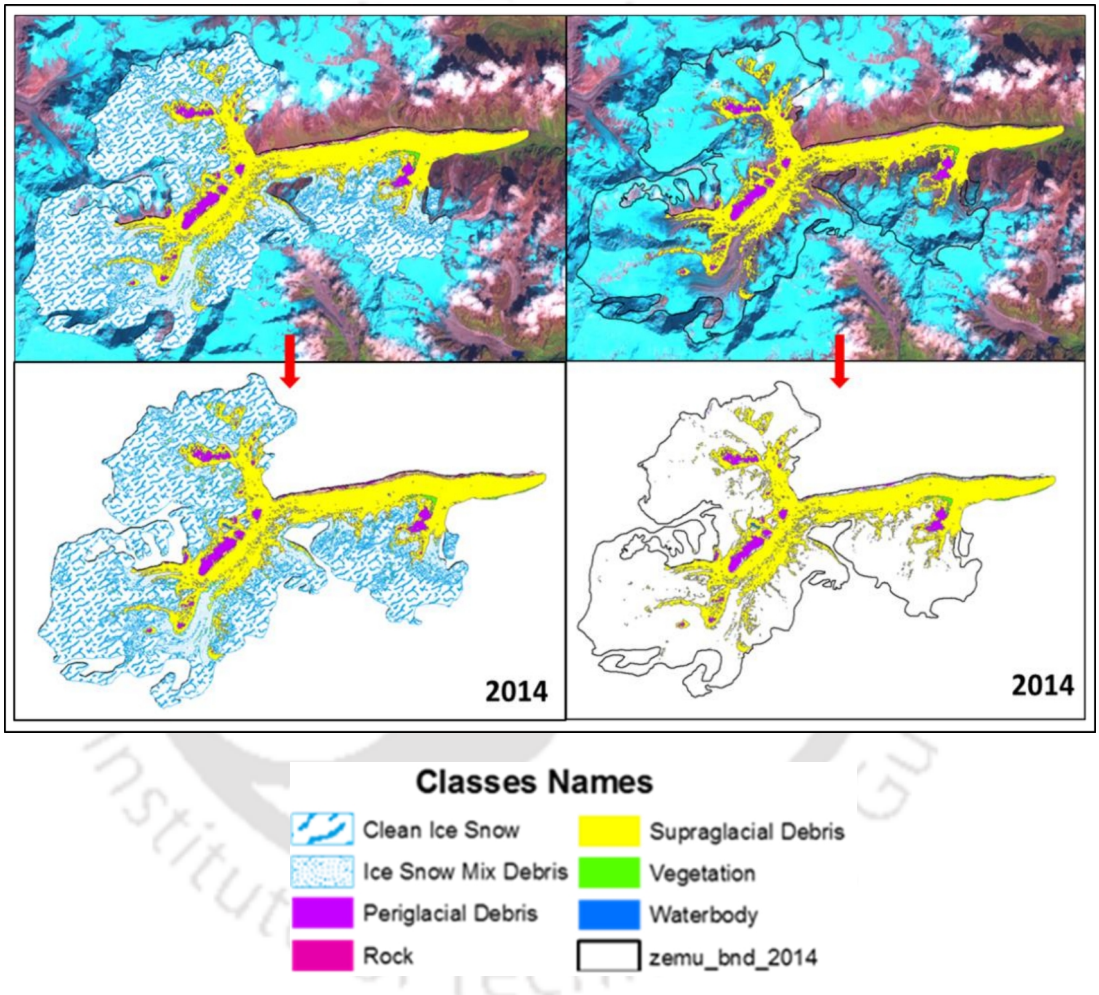


Fig. 5.18: SGD and PGD boundary and area characterization using semi-automated approach as per the hybrid classified map of the year 2014.

TH-1643_136104018

The delineation of the outer Zemu glacier boundary, as a whole, from the hybrid classified maps using semi-automated processing tasks considering slopes and elevation information matches, displayed reasonable good accuracy level when compared with the glacier boundaries extracted from the surveyed toposheet and ICIMOD WGI database (Figs. 5.19). The ICIMOD WGI database based glacier boundary is perfectly matched in the eastern and western portions of the valley glaciers (Fig. 5.18).

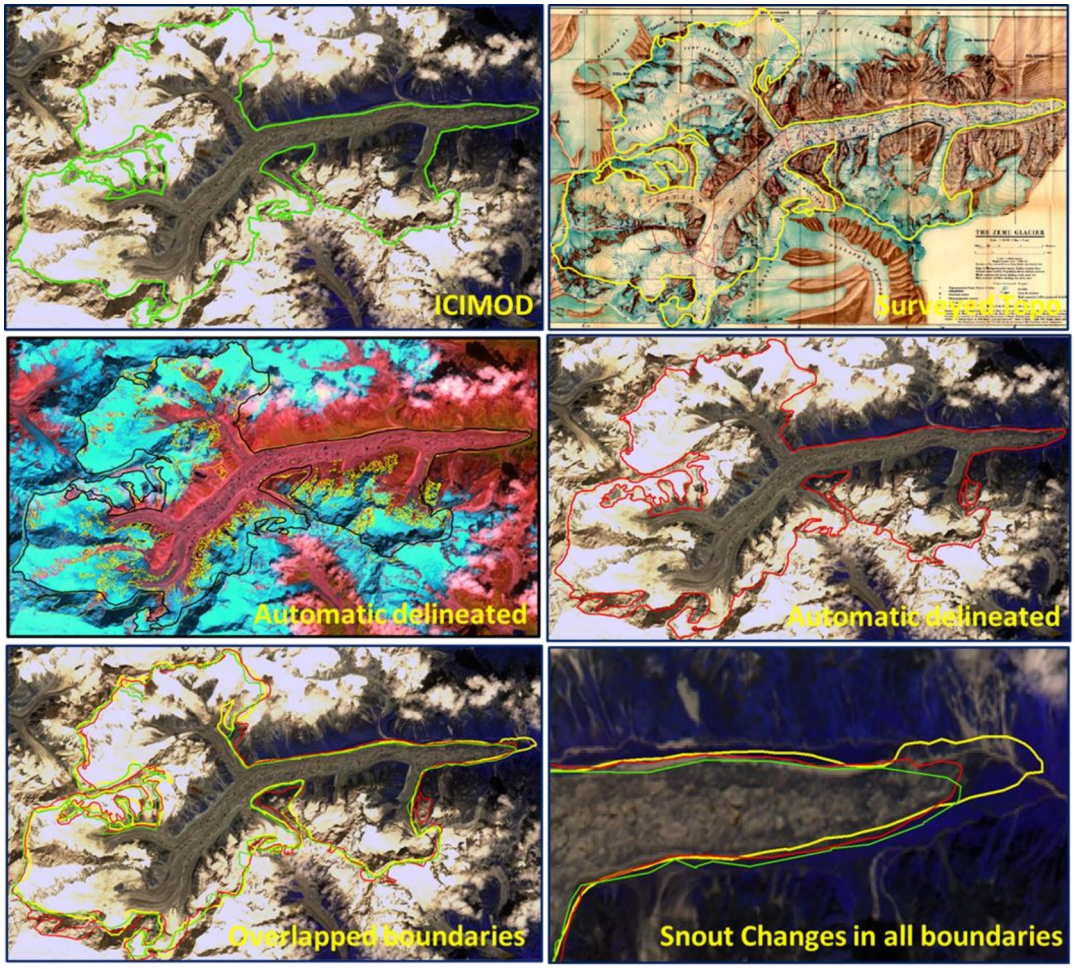


Fig. 5.19: Maps showing the semi-automated delineated boundary of the Zemu glaciers and its comparison with the surveyed toposheet and ICIMOD WGI database based glacier boundaries.

The current position of the snout in recently mapped glacier boundary (associated with SGD portion), highlighted in Fig. 5.19, clearly shows the recession of the glaciers during the last 74 years. While comparing it with ICIMOD WGI database (created in the year 2000), it also shows a slight fluctuation in the snout portion (Fig. 5.19). The recession in the glacier boundary, near to snout location, strongly supports the recession of the glaciers over Himalayas as reported by various authors (Immerzeel et al., 2013; Kulkarni et al., 2007). In the lower portion of the Zemu glacier (low elevation areas), large amount of the SGD can be

TH-1643_136104018

seen due to the less load carrying capacity of the glacier flowing in the snout direction, similar cause reported by the Tiwari et al. (2015). The different combination of the bands based satellite images (2009-2014) and Quickbird image also support that this region has strongly influenced by the SGD cover.

The automatic process of glacier boundary has given several anomalies, thus a semi-automated approach has been applied to delineate the Zemu glacier boundary and it gave satisfactory results. The surveyed toposheet (surveyed in 1935 at 1:25000 scale) and ICIMOD WGI (2000) database have helped to compare the present scenario (2009-2014), which also showed significant changes in the snout part of the glaciers. The comparisons have been done between the glacial area and elevation, in the temporal time duration (2009-2014), also give significant signatures of the climatic fluctuations over the Zemu glacier and its environment.

TH-1643_136104018

CHAPTER 6

INTEGRATED HYDROLOGICAL-HYDRODYNAMIC MODELING AND PROJECTED SCENARIOS

6.1 BRIEF FRAMEWORK

In this chapter, a hydrological modeling work has been presented. The Soil Water Assessment Tool (SWAT) model has been used to calibrate the main water balance components. SWAT Calibration and Uncertainty Program (CUP) based Sequential Uncertainty Parameter Fitting Approach (SUFI2), Generalized Likelihood Uncertainty Equation (GLUE) and Parametric Solution (ParaSol) methods applied for the model calibration, validation, parameterization sensitivity and uncertainty analysis. The watershed/water balance components such as precipitation, streamflow, snowfall, snowmelt, evapotranspiration (ET) and water yield have been computed at sub-catchment scale. For the streamflow simulation in SWAT, the Curve Number (CN) has been adjusted with the slopes. The projected scenarios for all the water balance components have been computed during 2006-2100 utilizing CMIP5 GCMs and RCP experiments. The snowmelt and snowfall contribution in the 21st century time scale is computed utilizing elevation band approach of SWAT model. The snowmelt runoff and rainfall runoff separation have been done using a mathematical improved version of Glacier Hydrological Model. The SWAT model based projected scenarios are coupled with the improved Glacier Hydrological Model (GSM-SOCONT) and then future projection (2006-2100) of snowmelt and streamflows have been calculated. In the projection scenarios, initial 2 years have been taken as the warm-up periods. Thus, the results of projected scenarios have been shown from the year 2008 to 2100.

For the hydrodynamic analysis of streamflows at the downstream of Teesta river channel, a one dimensional (1D) hydrodynamic model Mike 11 has been used. Mike 11 requires large number of physical, hydro-climatological and hydraulic parameters to setup the model. Therefore, in this research work, an integrated hydrological-hydrodynamic modeling framework has been developed. A coupling between SWAT and Mike 11 has been done to simulate and project the various hydrodynamic variables in the historical (1991-2005) and future times (2006-2008). For Mike 11 various cross sections are required to calculate the stage-discharge relationship at different points in the downstream of the Teesta river channel. Thus, a field survey has been done and various cross section are computed. Though, several cross sections are also calculated from the remote sensing based CARTOSAT DEM with 10 meter spatial resolution. The manning roughness, slopes and streamflow discharge have been

TH-1643_136104018

obtained from SWAT model. The observed datasets (1991-2005) of stream flows and precipitation are available at Chungthang and Lachung gauges and hence, utilized for the analysis. Using coupled approach between SWAT and Mike, the hydrodynamic variables such as water level, discharge and water velocity have been projected in the 21st century. The rating curve equations, based on the 21st century projected scenarios of water level and discharge, at Chungthang and Lachung gauges have also been developed.

6.2 METHOLOGY OF SWAT, GSM-SOCONT AND MIKE 11 MODELS

6.2.1 SWAT Model description and model setup

SWAT is a deterministic, lumped, semi-distributed and continuous time hydrological model, which is capable to simulate and forecast various water balance components on a daily, monthly and annual basis. SWAT is fully capable to simulating and forecasting surface water parameters, snowmelt hydrology parameters, groundwater parameters and water quality parameters at Hydrological Response Units (HRUs), sub-catchment scale and point source. The main water balance of SWAT model is given as below (Arnold et al., 2012; Arnold et al., 1998):

$$SW_{\mathrm{t}} = SW_{\mathrm{a}} + \sum_{i=1}^{n}\left(R_{\mathrm{day}} - Q_{\mathrm{sur}} - E_{\mathrm{a}} - W_{\mathrm{seep}} - Q_{\mathrm{gw}}\right) \quad \text{.....(6.1)}$$

where SW_t is the final soil water content (mmH_2O), SW_o the initial soil water content (mmH_2O), t time in days, R_{day} amount of precipitation on day i (mmH_2O), Q_{surf} the amount of surface runoff on day$i$ (mm H_2O), E_a the amount of evapotranspiration on day i (mmH_2O), W_{seep} the amount of percolation and bypass exiting the soil profile bottom on day i (mmH_2O) and Q_{gw} is the amount of return flow on day i (mmH_2O).

SWAT simulates streamflow by using Soil Conservation Services (SCS) curve number (CN) (USDA Soil Conservation Service 1972) method. In this study, a modified CN method has been used. The CN has been modified as per the calculated slopes of the selected study area. For the CNs modification, a modified CN equation, initially developed by Mishra et al. (2014) and Williams (1995), has been adopted and then SWAT derived CNs as per the respective landuse/landcover (LULC) class are adjusted. The initial CN equation is given as (Neistch et al., 2011):

$$Q_s = \frac{(R-I_a)^2}{R-I_a+S} \quad \text{..... (6.2)}$$

Where, Q_s is total surface runoff (mm), R is daily rainfall (mm), I_a is the initial abstraction such as infiltration and interception prior to runoff (mm), S is a retention parameter based on the combination of soil, LULC.

$$S = 25.4\left(\frac{1000}{CN} - 10\right) \quad \text{..... (6.3)}$$

TH-1643_136104018

Where CN is the curve number for the day. The initial abstractionsI_a, is generally approximated as 0.2S and the equation will be as:

$$Q_{surf} = \frac{(R_{day}-0.2S)^2}{(R_{day}+0.8S)} \quad \text{..... (6.4)}$$

Runoff will be occurred if $R_{day}>I_a$. The slopes are generated for each HRU and then a new modified curve number generated for each HRU as per the given equation (Mishra et al. (2014) :

$$CN2_\alpha = \frac{CN2*(322.79+15.63(\alpha)}{\alpha+323.52} \quad \text{..... (6.5)}$$

Where, $CN2_\alpha$ is the moisture condition II CN adjusted for slopeα is the fractional slope for each HRU. Here, the value of α varies from 0.14 to 1.4 (Mishra et al., 2014). The adjusted CNs and slopes are shown in Table (6.1). Likewise, CN2 stands for moisture condition II CN and CN3 stands for moisture condition III CN. In Table (6.1), the LULC classes defined as Forest (FRST), Shrubs (SHRB), Snow cover (SNOW), Glaciers (ICE) and pasture or grazing land (PAST).

Table 6.1: Adjusted CN as per the slopes at each HRU.

SBs	HRU	LULC	HRU Fraction	HRU Fractional Slopes	Slopes	CN2	CN3	Adjusted CN
1	1	FRST	0.01	0.15	14.78	65	82	69
1	2	FRST	0.01	0.08	7.53	65	82	67
1	3	FRST	0.01	0.02	2.44	65	82	63
1	4	FRST	0.07	0.5	49.59	65	82	71
1	5	FRST	0	0.16	15.51	60	79	65
1	6	FRST	0.03	0.5	50.2	60	79	66
1	7	SHRB	0.04	0.03	2.77	72	87	70
1	8	SHRB	0.06	0.08	7.59	72	87	73
1	9	SHRB	0.12	0.15	14.79	72	87	76
1	10	SHRB	0.2	0.41	40.8	72	87	77
1	11	SHRB	0.03	0.52	52.46	70	86	75
1	12	SHRB	0	0.16	15.58	70	86	74
1	13	SNOW	0.04	0.07	7.24	70	86	71
1	14	SNOW	0.03	0.03	2.84	70	86	68
1	15	SNOW	0.04	0.43	42.7	70	86	75
1	16	SNOW	0.03	0.14	14.1	70	86	74
1	17	ICES	0.01	0.08	7.59	70	86	72
1	18	ICES	0.02	0.15	15.06	70	86	74
1	19	ICES	0.11	0.44	44.13	70	86	75

TH-1643_136104018

1	20	ICES	0.02	0.42	42.49	65	82	71
1	21	ICES	0	0.16	15.87	65	82	69
1	22	PAST	0.02	0.07	7.48	70	86	72
1	23	PAST	0.03	0.15	14.57	70	86	74
1	24	PAST	0.04	0.36	36.01	70	86	75
1	25	PAST	0.02	0.03	2.77	70	86	68
2	1	FRST	0.25	0.56	56.2	65	82	71
2	2	FRST	0.02	0.08	7.61	65	82	67
2	3	FRST	0.04	0.15	15.01	65	82	69
2	4	FRST	0.01	0.15	15.45	60	79	65
2	5	FRST	0.07	0.64	64.34	60	79	66
2	6	SHRB	0.24	0.54	54.3	72	87	77
2	7	SHRB	0.04	0.15	15.1	72	87	76
2	8	SHRB	0	0.16	15.62	70	86	74
2	9	SHRB	0.05	0.6	59.58	70	86	75
2	10	SNOW	0.01	0.15	15.42	70	86	74
2	11	SNOW	0.06	0.55	55.33	70	86	75
2	12	SNOW	0	0.15	15.29	65	82	69
2	13	SNOW	0.02	0.57	57.3	65	82	71
2	14	ICES	0.13	0.52	51.96	70	86	75
2	15	ICES	0.02	0.15	15.5	70	86	74
2	16	ICES	0	0.16	15.61	65	82	69
2	17	ICES	0.05	0.55	54.94	65	82	71
3	1	FRST	0.01	0.4	2.35	65	82	71
3	2	FRST	0.16	0.4	53.06	65	82	71
3	3	FRST	0.03	0.4	15.16	65	82	71
3	4	FRST	0.01	0.4	7.54	65	82	71
3	5	FRST	0	0.4	2.71	60	79	66
3	6	FRST	0	0.4	7.36	60	79	66
3	7	FRST	0	0.4	14.75	60	79	66
3	8	FRST	0.03	0.4	57.71	60	79	66
3	9	FRSE	0.09	0.4	49.35	55	74	61
3	10	FRSE	0.01	0.4	7.54	55	74	61
3	11	FRSE	0.02	0.4	15.29	55	74	61
3	12	FRSE	0	0.4	14.88	50	70	57
3	13	FRSE	0	0.4	7.46	50	70	57
3	14	FRSE	0	0.4	3.04	50	70	57
3	15	FRSE	0.01	0.4	51.2	50	70	57

TH-1643_136104018

3	16	SHRB	0.23	0.4	53.21	72	87	77
3	17	SHRB	0.05	0.4	15.16	72	87	77
3	18	SHRB	0.02	0.4	7.67	72	87	77
3	19	SHRB	0	0.4	7.58	70	86	75
3	20	SHRB	0.01	0.4	15.09	70	86	75
3	21	SHRB	0.03	0.4	52.59	70	86	75
3	22	SNOW	0.01	0.08	7.58	70	86	72
3	23	SNOW	0.05	0.49	48.68	70	86	75
3	24	SNOW	0.02	0.15	14.9	70	86	74
3	25	SNOW	0	0.15	14.95	65	82	69
3	26	SNOW	0	0.08	7.71	65	82	67
3	27	SNOW	0.01	0.48	47.51	65	82	71
3	28	ICES	0.15	0.49	49.25	70	86	75
3	29	ICES	0.03	0.15	15.32	70	86	74
3	30	ICES	0.01	0.15	15.39	65	82	69
3	31	ICES	0.03	0.48	48.03	65	82	71
4	1	FRST	0.02	0.15	15.33	65	82	69
4	2	FRST	0.27	0.63	63.42	65	82	71
4	3	FRST	0.07	0.7	70.03	60	79	66
4	4	SHRB	0.21	0.59	59.48	72	87	77
4	5	SHRB	0.03	0.15	15.07	72	87	76
4	6	SHRB	0.05	0.6	60.37	70	86	75
4	7	SHRB	0	0.15	15.44	70	86	74
4	8	SNOW	0.01	0.08	7.87	70	86	72
4	9	SNOW	0.02	0.15	14.88	70	86	74
4	10	SNOW	0.06	0.51	51.15	70	86	75
4	11	SNOW	0.01	0.5	49.99	65	82	71
4	12	SNOW	0	0.15	15.45	65	82	69
4	13	ICES	0.03	0.15	15.21	70	86	74
4	14	ICES	0.18	0.52	52.42	70	86	75
4	15	ICES	0.04	0.51	51	65	82	71
4	16	ICES	0.01	0.15	15.36	65	82	69
5	1	FRST	0.05	0.68	68.46	60	79	66
5	2	FRST	0.01	0.15	15.37	65	82	69
5	3	FRST	0.11	0.56	55.95	65	82	71
5	4	FRST	0.01	0.15	15.35	60	79	65
5	5	FRST	0.09	0.62	62.33	60	79	66
5	6	SHRB	0.02	0.7	69.57	70	86	75
5	7	SHRB	0.08	0.54	54.39	72	87	77

TH-1643_136104018

5	8	SHRB	0.01	0.15	15.21	72	87	76
5	9	SHRB	0.01	0.15	15.14	70	86	74
5	10	SHRB	0.13	0.61	61.3	70	86	75
5	11	SNOW	0.01	0.08	7.67	70	86	72
5	12	SNOW	0.01	0.15	14.84	70	86	74
5	13	SNOW	0.03	0.42	42.25	70	86	75
5	14	SNOW	0	0.03	3.31	70	86	69
5	15	SNOW	0.07	0.49	48.89	65	82	71
5	16	SNOW	0.01	0.08	7.73	65	82	67
5	17	SNOW	0.02	0.15	14.88	65	82	69
5	18	ICES	0.01	0.15	15.35	70	86	74
5	19	ICES	0.07	0.47	46.98	70	86	75
5	20	ICES	0.2	0.5	50.38	65	82	71
5	21	ICES	0.03	0.15	15.25	65	82	69
6	1	FRST	0.14	0.4	64.01	60	79	66
6	2	FRST	0.01	0.4	15.37	60	79	66
6	3	FRST	0.02	0.4	15.45	65	82	71
6	4	FRST	0.23	0.4	63.27	65	82	71
6	5	SHRB	0.01	0.4	15.38	70	86	75
6	6	SHRB	0.07	0.4	54.49	70	86	75
6	7	SHRB	0.01	0.4	15.39	72	87	77
6	8	SHRB	0.14	0.4	61.73	72	87	77
6	9	SHRB	0.01	0.4	71.72	70	86	75
6	10	SNOW	0	0.08	7.65	65	82	67
6	11	SNOW	0.01	0.43	42.95	65	82	71
6	12	SNOW	0	0.15	15.2	65	82	69
6	13	SNOW	0.02	0.15	14.99	70	86	74
6	14	SNOW	0.01	0.08	7.79	70	86	72
6	15	SNOW	0.05	0.46	45.82	70	86	75
6	16	SNOW	0	0.15	15.07	65	82	69
6	17	SNOW	0.02	0.51	51.01	65	82	71
6	18	ICES	0.01	0.15	15.47	65	82	69
6	19	ICES	0.06	0.48	48.32	65	82	71
6	20	ICES	0.15	0.52	51.76	70	86	75
6	21	ICES	0.02	0.15	15.43	70	86	74
6	22	ICES	0.02	0.62	62.45	65	82	71
6	23	ICES	0	0.16	15.75	65	82	69
7	1	FRST	0.03	0.4	15.5	65	82	71
7	2	FRST	0.48	0.4	64.75	65	82	71

TH-1643_136104018

7	3	FRST	0.22	0.4	63.79	60	79	66
7	4	FRST	0.02	0.4	15.5	60	79	66
7	5	SHRB	0.01	0.4	67.75	70	86	75
7	6	SHRB	0.01	0.4	15.52	72	87	77
7	7	SHRB	0.1	0.4	62.36	72	87	77
7	8	SHRB	0.02	0.4	62.71	70	86	75
7	9	SHRB	0	0.4	15.35	70	86	75
7	10	ICES	0.01	0.53	53.36	65	82	71
7	11	ICES	0	0.15	15.38	65	82	69
7	12	ICES	0.01	0.15	15.5	70	86	74
7	13	ICES	0.08	0.54	53.65	70	86	75
7	14	ICES	0.01	0.54	53.53	65	82	71
7	15	ICES	0	0.16	15.67	65	82	69

6.2.2 Rationale behind the sub-watershed delineation and model simulation setup

SWAT model requires large number of physical and daily hydro-meteorological data sets along with number of parameters coefficient. The weather generator parameters such as daily precipitation, daily minimum and maximum temperature, daily humidity, daily wind speed and daily net solar radiation are necessarily required. The physical and topographical parameters such as LULC, Soil map and soil parameters and digital elevation model (DEM) are required to generate the drainage and physiographical characteristics of the selected study region. CARTOSAT DEM (30 meter spatial resolution) has used as an initial input parameter to determine the slope and drainage properties of the selected catchment. The topographic attributes of the sub-catchments such as area, slope and field slope length, were all derived from the CARTOSAT DEM. The data description has already been provided into the Chapter 3. A soil map along with 30 different soil parameters for the Indian regions is available for the download at SWAT portal and hence utilized for the study (*www.swat.tamu.edu/conferences/ international/2012/dataset/*), (FAO, 2005). Based on the above data inputs, SWAT model has been setup for the initial model simulation. The main steps are involved in the model setup viz. data preparation, sub-watershed discretization, HRU definition and overlay, writing database files, SWAT run and model simulation.

SWAT model primarily delineate the whole catchment into numbers of sub-catchments based on the area threshold (Neistch et al., 2011). The SWAT model divided the whole catchment into seven (7) numbers of sub-catchments. Each sub-catchment contains a main channel and many hydrologic response units (HRUs), which consist of homogeneous land use, soil type, and management practices. The contributions of each HRU are then aggregated for the sub-

TH-1643_136104018

catchment by a weighted average (Zhou et al., 2014). In SWAT, the main hydrological component such as runoff is then simulated for each HRU, and the contributions of each HRU are then aggregated for the sub-basin by a weighted average. Water is then routed to the outlet of the watershed. Likewise, SWAT also simulates snow accumulation and snowmelt at each HRU and the contributions of each HRU, are then aggregated for the sub-catchment. For future scenario generation, the SWAT model calculates the radiation and humidity based on the weather generator data sets. Thus, without these parameters, the effects on temperature and precipitation can be highlighted.

6.2.3 SWAT's Elevation band approach for snowfall and snowmelt calculation

In this research study, SWAT snowmelt hydrology and linked processes are performed at the sub-catchment scale (Fontaine et al., 2002). Therefore, each sub-catchment is divided into 10 elevation bands (SWAT maximum limit is 10 bands) in order to incorporate temperature and precipitation variations with respect to altitude (Neistch et al., 2011). The overall methodology can be grouped into different sections as:

(i) Temperature and precipitation lapse rate based on elevation bands:

For each sub-catchment, the lapse rates for precipitation p_{laps} (mmH_2O/km) and temperature t_{laps} (ºC/km) can be computed as (Eq…):

$$P_B = P + (Z_B - Z)\frac{p_{laps}}{days_{pcp,yr} \times 1000}$$

and

$$T_B = T + (Z_B - Z)\frac{t_{laps}}{1000} \quad \ldots\ldots\ldots\ldots\ldots\ldots\ldots\ldots \quad (6.6)$$

Where, P (mmH_2O), T (ºC) and Z (m) are the sub-watershed precipitation, temperature and recording gauge elevation, respectively; while P_B, T_B and Z_B are the adjusted precipitation, temperature and mean elevation for each elevation band. The variable $days_{pcp,\,yr}$ represents the mean annual number of days with precipitation. The temperature lapse rate can be computed using mean annual temperature. As per sub-watershed based delineation approach, temperatures can be adjusted within each elevation band by comparing the elevation band midpoint elevation (Z_B) within the station elevation (Z). The elevation difference is multiplied by the lapse rate to calculate a temperature difference between the station elevation and the elevation band. An updated elevation band mean temperature (T_B) is calculated by adding or subtracting the temperature difference to the temperature measured at the station elevation (T) as (Eq. 6.7)

$$T_B = T + (Z_B - Z)\frac{dT}{dZ} \quad \ldots\ldots\ldots\ldots\ldots\ldots\ldots\ldots \quad (6.7)$$

TH-1643_136104018

Where, $\frac{dT}{dZ}$ is the mean local lapse rate (t_{laps}) (°C/km) and can be calculate for all sub-watersheds. A lapse rate for annual precipitation can be formulated by mean annual precipitation versus station elevation. Adjusted precipitation in each elevation band (P_B) is based on the difference between the elevations of the sub basin meteorological station (Z) and each elevation band (Z_B) multiplied by the lapse rate of (mmH_2O/km) per event (P). In case, if the meteorological station is not available in the particular sub-watershed then next nearest meteorological station was considered for the lapse rate calculation. The equation can be defined as (Eq. 6.8):

$$P_B = P + (Z_B - Z)\frac{dP}{dZ} \quad \text{..... (6.8)}$$

Where, $\frac{dP}{dZ}$ is the mean local lapse rate (p_{laps}) and can be calculate for all sub-watersheds.

(ii) Snowfall/snowpack and snow water equivalent

The snowpack is represented in SWAT by means of the variable snow water equivalent (the mass of liquid water in the snowpack) *SWE* (mmH_2O), which increases with snowfall *SF* (mm H_2O) decreases with snowmelt *SM* (mmH_2O) or sublimation *ES* (mmH_2O) (Eq. 6.9):

$$SWE_{day} = SWE_{(day-1)} + SF - SM - E_s \quad \text{..... (6.9)}$$

In SWAT, snowmelt *SM* is controlled by the air and snowpack temperature, the melting rate and the areal coverage of snow. When daily mean air temperature is less than a snowfall temperature, as specified by the SWAT variable SFTMP, the precipitation within an HRU is classified as snow, and the liquid water equivalent is added to the already-present snowpack. The snowpack temperature is a function of the mean daily temperature during the preceding days and varies as a dampened function of air temperature (Anderson, 1976). The influence of the previous day's snowpack temperature on the current day's snowpack temperature is controlled by a lagging factor, (*TIMP)*, which intrinsically accounts for snowpack density, snowpack depth, exposure and other factors known to affect snowpack temperature (Eq. 6.10):

$$T_{snowpack(day)} = T_{snowpack(day-1)} \times (1 - TIMP) + T_{av}TIMP \quad \text{..... (6.10)}$$

Where, $T_{snowpack}$ (day) and $T_{snowpack\,(day\text{-}1)}$ are the snowpack temperature (^oC) on a given day and on the day preceding it, respectively, and T_{av} (^oC) is the mean air temperature for the same given day. The fraction of area covered by snow SNO_{cov} can be computed as (Eq. 6.11):

$$sno_{cov} = \frac{SNO}{SNO_{100}}\left(\frac{SNO}{SNO_{100}} + exp\left(cov_1 - cov_2\frac{SNO}{SNO_{100}}\right)\right) - 1 \quad \text{..... (6.11)}$$

TH-1643_136104018

Where *SNO* is the water content of the snow pack on a given day (mmH_2O), SNO_{100} is the threshold depth of snow at 100% coverage (mmH_2O), and cov_1 and cov_2 are coefficients that define the shape of the curve. Snow depth over an elevation band is assumed to be constant when the *SWE* exceeds SNO_{100} i.e. the areal depletion curve affects snowmelt only when the snowpack water content is between zero and SNO_{100}.

(iii) Snowmelt and glacier melt

Snowmelt rate is controlled by snowpack temperature and air temperature. A snowpack cannot begin to melt and release water before the entire pack has reached 0°C. The SWAT model does not calculate glacier melt contribution directly. It corresponds to snowmelt contribution mainly from the snowpack amount. The melt rate from a snowpack cannot be a fixed value; rather it changes in response to snowpack conditions (Fontaine et al., 2002). Glacier input data information is obtained from the Neistch et al. (2011) and Farinotti et al. (2009).

In this study, snowmelt and glacier melt are setup together into the SWAT model as a linear function of the difference between the average of the snowpack and glacier temperature ($T_{snowpack}$) and the maximum air temperature (T_{max}) on a given day and the base or threshold temperature for the snowmelt (Eq. 6.12). However, it is worth stating that due to the large number of glaciers over the Teesta river catchment, it was not possible to analyze the temporal mass balance of individual glaciers and melting rate at the HRU level. Hence, standard coefficient values are used in this study.

$$SM = b_{mlt} \times sno_{cov} \left[\frac{T_{snowpack}+T_{melt}}{2} - TMLT\right] \quad \text{(6.12)}$$

Where, b_{mlt} (mmH_2O/day-°C), is the melt factor for that day:

$$b_{mlt} = \frac{SMFMN+SMFMX}{2} + \frac{SMFMN-SMFMX}{2} sin\left(\frac{2\pi}{365}(d_n - 81)\right) \quad \text{(6.13)}$$

Eq. (6.13) has been adapted for application in the Northern Hemisphere: *SMFMN* is the melt factor for 21stJune, *SMFMX* is the melt factor for 21st December, and d_n represents the day of the year.

6.2.4 SWAT model calibration, validation, parameterization sensitivity and uncertainty analysis

The SWAT simulated results calibrated and validated in SWAT CUP packages. For the current research work, SUFI2, GLUE and ParaSol algorithms have been used for model parameterization and sensitivity analysis. The model calibration was performed using the concept of aggregate parameter selection (Yang et al., 2007). An 'aggregate parameter' is

TH-1643_136104018

defined by adding a term such as v_, a_ and r_ to the front of the original parameter to mean a replacement, an absolute increase and a relative change to the initial parameter value, respectively (Abbaspour, 2011). SWAT CUP comprises all sources of uncertainties such as model structure based uncertainty, parameter uncertainty and data input errors. Parameter uncertainty is usually caused as a result of inherent non-uniqueness of parameters (involved model calibration parameters) in inverse modeling due to wrong data inputs and parameterization. The adaptation of inverse modeling approach is a very popular method for the model calibration (Abbaspour et al., 2007).

The parameter sensitivity analysis helps to identify the significance of the particular parameter for the calibration process, whether the process is influenced by the parameter values if it changes. For this current study, a global sensitivity analysis approach has been applied. The parameter's sensitivity can be determined by the multiple regression system, which regresses Latin hypercube generated parameters against the objective function. The Latin Hypercube Sampling (LHS) method is considered as a highly efficient sampling method. It can reduce the sampling points within a certain space. In this study, the significance level P value test and statistical t-test are used to rank the high sensitive and non-sensitive parameter. If the P-values corresponded to 0 then it means that parameter is highly sensitive for the process. In global sensitivity outcomes, a t significance test (t-stat) is evaluated based on the significance level alpha ($\alpha = 0.05$) and P-values. The alpha value of 0.05 was chosen as the local significance level. Based on this significance level, values larger than 1.96 or lower than -1.96, respectively, indicate a significant ($p<0.05$) positive or negative trend. If the P values will be closer to zero, the corresponding values will be more significant for the trend (Abbaspour et al., 2011; Chamaille-Jammes, 2007). The SUFI2, GLUE and ParaSol methodology has been given in the methodology chart (Fig 6.1) and the procedures described as follows:

(i) SUFI2 algorithm:

In SUFI2, an iterative process is required for updating the old coefficient parameters into updated new coefficients during calibration to achieve the final estimates. SUFI2 accounts the parametric uncertainty through sequential and fitting processes. In SUFI2, the parametric errors can be identified in the final modeling outcomes as overestimation or underestimation (Abbaspour et al. 2011). Prior knowledge of parameter's coefficient and data quality checks are thus compulsory to minimize the uncertainty issues. SUFI2 algorithm basically assumes a large parameter uncertainty (or physically meaningful range that can be occurred due to used data inputs such as LULC, precipitation, temperature etc.) to ensure the observed data

TH-1643_136104018

fall into the 95PPU band for the first iteration and decrease the uncertainty in steps while monitoring the p-factor and r-factor for next several iterations (Abbaspour et al., 2007).

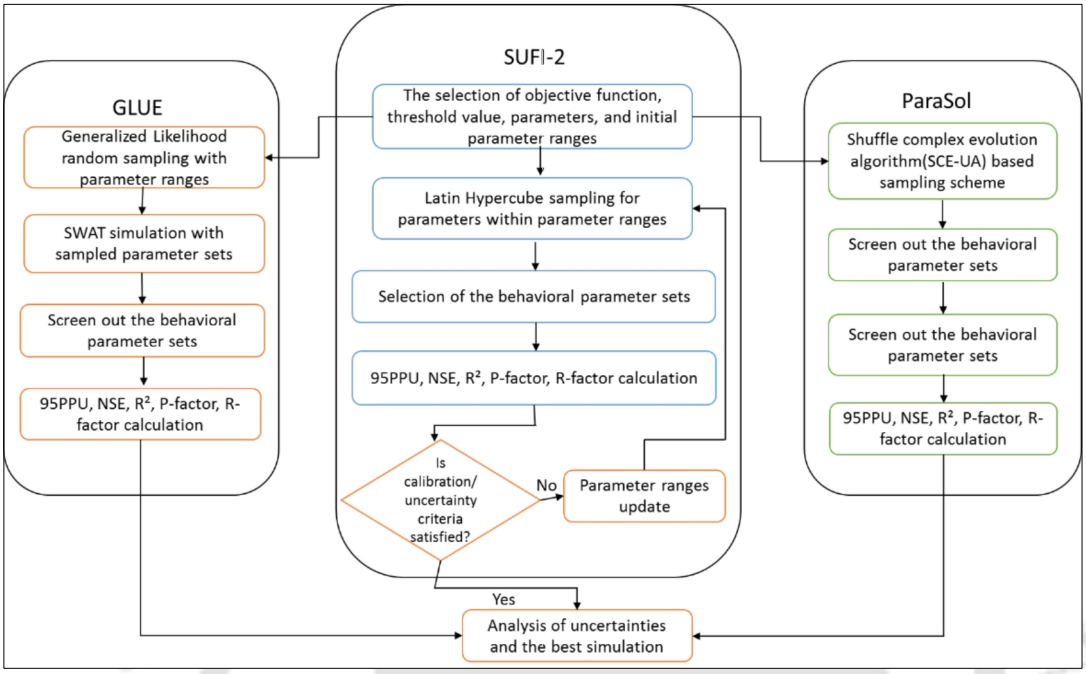


Fig. 6.1: Methodology chart of SUFI2, GLUE and ParaSol methods.

The 95PPU (95 % prediction uncertainty) can be calculated between the 2.5% and 97.5% levels of the cumulative distribution of an output variable obtained through Latin hypercube sampling, disallowing 5% of the very bad simulations (Abbaspour et al. 2011; Yang et al., 2007). The main goal of the SUFI2 approach is to minimize the overestimation or underestimation of modeling outcomes through iterative parameterization and search for bracketing most of the observed data with the smallest possible uncertainty band, which means the good results should have a relatively large p-factor with relatively small r-factor. The p-factor determines the percentage of simulated data falls into the observed dataset and the r-factor determines the uncertainty thickness in the simulated datasets when compared to observed datasets. Theoretically, the value of p-factor ranges between 0 to 100% and r-factor ranges between 0 to infinity. It means that the value of p-factor = 1 and r-factor = 0 corresponds to measured data equivalent to observed data. The degree to which away from these values can be utilized to judge the strength of the calibration. A larger P-factor can be achieved at the expense of a larger r-factor (Abbaspour et al. 2011). The mathematical expressions of SUFI2 algorithm can be defined into the following steps.

1. The first step, the objective function $g(\theta)$ and other parameter ranges $(\theta_{abs\,min}, \theta_{abs\,max})$ are defined.

TH-1643_136104018

2. Latin hypercube sampling is carried out the hypercube$[\theta_{min}, \theta_{max}]$, the corresponding objective functions are evaluated and the sensitivity matrix J and the parameter covariance matrix C are calculated according to equations (6.14 and 6.15)

$$J_{ij} = \frac{\Delta g_i}{\Delta \theta_j}, i = 1, \ldots\ldots, C_2^m, j = 1, \ldots . \mathrm{n} \ldots\ldots\ldots\ldots\ldots\ldots\ldots \quad (6.14)$$

$$\mathrm{C} = \mathrm{S_g^2}\,(\mathrm{J^T J})^{-1} \ldots\ldots\ldots\ldots\ldots\ldots\ldots\ldots\ldots\ldots\ldots\ldots\ldots\ldots \quad (6.15)$$

Where S_g^2 is the variance of the objective function values resulting from the number of model runs.

3. A 95% predictive interval of a parameter θ_j is computed as follows (Eq. 6.16):

$$\theta_{\mathrm{j,lower}} = \theta_{\mathrm{j}}^{*} - \mathrm{t_{v,0.025}}\sqrt{\mathrm{C_{jj,}}}\theta_{\mathrm{j,upper}}\theta_{\mathrm{j}}^{*} + \mathrm{t_{v,0.025}}\sqrt{\mathrm{C_{jj}}} \ldots\ldots\ldots\ldots\ldots\ldots \quad (6.16)$$

Where θ_j^* is the parameter θ_j for the best estimates (i.e. parameters which produce the optimal objective function), and v is the degrees of freedom (mn).

4. The 95PPU is calculated at the 2.5% and 97.5% levels of the cumulative distribution of an output variable obtained through Latin hypercube sampling, disallowing 5% of the very bad simulations (Eq. 6.17).

$$R - \text{ factor} = \frac{\frac{1}{\mathrm{n}}\sum_{\mathrm{t1=1}}^{\mathrm{n}}\left(\mathrm{y_{t1,97.5\%}^{M}} - \mathrm{y_{j,2.5\%}^{M}}\right)}{\sigma_{\mathrm{obs}}} \ldots\ldots\ldots\ldots\ldots\ldots\ldots\ldots\ldots\ldots\ldots\ldots\ldots \quad (6.17)$$

Where $y_{t1,97.5\%}^{M}$ and $y_{j,2.5\%}^{M}$ represents the upper and lower boundary of the 95PPU and σ_{obs} stands for the standard deviation of the measured data.

5. The goodness of fit and the degree to which the calibrated model accounts for the uncertainties are assessed by the above two measures. A uniform distribution in the parameter hypercube $[\theta_{min}, \theta_{max}]$ is interpreted as the posterior parameter distribution. Otherwise $[\theta_{min}, \theta_{max}]$ is updated according to the given formulas (Eqs. 6.18 and 6.19):

$$\theta_{\mathrm{j,min,new}} = \theta_{\mathrm{j,lower}} - \max\left(\frac{\theta_{\mathrm{j,lower}} - \theta_{\mathrm{j,min}}}{2}, \frac{\theta_{\mathrm{j,max}} - \theta_{\mathrm{j,upper}}}{2}\right) \ldots\ldots\ldots\ldots\ldots\ldots \quad (6.18)$$

$$\theta_{\mathrm{j,max,new}} = \theta_{\mathrm{j,upper}} + \max\left(\frac{\theta_{\mathrm{j,lower}} - \theta_{\mathrm{j,min}}}{2}, \frac{\theta_{\mathrm{j,max}} - \theta_{\mathrm{j,upper}}}{2}\right) \ldots\ldots\ldots\ldots\ldots\ldots \quad (6.19)$$

6. Finally the model is required number of iterations to be done for initialization of the best parameter ranges for processing the data.

(ii) GLUE method:

TH-1643_136104018

The GLUE method is initially produced by Beven and Binley (1992) to allow to find out the equifinality of model parameters in over-parameterized models. GLUE method adopts 'goodness of fit' criteria if there is no unique set of parameters. GLUE estimates the weights or probabilities that can be associated with multiple parameter sets, centered on the use of a likelihood measure to derive a posterior probability function. This is further used to derive the predictive probability of the output variables. A GLUE procedure can be grouped into three steps as given below:

1. The "generalized likelihood measure" $L(\theta)$ involves a group of parameter sets which are randomly sampled through the prior distribution. Each parameter set will be assessed as either "behavioral" or "non-behavioral" through a comparison of the "likelihood measure" as per the defined threshold value.

2. A "likelihood weight" can be determined from the behavioral parameters. The equation can be written as:

$$w_i = \frac{L(\theta_i)}{\sum_{k=1}^{N} L(\theta_i)} \quad \text{..... (6.20)}$$

Where, N is the number of behavioral parameters sets.

3. At last, the prediction uncertainty is described as prediction quantile from the cumulative distribution realized from the weighted behavioral parameters sets. The Nash-Sutcliffe (NS) coefficient is frequently used to measure for GLUE (Abbaspour, 2011).

(iii) ParaSol method:

In this method, a global optimization criteria can be optimized using objective functions. In this procedure, an uncertainty analysis can be performed under the choice of two statistical methods. ParaSol adopts Shuffle Complex (SCE-UA) algorithm, which minimize a function for up to 16 variables (Duan et al., 1992). SCE-UA algorithm used widely for watershed model calibration. This algorithm has been also used for various hydrological application such as subsurface hydrology, soil erosion, remote sensing and land surface modeling (Abbaspour, 2011). The two major steps of ParaSol method are given below:

1. In this method, the simulated outcomes are divided into "good" simulations and "not good simulations" by a threshold value. The threshold value can be defined by Bayesian statistics using probability density region for the model results.

2. The prediction uncertainty constructed equally from the good simulations.

6.2.5 Objective functions

TH-1643_136104018

The coefficient of determination (R^2) and Nash-Sutcliffe Equation *NSE* (Nash-Sutcliffe, 1970) have been used for the model optimization objective functions (Abbaspour, 2011). The equations are given below:

$$\text{Maximize} \quad R^2 = \frac{[\sum_i (Q_{m,i} - \bar{Q}_m)(Q_{s,i} - \bar{Q}_s)]^2}{\sum_i (Q_{m,i} - \bar{Q}_m)^2 \sum_i (Q_{s,i} - \bar{Q}_s)^2} \ldots\ldots\ldots\ldots\ldots\ldots\ldots\ldots (6.21)$$

Q is a variable (e.g. discharge), m and s stand for measured and simulated, respectively. i is the i^{th} measured or simulated data.

$$\text{Maximize} \quad NSE = 1 - \frac{\sum_i (Q_m - Q_s) i^2}{\sum_i (Q_{m,i} - \bar{Q}_m)^2} \ldots\ldots\ldots\ldots\ldots\ldots\ldots\ldots\ldots\ldots (6.22)$$

Where, Q is a variable (e.g. discharge), m and s stand for measured and simulated, respectively and bar stands for average.

6.3 SNOW WATER EQUIVALENT RECONSTRUCTION APPROACH

Snow water equivalent (SWE) reconstruction method can be used to calculate the amount of snow that existed in the particular point or area by back-calculating the melt snow amount which occurred prior to the complete removal of snow. The contamination of clouds can disrupts the accurate measurement of snow water equivalent, thus, a cloud free MODIS snow cover product has been taken into account. In this study, MOD09A1 based 8 daily extracted snow cover has been used to reconstruct snow water equivalent over the selected study region. Applications of snow covered area (SCA) and snow depletion curves (SDC) can be used to predict the snowmelt at a particular point or area in the temporal time, especially in the absence of ground based measurement techniques (Moloch and Margulis, 2008).

The meteorological data used in the study such as relative humidity, wind speed and net radiation were obtained from the SWAT model portal (*http://globalweather.tamu.edu/*). The daily average temperature is calculated from the IMD gridded observed datasets opted from IMD and IITM, Pune, India. In the selected study region of north Sikkim eastern Himalayas, no snow gauge site is available. Thus, field measurement based snow water equivalent has been calculated at several point locations over the study area. The snowmelt factor over the Himalayan terrain is opted from the analysis done by Singh and Kumar (1997). In the Himalayas, the snowmelt factor ($cm°C^{-1}day^{-1}$) varies from 0.4 to 0.75 (Singh et al., 2000; Singh and Kumar, 1997). The mathematic equations and steps to construct snow water equivalent are given as below (Moloch and Bales, 2006):

$$SWE_n = SWE_0 - \sum_{j=1}^{n} M_j \ldots\ldots\ldots\ldots\ldots\ldots\ldots\ldots (6.23)$$

TH-1643_136104018

Where, M_j = snowmelt for time step j, SWE_n = pixel-specific SWE at time n, and SWE_0 is the initial SWE. Here is noticeable that during melting season, the accumulated precipitation as snowfall does not consider for the evaluation. The above equation can be re-arranged as Eq. (6.24) to estimate SWE (Moloch and Margulis, 2008).

$$\text{When } SWE_n = 0, SWE_0 - \sum_{j=1}^{n} M_j \quad \ldots\ldots\ldots\ldots\ldots\ldots \quad (6.24)$$

In this, the model is run forward beginning on each 8 daily/monthly time step from 1st April to 15th March during 2001-2005. Here, SWE_0 is the SWE at the beginning (Maximum Snow) time step. The SWE_0 estimation calculated for each 8 day/monthly throughout the snowmelt season. The monthly SWE calculated based on the monthly scenarios, which average from 8 daily MODIS snow covers. The 8 daily basis SWE is performed for the year 2005 and then monthly mean results have been shown and compared with SWAT simulated monthly means snowmelts. The annual prediction of SWE has been done from the year 2001 to 2005 by taking monthly average of 8 daily MODIS (MOD09A1) derived snow covers.

As per the above Eq. (6.24), the time step at which SWE_n is equal to zero can be estimated using MODIS derived snow covers. Here, $SWE_n = 0$ and $SCA_n = 0$. This method has advantage in reconstructing daily estimates of SWE but in this study, a monthly and annual basis SWE is reconstructed.

In this method, monthly and yearly estimates of SCA are calculated from 8 daily MODIS SCA from 2000-2005, which is a cloud free product. The monthly and annual SCA were utilized to calculate the melt flux as:

$$M_j = Mp_j * SCA_j \quad \ldots\ldots\ldots\ldots\ldots\ldots\ldots\ldots\ldots\ldots \quad (6.25)$$

Where, Mp_j is the potential snowmelt, calculated assuming continuous snow cover over each pixel at each time step (monthly/yearly)

$$Mp_j = T_{dj} * a_r + R_{nj} * M_q \quad \ldots\ldots\ldots\ldots\ldots\ldots \quad (6.26)$$

Where, T_d is degree-days (the average 8 daily air temperature above 0°C), a_r = degree-day coefficient for melt factor ($cm°C^{-1}day^{-1}$), R_n is average 8 daily net radiation above 0 Wm^{-2} and M_q is energy to water depth conversation, taken as 0.026 $cmW^{-1}m^2day^{-1}$ (Moloch and Margulis, 2008). The a_r is a calibration parameter, which has been adopted in the range 0.4 to 0.75 (Singh and Kumar, 1997). The potential melt flux will be depend on various model forcing, which may vary as per the spatial resolution. Based on the MODIS derived snow covers, SDCs are derived in order to obtain 8 daily and monthly estimates of SCA used as (Neistch et al., 2011):

TH-1643_136104018

$$SCA_j = SCA_i - \left[\frac{(SCA_i - SCA_k)}{(\sum_{i=1}^{n} Mp_i - \sum_{k=1}^{n} Mp_k)}\right] \times \left[\left(\sum_{i=1}^{n} Mp_i - \sum_{j=1}^{n} Mp_j\right)\right] \ldots\ldots\ldots\ldots (6.27)$$

Where, SCA_j = SCA at time step j, SCA_i and SCA_k are MODIS (MOD09A1) derived observed SCA values prior to and after j, respectively. $\sum_{i=1}^{n} Mp_i$ and $\sum_{k=1}^{n} Mp_k$ are the cumulative potential snowmelt values corresponding to the satellite acquisition time steps i and k, respectively. The above equation shows a SDC during each period between observations based on the fraction of total cumulative potential melt for the particular time step. It is important to highlight that this method does not account snowfall inputs after the onset of the snowmelt season. Thus, mass input to the snowfall (snowpack) is insignificant after maximum accumulation.

6.4 IMPROVEMENTS IN GLACIO-HYDROLOGICAL MODEL FOR SNOWMELT RUNOFF ESTIMATION

A lumped conceptual glacio-hydrological model (GSM-SOCONT: Glacier and Snowmelt – Soil Contribution Model), initially developed by Schaefli et al. (2005) based on alpine catchment conditions. In this study, this model has been taken into consideration to separate snowmelt runoff, glacier melt runoff and rainfall runoff. This model takes mainly five basic physical and hydro-meteorological parameters such as daily precipitation, daily average temperature, daily potential evapotranspiration (PET), daily stream flows, daily net solar radiation and hypsometric curves for glacier and non-glacier parts. The observed streamflow (1991-2005) at Chungthang gauge station has been used for the model evaluation. The PET

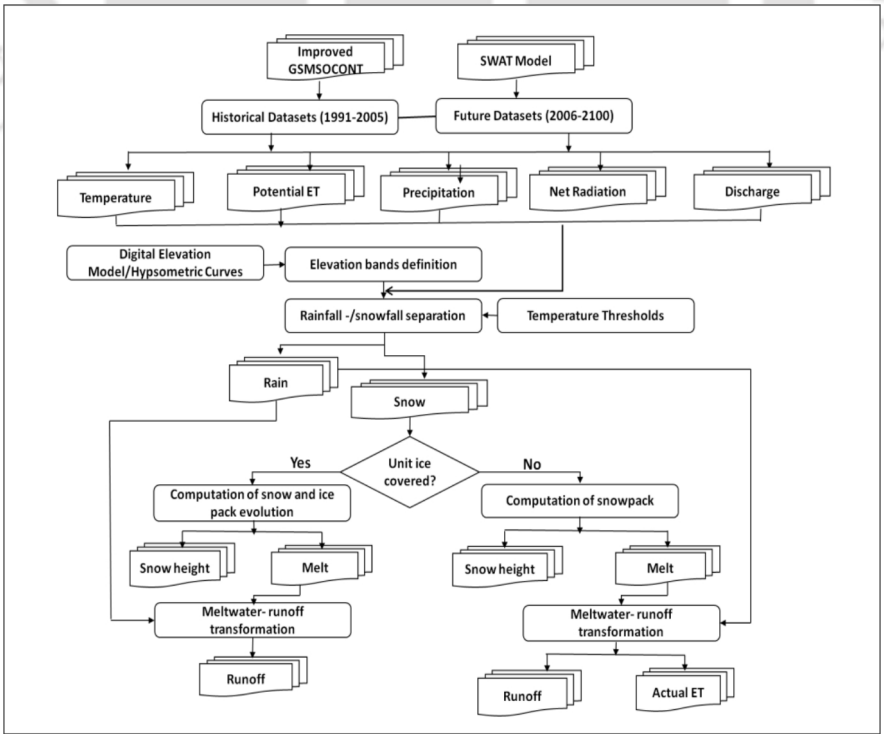


Figure 6.2: Flow chart of improved GSM-SOCONT coupled with SWAT.

TH-1643_136104018

and hypsometric curves are computed from the SWAT model.

The future projection (2006-2100) of streamflow and snowmelt are also evaluated from this model. Thus, a coupled approach has been presented to utilize the application of improved version of glacier snowmelt model over snowmelt induced Himalayan terrain catchment. The model results such as streamflow and snowmelt are evaluated at Chungthang gauge station (main outlet of the selected study region). The coupled approach diagram has been shown in Fig (6.2).

To make this model for Himalayan terrain conditions, several modifications and improvement are made in the model equations. As per the detailed literature review, it is resulted that the net solar radiation, and variable precipitation lapse rate (PLR) and temperature lapse rate (TLR) are additionally required for the accurate estimation of the snowmelt runoff, especially over Himalayan terrain conditions and for the present study area.

The model works based on the two level of discretization: (i) the separation between the permanent snow cover/ice-cover (glacier part) and (ii) non-glacier part. The glacier part and non-glacier part is mapped from IRS LISS3 satellite dataset. Based on the ratio of glacier part (around 21% for this catchment) and non-glacier part (79%), hypsometric curves and elevation bands have been defined. The glacier part of the catchment is supposed to be constant throughout the simulation periods (for few years). Then, the precipitation and temperature time series are interpolated for each elevation band according to its mean elevation. The interpolation is based on an altitude dependent regression of the observations at meteorological measurement stations located in or nearby the study catchments. For the temperature and precipitation time series, variable lapse rate is applied to the temperature series measured at the closest meteorological station. The equations and their improvements are given as:

At the whole catchment scale, the mean specific runoff Q (mm/d) at the catchment outlet can be computed as:

$$Q = \frac{1}{a_c}\sum_{i=1}^{2}\sum_{j=1}^{n_i} a_{i,j} \times Q_{i.j} \quad \ldots\ldots\ldots\ldots\ldots\ldots (6.28)$$

Where, I is an index for each of the two parts of the catchment and j an index for each of the n_i elevation bands in part i. $a_{i,j}$ (km^2) is the area of an elevation band j belongs to the catchment part I and $Q_{i.j}$(mm/d) the mean daily specific runoff the special unit, a_c (km^2) is the area of entire catchment.

(ii) Area covered by ice: The snow accumulation, snow melt and ice melt can be computed for each elevation band and then the average of all elevation band is

TH-1643_136104018

accounted at the main outlet of the selected study region (Chungthang). The aggregation rate of precipitation is determined based on a simple temperature threshold:

$P_{snow} = P_{tot}$, $P_{liq} = 0$, $T \leq T_0$

$P_{snow} = 0$, $P_{liq} = P_{tot}$, $T > T_0$

The potential snowmelt $M_{p,snow}$ (mm/d) is computed according to a degree-day approach:

$$M_{p,snow} = \begin{cases} a_{snow}\,(T - T_m) & T > T_m \\ 0 & T < T_m \end{cases}, \quad \ldots\ldots\ldots\ldots\ldots\ldots\ldots\ldots (6.29)$$

Where, P_{tot} (mm/d) is the total precipitation on a given day, P_{snow} (mm/d) is the snowfall and P_{liq} is rainfall. T (°C) is the mean daily air temperature and T_0 is defined as the temperature threshold. Here, an additional radiation component has been added to account the snow melt contribution due to net solar radiation. The improved equation is given as (Hock 1999):

$$M_{snow} = \begin{cases} \left(\frac{1}{n} MF + a_{snow}/a_{ice}\, I\right) & : \; T > 0 \\ 0 & : \; T < 0 \end{cases} \quad \ldots\ldots\ldots\ldots\ldots\ldots\ldots\ldots (6.30)$$

Where, MF is, a melt factor for the radiation, added into the above equation. The three parameters such asa_{snow}/a_{ice} is a radiation coefficient for snow and ice surface, I is potential clear-sky direct solar radiation at the ice or snow surface (Wm^{-2}) and T (°C) is air temperature. In the Himalayan terrains, the MF factor vary from 0.4 to 0.75 $cm°C^{-1}day^{-1}$. In this model, MF (for radiation) is taken as calibration parameters.

For the ice cover part (glaciers/permanent snow) of the catchment, the runoff model consists a linear reservoir approach. The general equation for the snow reservoir can be defined as follows:

$$Q_{snow}(t_{i+1}) = Q_{snow}(t_i) \times e^{-\frac{t_{i+1}-t_i}{k_{snow}}} + \left[P_{liq,snow}(t_{i+1}) + M_{snow}(t_{i+1})\right] \times \left(1 - e^{-\frac{t_{i+1}-t_i}{k_{snow}}}\right) \ldots\ldots\ldots\ldots\ldots\ldots\ldots (6.31)$$

Where, $Q_{snow}(t_i)$ (mm/d) is discharge from the snow contribution at time step t_i and $Q_{snow}(t_{i+1})$ is the discharge at the successive time step. k_{snow} (d) is the time constant of the reservoir. $P_{liq,snow}$ (mm/d) is the rainfall (liquid precipitation) falling on the snowpack. In the ice reservoir part, all the subscripts snow in the above equation will be replaced by the subscripts ice. The sum of the ice and snowmelt runoff contributed as total runoff from the ice covered part of the catchment.

TH-1643_136104018

(ii) Non-glaciated area: An equivalent rainfall P_{eq} (mm/d) with respect to the sum of the liquid precipitation and snowmelt, for every elevation band, is computed as:

$$P_{eq} = P_{liq} + M_{snow} \quad \text{.....(6.32)}$$

The equivalent rainfall-runoff transformation will lead to direct runoff and initial abstraction losses.

6.5 HYDRODYNAMIC MODEL MIKE 11 AND COUPLING WITH SWAT

Mike 11 is a one dimensional (1D) river modeling system formed by fully dynamic wave formulation of the Saint Venant equations (Soleymani and Delphi, 2012; Thompson et al., 2004). It is designed for the analysis of simple and complex river and channel systems. The fully hydrodynamic approach in Mike 11 system applies for the flood routing and reservoir operation, development of rating curves, water quality and non-cohesive sediment transport modules. In this study, Mike 11 is used for the analysis of discharge, water level, water velocities and development of rating curves in the historical and future times. These are some assumptions associated with Mike 11 as:

(i) Water is incompressible and homogenous

(ii) Flow is one-dimensional

(iii) Bottom slope of the stream is small

(iv) Manning's equation is used to describe resistance effects

(v) Flow everywhere is parallel to the bottom (e.g. wavelengths are large compared with water depths)

To setup the Mike 11, a physical and hydro-meteorological time series datasets such as stream channel network, catchment area boundary and projection parameter details, various cross sections (X-Sections) at different locations along the downstream of river channels, constant or time series discharge, constant or time series water level, hydrodynamic parameters, are necessarily required. To generate the point source discharge in Mike 11 NAM (default module), a daily precipitation, evapotranspiration, temperature, humidity and radiation datasets are required but these variables cannot be projected in Mike NAM, as per the CMIP5 GCMs. In the current study, a coupling between Mike 11 (fully hydrodynamic) and SWAT model has done to project the various hydrodynamic variables in the historical and 21st century. For futuristic projections of hydrodynamic variables such as water level, discharge and water velocity, 21st century projected scenarios of discharge, at various locations over the selected study region simulated from SWAT model, are taken into account. Thus, Mike NAM

TH-1643_136104018

is replaced by SWAT and coupled with Mike 11 for the 21st century projection of these hydrodynamic variables with reference to CMIP5 GCMs and RCP experiments. The other hydrodynamic variables such as manning roughness coefficient and catchment slopes are also taken from SWAT model and put into Mike 11 to reduce the global assumptions based selection of parameters, which can improve the computation of Mike 11. The hydrodynamic parameters details are given in Table 6.15

The mathematical formulation of Mike 11 can be written as follows:

$$\frac{\partial Q}{\partial x}+\frac{\partial A}{\partial t}=q \quad \text{(Continuity equation)} \quad (6.33)$$

$$\underbrace{\frac{\partial Q}{\partial t}}_{\text{Fully dynamic}}+\underbrace{\frac{\partial}{\partial x}\left(\alpha\frac{Q^2}{A}\right)}_{\text{Diffusive}}+\underbrace{gA\frac{\partial h}{\partial x}}_{\text{Kinematic}}+\frac{n^2 gQ|Q|}{AR^{4/3}}=0 \quad \text{(Momentum equation)} \quad (6.34)$$

where Q is the discharge (m^3/s) (dependent); A is the cross section (flow) area (m^2); q is the lateral inflow (m^2/s); h is the water level above a reference datum (m) (dependent); x is downstream direction (m) (independent); t is time (s) (independent); n is the Manning resistance coefficient ($s/m^{1/3}$); R is the hydraulic or resistance radius (m); g is the acceleration due to gravity (m^2/s) and a is the momentum distribution coefficient (e), introduced to account for the non-uniform vertical distribution of velocity in a given section. The above equation can be transformed to as set of implicit finite difference equations obtained from Navier-Stokes equation (Soleymani and Delphi, 2012) over a computational grid. Using Implicit numerical method, the main equations (Eq. 6.34) can be solved using the Lax-Wendroff scheme (Chow et al., 2010) as below (Eqs. 6.35 and 6.36):

$$Q_1=\frac{Q_{i-1}^{j}+Q_{i-1}^{j+1}+Q_{i+1}^{j}+Q_{i}^{j+1}}{4} \quad \ldots\ldots\ldots\ldots\ldots\ldots\ldots\ldots \quad (6.35)$$

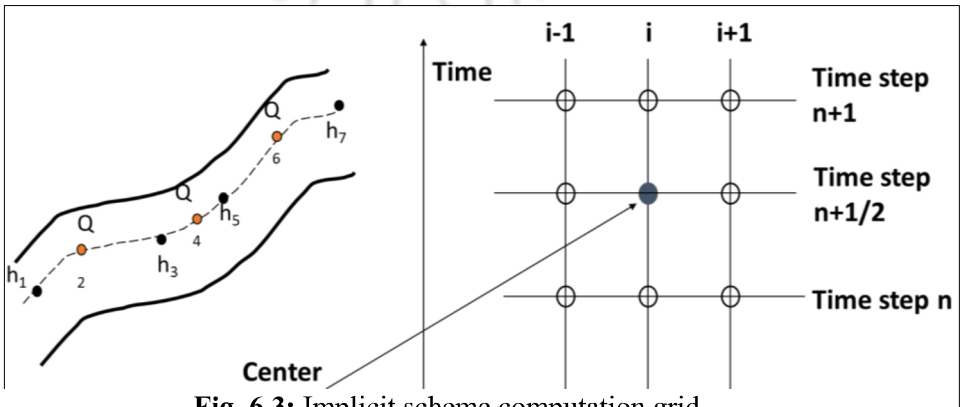


Fig. 6.3: Implicit scheme computation grid.

TH-1643_136104018

$$Q_2 = \frac{Q_i^j + Q_i^{j+1} + Q_{i+1}^j + Q_{i+1}^{j+1}}{4} \quad \ldots\ldots\ldots\ldots\ldots\ldots\ldots\ldots (6.36)$$

The boundary conditions (upstream and downstream), initial condition (time t = 0) and stability parameters such as courant condition (Cr < 1) to determine time step are necessary for the model simulation (Soleymaniand Delphi, 2012). The stability and hydrodynamic parameter details are given in Table 6.15 The coupled diagram of Mike 11 and SWAT has shown in Fig (6.4).

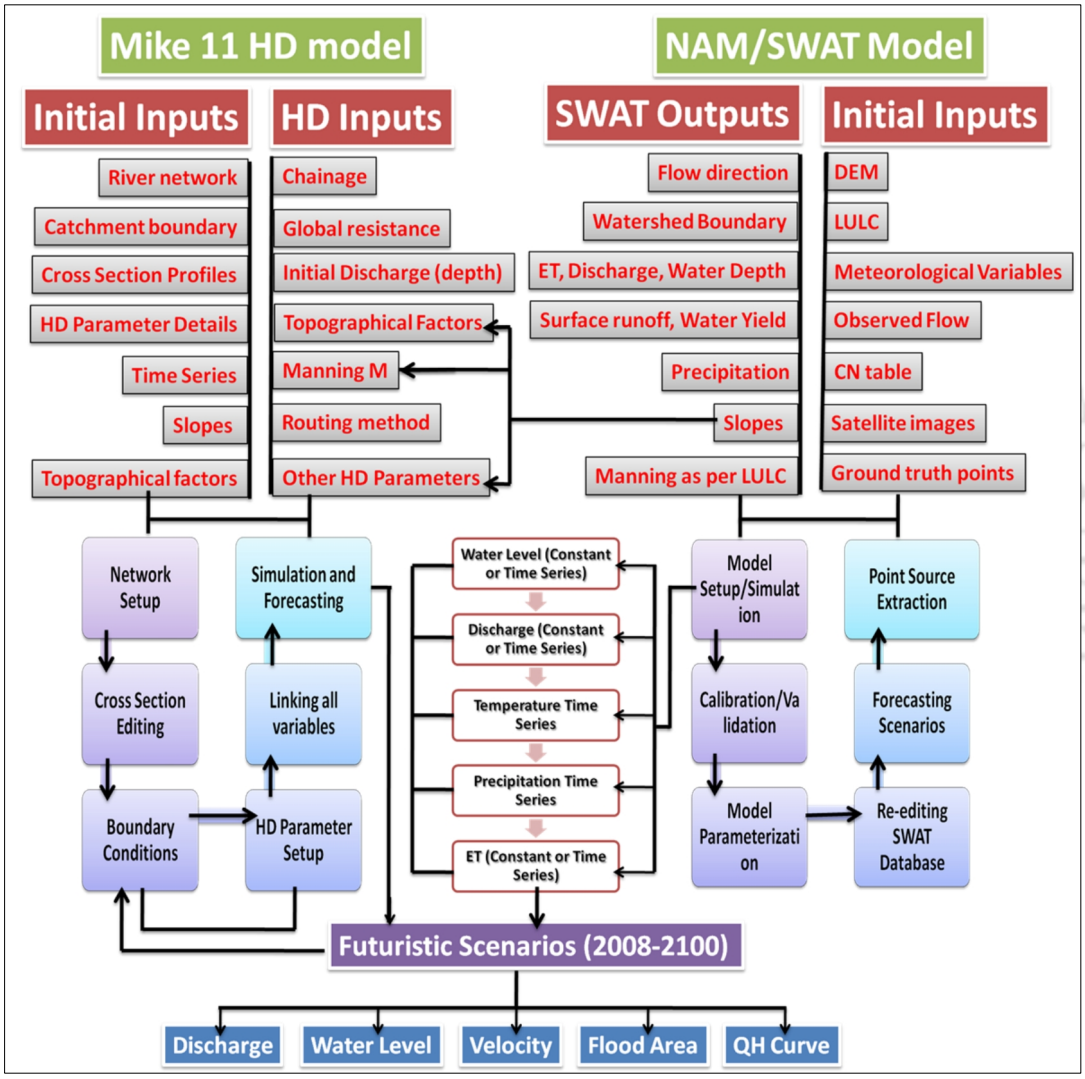


Fig. 6.4: A coupled modeling framework between Mike 11 and SWAT.

6.6 SWAT AND SWAT CUP BASED ANALYSIS RESULTS

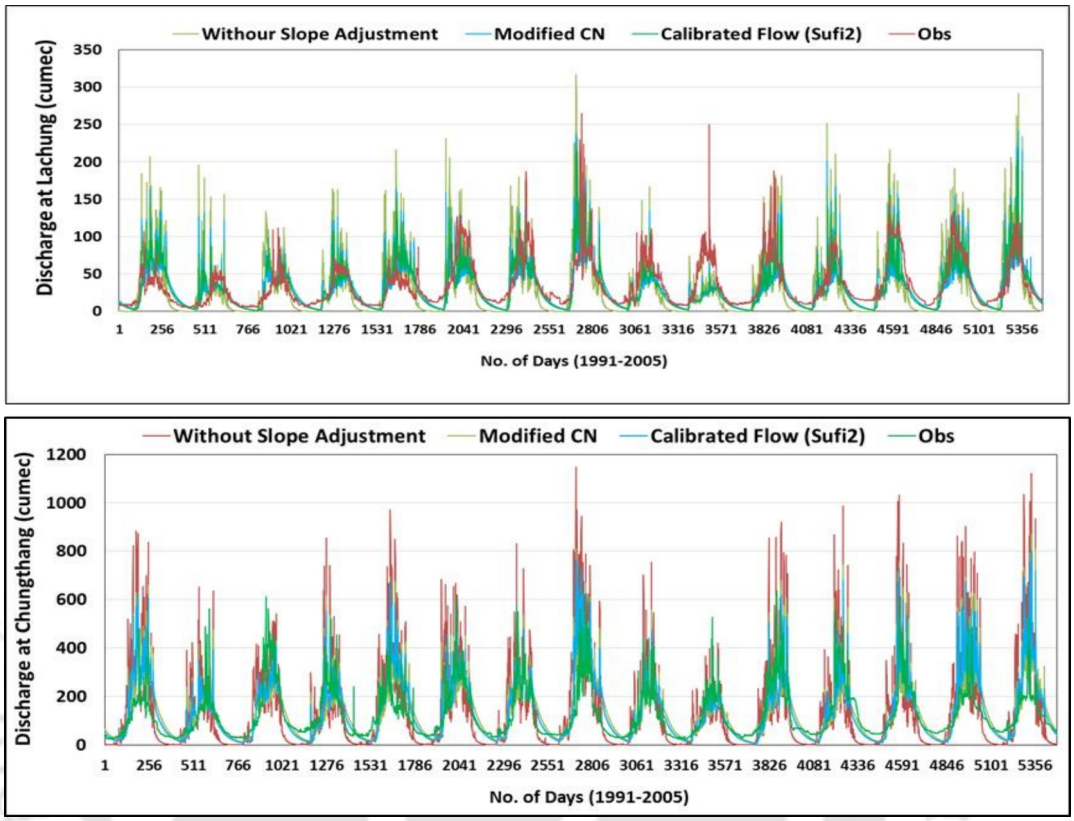
6.6.1 CN adjustment and improvement in SWAT simulated outcomes

SWAT physical and meteorological parameters such as LULC, soil map along with 30 surface and infiltration parameters, daily meteorological variables and DEM were setup into the model. To perform calibration, SWAT parameters are varied within a physically for each sub-

TH-1643_136104018

catchment (SB). In this research work, CN has been adjusted with the slopes at HRUs (Table 6.1).

(a)



(b)

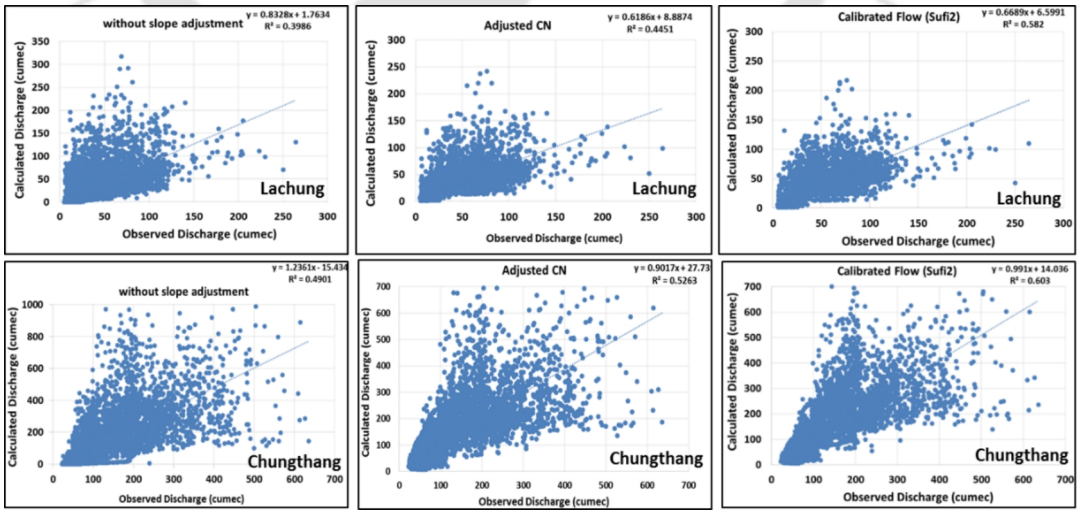


Fig. 6.5: Comparisons of SWAT simulated adjusted CN based streamflow, without adjusted CN based streamflow and calibrated flow with reference to observed streamflow: (a) time series of Lachung and Chungthang and (b) regression plots of Lachung and Chungthang.

TH-1643_136104018

The adjusted CN improved the accuracy of model simulated water balance components (e.g. streamflow). Figs. 6.5 (a) and 6.5 (b) show the results of adjusted CN based streamflow simulation, without adjusted CN based streamflow simulation and calibrated flow at the catchment outlets namely Lachung and Chungthang.

The streamflow is simulated for the year 1989 to 2005. The initial two years (1989-1990) were taken as warm-up period. The observed discharge is available at Lachung and Chungthang outlets for the years 1989 to 2005 and hence, utilized for the model simulation and calibration/validation. In Fig. 6.5 (a), without CN adjusted simulated streamflow looks over predicted than CN adjusted streamflow and calibrated flow at both the catchment outlets. These simulations are showing on a daily basis outcomes. In this time series plots, the calibrated flow and CN adjusted flow peaks are almost following the trends of observed data. But, the without CN adjusted flow peaks show very high values and peaks than observed and calibrated flows. This can be caused due to steep slopes over the catchment. As per the catchment topography, selected for the study, high steep slopes are identified at several locations of the study region (Table 6.1).

SWAT model calculates streamflow as per the CN method to account soil antecedent moisture conditions (AMC) (Arnold et al., 1998) and thus, for the steep slopes, CNs have been adjusted to improve the model simulation (Table 6.1) and Fig. 6.5(a). Fig. 6.5(b) shows the regression plots between the observed discharge and adjusted CN based streamflow, without adjusted CN based streamflow and calibrated flow at both the outlets. The calibrated and adjusted flow showed significant correlation with the observed flow data, while the without CN adjusted flow found highly over predicted at both the outlets. Among all the regression plots, calibrated flow showed best fit with the observed flow datasets. The overall results highlight that the CN adjustment improved the accuracy of the model simulated outcomes.

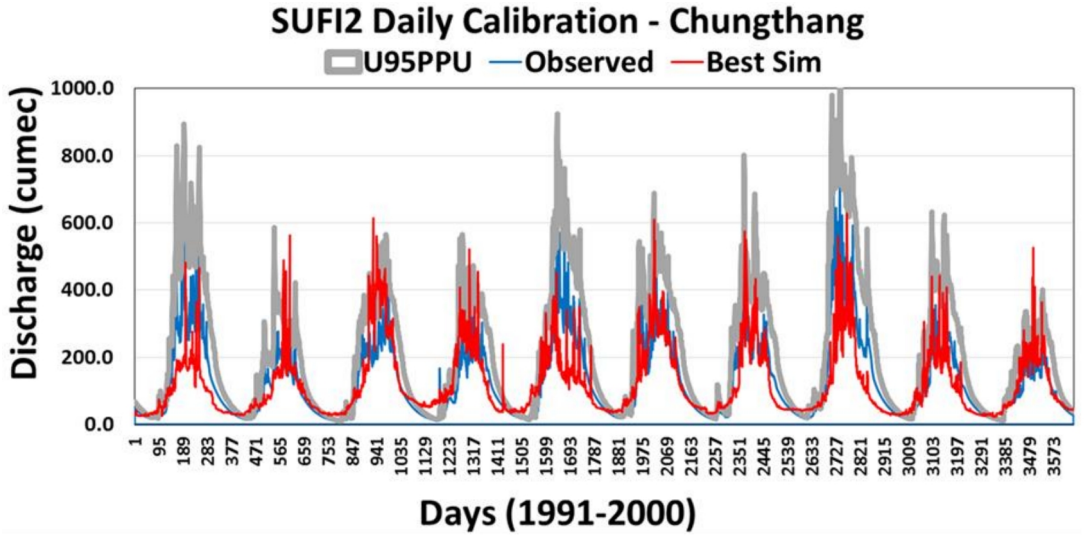
6.6.2 SWAT model calibration/validation, parameterization sensitivity and uncertainty analysis

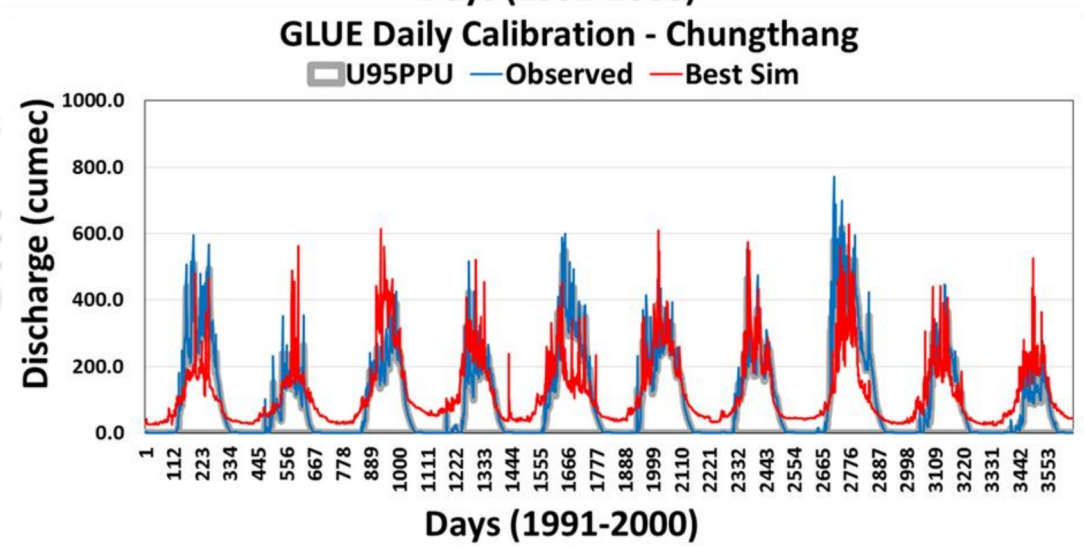
Streamflow has been calibrated and validated from 1991 to 2005. For the simulated streamflow, SWATCUP based SUFI2, GLUE and ParaSol optimization and sensitivity analysis programs have been applied utilizing observed streamflow datasets (1991-2005). Fig. 6.6 and Table 6.2 show the model calibrated final outcomes. These results were achieved by using around 5 iterations and 500 simulation steps for all the methods. The final results were shown as per the detailed sensitivity analysis utilizing these three optimization methods (e.g. SUFI2, GLUE and ParaSol). After sensitivity analysis, the final iteration parameters are used for the uncertainty analysis. In Fig. 6.6, the times series plots of streamflow between

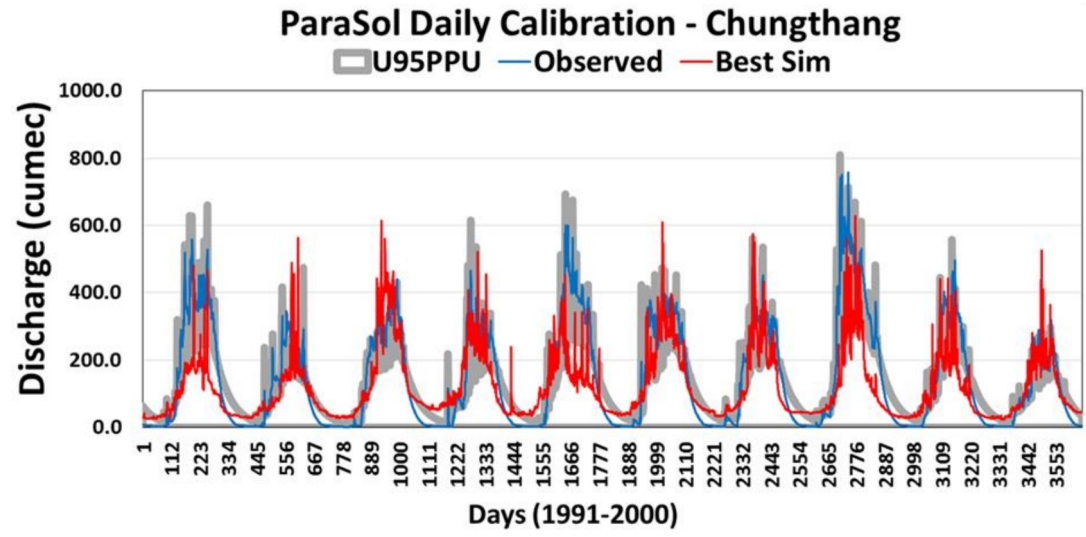
TH-1643_136104018

calibrated and observed datasets have been shown at Chungthang outlet. The overall results have shown in Table 6.2.

(a)







TH-1643_136104018

(b)

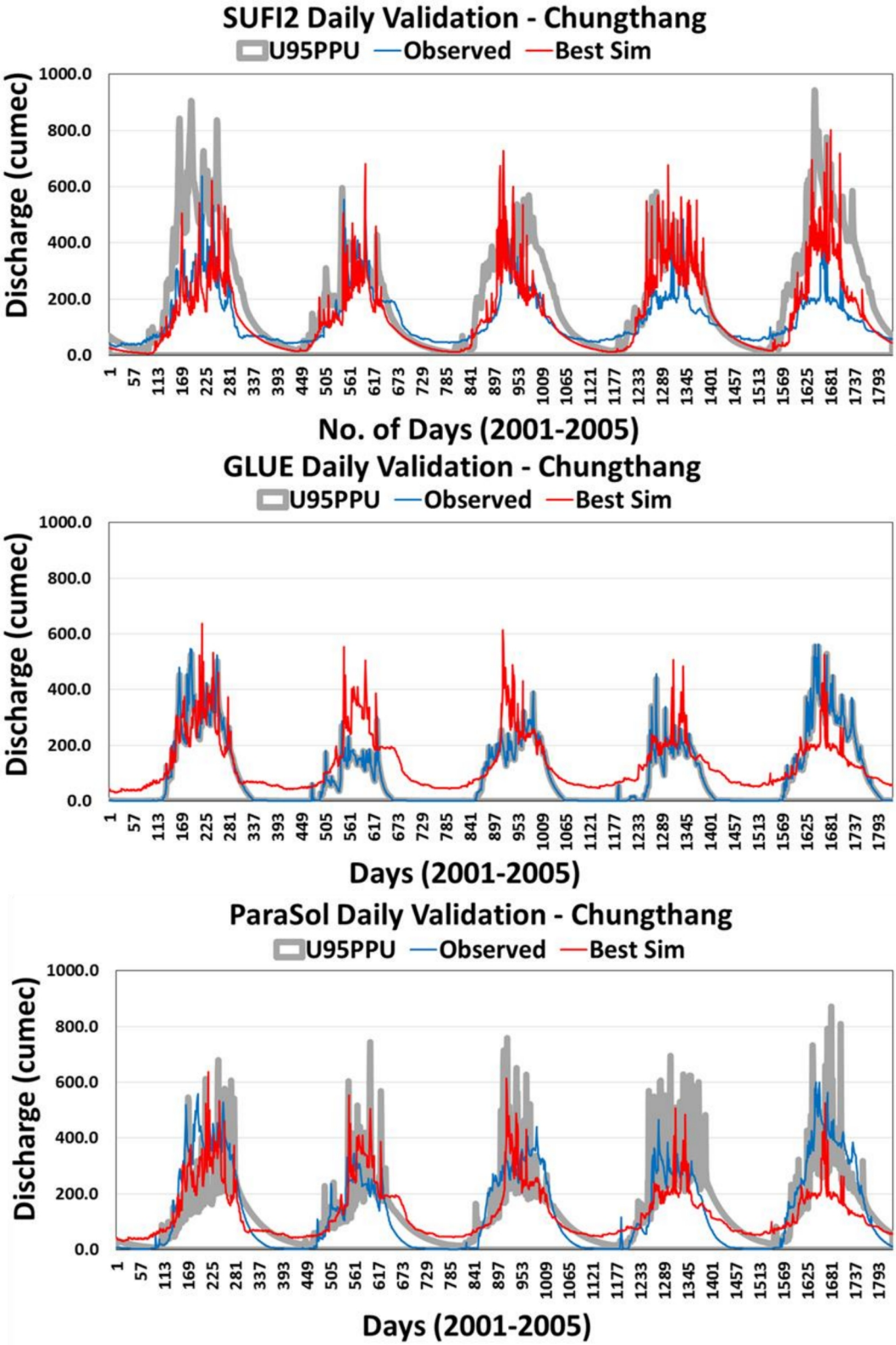


Fig. 6.6: Time series plots for the (a) calibration and (b) validation at main outlet of the catchment (Chungthang).

TH-1643_136104018

Fig. 6.6(a) shows the calibration time series (1991-2000) along with maximum 95PPU bands for all the methods. In this, the SUFI2 based calibrated streamflow showed better correlation with the observed datasets. In SUFI2, the calibrated streamflow is almost captured by the 95PPU band. In SUFI2, the high peak values (represents the monsoon duration flow) and extreme low peak values (represents the summer and winter duration flows) are well matching with the observed flow values. The GLUE based calibrated streamflow showed several extreme low peaks in their time series plot compare to observed data. The GLUE has under predicted the low flows, though it shows well agreement during the high peak flows.

The ParaSol method shows better agreement between the observed and calibrated flow. Though, it also predicted several extreme peaks and low peaks in their whole time series data values and can be visualized in Fig. 6.5(a). Fig. 6.5(b) shows the validation results of SUFI2, GLUE and ParaSol on a daily basis for the year 2001-2005. Similarly calibration, in validation also, SUFI 2 based calibration gave better correlation than GLUE and ParaSol. In this overall time series plots at Chungthang, the SUFI approach showed better agreement in predicting streamflow.

Table 6.2: Calibration (1991-2000)/validation (2001-2005) results as per SUFI2, GLUE and ParaSol on daily and monthly bases.

Method	Daily/Mon	Cal/Val	Outlet	p-factor	r-factor	R^2	NS	Mean Sim	Mean Obs
SUFI2	Daily	Cal	Lachung	0.48	0.32	0.52	0.38	40.53	32.56
			Chungthang	0.58	0.14	0.62	0.46	183.73	118.92
		Val	Lachung	0.54	0.45	0.60	0.53	39.07	39.77
			Chungthang	0.55	0.45	0.61	0.77	177.44	133.45
	Mon	Cal	Lachung	0.67	0.31	0.61	0.46	30.45	39.59
			Chungthang	0.62	0.26	0.76	0.48	132.32	118.41
		Val	Lachung	0.57	0.39	0.81	0.77	31.34	39.59
			Chungthang	0.55	0.49	0.78	0.64	143.43	132.83
GLUE	Daily	Cal	Lachung	0.49	0.66	0.47	0.29	33.54	32.55
			Chungthang	0.46	0.53	0.58	0.28	95.99	118.92
		Val	Lachung	0.42	0.59	0.51	0.43	33.57	39.77
			Chungthang	0.52	0.55	0.54	0.15	93.14	133.44
	Mon	Cal	Lachung	0.53	0.46	0.51	0.24	41.58	32.43
			Chungthang	0.47	0.55	0.63	0.52	115.06	118.41
		Val	Lachung	0.50	0.46	0.55	0.54	40.08	39.59
			Chungthang	0.52	0.54	0.66	0.52	108.77	132.83

TH-1643_136104018

ParaSol	Daily	Cal	Lachung	0.51	0.40	0.51	0.35	30.90	32.56
			Chungthang	0.52	0.43	0.52	0.23	135.66	118.92
		Val	Lachung	0.49	0.45	0.62	0.52	29.71	39.77
			Chungthang	0.42	0.52	0.54	0.33	146.65	133.45
	Mon	Cal	Lachung	0.58	0.46	0.63	0.46	24.04	32.43
			Chungthang	0.52	0.44	0.72	0.44	71.11	118.41
		Val	Lachung	0.57	0.46	0.70	0.52	26.39	39.59
			Chungthang	0.55	0.42	0.72	0.33	110.81	132.83

Table 6.2 shows the results of the streamflow calibration and validation on a daily as well as on a monthly basis. In Table (6.2), the p-factor and r-factor show the associated model uncertainty with simulated streamflow. For the measurement of goodness-of-fit, R^2 and NSE have been applied. These results show the best calibration outputs obtained in 5 iterations and 500 simulations/each iteration.

Table 6.3: Description of model calibration parameters.

Streamflow parameters selected for calibration and validation	Description
R__SNOCOVMX.bsn	Maximum snow water content (that corresponds to 100% snow cover)
R__HRU_SLP.hru	Average slope steepness (Fraction % of Area : 0 to 1)
R__SOL_K.sol	Soil hydraulic conductivity (mm/hr)
R__SNO50COV.bsn	Fraction of snow volume (that corresponds to 50% snow cover)
R__PLAPS.sub	Precipitation lapse rate (mm/km/day)
R__SFTMP.bsn	Snowfall temperature (°C)
V__GWQMN.gw	Threshold depth of water in shallow aquifer required for return flow (mmH_2O)
V__CH_N(2).rte	Manning roughness coefficient for main channel (Manning's N)
R__SOL_BD.sol	Moist bulk density (gm/cm^3)
R__SOL_AWC.sol	Available water capacity of the soil layer
V__GW_REVAP.gw	Groundwater 'revaporation' coefficient
R__SMTMP.bsn	Snowmelt base temperature (°C)
A__ALPHA_BF.gw	Baseflow alfa factor coefficient (0 to 1)

TH-1643_136104018

R__SMFMN.bsn	Melt factor for snow on December 21st (mm H_2O/day-°C)
R__SOL_Z.sol	Depth from soil surface to bottom layer (mm)
V__GW_DELAY.gw	Groundwater delay time (days)
A__TLAPS.sub	Temperature lapse rate (°C/km)
V__CH_K2.rte	Effective hydraulic conductivity (mm/hr)
R__SMFMX.bsn	Melt factor for snow on June 21st (mm H_2O/day-°C)
R__CN2.mgt	Curve number coefficient

In Table 6.2, the maximum p-factors and lowest r-factors for both the simulation steps (e.g. daily and monthly) are recorded for the SUFI2 approach. The GLUE is found less significant for this catchment and achieved lowest p-factors and highest r-factor values for both the simulation steps at both the catchment outlets. The monthly basis evaluation of objective functions such as p-factor, r-factor, and R^2 and NSE show better streamflow prediction results than daily basis predictions.

Tables (6.4 to 6.5) show the results of model calibration parameters and their optimization coefficient values evaluated using three methods such as SUFI2, GLUE and ParaSol. These tables show optimized coefficients on a daily basis calibration. The parameter sensitivity analysis is also done utilizing t-test and p-value test. Table 6.3 shows the full description of each selected calibration parameters. In these tables (Tables 6.4, 6.5 and 6.6), the initial coefficient values during 1st model iteration and final iteration have been shown. In SWAT CUP, there are three methods for optimizing the parameter coefficients such as "V__" (replacing the existing parameter value), "R__" (multiplying: 1 + a given value to the existing parameter value) and "A__" (adding a given value to the existing parameter value), applied. In SWATCUP, the default initial suggested ranges for few parameters, were not physically meaningful parameter ranges and thus, manual modifications have been applied to those parameters to make them physically meaningful within the minimum/maximum ranges. As per the SWATCUP literature review, fifteen, twelve and twelve (15, 12 and 12) parameters, which are most relevant to streamflow and snowmelt, have been selected for SUFI2, GLUE and ParaSol, respectively. The initial parameter ranges during 1st iteration modify the parameter values within their minimum and maximum ranges. In each simulation, the selected objective function (e.g. NSE and R^2) modifies the parameter range and calibrate the simulated and observed dataset values (e.g. streamflow). At the end of the iteration, as per the given objective function, it compares all the calculated parameter coefficients with the objective function (for this study it is selected as 0.5 for both the objective functions).

TH-1643_136104018

Table 6.4 shows the results of SUFI2 method. In Table (6.4), total 15 calibrated parameters were evaluated. Initially, during the 1st iteration, calibration is setup with the 15 different parameters relevant to the streamflow and snowmelt processes.

Table 6.4: Model parameterization and sensitivity analysis results on a daily basis process using SUFI2 approach.

Sl. No.	Parameter Name	1st Iteration			Final Iteration			Sensitivity Results	
		Min Value	Max Value	Fitted Value	Min Value	Max Value	Fitted Value	t-stat	p-value
1	R__CN2.mgt	-0.20	0.20	-0.02	-0.03	0.1	0.03	-6.87	0.00
2	V__ALPHA_BF.gw	0.00	0.30	0.14	0.17	0.26	0.18	-1.56	0.12
3	V__GW_DELAY.gw	10.00	450.00	15.13	2.00	27.19	14.67	-4.81	0.00
4	V__GWQMN.gw	0.00	2.00	1.82	0.91	2.73	2.54	-1.95	0.05
5	V__ESCO.hru	0.40	0.90	0.46	0.91	0.96	0.94	0.14	0.89
6	V__SFTMP.bsn	-2.00	5.00	-1.22	4.13	6.59	4.56	1.81	0.07
7	V__SMTMP.bsn	-2.00	4.50	0.87	-2.41	-0.05	-0.64	-1.84	0.07
8	V__SMFMX.bsn	0.00	5.00	2.14	NA	NA	NA	-0.55	0.58
9	V__SMFMN.bsn	0.00	5.00	1.44	NA	NA	NA	-1.94	0.05
10	V__TIMP.bsn	0.00	1.00	0.94	NA	NA	NA	-1.92	0.06
11	V__SNOCOVMX.bsn	0.00	500.00	389.17	5.47	10.85	9.56	2.08	0.04
12	V__SNO50COV.bsn	0.00	1.00	0.54	0.16	0.50	0.33	-4.22	0.00
13	R__SOL_AWC.sol	NA	NA	NA	-0.02	0.03	0.02	1.81	0.72
14	R__SOL_K.sol	NA	NA	NA	-0.84	-0.04	-0.81	1.96	0.05
15	R__HRU_SLP.hru	NA	NA	NA	-0.02	0.03	0.02	-1.95	0.52

Table 6.5: Model parameterization and sensitivity analysis results on a daily basis process using GLUE approach.

GLUE - Daily									
Sl. No.	Parameter Name	1st Iteration	Sensitivity Results			Final Iteration		Sensitivity Results	
		Min Value	Max Value	t-stat	p-value	Min Value	Max Value	t-stat	p-value
1	R__CN2.mgt	-2.00	2.00	3.95	0.00	-0.10	0.10	-30.99	0.00
2	V__ALPHA_BF.gw	0.10	0.30	0.68	0.50	0.80	0.25	0.13	0.90
3	V__GW_DELAY.gw	30.00	450.00	8.20	0.00	0.00	7.00	30.76	0.00
4	V__GWQMN.gw	0.00	2.00	-3.48	0.00	0.10	2.00	-1.34	0.18
5	V__GW_REVAP.gw	0.00	0.20	-11.92	0.00	-0.01	0.01	1.74	0.08
6	V__ESCO.hru	0.80	1.00	1.55	0.12	0.90	1.00	-0.24	0.81
7	V__ALPHA_BNK.rtc	0.00	1.00	1.38	0.17	0.10	1.00	-1.54	0.12
8	R__SOL_AWC(1).sol	-0.20	0.40	-2.72	0.01	-0.20	0.50	-2.73	0.01

TH-1643_136104018

9	R__SOL_K(1).sol	-0.80	0.80	12.09	0.00	-0.50	0.50	0.19	0.85
10	R__SOL_BD(1).sol	-0.50	0.60	12.29	0.00	-0.20	0.20	-0.23	0.82
11	V__SFTMP.bsn	-5.00	5.00	2.10	0.04	-1.00	5.00	-1.21	0.23
12	V__SMTMP.bsn	NA	NA	NA	NA	0.00	5.00	-0.31	0.76

Table 6.6: Model parameterization and sensitivity analysis results on a daily basis process using ParaSol approach.

Sl. No.	Parameter Name	1st Iteration		Sensitivity Results		Final Iteration			Sensitivity Results		
		Min Value	Max Value	Best Value	t-stat	p-value	Min Value	Max Value	Best Value	t-stat	p-value
1	R__CN2.mgt	-0.20	0.20	0.14	-5.69	0.00	-0.05	0.10	0.02	-11.3	0.00
2	V__ALPHA_BF.gw	0.00	0.10	0.08	-2.72	0.02	NA	NA	NA	NA	NA
3	V__GW_DELAY.gw	5.00	50.00	12.67	-1.64	0.10	10.00	20.00	16.88	9.96	0.00
4	V__GWQMN.gw	0.00	2.00	0.42	-1.04	0.30	1.00	2.00	1.01	-0.74	0.46
5	V__GW_REVAP.gw	0.00	0.20	0.07	-1.42	0.16	NA	NA	NA	NA	NA
6	V__ESCO.hru	0.80	1.00	0.96	1.47	0.14	0.80	1.00	1.00	1.40	0.16
7	V__ALPHA_BNK.rte	0.00	1.00	0.53	2.00	0.05	NA	NA	NA	NA	NA
8	R_SOL_AWC.sol	-0.20	0.40	-0.08	-0.54	0.59	NA	NA	NA	NA	NA
9	R_SOL_K.sol	-0.80	0.80	0.44	1.35	0.18	NA	NA	NA	NA	NA
10	R__SOL_BD.sol	-0.50	0.60	0.33	0.98	0.33	NA	NA	NA	NA	NA
11	V__SFTMP.bsn	-5.00	5.00	0.79	0.35	0.72	0.00	5.00	2.41	2.69	0.01
12	V__ALPHA_BF.gw	NA	NA	NA	NA	NA	0.20	0.80	0.33	-2.78	0.01

As per their sensitivity test results, only significant sensitive parameters were taken into the consideration for further iteration. However, if parameter found not significant and the results are not improved then the initial value of parameter (minimum/maximum ranges) has been modified to check the sensitivity of that parameter again. The best initial values is thus opted by applying trial and error method. In the table (6.5), CN2, GW_DELAY, SNOCOVMX and SNOCOV50 are found significant sensitive parameters. While in the final iteration, the CN2 was found most significant parameter for the calibration process. For these significant values, the corresponding P-values and t-stat values are found lower than 0.05 and greater than ± 1.96, respectively.

Table (6.5) shows the results of GLUE base calibration outcomes on a daily basis analysis. In this method, twelve most relevant parameters are taken and evaluated as per the literature suggested. In this method, during initial iteration process with 500 simulations, total eight parameter are found significant sensitive, as per the p-value and t-stat. In the final iteration, three out of twelve parameters are recorded significant sensitive, whose P-values are recorded

TH-1643_136104018

less than alpha < 0.05 significance level. In the final iteration (Table 6.5), CN2, GW_DELAY and SOL_AWC are found most significant parameters. Table 6.6 shows the calibrated outcomes of ParaSol method on a daily basis analysis. In this method, during first iteration, two parameter such as CN2 and GW_DELAY out of twelve different parameters are recorded significant sensitive, as per their t-stat and p-values. In the final iteration, three parameters such as CN2, ALFA_BF and SFTMP are recorded significant sensitive parameters. Among these three significant sensitive parameters, CN2 is found most significant for the ParaSol optimization process. The overall calibration and parameterization uncertainty analysis outcomes gave broad scope of the analysis to understand the catchment characteristics. SUFI has been found most powerful optimization tool for calibrating various watershed components.

6.6.3 Simulations, projection scenarios and changes in main watershed components under CMIP5 GCMs and RCP experiments

Fig. 6.7 shows the results of various water balance components simulated by SWAT on an annual basis for the historical/observed period (1991-2005). All the water balance components such as precipitation (precip mm), snowmelt (mm), potential ET (mm), ET (mm), seepage water (SW mm), percolation (mm), surface runoff (SURQ mm), groundwater flow (mm) and water yield (mm) show mixed responses among all as per their variability across the catchment. The snowmelt component shows higher contribution at SB1, SB2, SB3 and SB4 than others. Because these SBs are mostly covered by snow and glaciers throughout the years. Thus effective melt runoff contribution can be identified over these SBs.

For the projection of 21st century scenarios, downscaled daily minimum/maximum temperature and daily precipitation datasets as per the CMIP5 GCMs with their emission scenarios(RCP experiments), from low to high (RCP2.6, RCP4.5 and RCP8.5), utilized in the SWAT model. As per the IPCC (2013), it is reported that precipitation and water yield amount will be enhanced in the 21st century. In these plots, one can notice that the before 1998s precipitation and corresponding water yield showed higher increase than after 2000s. Thus, among all the above water balance components, precipitation, ET and water yield at each catchment level have been projected in the 21st century. The percolation and other infiltration parameters show enormous variability over the Teesta catchment. Percolation amount is contributed higher for the upstream portion of the study area such as SB1, SB2, SB3 and SB4.

Fig. (6.8) shows the projected scenarios for the precipitation as per CMIP5 ESM-2M (RCP2.6, RCP4.5, RCP8.5, and average of all RCPs) (Fig. 6.8a), CM3 (RCP2.6, RCP4.5, RCP8.5, and average of all RCPs) (Fig. 6.8b) and CM2P1 (RCP4.5, RCP8.5, and average of both the RCPs) at each catchment scale (Fig. 6.8c). All the projected scenarios show a significant increment

TH-1643_136104018

in the precipitation amount as it is showing consistent increasing trend in the progressive manner (from 2008 to 2100). All the RCPs from low emission scenario such as RCP2.6 and moderate to high emission scenario such as RCP4.5 to 8.5 show increase in precipitation. The extreme emission scenario based projection (RCP8.5) showed maximum increase in precipitation across all the catchment and GCMs. The average of all RCPs for the respective GCM also showed increase in precipitation. Fig. 6.8(a) shows several extreme peaks in the plots, which are occurred due to modeled extreme events. In Fig. (6.8), among all the GCMs and RCPs, it can be visualized that the precipitation will sudden increase after 2050s. In these plots, among all GCMs, it can also be observed that the upper SBs such as SB1, SB2, SB3 and SB4 showed higher increase than lower SBs such as SB5, SB6 and SB7.

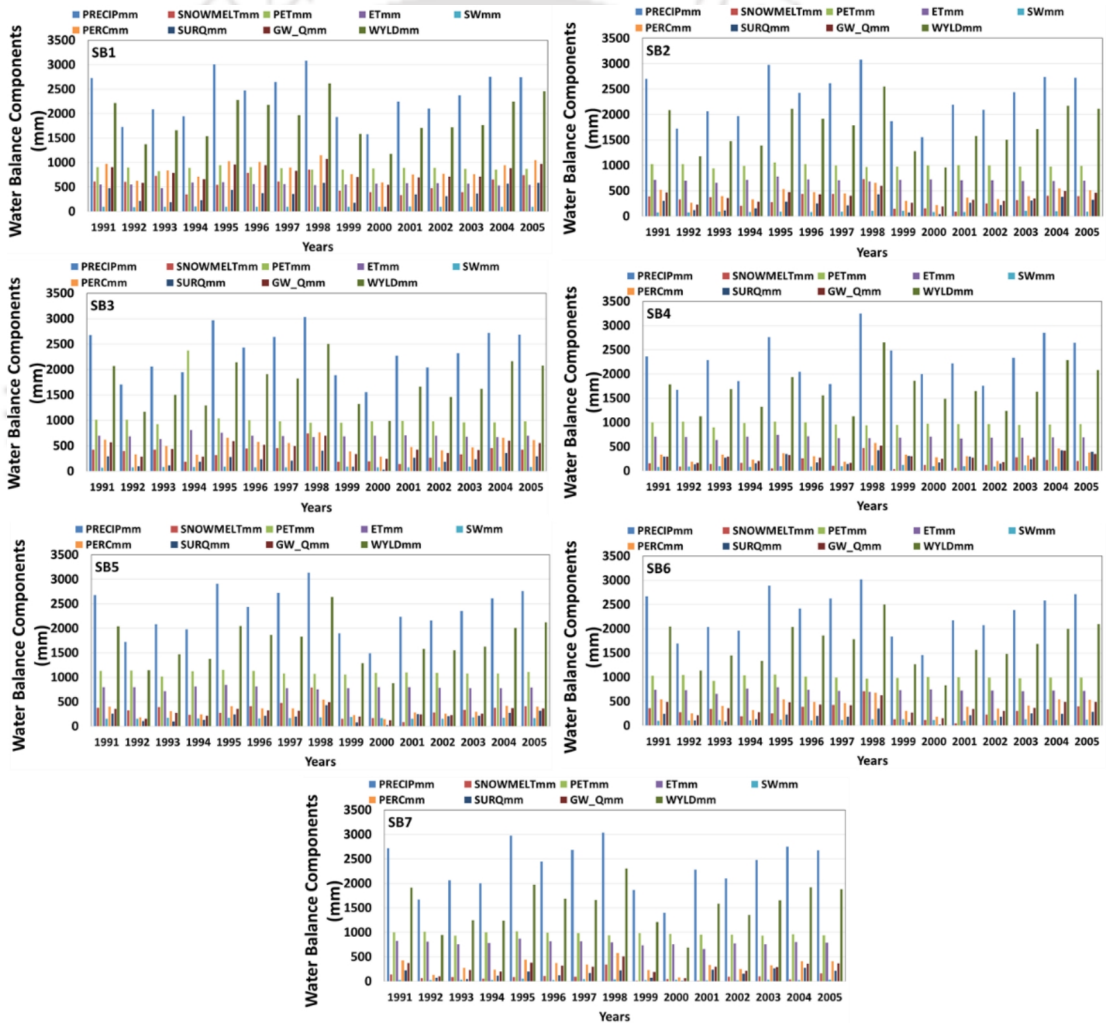


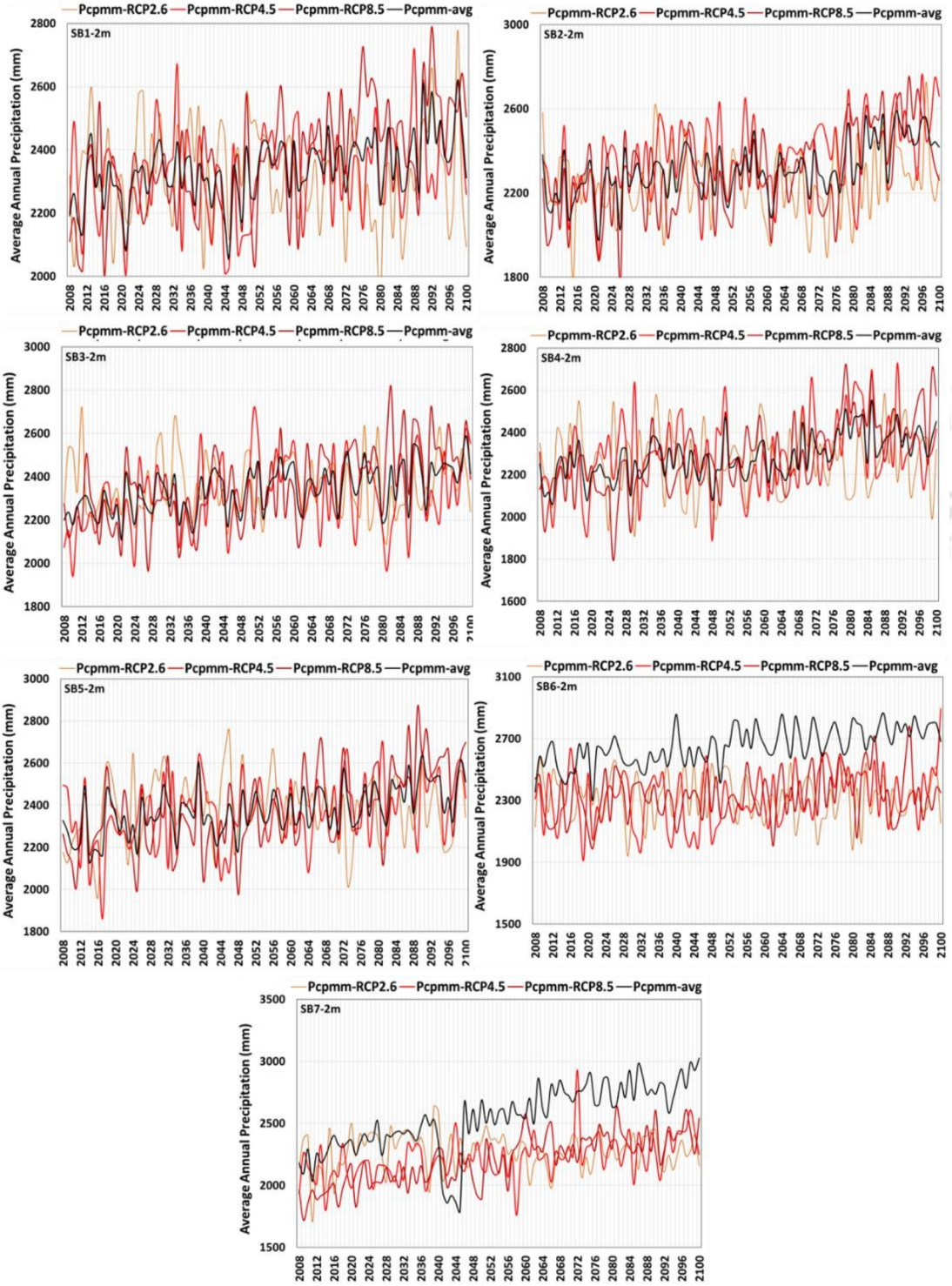
Fig. 6.7: SWAT simulated main water balance components (average annual) at each catchment (1991-2005).

Fig. 6.9 shows the projected scenarios for the ET as per CMIP5 ESM-2M (RCP2.6, RCP4.5, RCP8.5, and average of all RCPs) (Fig. 6.9a), CM3 (RCP2.6, RCP4.5, RCP8.5, and average of all RCPs) (Fig. 6.9b) and CM2P1 (RCP4.5, RCP8.5, and average of both the RCPs) at each

TH-1643_136104018

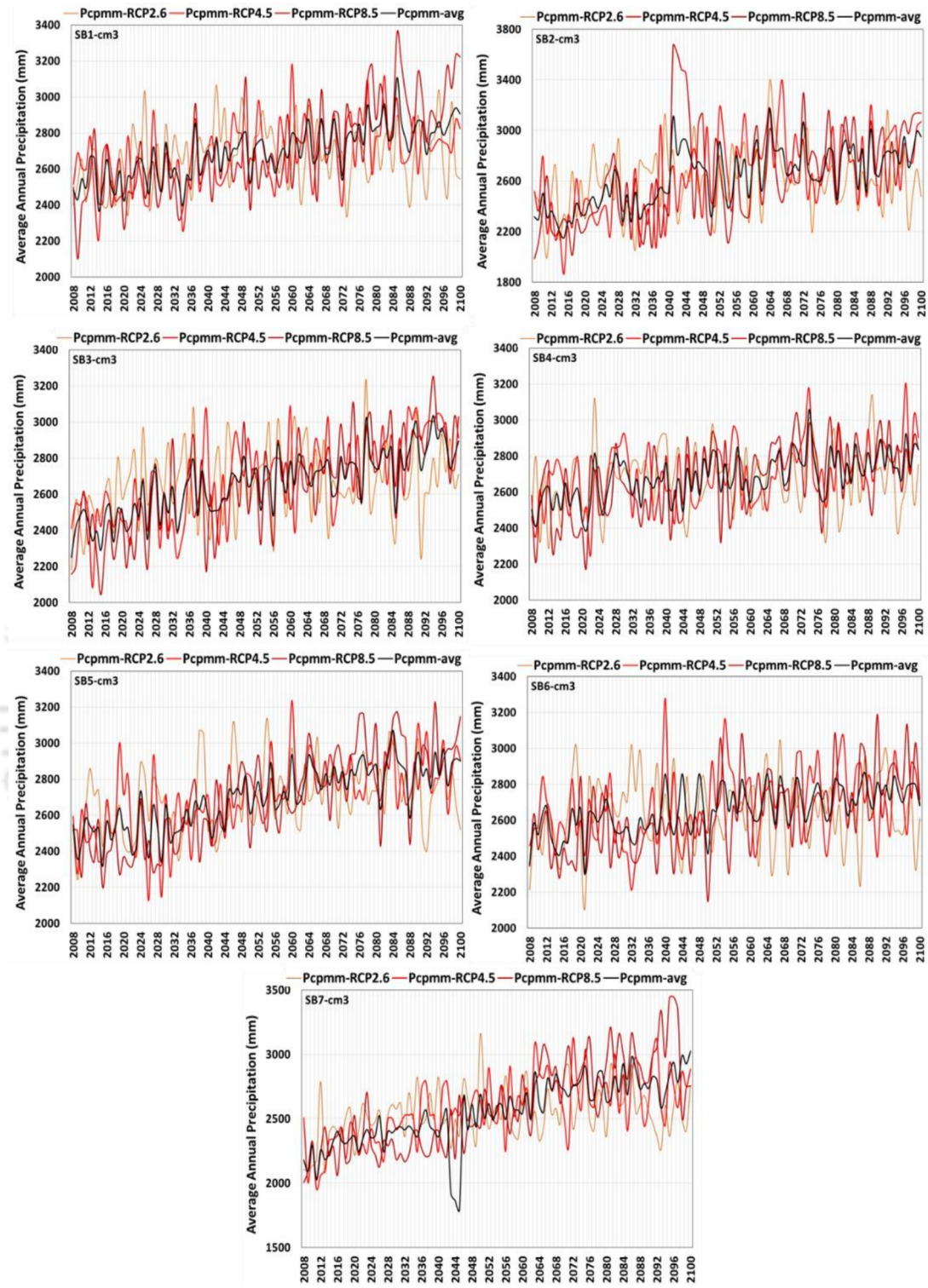
catchment scale (Fig. 6.9c). In Fig. (6.9a), as per the CMIP5 2M GCM, the SB1 shows decrease in ET, while SB7 shows increase in ET. The other SBs show slight increase (SB3 and SB6) and slight decrease (SB4 and Sb5). Similar trends were observed in the other CMIP5 GCMs and RCPs (Figs. 6.9b and 6.9c). Based on these trends, it is observed that the ET is highly variable component over this catchment.

(a)



TH-1643_136104018

(b)



TH-1643_136104018

(c)

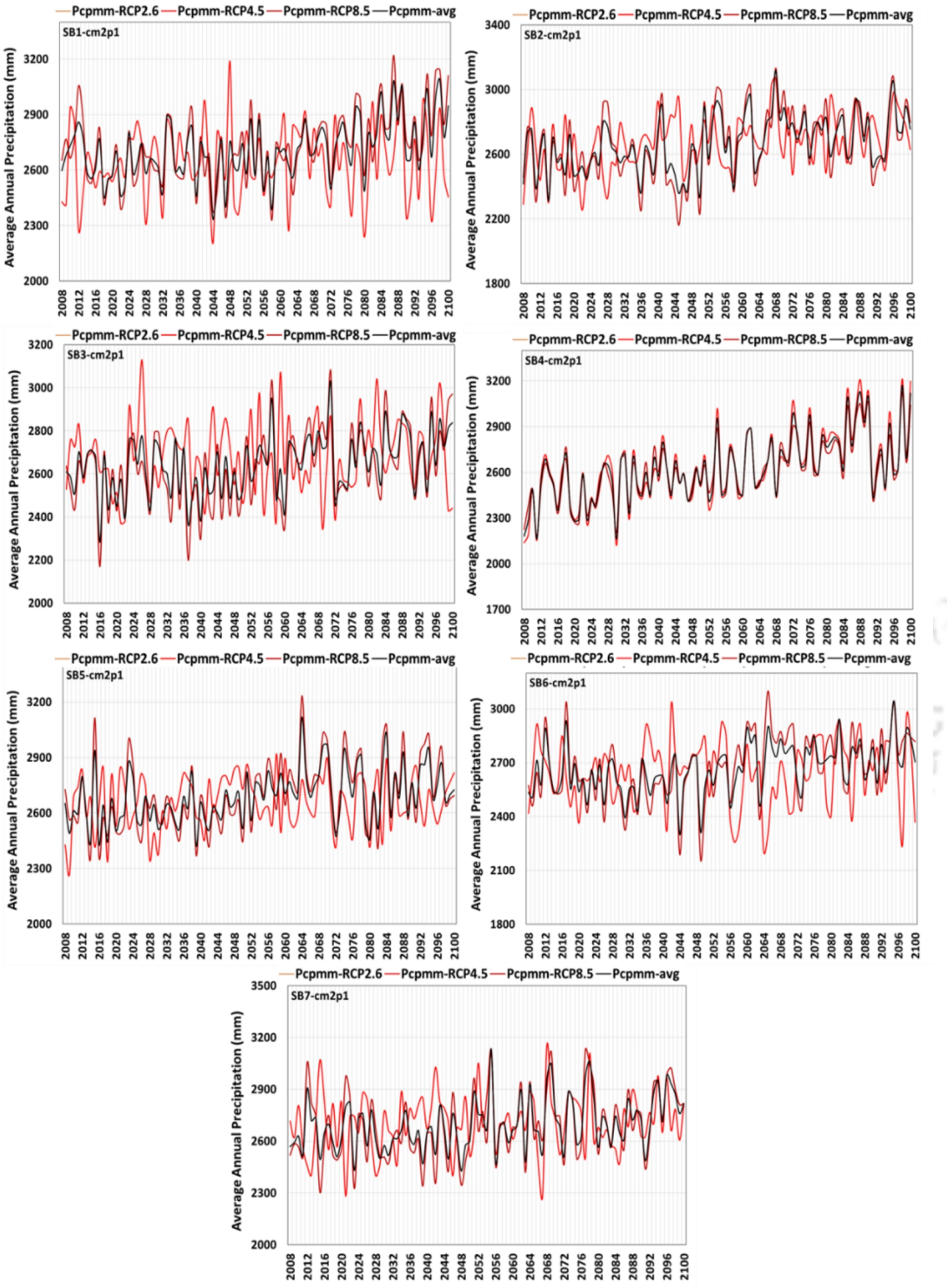
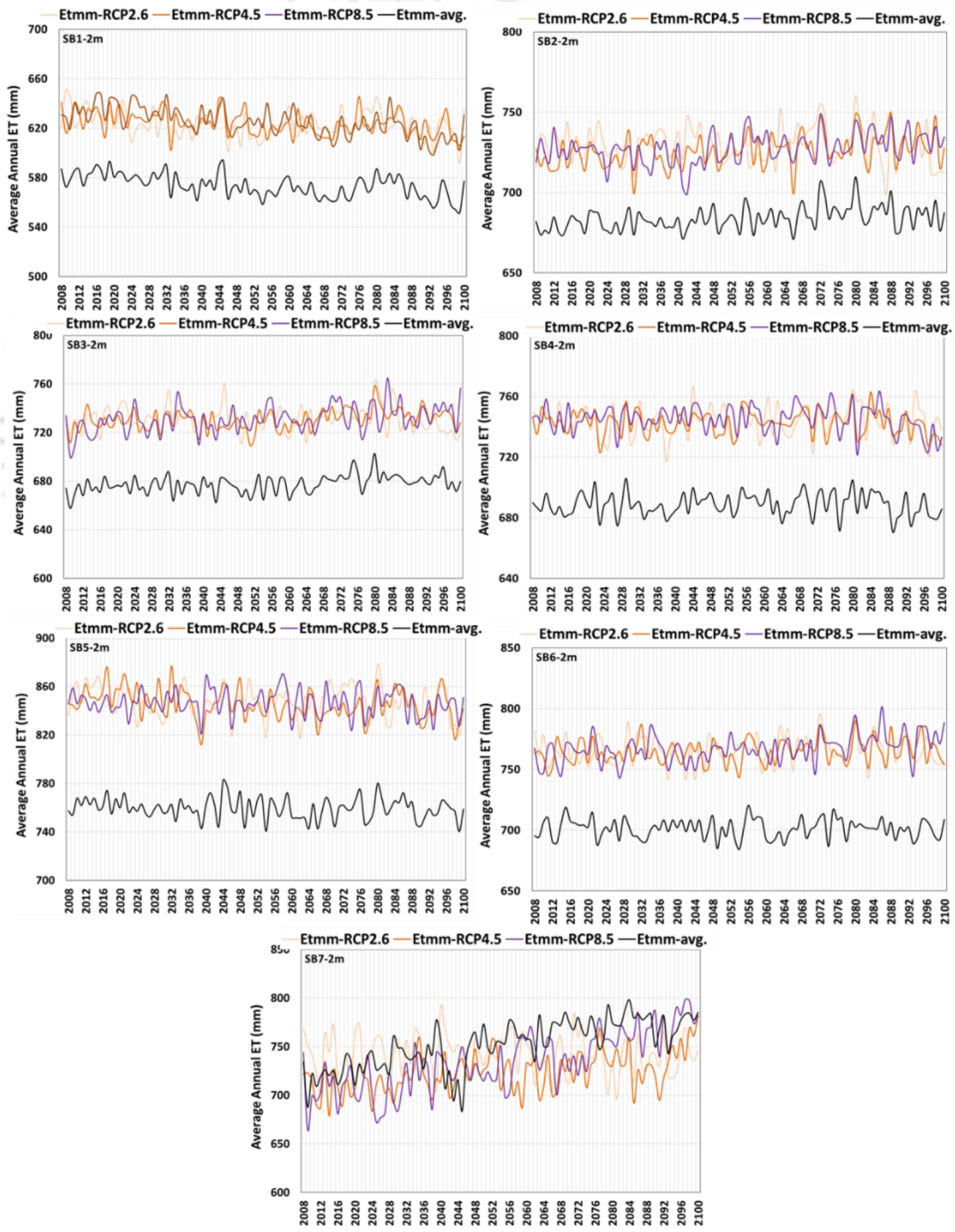


Fig.6.8: Projected precipitation (Pcp mm) scenarios during 2008-2100 at each catchment scale as per: (a) ESM-2M, (b) CM3 and (c) CM2P1 GCMs with their RCPs.

TH-1643_136104018

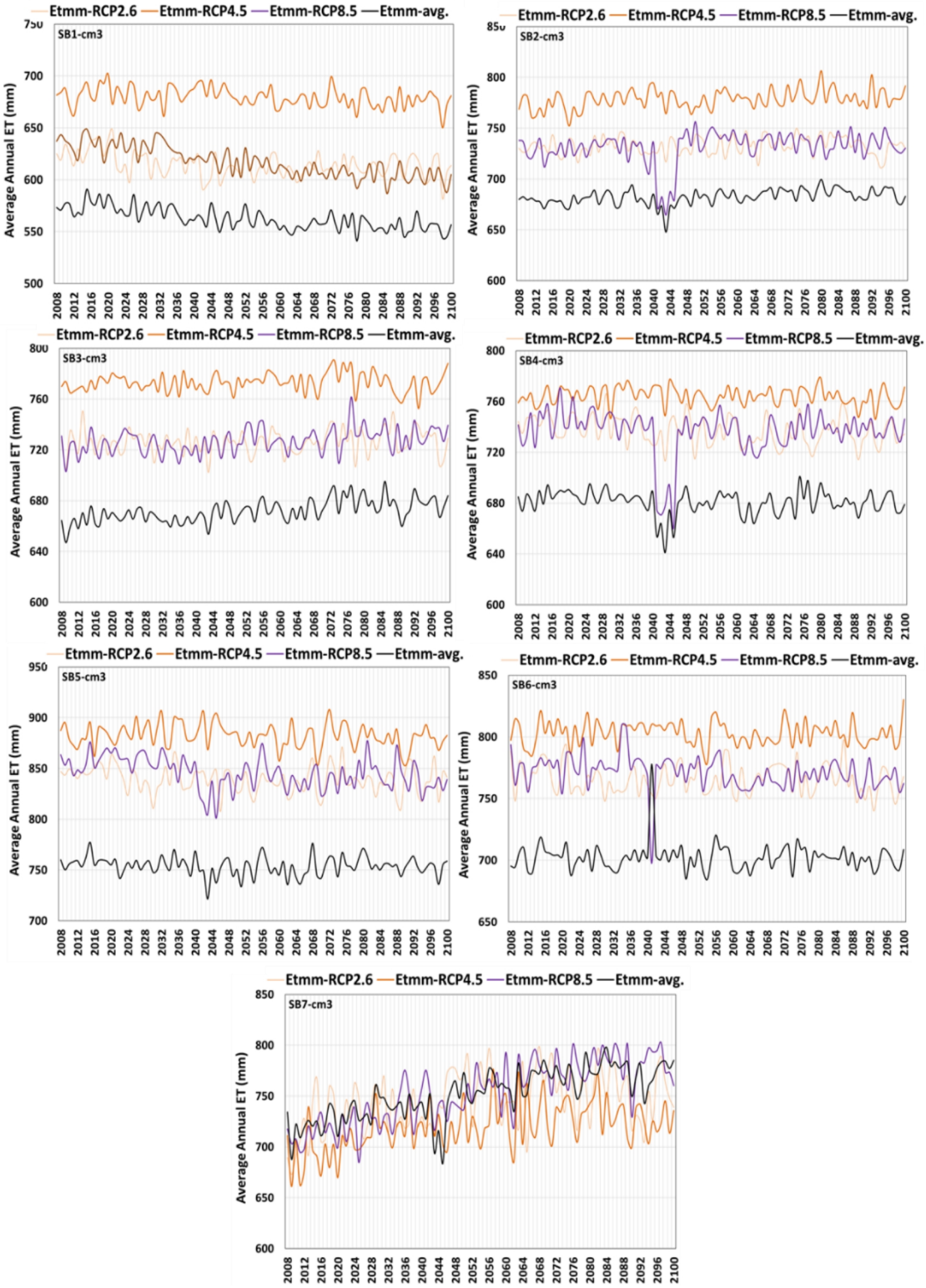
Fig. 6.8 shows the projected scenarios for the water yield as per CMIP5 ESM-2M (RCP2.6, RCP4.5, RCP8.5, and average of all RCPs) (Fig. 6.10a), CM3 (RCP2.6, RCP4.5, RCP8.5, and average of all RCPs) (Fig. 6.10b) and CM2P1 (RCP4.5, RCP8.5, and average of both the RCPs) at each catchment scale (Fig. 6.10c). The CMIP5 GCMs and RCPs show that water yield will increase over selected study catchment. All the GCM based projected scenarios revealed that Teesta river catchment water yield will be increased from SB1 to SB7 as precipitation will increase.

(a)



TH-1643_136104018

(b)



TH-1643_136104018

(c)

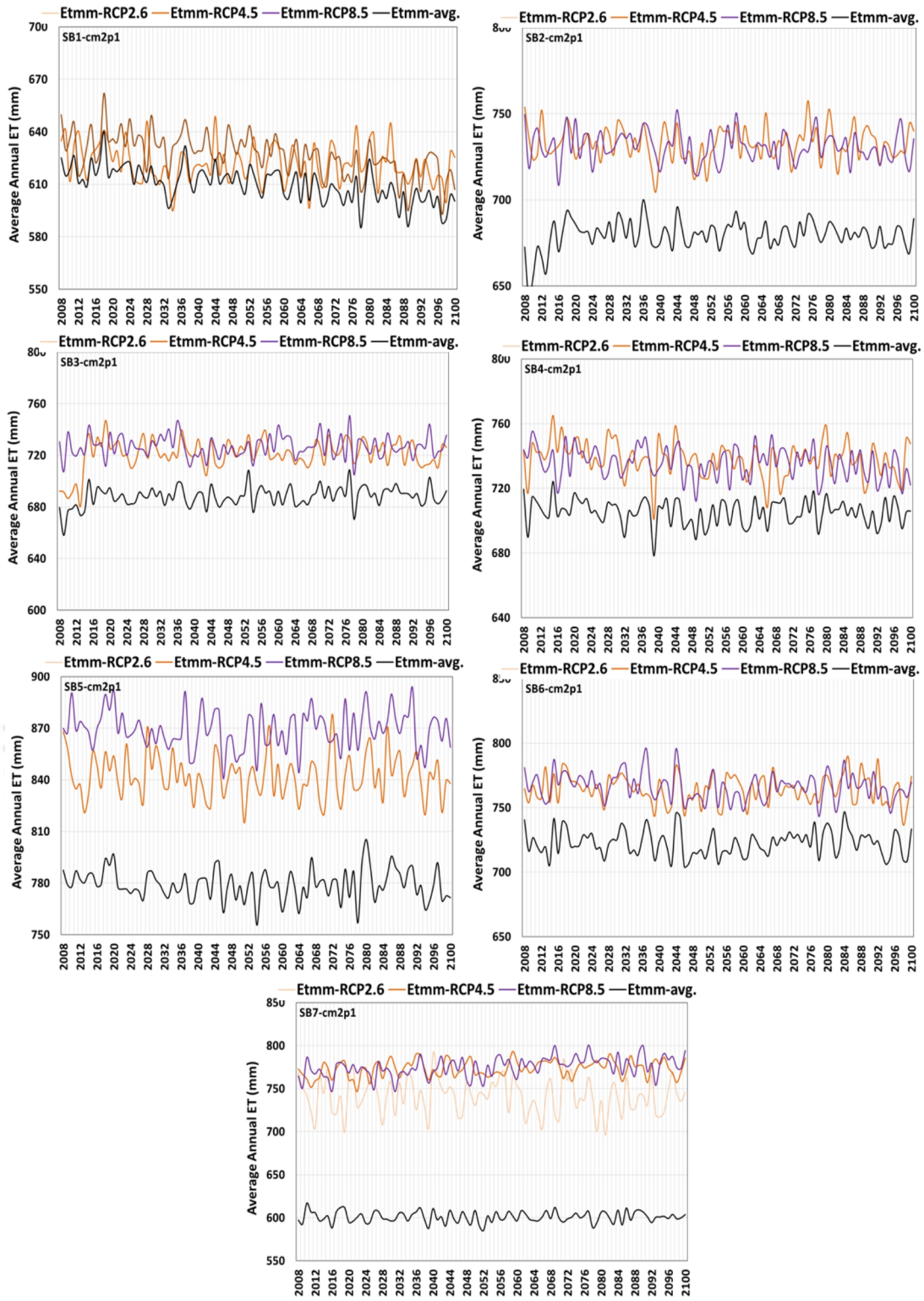
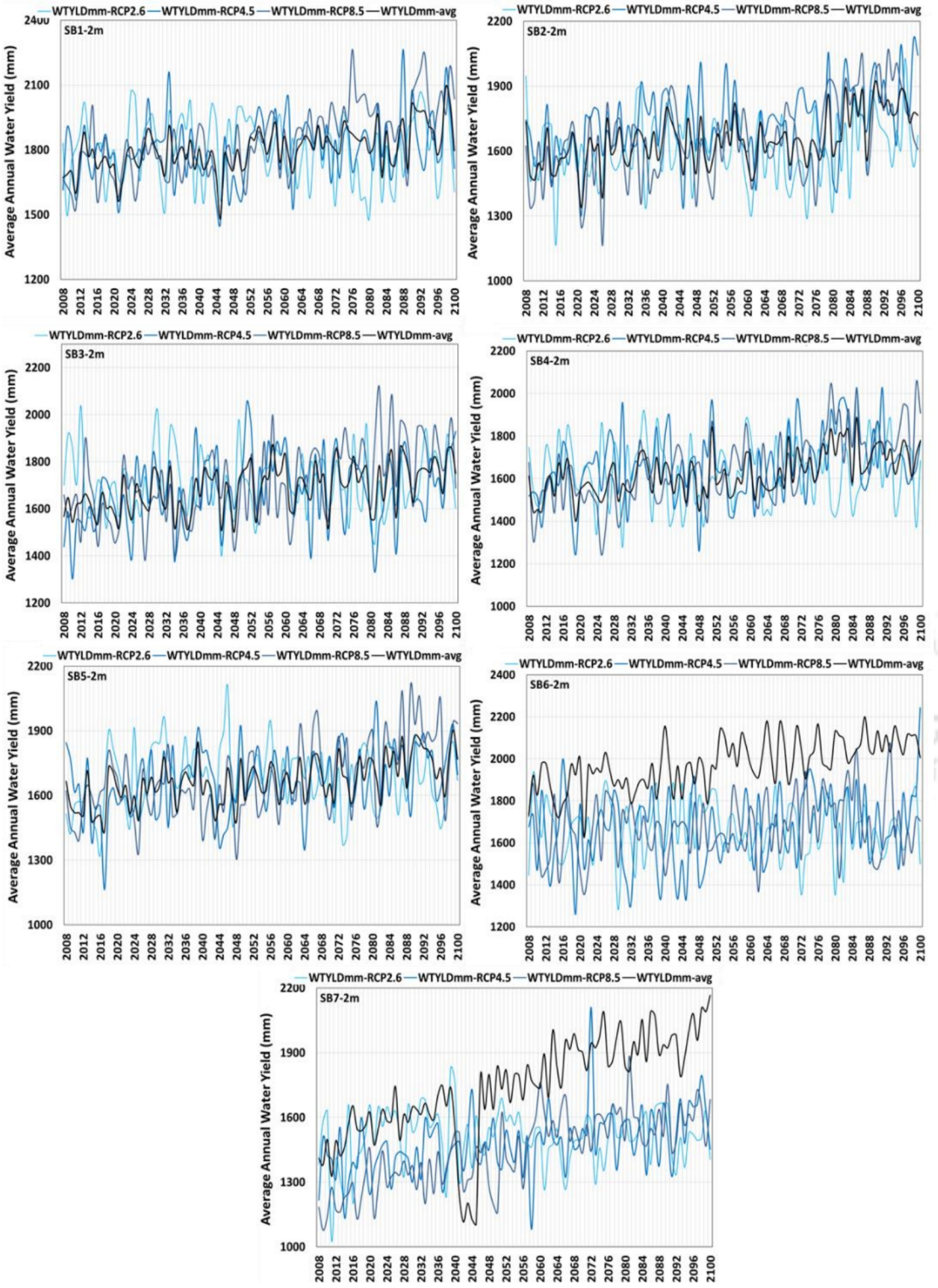


Fig. 6.9: Projected evapotranspiration (ET) scenarios during 2008-2100 at each catchment scale as per: (a) ESM-2M, (b) CM3 and (c) CM2P1 GCMs with their RCPs.

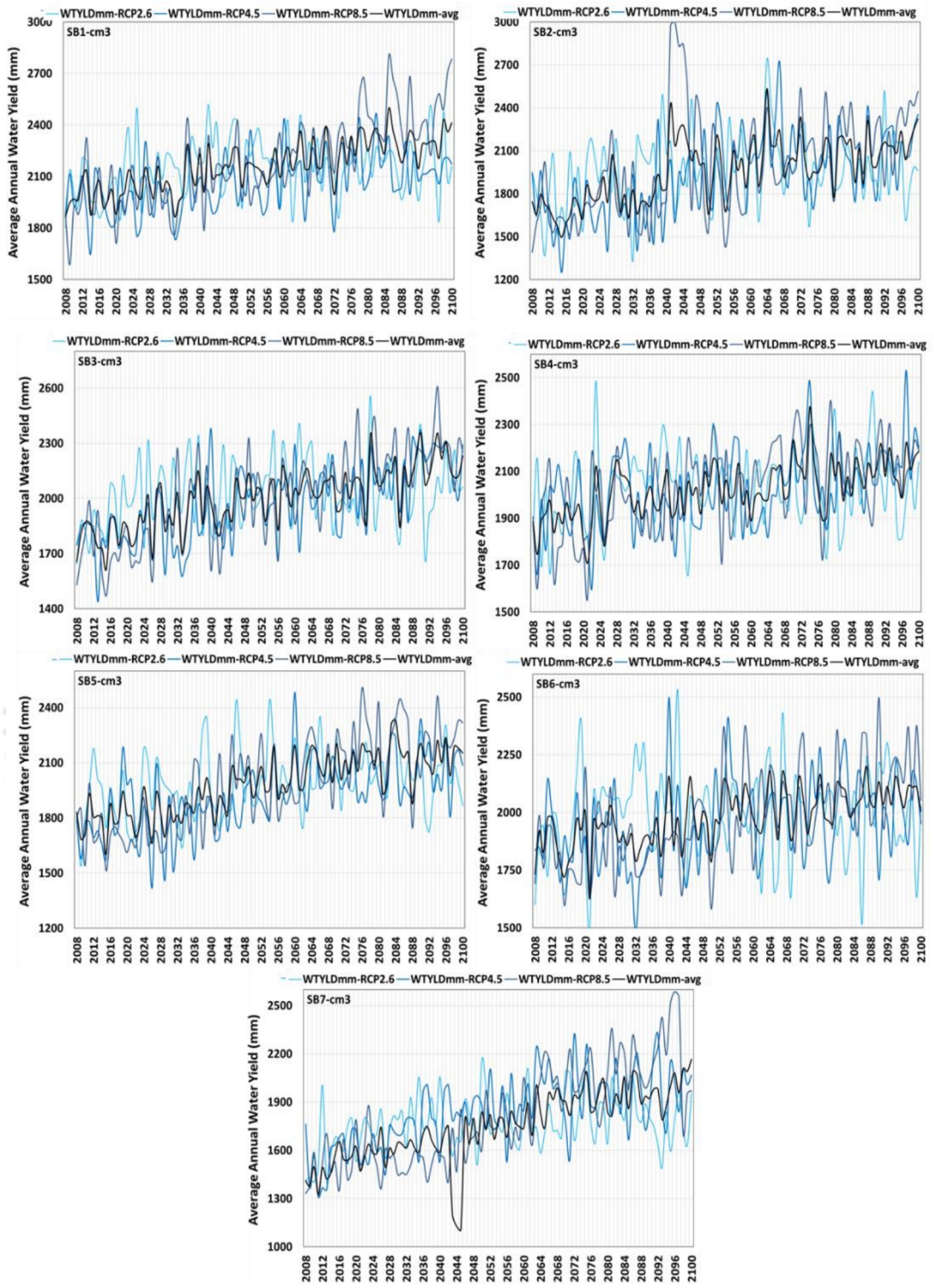
TH-1643_136104018

(a)



TH-1643_136104018

(b)



Here in these plots, as per the CMIP5 GCMs based including low (RCP2.6) to extreme emission scenario (RCP8.5), it can be concluded the precipitation and water yield will increase in the future over the Teesta river catchment. Though, their severity or extremity will

TH-1643_136104018

be enhanced after 2050s. Because in case of precipitation and water yield, it can be seen that the frequency of occurring extreme peaks are enhanced after 2050s.Several extreme events can also be notified in the projected scenarios. In case of the ET scenario, it is found that the ET will be most significant parameter of this catchment and will be varied from SB1 to SB7.

(c)

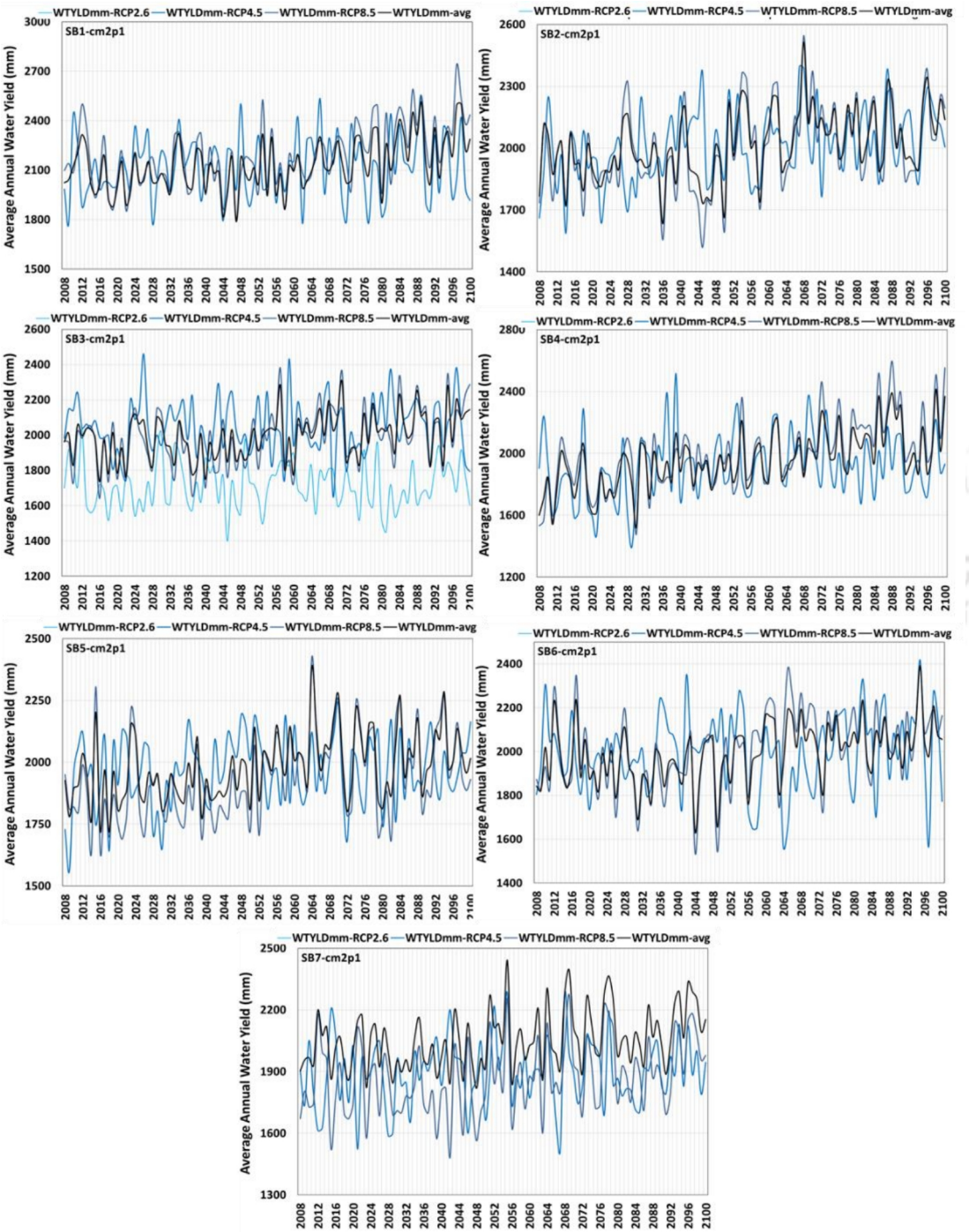


Fig. 6.10: Projected water yield scenarios during 2008-2100 at each catchment scale as per: (a) ESM-2M, (b) CM3 and (c) CM2P1 GCMs with their RCPs.

TH-1643_136104018

In this study, streamflow is considered most projecting component among all the water balance components. Therefore, a streamflow change (in amount) has been calculated for the streamflow based on the projected streamflow scenarios to see the magnitude of change. The streamflow change has been calculated for the each month at catchment scale. For the streamflow change, the whole time series is divided into two intra-decadal time series sets such as 2008-2050 (TS1) and 2058-2100 (TS2).

TS 2 is chosen is started from the year 2058, to maintain the uniqueness in doing the average for calculating percentage of change. Most of the months show significant increase in the streamflow amount except few ones (mostly July). The April month based observations shows highest growth in the streamflow at both the catchment (Table 6.7). The maximum limit is recoded (change in amount) as 135.7 for April month.

Figs. (6.11 and 6.12) shows the mean monthly projected scenarios of streamflows at Lachung and Chungthang outlet locations for the year 2008-2100. All the plots as per CMIP5 GCMs and RCPs showed consistent increasing trends in the 21st century. However, the magnitude change or increase/decrease variability in the streamflow are observed at both the locations. In Fig. 6.11, the months such as January, February, March, October and November show higher increase in the streamflow than other months. In Fig. 6.12, Chungthang shows almost increase in streamflow except July scenario. In the given projected time series plots, several extreme high peak flow events can be visualized.

In Fig. 6.12, the July month show decrease in streamflow over the Chungthang catchment. In Fig. (6.12), the December, January, October and November months show highest increase in the streamflow. The discharge can be enhance during this season due to faster snow melt. In this study, the streamflow also induced snow/glacier melt. Among all the GCMs, CM3 GSM showed maximum increase in their projected streamflows. All the scenarios, mean monthly and annual show that streamflow over catchment will be increased. In Figs. (6.11 and 6.12), March and April months show very lean flows except few scenarios.

TH-1643_136104018

TH-1643_136104018

Table 6.7: Change in Streamflows amount at Lachung and Chungthang between two intra-decades (2008-2050) and (2058-2100) as per CMIP5 GCMs and RCP experiments.

Outlets	Months	CM3 rcp26	CM3 rcp45	CM3 rcp85	CM3 avg	2M rcp26	2M rcp45	2M rcp85	2M avg	CM2P1 rcp45	CM2P1 rcp85	CM2P1 avg
Lachung	Jan	8.8	22.3	25.1	19.4	-2.2	11.3	23.3	12.2	3.4	27.7	19.3
	Feb	10.0	25.7	28.9	22.0	-3.1	13.3	28.6	14.4	3.9	34.1	23.1
	Mar	13.2	65.0	40.6	31.0	-2.4	20.2	44.8	20.4	5.2	49.0	35.6
	Apr	53.5	-0.7	73.1	135.7	6.7	90.9	26.4	41.2	-0.7	19.5	46.1
	May	3.6	13.1	11.7	7.9	2.2	3.9	-2.3	1.3	0.7	7.8	5.6
	Jun	9.8	25.0	25.7	16.8	1.3	6.9	9.6	6.9	3.7	14.8	12.0
	Jul	-4.2	-5.1	-11.8	-7.4	-3.5	-2.4	-4.9	-3.6	-6.0	-12.5	-10.7
	Aug	-2.1	6.2	7.7	-0.9	-0.1	3.3	8.7	4.2	1.5	3.0	2.8
	Sep	5.8	9.7	17.4	9.4	-2.8	7.2	9.7	5.7	1.3	24.2	17.7
	Oct	9.8	27.2	49.4	32.3	-2.3	18.4	40.6	20.4	7.8	42.0	33.1
	Nov	9.3	26.2	26.9	21.4	-2.3	13.0	26.9	14.1	3.8	33.3	19.5
	Dec	7.2	21.7	23.6	18.2	-2.5	11.3	22.7	12.0	3.1	26.1	17.9
Chungthang	Jan	5.7	24.0	34.5	21.4	-0.3	11.1	27.2	13.8	6.3	22.8	18.2
	Feb	6.7	32.8	39.9	25.1	-0.9	13.5	35.2	16.9	7.1	30.9	22.4
	Mar	33.5	58.1	89.7	53.1	0.8	23.9	50.3	25.7	4.0	14.4	34.3
	Apr	51.1	5.2	30.5	31.5	2.0	85.2	34.6	91.6	0.9	28.4	27.7

TH-1643_136104018

	May	5.9	15.4	19.7	13.2	1.4	4.2	3.3	3.6	3.3	6.3	5.2
	Jun	5.5	20.0	24.6	17.7	1.4	5.0	11.8	7.1	5.4	18.0	14.9
	Jul	-0.3	0.8	0.4	0.8	-0.9	0.2	1.2	0.3	-5.2	-7.6	-7.2
	Aug	-1.0	7.0	6.0	4.8	0.2	2.8	10.8	5.0	2.6	7.3	5.9
	Sep	4.9	10.1	14.8	11.0	-0.2	7.0	15.1	8.3	5.8	16.4	13.4
	Oct	6.0	24.9	52.7	30.5	-2.2	17.0	37.3	18.6	10.4	39.1	31.9
	Nov	6.4	25.8	44.2	25.3	-1.7	12.4	31.8	15.3	6.4	25.4	18.1
	Dec	4.9	21.4	33.0	20.2	-1.0	10.2	25.4	12.7	5.8	21.1	16.9

Indian Institute of Technology Guwahati

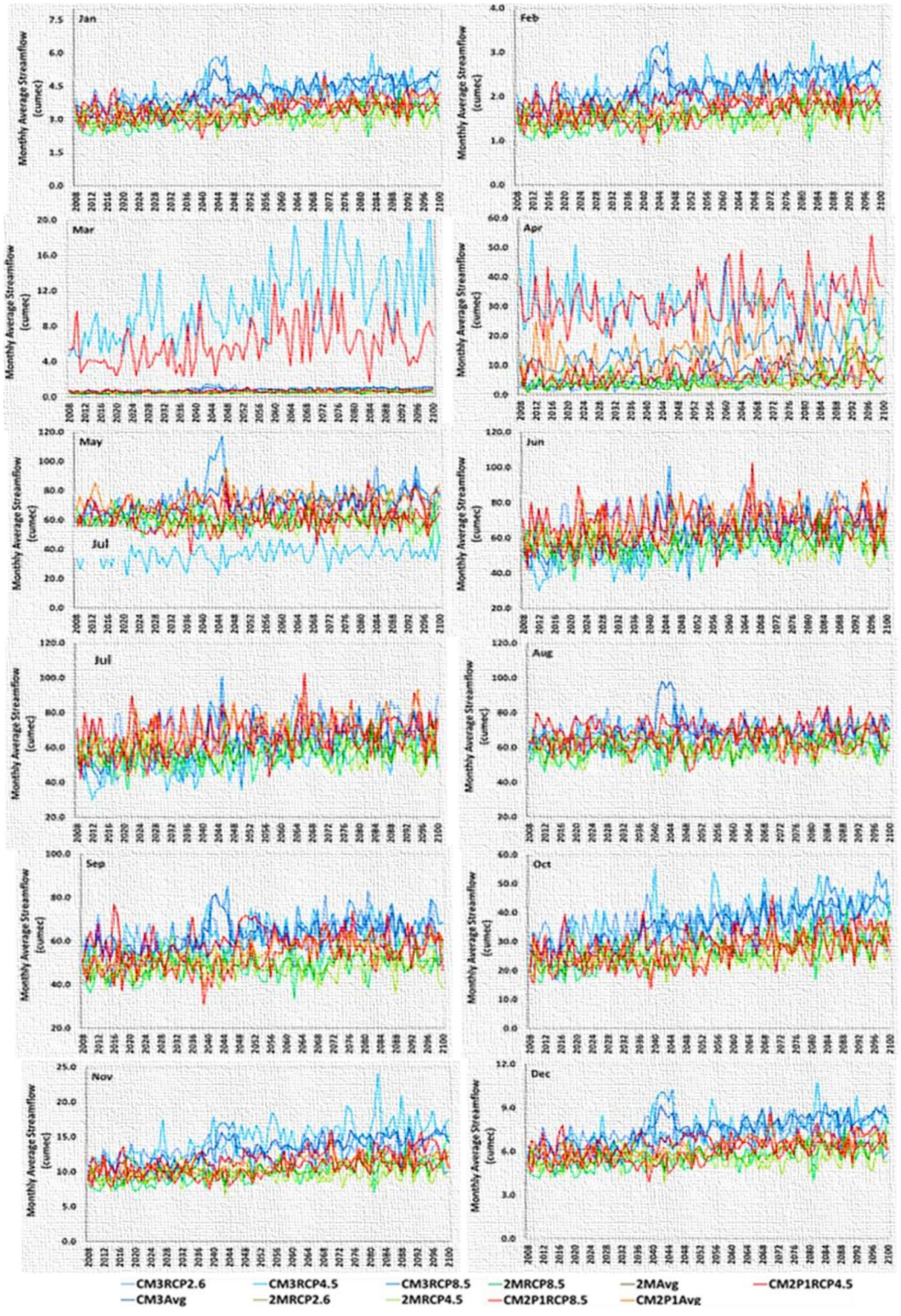


Fig. 6.11: Monthly projected trends of streamflow at Lachung outlet as per multimodel CMIP5 GCMs for the year 2008-2100.

TH-1643_136104018

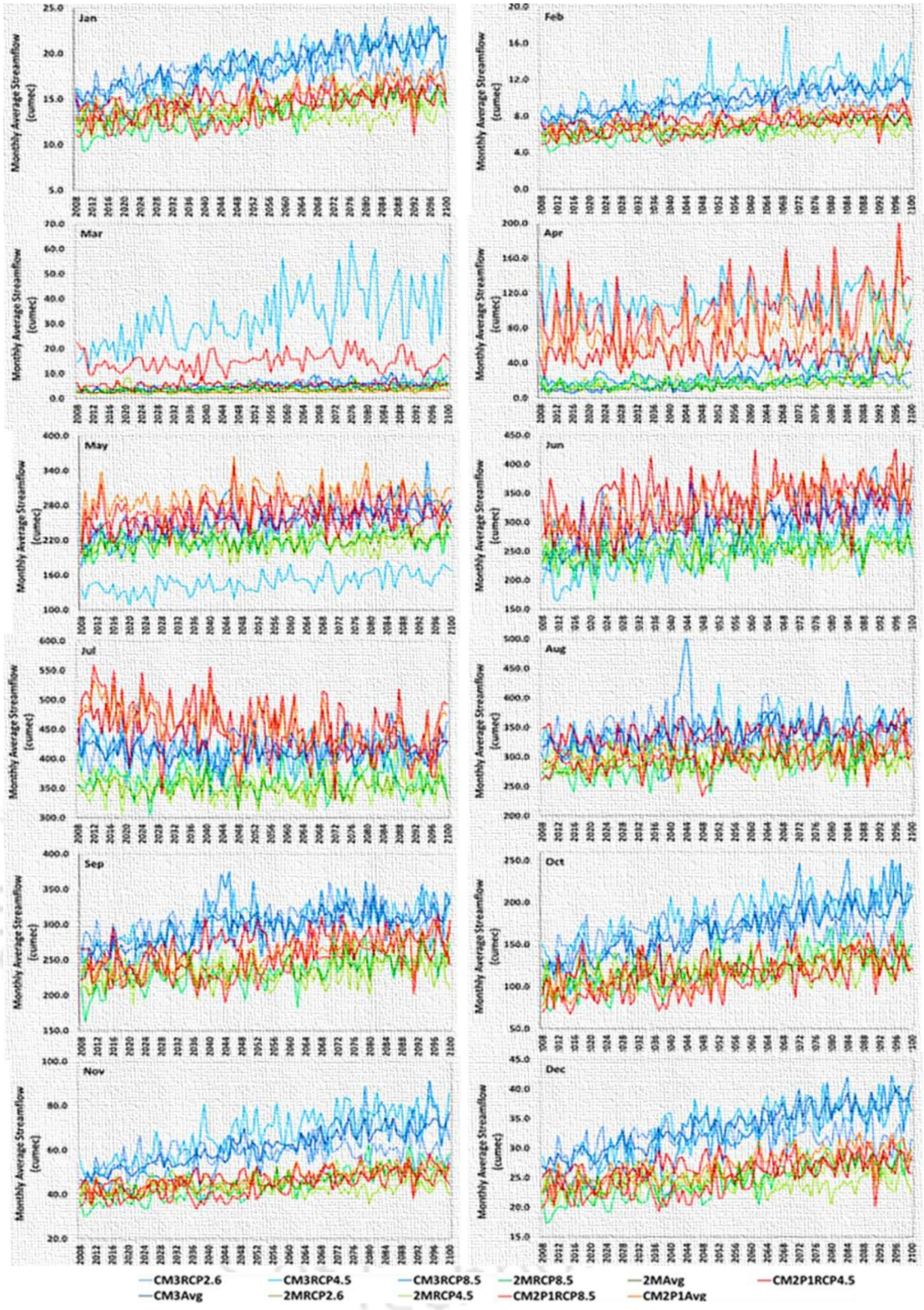


Fig. 6.12: Monthly projected trends of streamflow at Chungthang outlet as per multimodel CMIP5 GCMs for the year 2008-2100.

TH-1643_136104018

6.7 IMPROVED GSM-SOCONT MODEL: COUPLING AND COMPARISION WITH SWAT

The conceptual lumped linear reservoir approach based Glacier Hydrological Model (GSM-SOCONT) is modified and improved as per the Himalayan terrain conditions. In this model, the three main calibration parameters such as a_{snow_rad}, a_{ice_rad} and MF (melt factor) have been added to account for the net solar radiation effects on snowmelt process. The other parameters such as degree day factors for temperature (a_{snow}, a_{ice}), three linear reservoir coefficients (k_{slow}, k_{ice}, k_{snow}), maximum storage capacity of the slow reservoir (A), one non-linear reservoir coefficient for the direct runoff (β), melt factor (MF) also taken as existed initially. The TLR and PLR are varied for each elevation band. The calibration parameters and their performance details are given in the Table (6.8).

To setup the GSM-SOCONT model, the required inputs such as hypsometric curves (for glacier and non-glacier bands), daily PET, daily precipitation and daily average temperature have been taken. For the future projection of snowmelt and streamflows in the improved version of GSM-SOCONT model, projected watershed components such as daily streamflows, daily PET, resultant from SWAT model, have been selected to perform the study. Around 21% area of the catchment corresponded to ice/glacier covered and remaining areas come under non-glacier.

Therefore, four elevation bands created for the glacier part and 6 glacier bands are created for the non-glacier parts. The for each glacier band, TLR and PLR have been adjusted to define the precipitation and temperature. After doing the basic model input setup, various model parameters were optimized as listed in Table (6.8). The model parameterization and optimization results are given in Table (6.8). In Fig. (6.13), a separation of the rainfall discharge and icemelt + snowmelt from the total discharge have been shown. Fig. 6.13 shows the comparison in the observed discharge, model simulated discharge with radiation factor (Qsim_rad) and model simulated discharge without radiation (Qsim_wrad).

Table 6.8: Glacier Hydrological Model calibration parameter details and their coefficient values.

Times Series		Parameters	a_{ice} (temp.)	a_{sno} (temp.)	lk	A	beta	kgl	kn	a_{sno}w (rad)	a_{ice} (rad.)	MF (rad.)	RMSE
Historical Period	1991-2005	Initial Values	6	4.5	-8	1000	301	10	3	0	0	6	
		1st run with 500 iterations	5.62	5.12	-11.4	2360.7	324	24.52	12.04	0.25	0.08	1.66	6.78

TH-1643_136104018

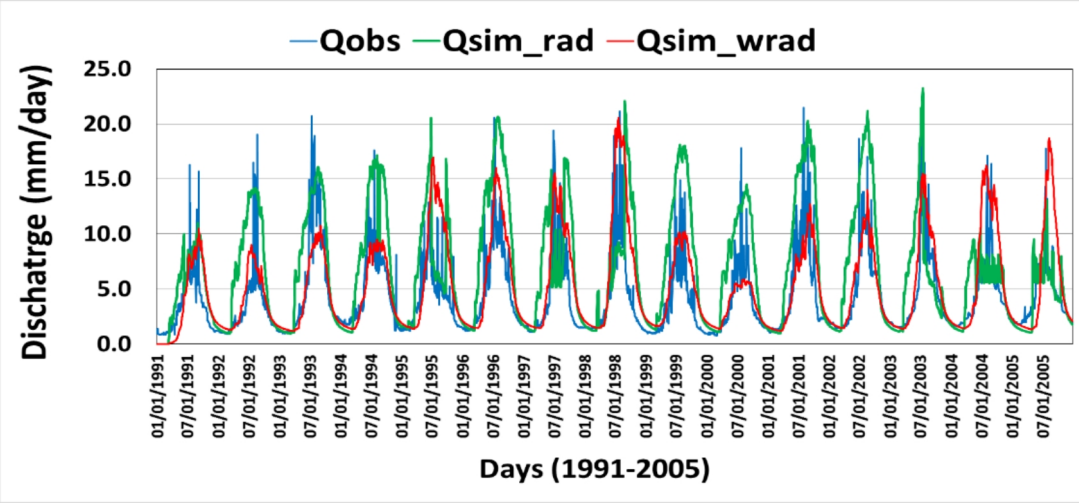
		2nd run with 500 iterations	0.05	2.46	-11.3	2674.2	975	6.84	23.29	0.86	0.02	4.17	4.24
		3rd run with 500 iterations	0.39	2.56	-7.97	1404	2516	16.2	8.7	0.57	0	4.04	6.85
		4th run with 500 iterations	0.21	1.64	-8.81	1515.7	2167	17.62	7.01	0.26	0.03	4.19	7.23
		5th run with 1000 iterations	0.11	1.65	-8.92	1523.5	2311	17.67	8.89	0.14	0.01	4.2	6.72
		6th run with 1000 iterations	0.03	2.34	-10.2	2601.7	984	6.53	23.44	0.27	0.01	4.22	6.33
		7th run with 500 iterations	0.1	2.28	-10.5	2580.8	903	5.48	24.13	0.57	0	4.02	5.92
CM3RCP2.6	2008-2100	Best Parameters Value	0.1	2.28	-10.5	2580.8	903	5.48	24.13	0.57	0	4.02	5.01
CM3RCP4.5		Best Parameters Value	0.03	2.27	-10.5	2542.7	929	5.4	21.06	0.74	0.01	4.31	6.29
CM3RCP8.5		Best Parameters Value	0.31	2.27	-10.5	2514.4	923	5.54	23.8	0.62	0.01	4.1	6.24
CM3Avg		Best Parameters Value	0.23	1.78	-10.5	2520.3	815	6.03	24.63	0.45	0.02	4.27	6.6
2MRCP2.6		Best Parameters Value	0.1	2.28	-10.5	2580.8	903	5.48	24.13	0.57	0	4.02	5.46
2MRCP4.5		Best Parameters Value	0.1	2.28	-10.5	2580.8	903	5.48	24.13	0.57	0	4.02	5.54

TH-1643_136104018

2M RCP 8.5		Best Parameters Value	0.03	2.27	-10.5	2542.7	929	5.4	21.06	0.74	0.01	4.31	6.15
2M Avg		Best Parameters Value	0.25	1.64	-10.3	2584	985	5.03	22.72	0.87	0	4.1	6.01
CM 2P1 4.5		Best Parameters Value	0.1	1.19	-10.4	2636.8	993	5.6	22.62	0.64	0.02	4.16	6.28
CM 2P1 RCP 8.5		Best Parameters Value	0.74	2.78	-10.1	2645.9	945	6.6	22.93	0.76	0.01	4.04	6.6
CM 2P1 Avg		Best Parameters Value	0.25	1.64	-10.3	2588.6	818	5.58	21.48	0.36	0	4.46	6.63

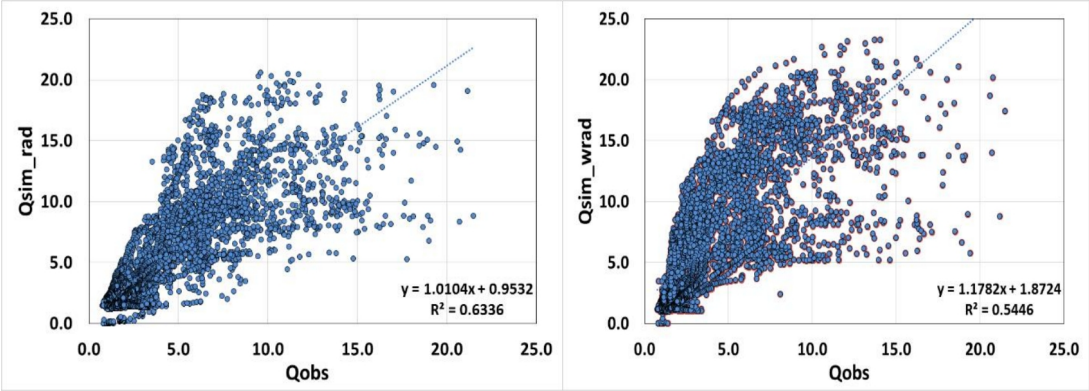
The regression plots show the line of fit between observed discharge and model computed discharge. The snowmelt contribution from non-glacier part and snowmelt+icemelt contribution from glacier part have been computed significantly and shown in Fig. 6.13 (c). In Fig. (6.13), the simulated discharge without radiation component has shown under predicted as compare to observed discharge. After adding radiation component with addition three parameters such as a_{snow_rad}, a_{ice_rad} and MF (melt factor), the computation efficiency of the modified significantly increased. The improvement in the simulated discharge can interpret in Fig. 6.13 (a).

(a)



TH-1643_136104018

(b)



(c)

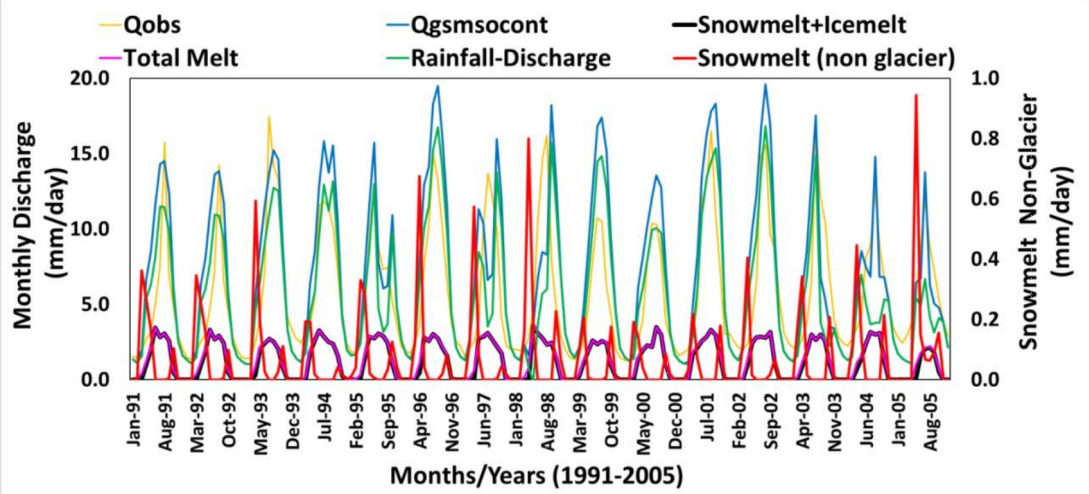


Fig. 6.13: Comparison of time series values simulated from GSM-SOCONT implementing radiation components: (a) Obs. vs Qsim_rad vs Qsim_wrad, (b) scatter plot between Qsim_rad vs Obs. discharge and (c) Separation of GSM-SOCONT simulated discharge (Qgsmscon).

Table 6.8 shows the model optimization results in two different time series domains such as historical (1991-2005) and futuristic (2008-2100) assessment under multimodel CMIP5 GCMs and RCPs. For optimizing best coefficient values of the selected model parameters, several iteration numbers are performed. It utilizes Monte-Carlo simulation based approach for the model optimization and parameter sensitivity analysis (Schaefli et al., 2005). The whole computation and optimized coefficients have been opted using 7 iterations.

The best parameter results and their annual average RMSE values have been shown. The overall results found reasonable accepted. Total 12 projected ensembles have been generated as per the CMIP5 GCMs and RCPs. To obtain the best simulation outcomes, five iteration along with 1000 simulation/each iteration/each projected scenario has been run. The best

TH-1643_136104018

computational outcomes identified by the calculated root mean square error (RMSE). The beast parameters were opted as per the minimum RMSE.

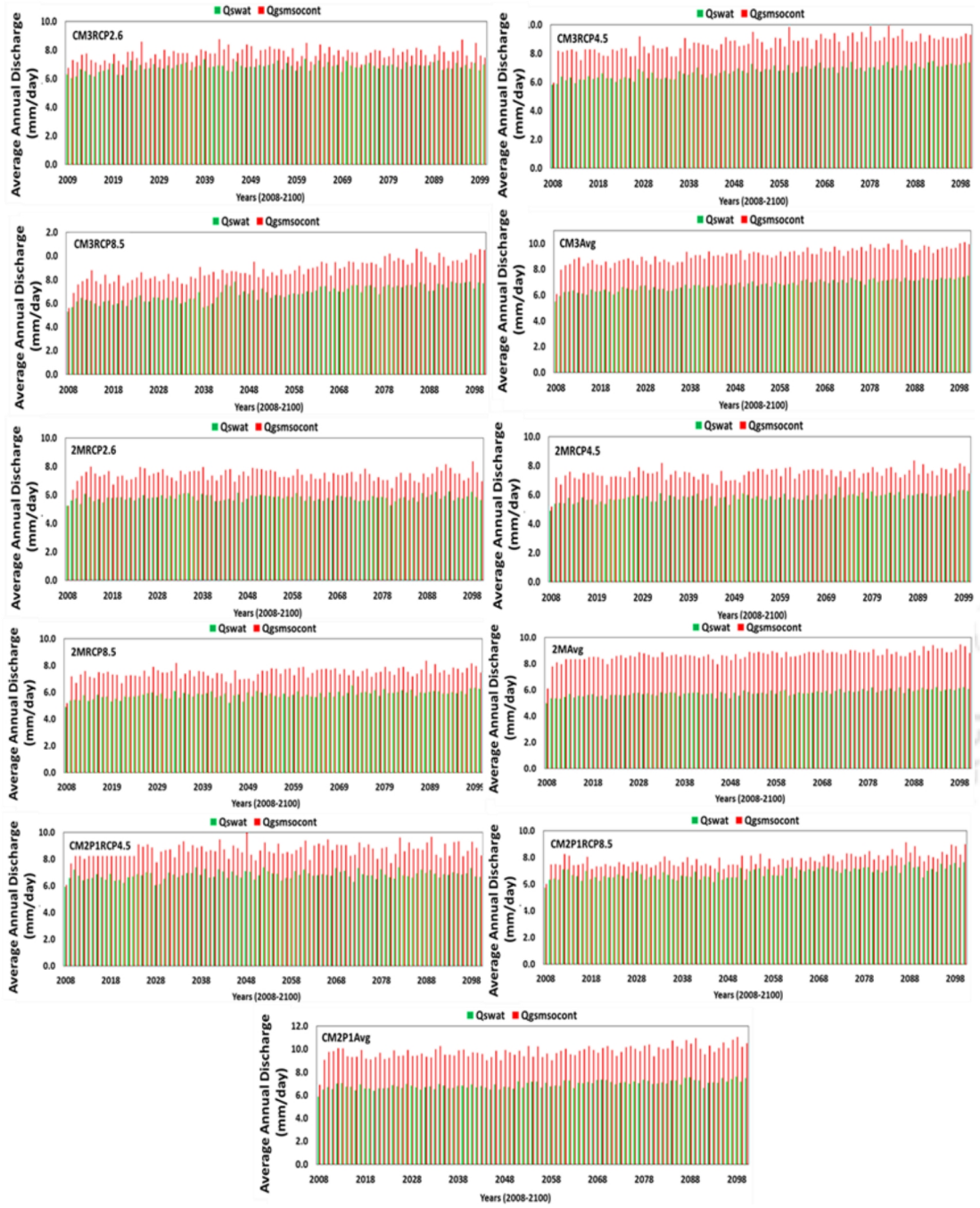


Fig. 6.14: Times series plots and comparison between the SWAT projected streamflows and improved GSM-SOCONT projected streamflows at the catchment outlet (Chungthang) (2008-2100).

Fig. 6.14 shows the annual time series plots for the future scenarios (2008-2100) which compare the streamflows simulated from SWAT and improved GSM-SOCONT. All the projected scenarios of streamflow show similar pattern and reasonable correlation between

TH-1643_136104018

them. In Fig. 6.14, one can notice that SWAT based streamflows little bit less predicted as compared to improved glacier hydrological model. This could be elaborate with the icemelt contribution, which is present in the improved version of glacier hydrological model. The average scenarios show slightly under predicted, while several scenarios show very less variations in the projected streamflows. In Fig. 6.14, projected scenarios show that the streamflow will be increased in the 21st century.

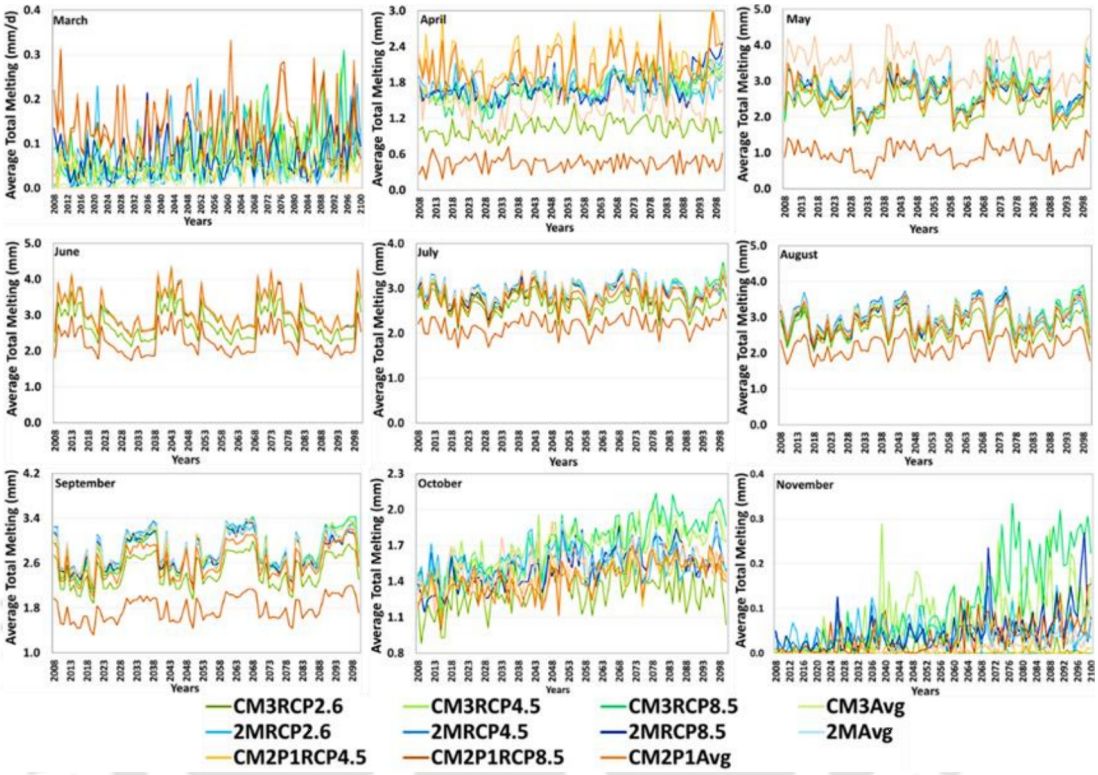
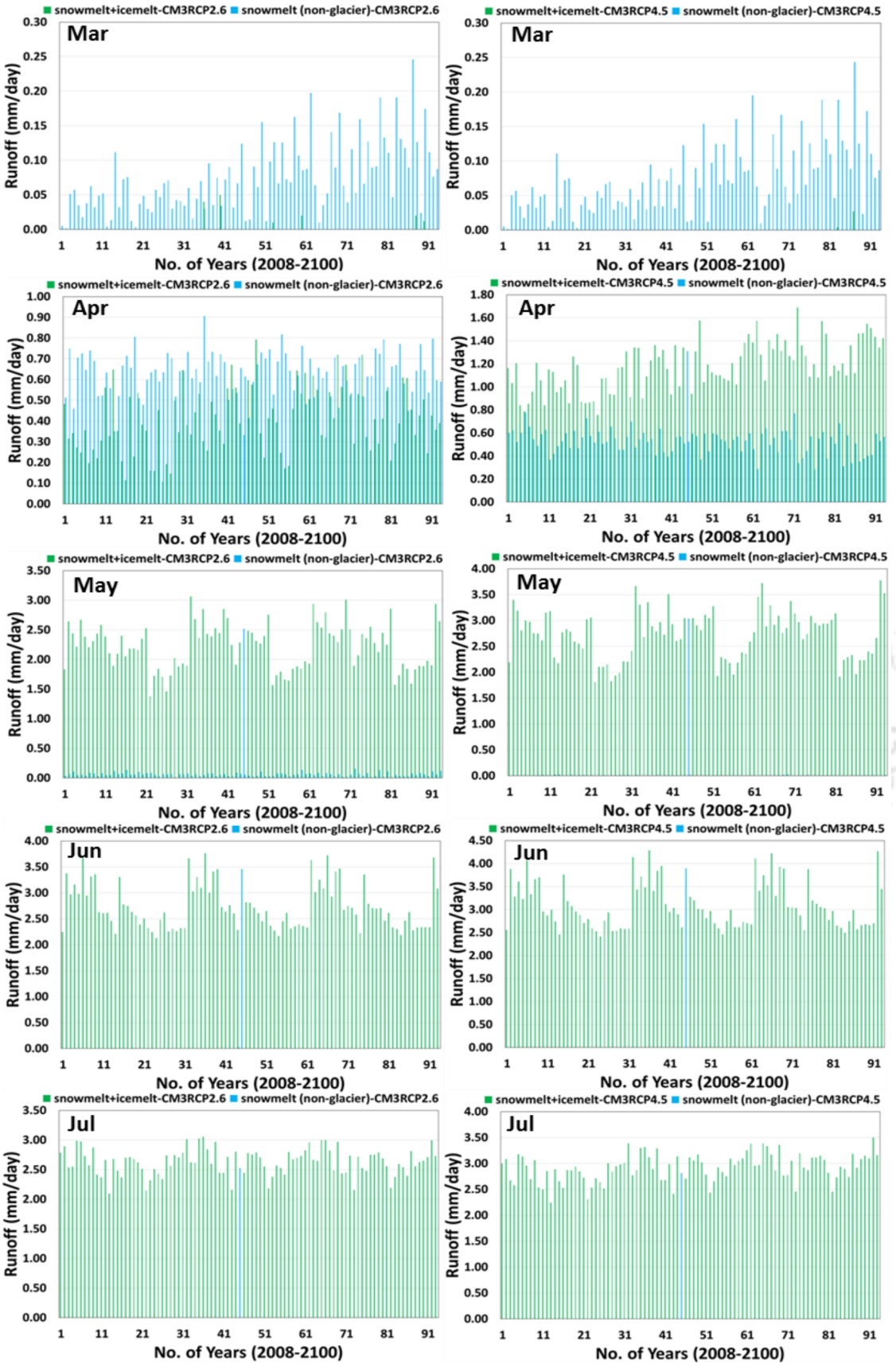


Fig. 6.15: Total snowmelt contribution at Chungthang outlet simulated from improved GSM-SOCONT model under CMIP5 GCMs and RCPs.

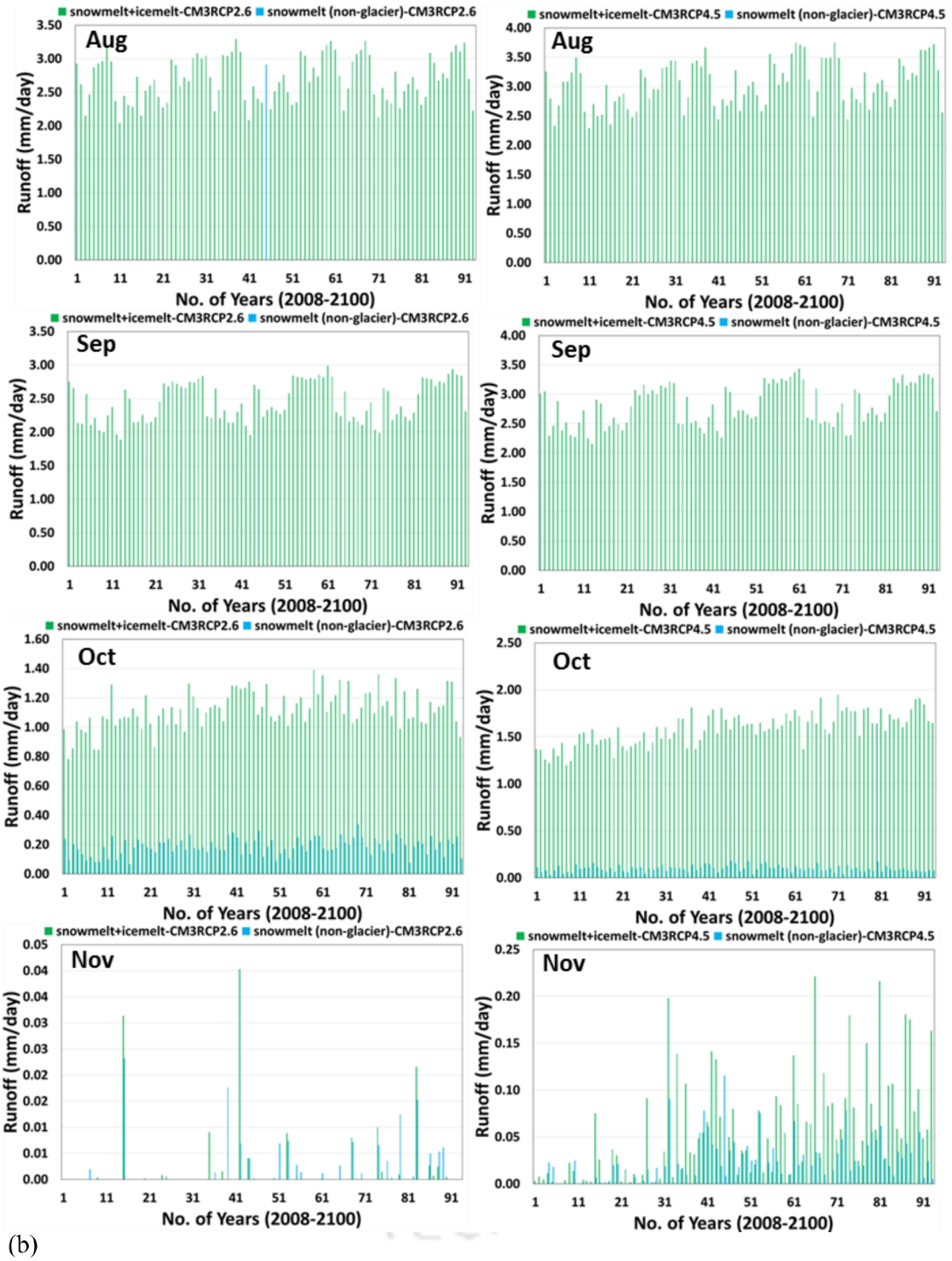
Fig. 6.15 shows the improved GSM-SOCONT model based projected total snowmelt contribution at the catchment outlet (Chungthnag) for the year 2008-2100 under CMIP5 . The model is initially evaluated for the war-up years (2006-2007). Most of the snowmelt contribution is recorded during March to November. In April, May and June months, it contributed enormously. It these months, the snowmelt ranges vary from 0.5 mm/day to 5 mm/day as shown in Fig. (6.15).

TH-1643_136104018



(a)

TH-1643_136104018



(b)

Fig. 6.16: Projected scenarios of icemelt/glacier melt runoff and snowmelt runoff (non-glacier) from improved GSM-SOCONT model for the year 2008-2100.

The October and November months also account snowmelt runoff because in these months significant amount of snowfall has recorded. As the snowmelt is projected for the long duration time series (2008-2100) under CMIP5 GCMs and RCPs, the trends show significant variability in the snowmelt runoff during 2008 to 2100. The monthly variations can also be seen in Fig. 6.15. The months such as March, April, September, October and Noverber show

TH-1643_136104018

a consistent increaseing trend in the snowmelt runoff during 2008 to 2100. These projections uncer CMIP5 GCMs and RCPs suggest, in 21st century, snowmelt will be faster than prersent and the snow melt variability will be increased.

Fig. 6.16 shows the projected scenarios (2008-2100) of icemelt + snowmelt contribution (glacier part) and snowmelt contribution (non-glacier part) at the Chungthang outlet computed from improved GSM-SOCONT model. The non glacier part snow cover and snow/ice cover/glaciers from glacir part start melting from March. In Fig. 6.16, it can onserve that upto April, the temporary snow cover, corresponded to non glacier part, generally melt. Though, the snow cover/ice which corresponded to glacier region, continue their melting till November. In Fig. 6.16, the separation of snowmelt from the glacier part and non-glacier part can be understood. In the months such as October and Noverber months, the Teesta river catchment contributes snowfall and thus, during these months, snowmelt has been accounted in Fig. 6.16. Though, these snow melt shows the projected scenarios from 2008-2100 under CMIP5, an increase in the snowmelt (both the glacier part and non-glacier part) has been recorded, especially during March, April, October and November. As per the literature review, these months are very critical for the snowmelt process and increase in these months, in the projected scenarios (2008-2100) can be a indication of glacier retreating over the selecetd study region.

6.8 ELEVATION BAND APPROACH FOR PROJECTING SNOWFALL-SNOWMELT AND THEIR CHANGE ASSESSMENT UNDER CMIP5 GCMs

SWAT model calculates snowfall and snowmelt runoff by utilizing elevation band approach and temperature index model (Neistch et al., 2011). In SWAT model for every sub-catchment, maximally 10 elevation bands can be computed and analyzed. The additional parameters such as TLR, PLR, degree day factor, melt rate coefficient and snow depletion curves (SDC) are computed to account the snowfall and snowmelt (Reference to previous work). To comprehend this objective, CMIP5 GCMs and RCPs based downscaled daily temperature and precipitation datasets and projected TLRs and PLRs at each catchment, were taken into account. The degree day melt factor, especially for Himalayan terrains, is opted from the detailed literature review (Singh and Kumar, 2009, Hook, 1996). It has improved the modeling accuracy.

The sub-catchment wise estimation of snowmelt runoff during historical time period (1991-2005) have been shown in Fig. 6.17. In Fig. (6.17), one can notice significant variations in the snowfall amount and snowmelt amount. The contribution of snowfall and snowmelt vary from sub-catchment (SB) 1 to SB7. The highest amount of snowfall and snowmelt are computed over the high elevation based SBs such as SB1, SB2, SB3 and SB4. Whereas, SB5, SB6 and

TH-1643_136104018

SB7 are recorded less contribution of snowfall and snowmelt. The snowfall and snowmelt amount fluctuate from 1991 to 2005. The initial years (1991-1998) of the time series (1991-2005) show higher amount of snowfall and snowmelt than later years (1999-2005).

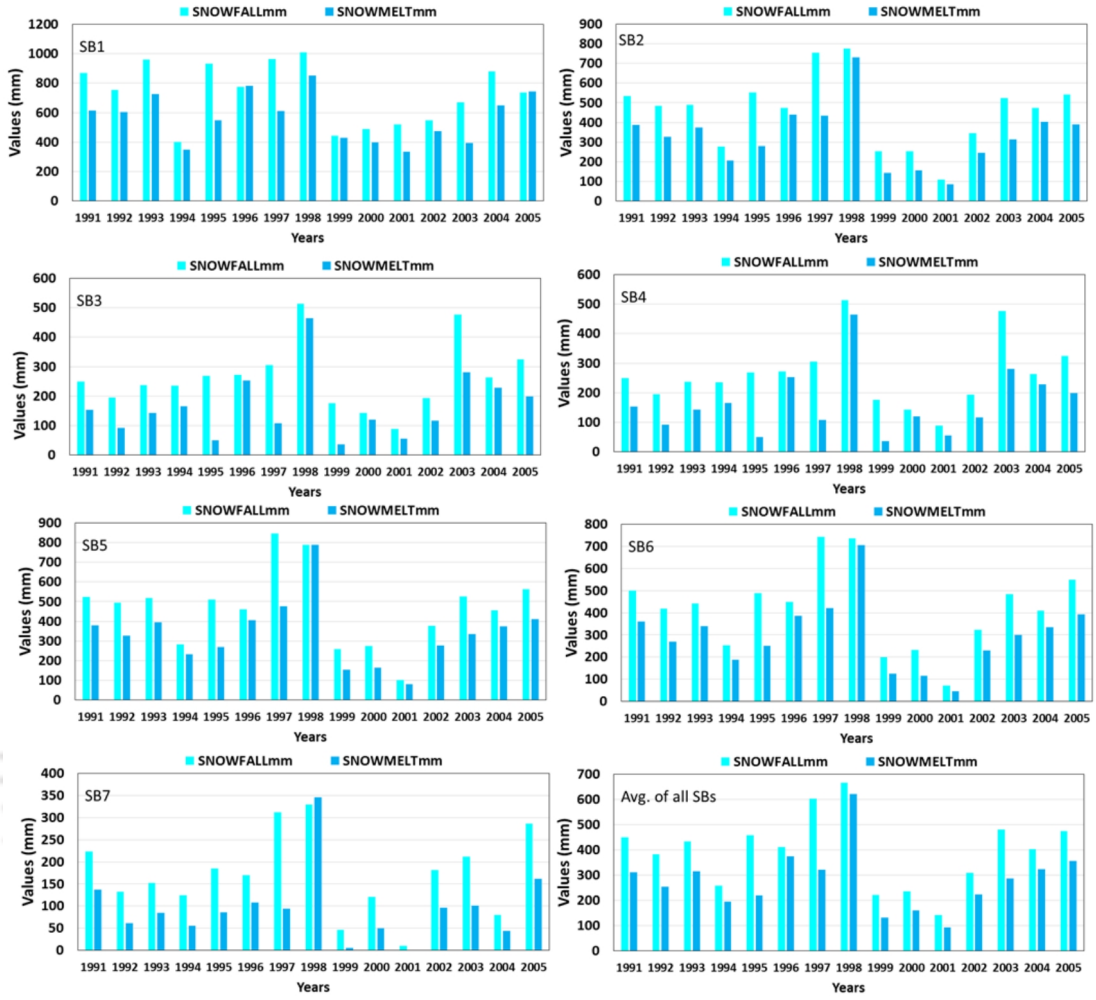


Fig. 6.17: Annual snowfall and snowmelt at each sub-catchment for the historical time (1991-2005) simulated from SWAT.

Figs. (6.19 and 6.21) show the monthly snowfall (snowpack) contribution at each sub-catchment (SB) scale projected using elevation band approach in SWAT. The snowfall has been projected for the year 2008-2100 and the initial 2 years datasets are taken as the warm-up years (2006-2008). The snowfall projected scenarios resulted for the year 2008-2100. The degree day approach based on temperature index model has been adopted for accounting snowfall at each-sub catchment. Different monthly TLRs and PLRs are calculated and defined for each sub-catchment. The snowfall is calculated based on the 10 elevation bands defined for each sub0catchment.

Figs. 6.18 and 6.19 show the monthly variations in snowfall at each sub-catchment (SB) scale in the 21st century time as per CMIP5 ESM-2M GCMs and RCPs (RCP2.6, RCP4.5, RCP8.5

TH-1643_136104018

and average of all RCPs). The plots show times series for the months which have contributed snowfall, because several months such as (May to September) did not account snowfall over the selected study region. The projected scenarios of snowfall show high spatial variability over the catchment in the given time (2008-2100). The SBs such as SB1, SB2, SB3 and SB4 show maximum amount of snowfall than other SBs. In these high elevation SBs, the maximum amount of snowfall vary from 60 mm to 300 mm, estimated especially in the winter months (November to April).

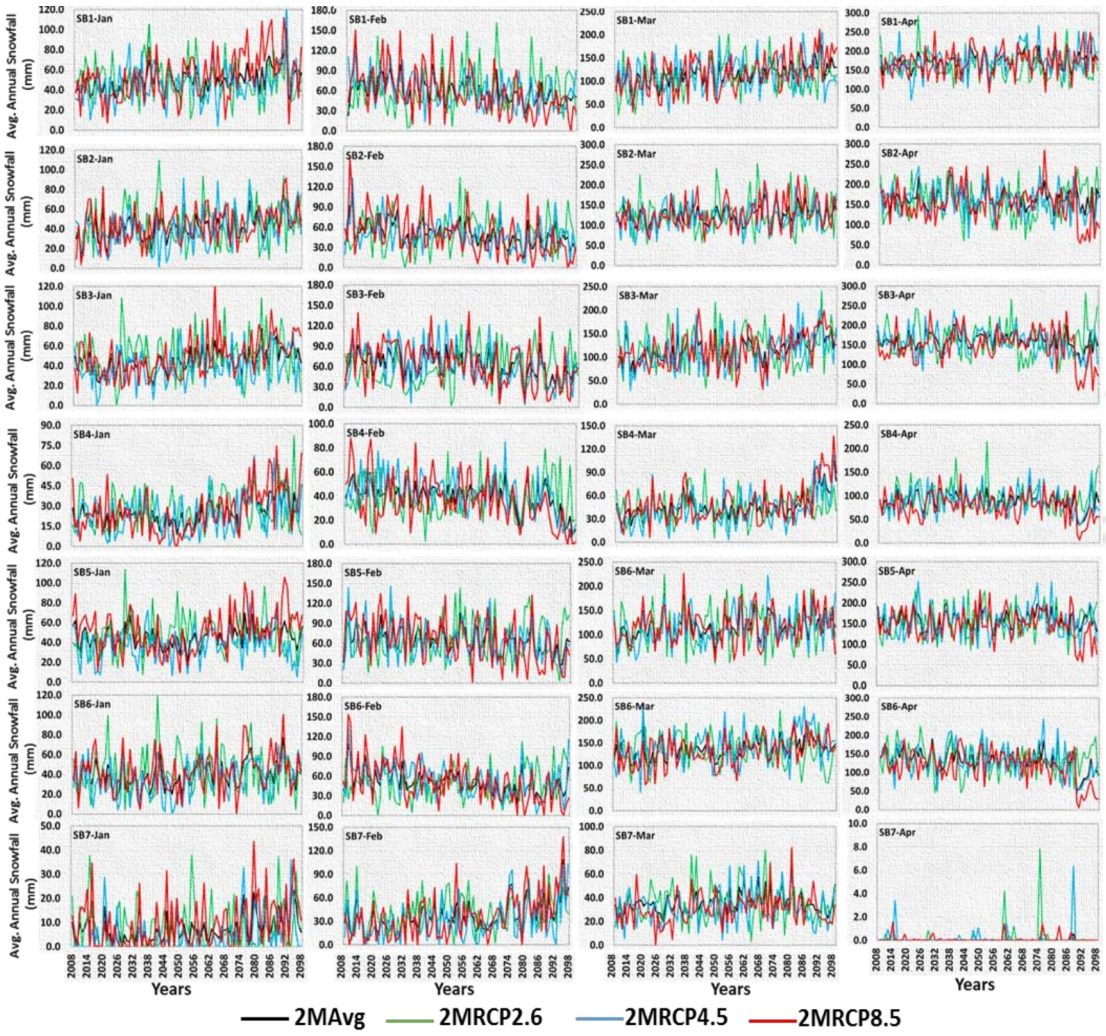


Fig. 6.18: SWAT simulated monthly variations in snowfall during January to April under CMIP5 ESM-2M GCMs and RCPs during 2008-2100.

TH-1643_136104018

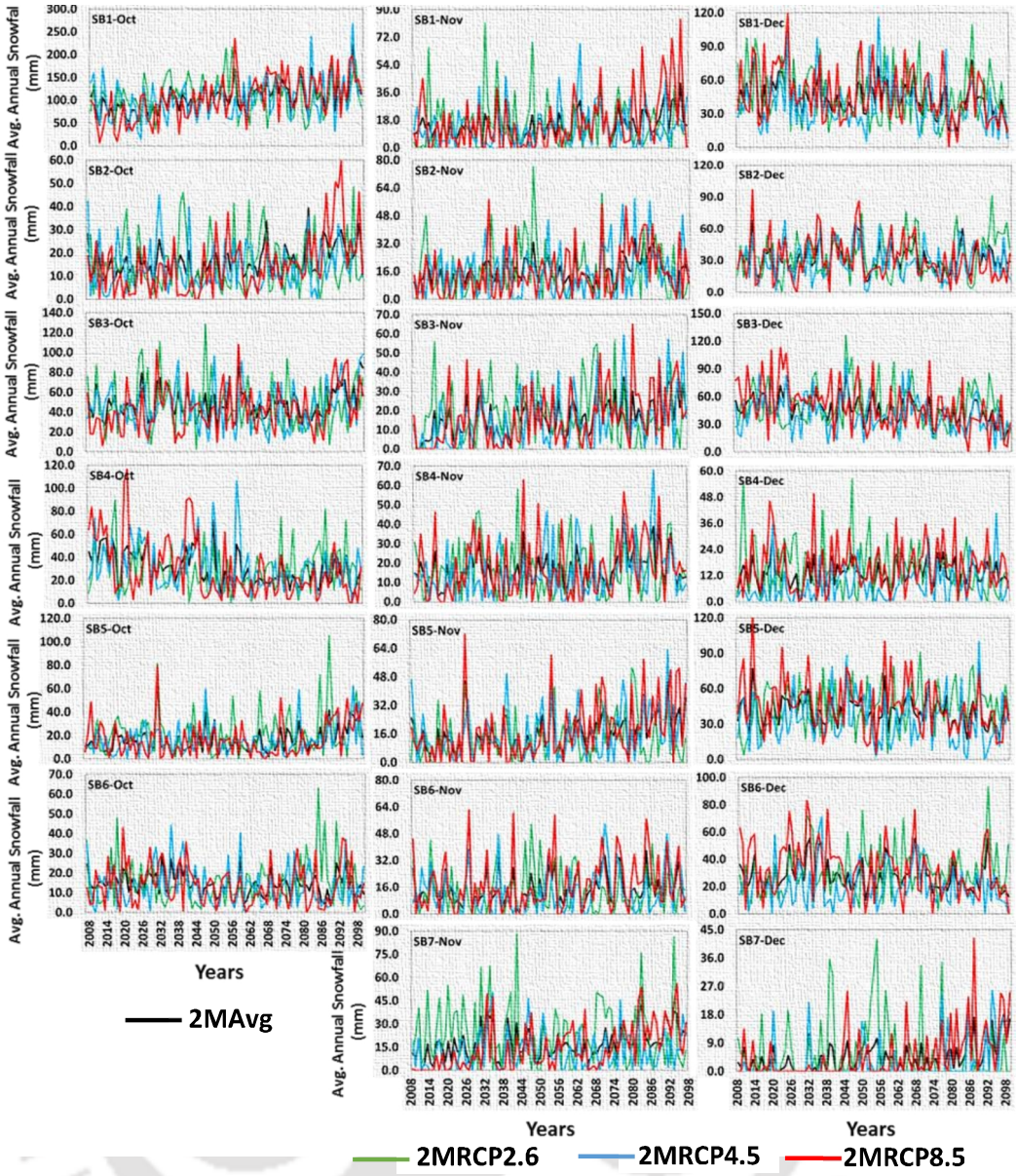


Fig. 6.19: SWAT simulated monthly variations in snowfall during October to December under CMIP5 ESM-2M GCMs and RCPs during 2008-2100.

Among all the months, February and March have contributed highest amount of snowfall. In Fig. (6.19), the October month contributes adequate amount of snowfall. In the Figs. 6.18 and (6.19), the months such as February, April, October and December show decrease in snowfall, while several months such January and March show slight increase in the snowfall amount, especially at high elevation SBs (e.g. SB1, SB2, SB3 and SB4). Each RCP of ESM-2M model shows enormous spatial variability from SB1 to SB7. Figs. (6.20) and (6.21) show the monthly variations in snowfall at each sub-catchment (SB) scale in the 21st century time as per CMIP5 CM3 GCMs and RCPs (RCP2.6, RCP4.5, RCP8.5 and average of all RCPs.

TH-1643_136104018

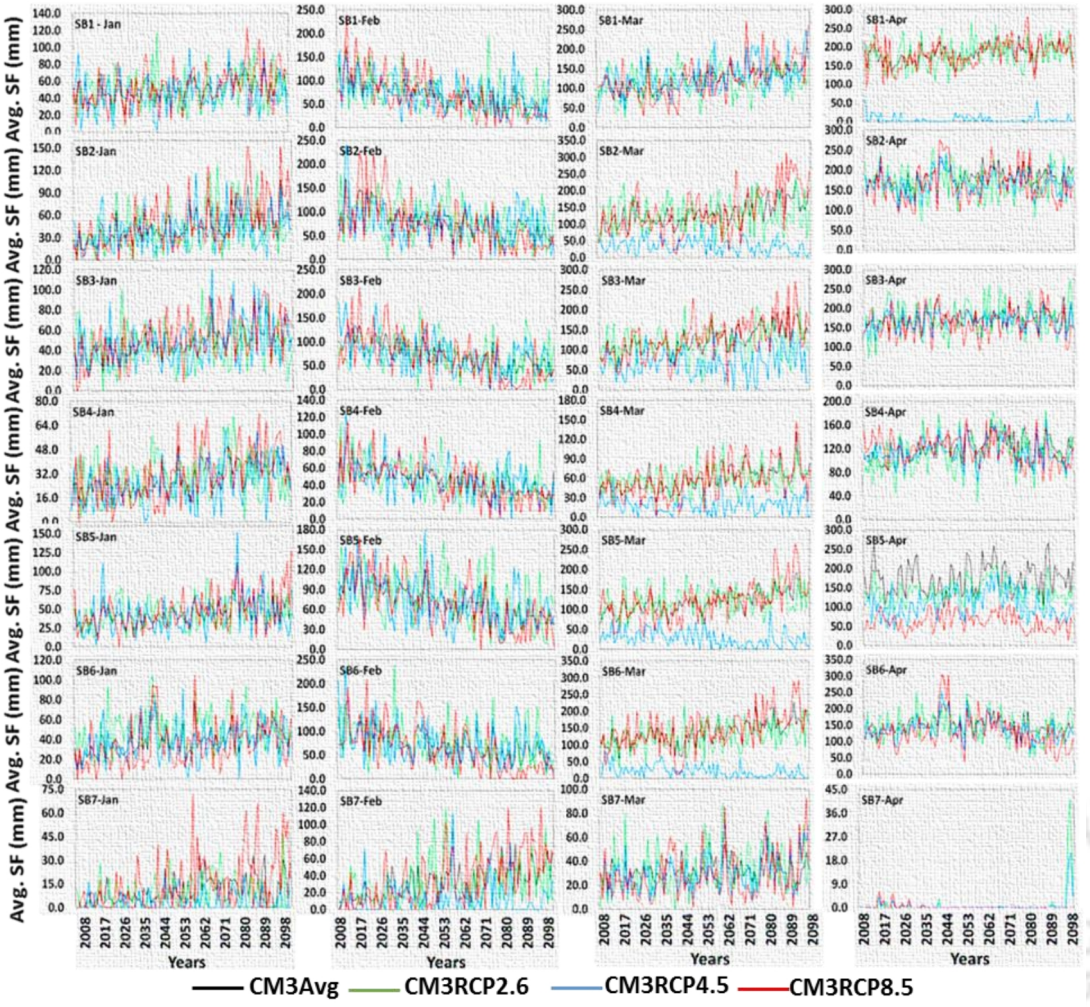


Fig. 6.20: SWAT simulated monthly variations in snowfall during January to April under CMIP5 CM3 GCMs and RCPs during 2008-2100.

In Figs. (6.20 and 6.21), almost similar trends were observed for the CMIP5 CM3 model. The February, April, October and December months show decrease in the snowfall, while January, March and November months show increase in the snowfall during 2008 to 2100 as per multiple RCPs. The increase in the snowfall is mostly observe at the high elevation SBs. While comparing the emission scenarios, the extreme scenario (RCP8.5) show maximum decrease in the snowfall during February, April and December Months. In October, it shows decrease in snowfall except SB1, SB2 and SB2. The low emission scenario (RCP2.6) and moderate emission scenario (RCP4.5) also exhibit high spatial variability in the increase and decrease trends. As per the projected scenarios, the peaks of increase and decrease of snowfall maximally fluctuated in the last decadal years (after 2060s) of the time series. The overall projected scenarios, as per CMIP5 GCMs and their emission scenarios, show that the snowfall variability will be enhanced in the future over the Teesta river catchment.

TH-1643_136104018

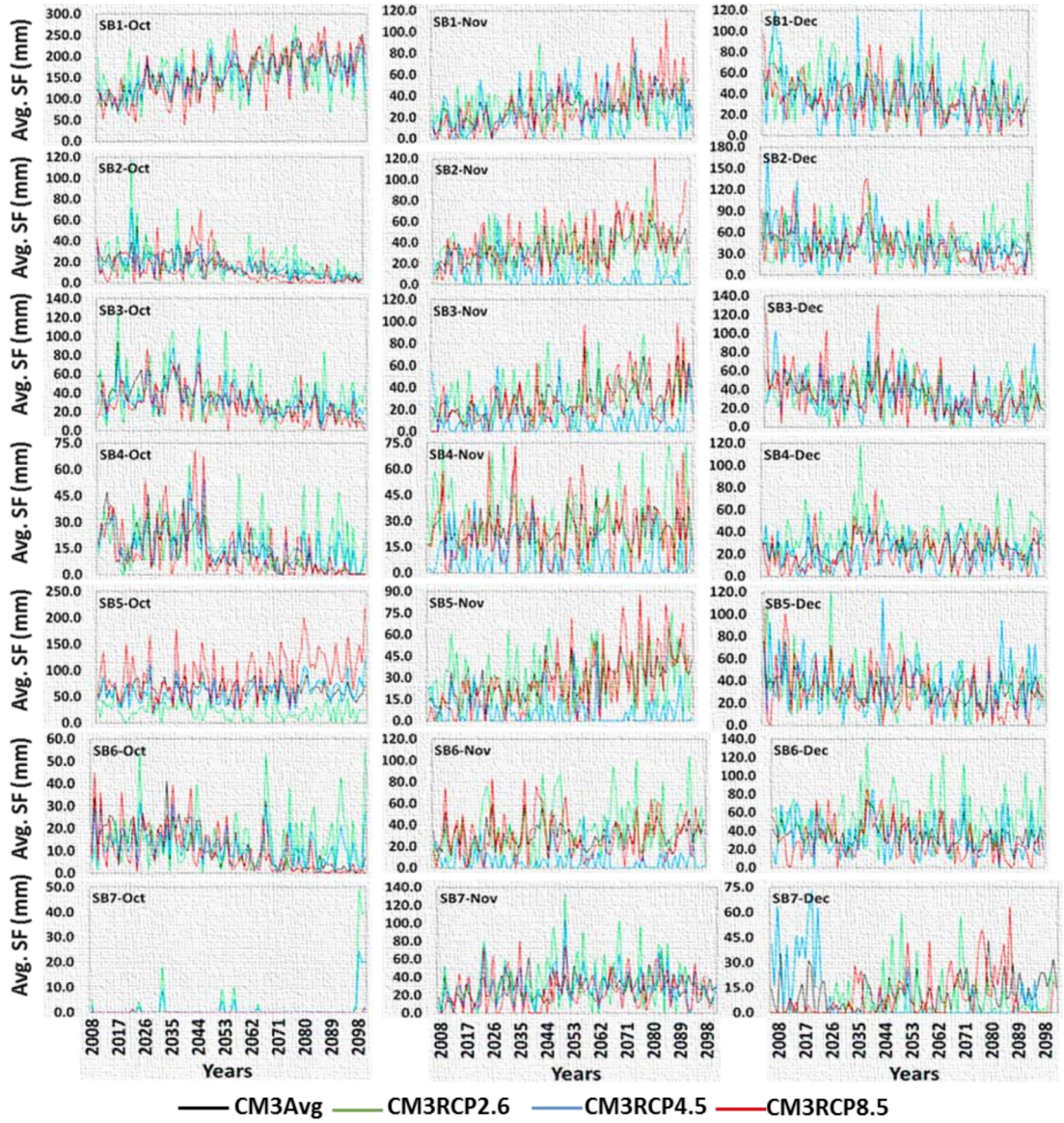


Fig. 6.21: SWAT simulated monthly variations in snowfall during October to December under CMIP5 CM3 GCMs and RCPs during 2008-2100.

Figs. (6.23, 6.24 and 6.25) show the SWAT simulated monthly variations in the snowmelt amount calculated at each sub-catchment in the projected time series (2008-2100) under CMIP5 ESM-2M (RCP2.6, RCP4.5 and RCP8.5), CM3 (RCP2.6, RCP4.5 and RCP8.5) and CM2P1 (RCP4.5 and RCP8.5) GCMs. In Figs. (6.23, 6.24 and 6.25), the projected scenario show high spatial variability in the snowmelt from SB1 to SB7 in the given time scale (2008-2100). In the winter months such as March and April, the low elevation SBs such as SB7, SB6 and SB5 show adequate amount snowmelt contribution from 2008 to 2100. These SBs corresponded with temporary snow cover, which melts earlier than permanent snow cover/ice/. In the high elevation SBs, snowmelt process starts from March and hence, the SBs such as SB1, SB2, SB3 and SB4 account snowmelt during April, May, June and July months (Figs. 6.23, 6.24 and 6.25).

TH-1643_136104018

However, as per the projected extreme emission scenarios such as RCP8.5, it shows that the snowmelt starts in the February and it melts unto May. In these Figs. (6.23, 6.24 and 6.25), it can also be observed that the snowmelt starts earlier winter months such as November and December. This highlights the shift in the projected snowmelt observed in the CMIP5 GCMs. Over the Teesta catchment, the upstream portion corresponded to high elevation and lower part corresponded with moderate to low elevation topography. Thus, snowfall and resultant snowmelt fluctuate throughout the year. As per the results revealed above, all these climate models altogether show enormous variability in the snowmelt over the selected study region.

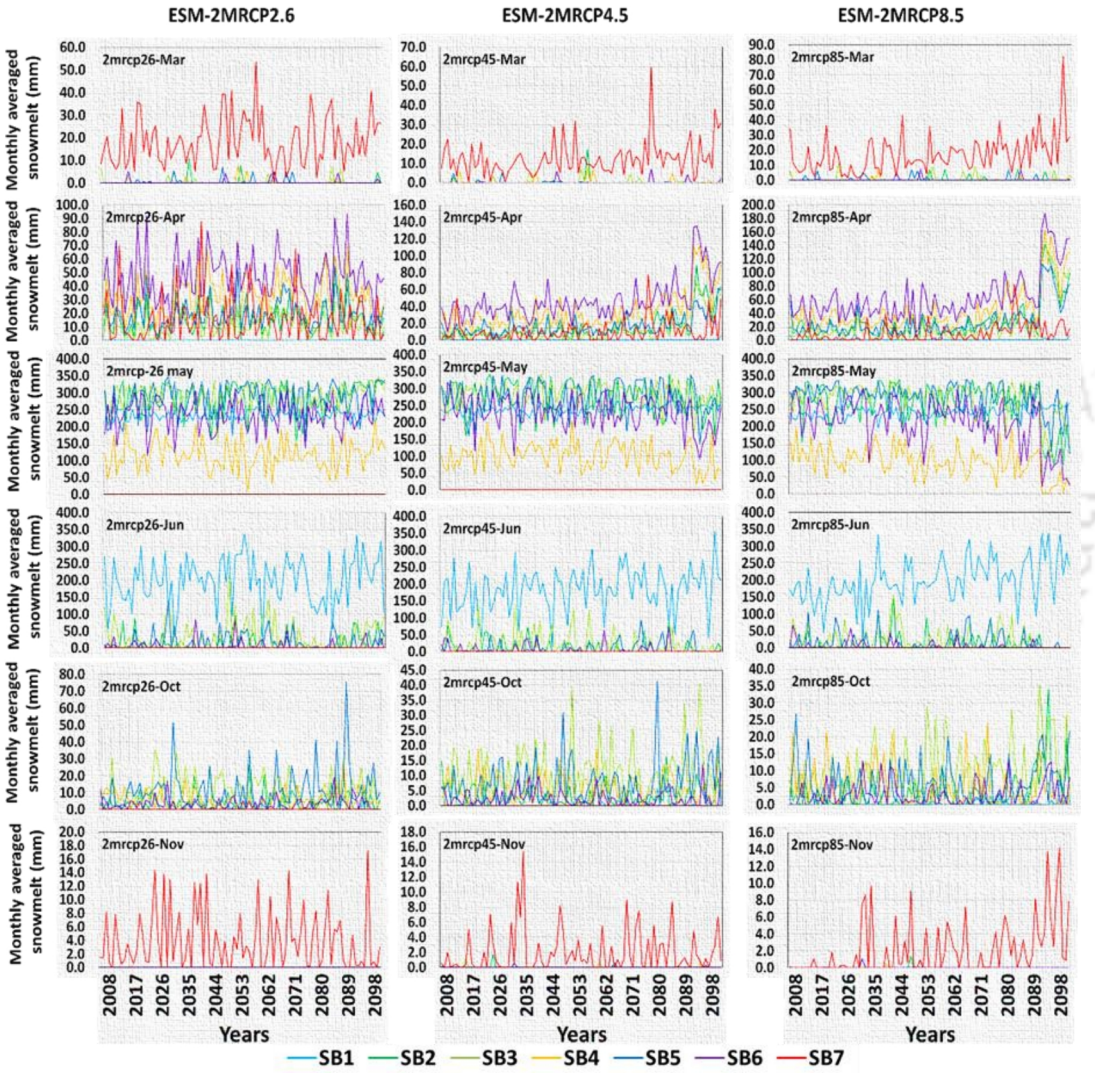


Fig. 6.22: SWAT simulated monthly variations in snowmelt during March to November under CMIP5 ESM-2M GCMs and RCPs during 2008-2100.

While comparing in the increase and decrease, most of scenarios (Figs. 6.23, 6.24 and 6.25), across all the sub-catchments, show slight increase in the snowmelt process. In the months such as March, April, October and November, consistent increase in the snowmelt, across the scenarios and sub-catchments, can observe in the progressive manner from the year 2008 to

TH-1643_136104018

2100. There is no consistent decrease trends observed for the snowmelt process during 2008-2100 in all the scenarios and SBs. The overall projected scenarios show that the severity of faster snowmelt will be enhance especially after 2050s (Figs. 6.23, 6.24 and 6.25).

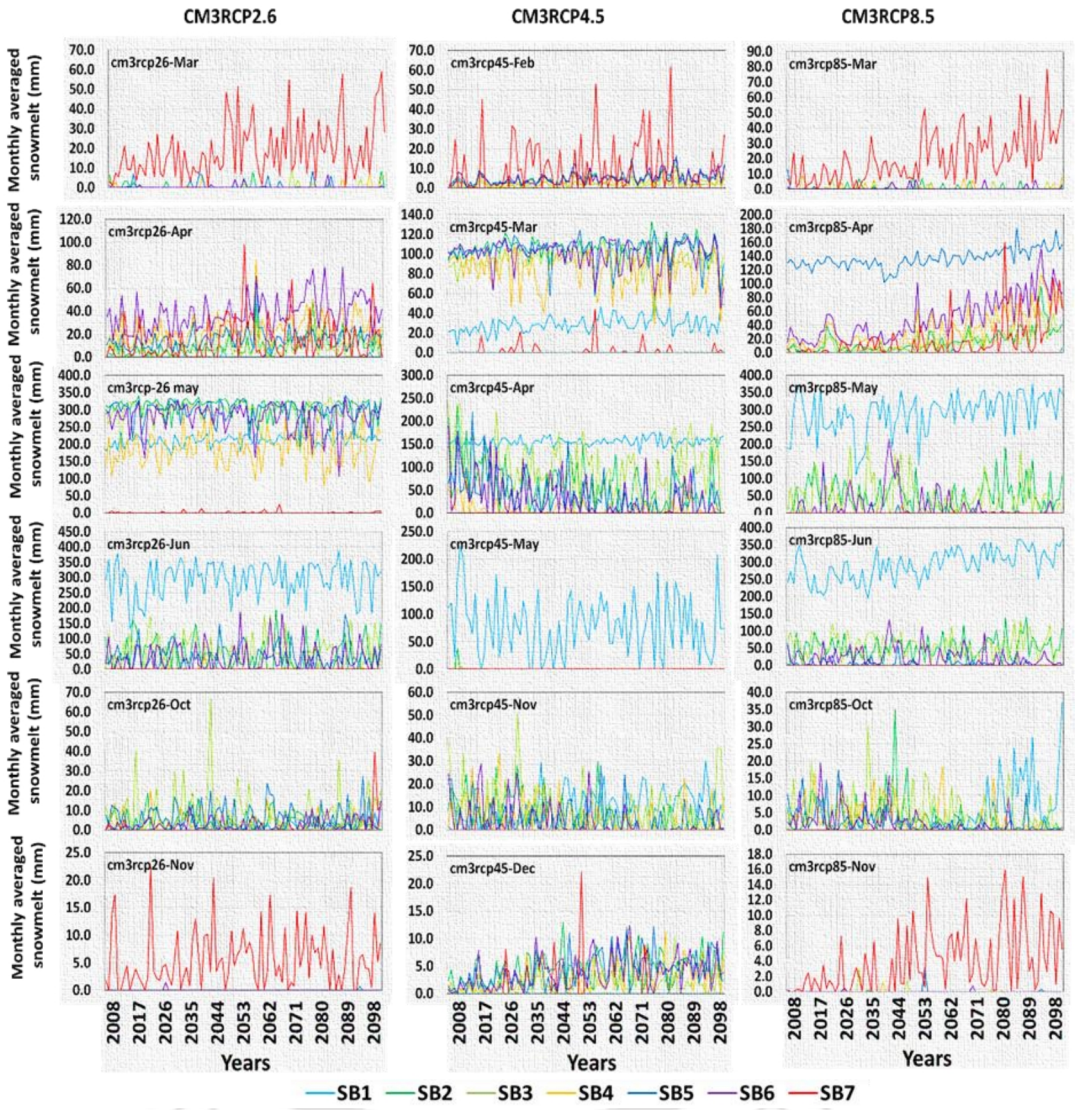


Fig.6.23: SWAT simulated monthly variations in snowmelt during March to November under CMIP5 CM3 GCMs and RCPs during 2008-2100.

TH-1643_136104018

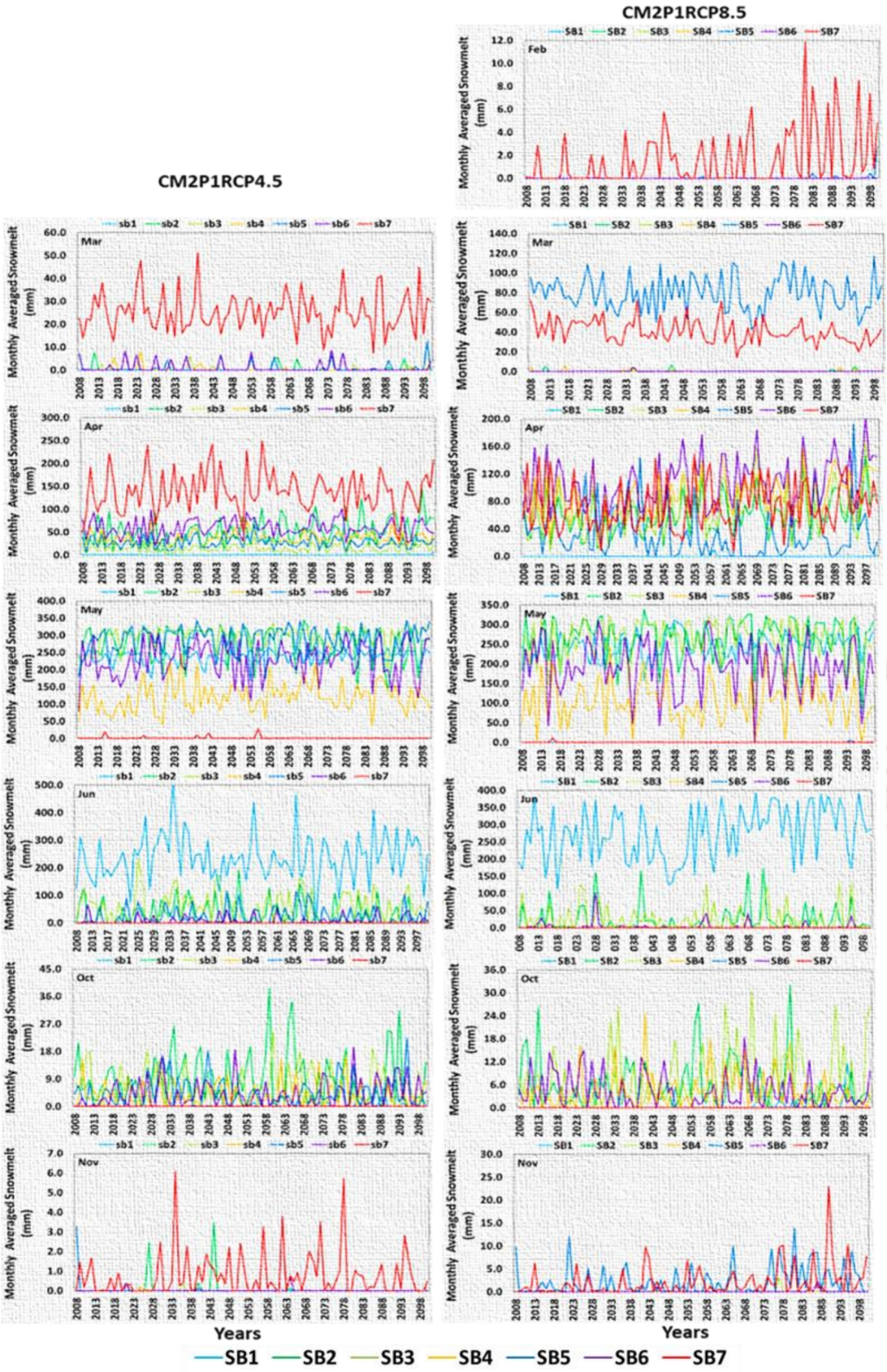


Fig. 6.24: SWAT simulated monthly variations in snowmelt during March to November under CMIP5 CM2P1 GCMs and RCPs during 2008-2100.

TH-1643_136104018

Table (6.9) shows the percent (%) of change in snowmelt and snowfall (average annual in mm) at the whole catchment scale during intra-decadal time series (TS) duration (TS1-2011-2035, TS2-2041-2065, and 2076-2100) as per resultant from SWAT model under CMIP5 GCMs. At catchment scale, Table (6.9) shows enormous variability in the snowmelt and snowfall during intra-decades. In the snowfall, mixed responses of increase and decease are obtained, while in snowmelt most of the trends show increase in snowmelt among the Inter comparison of times series (TS1 to TS2, TS1 to TS3 and TS2 to T3).

The moderate and extreme emission scenarios (e.g. RCP4.5 and RCP8.5) show significant increase and decrease in snowfall and snowmelt. In case of snowfall, among all the scenarios, the maximum decrease and increase are recorded as -142 and 60 (mm), respectively. In case of the snowmelt, the maximum increase is recorded as 124.7 (mm) and maximum decrease is recorded as -76.6 (mm) as per shown in Table (6.9).

Table 6.9: Percent (%) change statistics of average annual snowmelt and snowfall in intra-decadal time series (TS) domains (TS1-2011-2035, TS2-2041-2065, and 2076-2100) observed as per multi model GCMs and RCPs.

GCMs	RCPs	SBs	Snowfall			Snowmelt		
			TS1-TS3	TS1-TS2	TS2-TS3	TS1-TS3	TS1-TS2	TS2-TS3
CM3	RCP2.6	SB1	3.3	4.6	-1.3	4.5	5.2	-0.7
		SB2	-4.5	-4.1	-0.4	-5.2	-4.5	-0.7
		SB3	-3.8	-0.3	-3.5	-5.1	-0.2	-5
		SB4	0.2	-0.5	0.7	4.3	5.3	-1
		SB5	-1.1	2.5	-3.5	-1.2	3.5	-4.5
		SB6	0.4	2.2	-1.8	1.1	4	-2.8
		SB7	-35.3	-24.8	-23.2	-9.3	-12	3.1
	RCP4.5	SB1	4	4.3	-0.2	4.8	3.5	1.2
		SB2	-19.7	-6	-14.5	22.7	-8.9	15.1
		SB3	-7.4	-7	-0.4	-9.8	-8.7	-1.2
		SB4	-5	-4.2	-0.9	-7.9	-5.7	-2.3
		SB5	-20.5	-13.3	-8.3	23.1	15.7	-8.9
		SB6	-23.4	-17.9	-6.8	-24.7	-19.8	-6.1
		SB7	19.4	16.3	2.7	14	12.2	1.6
	RCP8.5	SB1	21	8	12	-16.7	8.9	23.5
		SB2	9.4	-0.3	9.8	10.1	-2.4	12.9
		SB3	0.1	-1	1.1	-1.8	-2	0.1
		SB4	5.8	21.1	-12.6	11.3	32.2	15.8

TH-1643_136104018

		SB5	20.1	7.2	12	20.4	7.7	11.8
		SB6	-3.5	11.6	-13.5	-2.2	16	-15.7
		SB7	-42	30.4	-50.8	29.2	24.7	68.5
ESM-2M	RCP2.6	SB1	-11.3	5.6	-16	1.6	6.7	-4.7
		SB2	2	-0.3	2.3	2.7	1.1	1.6
		SB3	-0.3	6.2	-6.2	0.5	8	-6.9
		SB4	-0.9	-6.2	5.7	-2.4	-9.5	7.9
		SB5	3.9	4.3	-0.4	5.3	6	-0.7
		SB6	-1.7	0.3	-2	-2.7	0.4	-3.1
		SB7	3	5.2	-2.1	9.1	15.7	-5.7
	RCP4.5	SB1	7.3	4.1	3	9.2	5.8	3.2
		SB2	7.3	4.1	3	9.2	5.8	3.2
		SB3	-0.9	4.6	-5.2	-2.1	4.9	-6.7
		SB4	3.1	0.4	2.7	5.6	2.3	3.2
		SB5	5.8	-0.5	6.3	6.8	0.9	5.8
		SB6	-1.8	-3.9	2.1	-1.8	-4.6	2.9
		SB7	-5.5	-29.6	34.1	34.7	-16.6	51
	RCP8.5	SB1	17.4	9.8	6.9	21.1	10.3	9.8
		SB2	-0.3	3.9	-4.1	-3.6	4.3	-7.6
		SB3	3.6	3.3	0.3	2.2	3.3	-1
		SB4	-2.9	-8.4	6	0.8	-9.6	11.6
		SB5	-2.1	-5.2	3.3	-5.3	-7.5	2.3
		SB6	-10	-1.9	-8.3	-11.2	-1.8	-9.5
		SB7	-40.3	34.8	-55.7	52.5	34.7	13.2

6.9 EVALUATION OF SWAT MODELED SNOWMELT USING SATELLITE SNOW COVER BASED SWE RECONSTRUCTION APPROACH

In this study, the snow water equivalent (SWE) based on reconstruction method is mainly applied to evaluate the SWAT model simulated and projected snowmelt. MODIS (MOD09A1) eight daily cloud free snow cover product for the year 2005 has been taken to calculate the SWE at each sub-catchments of the selected study region. The observed dataset such as precipitation, temperature and net radiation were available up to 2005, hence for the comparison purposes, MODIS snow cover product for the year 2005 has been utilized. In this reconstruction method, SWAT simulated snowmelt has been validated with the reconstructed SWE. The main purpose of this part of the research work is to compare the SWE derived from satellite snow cover and modeled datasets.

TH-1643_136104018

For the SWE reconstruction, 8 daily fractions snow covered area (SCA) is computed. However, for several scenes SCA is not much varied (<1km^2) and thus, next scene (8 daily MODIS snow cover) has been taken for the considerations. There is no Snow Gauge (SG)/Snow Telemetry (SNOTEL) site is available over the selected study region. To verify the SWE, it was necessary to conduct the field measurement and hence, snow density and snow depth were measured at the accessible locations of the selected study region. Around 32 snow depth and snow density samples were collected from different location over the field area i.e. Teesta catchment, a part of north Sikkim eastern Himalayas. The details of the samples are given in Table (6.10). The snow density is measured using Snow Density Gauge (Scientist 200: sample size 200 cc) by Brocks Range. The snow depth is measured using solid iron road by doing holes at the site. The depth is marked with the centimeter mapping scale.

The fractional SCA has been calculated at each catchment scale, values range from 0 to 1, to calculate the potential snow melt as per the 8 daily snow cover depletion curves (Eq. 6.27). The fractional SCA details has been shown in the Table (6.11). Apart from this, the other most important variable such as net radiation (Rn) has been averaged at 8 daily scale using daily datasets (Table 6.12).

Table 6.10: Field based measurement of snow density and snow depth samples over Teesta catchment.

Sl. No.	Sample Place	Lat	Long	Avg. Snow depth (cm)	Density (gm/cc)	SWE (cm)	Elevation (m)
S1	Near Yumthang Valley	27d 43m 506s	88d 44m 715s	24	0.26	6.24	2992
S2				25	0.26	6.5	
S3				26	0.27	7.02	
S4				80	0.28	22.4	
S5				28	0.28	7.84	
S6				25	0.3	7.5	
S7	Katau (Swastic Bridge)	24d 40m 557s	88d 47m 518s	28	0.31	8.68	3600
S8				29	0.32	9.28	
S9				30	0.32	9.6	
S10				35	0.32	11.2	
S11				40	0.32	12.8	
S12				33	0.31	10.23	
S13				30	0.31	9.3	
S14				31	0.31	9.61	
S15	Katau	24d 40m 358s	88d 47m 558s	36	0.33	11.88	3710
S16				50	0.32	16	
S17				40	0.32	12.8	

TH-1643_136104018

S18				44	0.32	14.08	
S19				38	0.34	12.92	
S20				41	0.34	13.94	
S21				40	0.31	12.4	
S22	Zero Point (Yumeshdong)			20	0.37	7.4	5200
S23				25	0.38	9.5	
S24				24	0.37	8.88	
S25				22	0.37	8.14	
S26				23	0.29	6.67	
S27				26	0.29	7.54	
S28				25.5	0.31	7.905	
S29	Near Lachung	27d 42m 838s	88d 45m.14s6	20	0.33	6.6	2850
S30				30	0.23	6.9	
S31				45	0.31	13.95	
S32				40	0.32	12.8	

Table 6.11: Sub-catchment (SB) wise snow cover fraction for the year 2005 extracted from MODIS (MOD09A1) cloud free snow cover datasets.

Months	SB1	SB2	SB3	SB4	SB5	SB6	SB7
	SCA (km^2)	SCA (km^2)	SCA (km^2)	SCA (km^2)	SCA (km^2)	SCA (km^2)	SCA (km^2)
April	221.528	210.580	377.371	329.716	204.780	237.628	149.610
May	195.980	152.620	307.392	199.633	133.300	161.853	90.150
May	181.816	82.640	205.858	85.648	88.960	148.759	78.132
May	140.172	55.160	179.026	80.497	63.100	108.610	62.250
June	52.590	39.622	77.921	17.300	19.534	64.612	57.090
July	60.590	31.760	64.183	17.100	19.310	15.450	7.650
July	22.800	23.390	59.675	15.450	18.670	7.691	1.510
Aug	22.620	6.400	47.439	4.400	2.140	1.289	1.030
Aug	22.140	6.010	40.780	4.230	0.810	0.429	0.000
Sep	18.850	1.000	29.685	2.360	0.210	0.000	0.000
Sep	0.000	0.000	0.000	0.000	0.000	0.000	0.000

TH-1643_136104018

The potential snow melt (M_{pj}) has been calculated as per the given Eq. 6.26. The M_{pj} calculated at each sub-catchment scale and the details are given in Table 6.13. For the calculation of $M_{pj,}$ the degree day factor was chosen as per the study conducted by Singh and Kumar (1996). Over the Himalayan regions, the snow degree day melt factor (a_r) for the temperature vary from 0.4 to 0.75 (cm/°C/day) and thus this factor has taken as the calibration parameter. In this study, it varies from SB1 to SB7 within the range as 0.45 to 6.0. In the satellite snow cover based SWE reconstruction method, the vegetation density and cloud contaminations can affect the accuracy of the SWE. Thus, cloud free MODIS datasets were accounted for the SCA generation. The vegetation and water pixels already removed by calculating Normalized Snow Difference Index (NDSI). Before applying NDSI, the Normalized Different Water

Table 6.12: Sub-catchment (SB) wise 8 daily average of net solar radiation for the year 2005.

Months	SB1	SB2	SB3	SB4	SB5	SB6	SB7
	Rn (w/cm^2)	Rn (w/cm^2)	Rn (w/cm^2)	Rn (w/cm^2)	Rn (w/cm^2)	Rn (w/cm^2)	Rn (w/cm^2)
April	0.07	0.07	0.07	0.07	0.07	0.07	0.07
May	0.07	0.07	0.07	0.07	0.06	0.06	0.06
May	0.05	0.05	0.04	0.03	0.03	0.04	0.04
May	0.04	0.04	0.03	0.03	0.03	0.03	0.03
June	0.03	0.04	0.03	0.03	0.03	0.03	0.03
July	0.02	0.04	0.03	0.04	0.03	0.03	0.03
July	0.03	0.03	0.02	0.02	0.01	0.02	0.01
Aug	0.04	0.05	0.03	0.03	0.03	0.03	0.03
Aug	0.02	0.04	0.04	0.04	0.04	0.04	0.03
Sep	0.03	0.04	0.04	0.04	0.03	0.04	0.04
Sep	0.03	0.04	0.04	0.04	0.03	0.04	0.04

TH-1643_136104018

Table 6.13: Sub-catchment (SB) wise M_{pj} for the year 2005.

Months	SB1	SB2	SB3	SB4	SB5	SB6	SB7
	M_{pj} (cm)	M_{pj} (cm)	M_{pj} (cm)	M_{pj} (cm)	M_{pj} (cm)	M_{pj} (cm)	M_{pj} (cm)
April	0.79	2.28	1.96	2.31	2.34	2.56	4.53
May	1.17	3.20	2.77	3.13	3.05	3.28	5.12
May	3.15	4.95	4.00	4.62	4.48	4.93	5.61
May	4.63	4.69	4.81	5.61	5.47	4.54	5.25
June	6.01	5.65	5.43	6.31	6.20	5.56	6.14
July	6.07	6.39	5.47	6.39	6.25	6.24	6.40
July	6.61	6.37	5.01	5.77	5.66	6.32	5.94
Aug	6.14	7.19	5.94	6.84	6.73	6.31	6.45
Aug	7.67	6.99	6.72	7.66	7.55	6.49	6.61
Sep	6.80	4.39	5.68	6.46	6.31	6.59	4.53
Sep	6.72	4.39	6.33	6.48	6.32	2.56	5.12

Then utilizing Eq. 6.25 M*j* (SWE) has been calculated at each sub-catchment scale. The satellite snow cover based reconstructed SWE (mm) has shown in Table (6.14). In this Table (6.14), it can be observed that the maximum amount of SWE has been computed from April to June. Thus, SWAT model based calculated SWE has been compared with satellite derived SWE. The results show feasible match with SWAT based outcomes. When compare with the field measurement, as shown in Table (6.10), reconstructed SWE found within the range of them. The field based measurement actually helped to understand the real time dynamics of the snow and glaciers. Hence, the empirical methods based computation of SWE has been improved.

Table 6.14: Sub-catchment (SB) wise M*j* (SWE) for the year 2005.

Months	SB1	SB2	SB3	SB4	SB5	SB6	SB7
	Mj (mm)	Mj (mm)	Mj (mm)	Mj (mm)	Mj (mm)	Mj (mm)	Mj (mm)
April	0	0	0	0	0	0	0
May	10.22	21.32	37.22	30.06	19.98	27.48	24.53

TH-1643_136104018

May	22.65	21.07	45.63	27.97	18.90	27.45	17.64
May	24.12	12.28	32.31	12.45	12.81	20.89	14.91
June	24.91	10.36	30.54	12.83	10.63	14.94	9.05
July	9.65	8.35	17.28	4.33	4.95	9.41	7.51
July	11.04	5.25	13.15	2.70	2.69	2.19	1.10
Aug	5.73	4.35	13.97	2.88	2.86	1.08	0.20
Aug	6.56	0.89	11.71	1.05	0.34	0.17	0
Sep	3.10	0.55	5.34	0.57	0.11	0.13	0
SWE-REC	118.01	84.41	188.62	94.84	73.27	103.74	74.94
SWAT	110.29	78.07	113.13	79.53	81.88	107.72	47.29

6.10. COUPLED APPROACH: MIKE 11 AND SWAT

The design flood stage is useful in the flood protection measures and to assess the flood vulnerability in extreme condition and different return periods. The four major hydraulic components, which are necessary for the flood study, have been computed in the historical/observed time series (1991-2005) and in the future time periods (2006-2100). In the study, Mike 11 hydrodynamic (HD) model is coupled with SWAT to generate the future projection of water level, discharge and water velocities.

This study routed from the upstream of Teesta and Lachung to their downstream. The Teesta flows approximately 180 km through a mountainous area of India before entering into the alluvial plains of north western part of Bangladesh. It keeps flowing in a braided course for a length of 96 km before crossing the India-Bangladesh border. After travelling 121 km, it joins the Jamuna River near Chilmari in Bangladesh. For the routing, an upstream catchment of Teesta river (up to Chungthang) has been selected and it travels around 85 km length from the origin to Chungthang. Lachung meets the Teesta at Chungthang after travelling around 25 km length. Thus, the cross sections in every 10 km river length have been calculated using manual survey by using Total Station.

The HD model setup is grouped into various sections such as River network linking (Fig. 6.25), river cross section and conveyance definition, boundary condition, HD parameter setup and simulation time step. Stage in river Teesta is also influenced during flood period by other rivers that have also been considered in the river network and calculated from the cross

TH-1643_136104018

sections. The HD parameter details are given in Table (6.15). SWAT generated outcomes of these watershed parameters utilized into Mike 11 model. SWAT also calculated Manning M and n in HRU level utilizing LULC and other topographical factors. Hence, these factors also utilized as outputs from the SWAT.

Table 6.15: Details of Mike 11 HD model parameters used as inputs to the model.

Parameter	Factor	Method/Values	Description
Initial Parameters	Initial Discharge	10 cumec	Discharge
	Initial Depth	0.5 cm	Water Level Depth
Wind Factor	Friction Factor	0.0024	Friction parameter value
	Topographical Factor	1	Slopes
Bed Resistant	Resistance Number	15 (10-100)	Manning parameter
	Approach	Uniform Section	
	Resistance Formula	Manning M/Chezy's Number	
Wave Approximation	Method	High Order Fully Dynamic	Routing method
Coefficient Values	Delta	0.6 (0.5 to 1.0)	for model stabilities
	Delhs	0.01	the minimum allowable water level differences across a weir
	Delh	0.1	controls the dimensions
	Alpha	1	velocity distribution coefficient
	Theta	1	a weighting factor for momentum equation
	Eps	0.0001	water surface slope uses in diffusive wave equation
	Dh Node	0.01	computational coefficient
	Zeta Min	0.1	minimum head loss coefficient
	Inter 1 Max	20	maximum number of iterations
	Nolter	1	no iterations

TH-1643_136104018

	Maxlter Steady	100	maximum number of iterations for steady condition
	Froude Max	-1	suppression term for convective acceleration
	Froude Exp.	-1	suppression term for convective acceleration

6.10.1 Mike 11 model setup and cross section profile

In this study, an unsteady flow routing model has been developed at different sections (Chainages: Ch) of the stream network (Figs. 6.25 to 6.28). The stream network for 1-D unsteady flow has been created in the model. Though, it can also be import from another source. If there is no difference in the stream channel length and flood plain flow paths from cross section to cross section are already known, then model provides the same outputs as compare to observe datasets.

In this study, several cross sections have been collected from the field measurement and few cross sections are generated from the CARTOSAT DEM. The cross sections should properly follow the river path. The longitudinal profile for Teesta river and Lachung river with the water level and discharges are highlighted in Figs. (6.26 to 6.28). The cross sections and their conveyance, at Lachung and Teesta Chainages, have been shown in Fig. (6.29). Channel and flood plain resistance factors for the given cross sections are calculated in the cross section editor file in Mike 11. The Manning's *n* value for each cross section is adopted from the SWAT model. SWAT calculates the accurate Manning' n value at each HRU using LULC and slopes.

The observed daily discharge datasets (1991-2005) are available at Lachung and Chungthang gauges and hence, utilized in the model. The SWAT calibrated flow at several locations along the Teesta and Lachung is also utilized in the model as a point source discharge datasets. To input the discharge data into Mike 11, boundary conditions have been setup. To make the data Mike11 readable, the discharge data sets from SWAT and observed gauge are converted into Mike 11 specified format. At Lachung and Teesta, observed gauge data and at another locations, SWAT calibrated point source discharge have been setup into the boundary condition.

TH-1643_136104018

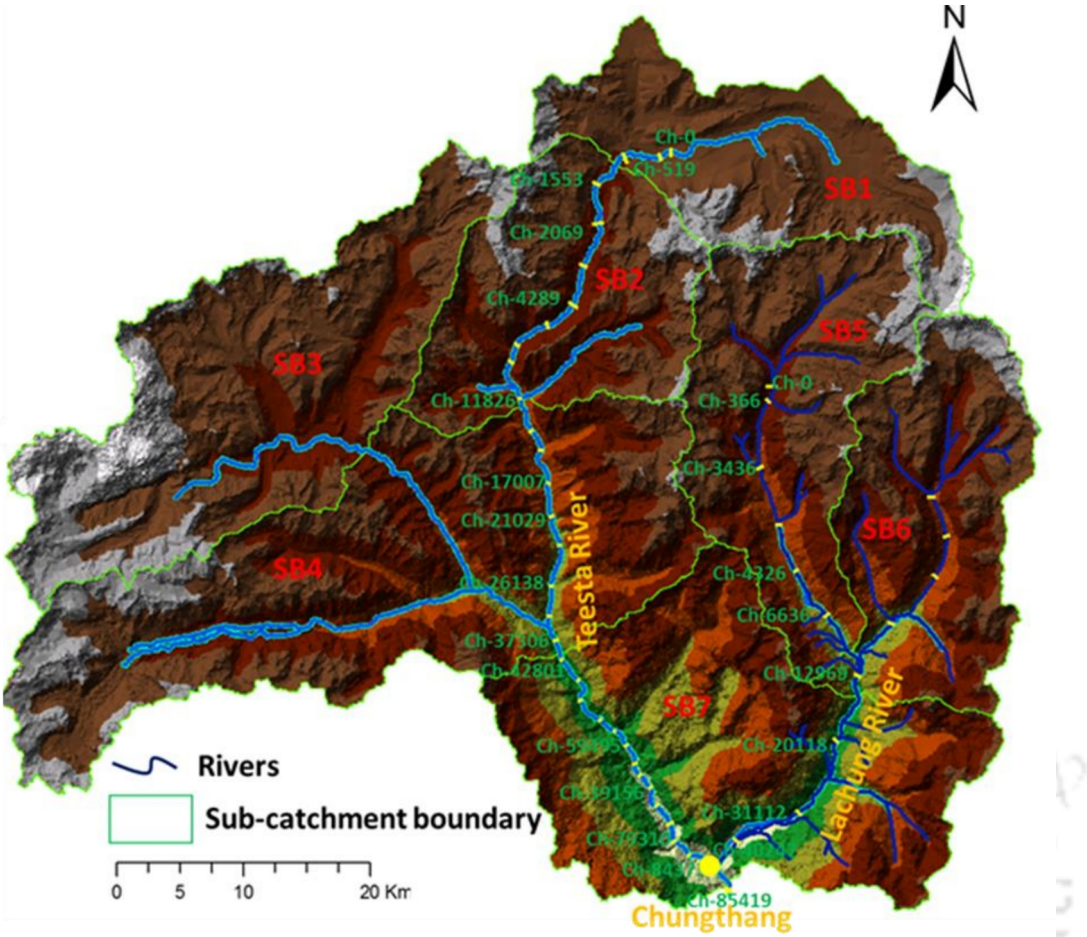


Fig. : 6.25 Teesta river cross section and stream network details.

Several hydrodynamic parameters are required for the model stability conditions. The hydrodynamic parameter file requires bed and flood plain resistance data for the river network. Bed and flood plain are input as Manning's *M* values. The resistance factor is input from one point to another point along the river flow path. Any local differences in resistance can be given into the cross section file at a specific cross section. The HD parameters, given in Table (6.15), are calculated from SWAT and some of them taken as the global values with reference to Mike 11 documentation and literature review. The *Delta* and *Delhs* coefficients are very sensitive for the model. The best Delta value is opted as 0.6 after doing several trial and error computations. All the input data and boundary layers were setup into the SWAT simulation file. The Teesta slopes are corresponded with very steep slopes thus, the model run time is taken as 1 minute to find the stability conditions.

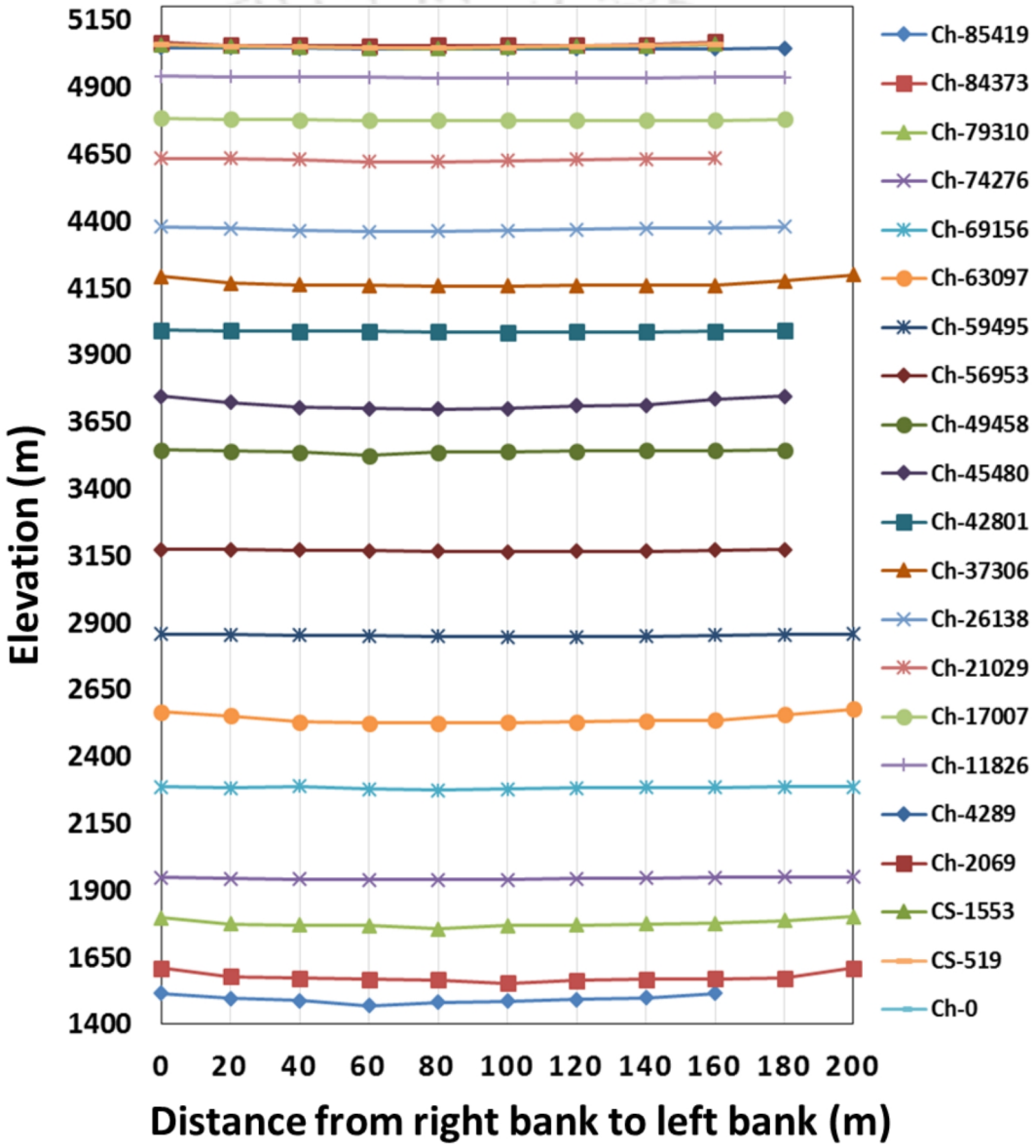
Mike 11 has been calibrated for the historical period from 1991 to 2005. The observed discharge datasets are available at Teesta and Lachung hence, Mike 11 generated discharge has been compared at both the gauge locations (Chainages in Mike 11). Based on the historical

TH-1643_136104018

data inputs, water level, water velocities, flooded area and discharge have been computed at different downstream Chainages. Based on the computed discharge and water level, a stage-discharge (Q-h) rating curves at different changes of river Teesta and Lachung have been produced (Figs 6.30 and 6.31)

Figs. (6.32 to 6.35) shows the comparison between observed discharge and Mike 11 simulated discharge. Figs. (3.36) show the computed water velocities and flooded area at different Chainages of Teesta and Lachung River.

(a)



TH-1643_136104018

(b)

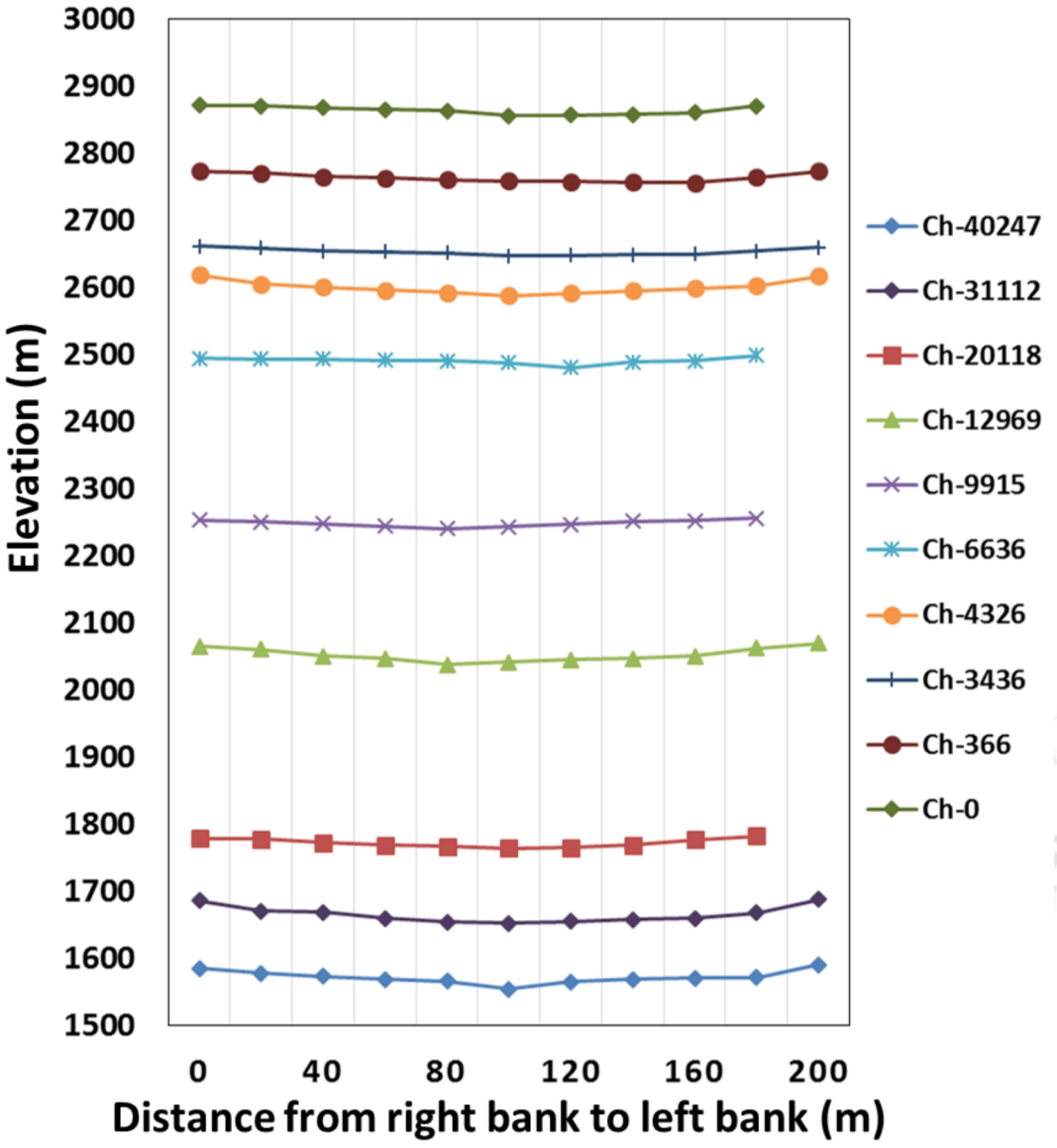


Fig. 6.26: Longitudinal Cross profile of Teesta River catchment showing maximum discharge at each cross sections: (a) Teesta river cross sections and (b) Lachung river cross sections.

TH-1643_136104018

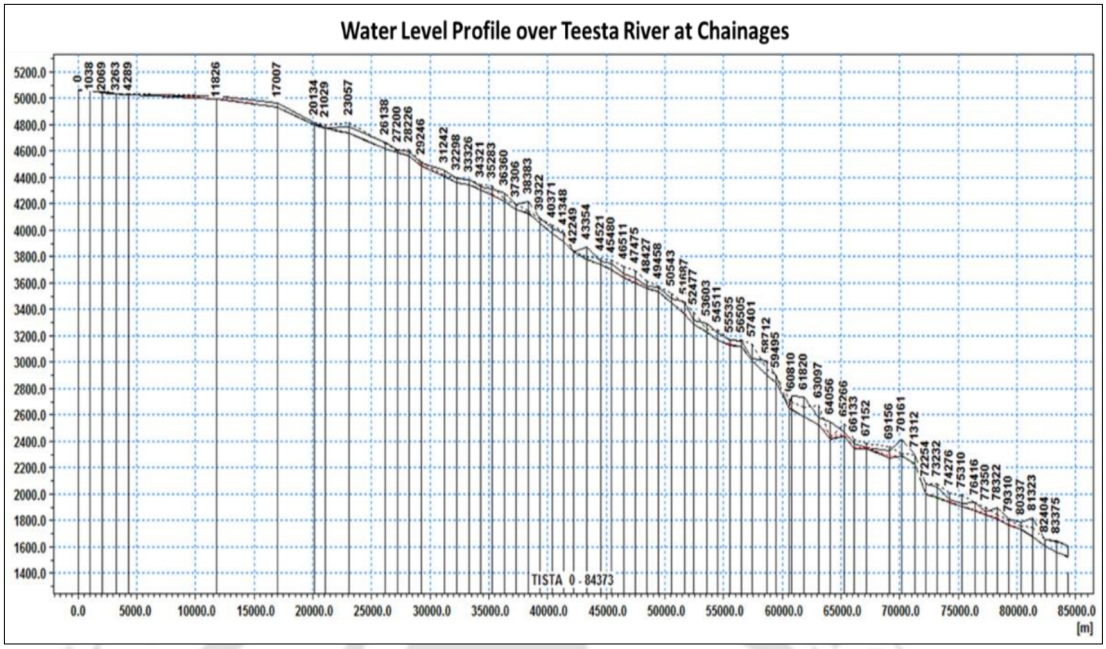


Fig. 6.27: Water Level at different Chainages/cross sections over Teesta River.

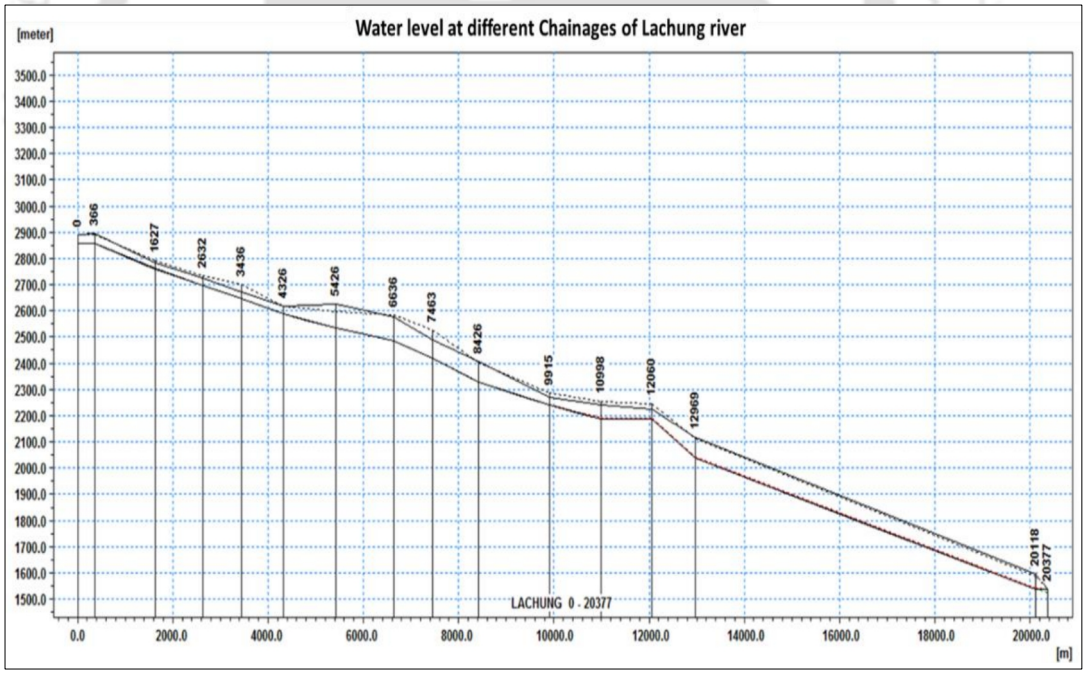


Fig. 6.28: Water Level at different chainages/cross sections over Lachung River.

6.10.2 Mike 11 historical simulations

As per the time series plot (Figs. 6.31 to 6.35), the Mike 11 calculated discharge, at both the Chainages, shows better agreement compare to observed discharge datasets. The Lachung corresponds to low flow than Teesta. Lachung meets the Teesta at Chungthang, thus at Chungthang it shows total contribution of the discharge from the whole catchment. Figs. (6.31

TH-1643_136104018

and 6.32) show the Mike 11 calculated discharge at different downstream changes of the Teesta and Lachung River. In this Fig. (), one can observe the increase in discharge amount in a progressive manner when it comes from upstream Chainages to downstream Chainages. At the origin of the Teesta river (Ch-519 and Ch-1153), it corresponded to 200 cumec, while at the downstream it corresponded to around 800 cumec. This shows the variability in the discharge over the steep slopes of the Teesta river catchment.

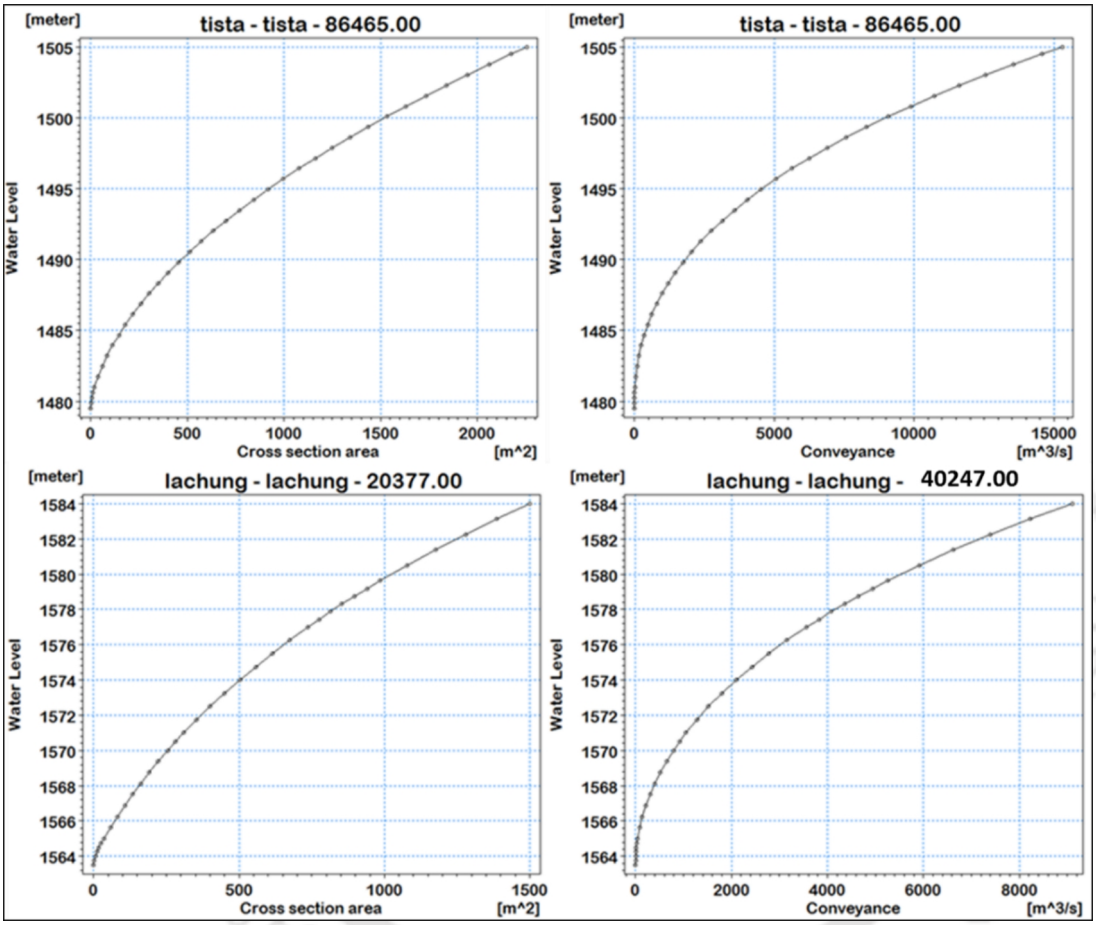


Fig. 6.29: Cross section details at Chungthang and Lachung Chainages (gauge).

In case of the Lachung River, the upstream Chainage (Ch-366) corresponded around 100 cumec flow, while at the downstream portion Chainage (Ch-12514), it corresponded around 300 cumec. Figs. (6.36 and 6.37) show the water velocity and flooded area over the Lachung and Teesta. In the Figs. (6.36), one can observe the water velocity varies around1.0 m/s to 8 meter/sec. Several values show extreme water velocity up to 10 m/s. The lowest value recorded at upstream and higher velocity values are recorded at downstream of the portion. In the Lachung River, the water velocity varies from 0.2 m/s to 3.8 m/s. Figs. (6.37) show the flooded area information at different Chainages of the Teesta and Lachung River.

TH-1643_136104018

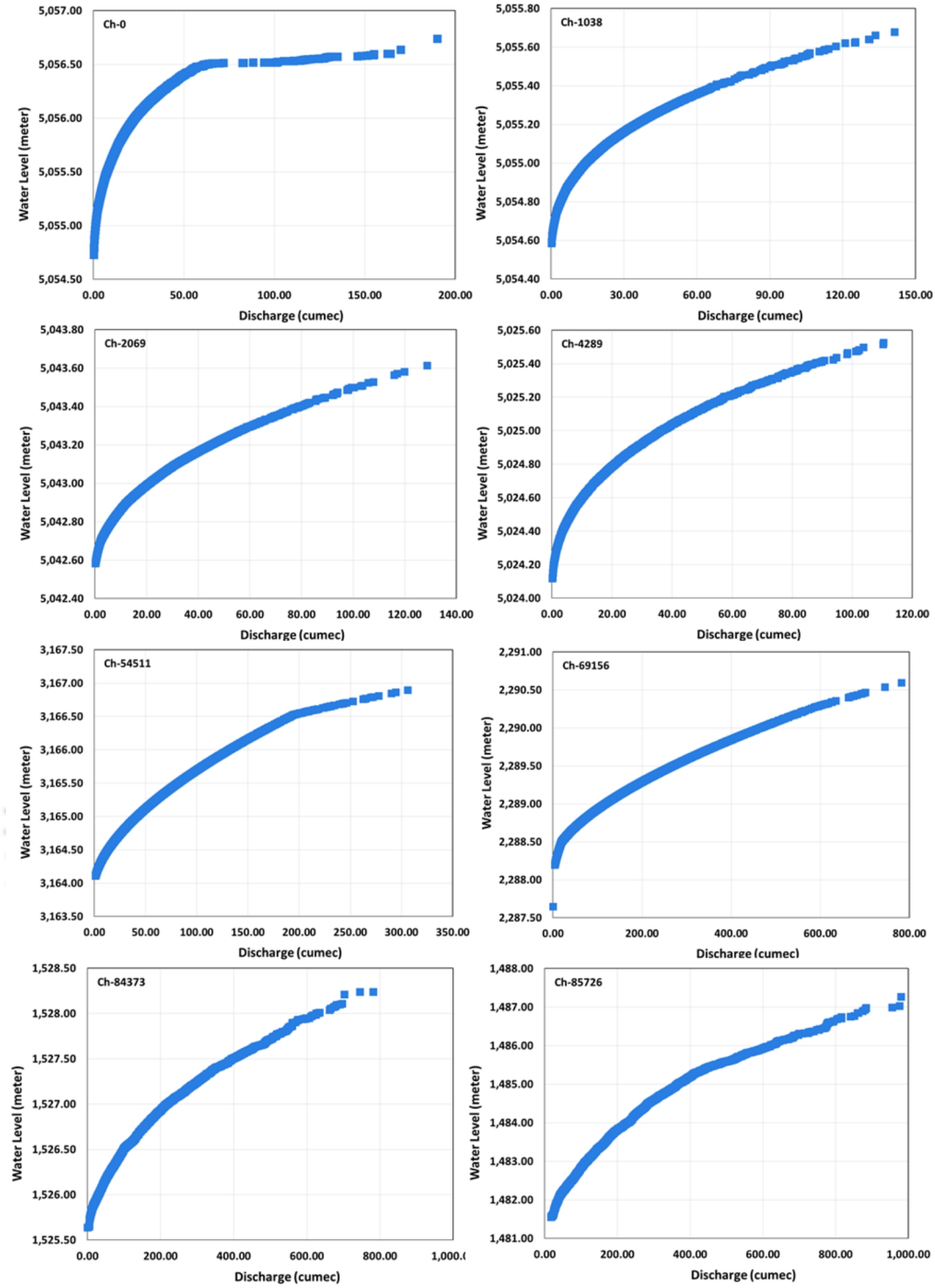


Fig: 6.30: Rating curves (stage-discharge) at different downstream Chainages of Teesta River computed from Mike 11. Changed.

TH-1643_136104018

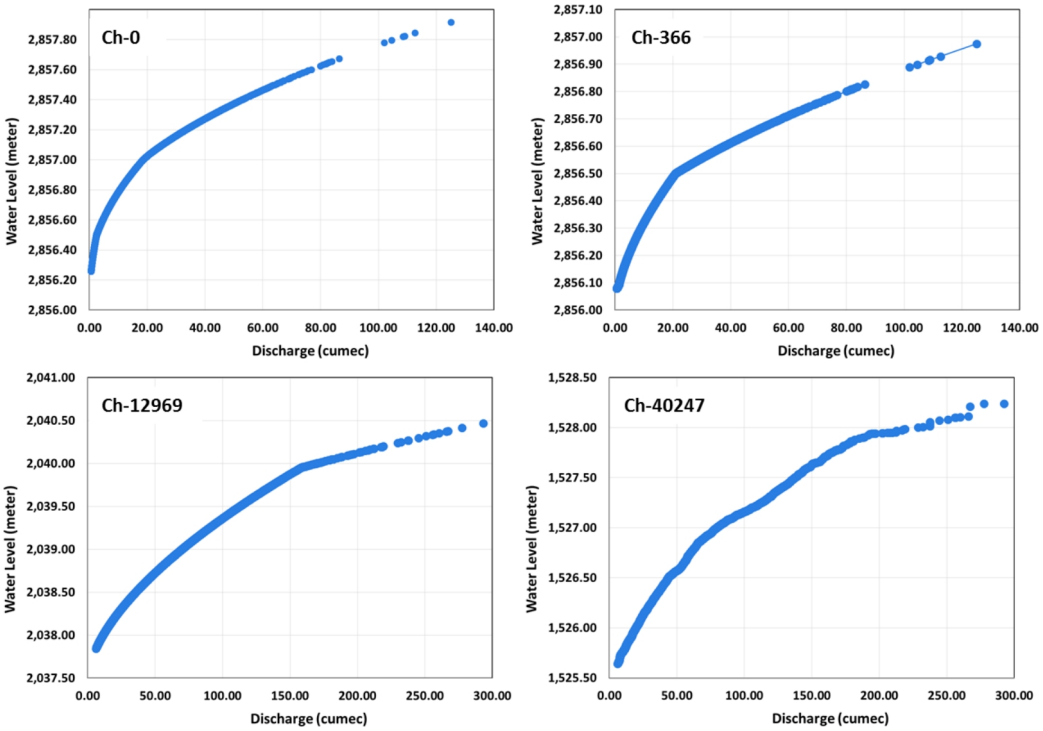


Fig: 6.31: Rating curves (stage-discharge) at different downstream Chainages of Lachung River computed from Mike 11.

6.10.3 Mike 11 21st century projections under CMIP5 CM3 GCM

For the future projection of water level, water velocities and discharge, the required time series of discharge and other parameters are input to the model. SWAT based projected discharge as per CMIP5 CM3 GCMs and RCPs, has been taken to setup the model for future projection. The coupling of SWAT and Mike has presented a novel approach for assessing the future changes in the downstream river flows, water level and water velocities. Mike 11. The projection scenarios of future water level, river discharge and water velocities as per the CMIP5 CM3 GCMs and RCPs have shown in Figs. (6.38 to 6.43).

The month wise projection scenarios have been carried out at the two main Chainages/outlet locations i.e. Chungthang and Lachung. Figs. (6.38-6.39) show the monthly projection of water level during monsoon seasons (May to October) from the year

TH-1643_136104018

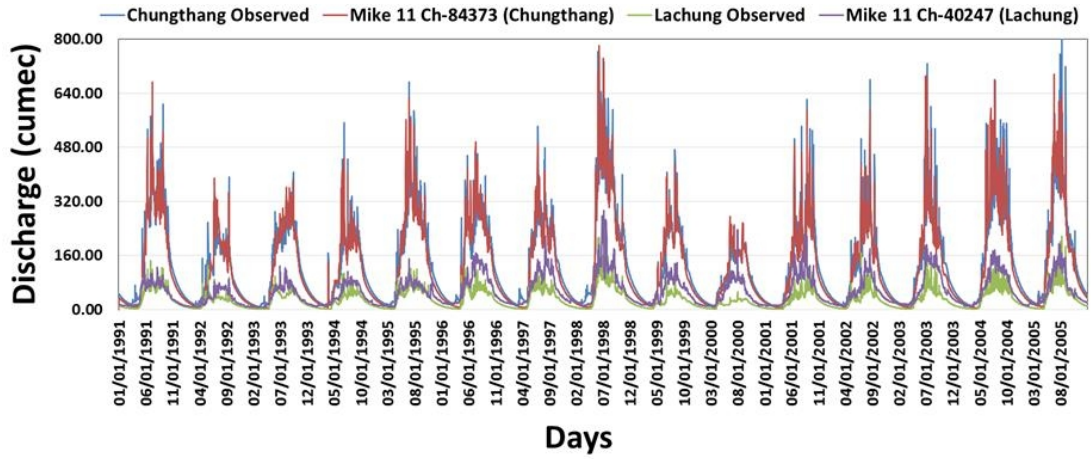


Fig.6.32: Comparison of Mike 11 simulated discharge and observed discharge at Chungthang and Lachung.

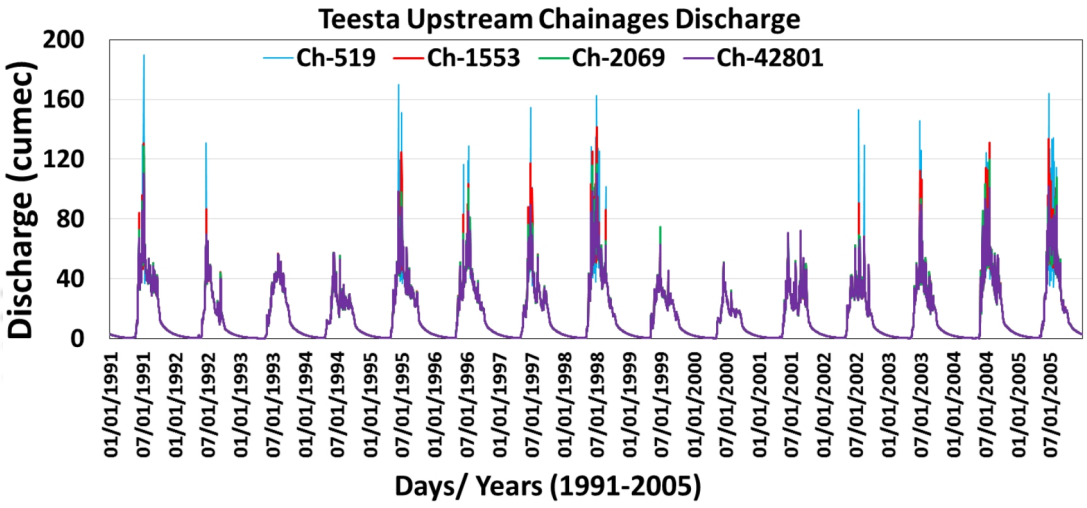


Fig. 6.33: Mike 11 simulated discharge at upstream Chainages at Teesta River.

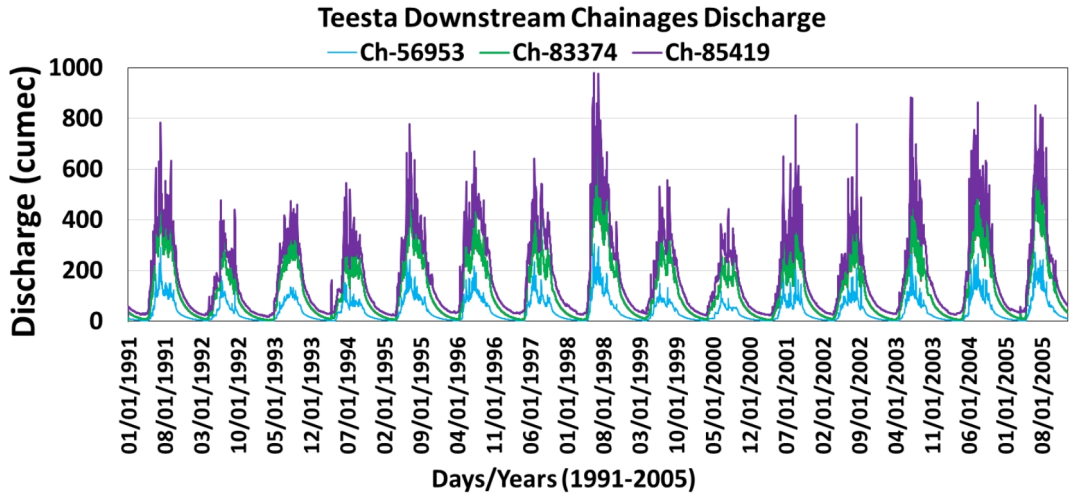


Fig. 6.34: Mike 11 simulated discharge at downstream Chainages at Teesta River.

TH-1643_136104018

2008-2009. The initial two year 2006-2007 were taken as the warm-up years in the Mike 11. In Figs. (6.40 and 6.41), one can observe the increase in water level during the monsoon season in the given time series except July. In July month, it shows slight decrease in water level. Among all the monsoon months, August has shown very clear consistent increase in the water level. In the projected scenarios of water level, several uneven extreme events can also be identified in the time series plots.

Figs. (6.40 and 6.41) show the Mike 11 based projected scenarios of monthly discharge during monsoon period at both the Chainages. In the projected time series, a consistent increase in the discharge amount is observed across all the months except July. In the projected discharge, the amount of discharge has been increased and it ranged up to 1200 cumec to 1400 cumec. Mike 11 shows very noteworthy projection scenarios of discharge and other variables. If one can compare the results of historical discharge at the same outlet i.e. Chungthang, it showed large variation in the future discharge amount. Apart from consistent increase trend (2008-2100). The amount of discharge is also increased during the monsoon period. Figs. (6.42 and 6.43) show the future projected month wise (monsoon period) water velocities at both the Chainages. Figs. (6.42 and 6.43) clearly show that the water velocity will be increased in the 21st century over the Teesta and Lachung river. At Teesta river, the maximum water velocities vary from 6.5 m/s to 8 m/s, while at Lachung river it varies from 1.7 m/s to 3 m/s during monsoon months.

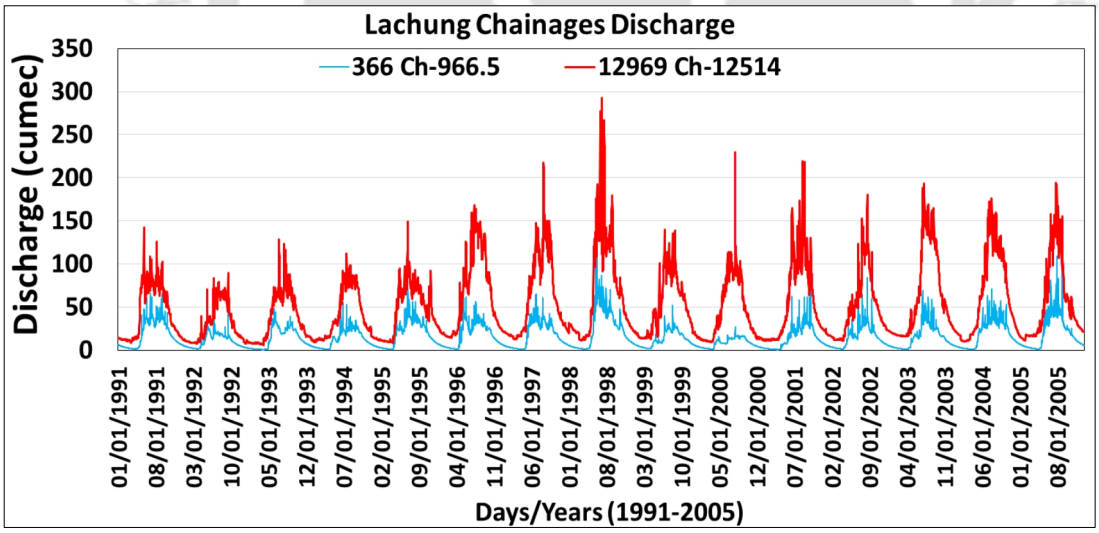
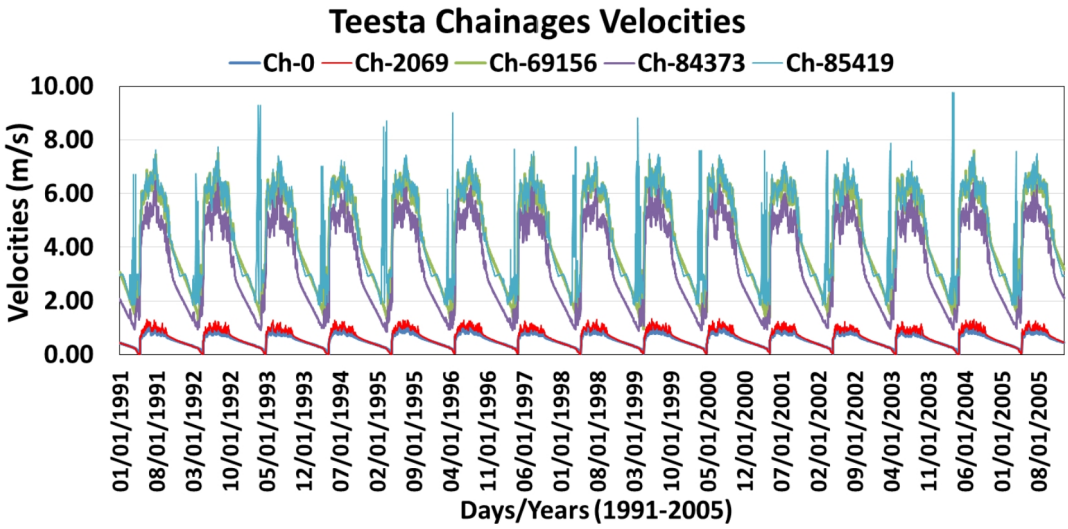


Fig.6.35: Mike 11 simulated discharge at upstream and downstream Chainages at Lachung river.

TH-1643_136104018

(a)



(b)

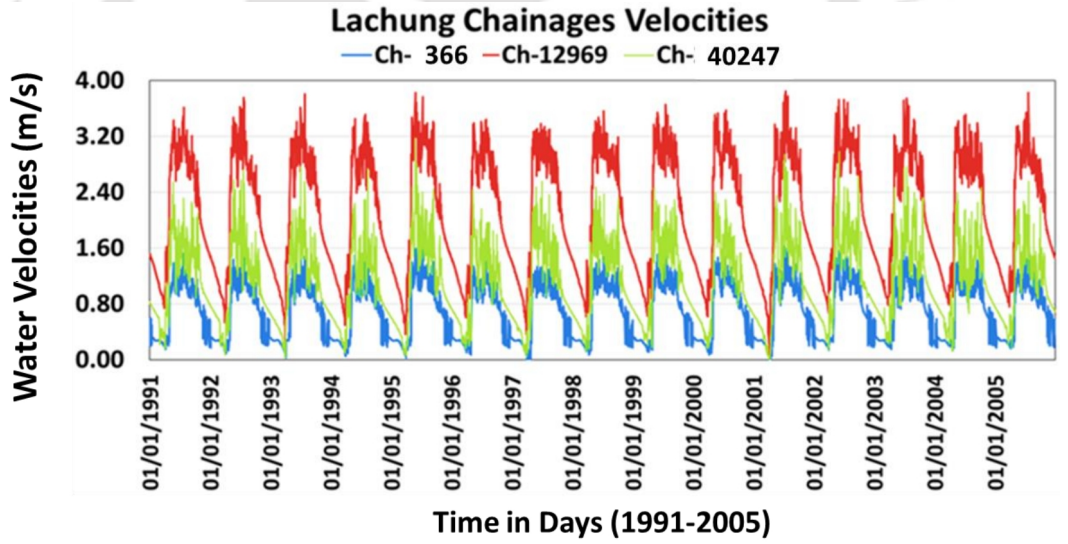


Fig. 6.36: Mike 11 simulated water velocities at downstream Chainages at (a) Teesta and (b) Lachung rivers.

As per the future time series, a consistent and progressive increase are projected in the water velocities in most of the monsoon months. The September and October months show very high increase in the water velocities. In the water velocities, several high velocity events also recorded. In the September and October months, as per the RCPs, the increments in the water velocity are recorded from 0.4 m/s to 1.0 m/s (2008-2100).

TH-1643_136104018

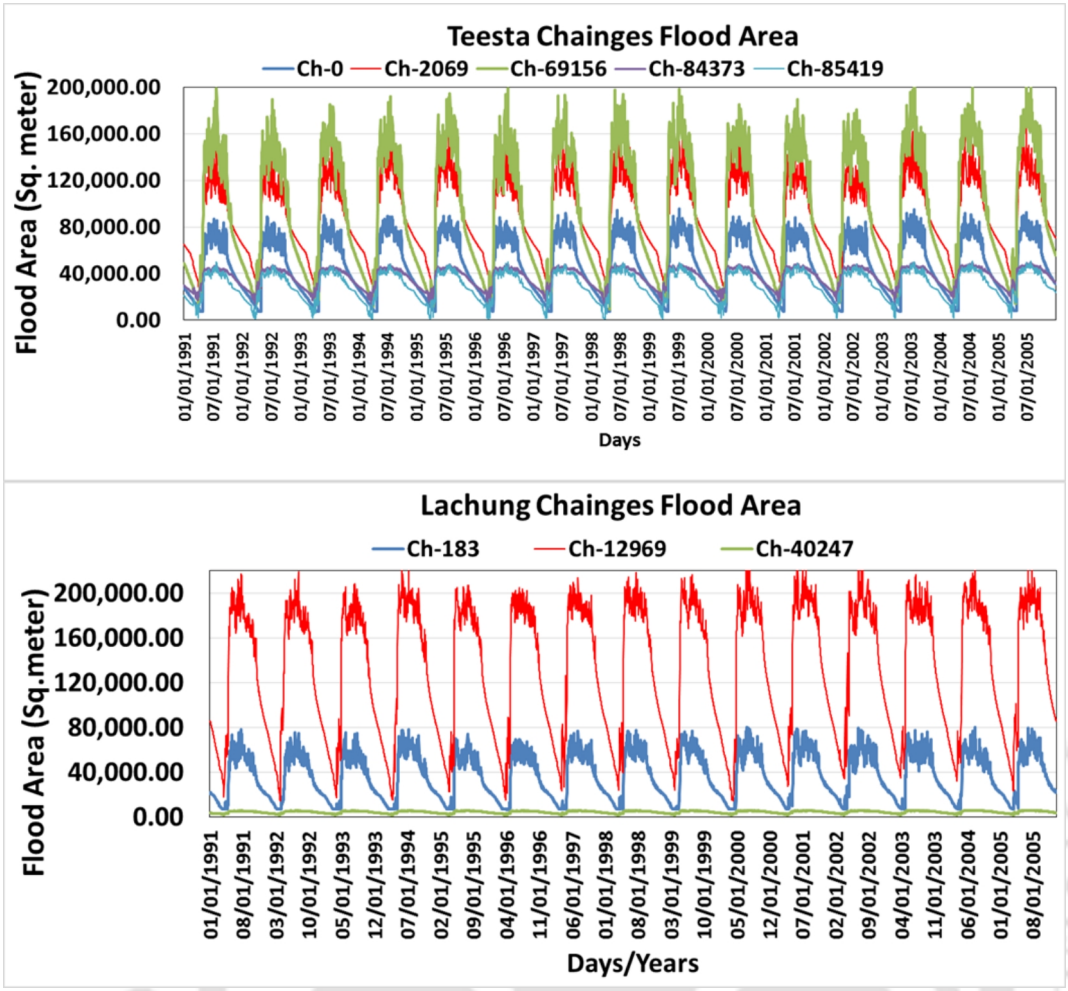


Fig. 6.37: Mike 11 simulated Flood Area (sq. meter) at downstream Chainages at Teesta and Lachung rivers.

6.10.4 Development of rating-curve equations

Based on the forecasted water level (h) and discharge (Q), as per CMIP5 CM3 GCMs with RCPs (RCP2.6, RCP4.5 and RCP8.5), rating curve equations have been developed. For the development of the rating curve equation, around 93 years monthly discharge datasets have been taken, which are projected from the Mike 11. The rating curve equations developed by Mosley and Mc Kercher (1993) has been considered for the development of the rating curve equations as given below:

$$Q = C(h - Z_0)^n$$

Where, Q = discharge, C and n are the constants, h = water level or height and Z_0 = height at which discharge is zero. Values of n and C have been determined as the calibration parameter.

TH-1643_136104018

Values of n for different cross section shapes are rectangular n = 1.67 and triangular n = 2.67 (Rahman et a., 2011).

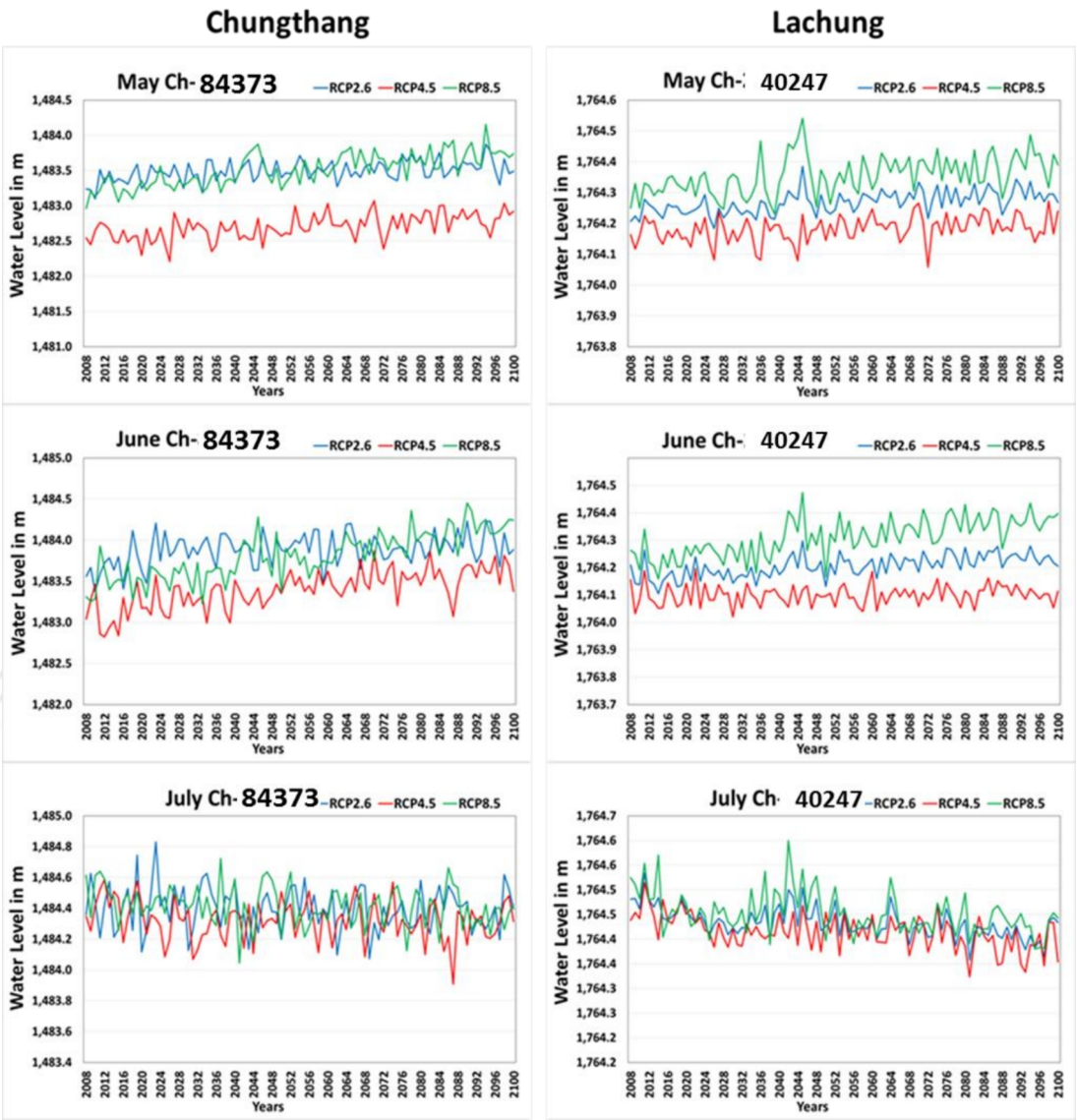


Fig.6.38: Future Water Level (August to October) at Lachung and Chungthang as per CMIP5 CM3 GCMs (2008-2100).

TH-1643_136104018

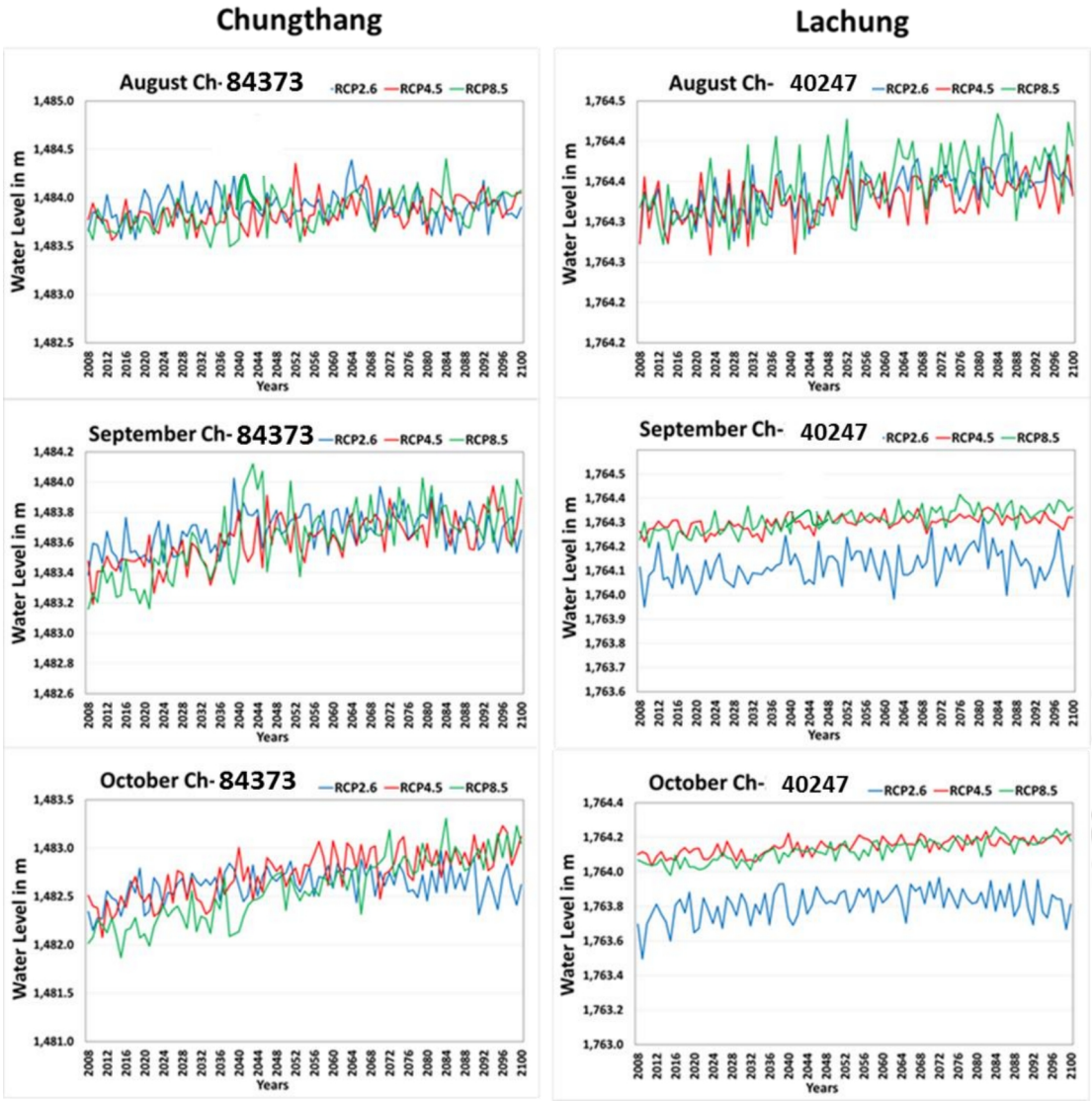


Fig. 6.39: Future Water Level (May to July) at Lachung and Chungthang as per CMIP5 CM3 GCMs (2008-2100).

TH-1643_136104018

(b)

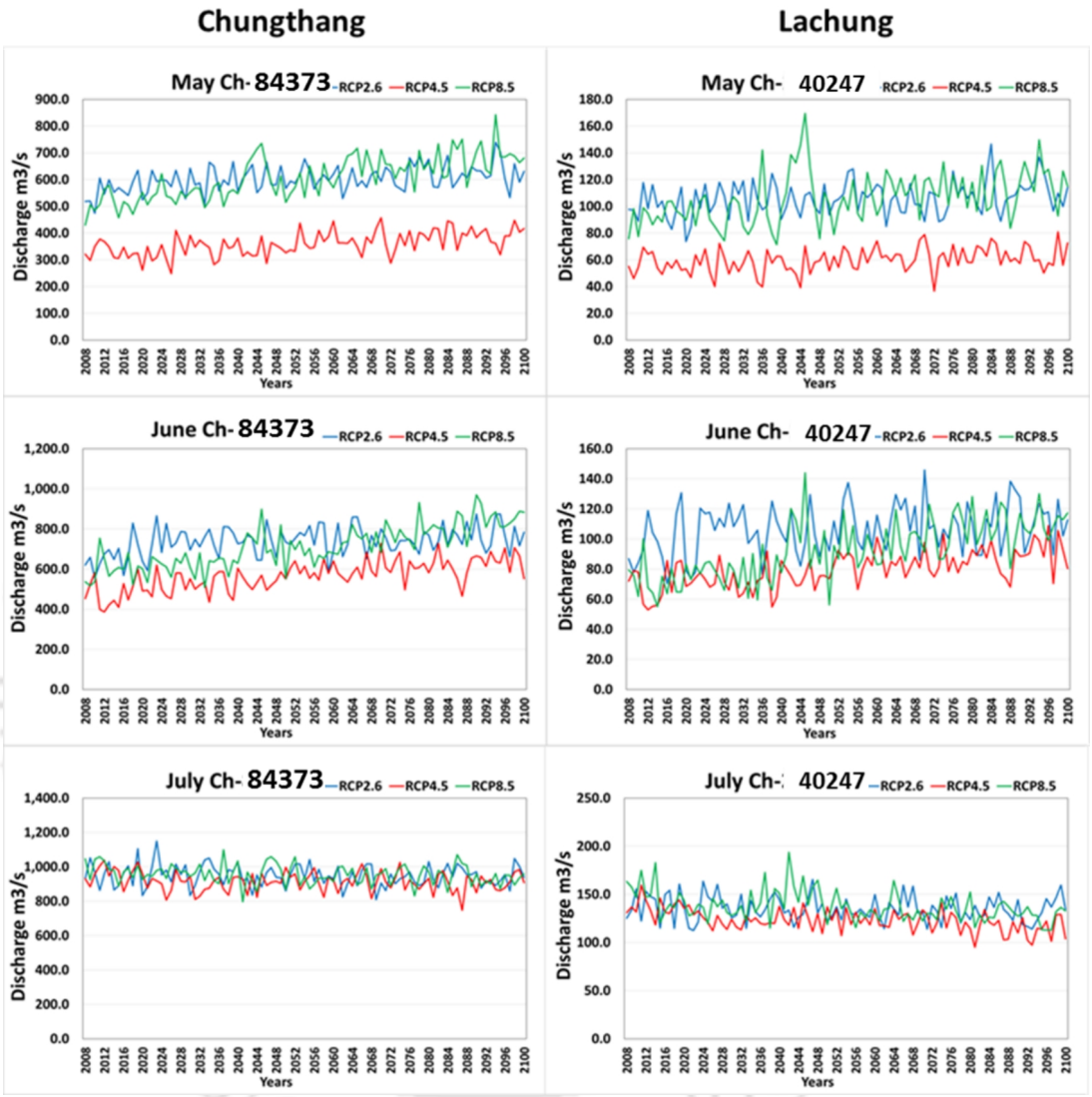


Fig. 6.40: Future Discharge (May to July) at Lachung and Chungthang as per CMIP5 CM3 GCMs (2008-2100).

TH-1643_136104018

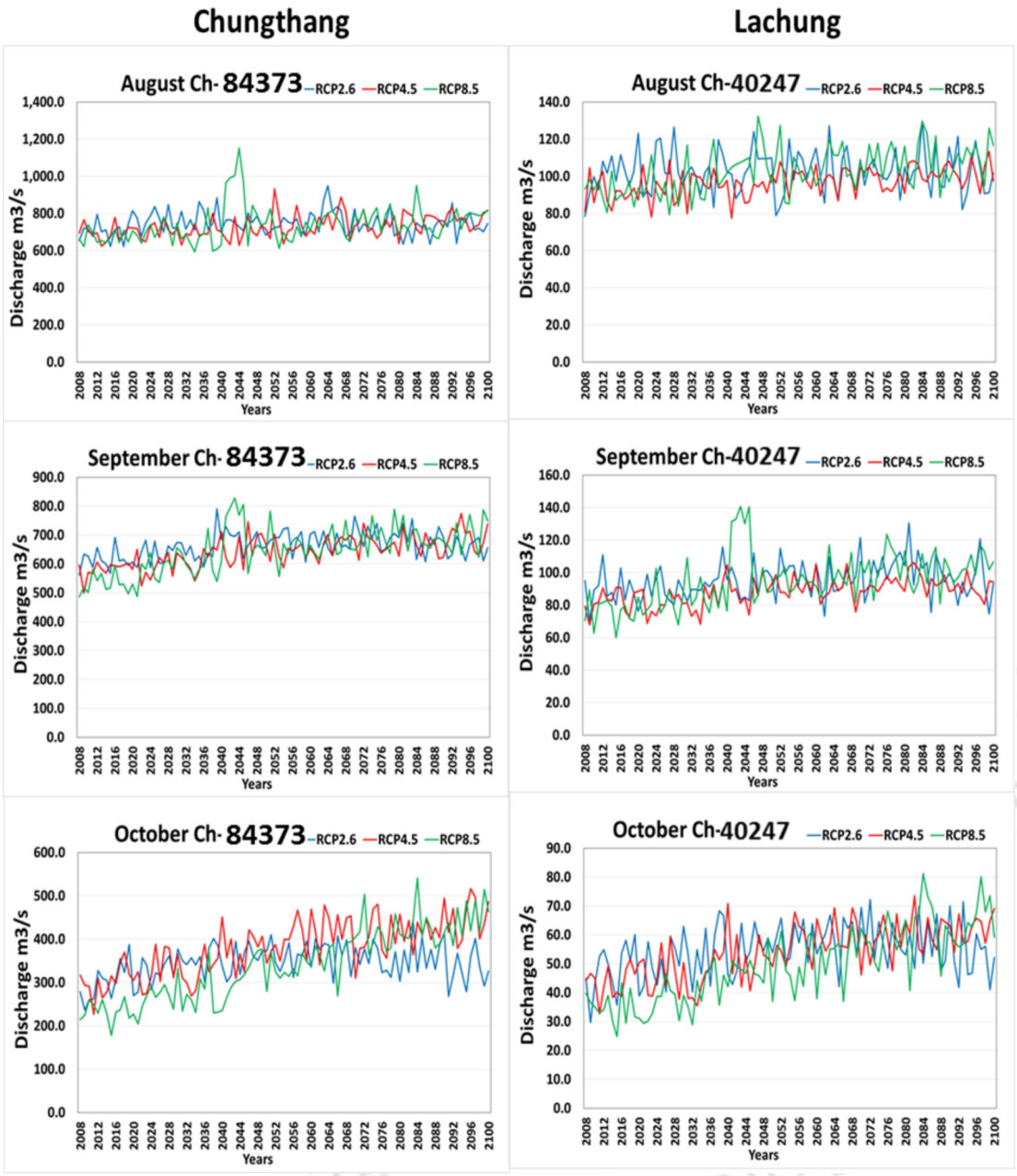


Fig. 6.41: Future Discharge (August to October) at Lachung and Chungthang as per CMIP5 CM3 GCMs (2008-2100).

TH-1643_136104018

(c)

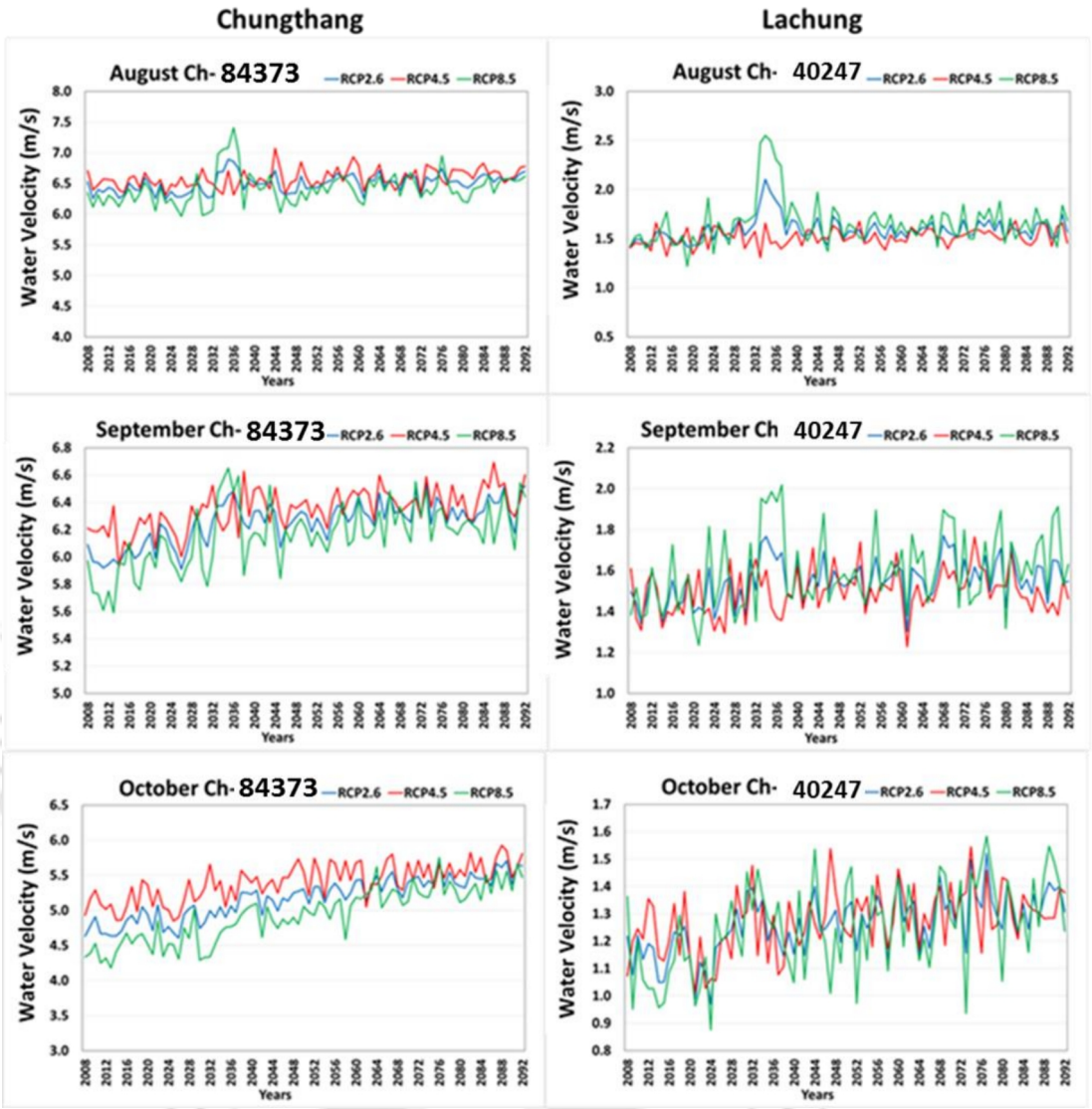


Fig. 6.42: Future Water Velocity (May to July) at Lachung and Chungthang as per CMIP5 CM3 GCMs (2008-2100).

TH-1643_136104018

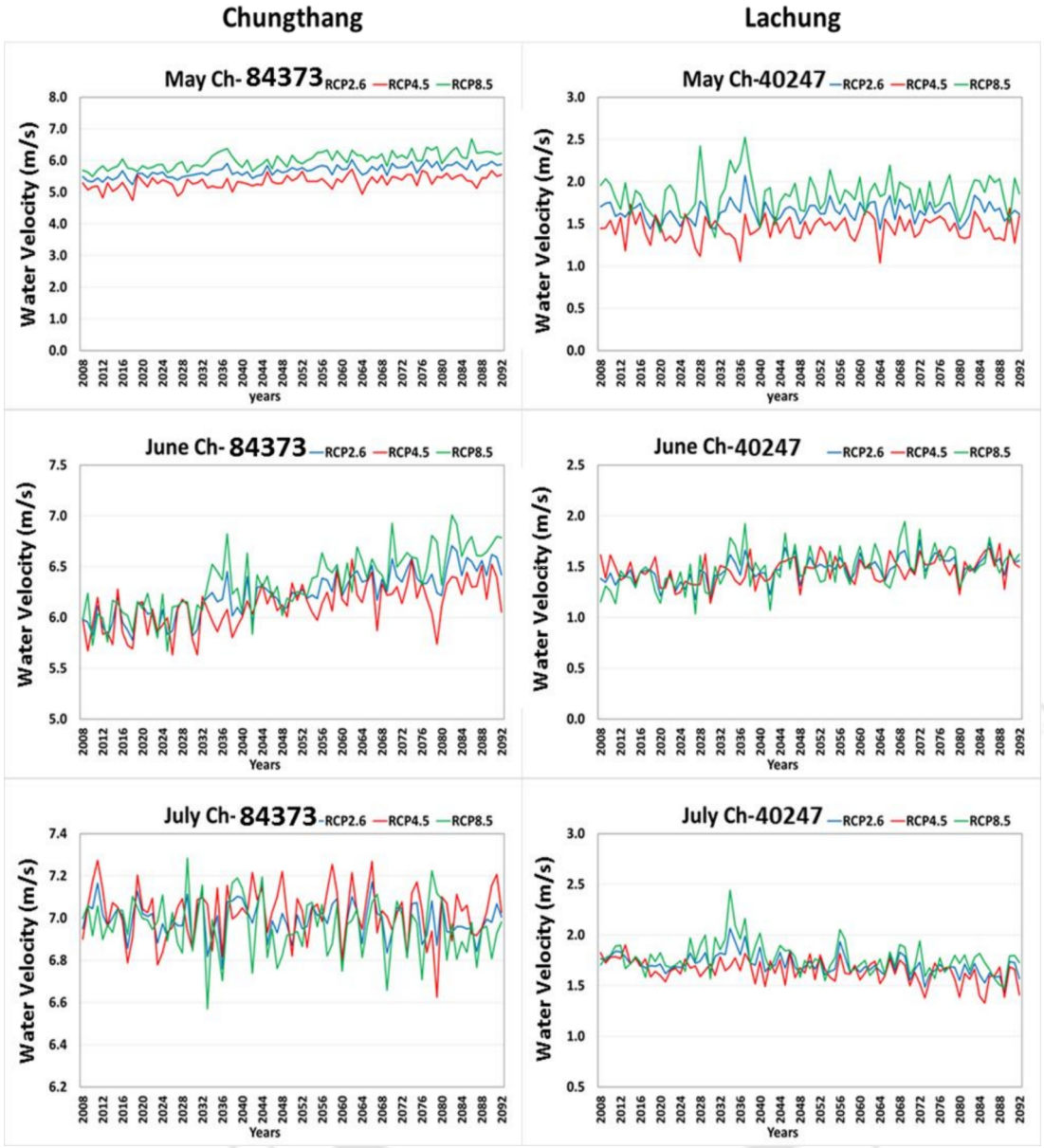


Fig. 6.43: Future Water Velocity (August to October) at Lachung and Chungthang as per CMIP5 CM3 GCMs (2008-2100).

As per the literature, Natural channels are generally parabolic in cross section. Therefore, here $n = 2$ is considered for the optimization. The statistical evaluation method such as coefficient of determination (R^2) has been considered for the evaluation between predicted discharge and projected discharge. The $R^2$is obtained greater than 0.85 in all the equations. The developed rating curve equations have been shown in Table (6.16). Using these rating curve equation at both the gauges i.e. Chungthang and Lachung, the flood stages and return periods can be computed for the 21st century in climate extreme conditions.

TH-1643_136104018

Table 6.16: Development of rating curve equation utilizing projected future water level and discharge (2008-2100).

RCPs-CM3 (2008-2100)	Q-h equation/**Optimization Coefficients	Cross Sections Chainages	
		86465 (Chungthang)	40247 (Lachung)
CM3RCP 2.6	**C	256.992	139.184
	**n	1.769	1.13
	Z_0 (where Q=0)	0.098	0.09
	$Q = C(h+Z_0)^{\wedge n}$	Q=256.992(h+0.098)^1.796	Q=139.184(h+0.09)^1.13
CM3RCP 4.5	**C	289.667	143.627
	**n	0.0826	0.661
	Z_0 (where Q=0)	0.095	0.028
	$Q = C(h+Z_0)^{\wedge n}$	Q=289.667(h+0.0826)^0.0826	Q=143.627(h+0.028)^0.661
CM3RCP 8.5	**C	361.7763	288.9974
	**N	0.971	1.228
	Z_0 (where Q=0)	0.11	0.069
	$Q = C(h+Z_0)^{\wedge n}$	Q=361.7763(h+0.11)^0.971	Q=288.997(h+0.069)^1.228

TH-1643_136104018

CHAPTER 7

CONCLUSIONS AND RECOMMENDATIONS FOR FUTURE WORK

The present study has performed to explore the present and future water resources of snow glacier induced Himalayan catchment namely Teesta river catchment, which is a part of North Sikkim state of India. In this study, to accomplish the impacts of climate change, CMIP5 GCMs with low and extreme emission scenarios (RCPs) based global predictors of climate, used for the downscaling of daily temperature and precipitation datasets at the point locations of Teesta river catchment. In this study, the effect of temperature and precipitation changes has been assessed in various manners over the water resources of Teesta river catchment.

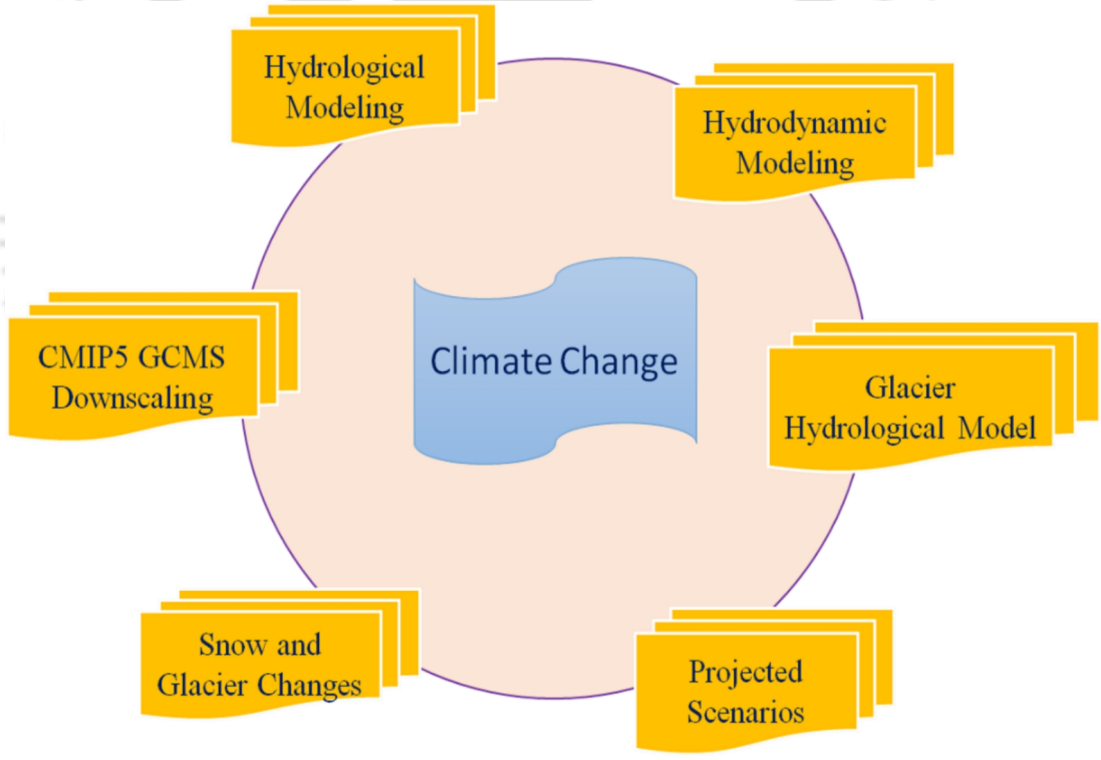


Fig. 7.1: Overall study based major components assessed in the historic and future time domains.

As per the current need, eight most important objectives are selected in this study, which are linked with each other. All the objectives are accomplished by adopting various mathematical methods, empirical methods, statistical-stochastic methods, integrated hydrological-hydrodynamic approaches and remote sensing based methods (Fig. 7.1). Based

TH-1643_136104018

on the selected objectives, following are the conclusive points notified in the overall study outcomes given below as:

7.1 DOWNSCALE SCENARIOS AND THEIR CONCLUSION

A statistical stochastic downscaling of daily temperature and daily precipitation datasets have been performed with reference to observed datasets under latest CMIP5 GCMs with representative concentration pathway based emission scenarios. For the downscaling of daily temperature and precipitation, 16 most relevant global GCM predictors adopted, as per the detailed literature review, to account the global climate impact on a regional scale. Based on the downscaled daily temperature and daily precipitation datasets, future projected scenarios (2006-2100) have been formulated to evaluate the 21st century climate variability and vulnerability over the snow glacier induced Teesta river catchment. The projected scenarios of temperature suggest that the temperature warming will be increased in the 21st century over the selected study region. The temperature will be increased from 1°C (as per the low and moderate emission scenarios: RCP2.6 and RCP4.5) to 2°C (as per the extreme emission scenario RCP8.5) by the end of the century 2100. The daily minimum and maximum temperature based extreme indices have been generated to assess the temperature extremity. The extreme indices based study outcomes show that the diurnal variation width (the gap between maximum and minimum temperature) will be decreased in the future, which highlight an increase in the both maximum and minimum temperature. The other extreme indices such as hottest days, coldest days, frost days and percentile based indices also show increase in the temperature. The non-parametric test such as Mann-Kendall show significant increments in the maximum and minimum temperature over the selected study region. As per the study observations, the minimum temperature is found most vulnerable than maximum temperature.

Similarly, the precipitation scenarios show high spatial variability in the selected study region. The annual precipitation trends show that precipitation amount will be increased in the 21st century. The precipitation extreme indices show significant variability, increase and decrease, over the selected study region. To account the topographical and local climate variations in the temperature and precipitation, temperature lapse rate (TLR) and precipitation lapse rate (PLR) are calculated and projected in the future time scale under CMIP5 GCMs. The TLR and PLR are calculated as per the existed altitudinal variations over the study region, which showed a high spatial variability from one sub-catchment to another sub-catchment. The annual TLR projected scenarios showed a consistent progressive decrease during 2006-2100, which shows that the temperature is enhancing over the glaciated region of Teesta river catchment. The upstream portion of the catchment

TH-1643_136104018

showed higher degree of warming than downstream portion. The PLR also exhibit significant variability over the selected study catchment.

7.2 REMOTE SENSING APPLICABILITY IN THE SNOW COVER AND GLACIAL CHANGE ANALYSIS

In the next portion of the study, satellite remote sensing based assessment of snow cover change and glacial extent change identification have been done. To fulfill this study objective, various remote sensing satellite sensor based high spatial resolution imageries, having multispectral and multitemporal quality, are utilized to perform the analysis. The snow depletion curves (SDC) have been made using cloud free MODIS snow cover and IRS LISS 3 datasets, which gave the present time scenario of snow cover changes. The SDCs show spatio-temporal variability in the snow covered area (SCA) over the Teesta river catchment. Based on the 15 years (2000-2014) monthly SCA statistics and percent of change analysis, calculated from MODIS and LISS 3, it shows high spatial and temporal variability in the SCA area. The elevation bands wise fractional snow covered area also show high spatial changeability in the Teesta river catchment. The glacial lakes and water bodies can be vulnerable to flash flood in the high elevative regions. Thus, based on the NDWI methods, around 73 glacial lakes and water bodies are extracted in the large temporal time domain (e.g. images are compared from 1990 to 2014) utilizing multispectral high resolution Landsat7/8 and LISS 3 satellite sensor datasets. Several glacial lakes, having size greater than 0.5 km^2, are significantly increasing their size from 1990 to 2014. These glacial lakes can be vulnerable for flash floods in the extreme conditions.

In this study, a novel approach has been formulated and presented to classify the debris cover of glaciers. The Zemu glacier has been analyzed for the classification of supraglacial debris and periglacial debris utilizing Landsat7/8 and LISS 3 imageries during 2009 to 2014. In this, multiple band combinations of optical and thermal infrared (TIR) bands from Landsat and LISS 3 sensors have been incorporated. The TIR bands showed significant scope of the study in glacier classification. This novel approach of glacier classification has been compared with previous other similar studies. In this study, the outcomes showed a better accuracy of the outcomes in the debris classification. The final delineated boundary of Zemu glacier (2014) is compared with the survey toposheet (1935) and ICIMOD World Glacier Inventory database (2000) and it showed noticeable glacial retreat at the snout portion of the Zemu glacier.

TH-1643_136104018

7.3 HYDROLOGICAL AND HYDRODYNAMIC MODELING APPLICATIONS IN THE ASSESSMENT OF WATERSHED COMPONENTS

The watershed components and various water balance parameters such as precipitation, snowfall, snowmelt, evapotranspiration (ET), water yield and streamflow have been analyzed at sub-catchment scale and point scale (e.g. Lachung and Chungthang) in the historical and future time scales under CMIP5 GCMs and RCPs. These watershed components are simulated and projected using SWAT model. The model calibration and uncertainty analysis done in the SWATCUP by the application of three different optimization methods such as SUFI2, GLUE and ParaSol. SUFI2 method is observed as the most realizable method to account the various sources of model uncertainties in the modeling outcomes and hence, the accuracy of the results have increased. The detailed parameterization and their sensitivity tests enhanced the understanding about the model processes and associated parameters. The daily precipitation and daily temperature datasets, from different CMIP5 GCMs and RCPs, have been used to project the future scenarios of these water balance components as shown in Appendix (A.1 and A.2).

The historical simulation of the streamflow at Chungthang and Lachung showed better correlation with the observed streamflow datasets. The SWAT based projected scenarios showed high increase in the precipitation, water yield and streamflow amount in the 21st century. The ET is highly fluctuated over the catchment. The elevation band approach utilizing maximum 10 numbers of elevation bands, defined at each sub-catchments, formulated to compute the snowfall and snowmelt. The snowfall is found highly variable in the projected scenarios. The snowmelt show consistent decrease in the future except few observations. For the accurate estimation of streamflow, the initially defined curve number (CN) values have been modified as per the slopes and adjusted CN values are used to perform the study. This modifications in the CN values significantly improved the streamflow discharge peaks.

The improved Glacio-Hydrological Model (GSMSOCONT) has been applied for separating the snow/icemelt contribution and snowmelt contribution from glaciated region and non-glaciated region, respectively. In this model, net radiation and three additional calibration parameters have been added to make the model reliable for the Himalayan terrain conditions. The improved GSMSOCONT is coupled with the SWAT for the historical calibration and future projection of snowmelt runoff computation. The projected scenarios of snowmelt showed significant variability over the study region. The monthly observations of the snowmelt showed that the rate of snow melting will be increased over the region. The earlier snow melting (starts in February) and shifts in melt process (up to December) are

TH-1643_136104018

also observed. As per the extreme emission scenario (RCP8.5), a faster snowmelt is observed. The percent (%) of change analysis of snowmelt clearly show that in the last decades of the 21st century, the rate of snow melting will be increased. The satellite snow cover based snow water equivalent (SWE) reconstruction method has been utilized to evaluated the SWAT simulated snowmelt and snowfall. The SWE reconstruction method utilized the cloud free 8 daily snow cover products. The SWE reconstructed results are compared with SWAT model outcomes and field measurement datasets and found better similarities among all the sources. The satellite based SWE is also compared with several previous studies and found very reliable outcomes in the present domain.

The future projection of various water levels, discharge and water velocities, at different Chainages of the Teesta and Lachung river have been computed. In the historical and projected scenarios, the maximum average water velocity ranges are calculated 6.5 m/s, which shows high velocity over the Teesta river, may be expected due to very steep slopes. The future outcomes from Mike 11 show significant increase in discharge, water level and water velocity at Lachung and Teesta river outlet points. Based on the calculated future water level and discharge, as per CM3 GCMs and RCPs, various rating curve equations have been developed. The rating curve equations, developed in this study, can be used to predict the future discharge at Lachung and Chungthang outlets in the future scenarios. The flood inundation and return periods can be computed from the rating curve equations.

In this study, an integrated hydrological-hydrodynamic coupled approach has been performed for the development of the rating curve equations utilizing projected discharge ad water level by coupling of the SWAT and Mike 11 models. These rating curve equations can be used in making reservoir operation policy for Chungthang Dam. In this study, a Glacier Hydrological Model is improved for the analysis of snowmelt for the Himalayan catchments by adding radiation factors. This study also highlighted the retreating over Zemu glaciers. For this, a novel approach by merging the optical and thermal bands from the Landsat and LISS 3 sensors are presented. The SWAT model based projected future discharge and water balance components shows that the severity of climate change issues will be more frequent in future. These projected scenarios can help to making a strategy for management of water resources for the Teesta river catchment.

7.4 RECOMMENDATIONS FOR FUTURE SCOPE

- In this study, GCMs with little bit coarser resolution datasets have been used to downscale the temperature and precipitation variables and thus, RCMs (Regional Climate Model) based availability of predictors can be useful to assess the global

TH-1643_136104018

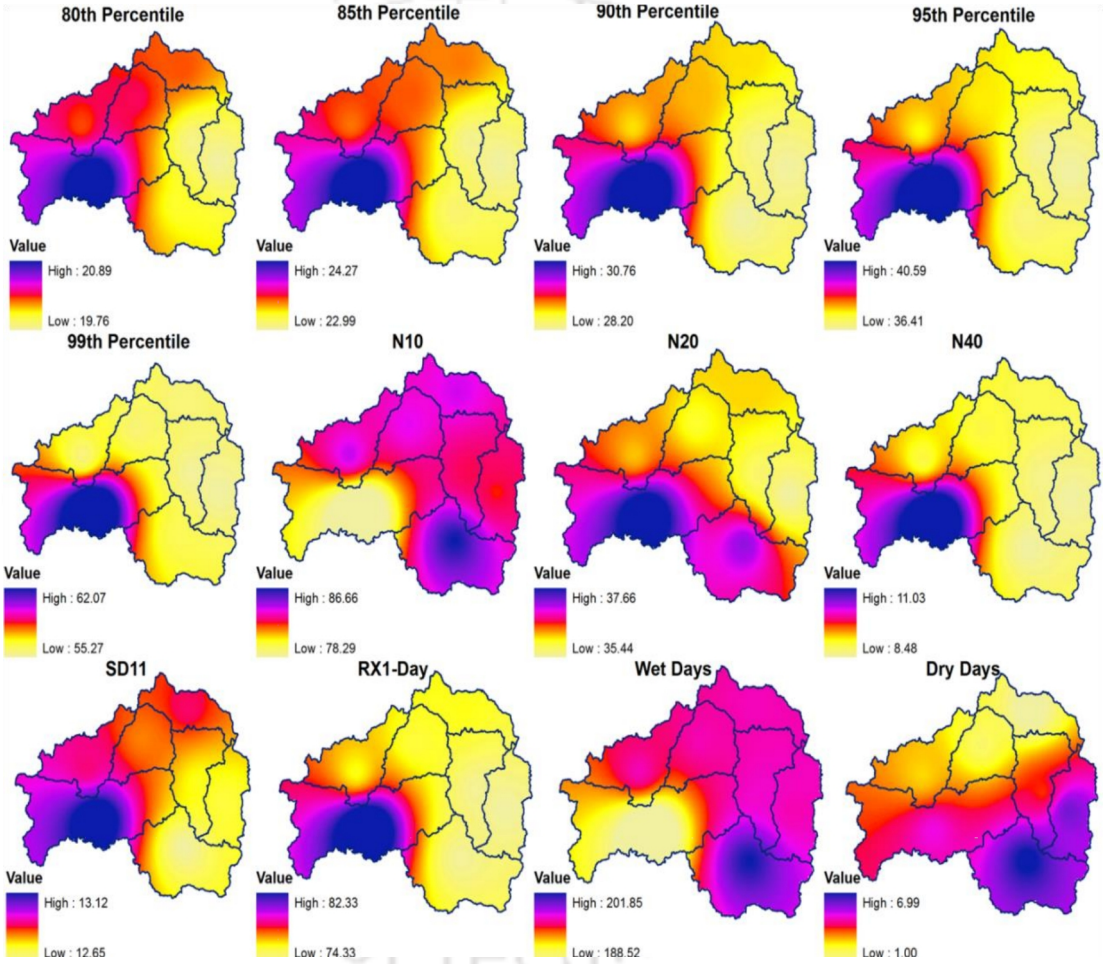
scale climate effects on the regional or point scale. The addition of monsoon conditions can increase the accuracy of the projected scenarios.

- The enhance the snow and glacier dynamics over the Teesta river catchment, instead of 8 daily MODIS snow cover products, daily snow cover products can be utilized. The daily SDC will provide a better estimation of the SCA over this region. The presented novel approach for debris cover of glacier classification can be applied in another similar studies. The present auto-mated approach of the glacier boundary delineation can be utilized in another studied to reduce the time as compare to manual delineation. The automated method of glacier mapping will be most reliable method for the other similar studies.
- The temperature extreme analysis shows that warming will be increased over the snow glaciated catchment of Teesta river. Thus, glacier retreating and snow melting will be faster than present. Glacial lakes are also found vulnerable and increasing their sizes. Thus, a detailed Glacial Lake Outburst Study (GLOF) with downstream flood hazard mapping is needed over this region.
- The SWAT model is used for the projection of various water balance components under the effect of temperature and precipitation changes. The other parameters were remain constant. Though, in other regions, where LULC changes are frequent, further, LULC and other soil changes (temporal changes) can also be incorporated into SWAT model to assess the future changes in water balance components.
- In this study, a one dimensional (1D) hydrodynamic model has been used to compute the flood parameters at different locations along the river path. Thus, 2D hydrodynamic model such as Mike 21 can be utilized for similar kind of studies. The field measurement based calculation of snow density and depth should be most frequent.
- Many hydropower projects have been proposed over the Teesta river catchment, thus, detailed study of watershed components, which have been computed and evaluated in this study, can be utilized for the detailed assessment of potential hydropower project sites. The hydrodynamic computations of future discharges and water levels could be helpful in making reservoir operation policies at the Chungthang gauge stations.
- However, various field based observations such as bed resistant factors and hydraulic structure properties are nor fully incorporated in this study. Thus, there is a scope to incorporate all these factors, based on the field measurement, in hydrodynamic computations of the river flow and water levels during extreme flood conditions.

TH-1643_136104018

APPENDIX A

A. 1 SPATIAL VARIATIONS IN EXTREME PRECIPITATION INDICES



TH-1643_136104018

TH-1643_136104018

A. 2 INTRA-DECADAL AVERAGE ANNUAL SCENARIOS OF MAIN WATER BALANCE COMPONENTS

A2.1 Water Yield and ET (2008-2100): CM3 GCM

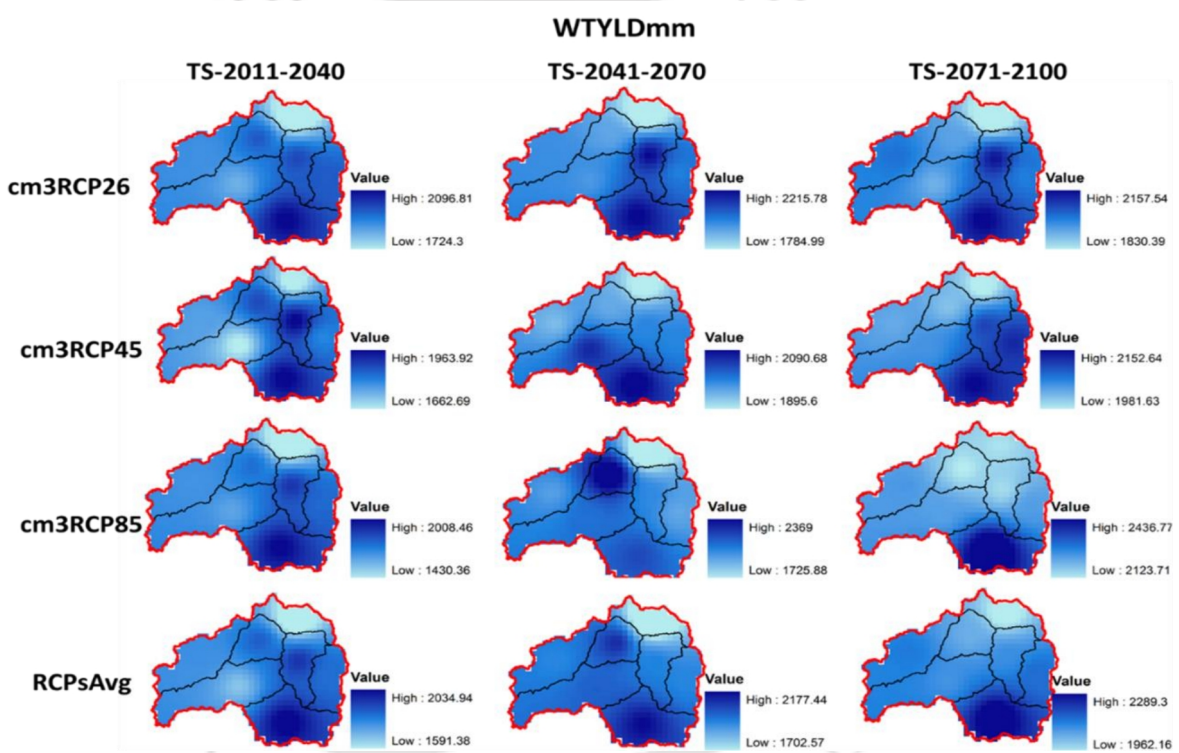


Fig. A.2: Water yield (2008-2100) for CM3 GCM.

TH-1643_136104018

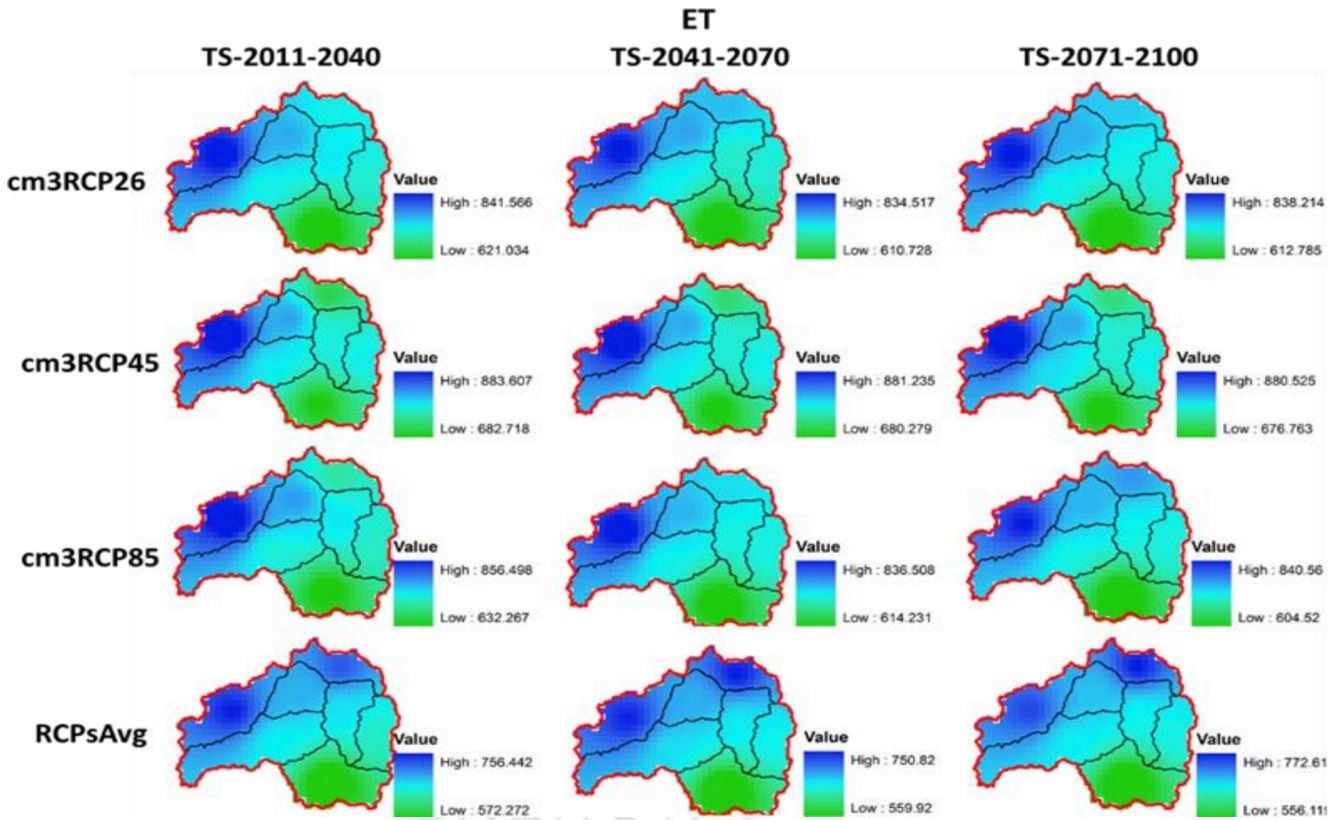


Fig. A.3: ET (2008-2100) for CM3 GCM.

TH-1643_136104018

A2.2 Water Yield and ET (2008-2100): ESM-2M GCM

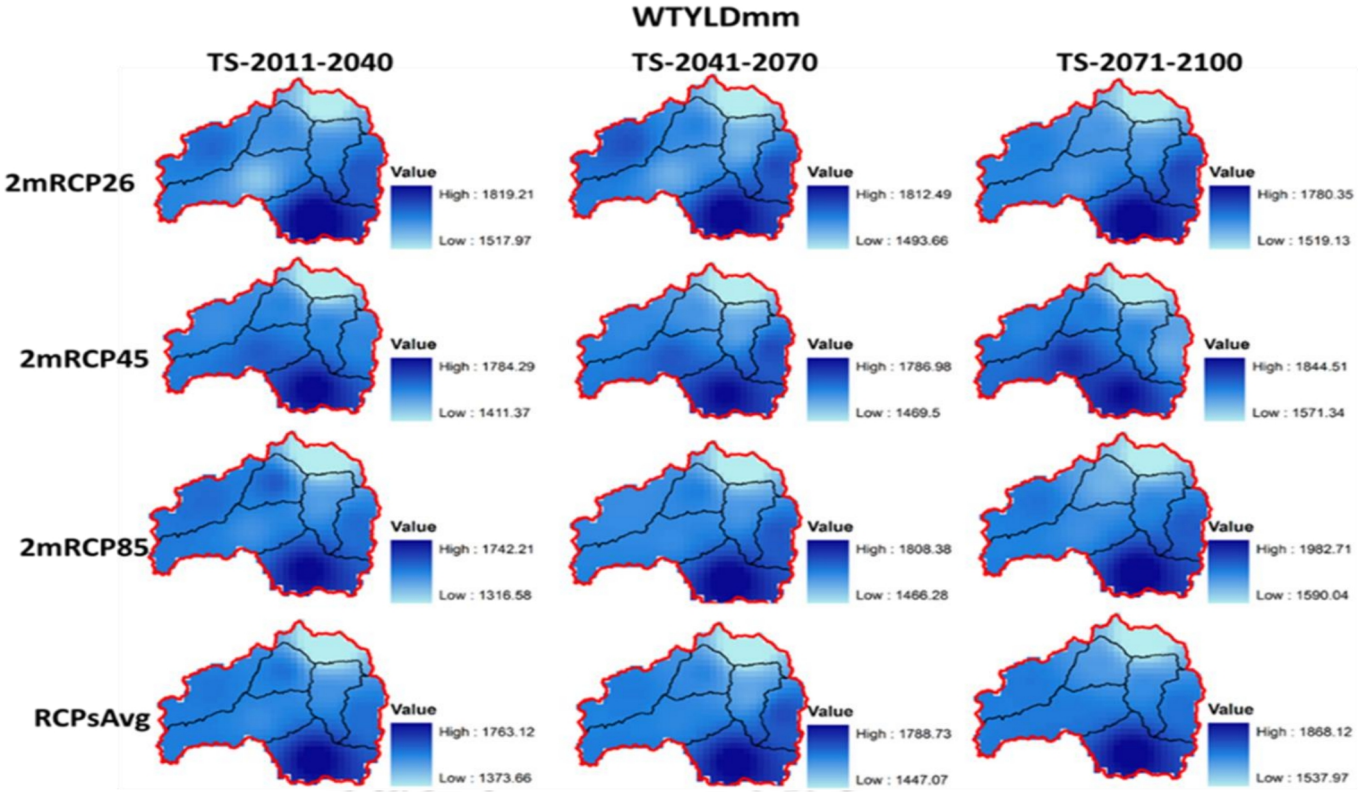


Fig. A.4: Water yield (2008-2100) for ESM2M GCM.

TH-1643_136104018

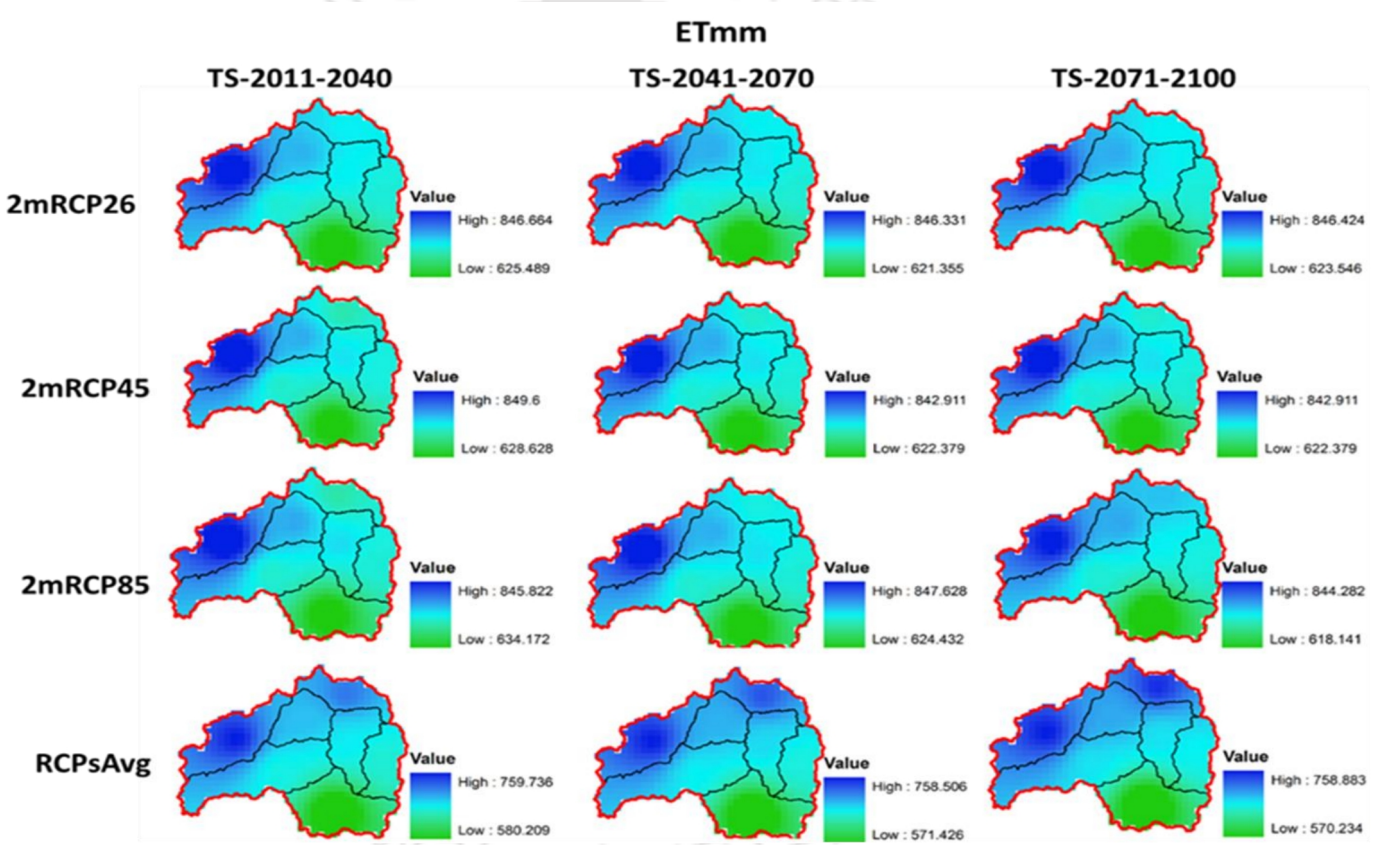


Fig. A.5: ET (2008-2100) for ESM2M GCM.

TH-1643_136104018

A2.3 Water Yield and ET (2008-2100): CM2P1 GCM

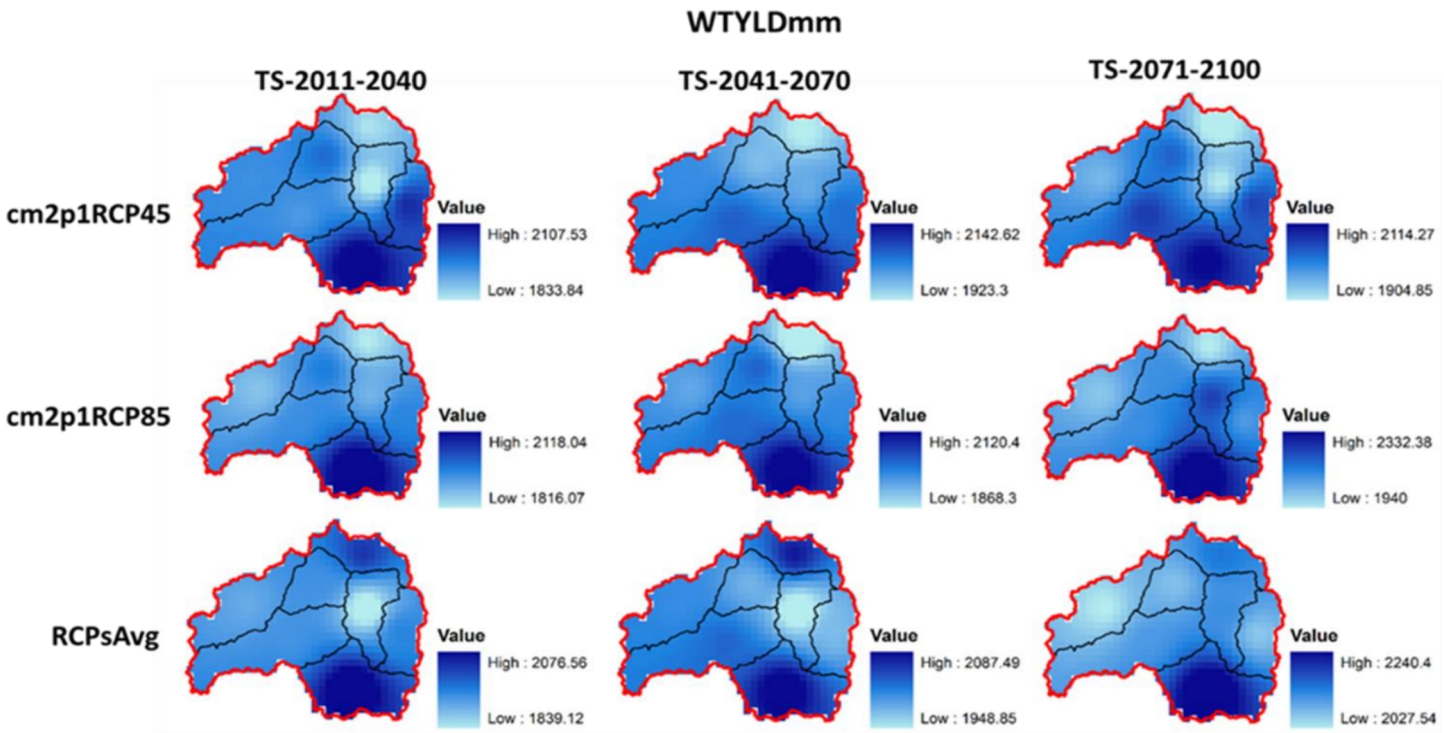


Fig. A.6: Water Yield (2008-2100) for CM2P1 GCM.

TH-1643_136104018

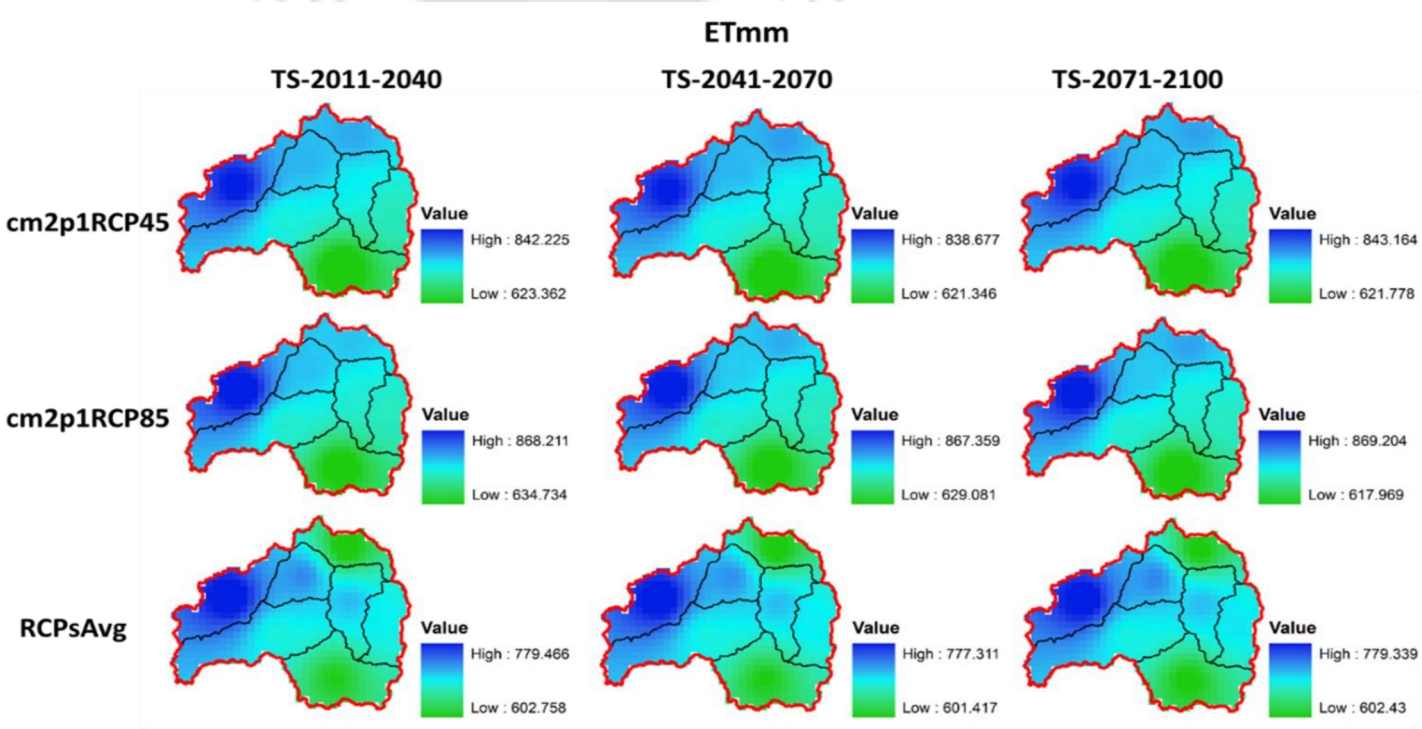


Fig. A.7: ET (2008-2100) for ESM2M GCM

TH-1643_136104018

A.3 Measurement of Snow density at Teesta catchment, North Sikkim Himalaya, India.



Fig. A.8: Measurement of snow density using Snow Density Gauge: Scientific 200.

TH-1643_136104018

A.3 Measurement of Cross Section using Total Stations at River Lachung, North Sikkim Himalaya, India.



Fig. A.9: Measurement of River Cross Section using Total Station.

REFERENCES

1. Abbaspour, K. C. (2011). SWAT-CUP4: SWAT Calibration and Uncertainty Programs – *A User Manual. Swiss Federal Institute of Aquatic Science and Technology, Eawag.*
2. Abbaspour, K. C., Yang, J., Maximov, I., Siber, R., Bogner, K., Mieleitner, J., Zobrist, J., and Srinivasan, R., (2007). *Modelling hydrology and water quality in the pre-alpine/alpine Thur watershed using SWAT. J. of Hydrol. 333,* 413-430.
3. Alifu, H., Tateishi, R., and Johnson, B. (2015). A new band ratio technique for mapping debris-covered glaciers using Landsat imagery and a digital elevation model. *International Journal of Remote Sensing*, *36*(8), 2063-2075.
4. Apurv, T., Mehrotra, R., Sharma, A., Goyal, M. K., and Dutta, S. (2015). Impact of climate change on floods in the Brahmaputra basin using CMIP5 decadal predictions. *Journal of Hydrology*, *527*, 281-291.
5. Arnell, N. W. (1999). Climate change and global water resources. *Global environmental change*, *9*, S31-S49.
6. Arnell, N. W., and Lloyd-Hughes, B. (2014). The global-scale impacts of climate change on water resources and flooding under new climate and socio-economic scenarios. *Climatic Change*, *122*(1-2), 127-140.
7. Arnold, J. G., Moriasi, D. N., Gassman, P. W., Abbaspour, K. C., White, M. J., Srinivasan, R., and Jha, M. K. (2012). SWAT. *Transactions of the ASABE*, *55*(4), 1491-1508.
8. Arnold, J., Srinivasan, R., Muttiah, R. S., and Williams, J. R., (1998). Large area hydrologic modeling and assessment – Part I: model development. *Journal of American Water Resource Assocciation. 34* (1): 73–89.
9. Arora, V. K., Boer, G. J., Friedlingstein, P., Eby, M., Jones, C. D., Christian, J. R., and Wu, T. (2013). Carbon–concentration and carbon–climate feedbacks in CMIP5 Earth system models. *Journal of Climate*, *26*(15), 5289-5314.
10. Awol, F. S., Drueckler, T., and Matz, S. (2015). *Hydropower Energy Simulation Using Mike 11 Model; A Case Study In South Germany's Small Run-Of-River Hydropower Plants.*

TH-1643_136104018

11. Bae D. H., Jung I. W., and Lettenmaier D. P. (2011). Hydrologic uncertainties in climate change from IPCC AR4 GCM simulations of the Chungju basin, Korea. *Journal of Hydrology* 401:90–105.
12. Bajracharya, S. R., Maharjan, S. B., Shrestha, F., Guo, W., Liu, S., Immerzeel, W., and Shrestha, B. (2015). The glaciers of the Hindu Kush Himalayas: current status and observed changes from the 1980s to 2010. *International Journal of Water Resources Development*, (ahead-of-print), 1-13.
13. Bajracharya, S. R., and Shrestha, B. (eds) (2011). *The status of glaciers in the Hindu Kush-Himalayan region. Kathmandu: ICIMOD.*
14. Barros, V. R., Field, C. B., Dokke, D. J., Mastrandrea, M. D., Mach, K. J., Bilir, T. E., and White, L. L. (2015). Climate change 2014: impacts, adaptation, and vulnerability. Part B: regional aspects. *Contribution of Working Group II to the Fifth Assessment Report of the Intergovernmental Panel on Climate Change*.
15. Basnett, S., Kulkarni, A. V., and Bolch, T. (2013). The influence of debris cover and glacial lakes on the recession of glaciers in Sikkim Himalaya, India. *Journal of Glaciology*, 59(218), 1035-1046.
16. Bates, P. D., and De Roo, A. P. J. (2000). A simple raster-based model for flood inundation simulation. *Journal of hydrology*, *236*(1), 54-77.
17. Bawa, K. S., and Ingty, T., (2012). Climate Change in Sikkim: A Synthesis. *Climate Change in Sikkim, Patterns, Impacts and Initiatives.* 19-48.
18. Bera, A. K., Singh, V., Bankar, N., Salunkhe, S. S., and Sharma, J. R. (2014). Watershed Delineation in Flat Terrain of Thar Desert Region in North West India–A Semi Automated Approach Using DEM. *Journal of the Indian Society of Remote Sensing*, *42*(1), 187-199.
19. Beven, K. and Binley, A., (1992). The Future of Distributed Models - Model Calibration and Uncertainty Prediction. *Hydrological Processes, 6*(3): 279-298.
20. Beven, K., Lamb, R., Quinn, P., Romanowicz, R., Freer, J., and Singh, V. P. (1995). Topmodel. *Computer models of watershed hydrology.* 627-668.
21. Bhambri, R., Bolch, T., and Chaujar, R. K. (2011). Mapping of debris-covered glaciers in the Garhwal Himalayas using ASTER DEMs and thermal data. *International Journal of Remote Sensing*, 32, 8095–8119.

TH-1643_136104018

22. Bhambri, R., Bolch, T., Chaujar, R. K., and Kulshreshtha, S. C. (2011). Glacier changes in the Garhwal Himalaya, India, from 1968 to 2006 based on remote sensing. *Journal of Glaciology*, *57*(203), 543-556.
23. Bhardwaj, A., Joshi, P. K., Sam, L., Singh, M. K., Singh, S., and Kumar, R. (2015). Applicability of Landsat 8 data for characterizing glacier facies and supraglacial debris. *International Journal of Applied Earth Observation and Geoinformation*, 38, 51-64.
24. Bhutiyani, M. R., Kale, V. S., and Pawar, N. J. (2008). Changing streamflow patterns in the rivers of northwestern Himalaya: implications of global warming in the 20th century. *Current Science*, *95*(5), 618-626.
25. Black P. E, (1995). Watershed Hydrology. *Book, Second Edition, ISBN-57504-027-551.48, GB980.B57 1996, dc-20.*
26. Blanford, H. F. (1884). On the connection of the Himalaya snowfall with dry winds and seasons of drought in India. *Proceedings of the Royal Society of London,* 37,1–23.
27. Bloschl, G., and Montanari, A. (2010). Climate change impacts—throwing the dice? *Hydrological processes*, *24*(3), 374-381.
28. Bolch, T., Kulkarni, A., Kaab, A., Huggel, C., Paul, F., Cogley, J. G. and Stoffel, M. (2012). The state and fate of Himalayan glaciers. *Science, 336*(6079), 310-314.
29. Bradley, R. S., Keimig, F. T., Diaz, H. F., and Hardy, D. R. (2009). Recent changes in freezing level heights in the Tropics with implications for the deglacierization of high mountain regions. *Geophysical Research Letters*, *36*(17).
30. Brooks, K. N. F., Folliott, P. F., and Magner, J. A. (2012). Book: Hydrology and the Management of Watersheds. John Wiley and Sons, 25-sep-2012 - Technology and Engineering -552 pages.
31. Burn, D. H., and Elnur, M. A. H. (2002). Detection of hydrologic trends and variability. *Journal of hydrology, 255*(1), 107-122.
32. Burn, D. H., Sharif, M., and Zhang, K. (2010). Detection of trends in hydrological extremes for Canadian watersheds. *Hydrological Processes*, *24*(13), 1781-1790.
33. Chang H., and Kwon W. T. (2007). Spatial variations of summer precipitation trends in South Korea, 1973–2005. *Environmental Research Letters* 2(4): 045012.

TH-1643_136104018

34. Change, I. C. (2013). The Physical Science Basis. Working Group I Contribution to the Fifth Assessment Report of the Intergovernmental Panel on Climate Change. *Cambridge, United Kingdom and New York, USA*.
35. Change, I. C. (2014). Impacts, adaptation, and vulnerability. Part A: global and sectoral aspects. *Contribution of working group II to the fifth assessment report of the intergovernmental panel on climate change*.
36. Chelamallu, H. P., Venkataraman, G., and Murti, M. V. R. (2014). Accuracy assessment of MODIS/Terra snow cover product for parts of Indian Himalayas. *Geocarto International*, *29*(6), 592-608.
37. Choi W, Tareghian R, Choi J, Hwang CS (2013) Geographically heterogeneous temporal trends of extreme precipitation in Wisconsin, USA during 1950–2006. *International Journal of Climatology* 34: 2841-2852.
38. Chow, V. T., Maidment, D. R., and Mays, L. W., (2010). *Applied Hydrology. McGraw Hill Edition. ISBN* -0-07-010810-2.
39. Christierson, B. V., Vidal, J. P., and Wade, S. D. (2012). Using UKCP09 probabilistic climate information for UK water resource planning. *Journal of Hydrology*, 424, 48-67.
40. Chu J. T, Xia J, Xu C. Y, and Singh V. P (2010). *Statistical downscaling of daily mean temperature, pan evaporation and precipitation for climate change scenarios in Haihe River, China. Theor. Appl. Climatol.* 99(1–2):149–161. DOI: 10.1007/s00704-009-0129-6.
41. Coe, M. T., Costa, M. H., and Howard, E. A., (2007). Simulating the surface waters of the Amazon River basin: impacts of new river geomorphic and flow parameterizations. *Hydrol. Process. 22* (14), 2542–2553.
42. Collins, D. N., Davenport, J. L., and Stoffel, M. (2013). Climatic variation and runoff from partially-glacierized Himalayan tributary basins of the Ganges. *Science of the Total Environment*, *468*, S48-S59.
43. Crosbie, R. S., Scanlon, B. R., Mpelasoka, F. S., Reedy, R. C., Gates, J. B., and Zhang, L. (2013). Potential climate change effects on groundwater recharge in the High Plains Aquifer, USA. *Water Resources Research*, *49*(7), 3936-3951.
44. Cunderlik, J. M., and Ouarda, T. B. (2009). Trends in the timing and magnitude of floods in Canada. *Journal of Hydrology*, *375*(3), 471-480.
45. Cunge, J. A., Holly, F. M., andVerwey, A., (1980). Practical Aspects of Computational River Hydraulics. *Pitman Advanced Publishing Program*.

TH-1643_136104018

46. Dai, A., Qian, T., Trenberth, K. E., and Milliman, J. D. (2009). Changes in continental freshwater discharge from 1948 to 2004. *Journal of Climate*, *22*(10), 2773-2792.
47. Dale, V. H., Joyce, L. A., McNulty, S., Neilson, R. P., Ayres, M. P., Flannigan, M. D., and Michael Wotton, B. (2001). Climate change and forest disturbances: climate change can affect forests by altering the frequency, intensity, duration, and timing of fire, drought, introduced species, insect and pathogen outbreaks, hurricanes, windstorms, ice storms, or landslides. *BioScience*, *51*(9), 723-734.
48. Dankers, R., Arnell, N. W., Clark, D. B., Falloon, P. D., Fekete, B. M., Gosling, S. N., and Wisser, D. (2014). First look at changes in flood hazard in the Inter-Sectoral Impact Model Intercomparison Project ensemble. *Proceedings of the National Academy of Sciences*, *111*(9), 3257-3261.
49. Paiva de, R. C. D., Buarque, D. C., Collischonn, W., Bonnet, M. P., Frappart, F., Calmant, S., andBulhões Mendes, C. A. (2013). Large-scale hydrologic and hydrodynamic modeling of the Amazon River basin. *Water Resources Research*, *49*(3), 1226-1243.
50. Deng, Z., Qiu, X., Liu, J., Madras, N., Wang, X., and Zhu, H. (2015). Trend in frequency of extreme precipitation events over Ontario from ensembles of multiple GCMs. *Climate Dynamics*, 1-13.
51. DHI, 2009. MIKE 11: A Modeling System for Rivers and Channels. Reference Manual. *Danish Hydraulic Institute, Denmark*.
52. Diallo I., Sylla M. B., Giorgi F., Gaye A. T., Camara M. (2012). Multimodel GCM-RCM ensemble-based projections of temperature and pre- cipitation over West Africa for the Early 21st century. *Int J Geo- phys*2012:1–19. DOI:10.1155/2012/972896.
53. Dietz, A. J., Kuenzer, C., and Conrad, C. (2013). Snow-cover variability in central Asia between 2000 and 2011 derived from improved MODIS daily snow-cover products. *International journal of remote sensing*, *34*(11), 3879-3902.
54. Doll, P., and Bunn, S. E. (2014). Impact of Climate Change on Freshwater Ecosystems due to Altered River Flow Regimes. *Climate change*.
55. Dosio, A., Panitz, H. J., Schubert-Frisius, M., and Luthi, D. (2015). Dynamical downscaling of CMIP5 global circulation models over CORDEX-Africa with COSMO-CLM: evaluation over the present climate and analysis of the added value. *Climate Dynamics*, *44*(9-10), 2637-2661.

TH-1643_136104018

56. Dunn-Sigouin, E., and Son, S. W. (2013). Northern Hemisphere blocking frequency and duration in the CMIP5 models. *Journal of Geophysical Research: Atmospheres*, *118*(3), 1179-1188.
57. Earl, L., and Gardner, A. (2016). A satellite-derived glacier inventory for North Asia. *Annals of Glaciology*, *57*, 50-60.
58. Easterling D. R, Horton B, Jones P. D, Peterson T. C, Karl T. R, Parker D. E, Salinger M. J., Razuvayev V., Plummer N., Jamason P., and Folland C. K. (1997). Maximum and minimum temperature trends for the globe. *Science* 277:364–367. DOI: 10.1126/*science*.277.5324.364
59. Elguindi, N., Somot, S., Déqué, M., and Ludwig, W. (2011). Climate change evolution of the hydrological balance of the Mediterranean, Black and Caspian Seas: impact of climate model resolution. *Climate dynamics*, *36*(1-2), 205-228.
60. Ellison, D., N Futter, M., and Bishop, K. (2012). On the forest cover–water yield debate: from demand-to supply-side thinking. *Global Change Biology*, *18*(3), 806-820.
61. Emanuel, K. (2013). Downscaling CMIP5 climate models shows increased tropical cyclone activity over the 21st century. *PNAS*.
62. ERDAS IMAGINE. (2014). ERDAS Imagine (2014) User Guide. *Atlanta, GA: ERDAS, Intergraph.*
63. Escurra, J. J., Vazquez, V., Cestti, R., De Nys, E., and Srinivasan R., (2014). *Climate change impact on countrywide water balance in Bolivia. Reg. Environ. Change.* 14, 727-742.
64. Etienne, S., and Paris, R. (2010). Boulder accumulations related to storms on the south coast of the Reykjanes Peninsula (Iceland). *Geomorphology*, *114*(1), 55-70.
65. Ferguson, R. I. (1999). Snowmelt runoff models. *Progress in Physical Geography*, *23*(2), 205-227.
66. Feyisa, G. L., Meilby, H., Fensholt, R., and Proud, S. R. (2014). Automated Water Extraction Index: A new technique for surface water mapping using Landsat imagery. *Remote Sensing of Environment*, *140*, 23-35.
67. Ficklin, D. L., and Barnhart, B. L. (2014). SWAT hydrologic model parameter uncertainty and its implications for hydroclimatic projections in snowmelt-dependent watersheds. *Journal of Hydrology*, *519*, 2081-2090.

TH-1643_136104018

68. Field, C. B. (2012). Managing the risks of extreme events and disasters to advance climate change adaptation: special report of the intergovernmental panel on climate change. *Cambridge University Press*. UK.
69. Field, C. B. (2014). Climate change 2014: impacts, adaptation, and vulnerability (Vol. 1). IPCC.
70. Forster, P. M., Andrews, T., Good, P., Gregory, J. M., Jackson, L. S., and Zelinka, M. (2013). Evaluating adjusted forcing and model spread for historical and future scenarios in the CMIP5 generation of climate models. *Journal of Geophysical Research: Atmospheres*, *118*(3), 1139-1150.
71. Frey, H., Paul, F., and Strozzi, T. (2012). Compilation of a glacier inventory for the western Himalayas from satellite data: methods, challenges, and results. *Remote Sensing of Environment*, *124*, 832-843.
72. Gafurov, A., and Bardossy, A. (2009). Cloud removal methodology from MODIS snow cover product. *Hydrology and Earth System Sciences*, *13*(7), 1361-1373.
73. Gao, B. C. (1996). NDWI—a normalized difference water index for remote sensing of vegetation liquid water from space. *Remote sensing of environment*, *58*(3), 257-266.
74. Gardelle, J., Berthier, E., and Arnaud, Y. (2012). Slight mass gain of Karakoram glaciers in the early twenty-first century. *Nature geoscience*, *5*(5), 322-325.
75. Gardner, A. S., Sharp, M. J., Koerner, R. M., Labine, C., Boon, S., Marshall, S. J., and Lewis, D. (2009). Near-surface temperature lapse rates over Arctic glaciers and their implications for temperature downscaling. *Journal of Climate*, *22*(16), 4281-4298.
76. Ghosh S., and Mujumdar P. P. (2008) Statistical downscaling of GCM simulations to streamflow using relevance vector machine. *Ad. Water Resour.* 31:132–146.
77. Ghosh, S., and Dutta, S. (2010). Impact of climate change on flood characteristics in Brahmaputra basin using a macro-scale distributed hydrological model. *Journal of earth system science*, *121*(3), 637-657.
78. Gong, X., and Richman, M. B. (1995). On the application of cluster analysis to growing season precipitation data in North America east of the Rockies. *J. Clim.* *8*(4), 897-931.

TH-1643_136104018

79. Goyal M. K, and Ojha C. S. P. (2010) Robust weighted regression as a down-scaling tool in temperature projections. *Int J Global Warming 2* (3):234–251. DOI:10.1504/IJGW.2010.036135.
80. Goyal M. K. (2014) Statistical Analysis of Long Term Trends of Rainfall during 1901–2002 at Assam, India. *Water Resources Management* 28: 1501-1515.
81. Goyal M. K. (2014). Recession Coefficient. *In Encyclopedia of Snow, Ice and Glaciers* (pp. 922-922). Springer Netherlands.
82. Goyal, M. K., Burn, D. H., and Ojha, C. S. P. (2012). Statistical downscaling of temperatures under climate change scenarios for Thames river basin, Canada. *International Journal of Global Warming*, *4*(1), 13-30.
83. Goyal, M. K., Gupta, V., (2014). Identification of homogeneous rainfall regimes in Northeast Region of India using fuzzy cluster analysis. *Wat. Res. Manage. 28*(13), 4491-4511.
84. Goyal, M. K., Singh, V., and Meena, A. H. (2015). Geospatial and hydrological modeling to assess hydropower potential zones and site location over rainfall dependent Inland catchment. *Water Resources Management*, *29*(8), 2875-2894.
85. Guan, Y., Zhang, X., Zheng, F., and Wang, B. (2015). Trends and variability of daily temperature extremes during 1960–2012 in the Yangtze River Basin, China. *Global and Planetary Change, 124,* 79-94.
86. Gupta, R. P. (2003). Remote sensing geology (second ed.). *New York: LLC: Springer-Verlag.*
87. Gurung, D. R., Giriraj, A., Aung, K. S., Shrestha, B., and Kulkarni, A. V. (2011). Snow-cover mapping and monitoring in the Hindu Kush-Himalayas. International Centre for Integrated Mountain Development (ICIMOD).
88. Gutmann, E., Pruitt, T., Clark, M. P., Brekke, L., Arnold, J. R., Raff, D. A., and Rasmussen, R. M. (2014). An intercomparison of statistical downscaling methods used for water resource assessments in the United States. *Water Resources Research*, *50*(9), 7167-7186.
89. Hagemann, S., Chen, C., Clark, D., Folwell, S., Gosling, S. N., Haddeland, I., and Wiltshire, A. (2013). Climate change impact on available water resources obtained using multiple global climate and hydrology models. *Earth System Dynamics*, *4*, 129-144.
90. Hagemann, S., Chen, C., Haerter, J. O., Heinke, J., Gerten, D., and Piani, C. (2011). Impact of a statistical bias correction on the projected hydrological

TH-1643_136104018

changes obtained from three GCMs and two hydrology models. *Journal of Hydrometeorology*, *12*(4), 556-578.

91. Hall, B. L., Denton, G. H., Overturf, B., and Hendy, C. H. (2002). Glacial Lake Victoria, a high-level Antarctic Lake inferred from lacustrine deposits in Victoria Valley. *Journal of Quaternary Science*, *17*(7), 697-706.
92. Hall, Dorothy K., George A. Riggs, and Vincent V. Salomonson. 2006, updated weekly. MODIS/Terra Snow Cover 8-day L3 Global 500m Grid V005, [list the dates of the data used]. Boulder, Colorado USA: National Snow and Ice Data Center. Digital media.
93. Hamilton, J. D. (1994). Time series analysis (Vol. 2). Princeton: Princeton university press.
94. Hantel, M., and Maurer, C. (2011). The median winter snowline in the Alps. *Meteorologische Zeitschrift*, *20*(3), 267-276.
95. Hao, L. and Naiman, D. Q. (Eds.). (2007). Quantile regression (No. 149). *Sage.*
96. Harding, R. J., Weedon, G. P., van Lanen, H. A., and Clark, D. B. (2014). The future for global water assessment. *Journal of Hydrology*, *518*, 186-193.
97. Hattermann, F. F., Kundzewicz, Z. W., Huang, S., Vetter, T., Gerstengarbe, F. W., and Werner, P. (2013). Climatological drivers of changes in flood hazard in Germany. *ActaGeophysica*, *61*(2), 463-477.
98. Havno, K., Madsen, M. N., Dorge, J., and Singh, V. P. (1995). MIKE 11-a generalized river modelling package. *Computer models of watershed hydrology.* 733-782.
99. Himalayan, N. D. A. (2009). No sign yet of Himalayan meltdown, Indian report finds.
100. Hirabayashi, Y., Mahendran, R., Koirala, S., Konoshima, L., Yamazaki, D., Watanabe, S., andKanae, S. (2013). Global flood risk under climate change. *Nature Climate Change*, *3*(9), 816-821.
101. Hooker, J. D. (2003). Himalayan Journals II (Vol. 9). Psychology Press.
102. Horton, B. (1995). Geographical distribution of changes in maximum and minimum temperatures. *Atmos. Res. 37*(103):101–117. DOI:10.1016/ 0169-8095(94)00083-P.
103. Horton, R., Yohe, G., Easterling, W. E., Kates, R., Ruth, M., Sussman, E., Whelchel, A., and Wolfe, D. (2013) Northeast. *In: National climate assessment, U.S. global change research program, chap 16.*

TH-1643_136104018

104. Hua, S., Liang, J., Zeng, G., Xu, M., Zhang, C., Yuan, Y., and Huang, L. (2015). How to manage future groundwater resource of China under climate change and urbanization: An optimal stage investment design from modern portfolio theory. *Water research*, *85*, 31-37.

105. Huang J, Zhang J, Zhang Z, Xu C,Wang B, and Yao, J. (2011) Estimation of future precipitation change in the Yangtze River basin by using statistical downscaling method. StochEnv Res Risk A 25(6):781– 792. DOI:10.1007/s00477-010-0441-9

106. Huang, G., Qin, X., He, L., Zhang, H., Li, Y., and Li, Z. (2015). Nonstationary desertification dynamics of desert oasis under climate change and human interference. Journal of Geophysical Research: Atmospheres.

107. Hunter N. M., Bates P. D., Matthew S., Horritt M. S., and Wilson M. D. (2007) Simple spatially-distributed models for predicting flood inundation: a review. *Geomorphology* 90:208–225.

108. Huss, M. (2011). Present and future contribution of glacier storage change to runoff from macroscale drainage basins in Europe. *Water Resources Research*, *47*(7).

109. Ichiyanagi, K., Yamanaka, M. D., Muraji, Y., and Vaidya, B. K. (2007). Precipitation in Nepal between 1987 and 1996. *International Journal of Climatology*, *27*(13), 1753-1762.

110. Immerzeel, W. W., Droogers, P., De Jong, S. M., and Bierkens, M. F. P. (2009). Large-scale monitoring of snow cover and runoff simulation in Himalayan river basins using remote sensing. *Remote sensing of Environment*, *113*(1), 40-49.

111. India-WRIS. (2012). River Basin Atlas of India, *RRSC-West, NRSC, ISRO, Jodhpur, India.*

112. IPCC (2007) Climate Change 2007: The physical science basis. *Contribution of Working Group I to the Fourth Assessment Report of the IPCC,* by Solomon S., Qin D., ManningM, Chen Z,Marquis M, Averyt M, Tignor M, Miller HL (eds). Cambridge University Press, Cambridge, UK.

113. IPCC (2012): Managing the Risks of Extreme Events and Disasters to Advance Climate Change Adaptation. *A Special Report of Working Groups I and II of the Intergovernmental Panel on Climate Change* [Field, C. B., V. Barros, T. F. Stocker, D. Qin, D. J. Dokken, K. L. Ebi, M. D. Mastrandrea, K. J. Mach, G. K. Plattner, S. K. Allen, M. Tignor, and P. M. Midgley (eds.)].

TH-1643_136104018

Cambridge University Press, Cambridge, UK and New York, NY, USA, 582 pp.

114. Jackson, C. R., Meister, R., and Prudhomme, C. (2011). Modelling the effects of climate change and its uncertainty on UK Chalk groundwater resources from an ensemble of global climate model projections. *Journal of Hydrology*, *399*(1), 12-28.

115. Jain S. K., and Kumar V. (2012) Trend analysis of rainfall and temperature data for India. *Current Science* 102: 37-49.

116. Jain, S. K., Tyagi, J., and Singh, V. (2010). Simulation of runoff and sediment yield for a Himalayan watershed using SWAT model. *Journal of Water Resource and Protection*, *2*(03), 267.

117. Jarosch, A. H., Anslow, F. S., and Clarke, G. K. (2012). High-resolution precipitation and temperature downscaling for glacier models. *Climate Dynamics*, *38*(1-2), 391-409.

118. Jena, S., Panda, R. K., andTripathy, S. (2015). Effect of climate change on groundwater recharge and long term sustainable utilisation of groundwater in the sub-humid, sub-tropical region of Eastern India. *InASABE 1st Climate Change Symposium: Adaptation and Mitigation Conference Proceedings* (pp. 1-1). American Society of Agricultural and Biological Engineers.

119. Johansen, K., Phinn, S., and Taylor, M. (2015). Mapping woody vegetation clearing in Queensland, Australia from Landsat imagery using the Google Earth Engine. *Remote Sensing Applications: Society and Environment*, *1*, 36-49.

120. Jones, C., and Carvalho, L. M. (2014). Sensitivity to Madden–Julian Oscillation variations on heavy precipitation over the contiguous United States. *Atmospheric Research*, *147*, 10-26.

121. Jones, P. D., Trenberth, K., Ambenje, P., Bojariu, R., Easterling, D., Klein, T., andZhai, P. (2007). Observations: surface and atmospheric climate change. In Climate Change 2007: The Physical Science Basis. Contribution of Working Group I to the Fourth Assessment Report of the Intergovernmental Panel on Climate Change, 235-336.

122. Joshi, S., Kumar, K., Joshi, V., and Pande, B. (2014). Rainfall variability and indices of extreme rainfall-analysis and perception study for two stations over Central Himalaya, India. *Natural hazards*, 72(2), 361-374.

TH-1643_136104018

123. Jung, I. W., Bae, D. H., and Lee, B. J. (2013). Possible change in Korean streamflow seasonality based on multi-model climate projections. *Hydrological Processes*, *27*(7), 1033-1045.

124. Kaab, A., Berthier, E., Nuth, C., Gardelle, J., and Arnaud, Y. (2012). Contrasting patterns of early twenty-first-century glacier mass change in the Himalayas. *Nature*, *488*(7412), 495-498.

125. Kagawa, S., Suh, S., Hubacek, K., Wiedmann, T., Nansai, K., and Minx, J. (2015). CO 2 emission clusters within global supply chain networks: Implications for climate change mitigation. *Global Environmental Change*.

126. Kalra, A., Piechota, T. C., Davies, R., and Tootle, G. A. (2008). Changes in US streamflow and western US snowpack. *Journal of hydrologic engineering*.

127. Kargel, J. S., Cogley, J. G., Leonard, G. J., Haritashya, U., and Byers, A. (2011). Himalayan glaciers: The big picture is a montage. *Proceedings of the National Academy of Sciences*, *108*(36), 14709-14710.

128. Kattelmann, R. (1987). Uncertainty in assessing Himalayan water resources. *Mountain Research and Development*, 279-286.

129. Kendall, M. G. (1975). Rank Correlation Methods, *Griffin, London*, 202 pp.

130. Khan, A., Naz, B. S., and Bowling, L. C. (2015). Separating snow, clean and debris covered ice in the Upper Indus Basin, Hindukush-Karakoram-Himalayas, using Landsat images between 1998 and 2002. *Journal of Hydrology*, *521*, 46-64.

131. Kharin, V. V., Zwiers, F. W., Zhang, X., andWehner, M. (2013). Changes in temperature and precipitation extremes in the CMIP5 ensemble. *Climatic Change*, *119*(2), 345-357.

132. Kim, C., Suh, M. S., and Hong, K. O. 2009. Bayesian Changepoint Analysis of the Annual Maximum of Daily and Sub daily Precipitation over South Korea. *Journal of Climate* 22(24): 6741–6757.

133. Knutti, R., andSedlacek, J. (2013). Robustness and uncertainties in the new CMIP5 climate model projections. *Nature Climate Change*, *3*(4), 369-373.

134. Koenker, R. (2005). *Quantile regression (No. 38).* Cambridge university press.

135. Krakauer, N. Y., Pradhanang, S. M., Panthi, J., Lakhankar, T., and Jha, A. K. (2015). Probabilistic Precipitation Estimation with a Satellite Product. *Climate*, *3*(2), 329-348.

TH-1643_136104018

136. Krishna, A. P. (2005). Snow and glacier cover assessment in the high mountains of Sikkim Himalaya. *Hydrological Processes*, *19*(12), 2375-2383.

137. Kulkarni, A. V., Bahuguna, I. M., Rathore, B. P., Singh, S. K., Randhawa, S. S., Sood, R. K., and Dhar, S. (2007). Glacial retreat in Himalaya using Indian Remote Sensing satellite data. *Current science*, *92*(1), 69-74.

138. Kulkarni, A. V., Rathore, B. P., Singh, S. K., Ajai., (2010). Distribution of seasonal snow covers in central and western Himalaya. *Annals of Glaciol.* 51, 123–128.

139. Kumar, R., Singh, R. D., and Sharma, K. D. (2005). Water resources of India. *Current science*, *89*(5), 794-811.

140. Kunkel, K., Stevens L., and Stevens S. (2013) Regional climate trends and scenarios for the U.S. National Climate Assessment. Part1. *Climate of the Northeast U.S. Tech. Rep. NESDIS 142-1, U.S. Department of Commerce National Oceanic and Atmospheric Administration.*

141. Lauwaet, D., Hooyberghs, H., Maiheu, B., Lefebvre, W., Driesen, G., Van Looy, S., and De Ridder, K. (2015). Detailed Urban Heat Island Projections for Cities Worldwide: Dynamical Downscaling CMIP5 Global Climate Models. *Climate*, *3*(2), 391-415.

142. Le Houerou, H. N. (1996). Climate change, drought and desertification. *Journal of Arid Environments*, *34*(2), 133-185.

143. Lee J. W., and Hong S. Y. (2013) Potential for added value to down- scaled climate extremes over Korea by increased resolution of a regional climate model. *TheorApplClimatol*. DOI:10.1007/ s00704-013-1034-6

144. Lee, J. W., Hong, S. Y., Chang, E. C., Suh, M. S., and Kang, H. S. (2014). Assessment of future climate change over East Asia due to the RCP scenarios downscaled by GRIMs-RMP. *Clim. Dynam.* 42(3–4):733–747. DOI: 10.1007/s00382-013-1841-6.

145. Li, J., Dong, W. J., Yang, and Z. W. (2012). Changes of climate extremes of temperature and precipitation in summer in eastern China associated with changes in atmospheric circulation in East Asia during 1960–2008. *Chin. Sci. Bull. 57* (15), 1856–1861.

146. Li, L., Vrieling, A., Skidmore, A., Wang, T., Muñoz, A. R., and Turak, E. (2015). Evaluation of MODIS Spectral Indices for Monitoring Hydrological Dynamics of a Small, Seasonally-Flooded Wetland in Southern Spain. *Wetlands*, *35*(5), 851-864.

TH-1643_136104018

147. Liang, X., Lettenmaier, D. P., Wood, E. F., and Burges, S. J. (1994). A simple hydrologically based model of land surface water and energy fluxes for general circulation models. *JOURNAL OF GEOPHYSICAL RESEARCH-ALL SERIES-*, *99*, 14-415.

148. Lie, L., Zeng, Z., and Zhang, B. (2012). Method for detecting snow lines from MODIS data and assessment of changes in the Nianqingtanglha Mountains of the Tibet plateau. *Selected Topics in Applied Earth Observations and Remote Sensing, IEEE Journal of*, *5*(3), 769-776.

149. Liu, H. L., Chen, X., Bao, A. M., and Wang, L. (2007). Investigation of groundwater response to overland flow and topography using a coupled MIKE SHE/MIKE 11 modeling system for an arid watershed. *Journal of Hydrology*, *347*(3), 448-459.

150. Liu, J., Song, M., Horton, R. M., and Hu, Y. (2013). Reducing spread in climate model projections of a September ice-free Arctic. *Proceedings of the National Academy of Sciences*, *110*(31), 12571-12576.

151. Liu, Z., and Todini, E.(2002). Towards a comprehensive physically-based rainfall-runoff model. *Hydrol. Earth Syst. Sci.* 6 (5), 859–881.

152. Loinaz, M. C., Davidsen, H. K., Butts, M., and Bauer-Gottwein, P. (2013). Integrated flow and temperature modeling at the catchment scale. *Journal of Hydrology*, 495, 238-251.

153. Lougeay, R. (1974). Detection of buried glacial and ground ice with thermal infrared remote sensing. In H. S. Santeford, and J. L. Smith (Eds.), Advanced concepts and techniques in the study of snow and ice resources. Washington, D. C: *National Academy of Sciences* (800 pp.).

154. Lu, G. Y., and Wong, D. W. (2008). An adaptive inverse-distance weighting spatial interpolation technique. *Computers andGeosc*. 34, 1044-1055.

155. Lutz, A. F., Immerzeel, W. W., Gobiet, A., Pellicciotti, F., andBierkens, M. F. P. (2013). Comparison of climate change signals in CMIP3 and CMIP5 multi-model ensembles and implications for Central Asian glaciers. *Hydrology and Earth System Sciences*, *17*(9), 3661-3677.

156. Madsen, H., and Skotner, C. (2005). Adaptive state updating in real-time river flow forecasting—A combined filtering and error forecasting procedure. *Journal of Hydrology*, *308*(1), 302-312.

157. Mahmood R., and Babel M. S. (2012). Evaluation of SDSM developed by annual and monthly sub-models for downscaling temperature and

TH-1643_136104018

precipitation in the Jhelum basin, Pakistan and India. *Theoretical and applied climatology*, *113*: 27-44.

158. Mall, R. K., Gupta, A., Singh, R., Singh, R. S., and Rathore, L. S. (2006). Water resources and climate change: an Indian perspective. *Current science*, *90*(12), 1610-1626.

159. Manandhar, S., Pandey, V. P., Ishidaira, H., and Kazama, F. (2013). Perturbation study of climate change impacts in a snow-fed river basin. *Hydrological Processes*, 27(24), 3461-3474.

160. Manjunath, K. R., Panigrahy, S., Kumari, K., Adhya, T. K., and Parihar, J. S. (2006). Spatiotemporal modelling of methane flux from the rice fields of India using remote sensing and GIS. *International Journal of Remote Sensing*, *27*(20), 4701-4707.

161. Mann H. B. (1975) Nonparametric tests against trend. *Econometrica*. 13:245-259.

162. Mann, M. E., and Gleick, P. H. (2015). Climate change and California drought in the 21st century. *Proceedings of the National Academy of Sciences*, *112*(13), 3858-3859.

163. Marston, R. A., Fritz, D. E. and Nordberg, V. 1997. The impact of debris torrents on substrates of mountain streams.*Geomorphologie: Relief, Processus, Environement* 1, 21-32.

164. Mastrandrea, M. D., Mach, K. J., Plattner, G. K., Edenhofer, O., Stocker, T. F., Field, C. B., andMatschoss, P. R. (2011). The IPCC AR5 guidance note on consistent treatment of uncertainties: a common approach across the working groups. *Climatic Change*, *108*(4), 675-691.

165. Meehl, G. A., Covey, C., McAvaney, B., Latif, M., and Stouffer, R. J. (2005). Overview of the coupled model intercomparison project. *Bulletin of the American Meteorological Society*, *86*(1), 89-93.

166. Meehl, G. A., Goddard, L., Murphy, J., Stouffer, R. J., Boer, G., Danabasoglu, G., and Stockdale, T. (2009). *Decadal prediction: can it be skilful.*

167. Meehl, G., Moss, R., Taylor, K., Eyring, V., Bony, S., Stouffer, R., and Stevens, B. (2014). Climate model intercomparisons: preparing for the next phase. *EOS, Transactions of the American Geophysical Union*, *95*, 77-78.

168. Mehdi, B., Lehner, B., Gombault, C., Michaud, A., Beaudin, I., Sottile, M. F., and Blondlot, A. (2015). Simulated impacts of climate change and agricultural land use change on surface water quality with and without

TH-1643_136104018

adaptation management strategies. *Agriculture, Ecosystems and Environment*, *213*, 47-60.

169. Miao, C., Duan, Q., Sun, Q., Huang, Y., Kong, D., Yang, T., and Gong, W. (2014). Assessment of CMIP5 climate models and projected temperature changes over Northern Eurasia. *Environmental Research Letters*, *9*(5), 055007.

170. Ministry of Water Resources. Hydro-meteorological data dissemination policy. *Government of India; 2013 [14 pp.]*

171. Mishra, S. K., Chaudhary, A., Shrestha, R. K., Pandey, A., and Lal, M. (2014). Experimental verification of the effect of slope and land use on SCS runoff curve number. *Water resources management, 28*(11), 3407-3416.

172. Mishra, S., Saravanan, C., Dwivedi, V. K., and Pathak, K. K. (2015). Discovering flood rising pattern in hydrological time series data mining during the pre-monsoon period. *Indian Journal of Marine Sciences*, *44*(3), 3.

173. Molotch, N. P., and Bales, R. C. (2006). SNOTEL representativeness in the Rio Grande headwaters on the basis of physiographics and remotely sensed snow cover persistence.*Hydrol Process, 20*:723–39.

174. Molotch, N. P., and Margulis, S. A. (2008). Estimating the distribution of snow water equivalent using remotely sensed snow cover data and a spatially distributed snowmelt model: A multi-resolution, multi-sensor comparison. *Advances in Water Resources*, *31*(11), 1503-1514.

175. Moss, R. H., Edmonds, J. A., Hibbard, K. A., Manning, M. R., Rose, S. K., Van Vuuren, D. P., and Wilbanks, T. J. (2010). The next generation of scenarios for climate change research and assessment. *Nature*, *463*(7282), 747-756.

176. Murphy, B. F., and Timbal, B. (2008). A review of recent climate variability and climate change in southeastern Australia. *International journal of Climatology*, *28*(7), 859-879.

177. Narsimlu, B., Gosain, A. K., and Chahar, B. R. (2013). Assessment of future climate change impacts on water resources of upper sind river basin, India using SWAT model. *Water resources management*, *27*(10), 3647-3662.

178. Nayak, (2006). *Master Thesis: An analysis using LISS 3 data for estimating water demand for rice cropping in parts of hirakud command area, Orissa, India*. IIRS. Dehradun, India.

TH-1643_136104018

179. Negi, H. S., Jassar, H. S., Saravana, G., Thakur, N.,Snehmani, K., and Ganju, A. (2013). Snow-cover characteristics using Hyperion data for the Himalayan region. *International Journal of Remote Sensing,* 34(6), 2140-2161.

180. Neitsch, S. L., Arnold, J. G., Kiniri, J. R., Williams, J. R., (2011). Soil water assessment tool theoretical documentation version 9. *Texas water resource institute of technical report No. 406,* Texas A and M University.

181. NRSC. (2010). *Wasteland Atlas of India*. National Remote Sensing Centre. Indian Space Research Organization (ISRO), Government of India. Hyderabad.

182. Pachauri, R. K., Allen, M. R., Barros, V. R., Broome, J., Cramer, W., Christ, R., and van Vuuren, D. (2014). Climate Change 2014: Synthesis Report. *Contribution of Working Groups I, II and III to the Fifth Assessment Report of the Intergovernmental Panel on Climate Change.*

183. Paeth, H., and Mannig, B. (2012). On the added value of regional climate modeling in climate change assessment. *ClimDynam 41*(3– 4):1057–1066. DOI:10.1007/s00382-012-1517-7.

184. Paiva, R. C. D. (2009). Large Scale Hydrological and Hydrodynamic Modeling: the Rio Solimões Case Study (in Portuguese). *M.Sc.* Dissertation, Instituto de PesquisasHidráulicas, Universidade Federal do Rio Grande do Sul. http://hdl.handle.net/ 10183/18927.

185. Palazzi, E., von Hardenberg, J., Terzago, S., and Provenzale, A. (2014). Precipitation in the Karakoram-Himalaya: a CMIP5 view. *Climate Dynamics*, *45*(1-2), 21-45.

186. Pall, P., Aina, T., Stone, D. A., Stott, P. A., Nozawa, T., Hilberts, A. G., and Allen, M. R. (2011). Anthropogenic greenhouse gas contribution to flood risk in England and Wales in autumn 2000. *Nature*, *470*(7334), 382-385.

187. Panday, P. K., Williams, C. A., Frey, K. E., and Brown, M. E. (2014). Application and evaluation of a snowmelt runoff model in the Tamor River basin, Eastern Himalaya using a Markov Chain Monte Carlo (MCMC) data assimilation approach. *Hydrological Processes*, *28*(21), 5337-5353.

188. Patil, S. D., Wigington, P. J., Leibowitz, S. G., Sproles, E. A., and Comeleo, R. L. (2014). How does spatial variability of climate affect catchment streamflow predictions?.*Journal of Hydrology*, *517*, 135-145.

189. Paudel, K. P., and Andersen, P. (2011). Monitoring snow cover variability in an agropastoral area in the Trans Himalayan region of Nepal using MODIS

TH-1643_136104018

data with improved cloud removal methodology. *Remote Sensing of Environment*, *115*(5), 1234-1246.

190. Paul, F., Huggel, C., and Kaab, A. (2004). Combining satellite multispectral image data and a digital elevation model for mapping debris-covered glaciers. *Remote Sensing of Environment*, *89*(4), 510-518.

191. Paz, A. R., Bravo, J. M., Allasia, D., Collischonn, W., Tucci, C. E. M., (2010). *Large-scale hydrodynamic modeling of a complex river network and floodplains. J. Hydrol.Eng. 15* (2), 152–165.

192. Portmann, F. T., Doll, P., Eisner, S., and Florke, M. (2013). Impact of climate change on renewable groundwater resources: assessing the benefits of avoided greenhouse gas emissions using selected CMIP5 climate projections. *Environmental Research Letters*, *8*(2), 024023.

193. Pramanik, N., Panda, R. K., and Sen, D. (2010). One dimensional hydrodynamic modeling of river flow using DEM extracted river cross-sections. *Water resources management*, *24*(5), 835-852.

194. Pratap, B., Dobhal, D. P., Bhambri, R., Mehta, M., and Tewari, V. C. (2015). Four decades of glacier mass balance observations in the Indian Himalaya. *Regional Environmental Change*, 1-16.

195. Pratap, B., Dobhal, D. P., Mehta, M., and Bhambri, R. (2014). Influence of debris cover and altitude on glacier surface melting: a case study on Dokriani Glacier, central Himalaya, India. *Ann Glaciol*, 56(70), 9-16.

196. Pushpadas, D., Schrum, C., and Daewel, U. (2015, April). Projected Climate change effects on North Sea and Baltic Sea: CMIP3 and CMIP5 Model-Based Scenarios. In *EGU General Assembly Conference Abstracts* (Vol. 17, p. 5470).

197. Qian, W. H., Fu, J. K., and Yan, Z. W., (2007). Decrease of light rain events in summer associated with a warming environment in China during 1961–2005. *Geophys. Res. Lett. 34, L11705.*

198. Racoviteanu, A. E., Williams, M. W., and Barry, R. G. (2008). Optical remote sensing of glacier characteristics: a review with focus on the Himalaya. *Sensors*, *8*(5), 3355-3383.

199. Racoviteanu, A., and Williams, M. W. (2012). Decision tree and texture analysis for mapping debris-covered glaciers in the Kangchenjunga area, Eastern Himalaya. *Remote Sensing*, *4*(10), 3078-3109.

200. Radic, V., Bliss, A., Beedlow, A. C., Hock, R., Miles, E., and Cogley, J. G. (2014). Regional and global projections of twenty-first century glacier mass

TH-1643_136104018

changes in response to climate scenarios from global climate models. *Climate Dynamics*, *42*(1-2), 37-58.

201. Rahimzadeh, F., Asgari, A., and Fattahi, E., (2009). *Variability of extreme temperature and precipitation in Iran during recent decades. Int. J. Climatol. 29* (3), 329–343.

202. Rahman, M. M., Arya, D. S., Goel, N. K., and Dhamy, A. P. (2010). Design flow and stage computations in the Teesta River, Bangladesh, using frequency analysis and MIKE 11 modeling. *Journal of Hydrologic Engineering*.

203. Raina V. K, and Srivastava D. (2008) Glacier atlas of India. Geological Society of India Bangalore.

204. Rangwala, I., and Miller, J. R. (2012). Climate change in mountains: a review of elevation-dependent warming and its possible causes. *Climatic Change*, *114*(3-4), 527-547.

205. Rangwala, I., Miller, J. R., Russell, G. L., and Xu, M. (2010). Using a global climate model to evaluate the influences of water vapor, snow cover and atmospheric aerosol on warming in the Tibetan Plateau during the twenty-first century. *Climate Dynamics*, *34*(6), 859-872.

206. Rao, K. D., Rao, V. V., Dadhwal, V. K., and Diwakar, P. G. (2014). Kedarnath flash floods: a hydrological and hydraulic simulation study. *Current Science*, *106*(4), 598.

207. Rashid, M. M., Beecham, S., and Chowdhury, R. K. (2015). Statistical downscaling of CMIP5 outputs for projecting future changes in rainfall in the Onkaparinga catchment. *Science of the Total Environment*, *530*, 171-182.

208. Rouholahnejad, E., Abbaspour, K. C., Vejdani, M., Srinivasan, R., Schulin, R., and Lehmann, A. (2012). A parallelization framework for calibration of hydrological models. *Environmental Modelling and Software*, *31*, 28-36.

209. Sayemuzzaman, M., and Jha, M. K. (2014). Seasonal and annual precipitation time series trend analysis in North Carolina, United States. *Atmospheric Research*, *137*, 183-194.

210. Schaper, J., and Seidel, K. (2000, June). Modelling daily runoff from snow and glacier melt using remote sensing data. *InProceedings of the 2nd EARSel Workshop—Special Interest Group Land Ice and Snow* (pp. 308-316).

211. Schaefli, B, Hingray, B., Niggli, M., and Musy, A. (2005). A conceptual glacio-hydrological model for high mountainous catchments. *Hydrology and Earth System Science Discussions.*

TH-1643_136104018

212. Scherler, D., Bookhagen, B., andStrecker, M. R. (2011). Spatially variable response of Himalayan glaciers to climate change affected by debris cover. *Nature geoscience*, *4*(3), 156-159.

213. Schickhoff, U., Bobrowski, M., Böhner, J., Burzle, B., Chaudhary, R. P., Gerlitz, L., andWedegartner, R. (2014). Do Himalayan tree-lines respond to recent climate change? An evaluation of sensitivity indicators. *Earth System Dynamics Discussions*, *5*(2), 1407-1461.

214. Sedlacek, J., Knutti, R., Martius, O., and Beyerle, U. (2012). Impact of a reduced Arctic sea ice cover on ocean and atmospheric properties. *Journal of Climate*, *25*(1), 307-319.

215. Sen, P. K., (1968). *Estimates of regression coefficients based on Kendall's tau. J. Am. Stat. Assoc.* 63, 1379–1389.

216. Seneviratne, S. I., Nicholls, N., Easterling, D., Goodess, C., Kanae, S., Kossin, J., and Zhang, X. (2012). *Managing the risks of extreme events and disasters to advance climate change adaptation a special report of Working Groups I and II of the Intergovernmental Panel on Climate Change (IPCC).*

217. Shah, R. D. T., Sharma, S., Haase, P., Jahnig, S. C., and Pauls, S. U. (2015). The climate sensitive zone along an altitudinal gradient in central Himalayan rivers: a useful concept to monitor climate change impacts in mountain regions. *Climatic Change*, 1-14.

218. Sharma, V., Mishra, V. D., and Joshi, P. K. (2014). Topographic controls on spatio-temporal snow cover distribution in Northwest Himalaya. *International Journal of Remote Sensing*, *35*(9), 3036-3056.

219. Shin, M. J., Guillaume, J. H., Croke, B. F., and Jakeman, A. J. (2015). A review of foundational methods for checking the structural identifiability of models: Results for rainfall-runoff. *Journal of Hydrology*, *520*, 1-16.

220. Shrestha, U. B., Gautam, S., and Bawa, K. S. (2012). Widespread climate change in the Himalayas and associated changes in local ecosystems. *PLoS One*, *7*(5), e36741.

221. Shukla, A., Gupta, R., and Arora, M. K. (2010). Delineation of debris-covered glacier boundaries using optical and thermal remote sensing data. *Remote Sensing Letters*, 1(1), 11-17.

222. Singh V. P., and Woolhiser D. A. (2002). Mathematical Modeling of Watershed Hydrology. *J. Hydrol. Eng. 2002.7*:270-292.

TH-1643_136104018

223. Singh, A. K., Madramootoo, C. A., and Smith, D. L. (2014). Impact of Different Water Management Scenarios on Corn Water Use Efficiency. *Transactions of the ASABE,57*(5), 1319-1328.

224. Singh, D., Jain, S. K., and Gupta, R. D. (2015). Statistical downscaling and projection of future temperature and precipitation change in middle catchment of Sutlej River Basin, India. *Journal of Earth System Science*, *124*(4), 843-860.

225. Singh, G., Venkataraman, G., Yamaguchi, Y., and Park, S. E. (2014). Capability Assessment of Fully Polari-metric ALOS–PALSAR data for Discriminating Wet Snow from Other Scattering Types in Mountainous Regions. *Geoscience and Remote Sensing, IEEE Transactions on*, *52*(2), 1177-1196.

226. Singh, P., and Kumar, N. (1996). Determination of snowmelt factor in the Himalayan region. *Hydrological sciences journal*, *41*(3), 301-310.

227. Singh, P., and Kumar, N. (1997). Impact assessment of climate change on the hydrological response of a snow and glacier melt runoff dominated Himalayan river. *Journal of Hydrology*, *193*(1-4), 316-350.

228. Singh, P., Kumar, N., and Arora, M. (2000). Degree–day factors for snow and ice for Dokriani Glacier, Garhwal Himalayas. *Journal of Hydrology*, *235*(1), 1-11.

229. Singh, V. P., and Frevert, D. K. (2002). *Mathematical models of large watershed hydrology*. Water Resources Publication.

230. Singh, V., Bankar, N., Salunkhe, S. S., Bera, A. K., and Sharma, J. R. (2013). Hydrological stream flow modeling on Tungabhadra catchment: parameterization and uncertainty analysis using SWAT CUP. *Current Science(Bangalore)*, *104*(9), 1187-1199.

231. Singh, V., Goyal, M. K., and Chu, X. (2015). Multicriteria Evaluation Approach for Assessing Parametric Uncertainty during Extreme Peak and Low Flow Conditions over Snow Glaciated and Inland Catchments. *Journal of Hydrologic Engineering*, 04015044.

232. Snehmani, Singh, M. K., Gupta, R. D., Bhardwaj, A., and Joshi, P. K. (2015). Remote sensing of mountain snow using active microwave sensors: a review. *Geocarto International*, *30*(1), 1-27.

233. Snell, S.E., (1998). Spatial Interpolation of Surface Air Temperatures Using Artificial Neural Networks: Evaluating Their Use for Downscaling GCMs. J. of Clim. 13, 886-895.

TH-1643_136104018

234. Snell, S.E., Gopal, S., Kaufmann, R.K., (2000). Spatial interpolation of surface air temperatures using artificial neural networks: Evaluating their use for downscaling GCMs. J. of Climate. 13, 886-895.

235. Sonali, P., and Nagesh, K.D. (2013). Review of trend detection methods and their applicationto detect temperature changes in India. J.Hydrol. 476,212–227.

236. Song, X., Song, S., Sun, W., Mu, X., Wang, S., Li, J., and Li, Y. (2015). Recent changes in extreme precipitation and drought over the Songhua River Basin, China, during 1960–2013. *Atmospheric Research*, *157*, 137-152.

237. Sorg, A., Bolch, T., Stoffel, M., Solomina, O., andBeniston, M. (2012). Climate change impacts on glaciers and runoff in Tien Shan (Central Asia). *Nature Climate Change*, *2*(10), 725-731.

238. Srivastava, D. (2012). Status Report on Gangotri glacier. *Science and Engineering Research Board, Department of Science and Technology, New Delhi, Himalayan glaciology technical report*, (3).

239. Srivastava, D., Kumar, A., Verma, A., and Swaroop, S. (2014). Analysis of Climate and Melt-runoff in Dunagiri Glacier of Garhwal Himalaya (India). *Water resources management*, *28*(10), 3035-3055.

240. Stocker, B. D., Roth, R., Joos, F., Spahni, R., Steinacher, M., Zaehle, S., and Prentice, I. C. (2013). Multiple greenhouse-gas feedbacks from the land biosphere under future climate change scenarios. *Nature Climate Change*, *3*(7), 666-672.

241. Subash N., and Sikka A. K. (2014). Trend analysis of rainfall and temperature and its relationship over India. *Theoretical and applied climatology 117*(3-4): 449-462.

242. Tang Q. H, and Lettenmaier D. P. (2012). 21st century runoff sensitivities of major global river basins. *Geophysical Research Letters 39*: L06403.

243. Tang, B. H., Shrestha, B., Li, Z. L., Liu, G., Ouyang, H., Gurung, D. R., and San Aung, K. (2013). Determination of snow cover from MODIS data for the Tibetan Plateau region. *International Journal of Applied Earth Observation and Geoinformation*, *21*, 356-365.

244. Tareghian, R. and Rasmussen, P. (2013). Analysis of Arctic and Antarctic sea ice extent using quantile regression. *International Journal of Climatology*, *33*(5), 1079-1086.

245. Tatsumi, K., Oizumi, T., and Yamashiki, Y. (2015). Effects of climate change on daily minimum and maximum temperatures and cloudiness in the Shikoku

TH-1643_136104018

region: a statistical downscaling model approach. *Theoretical and Applied Climatology*, *120*(1-2), 87-98.

246. Taye, M. T., and Willems, P. (2013). Influence of downscaling methods in projecting climate change impact on hydrological extremes of upper Blue Nile basin. *Hydrology and Earth System Sciences Discussions*, *10*(6), 7857-7896.

247. Taylor, K. E., Stouffer, R. J., and Meehl, G. A.(2012): An Overview of CMIP5 and the Experiment Design (link is external). *Bulletin of the American Meteorological Society*, 93, 485–498. DOI: 10.1175/BAMS-D-11-00094.1.

248. Tennant, C. J., Crosby, B. T., and Godsey, S. E. (2015). Elevation-dependent responses of streamflow to climate warming. *Hydrological Processes*, *29*(6), 991-1001.

249. Thibeault, J. M., and Seth, A. (2014). Changing climate extremes in the Northeast United States: observations and projections from CMIP5. *Climatic Change*, *127*(2), 273-287.

250. Thome, K. J. (2001). Absolute radiometric calibration of Landsat 7 ETM+ using the reflectance-based method. *Remote Sensing of Environment*, *78*(1), 27-38.

251. Thompson, J. R., Sorenson, H. R., Gavin, H., andRefsgaard, A. (2004). Application of the coupled MIKE SHE/MIKE 11 modelling system to a lowland wet grassland in southeast England. *Journal of Hydrology*, *293*(1), 151-179.

252. Tiwari, R. K., Arora, M. K., and Gupta, R. P. (2014). Comparison of maximum likelihood and knowledge-based classifications of debris cover of glaciers using aster optical-thermal imagery. *Remote Sensing of Environment*.

253. Vansteenkiste, T., Tavakoli, M., Van Steenbergen, N., De Smedt, F., Batelaan, O., Pereira, F., andWillems, P. (2014). Intercomparison of five lumped and distributed models for catchment runoff and extreme flow simulation. *Journal of Hydrology*, *511*, 335-349.

254. Vaughan, D. G., Comiso, J. C., Allison, I., Carrasco, J., Kaser, G., Kwok, R., and Zhang, T. (2013). Observations: cryosphere. *Climate change*, 317-382.

255. Vermote, E. (2015). *MOD09A1 MODIS/Terra Surface Reflectance 8-Day L3 Global 500m SIN Grid V006. NASA EOSDIS Land Processes DAAC*. http://DOI.org/10.5067/MODIS/MOD09A1.006

TH-1643_136104018

256. Vicente-Serrano, S. M., El Kenawy, A., Azorin-Molina, C., Chura, O., Trujillo, F., Aguilar, E., and Friend, F. (2015). Average monthly and annual climate maps for Bolivia. *Journal of Maps*, (ahead-of-print), 1-16.

257. Vieli, A. (2015). Glacier change: Dynamic projections. *Nature Geoscience*, *8*(5), 332-333.

258. Viney, N. R., Sivapalan, M., Deeley, D., (2000). A conceptual model of nutrient mobilisation and transport applicable at large catchment scales. *J. Hydrol. 240* (1–2), 23–44.

259. Viviroli, D., Zappa, M., Gurtz, J., and Weingartner, R. (2009). An introduction to the hydrological modelling system PREVAH and its pre-and post-processing-tools. *Environmental Modelling and Software*, *24*(10), 1209-1222.

260. Wang, B. L., Zhang, M. J.,Wei, J. L.,Wang, S. J., Li, S. S., Ma, Q., Li, X. F., Pan, S. K., (2013). Changes in extreme events of temperature and precipitation over Xinjiang, northwest China, during 1960–2009. *Quat. Int. 298*, 141–151.

261. Wang, L., Ranasinghe, R., Maskey, S., van Gelder, P. H. A. J., andVrijling, J. K. (2015). Comparison of empirical statistical methods for downscaling daily climate projections from CMIP5 GCMs: a case study of the Huai River Basin, China. *International Journal of Climatology*.

262. Wardlaw, R., and Sharif, M. (1999). Evaluation of genetic algorithms for optimal reservoir system operation. *Journal of water resources planning and management, 125*(1), 25-33.

263. Wetterhall, F., Bardossy, A., Chen, D., Halldin, S., and Xu, C. Y. (2006). Daily precipitation-downscaling techniques in three Chinese regions. *Water resources research*, *42*(11).

264. Whitehead, P. G., Barbour, E., Futter, M. N., Sarkar, S., Rodda, H., Caesar, J., andSalehin, M. (2015). Impacts of climate change and socio-economic scenarios on flow and water quality of the Ganges, Brahmaputra and Meghna (GBM) river systems: low flow and flood statistics. *Environmental Science: Processes and Impacts*.

265. Whitfield, P. H., Bodtker, K., and Cannon, A. J. (2002). Recent variations in seasonality of temperature and precipitation in Canada, 1976–95. *Int. J. Climatol. 22*(13), 1617-1644.

TH-1643_136104018

266. Wilby R. L., Dawson C. W., Murphy C., O'Connor P., and Hawkins E. (2014). The Statistical Downscaling Model– Decision Centric (SDSM-DC): conceptual basis andapplications. Clim. Res., 61: 259-276.

267. Wilby R. L., Whitehead P. G, Wade A. J., Butterfield D., Davis R. J., Watts G. (2006). *Integrated modelling of climate change impacts on water resources and quality in a lowland catchment: River Kennet, UK. J. Hydrol 330*(1–2):204–220. DOI:10.1016/j.jhydrol.2006.04.033.

268. Willems, P. (2015). Extreme value analysis of extremes of inland and coastal water systems and impacts of climate change.

269. Willems, P., Mora, D., Vansteenkiste, Th., TeferiTaye, M., and Van Steenbergen, N. (2014). Parsimonious rainfall–runoff model construction supported by time series processing and validation of hydrological extremes – Part 2*: Intercomparison of models and calibration approaches. J. Hydrol. 510*, 591–609.

270. Winkler, J. A., (2014). Selection of climate information for regional climate change assessments using regionalization techniques: *an example for the Upper Great Lakes Region, USA. Int. J. Climatol. 45,* 1027-1040.

271. Wojcik, R. (2015). Reliability of CMIP5 GCM simulations in reproducing atmospheric circulation over Europe and the North Atlantic: a statistical downscaling perspective. *International Journal of Climatology*, *35*(5), 714-732.

272. Wong, P. P., Losada, I. J., Gattuso, J. P., Hinkel, J., Khattabi, A., McInnes, K., andBilir, T. E. (2014). Climate change 2014: impacts, adaptation, and vulnerability. Part A: global and sectoral aspects. *Contribution of Working Group II to the Fifth Assessment Report of the Intergovernmental Panel on Climate Change*.

273. Wu, P., Christidis, N., and Stott, P., (2013). Anthropogenic impact on Earth's hydrologicalcycle. *Nat. Clim. Change*. http://dx.doi.org/10.1038/NCLIMATE1932.

274. Wuebbles, D., Meehl, G., Hayhoe, K., Karl, T. R., Kunkel, K., Santer, B., and Sun, L. (2014). CMIP5 climate model analyses: climate extremes in the United States. *Bulletin of the American Meteorological Society*, *95*(4), 571-583.

275. Wurbs, R. A., Muttiah, R. S., and Felden, F. (2005). Incorporation of climate change in water availability modeling. *Journal of Hydrologic Engineering*.

TH-1643_136104018

276. Xu, C. Y., and Singh, V. P. (1996). A review on monthly water balance models for water resources investigations. *Water Resources Management*, *12*(1), 20-50.

277. Yamazaki, D., Baugh, C. A., Bates, P. D., Kanae, S., Alsdorf, D. E., and Oki, T. (2012). Adjustment of a spaceborne DEM for use in floodplain hydrodynamic modeling. *Journal of Hydrology*, *436*, 81-91.

278. Yang, Y., Zheng, H., and Chen, H. (2015). Automated Cloud Detection Algorithm for Multi-spectral High Spatial Resolution Images Using Landsat-8 OLI. In *Advances in Image and Graphics Technologies* (pp. 396-407). Springer Berlin Heidelberg.

279. Yazdi, J., and Neyshabouri, S. S. (2012). A simulation-based optimization model for flood management on a watershed scale. *Water resources management*, *26*(15), 4569-4586.

280. Zhang, Q., Singh, V. P., Sun, P., Chen, X., Zhang, Z., and Li, J. (2011). Precipitation and streamflow changes in China: changing patterns, causes and implications. *J. Hydrol. 410*, 204–216.

281. Zhang, Q., Xu, C. Y., and Zhang, Z. (2009). Observed changes of drought/wetness episodes in the Pearl River basin, China, using the standardized precipitation index and aridity index. *Theoretical and Applied Climatology*, *98*(1-2), 89-99.

282. Zhang, X., Xu, Y. P., and Fu, G. (2014). Uncertainties in SWAT extreme flow simulation under climate change. *J. Hydrol. 515*, 205-222.

283. Zhang, X., Zwiers, F. W., Hegerl, G. C., Lambert, F. H., Gillett, N. P., Solomon, S., and Nozawa, T. (2007). Detection of human influence on twentieth-century precipitation trends. *Nature*, *448*(7152), 461-465.

284. Zhang, Z., Lu, W., Chu, H., Cheng, W., and Zhao, Y. (2014). Uncertainty analysis of hydrological model parameters based on the bootstrap method: A case study of the SWAT model applied to the Dongliao River Watershed, Jilin Province, Northeastern China. *Science China Technological Sciences*, *57*(1), 219-229.

285. Zhao, H., Zhang, J., James, R. T., and Laing, J. (2012). Application of MIKE SHE/MIKE 11 model to structural BMPs in S191 Basin, Florida. *J Environ Inform*, *19*(1), 10-19.

286. Zhao, N., Chen, C. F., Zhou, X., and Yue, T. X. (2015). A comparison of two downscaling methods for precipitation in China. *Environmental Earth Sciences*, *74*(8), 6563-6569.

TH-1643_136104018

287. Zhou, L., Dickinson R. E, Tian Y., Vose R. S., and Dai Y. (2007).Impact of vegetation removal and soil aridation on diurnal temperature range in a semiarid region: application to the Sahel. *ProcNatlAcadSci USA 104*(46):17937–17942. DOI: 10.1073/ pnas.0700290104.

TH-1643_136104018